

**A Biophysically Based Coupled Model Approach  
For the Assessment of Canopy Processes  
Under Climate Change Conditions**

Dissertation der Fakultät für Geowissenschaften  
der Ludwig-Maximilians-Universität München



vorgelegt von:

*Tobias Benedikt Hank*

aus München

Eingereicht am 30. April 2008

1. Gutachter: Prof. Dr. Wolfram Mauser

2. Gutachter: Prof. Dr. Ralf Ludwig

Tag der mündlichen Prüfung: 27. Juni 2008

*“They say, a little knowledge is a dangerous thing,  
but it's not one half so bad as a lot of ignorance.”*

- TERRY PRATCHETT

## Acknowledgements

The successful fulfilment of the many challenges small and large that are accompanying a project like the one that is now lying before us, naturally is based on the interaction of coincidences and foreordinations as well as it is the consequence of the endeavours of many helping hands. It here is my intention to express the gratitude that I feel for the great number of good things that have happened to me on my way.

During the past years I had the chance to work in a variety of projects, where I gradually learned to recognize the wide scope of research that is covered by the scientific branch of Geography. First as a student assistant and then later as a graduate student in the scope of my diploma thesis, I was introduced to the art of computational vegetation and landsurface modelling, surely placing the headstone for my later work during my dissertational studies.

My employment at the Department of Geography of the Ludwig-Maximilians-Universität Munich can be considered as a particular personal chance. I was allowed to work at an internationally respected institution in the middle of the beautiful city of Munich and I cannot veil the pride of being part of one the most respected and venerable Universities of Europe.

The realization of the work that I was entrusted with was enabled through the support of two public organizations. In the frame of the project “Coupled Analysis of Vegetation Chlorophyll and Water Content Using Hyperspectral, Bidirectional Remote Sensing”, which was financed by the German Research Foundation (DFG), I was able to collect detailed in-field data, deepening my insight into plant physiological coherences. The adaptation of computational modelling techniques was enabled by help of the cooperative project “GLOWA - Global Change and the Hydrological Cycle”, funded by the Federal Ministry of Education and Research (BMB+F). To both organisations, the DFG and the BMB+F, I would like to express my honest thanks for their combined financial support.

From the many people that have directly or indirectly contributed to this project, my deepest thanks go to the person that made the completion of this work possible in the first place, my doctoral advisor Professor Dr. Wolfram Mauser. As the head of the Chair of Geography and Remote Sensing at the Department of Geography of the Ludwig-Maximilians-Universität of Munich, he not only provided me with excellent working conditions in form of a fully equipped workspace, huge amounts of calculation capacity and access to the full infrastructure of the working group, he also created a professional environment for me, where I was able to work in the middle of a diligent team that covers a wide range of specialized research fields. Professor Mauser also introduced me to the PROMET model and provided many assistant routines. For his constructive criticism, his open mind towards own ideas, his ability to pinpoint the essentials



of our work and his reassuring help with many tight situations, I would like to thank him profoundly.

I would also like to express deep thanks to Professor Dr. Ralf Ludwig for the generous acceptance of the efforts associated with the second review of this thesis.

My sympathy for the studying of plant physiological processes was enhanced by the scientific contributions of my dear colleague and project partner Dr. Natascha Oppelt. For her reliable help with professional and personal questions and her will to struggle through the administrative obstacles of project management for both of us, I would like to thank her very much.

I also wish to thank Dr. Heike Bach from VISTA - Remote Sensing in Geosciences GmbH for the continuous development of the PROMET Model and for the contribution of numerous assistant routines.

Great thanks also go to Professor Dr. Karl Schneider from the workgroup Hydrogeography and Climatology of the Institute of Geography of the University of Cologne for generously passing on his knowledge on the dynamic modelling of canopy related land surface processes.

The work at the Chair of Geography and Remote Sensing was accompanied by a constant reciprocal flux of discussion and help from my fellow Ph.D. students. First of all there are to mention Matthias Bernhardt and Thomas Marke, who both luckily survived sharing the office with me and whom I would like to thank for the cooperative and entertaining time during the past years. Also big thanks go to Markus Probeck for assisting me with my first steps of programming and for his help with the untangling of foreign code. For their cooperative assistance with the most diverse challenges concerning the PROMET model, I would like to thank my fellow Ph.D. students Markus Muerth and Monika Prasch. Also thanks for the wonderful time go to my other Ph.D. colleagues, as there are alphabetically arranged Carola Weiss, Daniel Waldmann, Khaled Haider, Monika Tepfenhart and Susan Niebergall.

Additional thanks are due to my colleagues from the faculty, Dr. Ulrich Strasser for his most entertaining and diverting discussions during the lunch breaks and Dr. Alexander Löw for his tolerating assistance with programming questions. I would also like to thank Dr. Marco Braun and Dr. Christoph Heinzeller for their reassuring way of sharing their experiences with the graduation process. Also thanks go to Mrs. Vera Erfurth, who has been a reliable contact for the diverse questions of every day problems during the past years.

In the scope of the diverse field campaigns that have contributed data to this project, a multitude of student assistants was engaged. Thanks in alphabetical order go to Andrea Reiter, Claudia Hundseher, Frank Färber, Franziska Koch, Inga May, Jens Neumeister, Johanna Dall' Amico, Julia Jaenicke, Nathalie Ohl, Sascha Berger and Stephanie Wegscheider.

Many thanks go to the proprietors of the test sites that were part of the diverse sampling campaigns. Special thanks are due to Max Stürzer senior and to Max Stürzer junior for

permitting the plant physiological sampling campaigns to be conducted on their acres during consecutive years as well as for the provision of the digital yield map.

Also thanks go to the Bavarian land surveying office for the generous provision of the high resolution digital elevation model and the orthorectified aerial photographs of the field test sites. It is of personal concern to me to express my thanks to Mr Akira Araki and the Yamaha Motor Corporation Ltd. for the construction of the Vmax and also to the members of the Bavarian Vmaxxers regulars table "*Bayernmaxxer*" for the welcome moments of diversion in times of exertion.

I dearly want to thank my girlfriend Christina Walter, who has been a source of confidence and strength in times of strain and who has uncomplainingly suffered the phases of neglect during the final stage of this work.

Last but not least, the thanks for the completion of this thesis are due to my family. The support of my parents, step-parents and sisters, who did not fail to help and assist in every way possible, has paved the way of my life ever since. My dearest thanks go to my mother for her love beyond measure and her undying trust in me and the things I do. To her, this work is dedicated.

# Table of Contents

<b>Acknowledgements</b>	I
<b>Tables</b>	
Table of Contents	IV
List of Figures	VIII
List of Tables	XXI
List of Equations	XXIV
List of Acronyms	XXIX
<b>1. Introduction</b>	
1.1 Physically based Modelling and Climate Change	001
1.2 State of the Art	002
1.3 Motivation and Goals of the Thesis	004
1.4 Biological Modelling	008
1.5 Photosynthetic Processes	009
1.5.1 “Light” Reaction	010
1.5.2 “Dark” Reaction (Carbon Fixation)	012
1.5.2.1 The Calvin-Cycle of C <sub>3</sub> Plants	012
1.5.2.2 The Hatch-Slack-Cycle of C <sub>4</sub> Plants	014
1.6 The Leaf Photosynthesis Model by Farquhar, von Caemmerer and Berry	015
<b>2. The Upper Danube Catchment</b>	
2.1 Natural Realities	017
2.2 Geology and Geomorphology	019
2.3 Climate	021
2.4 Hydrology	023
2.5 Soils	025
2.6 Vegetation	026
2.7 Socio-Economic Aspects	027

<b>3. Coupling a Physically Based Landsurface Model with a Biological Description of Canopy Processes</b>	
3.1 The Landsurface Simulator PROMET	029
3.2 Adapting PROMET to the physically based Modelling of Photosynthesis	030
3.3 The PROMET Biological Model	031
3.3.1 Radiation	031
3.3.2 Surface Processes	036
3.3.2.1 Wind Velocity within the Canopy	036
3.3.2.2 Interception Evaporation	039
3.3.3 Biological Processes	044
3.3.3.1 Model Initialization	044
3.3.3.2 Agricultural Management	049
3.3.3.3 Leaf Energy Balance	051
3.3.3.4 Iterative Determination of the Leaf Temperature	052
3.3.3.4.1 Longwave Emission	055
3.3.3.4.2 Conductive Heat Loss	056
3.3.3.4.3 Latent Heat Loss	057
3.3.3.5 Net Primary Production	059
3.3.3.5.1 Carboxylation Limitations	059
3.3.3.5.2 CO <sub>2</sub> Diffusion	063
3.3.3.5.3 Analytical Solution	064
3.3.3.5.4 Stomatal Conductance	070
3.3.3.6 Plant Growth	073
3.3.3.6.1 Phenology	073
3.3.3.6.1.1 Crop Phenology	073
3.3.3.6.1.2 Grassland and Natural Vegetation Phenology	077
3.3.3.6.1.3 Forest Phenology	077
3.3.3.6.1.3.1 Deciduous Trees	077
3.3.3.6.1.3.2 Coniferous Trees	080
3.3.3.6.2 Carbon Allocation	081
3.3.3.6.3 Aboveground Parameters	084
3.3.3.6.4 Root Growth	086
3.3.4 Input Parameters	089
3.3.4.1 Spatial Parameters	090
3.3.4.1.1 Landuse	090
3.3.4.1.2 Soil Texture	092
3.3.4.1.3 Digital Elevation Model	093

3.3.4.1.4	Mask and Subcatchments	094
3.3.4.2	Parameter Attributes	095
3.3.4.2.1	Landuse Parameters	095
3.3.4.2.2	Soil Parameters	097
3.3.4.3	Observational Networks	098
<b>4.</b>	<b>Model Validation</b>	
4.1	Field Scale Validation	100
4.1.1	Selection of Test Sites	100
4.1.2	Test Sites 2004	102
4.1.3	Test Sites 2005	103
4.1.4	Field Campaign	103
4.1.4.1	Defining a Sampling Pattern	104
4.1.4.2	Field Methods	105
4.1.4.2.1	Meteorology	105
4.1.4.2.2	Phenology	105
4.1.4.2.3	Canopy Height	106
4.1.4.2.4	Stand Density	107
4.1.4.2.5	Dry Biomass	107
4.1.4.2.6	Leaf Area Index (LAI)	108
4.1.5	Field Scale Modelling	109
4.1.6	Field Scale PROMET vs. Field Measurements	112
4.1.6.1	Meteorology	112
4.1.6.2	Winter Wheat 2004	113
4.1.6.3	Winter Wheat 2005	117
4.1.6.4	Maize 2004	117
4.1.6.5	Maize 2005	120
4.1.6.6	Yield	121
4.2	Meso Scale Validation	124
4.2.1	PROMET vs. Field Measurements for Selected Proxels	124
4.2.1.1	Intensive Grassland	126
4.2.1.2	Extensive Grassland	127
4.2.1.3	Spring Crops (Oat)	129
4.2.2	Relating the Coupled Approach to a Reference Model	131
4.2.2.1	The Penman-Monteith-PROMET	132
4.2.2.2	PROMET_Biological vs. PROMET_Penman-Monteith	132
4.2.2.2.1	Selected Reference Proxels	133

---

4.2.2.2	Spatial Statistics	137
4.2.3	Consulting External Data	141
4.2.3.1	Deciduous Forest Phenology	142
4.2.3.2	Coniferous Forest Phenology	147
<b>5.</b>	<b>Modelling Climate Scenarios</b>	
5.1	The IPCC CO <sub>2</sub> -Emissions-Scenarios	152
5.1.1	The Scenario Families	153
5.2	Adapting PROMET to the Simulation of Climate Scenarios	156
5.2.1	Modelling the Increase of Atmospheric Carbon Dioxide	156
5.2.2	Modelling the Corresponding Change of Temperature and Rainfall	159
5.2.3	Selected Scenario Storylines	162
<b>6.</b>	<b>The Scenario Results</b>	
6.1	Phenology	165
6.2	Biological Productivity	168
6.3	Drought Stress	171
6.4	Water Cycle Components	173
<b>7.</b>	<b>Conclusion and Outlook</b>	179
<b>8.</b>	<b>Summary</b>	183
<b>9.</b>	<b>Zusammenfassung (German)</b>	188
<b>10.</b>	<b>References</b>	194
<b>11.</b>	<b>Curriculum Vitae</b>	210
<b>12.</b>	<b>Appendix</b>	Separate Volume

## List of Figures

<b>Figure</b>	<b>Caption</b>	<b>Page</b>
Fig. 1.01:	Cycle of modelled scales. Chloroplast image inspired by MOORE ET AL. (1998). -----	007
Fig. 1.02:	Definition of the river drainage area through a watershed, based on the terrain topography. -----	007
Fig. 1.03:	The role of models in a scientific method, modified after JONES (1992). ----	008
Fig. 1.04:	Cut through a chloroplast, inspired by MOORE ET AL. (1998). -----	010
Fig. 1.05:	Absorption spectra of chlorophyll a (680), b and carotene that apply to PSII. Modified after JONES (1992). -----	010
Fig. 1.06:	Electron transport chain passing the photosystems II and I. -----	011
Fig. 1.07:	Calvin cycle of the carbon fixation in C <sub>3</sub> plants, indicating the energy consumption for the fixation of 3 carbon dioxide molecules. -----	013
Fig. 1.08:	C <sub>4</sub> cycle of carbon fixation, indicating the additional energy consumption for the regeneration of the PEPcase. -----	014
Fig. 1.09:	Representation of the general assumptions of the “Farquhar et al.” model of photosynthesis. -----	016
Fig. 2.01:	The Upper Danube catchment defined by the gauge “Achleiten” (287 m a.s.l.) in relation to the entire Danube river system, including the major tributaries (Backdrop: World map taken from ESRI Globe Data). -----	018
Fig. 2.02:	The Upper Danube catchment area in relation to the Central European countries that are part of it (Base data: ESRI World Database). -----	019
Fig. 2.03:	Three-Dimensional bird’s eye view of the Upper Danube catchment seen from the West, based on a 1 x 1 km resolution DEM applying a superelevation factor of 10. Indication of the major low and high mountain ranges. -----	020
Fig. 2.04:	Geologic map of the Upper Danube Basin, modified after BARTHEL ET AL. (2005). -----	020
Fig. 2.05:	Interpolated long-term precipitation for the Upper Danube catchment discerned into the hydrological summer (May-October) and winter half-year (November-April), indicating the orographically induced South-to-North climate gradient. The displayed precipitation sums are interpolated model results for the 30-year time period from 1971-2000. -----	022

<b>Figure</b>	<b>Caption</b>	<b>Page</b>
Fig. 2.06:	Modelled long term duration of the snow cover (left, base data: MAUSER ET AL. 2007) and interpolated annual mean temperature (right) of the Upper Danube Basin, indicating the orographically induced South-to-North climate gradient. The snow cover duration and the temperature map both show averaged model results, calculated for a 30-year time period (1971 – 2000). -----	023
Fig. 2.07:	The Upper Danube catchment defined by the Austrian gauge “Achleiten” (287 m a.s.l.) with its major tributaries and urban settlements in relation to the central European countries that are part of it. -----	024
Fig. 2.08:	Topographic situation of the Upper Danube catchment including the major cities, traffic routes, rivers and surface water bodies (base data: ESRI World Database). -----	027
Fig. 3.01:	Exterior model design of the PROMET landsurface simulator. -----	029
Fig. 3.02:	Interior top down model cycle of the PROMET model. -----	030
Fig. 3.03:	Course of the extinction coefficient for ellipsoidal canopies in dependence of the solar zenith angle. -----	032
Fig. 3.04:	Variability of the surface albedo, as a combination of bare soil and canopy reflectance characteristics, in dependence of the solar zenith angle and the grade of development of the vegetation cover. -----	033
Fig. 3.05:	Fraction of reflected, absorbed and transmitted direct shortwave radiation for two canopy layers (left) and distribution of the longwave radiation within the two layered canopy structure (right). -----	036
Fig. 3.06:	Derivation of the momentum roughness parameter (left) and the zero plane displacement height (right) from data measured by SHAW AND PEREIRA (1982). Please note that the coefficient of determination ( $r^2$ ) is correlated with the order of the polynomial and therefore is overestimated in both figures. -----	037
Fig. 3.07:	Vertical wind profile over a canopy surface indicating the parameters that are involved in the calculation of the surface friction (inspired by DINGMAN 1994). -----	038
Fig. 3.08:	Components of the PROMET surface water balance. -----	039
Fig. 3.09:	Correlation of leaf area and canopy closure (left) and variability of the interception capacity of the canopy in dependence of the leaf area and the fractional cover (right). -----	040
Fig. 3.10:	Temperature dependency of the latent heat of vaporization (left), the saturation vapour pressure (middle) and the slope of the saturation vapour pressure curve (right). -----	041



<b>Figure</b>	<b>Caption</b>	<b>Page</b>
Fig. 3.11:	Model results for the interception evaporation from the needles of a coniferous stand in the central region of the Upper Danube catchment for the 11 <sup>th</sup> of July 1998. -----	042
Fig. 3.12:	Measured precipitation and modelled intercepted rainfall for a winter wheat stand during the model season 1998/1999. -----	043
Fig. 3.13:	Model hierarchy of the 27 integrated landuse categories. -----	044
Fig. 3.14:	Flowchart of the biological subroutines of PROMET. -----	045
Fig. 3.15:	Phases of LAI development (left) and LAI curves for selected crops used for the initialization of the first time step. -----	046
Fig. 3.16:	Relation of long-term annual mean temperature and terrain elevation for coniferous sites within the Upper Danube Basin (left) and factor reducing the leaf area of coniferous forest in dependence of the annual mean temperature of the last modelled year (right). -----	047
Fig. 3.17:	Initial root length density distribution into four soil layers. -----	048
Fig. 3.18:	Combine harvester yield measurements for the test sites "Kochfeld" and "Hofanger" (compare section 4.1) in front of a GIS based land use map (left). Derivation of a relation between dry grain mass and measured grain yield (right). -----	050
Fig. 3.19:	Components of the leaf energy balance of PROMET biological. -----	051
Fig. 3.20:	Iteration loop for the calculation of the leaf energy balance, indicating that one model time step requires the initialization of four iterations per raster element. -----	052
Fig. 3.21:	Initial estimate for the iterative solution of the leaf energy balance. The exemplary initial estimate is far too high (left), so the iteration is started with the initial intermediate temperature being applied as upper boundary (right). -----	053
Fig. 3.22:	Exemplary results of the iteration steps 1 and 2. For the first iteration step, the intermediate temperature was assumed too low (left), so that for the second iteration step it is used as the lower temperature boundary (right). -	054
Fig. 3.23:	Exemplary results of the iteration steps 3 and 4. For the third iteration step, the leaf temperature again is assumed too low, only to meet the requirements of the threshold with the fourth iteration. -----	054
Fig. 3.24:	Daily course of the modelled leaf temperature of a wheat stand on a hot summer day (20 <sup>th</sup> of July 1998), discerned into two canopy layers as well as into sunlit and shaded leaves. -----	055
Fig. 3.25:	Coefficient of the thermal conductivity of air in dependence of the air temperature (left) and thickness of the boundary layer in dependence of the wind velocity and the width of the leaf (right). -----	056

Figure	Caption	Page
Fig. 3.26:	Thickness of the boundary layer in dependence of the wind velocity. -----	057
Fig. 3.27:	Arrhenius-function of the simple type for the calculation of the temperature dependency of the Michaelis-Menten constant for Oxygen (left) and complex Arrhenius-function for the calculation of the maximum velocity of carboxylation for a range of common leaf temperatures (right). -----	061
Fig. 3.28:	Exemplary model results for the photosynthetic activity of a deciduous forest on the 7 <sup>th</sup> of May 2003, indicating the parallel development of the daily course of net primary production and the directly related stomatal conductivity. The graphs show model results that were averaged for the sunlit and the shaded parts of the two canopy layers. -----	069
Fig. 3.29:	The dependence of stomatal aperture on the cell water content is represented in the model through a direct linkage with the soil water storage of the rooted soil layers. -----	070
Fig. 3.30:	Model soil profile indicating the root distribution of a fully developed deciduous forest and the soil moisture situation of four soil layers as well as the precipitation during a dry period of the summer of 2003. For this example, the inhibition of the stomatal conductance due to the soil moisture is determined through the hydrological dynamics in the soil layer 3. -----	072
Fig. 3.31:	Exemplary response curve of the hourly temperature effect for three different sets of cardinal temperatures that apply to winter wheat crops. ----	074
Fig. 3.32:	Dependence of the vernalisation effect on the absolute number of effective vernalisation days (left). Exemplary light effect for winter wheat in dependence of the photoperiodic day length (right). -----	076
Fig. 3.33:	Exemplary curve of the modelled phenologic development for the wheat test site "Hofanger" ( <i>see section 4.1</i> ) during the summer months of the season 2004, indicating the accumulation of the development rate and the thresholds that initiate the transition to the next phenological stage. -----	077
Fig. 3.34:	Left: Critical temperature sum for the leaf emergence ( $TT_{crit}$ ) of different deciduous tree types. Right: Example of modelled leaf emergence for a deciduous forest in the East of the Upper Danube Basin indicating the variables involved (model year 1998, 467 m a.s.l.). -----	079
Fig. 3.35:	Example of modelled defoliation for a deciduous forest in the East of the Upper Danube Basin (model year 1987, 467 m a.s.l.) showing hourly values of air temperature and the resulting frost sum as well as the critical boundaries of 0 °C for the air temperature (dashed) and -3.0 °C for the frost sum (solid). -----	080
Fig. 3.36:	Left: Critical temperature sum for the mayshoot ( $TT_{crit}$ ) of different coniferous tree types. Right: Example of modelled mayshoot for a coniferous forest in the middle of the Upper Danube Basin indicating the variables involved (model year 1998, 554 m a.s.l.). -----	081
Fig. 3.37:	Maintenance respiration in dependence of the air temperature. -----	082

<b>Figure</b>	<b>Caption</b>	<b>Page</b>
Fig. 3.38:	Allocation of the distribution of the net primary production to the different plant parts in dependence of the phenological phase. Exemplary parameters for winter wheat. -----	083
Fig. 3.39:	Modelled accumulation of biomass and distribution to the different plant parts in dependence of the phenological stage. Exemplary course of development for a winter wheat site during the growth season 2003/2004. -	083
Fig. 3.40:	Derivation of the leaf mass per leaf area for winter wheat, based on field measurements of the vegetation period 2004. Correlation of measured LAI with measured dry leaf mass (left) and course of the leaf mass area with increasing LAI values (right). -----	084
Fig. 3.41:	Courses of modelled leaf area values for coniferous forest depending on the annual mean air temperature as well as on the incidence of mayshoot.	085
Fig. 3.42:	Soil profile with four layers and root system, explaining the rooted fraction of a soil layer (left) and dependence of the soil moisture deficit factor on the amount of total extractable soil water (right). -----	087
Fig. 3.43:	Root preference factor according to soil grain size and soil compactness (left: colour chart, right: diagram). -----	087
Fig. 3.44:	Exemplary course of modelled root development of a winter wheat site in the middle of the Upper Danube Basin (352 m a.s.l.) from the 15 <sup>th</sup> of October 1998 to the 18 <sup>th</sup> of August 1999. Rooting depth of the winter crop penetrating the four layers of the soil profile (left) and corresponding development of the root length densities for each soil layer (right). -----	089
Fig. 3.45:	Aggregated land use map of the Upper Danube Basin based on the EEA CORINE Land cover classification, corrected and adjusted to match the regional agricultural statistics. -----	090
Fig. 3.46:	Areas of the Upper Danube, covered by the discerned land use categories with their accumulated area percentages. -----	091
Fig. 3.47:	Map of aggregated soil texture types, based on the German Soil Survey Map 1 : 1000 000 (BGR 2002). -----	092
Fig. 3.48:	Areas of the Upper Danube, covered by the explicit soil texture categories with their accumulated area percentages. -----	092
Fig. 3.49:	Top left: Digital elevation model mosaic for the Upper Danube Basin (relief 2 x vertical exaggeration); Top right: Slope derived from the DEM; Bottom left: Hypsometric curve, statistics and percentages of terrain exposure derived from the DEM; Bottom right: Terrain orientation (9 major categories) derived from the DEM. -----	093
Fig. 3.50:	Mask layer as applied for the model runs, including the major Upper Danube subcatchments. -----	094

<b>Figure</b>	<b>Caption</b>	<b>Page</b>
Fig. 3.51:	Map of the weather stations used for the meteorological interpolation for the Upper Danube Basin, indicating the spatial pattern and the elevations of the observation sites. -----	099
Fig. 4.01:	Test sites 2004/2005 embedded in a generalised landuse map (generated from field data 2005) with their relative position within the Upper Danube Basin (left). Background: Digital orthorectified aerial photograph mosaic of the season 2003 kindly provided by the Bavarian Land Surveying Office. ---	101
Fig. 4.02:	3D-Block image of the test sites “Hofanger” (left) and “Argelsried” (right), indicating the geometry and the terrain situation of the fields as well as the position of the sampling points of the field campaign. The images include four layers (aerial photograph, landuse map, soil map, digital elevation model). -----	102
Fig. 4.03:	3D-Block image of the test sites “Kochfeld” (left) and “Hochstadt” (right), indicating the geometry and the terrain situation of the fields as well as the position of the sampling points of the field campaign. The images include four layers (aerial photograph, landuse map, soil map, digital elevation model). -----	103
Fig. 4.04:	GPS positioning of sampling points (left) and general pattern for the positioning of sampling points within a test field (right). -----	104
Fig. 4.05:	Weather station Nr. 72 of the agro-meteorological network Bavaria ( <a href="http://www.lfl.bayern.de">www.lfl.bayern.de</a> ). -----	105
Fig. 4.06:	Decimal code of BBCH growth stages with their corresponding observable features. Modified after BIOLOGISCHE BUNDESANSTALT FÜR LAND- UND FORSTWIRTSCHAFT (1997). -----	106
Fig. 4.07:	Principle of measuring the height of a canopy in the field. -----	106
Fig. 4.08:	Method of the stand density measurements of the season 2004 (left) and 2005 (right). -----	107
Fig. 4.09:	Weighing chain for the determination of the dry biomass for different plant parts. -----	108
Fig. 4.10:	Principle of a leaf area measuring cycle with the LI-COR LAI-2000 instrument. -----	109
Fig. 4.11:	10 x 10 m resolution GIS data set for the field scale modelling of the 2004 wheat test site “Hofanger”. Top left: Mask layer, top middle: Soil particle size, top right: Land use, bottom left: Elevation [m a.s.l.], bottom middle: Slope [%] and bottom right: Aspect. All figures comprise an area of 890 by 680 m. -----	110
Fig. 4.12:	10 x 10 m resolution GIS data set for the field scale modelling of the 2005 wheat test site “Kochfeld”. Top left: Mask layer, top middle: Soil particle size, top right: Land use, bottom left: Elevation [m a.s.l.], bottom middle: Slope [%] and bottom right: Aspect. All figures comprise an area of 630 by 410 m. -----	110

Figure	Caption	Page
Fig. 4.13:	10 x 10 m resolution GIS data set for the field scale modelling of the 2004 maize test site "Argelsried". Top left: Mask layer, top middle: Soil particle size, top right: Land use, bottom left: Elevation [m a.s.l.], bottom middle: Slope [%] and bottom right: Aspect. All figures comprise an area of 530 by 410 m. -----	111
Fig. 4.14:	10 x 10 m resolution GIS data set for the field scale modelling of the 2005 maize test site "Hochstadt". Top left: Mask layer, top middle: Soil particle size, top right: Land use, bottom left: Elevation [m a.s.l.], bottom middle: Slope [%] and bottom right: Aspect. All figures comprise an area of 1000 by 680 m. -----	111
Fig. 4.15:	Subset of German-Weather-Service stations applied for the modelling of the field scale in the test area Gilching. -----	112
Fig. 4.16:	Interpolated vs. measured precipitation and temperature for the weather station No. 72 of the agro-meteorological network Bavaria. Annual course (left) and correlation (right) for the growth cycle of the wheat test field "Hofanger" from October 2003 to August 2004. -----	113
Fig. 4.17:	Modelled vs. measured aboveground dry biomass for the sampling period of the wheat test field "Hofanger" from April 1 <sup>st</sup> to August 31 <sup>st</sup> 2004. Course of development (left) and correlation including coefficients of determination and Nash-Sutcliffe coefficients (right) discerned into the plant parts leaf (top), stem (middle) and grain (bottom). -----	114
Fig. 4.18:	Modelled vs. observed plant phenology. Course of development (left) and correlation (right) for the sampling period of the wheat test field "Hofanger" from April 1 <sup>st</sup> to August 31 <sup>st</sup> 2004. -----	115
Fig. 4.19:	Modelled vs. observed leaf area index. Course of development (left) and correlation (right) for the sampling period of the wheat test field "Hofanger" from April 1 <sup>st</sup> to August 31 <sup>st</sup> 2004. -----	116
Fig. 4.20:	Modelled vs. observed overall canopy height. Course of development (left) and correlation (right) for the sampling period of the wheat test field "Hofanger" from April 1 <sup>st</sup> to August 31 <sup>st</sup> 2004. -----	116
Fig. 4.21:	Modelled vs. measured aboveground dry biomass for the sampling period of the maize test field "Argelsried" from May 1 <sup>st</sup> to September 30 <sup>th</sup> 2004. Course of development (left) and correlation including coefficients of determination and Nash-Sutcliffe coefficients (right) discerned into the plant parts leaf (top), stem (middle) and grain (bottom). -----	118
Fig. 4.22:	Figure 4.22: Modelled vs. observed plant phenology. Course of development (left) and correlation (right) for the sampling period of the maize test field "Argelsried" from May 1 <sup>st</sup> to September 30 <sup>th</sup> 2004. -----	
Fig. 4.23:	Modelled vs. observed leaf area index. Course of development (left) and correlation (right) for the sampling period of the maize test field "Argelsried" from May 1 <sup>st</sup> to September 30 <sup>th</sup> 2004. -----	119

<b>Figure</b>	<b>Caption</b>	<b>Page</b>
Fig. 4.24:	Modelled vs. observed overall canopy height. Course of development (left) and correlation (right) for the sampling period of the maize test field "Argelsried" from May 1 <sup>st</sup> to September 30 <sup>th</sup> 2004. -----	120
Fig. 4.25:	Yield map based on a combine measurement in full and resampled resolution compared to the modelled yield of the season 2004 for the wheat test site "Hofanger". -----	121
Fig. 4.26:	Spatial pattern of the absolute differences between measured and modelled yield (right) and histogram of the area percentages with their corresponding deviations (left) for the wheat test site "Hofanger" season 2004 (right). -----	122
Fig. 4.27:	Field scale model results for the accumulated overall biomass (root, stem, grain and leaf) for the respective growth cycles of the four test sites "Hofanger" (top left), "Kochfeld" (top right), "Argelsried" (bottom left) and "Hochstadt" (bottom right). The backdrop shows orthorectified b/w aerial photographs recorded during the aerial survey 2003 that were kindly provided by the Bavarian Land Surveying Office. -----	123
Fig. 4.28:	Available test sites for different landuse categories with their spatial situation compared to the 1x1 km landuse majority applied for the mesoscale model runs. Indication of the position of the general test area in the heart of the Upper Danube Basin. -----	125
Fig. 4.29:	Course of modelled and measured total aboveground dry biomass of the intensive grassland test site "Unterbrunn". Results from a single proxel, modelled at a resolution of 1 x 1 km, compared to field measurements of the season 1999. -----	126
Fig. 4.30:	Modelled vs. measured dry biomass (left) and canopy height (right) of the intensive grassland test site "Unterbrunn" for the growth season 1999. -----	127
Fig. 4.31:	Course of modelled and measured dry biomass of the extensive grassland test site "Inning 2". Results from a single proxel, modelled at a resolution of 1 x 1 km, compared to field measurements of the seasons 1999, 2000 and 2001. -----	127
Fig. 4.32:	Course of modelled and measured dry biomass, indicating the errors that possibly occur due to the modelling of management measures (left), and modelled versus measured dry biomass of the extensive grassland test site "Inning 2" for the season 1999. -----	128
Fig. 4.33:	Modelled vs. measured aboveground dry biomass for the sampling period of the oat test site "St. Gilgen" from April 1 <sup>st</sup> to August 31 <sup>st</sup> 1999. Course of development (left) and correlation including coefficients of determination (right) discerned into the plant parts leaf (top), stem (middle) and grain (bottom). -----	129
Fig. 4.34:	Modelled vs. observed plant phenology. Course of development (left) and correlation (right) for the sampling period of the oat test site "St. Gilgen" from April 1 <sup>st</sup> to August 31 <sup>st</sup> 1999. -----	130

<b>Figure</b>	<b>Caption</b>	<b>Page</b>
Fig. 4.35:	Modelled vs. observed overall canopy height. Course of development (left) and correlation (right) for the sampling period of the oat test site "St. Gilgen" from April 1 <sup>st</sup> to August 31 <sup>st</sup> 1999. -----	131
Fig. 4.36:	Modelled annual evapotranspiration of the hydrological year 1999, discerned into transpiration (left), interception evaporation (middle) and soil evaporation (right) for 22 different vegetation landuse proxels. Correlation between modelled results applying the Penman-Monteith approach and the biological model. -----	133
Fig. 4.37:	Daily rates of transpiration of a silage proxel, calculated via the biological and the Penman-Monteith model for the hydrological year 1999. Annual course (left) and correlation of both models (right). -----	135
Fig. 4.38:	Daily rates of interception evaporation of a silage proxel, calculated via the biological and the Penman-Monteith model for the hydrological year 1999. Annual course (left) and correlation of both models (right). -----	136
Fig. 4.39:	Daily rates of soil evaporation of a silage proxel, calculated via the biological and the Penman-Monteith model for the hydrological year 1999. Annual course (left) and correlation of both models (right). -----	136
Fig. 4.40:	Modelled evapotranspiration for a 46-year period (1961-2006), averaged for the Upper Danube catchment area. Annual course (left) and correlation (right) of the evapotranspiration modelled by the PROMET_Biological model and the PROMET_Penman-Monteith model. -----	137
Fig. 4.41:	Correlation of the long-term (1961-2006) average evapotranspiration (left) and transpiration (right) modelled by the PROMET_Biological model and the PROMET_Penman-Monteith model. -----	138
Fig. 4.42:	Map of deviation between the long-term (1961-2006) average evapotranspiration modelled by the PROMET_Biological model and the PROMET_Penman-Monteith model. -----	139
Fig. 4.43:	Correlation of modelled runoff for the gauge "Achleiten" by the PROMET_Biological model and the PROMET_Penman-Monteith model (1961-2006, left) and correlation of modelled and measured runoff for the main gauge of the Upper Danube catchment (1970-2003, right). -----	140
Fig. 4.44:	Terrain elevation within the Upper Danube Basin indicating the spatial distribution and the percentage of the altitudinal vegetation belts. -----	141
Fig. 4.45:	DOY of the mean and extreme modelled initiation of leaf emergence for deciduous trees in the Upper Danube Basin from 1961 to 2006, discerned into two altitudinal vegetation zones (left). Corresponding trends for the 46-year period 1961-2006 (right). -----	142
Fig. 4.46:	DOY of the mean and extreme modelled initiation of defoliation for deciduous trees in the Upper Danube Basin from 1961 to 2006, discerned into two altitudinal vegetation zones (left). Corresponding trends for the 46-year period 1961-2006 (right). -----	142

Figure	Caption	Page
Fig. 4.47:	Mean and extreme duration of the modelled vegetation period for deciduous trees in the Upper Danube Basin from 1961 to 2006, discerned into two altitudinal vegetation zones (left). Corresponding trends for the 46-year period 1961-2006 (right). -----	143
Fig. 4.48:	Moving 10-year averages of modelled leaf emergence, defoliation and the resulting vegetation period from 1965 to 2001, based on modelled data for the years 1961-2006. -----	144
Fig. 4.49:	10-year average of the initiation of leaf emergence, modelled by PROMET for the Upper Danube Basin 1961-1970 (left) and 1997-2006 (right). -----	144
Fig. 4.50:	10-year average of the initiation of defoliation, modelled by PROMET for the Upper Danube Basin 1961-1970 (left) and 1997-2006 (right). -----	145
Fig. 4.51:	Change of the modelled 10-year average of the duration of the active growth period for deciduous trees (1997-2006 compared to 1961-1970) in the Upper Danube Basin. -----	145
Fig. 4.52:	Modelled average and extreme incidence of coniferous mayshoot for the Upper Danube Basin (1961-2006), discerned into three altitudinal vegetation zones (left). Corresponding trends for the 46-year period 1961-2006 (right). -----	147
Fig. 4.53:	Modelled 10-year average of the initiation of mayshoot for coniferous trees 1961-1970 (left) compared to 1997-2006 (right) for the Upper Danube Basin. -----	148
Fig. 4.54:	Change of the modelled 10-year average of the incidence of mayshoot for coniferous trees (1997-2006 compared to 1961-1970) in the Upper Danube Basin. -----	149
Fig. 4.55:	International Phenological Gardens located next to and within the Upper Danube Basin. -----	150
Fig. 4.56:	Course of observed and modelled incidence of mayshoot of <i>picea abies</i> for a time series from 1961 to 1993 (left) and correlation of modelled and observed (middle) mayshoot dates. -----	151
Fig. 5.01:	Anthropogenic emissions of CO <sub>2</sub> (left) and resulting atmospheric CO <sub>2</sub> concentrations (right) for six illustrative SRES scenarios for a time frame from 1990 to 2100 (IPCC 2007, modified). -----	154
Fig. 5.02:	Global average temperature projections for the six illustrative SRES scenarios. The shading is the envelope based on all six model projections (with climate sensitivity in the range 1.7 to 4.2 °C). The bars on the right hand side indicate the range produced by different models for the respective storylines (IPCC 2007, modified). -----	155
Fig. 5.03:	Annual emissions of carbon due to human activity according to the IPCC A1B storyline (IPCC 2000, left) and resulting atmospheric CO <sub>2</sub> concentrations (right) for a time period of 1970 to 2060. -----	157



<b>Figure</b>	<b>Caption</b>	<b>Page</b>
Fig. 5.04:	Monthly addends or minuends respectively for the simulation of the seasonal amplitude of the atmospheric CO <sub>2</sub> concentration, based on measurements taken from OHTAKI (1982). -----	158
Fig. 5.05:	Seasonal variation of the hourly addends or minuends respectively for the simulation of the diurnal amplitude of the atmospheric CO <sub>2</sub> concentration, based on measurements taken from OHTAKI (1982). -----	158
Fig. 5.06:	Modelled atmospheric CO <sub>2</sub> concentration for a summer day (25 <sup>th</sup> of July 2010, left), for the course of the year 2010 (middle) and for a time period from 2010-2060 (right). -----	159
Fig. 5.07:	Observed annual mean air temperature of the meteorological stations that were applied for the modelling of the Upper Danube Basin (1960-2006), relative to the average annual temperature of 1960, including the trend of the regional temperature increase. Both are compared to the global relative temperature increase as it is assumed by the IPCC A1B scenario (IPCC 2007). -----	159
Fig. 5.08:	Generation of artificial meteorological data applying a stochastic weather generator. -----	161
Fig. 5.09:	Annual mean temperatures relative to the 10-year average of 1991-2000 observed by the meteorological stations, which were applied for the modelling of the Upper Danube (solid, see section 3.3.4.3), and stochastically rearranged annual mean temperatures, applying a local impact factor of 1.7 to the IPCC A1B scenario (dashed). -----	161
Fig. 5.10:	Development of the modelled annual mean temperature for the Upper Danube Basin. Model results based on observed data (1960-2006) and modelled temperatures applying to the regionally adapted IPCC A1B climate scenario (2011-2060), including the respective standard deviations from the area average. -----	163
Fig. 5.11:	Development of the annual sums of precipitation for the Upper Danube Basin. Model results based on observed data (1960-2006) and modelled rainfall applying to the regionally adapted IPCC A1B climate scenario (2011-2060), including the respective standard deviations from the area average. -----	163
Fig. 5.12:	Development of annual precipitation sums for the Upper Danube Basin discerned into the summer (May-October) and winter half-year (November-April). Model results based on observed data (1960-2006) and modelled rainfall applying to the regionally adapted IPCC A1B climate scenario (2011-2060), including the respective standard deviations from the area average. -----	164
Fig. 6.01:	Course of the average duration of the vegetation period of deciduous trees within the Upper Danube Basin, modelled for the reference period from 1961 to 2006 and for the modified IPCC A1B scenario from 2011 to 2060, including the moving 10-year average and the respective standard deviations from the area mean. -----	165

<b>Figure</b>	<b>Caption</b>	<b>Page</b>
Fig. 6.02:	Course of the average incidence of mayshoot of coniferous trees within the Upper Danube Basin, modelled for the reference period from 1961 to 2006 and for the modified IPCC A1B scenario from 2011 to 2060, including the moving 10-year average and the respective standard deviations from the area mean. -----	166
Fig. 6.03:	Map of change of the average duration of the vegetation period of deciduous trees (left) and of the incidence of mayshoot of coniferous forests (right) within the Upper Danube Basin, picturing the difference between the model results achieved for the reference period from 1961 to 2006 and for the modified IPCC A1B scenario from 2011 to 2060. -----	167
Fig. 6.04:	Course of the average annual accumulation of dry biomass for the Upper Danube Basin, modelled for the reference period from 1961 to 2006 and for the modified IPCC A1B scenario from 2011 to 2060, including the moving 10-year average and the respective standard deviations from the area mean. -----	168
Fig. 6.05:	Biological productivity of an intensive grassland proxel from the middle of the Upper Danube catchment (457 m a.s.l.), calculated for the reference period (1961-2006) and for three different future storylines including the modified A1B scenario with and without assumed CO <sub>2</sub> increase and the unbiased baseline scenario (2011-2060). -----	169
Fig. 6.06:	Map of change of the average annual accumulation of dry biomass (left) and of the average annual count of water stress days (right) for the Upper Danube Basin, picturing the difference between the model results achieved for the reference period from 1961 to 2006 and for the modified IPCC A1B scenario from 2011 to 2060. -----	170
Fig. 6.07:	Course of the average annual count of water stress days within the Upper Danube Basin, modelled for the reference period from 1961 to 2006 and for the modified IPCC A1B scenario from 2011 to 2060, including the moving 10-year average and the respective standard deviations from the area mean. -----	172
Fig. 6.08:	Course of the average annual sum of transpiration within the Upper Danube Basin, modelled for the reference period from 1961 to 2006 and for the modified IPCC A1B scenario from 2011 to 2060, including the moving 10-year average and the respective standard deviations from the area mean. -----	174
Fig. 6.09:	Annual sums of transpiration of an intensive grassland proxel from the middle of the Upper Danube catchment (457 m a.s.l.), calculated for the reference period (1961-2006) and for three different future storylines including the modified A1B scenario with and without assumed CO <sub>2</sub> increase and the unbiased baseline scenario (2011-2060). -----	175
Fig. 6.10:	Course of the average annual sum of evapotranspiration within the Upper Danube Basin, modelled for the reference period from 1961 to 2006 and for the modified IPCC A1B scenario from 2011 to 2060, including the moving 10-year average and the respective standard deviations from the area mean. -----	176

---

<b>Figure</b>	<b>Caption</b>	<b>Page</b>
Fig. 6.11:	Map of change of the average annual sum of transpiration (left) and evapotranspiration (right) within the Upper Danube Basin, picturing the difference between the model results achieved for the reference period from 1961 to 2006 and for the modified IPCC A1B scenario from 2011 to 2060. -----	176
Fig. 6.12:	Monthly average rates of discharge for the main gauge of the Upper Danube Basin "Achleiten" (287 m a.s.l.). Measured data (1970-2003) and modelled runoff for the reference period (1970-2006) and the modified IPCC A1B climate scenario (2011-2060). -----	177

## List of Tables

<b>Table</b>	<b>Caption</b>	<b>Page</b>
Tab. 3.01:	Initialisation of the leaf angles and the corresponding shape parameters for two canopy layers. -----	032
Tab. 3.02:	Initial root depth according to the initial growth stage. -----	048
Tab. 3.03:	Parameters used for the transformation of harvested biomass [kg m <sup>-2</sup> ] to yield [t ha <sup>-1</sup> ]. -----	050
Tab. 3.04:	Initialisation of the auxiliary variables applied to the analytical solution of the photosynthesis related equation system, depending on the nature of the limitation of the carbon fixation rate. -----	065
Tab. 3.05:	Initialization of the auxiliary variables $o_{1-4}$ applied to the solution of the cubic equation system for the determination of the net photosynthesis rate and initialization of the auxiliary variables $kappa$ , $beta$ , $gamma$ and $lambda$ for the calculation of the internal CO <sub>2</sub> concentration. -----	066
Tab. 3.06:	Initialisation of the auxiliary variables $p$ , $q$ , $r$ , $s$ , $t$ , $y$ and $dis$ applied to the solution of the cubic equation for np. -----	066
Tab. 3.07:	Initialisation of the auxiliary variables $v1$ and $v2$ applied to the solution of the reduced equation for np. -----	067
Tab. 3.08:	Initialization of the auxiliary variables $o_{2-4}$ applied to the solution of the quadratic equation system for the determination of the net photosynthesis rate. -----	068
Tab. 3.09:	Phenological stages in PROMET and their relation to the international BBCH code. -----	073
Tab. 3.10:	Parameters used for the description of the phenological behaviour of deciduous and coniferous trees (MENZEL 1997). -----	080
Tab. 3.11:	Divisors for the reduction of pure glucose to dry biomass (SCHNEIDER 1999). -----	082
Tab. 3.12:	Crop input parameters required for the PROMET biological model. -----	096
Tab. 3.13:	Soil input parameters, analogously required for both, the Penman-Monteith and the biological PROMET model. -----	098
Tab. 4.01:	GPS - Coordinates of the sampling points of the four test fields (Geographic, WGS 84). -----	104
Tab. 4.02:	Assessment of the model results for the aboveground physiological plant parameters of the wheat test site "Hofanger" (April 1 <sup>st</sup> to August 31 <sup>st</sup> 2005) in comparison with field measurements. -----	117

<b>Table</b>	<b>Caption</b>	<b>Page</b>
Tab. 4.03:	Assessment of the model results for the aboveground physiological plant parameters of the maize test site "Hochstadt" (May 1 <sup>st</sup> to September 30 <sup>th</sup> 2005) in comparison with field measurements. -----	120
Tab. 4.04:	Adjustment of the 1 x 1 km model landuse map due to the representation of the available test fields at their exact geographic position. -----	126
Tab. 4.05:	Annual sums of evapotranspiration components [mm] for the hydrological year 1999, modelled with the Penman-Monteith approach and deviations of the results achieved with the biological model. -----	134
Tab. 4.06:	Spatial correlation of the annual average evapotranspiration [mm] of both, the PROMET-Penman-Monteith and the PROMET_Biological model. Compared model results for the hydrological years of 1961 to 2006, calculated for the Upper Danube Basin. -----	138
Tab. 4.07:	Results for the correlation of modelled and measured runoff (1970-2003) at the main gauge of the Upper Danube catchment for the two different model approaches. -----	140
Tab. 4.08:	Average incidence of the leaf emergence of beech trees ( <i>fagus sylvatica</i> ) based on observed long time data (1963-1993) of International Phenological Gardens in Europe (MENZEL 1997) and modelled results for the Upper Danube Basin. -----	146
Tab. 4.09:	Average incidence of the defoliation of beech trees ( <i>fagus sylvatica</i> ) based on observed long time data (1963-1993) of International Phenological Gardens in Europe (MENZEL 1997) and modelled results for the Upper Danube Basin. -----	147
Tab. 4.10:	Average incidence of the mayshoot of spruce trees ( <i>picea abies</i> ) based on observed long time data (1963-1993) of International Phenological Gardens in Europe (MENZEL 1997) and modelled results for the Upper Danube Basin. -----	149
Tab. 5.01:	IPCC scenario families, discerned into scenario groups with their major characteristics (IPCC 2000). -----	152
Tab. 5.02:	Projected globally averaged surface warming at the end of the 21 <sup>st</sup> century for different model cases (IPCC 2007). -----	154
Tab. 5.03:	Parameters for the conversion of annual CO <sub>2</sub> emissions to atmospheric CO <sub>2</sub> concentrations. -----	156
Tab. 5.04:	Statistical features of the meteorological input data, summarized for the reference and the scenario model period. -----	164
Tab. 6.01:	Trends of the moving 10-year average of the modelled phenological behaviour of forest trees within the Upper Danube Basin and modelled average incidence of the major phenological phases, discerned into the reference period from 1961 to 2006 and the scenario period from 2011 to 2060. -----	167

---

<b>Table</b>	<b>Caption</b>	<b>Page</b>
Tab. 6.02:	Trends of the moving 10-year average of the modelled biological productivity within the Upper Danube Basin and modelled average biomass allocation, discerned into the reference period from 1961 to 2006 and the scenario period from 2011 to 2060. -----	169
Tab. 6.03:	Trends of the moving 10-year average of the modelled water stress events within the Upper Danube Basin and modelled average count of water stress days per year, discerned into the reference period from 1961 to 2006 and the scenario period from 2011 to 2060. -----	173
Tab. 6.04:	Trends of the moving 10-year average of the modelled transpiration and evapotranspiration within the Upper Danube Basin and modelled average of both water cycle components, discerned into the reference period from 1961 to 2006 and the scenario period from 2011 to 2060. -----	174

## List of Equations

<b>Equation</b>	<b>Caption</b>	<b>Page</b>
Eq. 1.01:	General mass equation of photosynthesis. -----	009
Eq. 1.02:	Mass equation of PGA formation (HOPKINS 1999). -----	012
Eq. 1.03:	Mass equation of RuBP regeneration (HOPKINS 1999). -----	013
Eq. 3.01:	Extinction coefficient for direct radiation (CAMPBELL 1986). -----	032
Eq. 3.02:	Shape parameter for different leaf angles (CAMPBELL 1986). -----	032
Eq. 3.03:	Canopy hemispherical reflection coeff. (CAMPBELL AND NORMAN 1998). ---	033
Eq. 3.04:	Canopy albedo for a well developed canopy. -----	033
Eq. 3.05:	Canopy albedo adjusted to a less well developed canopy. -----	033
Eq. 3.06:	Illuminated leaf area in vegetation layer 1 (BALDOCCHI ET AL. 1987). -----	034
Eq. 3.07:	Illuminated leaf area in vegetation layer 2 (BALDOCCHI ET AL. 1987). -----	034
Eq. 3.08:	Reciprocal fractions of shaded leaf area for both canopy layers. -----	034
Eq. 3.09:	Intercepted shortwave diffuse radiation (CAMPBELL AND NORMAN 1998). --	034
Eq. 3.10:	Transmitted fraction of dir and dif PAR (CAMPBELL AND NORMAN 1998). ---	035
Eq. 3.11:	Absorbed energy input for the biological processes. -----	035
Eq. 3.12:	Energy budget of the upper canopy layer. -----	035
Eq. 3.13:	Energy budget of the lower canopy layer. -----	035
Eq. 3.14:	Logarithmic wind profile (CIONCO 1965, OKE 1978, DINGMAN 1994). -----	036
Eq. 3.15:	Roughness length of a vegetated surface (CAMPBELL AND NORMAN 1998).	037
Eq. 3.16:	Displacement height of a veg. surface (CAMPBELL AND NORMAN 1998). ----	037
Eq. 3.17:	Friction velocity due to friction of the wind with the surface (OKE 1978). ---	038
Eq. 3.18:	Landsurface water balance as modelled in PROMET. -----	039
Eq. 3.19:	Variable interception capacity of the canopy (GASH 1979). -----	040
Eq. 3.20:	Degree of canopy closure derived from the LAI. -----	040
Eq. 3.21:	Potential evaporation (PRIESTLEY AND TAYLOR 1972). -----	041

Equation	Caption	Page
Eq. 3.22:	Energy balance with incoming and outgoing SW and LW radiation. -----	041
Eq. 3.23:	Slope of the saturation vapour pressure curve (MURRAY 1967). -----	041
Eq. 3.24:	Latent heat of vaporization (BAUMGARTNER AND LIEBSCHER 1996). -----	041
Eq. 3.25:	Aerodynamic resistance (CAMPBELL AND NORMAN 1998). -----	042
Eq. 3.26:	Psychrometric constant (MURRAY 1967). -----	042
Eq. 3.27:	Conversion of potential interception evaporation. -----	042
Eq. 3.28:	Initial LAI, if $d$ is lower than $d_{incstart}$ or $d$ is greater than $d_{decend}$ . -----	046
Eq. 3.29:	Initial LAI, if $d$ is greater than $d_{incstart}$ and $d$ is lower than $d_{incend}$ . -----	046
Eq. 3.30:	Initial LAI, if $d$ is greater than $d_{incend}$ and $d$ is lower than $d_{incstart}$ . -----	046
Eq. 3.31:	Initial LAI, if $d$ is greater than $d_{decstart}$ and $d$ is lower than $d_{decend}$ . -----	046
Eq. 3.32:	LAI reduction factor due to annual mean temperature. -----	047
Eq. 3.33:	Initial leaf area for pixels in “cold” sites. -----	047
Eq. 3.34:	Height of the canopy due to a relation of leaf area and plant height. -----	048
Eq. 3.35:	Initial leaf biomass through “LAI-to-leaf-mass-per-area” relation. -----	048
Eq. 3.36:	Initial root length density distribution (ADIKU ET AL. 1996). -----	048
Eq. 3.37:	Harvestable portion of the accumulated biomass. -----	049
Eq. 3.38:	Linear interpolation for estimation of an intermediate leaf temperature. ----	053
Eq. 3.39:	Emission of heat from the leaf according to the Stefan-Boltzmann-Law. --	055
Eq. 3.40:	Temperature gradient between air and estimated leaf temperature. -----	056
Eq. 3.41:	Thermal conductivity of the air according to NOBEL (1991). -----	056
Eq. 3.42:	Thickness of the boundary layer according to NOBEL (1991). -----	056
Eq. 3.43:	Sensible heat flux from the leaf (NOBEL 1991). -----	057
Eq. 3.44:	Conductance of the boundary layer for water vapour (NOBEL 1991). -----	057
Eq. 3.45:	Diffusion coefficient of water vapour (NOBEL 1991). -----	058
Eq. 3.46:	Reduction of boundary layer cond. for needles (JARVIS ET AL. 1976). -----	058
Eq. 3.47:	Overall conductivity of the leaf. -----	058
Eq. 3.48:	Flux of transpired water for the estimated leaf temperature. -----	059



Equation	Caption	Page
Eq. 3.49:	Conversion of flux density to latent energy (NOBEL 1991). -----	059
Eq. 3.50:	Total heat loss of the leaf for the currently estimated leaf temperature. ----	059
Eq. 3.51:	Rate of net photosynthesis (FARQUHAR ET AL. 1980). -----	060
Eq. 3.52:	CO <sub>2</sub> compensation point following FALGE (1997). -----	060
Eq. 3.53:	Arrhenius-function of the simple type (MEDLYN ET AL. 2002b). -----	060
Eq. 3.54:	Rate of Carboxylation (FARQUHAR ET AL. 1980). -----	061
Eq. 3.55:	Rate of Oxygenation (FARQUHAR ET AL. 1980). -----	061
Eq. 3.56:	Arrhenius-function of the complex type (MEDLYN ET AL. 2002a AND b). ----	061
Eq. 3.57:	Electron limited carboxylation (FARQUHAR AND VON CAEMMERER 1982). ---	062
Eq. 3.58:	Simplified description of electron limited carboxylation for C <sub>3</sub> crops. -----	062
Eq. 3.59:	Electron limited carboxylation for C <sub>4</sub> crops (CHEN ET AL. 1994). -----	062
Eq. 3.60:	Maximum rate of the electron transport through photo system II. -----	062
Eq. 3.61:	Light dependency of photosynthesis (FALGE 1997). -----	063
Eq. 3.62:	Internal concentration of CO <sub>2</sub> (YIN AND VAN LAAR 2005). -----	063
Eq. 3.63:	Stomatal conductance for H <sub>2</sub> O (BALL ET AL. 1987). -----	064
Eq. 3.64:	CO <sub>2</sub> concentration at the leaf surface applying Fick's diffusion law. -----	064
Eq. 3.65:	Internal concentration of CO <sub>2</sub> (BALDOCCHI 1994). -----	065
Eq. 3.66:	Internal concentration of CO <sub>2</sub> applying Fick's diffusion law. -----	065
Eq. 3.67:	Conversion of Internal concentration of CO <sub>2</sub> (BALDOCCHI 1994). -----	065
Eq. 3.68:	Cubic equation for np (BALDOCCHI 1994). -----	065
Eq. 3.69:	Normal form of the cubic equation for np (BALDOCCHI 1994). -----	066
Eq. 3.70:	Reduced equation via substitution (BALDOCCHI 1994). -----	066
Eq. 3.71:	One real solution for np, if $p$ is greater than zero (BALDOCCHI 1994). -----	067
Eq. 3.72:	One real solution for np, if $p <$ than zero and $dis >$ zero. -----	067
Eq. 3.73a:	Three real solutions for np, if $p <$ zero and $dis \geq$ zero. Solution 1. -----	067
Eq. 3.73b:	Three real solutions for np, if $p <$ zero and $dis \geq$ zero. Solution 2. -----	067
Eq. 3.73c:	Three real solutions for np, if $p <$ zero and $dis \geq$ zero. Solution 3. -----	067

<b>Equation</b>	<b>Caption</b>	<b>Page</b>
Eq. 3.74:	Quadratic equation for $n_p$ , if $\kappa$ equals zero. -----	068
Eq. 3.75a:	Reduced quadratic equation for $n_p$ , solution 1. -----	068
Eq. 3.75b:	Reduced quadratic equation for $n_p$ , solution 2. -----	069
Eq. 3.76:	Loading function for stomatal resistance (JARVIS AND MORISON 1981). ----	071
Eq. 3.77:	Weighted reduction of the stomatal sensitivity coefficient <i>g<sub>fac</sub></i> . -----	071
Eq. 3.78:	Average daily thermal time. -----	074
Eq. 3.79:	Response function of hourly temperature effect (YIN AND VAN LAAR 2005).	074
Eq. 3.80:	Hourly thermal time (YIN AND VAN LAAR 2005). -----	075
Eq. 3.81:	Hourly vernalisation effect (YIN AND VAN LAAR 2005). -----	075
Eq. 3.82:	Overall vernalisation effect. -----	075
Eq. 3.83:	Declination of the sun. -----	075
Eq. 3.84:	Daily photoperiod (YIN AND VAN LAAR 2005). -----	076
Eq. 3.85:	Light effect curve (STRECK ET AL. 2003). -----	076
Eq. 3.86a:	Daily development rate for vegetative growth. -----	076
Eq. 3.86b:	Daily development rate for generative growth. -----	076
Eq. 3.87:	Accumulation of chill days during endogenous dormancy (MENZEL 1997).	078
Eq. 3.88:	Accumulation of thermal degree days. -----	078
Eq. 3.89:	Accumulation of chill days during exogenous dormancy (MENZEL 1997). --	078
Eq. 3.90:	Critical temperature threshold for emergence (CANNEL AND SMITH 1983). -	079
Eq. 3.91:	Estimation of the maintenance respiration (JONES 1991). -----	082
Eq. 3.92:	Conversion of GPP to NPP and from carbon to glucose (MCCREE 1970). -	082
Eq. 3.93:	Leaf biomass senescence. -----	084
Eq. 3.94:	Actual green leaf area due to leaf biomass and leaf mass area. -----	085
Eq. 3.95:	Canopy height as a linear function of the leaf area. -----	085
Eq. 3.96:	Increase of root length (RITCHIE 1998). -----	086
Eq. 3.97:	Soil moisture deficit factor (SCHNEIDER 1999). -----	086
Eq. 3.98:	Root depth on a model day <i>i</i> . -----	088

<b>Equation</b>	<b>Caption</b>	<b>Page</b>
Eq. 3.99:	Root length density factor of soil layer I (SCHNEIDER 1999). -----	088
Eq. 3.100:	Nitrogen deficit factor JONES AND KINIRY (1986). -----	088
Eq. 3.101:	Root length density at a model time step i for each soil layer I. -----	088
Eq. 3.102:	Elevation of photosynthetic capacity of grassland for warm sites. -----	096
Eq. 3.103:	Elevation factor of elevation and annual mean temperature. -----	097
Eq. 3.104a:	Elevation adjustment of carboxylation capacity of deciduous tree types. --	097
Eq. 3.104b:	Elevation adjustment of carboxylation capacity of coniferous tree types. --	097
Eq. 3.105:	Maximum rate of electron transport scaled to the carboxylation capacity. -	097
Eq. 3.106:	Respiration capacity scaled linearly to the carboxylation capacity. -----	097
Eq. 4.01:	Conversion of plant sample weight to wet biomass per m <sup>2</sup> . -----	108
Eq. 4.02:	Conversion of plant sample weight to dry biomass per m <sup>2</sup> . -----	108
Eq. 4.03:	Penman-Monteith equation of evapotranspiration (MONTEITH 1965). -----	132
Eq. 5.01:	Conversion of annual carbon emission from gigatons to mol. -----	157
Eq. 5.02:	Approximation of global air mass. -----	157
Eq. 5.03:	Approximation of annual CO <sub>2</sub> increase (SHAFFER AND SARMIENTO 1995). -	157
Eq. 5.04:	Third order polynomial of modelled atmospheric CO <sub>2</sub> concentration. -----	158
Eq. 5.05:	Covariance of temperature and precipitation (MAUSER ET AL. 2007). -----	160
Eq. 6.01:	Averaging of water stress days for the catchment area. -----	172

## List of Acronyms

<b>Acronym</b>	<b>Translation</b>
AMT	= <b>A</b> nual <b>M</b> ean <b>T</b> emperature
APAR	= <b>A</b> bsorbed <b>P</b> hotosynthetically <b>A</b> ctive <b>R</b> adiation
ASCII	= <b>A</b> merican <b>S</b> tandard <b>C</b> ode for Information Interchange
ADP	= <b>A</b> denosine- <b>D</b> i- <b>P</b> hosphate
ATP	= <b>A</b> denosine- <b>T</b> ri- <b>P</b> hosphate
AVG	= <b>A</b> verage
BACROS	= <b>B</b> asic <b>C</b> rop Growth <b>S</b> imulator
BAHC	= <b>B</b> iological <b>A</b> spects of the <b>H</b> ydrological <b>C</b> ycle
BEAM	= <b>B</b> asic <b>E</b> RS & <b>E</b> NVISAT <b>A</b> TSR and <b>M</b> ERIS toolbox
BGC	= <b>B</b> iogeochemical Model
BMB+F	= <b>B</b> undesministerium für <b>B</b> ildung und <b>F</b> orschung [M. Education and Research]
CAM	= <b>C</b> rassulacean <b>A</b> cid <b>M</b> etabolism
CASA	= <b>C</b> arnegie <b>A</b> mes <b>S</b> tanford <b>A</b> pproach
CD	= <b>C</b> hill <b>D</b> ay
CERES	= <b>C</b> rop <b>E</b> nvironment <b>R</b> esource <b>S</b> ynthesis
CH <sub>2</sub> O	= Glucose
CO <sub>2</sub>	= Carbon dioxide
DEM	= <b>D</b> igital <b>E</b> levation <b>M</b> odel
DEMETER	= <b>D</b> ynamic <b>E</b> nergetic <b>M</b> odels of <b>E</b> arth's <b>T</b> errestrial <b>E</b> cosystem and <b>R</b> esources
DFG	= <b>D</b> eutsche <b>F</b> orschungsgemeinschaft [German Research Foundation]
DGPS	= <b>D</b> ifferential <b>G</b> lobal <b>P</b> ositioning <b>S</b> ystem
DGVM	= <b>D</b> ynamic <b>G</b> lobal <b>V</b> egetation <b>M</b> odel
DMT	= <b>D</b> aily <b>M</b> ean <b>T</b> emperature
DOI	= <b>D</b> igital <b>O</b> bject <b>I</b> dentifier
DOLY	= <b>D</b> ynamical <b>G</b> lobal <b>P</b> hytogeography Model
DOY	= <b>D</b> ay of <b>Y</b> ear

<b>Acronym</b>	<b>Translation</b>
DTM	= <b>D</b> igital <b>T</b> errain <b>M</b> odel
DWD	= <b>D</b> eutscher <b>W</b> etterdienst [German Weather Service]
ELCROS	= <b>E</b> lementary <b>C</b> rop Growth <b>S</b> imulator
ENVISAT	= <b>E</b> nvironment <b>S</b> atellite
ESA	= <b>E</b> uropean <b>S</b> pace <b>A</b> gency
ESRI	= <b>E</b> nvironmental <b>S</b> ystems <b>R</b> esearch <b>I</b> nstitute
ET	= <b>E</b> vapotr <b>anspiration</b>
FAO	= <b>F</b> ood and <b>A</b> griculture <b>O</b> rganization of the United Nations
fAPAR	= <b>F</b> raction of <b>A</b> bsorbed <b>P</b> hotosynthetically <b>A</b> ctive <b>R</b> adiation
fPAR	= <b>F</b> raction of <b>P</b> hotosynthetically <b>A</b> ctive <b>R</b> adiation
FBM	= <b>F</b> r Frankfurt <b>B</b> iosphere <b>M</b> odel
FC	= <b>F</b> ractional <b>C</b> over
FORTRAN	= <b>F</b> ormula <b>T</b> ranslation
G3P	= <b>G</b> lyceraldehyde- <b>3</b> - <b>P</b> hosphate (Triose Sugar-Phosphate)
GCM	= <b>G</b> eneral <b>C</b> irculation <b>M</b> odel
GDP	= <b>G</b> ross <b>D</b> omestic <b>P</b> roduct
GECROS	= <b>G</b> enotype by <b>E</b> nvironment Interaction on <b>C</b> rop Growth <b>S</b> imulator
GEM	= <b>G</b> lobal <b>E</b> nvironmental <b>M</b> odel
GHG	= <b>G</b> reen <b>H</b> ouse <b>G</b> as
GIS	= <b>G</b> eographic <b>I</b> nformation <b>S</b> ystem
GLOWA	= <b>G</b> lobaler <b>W</b> andel des Wasserkreislaufs [Global Change and the Hyd. Cycle]
GPP	= <b>G</b> ross <b>P</b> rimary <b>P</b> roduction
GPS	= <b>G</b> lobal <b>P</b> ositioning <b>S</b> ystem
H <sub>2</sub> O	= Water
IAA	= <b>I</b> ndole-3- <b>A</b> cetic <b>A</b> cid
IBIS	= <b>I</b> ntegrated <b>B</b> iosphere <b>S</b> imulator
IGBP	= <b>I</b> nternational <b>G</b> eosphere <b>B</b> iosphere <b>P</b> rogramme
IPCC	= <b>I</b> ntergovernmental <b>P</b> anel on <b>C</b> limate <b>C</b> hange
IPG	= <b>I</b> nternational <b>P</b> henological <b>G</b> arden

<b>Acronym</b>	<b>Translation</b>
LAI	= <b>Leaf Area Index</b>
LHC	= <b>Light Harvesting Complex</b>
LMA	= <b>Leaf Mass Area</b>
LMU	= <b>Ludwig-Maximilians-Universität</b>
LOD	= <b>Length of Day</b>
LPJ	= <b>Lund-Potsdam-Jena biogeographical equilibrium model</b>
LPJmL	= <b>LPJ for managed Lands</b>
LW	= <b>Long Wave</b>
MAPSS	= <b>Mapped Atmosphere-Plant-Soil System</b>
MERIS	= <b>Medium Resolution Imaging Spectrometer</b>
NADPH	= <b>Nicotine-Adenine-Dinucleotid-Phosphate</b>
NIR	= <b>Near Infra Red</b>
NPP	= <b>Net Primary Production</b>
N.-S.	= <b>Nash-Sutcliffe efficiency coefficient</b>
O <sub>2</sub>	= <b>Oxygen</b>
OAA	= <b>Oxaloacetate</b>
P680	= <b>Photosystem II with chlorophyll a absorption peak at 680 nm</b>
P700	= <b>Photosystem I with chlorophyll a pigment absorption peak at 700 nm</b>
PAR	= <b>Photosynthetically Active Radiation</b>
PCR	= <b>Photosynthetic Carbon Reduction</b>
PBM	= <b>Potsdam Biosphere Module</b>
PEP	= <b>Phosphoenol Pyruvate</b>
PEPcase	= <b>Phosphoenol Pyruvate Carboxylase</b>
PFT	= <b>Plant Functional Type</b>
PGA	= <b>Phosphoglycerate Acid</b>
PID	= <b>Pixel Identification Number</b>
PIXEL	= <b>Picture Element</b>
P.-M.	= <b>Penman-Monteith approach</b>
PROMET	= <b>Process of Radiation Mass and Energy Transfer Model</b>

<b>Acronym</b>	<b>Translation</b>
PROXEL	= <b>Process Pixel</b>
PSI	= <b>Photosystem I</b>
PSII	= <b>Photosystem II</b>
PSN	= <b>Net Photosynthesis</b>
RLD	= <b>Root Length Density</b>
RTM	= <b>Radiative Transfer Model</b>
RuBisCO	= <b>Ribulose-1.5-Biphosphate-Carboxylase/Oxigenase</b>
RuBP	= <b>Ribulose-1.5-Biphosphate</b>
SRES	= <b>Special Report on Emissions Scenarios</b>
SRTM	= <b>Shuttle Radar Topography Mission</b>
STD. DEV.	= <b>Standard Deviation</b>
SUCROS	= <b>Simple and Universal Crop Growth Simulator</b>
SVPC	= <b>Saturation Vapour Pressure Curve</b>
SW	= <b>Shortwave</b>
TBL	= <b>Thickness of the Boundary Layer</b>
TCA	= <b>Thermal Conductivity of Air</b>
TDD	= <b>Thermal Degree Day</b>
TEM	= <b>Terrestrial Ecosystem Model</b>
TOA	= <b>Top of Atmosphere</b>
USGS	= <b>United States Geological Survey</b>
UTC	= <b>Coordinated Universal Time</b>
UTM	= <b>Universal Transverse Mercator Projection</b>
VISAT	= <b>Visualization and Analysis Tool</b>
WGEN	= <b>Stochastic Weather Generation Model</b>
WSD	= <b>Water Stress Day</b>
YBP	= <b>Years Before Present</b>

# 1. Introduction

## 1.1 Physically based Modelling and Climate Change

The knowledge and public acceptance of the fact that the climatic conditions of the world are changing has finally found its way from the desks of scientists into the consciousness of the open public (IPCC 2001, 2007). Now that the world is aware of the changes that will happen and in some places already can be experienced, the interest in the possible effects of a changing climate is escalating. The most important question in that context will be how to deal with a changing climate and how to oppose the effects that are accompanying the change. A major part of the answer to that question is embedded in the knowledge about the extent and force of the reactions that will be provoked in our environment by the climate change.

The currently discussed future scenarios cover a wide range. On one hand exaggerated future projections that are envisioning disastrous cataclysms are broadcasted mostly by the yellow press, while on the other hand studies that are trying to play the effects of a changing climate down still are circulating (WEINGART ET AL. 2000). Somewhere between those extreme opinions lies a variety of possible future projections that are based on physical principles and can be derived from a detailed analysis of scientific calculations. These calculations have to be accompanied by probabilities that describe the likelihood of incidence of the projected change scenarios. Physically based computational models here provide an excellent didactic method to widen the understanding of the processes involved and to unveil the interconnectedness of the manifold cycles that are working together at the landsurface to form the landscape environment (JONES 1992, PENG 2000).

When investigating the impacts of climate change with physically based methods, it is necessary to construct a mechanism that is capable of mapping the current and the historic situation with the best possible quality. The basic demand for this instrument would be a reliable physical accuracy, requiring that all determinant physical parameters are taken into account.

One of the physical components that are likely to react to climate change in a most sensitive way is the vegetation cover (HUNTLEY 1991). Through its multiple and diverse functionality, the living canopy functions as a connecting element between the processes that occur in the soil and the atmosphere. The living vegetation is anchoring soil and land, especially in extreme environments and therefore plays the role of an important erosion inhibitor (DE BAETS ET AL. 2007). For man and animal the stability of agricultural production is of major concern, as plants are a resourceful reserve of food (ACC AND SCN 2004). Also the cultivation of crops that are intended as an additional source of renewable energy has gained importance over the last years (HALL ET AL. 1993). Photosynthetic reactions that are proceeding in every green plant as



long as energy is provided by the sunlight, contribute to the world climate according to their functionality as carbon dioxide sinks (BETTS ET AL. 1997, CAO AND WOODWARD 1998). And last but not least the plant growth activity greatly influences the water balance on all scales from micro climates within the living canopy up to the scale of the global water balance, by on one hand shading the earth and with that inhibiting the soil evaporation and by contributing largely to the atmospheric water vapour content through transpiration processes on the other (NEILSON AND MARKS 1994). The importance of the vegetation cover becomes even more apparent, when we consider that the great majority of the land biomass on the earth today consists of vegetation phytomass (HUNTLEY 1991). A deeper understanding of how the vegetation responds to climate change therefore will be of paramount importance, if possible reactions of the entire biosphere to climate change shall be assessed (PRENTICE ET AL. 1991, PENG ET AL. 1998, CRAMER ET AL. 1999).

When the task of the assessment of climate change effects with the help of physical models is approached, a detailed description and reproduction of the vegetation dynamics is indispensable and has to be given a high priority. This work consequently endeavours to clear the way towards an enhanced understanding and an improved prediction of climate change effects on vegetation dynamics by extending an existing hydrological land surface model, that already has proven its reliability and stability, by a biophysically based simulation of photosynthetic behaviour that will be able to trace the sensitivity of the living canopy with respect to temperature change and rising atmospheric CO<sub>2</sub> concentrations.

## **1.2 State of the Art**

Climate change is a major issue that is worked on by scientists of the most diverse fields. Recent studies cover the effects of climate change from the scientific view of biologists, oceanographers, zoologists, foresters, hydrologists, agronomists, politicians, economists et cetera. Since this work mainly gives attention to climatic changes that are directly influencing physical processes at the land surface and are affecting the life of humans and animals in a primary way, political and socioeconomic studies are neglected here and the focus is drawn towards physical and biological research.

During the past years an increasing number of published studies can be observed that are treating the application of computational models for mathematical predictions and the support of quantitative conclusions (JONES 1992). However, the latest cognitions have revealed that the majority of the models that are applied to the assessment of climate change effects still are lacking an adequately detailed description of the living canopy (BETTS ET AL. 2007). A more or less static representation of the canopy in a model is neglecting the respiration and gas exchange processes that occur in the real landscape and cannot satisfy a detailed future

projection of climate change effects. In opposition to those models, the green vegetation is actively reacting to the changing atmospheric conditions (SELLERS ET AL. 1996). Recent studies could prove that the vivid interaction between the canopy and the atmosphere is a determinant and highly variable process, which is influencing the atmospheric water vapour content and as a consequence also the water balance of the land surface (BETTS ET AL. 2007). This is mainly due to changes of the gas exchange behaviour of green vegetation under elevated atmospheric CO<sub>2</sub> concentrations (CHEN 1994, FIELD ET AL. 1995). This so called 'physiological forcing' (BETTS ET AL. 2007) has already been detected in observational records of increasing average continental runoff over the twentieth century (GEDNEY ET AL. 2006). It has been found in various studies that the increase of continental runoff is the consequence of a reduced transpiration activity of the vegetation cover (SELLERS ET AL. 1996, BETTS ET AL. 1997, HUNGATE ET AL. 2002, LONG ET AL. 2006), which leads to a higher supply of water on the land surface and in the near surface soil layers (WIGLEY AND JONES 1985). Other studies that are not taking the dynamic vegetation response to elevated atmospheric CO<sub>2</sub> concentrations and rising annual mean temperatures into account and are solely relying on the so called 'radiative forcing' of climate change (ARNELL AND LIU 2001, WARREN 2006, DE WIT AND STANKIEWICZ 2006) are not able to trace these sensitive changes of the landsurface water household. The composition of a highly dynamic vegetation model that is capable of a response to climate change induced variations of the meteorological driving forces therefore is one of the major concerns of this thesis.

The computational modelling of vegetation dynamics dates from early pioneers like the JABOWA model, which was developed by Botkin et al. in the early seventies of the previous century (BOTKIN ET AL. 1972). The early models that were applying the aid of computers were developed for forested areas only and initiated a whole science of computer aided vegetation modelling that soon developed from the mapping of mere forest areas also to the modelling of other vegetation types (BOX 1981, PENG 2000). Nowadays, various models exist that are mapping environmental vegetation processes on a very detailed level. On the global scale here will have to be mentioned the BIOME model family developed by PRENTICE ET AL. (1992) as an example for static biogeographical models. The BIOME model again has encouraged the development of a series of static ecophysiological models like CENTURY (PARTON ET AL. 1993), the FOREST-BioGeoChemical model (BGC, RUNNING AND COUGHLAN 1988), the Global Environmental Model (GEM, RASTETTER ET AL. 1991), the Terrestrial Ecosystem Model (TEM, RAICH ET AL. 1991) or the Frankfurt Biosphere Model (FBM, LÜDEKE ET AL. 1994).

Soon the static biogeographical models were enhanced to meet the demand of a dynamic description of vegetation activity. As examples may serve the BIOME2 and BIOME3 models by HAXELTINE AND PRENTICE (1996 AND 1997), the Dynamical Global Phytogeography Model (DOLY, WOODWARD ET AL. 1995), the Mapped Atmosphere-Plant-Soil System (MAPSS, NEILSON 1995), the family of Dynamic and Energetic Models of Earth's Terrestrial Ecosystem

and Resources (DEMETER, FOLEY 1995) or the LPJ Model (SITCH ET AL. 2003) that also has also been adapted to a simulation of managed lands (LPJml, BONDEAU ET AL. 2007) with its most recent derivate, which is the Potsdam Biosphere Module (PBM, CRAMER ET AL. 2004).

The need to develop models that are capable of mapping the carbon feedbacks of the canopy dynamically over time and space lead to a series of models like the Integrated Biosphere Simulator Model (IBIS, FOLEY ET AL. 1996), the HYBRID model (FRIEND ET AL. 1997), the Carnegie Ames Stanford Approach (CASA, POTTER AND CLOOSTER 1999) and to model combinations like MAPSS-CENTURY (LENIHAN ET AL. 1998) or TEM-DVM (PAN ET AL. 2000).

Besides canopy models that are currently applied to a modelling of the global vegetation activity, even more precise and detailed models exist that are applied to regional forestry or agricultural objectives. Here the Crop Environment Resource Synthesis model family (CERES, JONES AND KINIRY 1986, RITCHIE 1991) is one of the agricultural models that is most commonly applied and is constantly enhanced with respect to the mapping of different cultivars. Other determinant and complex general growth models emanate from the so called 'School of de Wit' (BOUMAN ET AL. 1996) that can look back on a series of continuous development from the initial elementary crop growth simulator (ELCROS, DE WIT ET AL. 1970), over the basic crop growth simulator (BACROS, DE WIT ET AL. 1978), the simple and universal crop growth simulator (SUCROS1, VAN KEULEN ET AL. 1982, GOUDRIAAN AND VAN LAAR 1994, SUCROS 2, VAN LAAR ET AL. 1997), up to the latest development of the 'School of de Wit' model family, which is represented by the genotype by environment interaction on crop growth simulator (GECROS, YIN AND VAN LAAR 2005). Other models that are predominantly applied for agricultural purposes can be represented by WANGRO (KANNEGANTI AND FICK 1991), the AGROSIM model compilation (MIRSCHER AND WENKEL 2007) or the MODWht model (RICKMAN ET AL. 1996).

### **1.3 Motivation and Goals of the Thesis**

With exception of the latest development of the school of de Wit model family (GECROS), none of the models listed in section 1.2 is capable of mapping an adequately dynamic interactive reaction of the vegetation cover with respect to carbon dioxide and temperature, as far as it is known to the author.

In this work, a biochemically based assimilation model for C<sub>3</sub> grasses (FARQUHAR, VON CAEMMERER AND BERRY 1980) is applied in combination with enhancements concerning the mathematic description of C<sub>4</sub> photosynthesis (CHEN ET AL. 1994) and forest growth (FALGE 1997). The photosynthesis model is combined with a model of stomatal conductance (BALL, WOODROW AND BERRY 1987) to enable the hydrological landsurface model PROMET (MAUSER AND BACH 2008) to the simulation of dynamic vegetation processes, including an explicit simulation of the leaf gas exchange. Through the detailed description of biochemical processes

within the leaf and the explicit simulation of the gas exchange between leaf and atmosphere, a direct interconnection of the modelled processes to external climate relevant parameters is established. Thus, a dynamic reaction of the modelled biochemistry to environmental parameters like air pressure, radiation, atmospheric carbon dioxide concentration and temperature can be mapped by the model, which is a basic prerequisite for the assessment of climate change effects that are related to vegetation activity.

The scientific aim and central target of this work is the investigation of vegetation behaviour under changing climatic conditions and the quantification of the effect that the vegetation dynamics impose on the hydrology of a river catchment. In this regard it will be of particular interest that diverging processes have to be expected when the canopy is exposed to a changing climate. On one hand rising temperatures and rising atmospheric CO<sub>2</sub> concentrations are pointing towards an increase of growth activity, due to the fact that all chemical processes are supposed to be accelerated when exposed to higher temperatures according to the van't Hoff rule. Also numerous publications have shown that elevated CO<sub>2</sub> concentrations may result in somewhat higher plant productivities (WONG 1979, SELLERS ET AL. 1996, FIELD ET AL. 1995, KÖRNER 2000, LONG ET AL. 2006), although in the meantime it has been found that these changes are mostly due to changed environmental conditions, while the photosynthetic reaction itself is rapidly adapting to the enriched CO<sub>2</sub> supply (KÖRNER 2006). On the other hand, the changing climate not only affects the photosynthetic processes, but also has an impact on the whole landsurface water balance. An increase of the average temperature may result in a lower water supply that may again lead to an increase of drought stress. The future balance of growth enhancing (rising levels of temperature and CO<sub>2</sub>) and growth inhibiting (increased frequency of water stress, decline of summer precipitation) processes will decide, whether the expected higher vegetation activity will be reduced or even be compensated by drought stress in the near future.

For the investigation of the future behaviour of the vegetation processes, computer aided modelling techniques are applied on a physical basis. As could be shown in section 1.2, a great variety of modelling approaches for different purposes that are related with plant growth already exists. The scientific challenge of this work therefore is not the development of another vegetation model. It rather is the review of existing modelling approaches, the understanding of the concerned processes, the selection of adequate methods and finally their combination and integration into a functioning modelling system that is capable of giving quantitative answers to climate change enquiries. This is a comprehensive task that requires an intensive engagement with different natural sciences on a very detailed level. The awareness of the interconnectedness of natural processes, disregarding the boundaries of single scientific niches, is one of the most determinant advantages that distinguish the science of Geography. The consolidation of methods that descend from different branches of the natural sciences therefore

is an appealing task for a universal scientist, who is not afraid of penetrating scientific grounds of neighbour sciences in order to tide over joints in science that actually are an interconnected system in nature.

The spatial extent of this study is limited to the watershed boundary of the Upper Danube catchment (see section 2), while the temporal dimension is separated into two time segments. A so called “reference” period, ranging from 1960 to 2006 and a “scenario” period that comprises the forthcoming 50 years from 2011 to 2060. The reason for choosing a scenario time frame that is relatively short compared to other projections, for example those introduced by the Intergovernmental Panel on Climate Change that partly cover ranges of up to 500 years into the future (IPCC 2001, 2007), is twofold. On one hand the proposed time frame is appealing because a great number of our contemporaries are likely to experience the manifestation of the possible changes in person. The other reason, why a limitation to 50 years was chosen for this task, is founded on restrictions that accompany the generation of artificial meteorology data for the scenario model runs. The stochastic generation of artificial weather data as applied here (see section 5.3.2, MAUSER ET AL. 2007) is limited by the data base of measured meteorological observations that can be integrated into the generation of the chain of artificial weather events. Since the observed regional meteorological data that could be acquired for this study only covers 46 years from 1960 to 2006, saturation effects that manifest in statistic repetitions of observed extremes occur, when the time frame and the connected scenario changes exceed a critical range. The limitation of the spatial extent to the Upper Danube catchment is due to several reasons. Most important, the scientific exchange with the GLOWA-DANUBE cooperative project, founded by the German Ministry of Education and Research (BMB+F), allowed for the acquisition of a comprehensive data base. The Upper Danube catchment is a rewarding subject for investigation, since it is a very heterogeneous landscape ranging from plain periglacial brash fields up to high alpine zones. It is a region that is economically active and densely inhabited, combining a huge variety of land uses that are formed by the antithetic demands of heavy and high tech industry, recreation and intensive agriculture, large forested areas and steep alpine rocks, big cities and rural villages. For hydrological applications, a river basin generally is an appealing entity due to the fact that the water balance can be controlled and verified with help of the measured runoff at the benchmark gauge, where the main stream drains the water basin. Last but not least the Upper Danube Basin is the region that I live in, which is the reason why I personally am most highly interested in the changes that will be of consequence for the environment and the people that are living in this part of central Europe.

Concerning the methods, the physically based hydrological landsurface model PROMET (MAUSER AND BACH 2008) forms an excellent basis for this work. The model has already proven its stability and capacity for hydrological applications on the landscape scale (MAUSER AND STRASSER 1997, MAUSER AND SCHÄDLICH 1998, STRASSER 1998, LUDWIG 2000). Due to its

modular architecture, additional extensions can easily be integrated, gradually enhancing the models functionality.

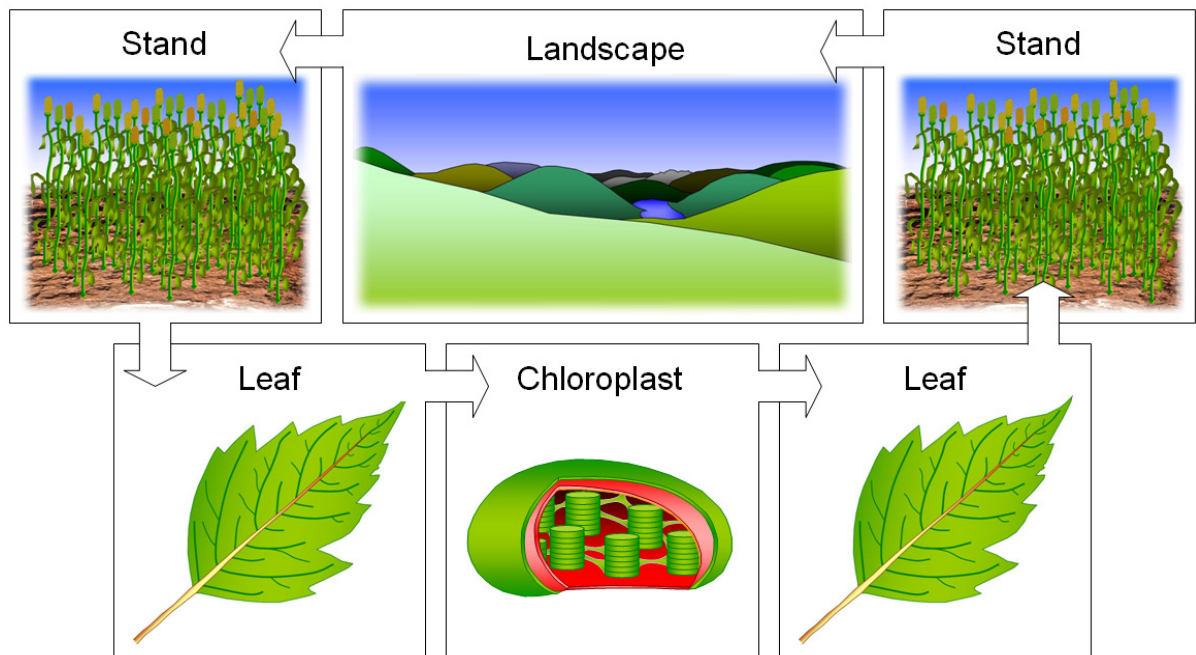


Figure 1.01: Cycle of modelled scales. Chloroplast image inspired by MOORE ET AL. (1998).

Besides the actual physical modelling, the scale that is used to comprehend the single modelling steps is a determinant factor. For this work, a modelling approach was applied that finds its beginning at the scale of a landscape or mesoscale, where the meteorology that powers the model is interpolated. The general energy flux then is directed to the leaves of the canopy and from there on to the microscale of the chloroplast level, where the processes of photosynthesis are modelled explicitly, based on mitochondrial activities. The products of the chloroplast photosynthesis then are scaled up to the leaf level and from there are scaled further back to the entire landscape in a last step (fig. 1.01).

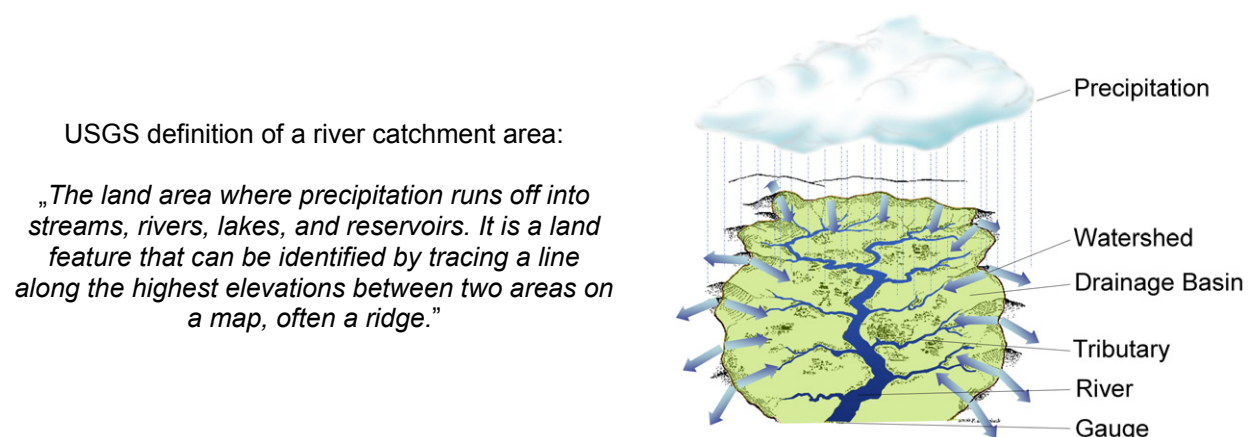


Figure 1.02: Definition of the river drainage area through a watershed, based on the terrain topography.

The term landscape in this context refers to the natural entity of a river catchment (*fig. 1.02*). The drainage basin offers ideal natural boundaries for modelling approaches, due to several reasons. On one hand, the river catchment is a naturally defined area that does not necessarily follow administrative borders and represents a natural landscape unit (HEATHCOTE 1998). On the other hand, the boundaries of a river catchment allow for a validation of the model results simply because the water balance can be retraced by comparing the model results with measured runoff data from the basin gauge. In comparison with the measurement of evapotranspiration and precipitation respectively, the recording of runoff rates can be accomplished with relatively high precision.

## 1.4 Biological Modelling

A model is a representation of a real system, such as a plant in this context, which can be used to simulate certain features of the more complex real system (JONES 1992). The description of the investigated process can either be empirical, or a simulation that is based on a mathematical abstraction of the system under consideration. A mathematical model will include a concise formulation of a hypothesis, so that it can be applied to the generation of predictions. Those predictions again can be tested by measurements either in the laboratory or in the field and may bring about a refinement of the initial hypothesis (*fig. 1.03*).

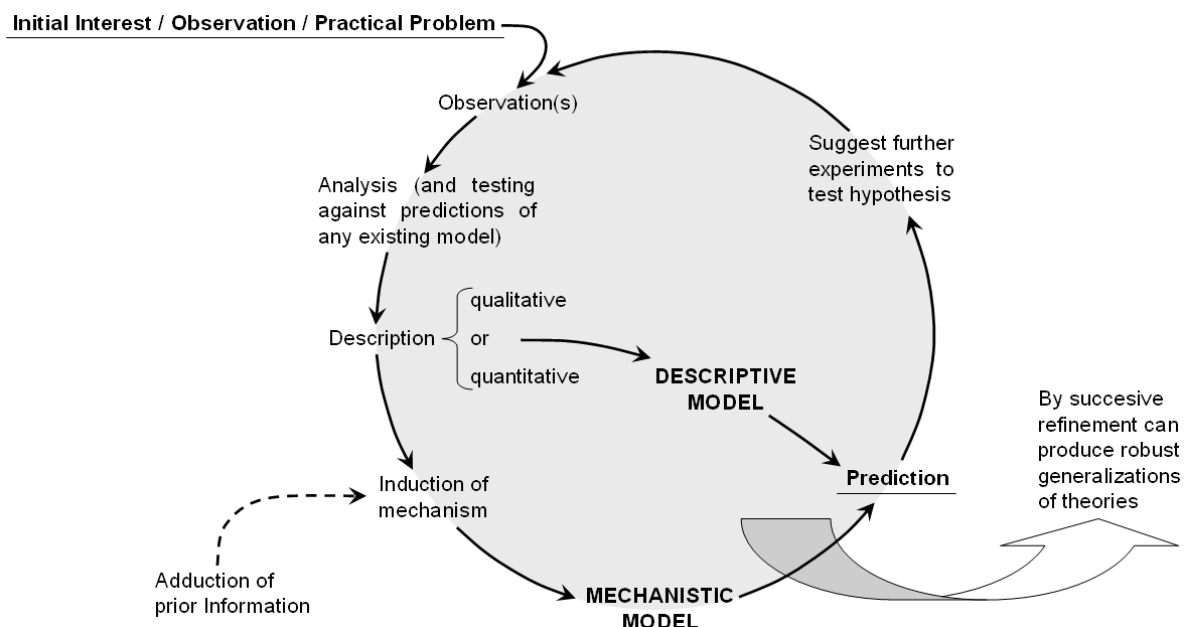


Figure 1.03: The role of models in a scientific method, modified after JONES (1992).

Biological systems are very complex, so that a complete mathematical description is rarely achieved. Simplifying assumptions therefore have to be made in every study, but can be refined

through an intensive testing of the model. An accurately validated mathematical model has specific advantages that can be summarized according to JONES (1992):

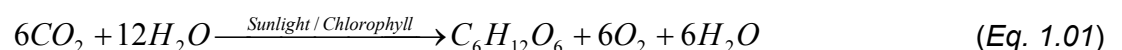
- It constitutes precise statements of hypotheses.
- It is inherently testable.
- It can explain or describe a large number of separate observations in a concise form.
- It helps to identify those areas where knowledge is lacking and further experiments or observations are required.
- It can be used to predict system behaviour in untried combinations of conditions.
- It can be used as a management tool.

In the domain of plant growth and environmental modelling, different mathematical model approaches have been developed. A general distinction has to be made between empiric models that do not attempt to describe the mechanisms involved and mechanistic models that apply well-known physical processes to the explanation of a phenomenon on a very detailed level. Both types may return reliable results, but it is a model of the latter kind that holds the largest potential for accurate predictions under a wide range of conditions (JONES 1992).

The mathematical models may be further discerned into deterministic or stochastic and again into dynamic or static models. Deterministic models define the model output according to the applied inputs, while stochastic models incorporate an element of randomness. However, most biological models are of the deterministic kind, due to reasons of simplicity. Also the model applied in this work belongs to this kind of mathematical models. Static models are used for the simple description of a final result, while dynamic models, such as the one that is introduced here, include a treatment of the time dependence of a process and therefore are particularly appropriate for the simulation of processes like plant growth or yield production (JONES 1992).

## 1.5 Photosynthetic Processes

Before the modelling approaches for the simulation of photosynthetic processes are presented in detail, the terms and definitions involved must be introduced. Most commonly known is the basic equation of photosynthesis (*eq. 1.01*), which describes the process of the transformation of carbon dioxide to glucose under use of sunlight energy that is absorbed by the chlorophyll in the leaves of green plants.



Less widely known are the chemical processes that are contributing to this conversion and the role of the enzymes that are catalyzing the associated reactions. Basic requirements for a functioning photosynthetic reaction are the availability of energy, water and carbon dioxide.



While the leaves are collecting energy through the specific absorption behaviour of the chlorophyll, the water is transported from the roots via the xylem of the stem and the carbon dioxide is made available through an active gas exchange thanks to the stomata of the leaf (LARCHER 1995).

The fluxes of the associated molecules are directed into the chloroplasts, which are filled with stacks of so called thylakoids (the grana) and an aqueous space that is surrounding the grana (*fig. 1.04*, MOORE ET AL. 1998). The actual photosynthesis is a two stage process, consisting of a so called “light” or light dependent and a “dark” or to some degree light independent reaction. The term “light” reaction summarizes the processes that happen in the grana of the chloroplast (*fig. 1.04*), where energy-transport-molecules, namely Adenosine-Tri-Phosphate (ATP) and Nicotine-Adenine-Dinucleotid-Phosphate (NADPH), are constructed, using the absorbed sunlight energy. During this process of energy conversion from radiation into a stable chemical form of energy,  $H_2O$  molecules are split and pure oxygen ( $O_2$ ) is released. The energy stored in the ATP and NADPH molecules is consumed by the “dark” reaction that takes place within the stroma of the chloroplasts.

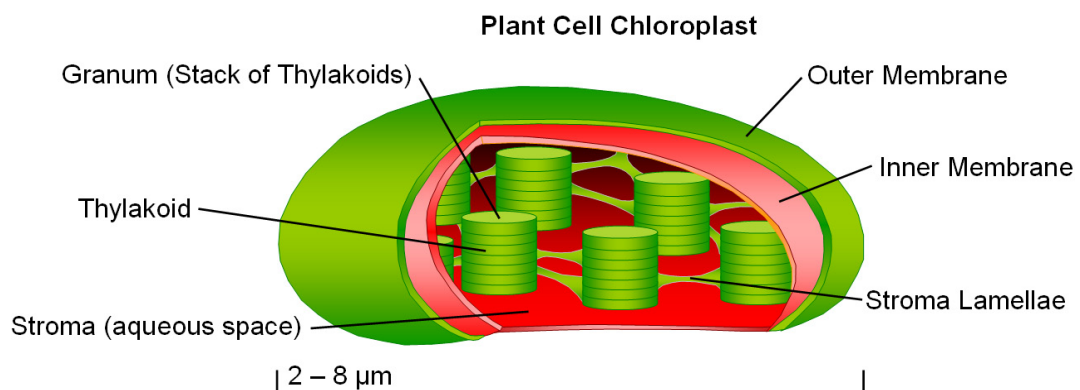


Figure 1.04: Cut through a chloroplast, inspired by MOORE ET AL. (1998).

### 1.5.1 „Light“ Reaction

Like antennae, the leaves are collecting sunlight energy for the plant. For the photosynthesis, only the part of the solar radiation is valuable that is absorbed by either chlorophyll *a* or *b* or by accessory pigments such as carotenoids that are covering the surface of the thylakoids. However, it has been found that the main light harvesting is done by the different types of chlorophyll, while the accessory pigments are mainly required to protect the chlorophyll against photodestruction in times of excess light (HOPKINS 1991). The chloroplast pigments all have their absorption maxima in the blue and in the red spectral domain (*fig. 1.05*, JONES 1992).

The thylakoids, which consist of stacked chlorophyll and accessory pigments, represent a multimolecular functioning unit that is termed a “photosystem”. Due to the fact that a single chlorophyll molecule is very small and would only be struck by the sunlight photons a few times

per second (HOPKINS 1999), the chlorophyll molecules are organized as so called light-harvesting complexes (LHC) that are concentrating the incoming energy and are transferring it into the reaction centre of the photosystem.

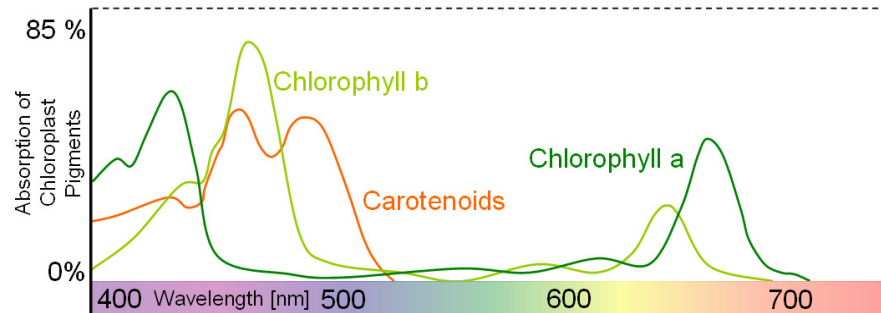


Figure 1.05: Absorption spectra of chlorophyll a (680), b and carotene that apply to PSII. Modified after JONES (1992).

Eukaryotes, like all higher plants, are equipped with two different photosystems, I (PSI) and II (PSII) that are linked by a multiprotein aggregate termed the cytochrome complex (*fig. 1.06*). The light harvesting is conducted by chlorophyll *P680* (Chlorophyll a with a relative absorption maximum at 680 nm, *fig. 1.05*) for PSII and for PSI by chlorophyll *P700* (Chlorophyll a with a relative absorption maximum at 700 nm). Within the photosystem II, electrons are excited by the incoming sunlight. Their energy is used to generate ATP compounds, a process termed photophosphorylation (*fig. 1.06*).

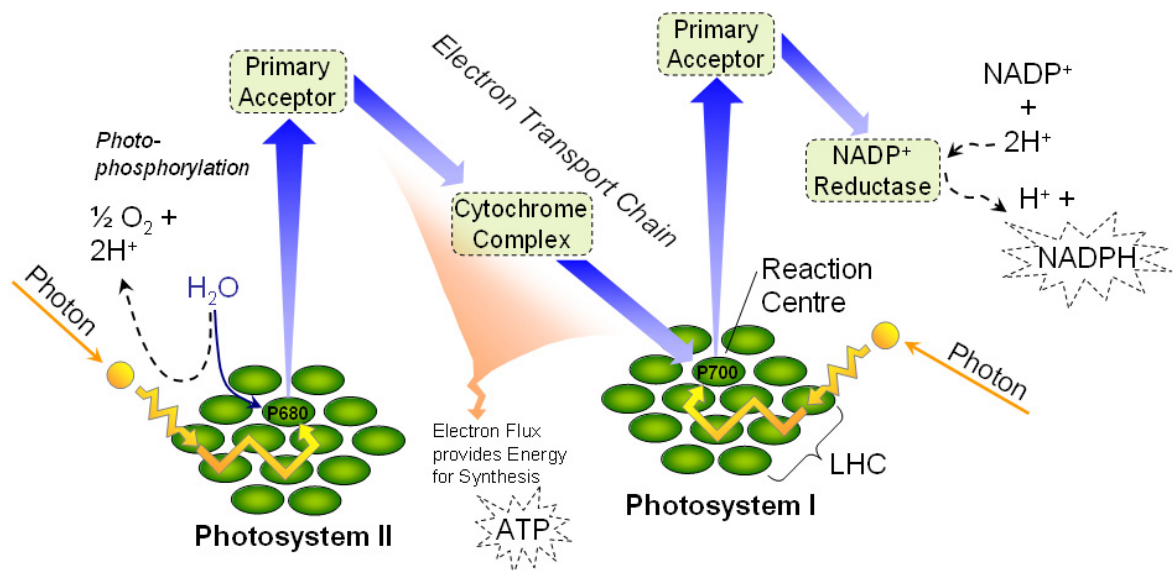


Figure 1.06: Electron transport chain passing the photosystems II and I.

The photophosphorylation can either be conducted in form of a non-cyclic electron transport (as shown in *fig. 1.06*) where ATP for the reduction of  $\text{CO}_2$  is produced, but also a cyclic electron transport through PSII is possible that generates additional ATP required for the support of other metabolic activities in the chloroplast. Thereby, the electrons pass a redox chain, leading

through the cytochrome complex, where a reductant termed “ferredoxine” is produced. During the cyclic or non-cyclic photophosphorylation, water (H<sub>2</sub>O) is split into hydrogen (H) and oxygen (O<sub>2</sub>). In case of a non-cyclic electron transport, the electrons are transported into the photosystem I after the photophosphorylation has taken place, where the electron level is even more elevated through the energy provided by the chlorophyll *P700*, finally resulting in the generation of NADPH.

Following that scheme, a continuous electron flux occurs within the thylakoids, where low level electrons are extracted from water, their energy level is elevated and a strong reductant (ferredoxine) is produced that is applied to the reduction of NADP<sup>+</sup> to NADPH (*fig. 1.06*). This NADPH also is a strong reductant, which is soluble in water and therefore is a mobile carrier for electron energy. NADPH diffuses freely through the stroma, where it is used to reduce CO<sub>2</sub> in the carbon reduction cycle (see section 1.5.2). During that process, oxygen is released and energy is stored within stable chemical compounds.

## 1.5.2 „Dark“ Reaction (Carbon Fixation)

Within the stroma of the chloroplast, the products of the “light” reaction are used to generate carbohydrates by establishing a covalence bond between the free hydrogen and the carbon dioxide from the surrounding air. This is where carbon is fixed from the atmosphere, a process that, regardless of its name, is not entirely independent from direct illumination, since some of the enzymes need an activating energy impulse in addition to the energy that is transported via ATP and NADPH (HOPKINS 1999). The photosynthetic carbon reduction (PCR) is different for C<sub>3</sub> and C<sub>4</sub> plants. While for C<sub>3</sub> plants the Calvin-pathway is cycled, for C<sub>4</sub>-plants the Hatch-Slack-Cycle is passed before the Calvin-Cycle is set into action. Also a third variation of the pathway of carbon fixation exists in species that are specially adapted to arid environments. It is termed the Crassulacean-Acid-Metabolism (CAM). Since no families of CAM-species are modelled within the area of this study, this alternative is neglected here.

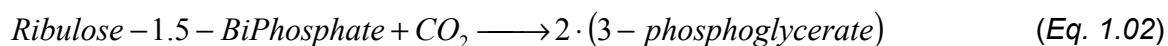
### 1.5.2.1 The Calvin-Cycle of C<sub>3</sub> Plants

The carbon fixation itself is conducted with the help of energy that is transported into the stroma through the NADPH compounds. The cycling process that applies to C<sub>3</sub> plants is termed the Calvin cycle or Calvin-Benson cycle, according to the scientists that paved the way for a deeper understanding of the carbon reduction processes, Melvin Calvin and Andrew Benson (BASSHAM ET AL. 1950).

The CO<sub>2</sub> that enters the leaf via the stomata is fixed by Ribulose-Biphosphate (RuBP), a sugar molecule. The reaction is catalysed by the receptor enzyme Ribulose-1.5-BiPhosphate-Carboxylase. Due to its ability to catalyse a similar reaction not only for carbon dioxide but also

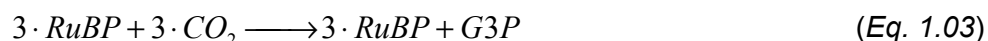
for oxygen, the molecule is also called RuBP Carboxylase/Oxygenase (RUBISCO). Amounting to about 50 percent of the soluble protein within the leaves of green plants, RUBISCO is supposed to be the most abundant protein on earth (HOPKINS 1999).

Through RUBISCO and CO<sub>2</sub>, a six-carbon intermediate molecule is formed, which is transient and unstable, so that it quickly is hydrolyzed to two molecules of 3-phosphoglycerate (3-PGA, eq. 1.02).



The first stable product in the cycle of carbon fixation therefore is a three-carbon molecule, which is the reason for this way of carbon fixation being referred to as the C<sub>3</sub> cycle (HOPKINS 1999).

Within the Calvin-cycle, two processes require the energy that has been stored by the “light” reaction in form of ATP and NADPH, as there are the reduction of 3-PGA on one hand and the regeneration of the RuBP receptor molecule on the other. The 3-PGA is reduced to a triose sugar-phosphate (glyceraldehyde-3-phosphate, G3P) through a two-step reaction, where the intermediate form of 1,3-BiPhosphateGlycerate is rapidly passed. The G3P is exported to the cytoplasm where the triose molecules are joined to synthesize fructose-phosphate and glucose-phosphate. Those triose phosphates later are used in a competitive process for the synthesis of either starch that is stored within the chloroplasts or sucrose, which is exported into the cytosol. The regeneration of the RuBP receptor enzyme is accomplished by a series of reactions, whose net message is that the uptake of three CO<sub>2</sub> molecules is needed for the regeneration of three RuBP molecules (eq. 1.03).



The regeneration of the receptor enzyme therefore equals the speed of the cycle (fig. 1.07). Equation 1.03 indicates that only every third turn of the cycle, that is to say every third CO<sub>2</sub> molecule that is taken up, produces an additional glycerol-aldehyde-3-phosphate (G3P), so that in total 12 turns of the cycle are necessary for the generation of one glucose molecule, which is the final product of the photosynthesis.

The energy consumed by both processes, the RuBP regeneration and the 3-PGA reduction, amounts to 2 molecules of NADPH and 3 molecules of ATP that are required for the reduction of each molecule of CO<sub>2</sub>. Since the activity of RUBISCO is highly sensitive to light, independent of the amount of available energy through ATP and NADPH, the rate of photosynthesis is a very variable process.

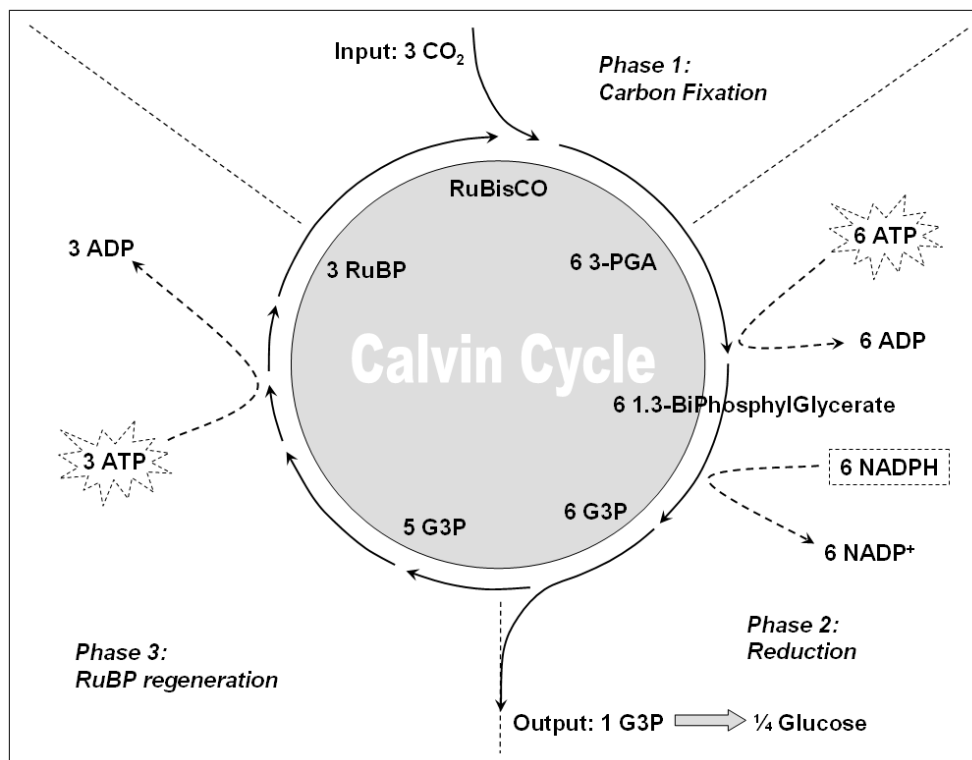


Figure 1.07: Calvin cycle of the carbon fixation in  $C_3$  plants, indicating the energy consumption for the fixation of 3 carbon dioxide molecules.

### 1.5.2.2 The Hatch-Slack-Cycle of $C_4$ Plants

The discovery of the cycle of  $C_4$  carboxylation can be traced to the scientists H. P. Kortschak, M. D. Hatch and C. R. Slack (KORTSCHAK ET AL. 1965, HATCH AND SLACK 1966). Consequently the  $C_4$  pathway is also termed the Hatch-Slack-Kortschak-Cycle. For  $C_4$ -plants, the process of carbon fixation is different from that of the  $C_3$ -plants, mainly due to some general anatomic differences.  $C_4$ -plants incorporate two different photosynthetic tissues, the bundle sheath cells on one hand and the mesophyll on the other. Being traced back to the German anatomist G. Haberlandt, this special characteristic is internationally known as the “Kranz”-anatomy (TAIZ AND ZEIGER 2000).

The  $C_4$  cycle is determined by the enzyme phosphoenol pyruvate carboxylase (PEPcase), which catalyzes the carboxylation of phosphoenol pyruvate (PEP) using  $\text{HCO}_3^-$  as the substrate rather than  $\text{CO}_2$ . The product of this reaction is oxaloacetate (OAA), a four carbon molecule that is moderately unstable and is quickly transformed to a more stable acid, either by reduction to malate or by transamination to aspartate, which then is transported from the mesophyll into the bundle sheath cells. There, the acid undergoes a carboxylation that results in available  $\text{CO}_2$  that is used for the reduction of triose sugars via the PCR-cycle analogue to the Calvin-cycle of  $C_3$ -plants. The PEPcase of  $C_4$ -plants therefore plays a role similar to that of RUBISCO for  $C_3$ -plants. The great difference to the  $C_3$  pathway is based on the fact that  $\text{CO}_2$  is assimilated in the mesophyll and then is transported into the bundle sheath cells via  $C_4$  acids. In the bundle sheath, the acids are decarboxylated and release their stored  $\text{CO}_2$  again directly at the site of

the PCR. Due to their ability to artificially concentrate  $\text{CO}_2$  at the site of carboxylation, the  $\text{C}_4$ -plants are not as sensitive to external  $\text{CO}_2$  concentrations as  $\text{C}_3$ -plants.

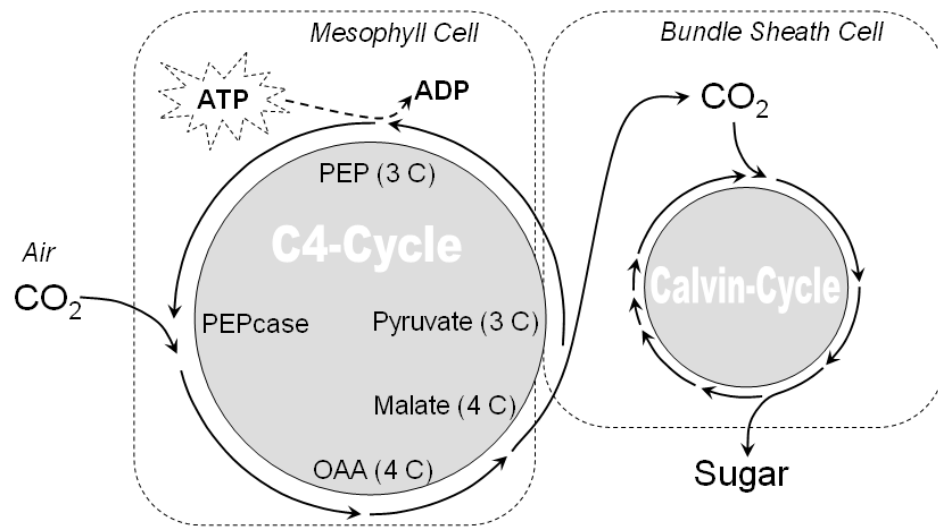


Figure 1.08:  $\text{C}_4$  cycle of carbon fixation, indicating the additional energy consumption for the regeneration of the PEPcase.

Under optimal conditions,  $\text{C}_4$  species are able to assimilate  $\text{CO}_2$  at rates two or three times that of  $\text{C}_3$  species. But not all of this advantage is converted into photosynthetic productivity because the concentration of  $\text{CO}_2$  in the bundle sheath cells costs additional energy. For each assimilated  $\text{CO}_2$  molecule, two ATP molecules must be expended for the regeneration of PEP in addition to the ATP and NADPH that is required for the maintenance of the PCR cycle (fig. 1.08). The overall energy consumption of the  $\text{C}_4$  photosynthesis therefore amounts to 2 molecules of NADPH and 5 molecules of ATP per molecule of fixed  $\text{CO}_2$ .

## 1.6 The Leaf Photosynthesis Model by Farquhar, von Caemmerer and Berry

The core model that is applied in this work for the modelling of the photosynthetic productivity is based on the biochemical model for photosynthetic  $\text{CO}_2$  assimilation by G. D. Farquhar, S. von Caemmerer and J. A. Berry (FARQUHAR ET AL. 1980). The model was initially developed for the modelling on the leaf scale only. However, it has become one of the most important biological models and has largely contributed to the enhancement of the understanding of photosynthetic activity (FARQUHAR ET AL. 2001). Keeping in mind the models origin as a leaf model, the adaptation to the simulation of the photosynthetic behaviour of a whole landscape is an appealing challenge for this work. Other contributions (i.e. FIELD ET AL. 1996, FIELD 2000) are showing that the adaptation of the “Farquhar”-model on the global scale is currently in progress.

The mathematical description of photosynthetic activity, as proposed by Farquhar et al., is a further development of the early photosynthesis models developed by HALL AND BJÖRKMANN (1975), PEISKER (1976) and BERRY AND FARQUHAR (1978). Since its publication in 1980, the model has been improved and enhanced continually (FARQUHAR AND VON CAEMMERER 1982, VON CAEMMERER 2000, BUCKLEY AND FARQUHAR 2004, MCNEVIN ET AL. 2006).

The model simulates various aspects of the biochemistry of photosynthetic carbon assimilation in  $C_3$  species. The most determinant of them include the kinetic properties of ribulose biphosphate carboxylase/oxygenase (RUBISCO), the requirements for the photosynthetic carbon reduction and photorespiratory carbon oxidation cycles, the dependence of electron transport on photon flux and the presence of a temperature dependent upper limit to electron transport.

The outstanding character of the model is based on its unique way to describe the rate of net photosynthesis as the result of the competing processes of carboxylation and oxygenation, which again are limited on one hand by the fixation capacity of RUBISCO and on the other by the rate of the electron transport through the photosystems (*fig. 1.09*). The rate of the electron transport again determines the regeneration of the receptor enzyme RuBP (see section 1.5.2.1), so that the limiting processes in the model are interconnected.

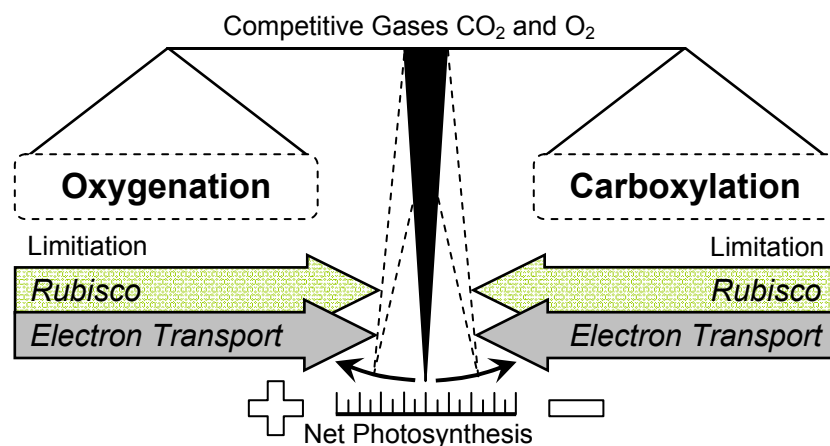


Figure 1.09: Representation of the general assumptions of the "Farquhar et al." model of photosynthesis.

While the availability of RUBISCO in the model mainly is determined by the CO<sub>2</sub> supply, the electron transport greatly depends on the amount of absorbed light quanta (FALGE 1995). The resulting rate of photosynthesis therefore is not only the product of environmental conditions, but is controlled by two determinant limiting processes that again are highly sensitive to external environmental conditions such as the atmospheric CO<sub>2</sub> concentration, air and leaf temperature or the radiation budget. A detailed description of the mathematic content of the model, as it was implemented into the PROMET model environment, is given in section 3.3.3.5.

## 2. The Upper Danube Catchment

Since the issues of this work are closely connected to the requirements and the objectives of the GLOWA-Danube cooperative project, the area of this study is limited to the watershed boundaries of the river Danube and again restricted to the catchment area of the Upper Danube. The Upper Danube catchment is defined by the area drained via the gauge “Achleiten” in Austria. The gauge Achleiten is located shortly downstream the city of Passau and drains an area of more than  $76 \times 10^3 \text{ km}^2$ . The resulting catchment area has a geographic extension of roughly  $8.5^\circ \text{ E}$  to  $14^\circ \text{ E}$  and of  $46^\circ \text{ N}$  to  $50^\circ \text{ N}$  (*fig. 2.01*).

As has been mentioned in section 1.3, the selection of this area was based on various reasons, among them being the diversity with respect to the natural environment and the socio-economic characteristics of the area that is drained by the Danube. The general characteristics of the Upper Danube catchment can give an insight into the natural diversity of the river basin and are briefly introduced in the following. For a more detailed characterization of the Upper Danube Basin it is referred to BRAUN (2007).

### 2.1 Natural Realities

The Danube has a great historic and economic significance, which can be traced back to an outstanding characteristic that distinguishes this river from other European streams. It is flowing over a great distance in an East-West direction, while most other navigable European rivers like the Rhine, Elbe, Oder, Rhône or Volga are either streaming North- or Southward.

With a length of 2 857 km from well to estuary, the Danube represents the second largest river in Europe, being only exceeded by the Volga with a total length of 3 685 km. For comparison, the world's longest river, the Nile with a total length of 6 671 km, is flowing more than twice the distance of the Danube River. Nonetheless, the Danube extends from  $8^\circ 09' \text{ E}$  to  $29^\circ 45' \text{ E}$  and encompasses a total area of  $817 \times 10^3 \text{ km}^2$ , where it unites versatile landscapes that represent an overview of the central European landscape diversity (*fig. 2.01*). The basin area covers large parts of the Alps, comprising glaciated mountains, forested low mountain ranges, hill countries and vast periglacial brash plains. The full catchment stretches across 18 European countries, from the Danube source at the confluence of the headstreams Brigach and Breg in the East of Donaueschingen in Southern-Germany, to its destination near the seaport Constanta in Eastern-Romania, where the Danube discharges into the Black Sea (RZD 1986, *fig. 2.01*).

The upper part of the catchment, referred to as the “Upper Danube” in the following, is delineated at the gauge Achleiten (287 m a.s.l.) shortly below the city of Passau, where the



Danube tributaries Inn and Ilz are discharging into the main stream (*fig. 2.01* and *fig. 2.06*). The catchment upstream from this point covers an area of 76 653 km<sup>2</sup> with a river length of approximately 580 km (BLFW 1999).

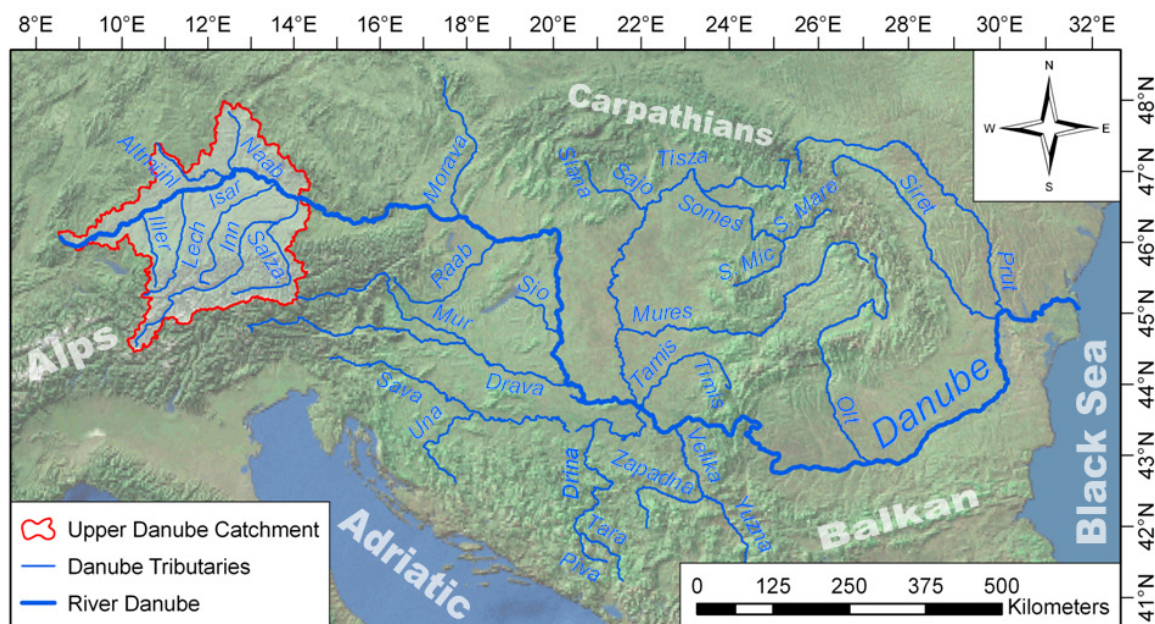


Figure 2.01: The Upper Danube catchment defined by the gauge “Achleiten” (287 m a.s.l.) in relation to the entire Danube river system, including the major tributaries (Backdrop: World map taken from ESRI Globe Data).

If the catchment area is categorized into natural landscape units, the low mountain ranges of the Black Forest to the West, the Swabian and the Franconian Alb to the North, the Bavarian and Bohemian Forest in the East have to be discerned from the hilly Alpine Foreland and the high Alps in the South (*fig. 2.03*). In the central region of the catchment, large fen landscapes are found such as the Donauried, the Donaumoos and the Dungau.

Five European countries are part of the territory of the Upper Danube, while the largest part is situated in Germany in the states of Bavaria (62 %) and Baden-Württemberg (11 %). One of the main tributaries to the Danube, the Inn (*fig. 2.01* and *2.06*), has its headwater located in Austria (24 %) with minor parts in Switzerland (2 %) and Italy (< 1 %). Additionally, a small part in the East of the catchment belongs to the Czech Republic (BLFW 1999, *fig. 2.02*).

The Western and Northern boundary of the Upper Danube Basin is defined by the so called European watershed that divides the catchment of the river Rhine from the Danube drainage basin. In the North, the drainage system of the river Elbe borders the Danube basin, while the neighbouring river systems in the South belong to the streams Po and Etsch, who have their headwaters located in the Italian Alps. Towards the East, the adjacent basins belong to the central part of the Danube catchment itself (*fig. 2.01*). Within the Upper Danube Basin, the major tributary rivers that are entering the main stream from the orographically sinistral side include the Wörnitz, the Altmühl, the Naab and the Regen, while on the dextral side the Iller, the Lech, the Isar and the Inn are joining the Danube river. Among those, the Inn is the largest

contributor to the Danube, covering a catchment area of  $26.13 \times 10^3 \text{ km}^2$ . The part of the Upper Danube catchment that is accessed by the Inn is the part of the basin that reaches farthest into the Alps and includes high alpine territory, the highest point being located at Piz Bernina with 4049 m a.s.l. (RZD 1986, BLFW 1999).

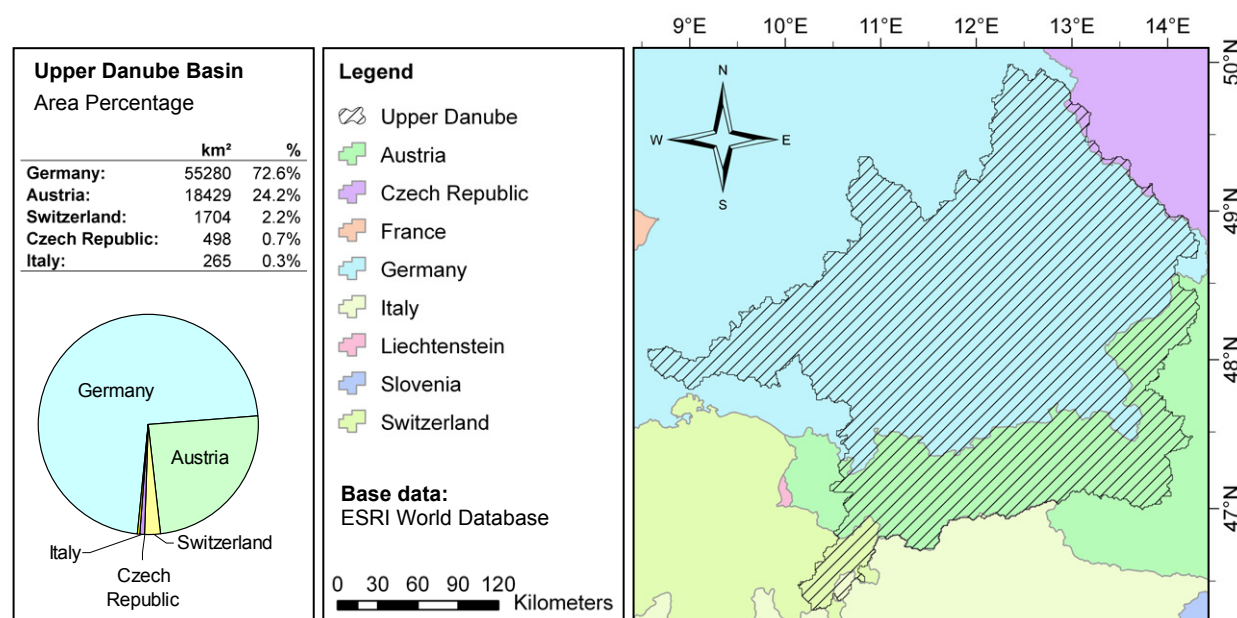


Figure 2.02: The Upper Danube catchment area in relation to the Central European countries that are part of it (Base data: ESRI World Database).

## 2.2 Geology and Geomorphology

The area is characterized by a variety of geological media that allow for a rough geographical classification. Here will have to be discerned a high alpine part from the alpine foreland and the region of the low mountain ranges of the Swabian and Franconian Albs (MEYNEN AND SCHMITHÜSEN 1953, *fig. 2.03*).

The central Alps are primarily composed of crystalline shale and granite, while the Northern rim and the foothills consist of limestone, which is locally moulded with typical alteration formations. Especially the karst alteration has to be mentioned here that most intensively determines the surface morphology through calcite solution processes and can be observed in all limestone based parts of the Alps (LANGENSCHIEDT 2001, FISCHER 2006). Directing the view further to the North, the foothills of the Alps are followed by clastic sedimentations of the flysch zone and a narrow band of rock formations termed the helvetic nappes (RAMSAY 1981). Large deposits of folded Molasse sediments, a by-product of erosion processes that occurred during the genesis of the Alps, form the Southern part of the alpine foreland (*fig. 2.04*). The Molasse is covered in most places by quarternary unconsolidated sediments of the Würm glacial period. In some parts of the alpine foreland, aeolian loess sediments cover the glacial rubbles and allow for the genesis of fertile soils. With the end of the Würm ice age about 12 000 years before present, the

melting glacial ice cover left a landscape that is shaped with typical fluvial and fluvio-glacial landforms. The large surface water bodies of the Chiemsee, Ammersee and Starnberger See are some of the more prominent vestiges of the glacial period (MEYER AND SCHMIDT-KALER 1997).

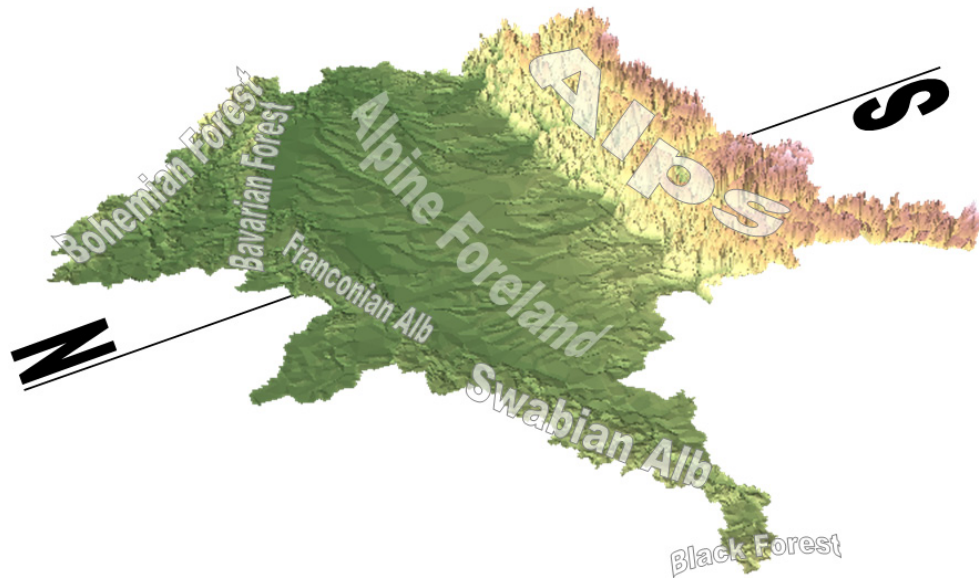


Figure 2.03: Three-Dimensional bird's eye view of the Upper Danube catchment seen from the West, based on a 1 x 1 km resolution DEM applying a superelevation factor of 10. Indication of the major low and high mountain ranges.

Beyond the reach of the glacial ice masses, the coverage of which still can be reconstructed through the arched ridges of the terminal moraines, the Molasse basin continues towards the North (fig. 2.04).

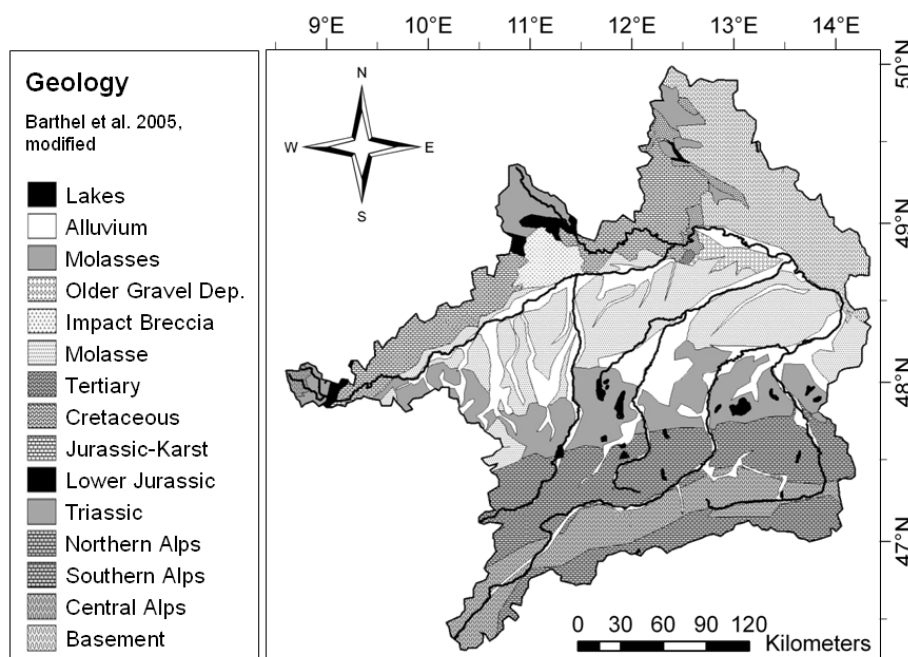


Figure 2.04: Geologic map of the Upper Danube Basin, modified after Barthel et al. (2005).

In the North, the Molasse is shaping a hilly landscape that is termed the tertiary hill country. The tertiary hills are partially divided by gravel plains of the larger rivers. Also the Danube River has carved its valley through these tertiary deposits, passing the Jurassic plateaus of the Swabian and the Franconian Jura, which are located in the North, as well as the crystalline mountains of the Bavarian Forest in the Northeast (JERZ 1993).

## 2.3 Climate

The climate of the Upper Danube area shows the typical characteristics of a seasonal climate zone. A temperature maximum in July and a minimum at the end of January are pointing towards a temperate continental climate. According to the genetic "Flohn" classification, the area is categorized as a transition climate of the extra tropical zone of Westerlies (FLOHN 1971). Following the effective "Köppen and Geiger" classification system (KÖPPEN 1936), the region is assigned to the *Cfb*-climate zone, indicating a cool, ever moist and temperate climate. Applying another effective global classification system following Troll and Paffen, the Upper Danube falls into the category of moderately cool climates. It is represented by the III3 climate zone, which describes a sub-oceanic transition climate with annual temperature amplitudes of 16 to 26 K and mild and moderately cool winters respectively, the coldest month not falling below an average temperature of -3 °C. The precipitation maximum occurs in the summer season, which is characterized by moderately warm temperatures and by a relatively long duration. The average vegetation period is supposed to last more than 200 days per year (TROLL AND PAFFEN 1964).

The weather in the Upper Danube area is dominated by patterns that are due to prevailing Westerlies, since the whole basin is located in the Northern mid-latitude temperate zone. The summer is characterized by North-Westerly and Westerly winds that change their direction of origin to mostly South-West during the winter. The summers are characterized by heavy rainfall due to the barrier effect of the Alps, which is fetching great amounts of humidity out of the steady North-West winds. By this effect, advection currents from the Northern Atlantic tend to bring enduring and yielding precipitation to the windward side of the Alps. During Southerly storms, the Upper Danube Basin happens to be situated on the leeward side of the Alps, where "Foehn" events occur. This local weather phenomenon is a common feature in the area's weather patterns, its influence sometimes extending as far to the North as the Danube valley. Mean annual precipitation sums are ranging from approximately 700 mm in the Danube valley to 1500 mm around the alpine foothills (*fig. 2.05*). At higher alpine elevations, larger precipitation sums that notably peak above 2000 mm have been recorded. The accumulation of precipitation along the successive alpine mountain ranges that occurs during Northerly meteorological conditions, greatly contributes to this increase of annual precipitation sums from North to South.



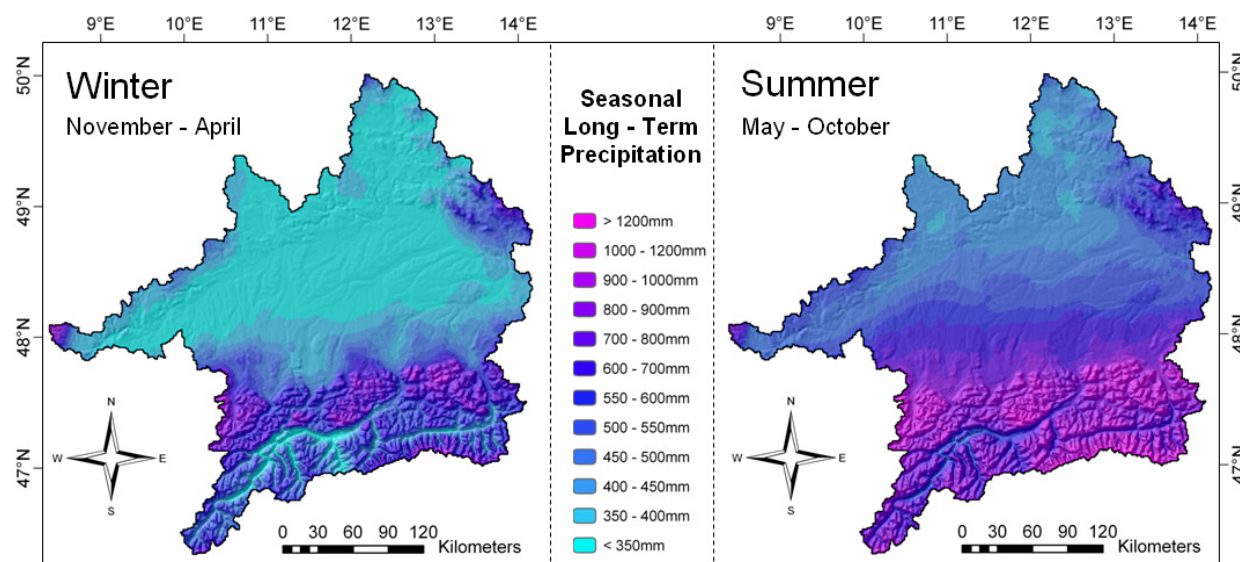


Figure 2.05: Interpolated long-term precipitation for the Upper Danube catchment discerned into the hydrological summer (May-October) and winter half-year (November-April), indicating the orographically induced South-to-North climate gradient. The displayed precipitation sums are interpolated model results for the 30-year time period from 1971-2000.

This gradient of precipitation applies to winter and summer rainfalls (*fig. 2.05*). The more elevated parts of the Black and the Bavarian Forest are also receiving annual precipitation sums of up to 1500 mm. While the plateaus of the Swabian and Franconian Alb also represent humid regions and tend to exceed 1000 mm a<sup>-1</sup>, the lowest precipitation sums are recorded in the basins of the rivers Altmühl and Naab as well as inside the ridge of the impact crater of the Nördlinger Ries, which dates from the Miocene (BMU 2003). Low annual rainfall also is reported from some of the central alpine valleys. The German part of the catchment (73 % of the total area, *fig. 2.02*), reaches an annual mean precipitation sum of 950 mm with the maximum of rainfall occurring in the summer (*fig. 2.05, right*). Especially in the alpine foreland, extreme local weather events like thunderstorms may bring up to 200 mm of precipitation per day during the summer months (RZD 1986).

The duration of the snow cover is another important landscape characteristic that can be applied for the description of the climatic conditions (*fig. 2.06, left*). 40 - 60 days of annual snow cover are reported for large parts of the catchment area, while the duration may exceed 100 days in the mountainous parts at higher elevations. In the Alps, the snow cover may last around six to eight months of the year at elevations of 2000 m. With an increasing gradient, ranging from the outskirts to the central Alps, the elevation of a perennial snow cover lies between 2900 and 3200 m a.s.l. (RZD 1986). Last but not least, the snow cover stability depends on the distribution of the annual mean temperature, which again is greatly influenced by the orography of the area (*fig. 2.06, right*). While the mean temperature in large parts of the alpine foreland levels around 7 – 8 °C, some favoured locations along the Danube River and in the lower parts of its tributaries may report annual mean temperatures of 8 to 10 °C. Annual temperature averages below the freezing point are commonly recorded in the mountains.

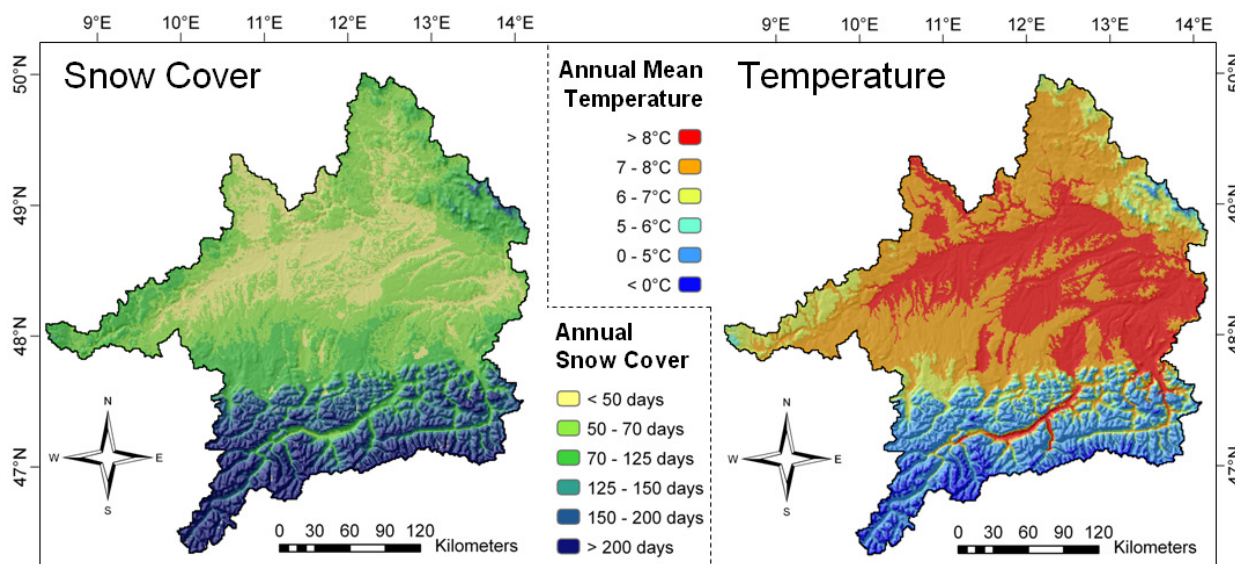


Figure 2.06: Modelled long term duration of the snow cover (left, base data: MAUSER ET AL. 2007) and interpolated annual mean temperature (right) of the Upper Danube Basin, indicating the orographically induced South-to-North climate gradient. The snow cover duration and the temperature map both show averaged model results, calculated for a 30-year time period (1971 – 2000).

The highest monthly mean temperatures are observed in July with 16 to 18 °C, while the coldest month turns out to be January, when mean temperatures between –2 and –3 °C are recorded. According to the general elevation gradient, the temperatures in the mountainous parts of the catchment decline with increasing altitude. The temperature gradient can be expressed with a rate of 0.5 - 0.7 K per 100 m in the summer, while the gradient is reduced to 0.2 - 0.4 K per 100 m during wintertime, due to frequent atmospheric inversion weather patterns (RZD 1986). It is a common feature of terrain with high relief energy, such as the Upper Danube Basin, that pronounced small-scale variations of climate often occur due to the local diversity of the radiation budget, air temperature, cloud cover, wind conditions and precipitation.

## 2.4 Hydrology

During the younger Tertiary and the advanced Pleistocene (approx. 1.7 m ybp), the drainage system in the alpine foreland was influenced by tectonic activities. Especially the Rhine rift, that has been caving in since the Eocene and still is sinking deeper today, has determined the diverging flow directions of the Danube and the Rhine river system (KLÜPFEL 1926).

The early ancestor of the Danube river system, the Aare-Danube, was established in the Miocene (25 - 5 m ybp), taking a course along the Northern rim of the alpine Molasse basin and collected the waters that were flowing from the Alps in a Northerly direction. The Aare-Danube to that time was a big alpine river that also gathered great water masses from the Swiss midlands, a process that can still be reconstructed by comparing alpine gravel samples from the Alb plateau and the Swiss Jura. Other gravel findings indicate that the Aare-Danube also received discharges from the Southern- and Mid-Black Forest. To that time, also large parts of

the Neckar basin were drained into the Molasse basin and only the northernmost part of the Neckar already belonged to the Ur-Rhine catchment. During the middle of the Pliocene (5 – 1.7 m ybp), the erosion power of the Aare was outmatched by the tectonic elevation of the Black Forest, so that the Aare was truncated from the Danube river system and changed its course towards the Mediterranean, depriving the Danube of one of its main alpine tributaries.

During the high Pliocene, the accelerated descend of the Upper Rhine Graben led to a crossing of the Kaiserstuhl watershed by the Ur-Rhine. This again changed the course of the Aare and integrated the Aare into the Rhine river system, strongly enforcing the erosion power of the Rhine. The regressive erosion of the Rhine again was strengthened by large masses of melting water during the Würm ice age, finally leading to the carving of the Wutach valley. That way, the Danube lost another determinant tributary to the Rhine river system. The Wutach erosion is still going on today, gradually shifting the Rhine-Danube watershed and cutting off more and more of the Danube catchment. It is expected that in geologic times the upper part of the Danube will completely change its course and become a tributary to the Rhine river system.

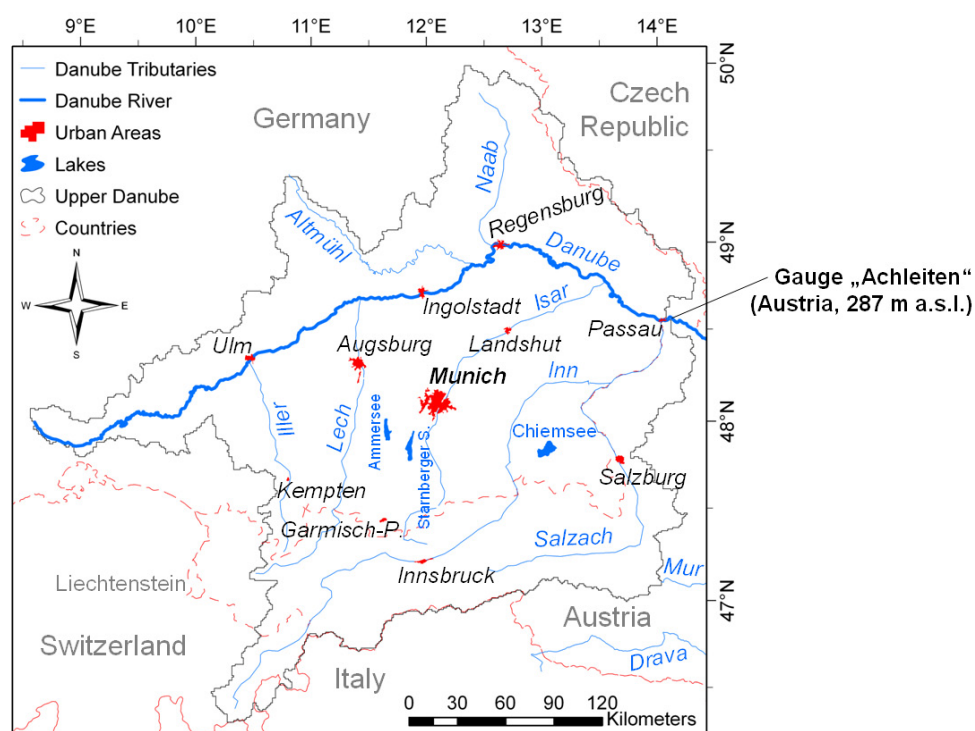


Figure 2.07: The Upper Danube catchment defined by the Austrian gauge "Achleiten" (287 m a.s.l.) with its major tributaries and urban settlements in relation to the central European countries that are part of it.

Nowadays, the alpine foreland is intersected by a number of rivers that are flowing from the Alps in a Northerly direction. Their course is deflected by the Danube, who is taking a course parallel to the mountain range of the Alps. The great number of tributaries is strongly influencing the flow regime of the Danube. Along the course of the main river, the hydrologic flow regime changes several times, according to the influence that the flow regimes of its affluents are taking. The alpine tributaries are characterized by a maximum discharge during the summer

months due to snow melt and glacier runoff, while the rivers coming from the North can be described as a pluvial regime type with their runoff maxima in the winter. Frequent flood situations during the early summer months are a common phenomenon due to the high precipitation rates along the northward side of the Alps.

The mean discharge rate of the Upper Danube measured at the gauge Achleiten near the city of Passau (*fig. 2.07*) lies around  $1420 \text{ m}^3 \text{ s}^{-1}$  (LUDWIG ET AL. 2003), more than half of this amount being contributed by the large catchment of the tributary Inn, whose drainage area reaches far into the Alps (BLFW 1999). Most of the rivers nowadays are regulated by dams and hydropower stations, so that a natural condition of discharge no longer can be found in the hydrographs of the Danube tributaries. Also the natural erosion capacity and sediment transportation is inhibited by the structures that control the discharge rates. The Pleistocene glaciations intensively formed the South of the Upper Danube and left a multitude of Lakelands, which are now also contributing to a balanced hydrograph, thanks to the compensating effect of their retention potential.

## 2.5 Soils

Regional variations of the factors and processes of soil formation such as bedrock, terrain, climate, vegetation or time, lead to the development of a multitude of different soil types in the Upper Danube Basin. The soil textures are ranging from loamy clays to grainy sand and, due to the great natural disparities, the variety of soil types ranges from weakly developed Leptosols in the mountain regions to fertile Luvisols that have been developing on aeolian loess sediments since the ice ages and nowadays are used intensively for agricultural purposes.

According to the climatic gradient, the young soils in the Alps are not very strongly developed in depth. They are discerned by the type of bedrock into Lithics or rendzic and umbric Leptosols. In the forested altitudinal belts, Regosols and some chromic Cambisols are developed on carbonate rocks, while the crystalline bedrock regions of the central Alps more favoured the development of umbric Leptosols and albic Luvisols. Along the valley floors, eutric Leptosols, Luvisols, Cambisols as well as gleyic Luvisols and Gleysols occur locally. On the moraine ridges that pervade the alpine foreland as well as on the permeable gravel plains, mainly Luvisols are developed. Some rendzic Leptosols are found in the gravel basin that surrounds the city of Munich. The loess sediments in the tertiary hill country encouraged the development of Luvisols and Cambisols. Depending on the ground water level, gleyic Luvisols and Gleysols are frequent. Along the courses of the numerous rivers, brooks and ditches that are found throughout the Upper Danube area, Fluvisols are found. The postglacial Lakelands are blotched with vast fens yielding peaty soils that are economically exploited in many places. The Swabian and Franconian low mountain ranges are mostly covered by rendzic Leptosols and chromic



Cambisols, which are predominant on the upper Jurassic, while Vertisols and gleyic Luvisols are found on brown and lower Jurassic bedrock. On the crystalline rock formations of the Bavarian, Bohemian and the Black Forest, umbric Leptosols and fertile Cambisols dominate, which tend to podsolize on granite and gneissic rock (KUNTZE ET AL. 1994, HINTERMAIER-ERHARD AND ZECH 1997).

## 2.6 Vegetation

The economically propelled anthropogenic influence in the basin of the Upper Danube has diluted the natural distribution of vegetation types over the centuries. Under natural conditions, the spatial distribution of plant biomes is a product of the climatic, geologic and geomorphologic properties of the landscape.

In the case of the Upper Danube Basin, the potential natural vegetation would largely be represented by deciduous and mixed forests in almost all of the area (RZD 1986). Under undisturbed natural conditions, deciduous forests dominated by beech (*fagus sylvatica*) and oak species (*quercus robur* and *quercus petraea*) would inhabit the parts of the basin that lie below the critical altitudinal belts, where climatic conditions inhibit the prevalence of the species.

The situation today reveals, that man has claimed most of the territory that provides suitable conditions for agricultural purposes, while the forest stands have shifted to sites that are not accessible for mechanically supported cultivation techniques. Local phenomena of the alpine Foreland that visualize the process of forest suppression, are the steep moraine ridges that in some places are the only forested arcs that intersect the rural landscape.

Economic forestry has substituted the natural vegetation by large plantings of spruce (*picea abies*), so that only few pure deciduous forests still are found. Wherever lack of human impact allows for a natural vegetation development, zones that are unique and rich in species remain. The stripes of forest that are lining the alluvial zones of the Danube and its tributaries may serve as an example for undisturbed vegetation. In the more elevated montane and subalpine altitudinal belts of the mountainous areas, mixed mountain forests composed of spruce, white fir (*abies alba*) and beech as well as coniferous forests are situated. Anthropogenic influence has led to a domination of spruce in the alpine surroundings as well, so that the timberline, which is found at about 1800 – 1900 m in the Upper Danube catchment, is also composed of spruce trees.

The central part of the Alps, which is receiving noticeable less precipitation than the Northern rim (fig. 2.05), also inhabits spruce in the lower stands, while larch (*larix decidua*) and more scarcely swiss stone pine (*pinus cembra*) and mountain pine (*pinus mugo*) climb heights up to the elevated central alpine timberline at 2400 m. Above this altitude, only grasses (*carex curvula*) and ericaceae (i.e. *calluna vulgaris*) remain, representing native species that are

adequately adapted to the extreme alpine environment (ELLENBERG 1996). In the South of Bavaria, some of the once widespread moorlands have been preserved in their natural state and are no longer exploited through the commercial extraction of peat.

## 2.7 Socio-Economic Aspects

The landscape of the Upper Danube catchment has been intensely influenced, formed and modified by the activity of man. The area is inhabited by about 11 million people, resulting in a dense population of more than 100 inhabitants per square kilometre, combined with a vivid economic activity. The largest settlements of the area are the agglomerations of Munich with 1.2 million inhabitants, followed by Augsburg with 260.000 and Ingolstadt with a population of 115.000 respectively (LUDWIG ET AL. 2003). Besides the high alpine crests, the whole area is well connected to public infrastructure and is easily accessible due to a dense traffic network (fig. 2.08).

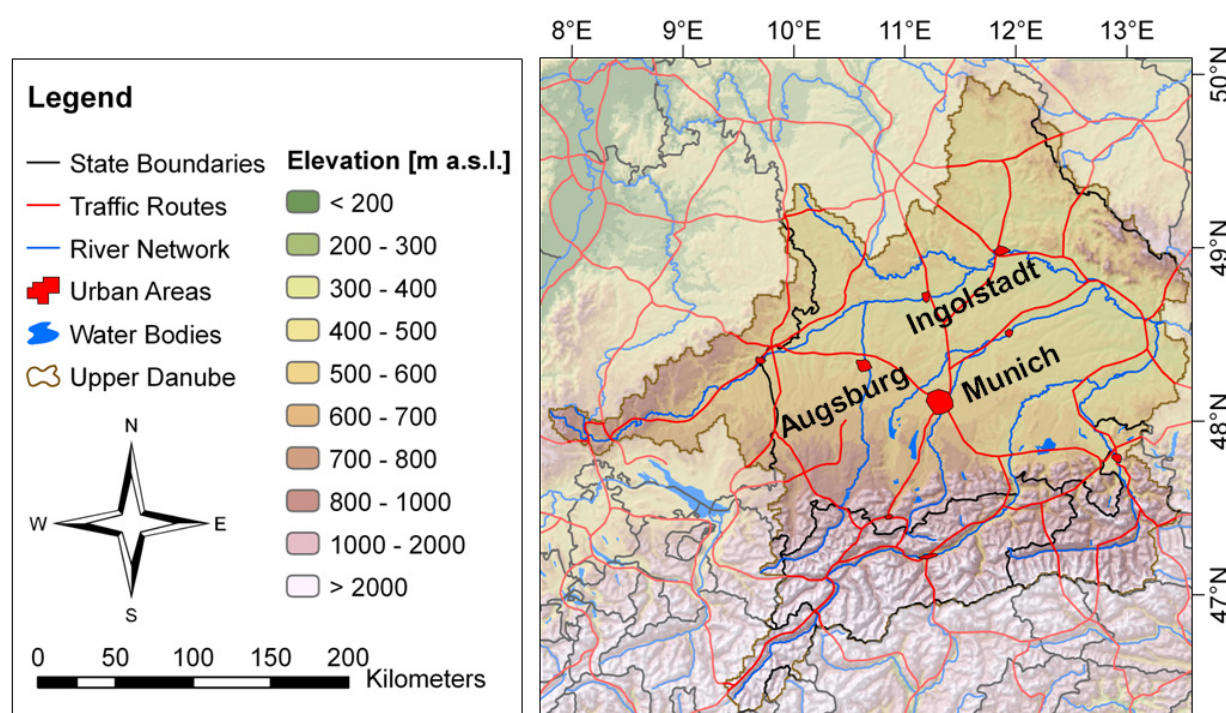


Figure 2.08: Topographic situation of the Upper Danube catchment including the major cities, traffic routes, rivers and surface water bodies (base data: ESRI World Database).

Surrounding the major cities, important industries have been established, while nearly all of the rural landscape is used agriculturally. Agriculture either manifests in form of meadows and pastures, that nourish a multitude of dairy and meat farms, or in form of acres applied for the production of cereals and silage crops. Pastures even are found in the high and remote areas of the mountains. Common arable crops include winter and summer grains (mainly *triticum aestivum* L., *hordeum vulgare* L., *secale cereale* L.) as well as maize (*zea mays* L.). More

regionally concentrated, sugar-beet (*beta vulgaris*), potatoes (*solanum tuberosum L.*), canola (*brassica napus L.*) as well as specialized crops like hop (*humulus L.*) and asparagus (*asparagus L.*) are cultivated. It has to be mentioned that the agricultural landscape within the Upper Danube Basin is relatively small parcelled, compared to other European regions (BAYERISCHES STAATSMINISTERIUM FÜR LANDWIRTSCHAFT UND FORSTEN 2006). The climatically favourable low basins along the river Danube itself offer preferable conditions for agricultural purposes. With increasing elevation, the acres are repelled by extended pastures and grasslands, so that also the higher terrain, which rather limits agricultural productivity due to the colder climate, is used extensively.

One strong pillar of the tertiary industry in the Upper Danube is tourism. Especially the regions of the Alps and the Bavarian Forest are attractive for tourists, but also the cities of Munich and Salzburg as well as the numerous architectural relics such as castles and fortresses that date from the monarchic times, are helping to develop the tourism into an economic branch of substantial size.

The management of water resources is a topic widely pursued in the Upper Danube catchment by public and private institutions. The management not only includes the fresh water supply for people, trade and industries, but also flood protection and low flow management as well as the operation of hydropower facilities. Another issue of water management is the controlling of shipping traffic along the navigable routes of the Danube river system. The Rhine-Main-Danube-Channel connects the navigable part of the Danube below the estuary of the Altmühl to the Rhine-Main river system, forming an important international waterway that ranges from the Black Sea up to the North Sea. This hydrologic connection leads to an artificial export of water from the Danube basin into the Rhine-Main basin (LUDWIG ET AL. 2003).

Water management interventions led to a profound redesign of the natural watercourses according to the perceptions of hydraulic engineering. Especially the production of hydro power, but also flood protection measures, led to river regulations and to the construction of dams and storage reservoirs throughout the catchment area. Today, the Danube and its tributaries are largely regulated with numerous flow barrages and reservoir power stations. This process is accompanied by a substantial shortening of the natural river courses and a reduction of retention basins, delicately increasing the flood potential. Recent developments show the effects of a change in hydrological engineering that manifests in the reconstruction of retention areas and a renaturalisation of river courses according to the goals of the European water framework directive.

### 3. Coupling a Physically Based Landsurface Model with a Biological Description of Canopy Processes

#### 3.1 The Landsurface Simulator PROMET

The process of radiation mass and energy transfer model PROMET, developed and enhanced by MAUSER AND BACH (2008), is a physically based process model that simulates a wide variety of landsurface parameters. It is designed for world wide application and can be operated on different scales (MAUSER AND SCHÄDLICH 1998). PROMET has been adapted to fit within the DANUBIA modelling framework (MAUSER AND LUDWIG 2002) and is used as land surface core model of the climate change decision support system DANUBIA (LUDWIG ET AL. 2005). The main task of the model is the solution of the energy and water balance at the land surface, while all determinant fluxes are taken into account. It is developed in FORTRAN77 and FORTRAN90 code, guaranteeing high computational performance. PROMET requires input data in form of a raster based geographic information system (GIS, *fig. 3.01*). In addition, parameter sets that characterize the soil and vegetation properties as well as meteorological inputs are needed.

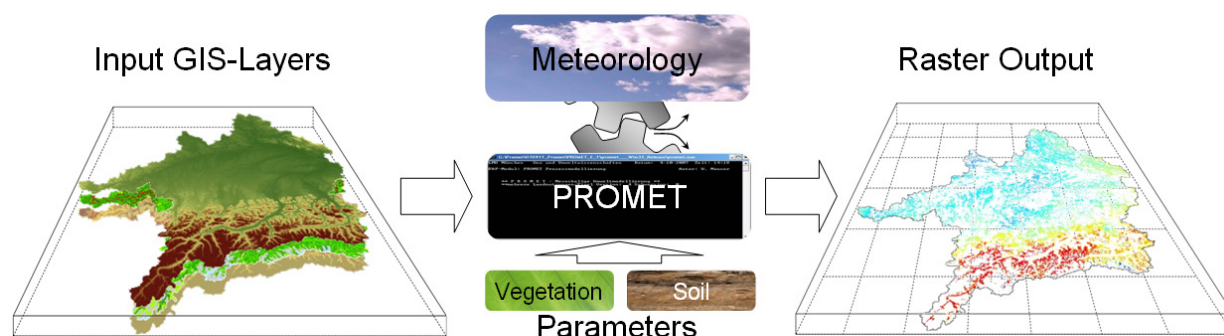


Figure 3.01: Exterior model design of the PROMET landsurface simulator.

The time step of the calculation is variable, but was set to one hour for all calculations presented in the context of this work. Within some submodels, like for the soil percolation, this frequency is overclocked to guarantee a numerically stable mapping of the fluxes. Every point of the raster array is calculated successively for each time step. The model can be preset to produce spatial results in form of GIS layers but is also applicable for single point or network calculations, which are stored as tables. The frequency of the output data normally matches the modelling time step, but the results can also be displayed and stored as aggregated daily, monthly or annual

values. The internal model architecture generally follows a top down cycle (*fig. 3.02*). The main model components are represented by:

- the interpolation of the input meteorology (MAUSER AND BACH 2008),
- the distribution of the incoming energy and the solution of the surface energy and water balance (CAMPBELL AND NORMAN 1998, OKE 1978, DINGMAN 1994),
- the simulation of the snow cover processes (STRASSER 1998),
- the straightforward vegetation model (BALDOCCHI ET AL. 1987),
- the soil percolation model (EAGLESON 1978).

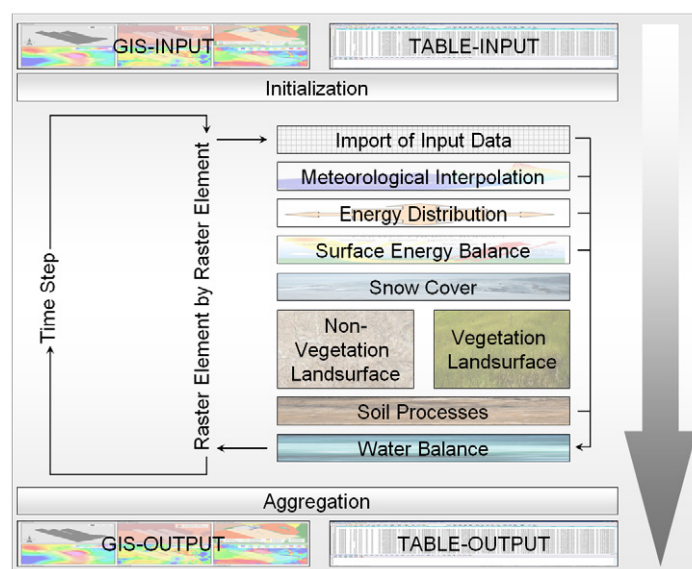


Figure 3.02: Interior top down model cycle of the PROMET model.

### 3.2 Adapting PROMET to the physically based Modelling of Photosynthesis

The PROMET model provides an excellent basis for a further development with regard to canopy processes. The GIS structure and the module based architecture allow for an easy coupling of additional modules. The core of the traditional calculation of the landsurface evapotranspiration in PROMET is based on the Penman-Monteith equation (PENMAN 1956, MONTEITH 1965). The resistances of the vegetation cover and the biomass generation, which are needed for the solution of that equation, are provided through a relatively straightforward vegetation model after BALDOCCHI ET AL. (1987). The carbon fluxes as well as the detailed energy fluxes are not taken into account so far. If the possible reactions of the landscape water household to a changing climate shall be investigated, the rough representation of the vegetation cover does not longer seem appropriate. The manifold interactions of the carbon dioxide supply with transpiration rates and biomass production, that again delicately affect the water balance of the landsurface, can only be mapped with a more sophisticated vegetation

model. Due to that reason, a vegetation module that is based on the detailed modelling of photosynthetic processes, considering the leaf energy balance as well as the leaf gas fluxes, was integrated into the PROMET model structure. The integration of the new vegetation module was designed in a way that still allows the calculation of the more static Penman-Monteith approach as an alternative. The explicit calculation of active plant growth though requires an extra set of input parameters (see section 3.3.4).

### 3.3 The PROMET Biological Model

In addition to the already available functionality of PROMET, the explicit biological module consists of five steps that are processed subsequently:

- Import of the parameters for all landuse categories.
- Initialization of the biological variables.
- Distribution of the incoming radiation.
- Steering of the biological routines via a management module.
- Computation of the leaf energy balance including the photosynthesis.
- Modelling of physical plant growth.
- Solution of the land surface energy balance.

The following section intends to give an insight into the chain of submodels and the modelled processes that are directly connected to the biological routines of the latest version of PROMET. A list of the applied mathematical symbols is given in the appendix (A.1). For further information concerning the modelling of inanimate landscape processes, it is referred to MUERTH (2008) for the soil and surface energy balance and to MARKE (2008) for meteorological scaling methods.

#### 3.3.1 Radiation

As mentioned above, PROMET follows a top down approach for its model cycle. The beginning of the calculation therefore is marked by the import of the meteorological parameters and commences with the distribution of the incoming energy into the canopy. Since the PROMET biological routines are the major topic of this work, only the irradiative processes that are directly connected with the vegetated land surface are described here.

The major force that is driving the processes at the land surface is the incoming radiation. Since the vegetated land surface in PROMET is modelled as a two layered canopy, the distribution of the incoming energy into the canopy has to be performed for the two layers successively. Only the amount of energy that is intercepted by the leaves is available for the biological processes, so that in a first step, a coefficient that describes the extinction of a solar beam by the leaves is determined. CAMPBELL AND NORMAN (1998) decided that the leaf properties of a crop could best be described through a random ellipsoidal distribution of the leaves. The extinction coefficient

for direct radiation ( $K_{ed}$ ) is calculated following CAMPBELL (1986) in dependence of a shape parameter ( $\chi$ ) and the solar zenith angle ( $\Psi$ , eq. 3.01).

$$K_{ed}(\Psi) = \frac{\sqrt{\chi^2 + \tan^2 \Psi}}{\chi + 1.774 \cdot (\chi + 1.182)^{-0.733}} \quad (\text{Eq. 3.01})$$

Here, the shape parameter ( $\chi$ ) is determined from the leaf angle ( $\beta_l$ ). For spherical leaf angle distributions, the parameter approaches a value of one, while for vertical leaf angles it becomes zero (eq. 3.02).

$$\chi(\beta_l) = \frac{-169.4338 \cdot \beta_l}{1 - 1.1222 \cdot \beta_l + 0.0009 \cdot \beta_l^2} \quad (\text{Eq. 3.02})$$

In order to simplify the calculations, the leaf angles in PROMET are set static for both canopy layers but are discerned into forested and non-forested categories according to table 3.01.

Table 3.01: Initialisation of the leaf angles and the corresponding shape parameters for two canopy layers.

	$\beta_l$ (Forest)	$\beta_l$ (Other)	X (Forest)	X (Other)
Upper layer:	40.11°	79.64°	2.28	0.31
Lower layer:	29.79°	63.02°	3.66	0.84

The extinction coefficient then is variable, depending on the solar zenith angle (fig. 3.03).

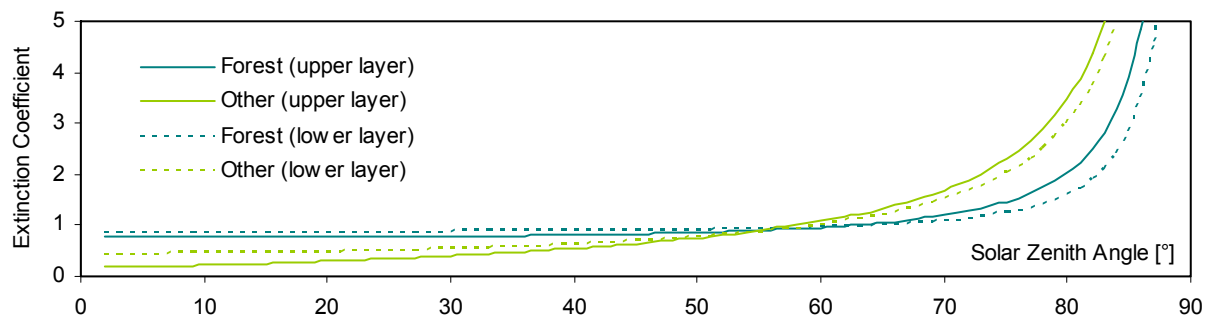


Figure 3.03: Course of the extinction coefficient for ellipsoidal canopies in dependence of the solar zenith angle.

The required solar zenith angle is determined for the current latitude and model hour. With the help of the extinction coefficient, the proportion of reflected sunlight, i.e. the albedo of the canopy ( $A_c$ ), can be determined following CAMPBELL AND NORMAN (1998). The canopy albedo depends on the sun elevation angle, which is expressed through the extinction coefficient mentioned above. It also is a function of the density of the canopy and of the albedo of the bare soil ( $A_s$ ) that is lying beneath the vegetation cover. Before the albedo can be determined, the canopy hemispherical reflection coefficient ( $\rho_{cpy}^H$ ) has to be calculated in dependence of the leaf



absorptivity for different wavelengths (eq. 3.03), accounting for the fact that leaves naturally are not black bodies. The absorptivity of the leaf for the photosynthetically active radiation range ( $\alpha_{par}$ ) is assumed with 89 %, while for the near infrared an absorptivity of 45 % is used ( $\alpha_{nir}$ , (EVANS 1987, BJÖRKMAN AND DEMMING 1987). The canopy hemispherical reflection coefficient then is the average of both spectral ranges (eq. 3.03).

$$\rho_{cpy}^H = 0.5 \cdot \left( \frac{1 - \sqrt{\alpha_{par}}}{1 + \sqrt{\alpha_{par}}} + \frac{1 - \sqrt{\alpha_{nir}}}{1 + \sqrt{\alpha_{nir}}} \right) \quad (\text{Eq. 3.03})$$

For a well developed canopy, as well as during the night, the underlying soil is neglected, so that the canopy albedo ( $A_c$ ) can be written as (eq. 3.04):

$$A_c = \frac{\rho_{cpy}^H \cdot 2 \cdot K_{ed}}{K_{ed} + 1} \quad (\text{Eq. 3.04})$$

For a less well developed canopy, the albedo has to be adjusted according to the fraction of bare soil that is shining through (eq. 3.05). Naturally, this process only is relevant during day time. The leaf absorptivity for the whole shortwave spectrum ( $\alpha_{sw}$ ) is applied here with an assumed average value of 70 % (EVANS 1987).

$$A_c = A_c - (A_c - A_s) \cdot e^{-2 \cdot \alpha_{sw} \cdot K_{ed} \cdot LAI} \quad (\text{Eq. 3.05})$$

The influence of the bare soil albedo, assumed with 20 %, on the total surface albedo, decreases with increasing leaf area values (LAI, fig. 3.04).

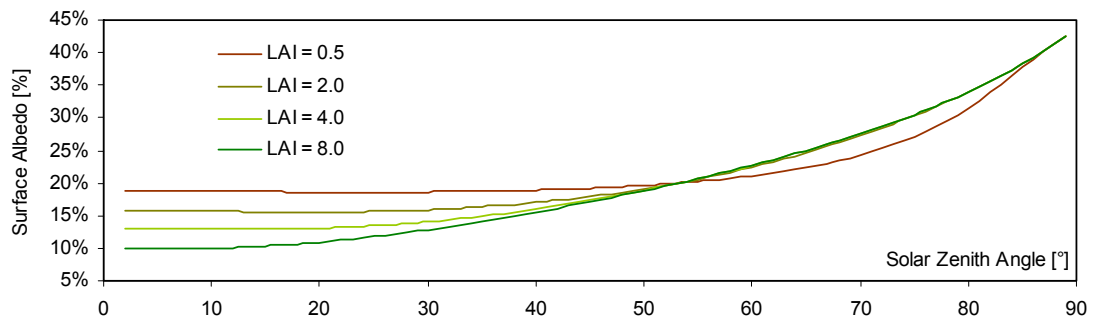


Figure 3.04: Variability of the surface albedo, as a combination of bare soil and canopy reflectance characteristics, in dependence of the solar zenith angle and the grade of development of the vegetation cover.

The amount of energy that is not reflected due to the canopy albedo will enter the canopy and has to be distributed to the two canopy layers. This includes the calculation of the sunlit or respectively shaded areas within the canopy layers, as well as an estimate of the fraction of



radiation that is transmitted through the canopy and will be available for soil processes beneath the vegetation layers.

During the night, when the solar zenith angle surmounts  $90^\circ$ , the whole canopy is assumed to be shaded. Consequently, the fraction of shaded leaf area is set to 100 % for all vegetation layers and no shortwave radiation is absorbed by the canopy. As soon as the sun is rising, the leaf area in the upper vegetation layer that is illuminated by direct sunlight ( $LA_{sun1}$ ) is determined as a function of the total leaf area in the upper layer ( $LA_1$ ) and the solar zenith angle ( $\Psi$ ) following BALDOCCHI ET AL. (1987, eq. 3.06).

$$LA_{sun1} = 1 - e^{\frac{-1 \cdot LA_1}{[2 \cdot \cos(\psi)]^2}} \quad (\text{Eq. 3.06})$$

The leaf area of the upper layer, which is shading the canopy beneath, has to be taken into account for the lower vegetation layer, so that equation 3.06 has to be modified (eq. 3.07).

$$LA_{sun2} = \left\{ 1 - e^{\frac{-1 \cdot (LA_1 + LA_2)}{[2 \cdot \cos(\psi)]^2}} \right\} - LA_{sun1} \quad (\text{Eq. 3.07})$$

From the respective sunlit leaf areas, the reciprocal fractions of shaded leaf area ( $S_{f1/2}$ ) can be derived for both canopy layers (eq. 3.08).

$$S_{f1/2} = 1 - \left( \frac{LA_{sun1/2}}{LA_{1/2}} \right) \quad (\text{Eq. 3.08})$$

The fraction of the incoming shortwave direct radiation has already been determined as the remainder of the incoming direct radiation that is not reflected due to the canopy albedo. For the incoming shortwave diffuse radiation, the intercepted portion ( $K_{dif}$ ) is calculated following CAMPBELL AND NORMAN (1998) as an exponential function of the overall leaf area (eq. 3.09).

$$K_{dif} = 0.8933 \cdot e^{0.0392 \cdot (LA_1 + LA_2)} \quad (\text{Eq. 3.09})$$

For the biological processes within the leaf, only the fraction of the incoming energy is of importance that is featuring a wavelength within the photosynthetically active spectral domain, i.e. the PAR. But only the fraction of the PAR that remains in the leaf and is not transmitted to the soil is available for the photosynthesis model. The transmitted fraction of direct and diffuse

PAR ( $tPAR_{dir/dif}$ ) therefore has to be determined as a function of the leaf absorptivity for the PAR and the extinction coefficients for direct and diffuse shortwave radiation, also considering the total leaf area (eq. 3.10).

$$tPAR_{dir} = e^{-1 \cdot \alpha_{par} \cdot K_{ed} \cdot (LA_1 + LA_2)} \quad tPAR_{dif} = e^{-1 \cdot \alpha_{par} \cdot K_{dif} \cdot (LA_1 + LA_2)} \quad (Eq. 3.10)$$

The total absorbed energy input for the biological processes ( $aPAR_{dir/dif}$ ) through incoming shortwave radiation ( $SW_{dir/dif}$ ) then can be expressed as (eq. 3.11).

$$aPAR_{dir/dif} = SW_{dir/dif} \cdot fPAR \cdot \left(1 - tPAR_{dir/dif}\right) \quad (Eq. 3.11)$$

Equation 3.11 naturally only applies to the upper canopy layer. For the lower layer, the energy that already has been absorbed by the leaves above has to be subtracted. The fraction of photosynthetically active radiation in relation to the whole shortwave spectrum ( $fPAR$ ) is assumed to be constant at an average value of roughly 50 % according to own spectrometer sky measurements. For the long wave radiation, which is continuously entering the canopy irrespective of the model time, the absorptance is calculated differently for the two canopy layers. While for the upper vegetation layer, the incoming long wave radiation from the atmosphere ( $LW$ ) is coming from above, the lower vegetation layer is emitting long wave radiation according to its temperature ( $T_{c2}$ ) following the Stefan-Boltzmann law of emission and is adding this radiated energy to the energy budget of the upper layer ( $aLW_1$ , eq. 3.12).

$$aLW_1 = (\alpha_{lw} \cdot LW) + (\alpha_{lw} \cdot \sigma \cdot T_{c2}^4) \quad (Eq. 3.12)$$

The absorptivity for long wave radiation ( $\alpha_{lw}$ ) is set variable for different canopies (93 - 98 %). The symbol  $\sigma$  represents the natural Stefan-Boltzmann constant. The lower canopy layer again is supposed to be shielded from the atmospheric long wave radiation, but receives long wave energy due to emissions of the upper canopy layer from above ( $T_{c1}$ ). From below, the soil surface is contributing the energy that is emitted according to its temperature ( $T_s$ , eq. 3.13).

$$aLW_2 = (\alpha_{lw} \cdot \sigma \cdot T_{c1}^4) + (\alpha_{lw} \cdot \sigma \cdot T_s^4) \quad (Eq. 3.13)$$

When the absorbed portions of the incoming radiation from the direct and the diffuse short wave, as well as from the long wave input have been determined, the energy budget is passed on to the biological submodel. Figure 3.05 illustrates the various energy fluxes that are involved with the distribution of the energy within the canopy.

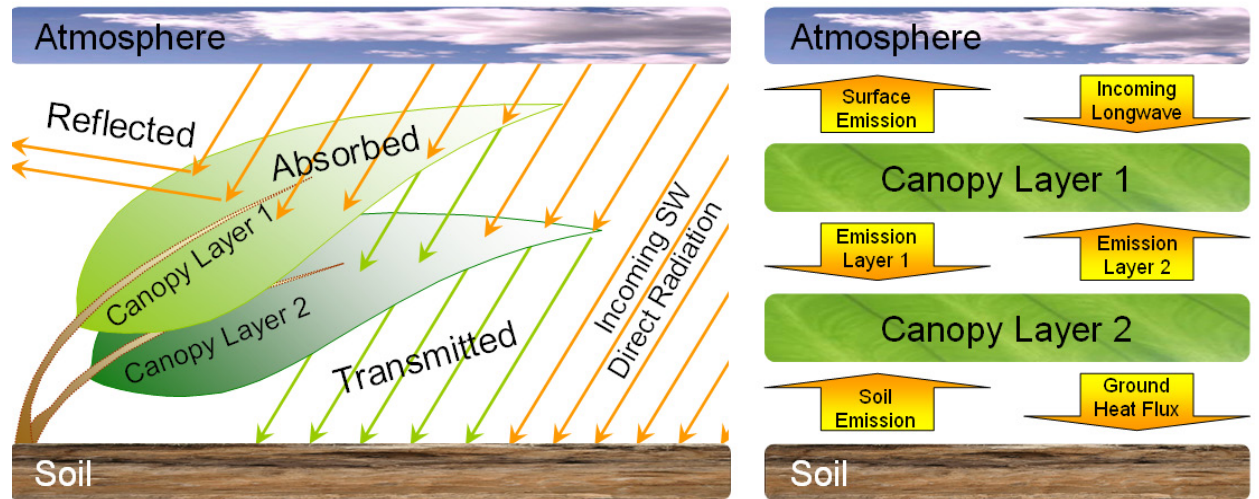


Figure 3.05: Fraction of reflected, absorbed and transmitted direct shortwave radiation for two canopy layers (left) and distribution of the longwave radiation within the two layered canopy structure (right).

### 3.3.2 Surface Processes

Before all requirements of the biological submodels are met, two important surface parameters have to be considered, as there is the circulation of air through the canopy and the interception of precipitation through the plant organs. The wind velocity within the canopy greatly influences the heat dissipation from the leaves, while the evaporation of intercepted water from a wet leaf surface determines the leaf energy budget by converting the incoming radiation into latent evaporation energy, which then is no longer available for the photosynthesis. Both therefore are processes that most sensitively interact with the biological core model, so they are briefly introduced in this section.

#### 3.3.2.1 Wind Velocity within the Canopy

The wind velocity that enters the model via the imported meteorology is a measured speed that is interpolated from anemometer measurements, which usually are taken at a standard measuring height of ten meters above the ground. This velocity normally does not apply to the real horizontal movement of air that can be experienced at the ground level, due to the retarding effect of the surface roughness. Within a dense canopy, the wind is even more limited, so that an isolated microclimate can develop within the stand that is scarcely stirred by external influences (OKE 1978). The measured wind speed is regulated down to the canopy level by applying a logarithmic wind profile (eq. 3.14, CIONCO 1965, OKE 1978, DINGMAN 1994).

$$u(z) = \frac{u^*}{K} \cdot \ln\left(\frac{z - dis_0}{z_m}\right) \quad (\text{Eq. 3.14})$$

For equation 3.14, the parameter  $u(z)$  is the wind velocity at a certain height above the ground ( $z$ ),  $z_m$  is the roughness length,  $K$  is the von Karman constant and  $u^*$  is the friction velocity. For the roughness length, as well as for the displacement height, reasonable approximations exist that apply to dense vegetation types (JARVIS ET AL. 1976, CAMPBELL AND NORMAN 1998), but since it is agreed, that in reality they vary with wind speed and canopy structure (MONTEITH 1976, MONTEITH AND UNSWORTH 1990, JONES 1992), they are modelled explicitly here.

The roughness of the vegetated land surface is primarily determined by the currently developed leaf area and the overall height of the canopy. The roughness length ( $z_m$ ) is a measure of the form drag and the skin friction of the layer of air that interacts with the surface (CAMPBELL AND NORMAN 1998, p. 69). It can be approximated through a fifth degree polynomial that is based on measured data of the momentum roughness parameter (eq. 3.15, fig. 3.06, left, SHAW AND PEREIRA 1982), which is multiplied by the overall canopy height ( $H_c$ ).

$$z_m = H_c \cdot \left[ \begin{array}{l} (0.0011 \cdot LAI^5) - (0.0155 \cdot LAI^4) + \\ (0.0821 \cdot LAI^3) - (0.1957 \cdot LAI^2) + \\ (0.1881 \cdot LAI) + 0.659 \end{array} \right] \quad (\text{Eq. 3.15})$$

A solid surface exerts a certain drag on the wind that is flowing above it. The wind speed will decrease logarithmically until it finally is zero when the observed height equals the surface height. The plane, where the wind profile converges to zero, is elevated from the ground for canopies. The displacement from the ground of the so called zero plane is termed as the displacement height ( $dis_0$ ). Like the roughness length, it depends on the leaf area as well as on the canopy height and can likewise be approximated via a polynomial (eq. 3.16, fig. 3.06, right, SHAW AND PEREIRA 1982).

$$dis_0 = H_c \cdot \left[ - (0.0088 \cdot LAI^2) + (0.0985 \cdot LAI) + 0.4766 \right] \quad (\text{Eq. 3.16})$$

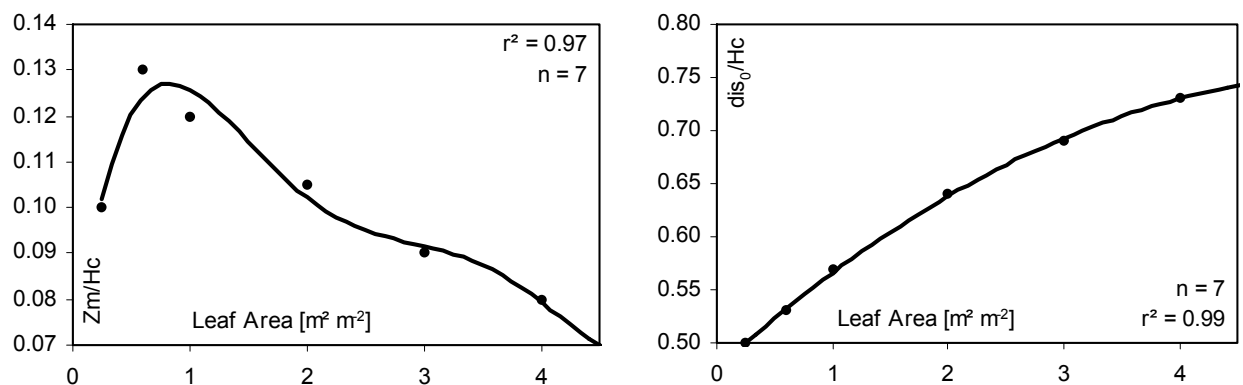


Figure 3.06: Derivation of the momentum roughness parameter (left) and the zero plane displacement height (right) from data measured by SHAW AND PEREIRA (1982). Please note that the coefficient of determination ( $r^2$ ) is correlated with the order of the polynomial and therefore is overestimated in both figures.

Figure 3.06 illustrates the stability of the polynomials (eqs. 3.15 and 3.16) for small leaf areas. For leaf areas higher than 4.5, both parameters are assumed to converge at the level of LAI 4.5. With the help of the roughness length ( $z_m$ ), the zero plane displacement height ( $dis_0$ ), the height of the wind measurement ( $H_m$ ) and the natural von Karman constant ( $K = 0.41$ ), the friction velocity ( $u^*$ ) can be determined. The friction velocity is directly proportional to the wind speed measured at height  $z$  and depends on the friction of the wind with the surface. It has a physical unit of  $m\ s^{-1}$  (eq. 3.17, OKE 1978), although a direct interpretation is not recommended (CAMPBELL AND NORMAN 1998).

$$u^* = \frac{u(z) \cdot K}{\ln\left(\frac{H_m + H_c - dis_0}{z_m}\right)} \quad (\text{Eq. 3.17})$$

When the results of the equations 3.15, 3.16 and 3.17 are inserted into equation 3.14, the wind speed within each canopy layer can be determined according to the measured wind speed at the measuring height and the current development of the vegetation cover. The parameters involved with the calculation of the wind profile are illustrated in figure 3.07.

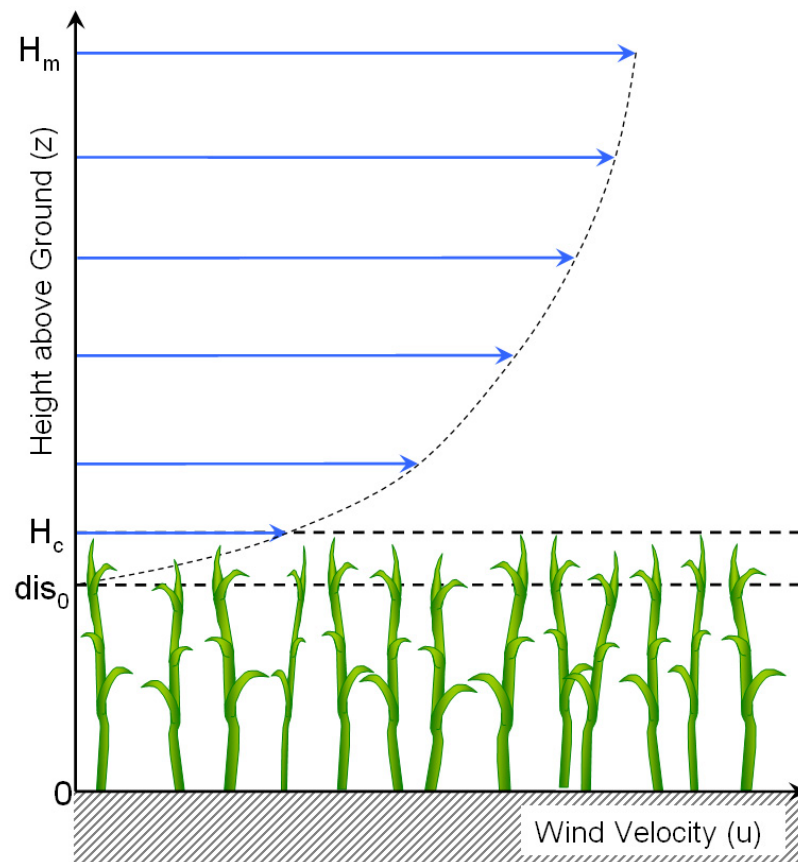


Figure. 3.07: Vertical wind profile over a canopy surface indicating the parameters that are involved in the calculation of the surface friction (inspired by DINGMAN 1994).

### 3.3.2.2 Interception Evaporation

In PROMET, the temperature of the landsurface is determined by an iterative distribution of the incoming energy into the latent heat flux, the ground heat flux and the sensible heat flux. While for the surface temperature of the vegetated land surface the biological processes play an important role (see section 3.3.3.5), the latent heat flux of the inanimate land surface consists of the soil and the interception evaporation.

The amount of water that enters the soil directly after a rainfall event is referred to as effective precipitation (BAUMGARTNER AND LIEBSCHER 1996). However, a large portion of the rainfall is intercepted either by anthropogenic structures like buildings, roads or parking areas or by the surface of the leaves and twigs of the vegetation cover (DYCK AND PESCHKE 1995, BAUMGARTNER AND LIEBSCHER 1996). The interception evaporation is a determinant component of the landsurface water balance as it is modelled in PROMET (eq. 3.18, fig. 3.08):

$$(P_{eff} + P_{int}) = (R_s + R_i) + (E_T + E_I + E_S) + (\Delta s_{snow} + \Delta s_{soil}) \quad (Eq. 3.18)$$

Thereby  $P_{eff}$  is the effective precipitation,  $P_{int}$  is the intercepted precipitation,  $R_s$  is the surface runoff,  $R_i$  is the interflow beneath the surface,  $E_T$  is the transpiration through the canopy,  $E_I$  is the interception evaporation,  $E_S$  is the soil evaporation and  $\Delta s_{snow/soil}$  represents the change of the snow or soil water storage respectively. Figure 3.18 outlines the hydrological components of the surface water balance that are accounted for in PROMET.

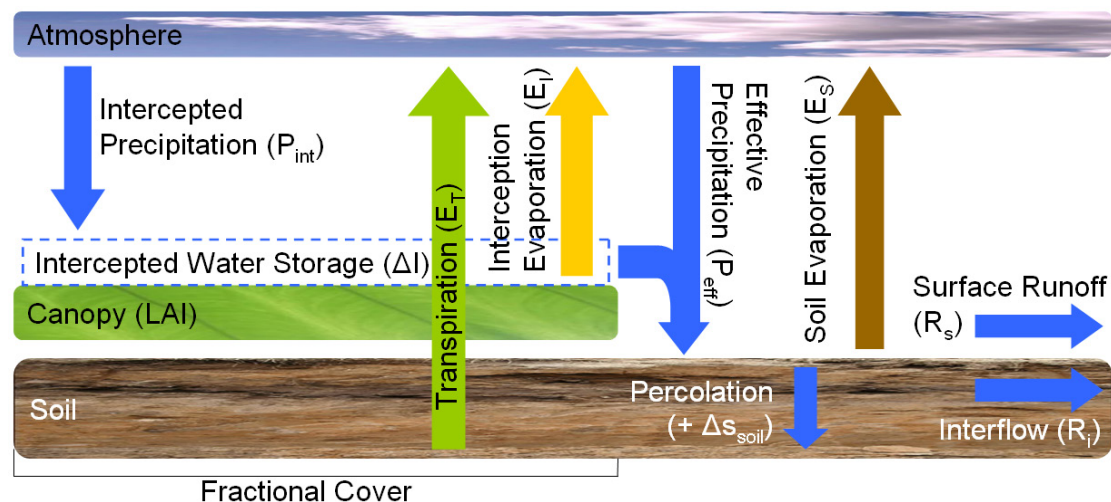


Figure 3.08: Components of the PROMET surface water balance.

While for non-vegetated land use categories, the amount of rainfall that can potentially be intercepted before it penetrates the soil is assumed to be static during the year (GRIMMOND AND OKE 1991), the seasonal variability of the storage capacity of the canopy is determined in dependence of the leaf area and the fractional cover for the vegetated land surface (eq. 3.19, fig. 3.09, GASH 1979, VAN DIJK AND BRUIJNZEEL 2001, WOHLFAHRT ET AL. 2006).

$$\Delta I_{\max} = \cdot fCOVER \cdot (0.935 + 0.498 \cdot LAI - 0.00575 \cdot LAI^2) \quad (\text{Eq. 3.19})$$

For small leaf areas, it has to be taken into account that not the whole proxel that is receiving precipitation may be vegetated, so the interception capacity has to be reduced according to the fractional cover of the canopy ( $fCOVER$ , *fig. 3.09, left*). The fractional cover describes the degree of canopy closure and is derived from the LAI using a simple exponential function (*eq. 3.20*).

$$fCOVER = 1 - e^{-1 \cdot LAI} \quad (\text{Eq. 3.20})$$

For anthropogenic structures, as well as for canopies that are defoliated ( $LAI = 0$ ), a basic interception capacity ( $\Delta I_{\max}$ ) of 0.935 mm is assumed (GRIMMOND AND OKE 1991, GASH ET AL. 2007).

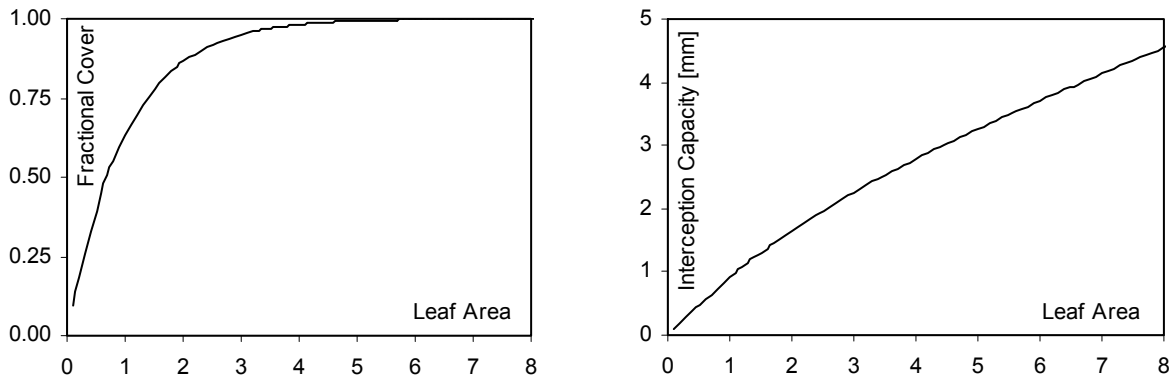


Figure 3.09: Correlation of leaf area and canopy closure (left) and variability of the interception capacity of the canopy in dependence of the leaf area and the fractional cover (right).

The simulation of the filling and drainage of the storage of intercepted water follows a simplified method that is based on the assumptions of GASH (1979). The most determinant assumptions in that context are:

- No evaporation takes place until the rainfall has ceased.
- No water drips from the leaves until the interception storage is filled completely.

Conversely this means that, if the storage for intercepted water is filled, all the rainfall that is additionally falling onto the leaves will drip off and will be added to the effective precipitation. The rest of the precipitation, staying on top of the canopy, evaporates as soon as the rainfall stops and enough energy for the evaporation is available. In PROMET, the latent energy of the evaporation of intercepted water ( $E_p$ ) is modelled parallel to the potential evaporation of open water bodies, applying a reduced form of the Penman-Monteith approach by using the Priestley-Taylor equation (*eq. 3.21*, PRIESTLEY AND TAYLOR. 1972).

$$E_p = \frac{R_n \cdot s(T_l) + \left[ p \cdot c_p \cdot (e_s \cdot r_a) \right]}{s(T_l) \cdot \gamma} \quad (\text{Eq. 3.21})$$

For equation 3.21,  $R_n$  is the energy balance (see eq. 3.22),  $s(T_l)$  is the slope of the saturation vapour pressure curve in dependence of the leaf temperature (see eq. 3.23),  $p$  is the density of air,  $c_p$  is the specific heat of air,  $e_s$  is the saturation deficit,  $r_a$  is the aerodynamic resistance and  $\gamma$  is the psychrometric constant (see eq. 3.26).

The energy balance can be written as equation 3.22 with  $O_{sw}$  and  $O_{lw}$  standing for the outgoing short and long wave radiation respectively.

$$R_n = (SW_{dir} + SW_{dif} + LW) - (O_{sw} + O_{lw}) \quad (\text{Eq. 3.22})$$

The slope of the saturation vapour pressure curve ( $s(T_l)$ ) also depends on the temperature ( $T_l$ ), the gas constant ( $R$ ), the molar mass of water ( $M_{H_2O}$ ), the saturation pressure ( $e$ ) as well as on the latent heat of vaporization ( $L$ ) and can be determined following MURRAY (1967, eq. 3.23).

$$s(T_l) = \left( \frac{M_{H_2O} \cdot 1000}{R} \right) \cdot \left( \frac{e \cdot L}{T_l^2 \cdot 100} \right) \quad (\text{Eq. 3.23})$$

The latent heat of vaporization is a linear function of the temperature (eq. 3.24) following BAUMGARTNER AND LIEBSCHER (1996).

$$L = 2501 - [2.361 \cdot (T_l - 273.16)] \quad (\text{Eq. 3.24})$$

Figure 3.10 illustrates the temperature dependency as well as the interconnectedness of the parameters  $L$ ,  $e$  and  $s(T_l)$ .

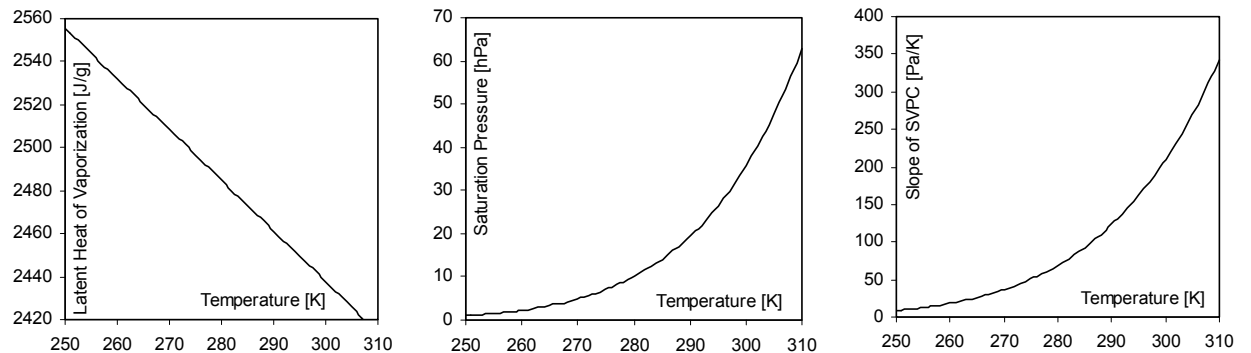


Figure 3.10: Temperature dependency of the latent heat of vaporization (left), the saturation vapour pressure (middle) and the slope of the saturation vapour pressure curve (right).



The aerodynamic resistance ( $r_a$ ) with a physical unit of  $\text{s m}^{-1}$  is derived through an empirical relation to the wind velocity (eq. 3.25, CAMPBELL AND NORMAN 1998, p. 103), the latter being determined according to the methods described in the previous section.

$$r_a = \frac{54}{u(z)} \quad (\text{Eq. 3.25})$$

The psychrometric constant by definition is not a constant as implied by its name, but depends on the air pressure (eq. 3.26) with  $M_{\text{H}_2\text{O}}$  and  $M_{\text{air}}$  representing the molar masses of water and air respectively.

$$\gamma = \frac{c_p \cdot P}{L} \cdot \left( \frac{M_{\text{H}_2\text{O}}}{M_{\text{air}}} \right) \quad (\text{Eq. 3.26})$$

When all involved parameters are finally determined, the potential interception evaporation ( $E_i$ ) has to be converted from a latent heat flux with the physical unit of  $\text{W m}^{-2} \text{h}^{-1}$  to a mass flux in  $\text{mm h}^{-1}$ , while at the same time it has to be limited to the amount of water that currently is stored within the interception storage ( $\Delta I$ , eq. 3.27).

$$E_i = \text{MIN} \left\{ \Delta I; \frac{E_p \cdot 3.6}{L} \right\} \quad (\text{Eq. 3.27})$$

As long as there is water in the interception storage, the incoming energy is used for the evaporation of the intercepted water and only a minimum amount is provided for the maintenance of the biological processes. However it is assumed, that stomatal gas exchange can happen as long as the leaves are wet, but only from the lower side of the leaves, which is supposed to be the dry one.

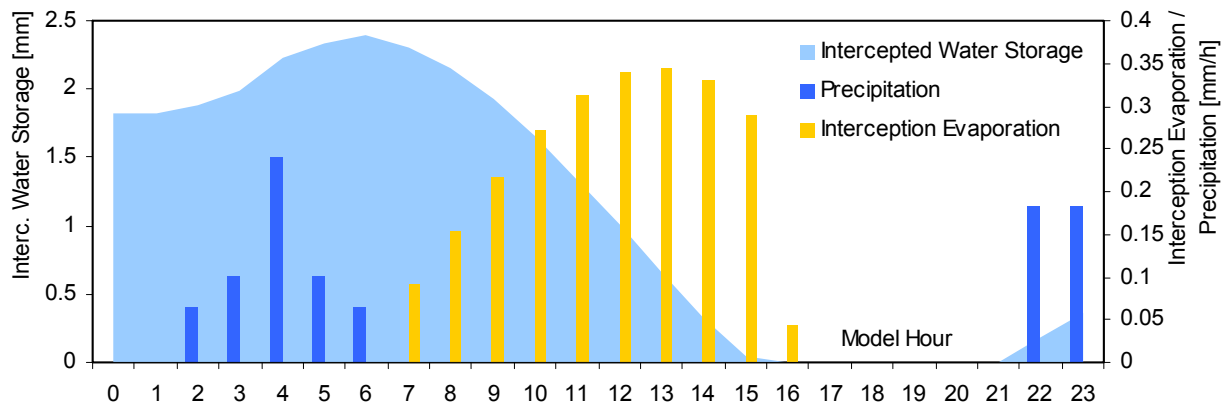


Figure 3.11: Model results for the interception evaporation from the needles of a coniferous stand in the central region of the Upper Danube catchment for the 11<sup>th</sup> of July 1998.

Figure 3.11 displays exemplary model results for the interception evaporation of a coniferous forest on a randomly chosen summer day (11<sup>th</sup> of July 1998). At the beginning of the day, the needles already are wet from a previous rainfall event. Approximately 1.8 mm of precipitation is suspended within the canopy, but since there is no energy input during the night, nothing evaporates from the intercepted storage. During the early morning hours, another 0.6 mm of rainfall are added to the storage of intercepted water, so that the total amount of intercepted water increases to 2.4 mm. At the beginning of July the forest is fully developed and has a maximum interception capacity of 4.7 mm. Consequently, no water drips off onto the ground. When the rainfall stops at 7 am, the sun has already risen and the intercepted water starts to evaporate. Since the exemplary day is a very cloudy day (average cloud cover is 88 percent), the needles take about ten hours until they are completely dry at 4 pm. During the late afternoon hours, the biological processes finally receive the total amount of incoming energy. After sunset at 9 pm it starts to rain again and the needles are wetted with about 0.3 mm of intercepted water until midnight. According to this example, the interception of rainfall leads to a constant cycle of wetting and drying in the course of the model year (fig. 3.12).

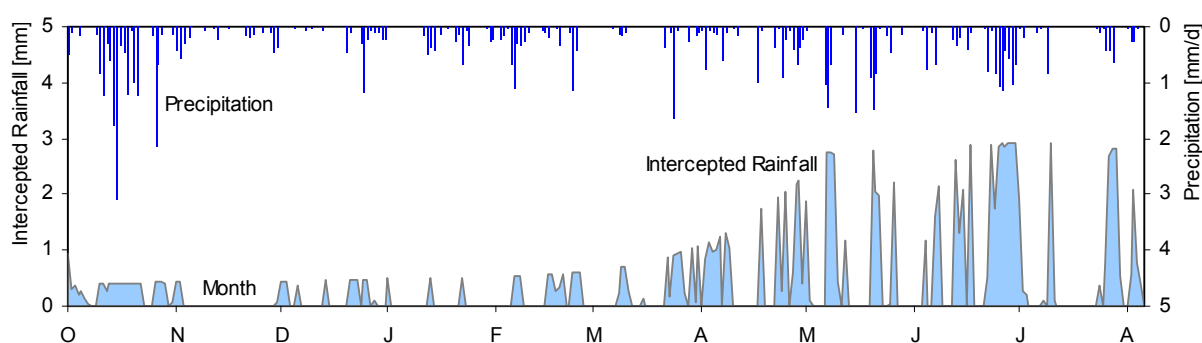


Figure 3.12: Measured precipitation and modelled intercepted rainfall for a winter wheat stand during the model season 1998/1999.

Figure 3.12 clearly explains the interrelation of precipitation and the amount of rainfall that is intercepted by the canopy. This example, taken from a winter wheat site, demonstrates the dynamics of the annual course of the intercepted water storage, whose holding capacity is highly dependent on the development of the crop. During the winter months, the sparse canopy is only capable of holding 0.5 mm of the incoming precipitation, so the major part of the rainfall drips off from the leaves onto the ground and enters the soil. During the early summer months, the crop develops rapidly and the potential storage capacity for intercepted precipitation increases with the newly developed leaf area. The increased frequency of thunderstorms, with high precipitation rates during the summer months, results in periods of constantly wet leaves. Due to the high radiation input in the summer, the whole storage of intercepted water can be evaporated during the course of one day.

### 3.3.3 Biological Processes

With exception of the initialization section, which only is passed once for all of the 27 landuse categories that are implemented in PROMET (*fig. 3.13*) during the first model time step, the biological subroutines of PROMET consist of a chain of submodels that are cycled successively for every element of the raster data set at each model time step (*fig. 3.14*).

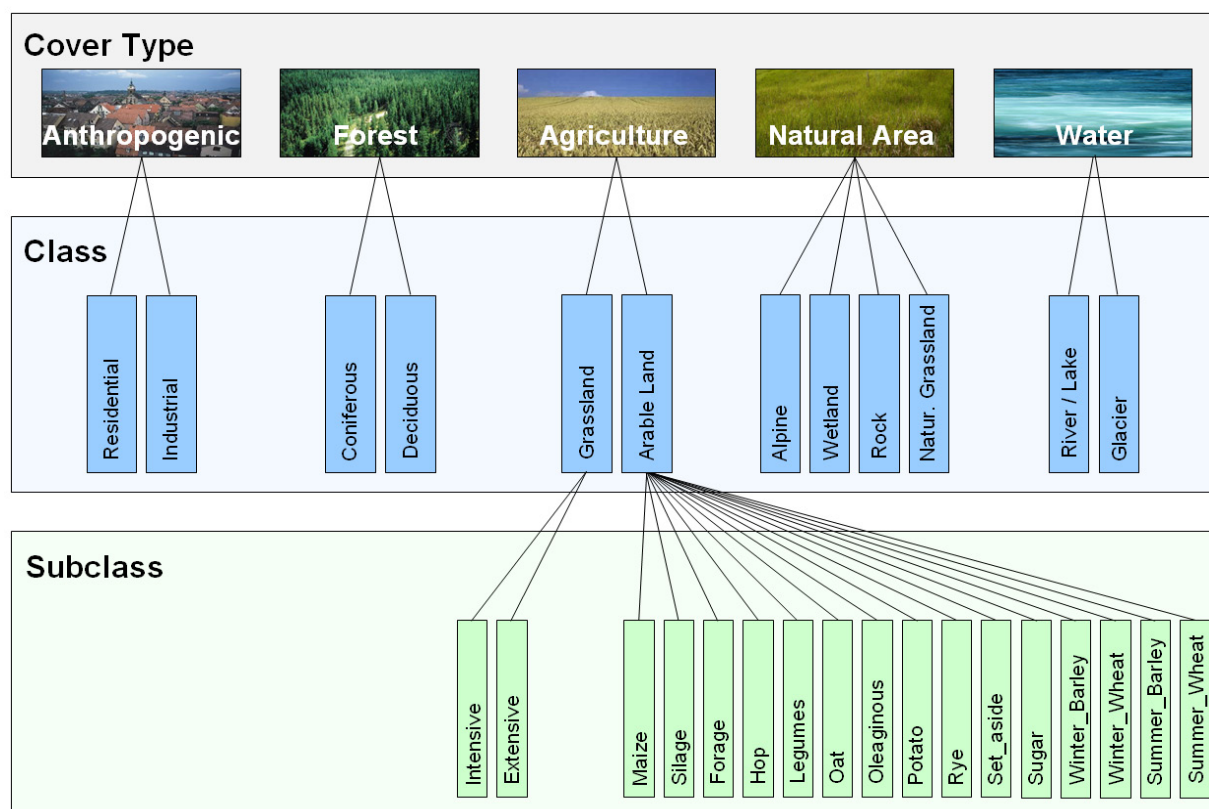


Figure 3.13: Model hierarchy of the 27 integrated landuse categories.

#### 3.3.3.1 Model Initialization

When the model run is started, the input parameters that correspond with the different landuse categories and are needed for the calculation of the biological submodels are read from parameter files and stored within the internal GIS structure. All crop specific information, concerning the 27 different landcover categories that are accounted for in the model, is arranged following a strict hierarchy that allows for a clear differentiation between the different landuse types (*fig. 3.13*). This enables the model to access the correct parameters unmistakably for each vegetation type from all subroutines. The land cover hierarchy also includes information, if the currently modelled pixel is a vegetated or a non-vegetated surface type. For non-vegetated surface types, the biological submodels are skipped. In PROMET, it also is assumed that no biological activities take place beneath a closed snow cover. The biological routines, with exception of the progress of the phenological stages, consequently do not run if a snow cover is modelled for a proxel at the current time step.

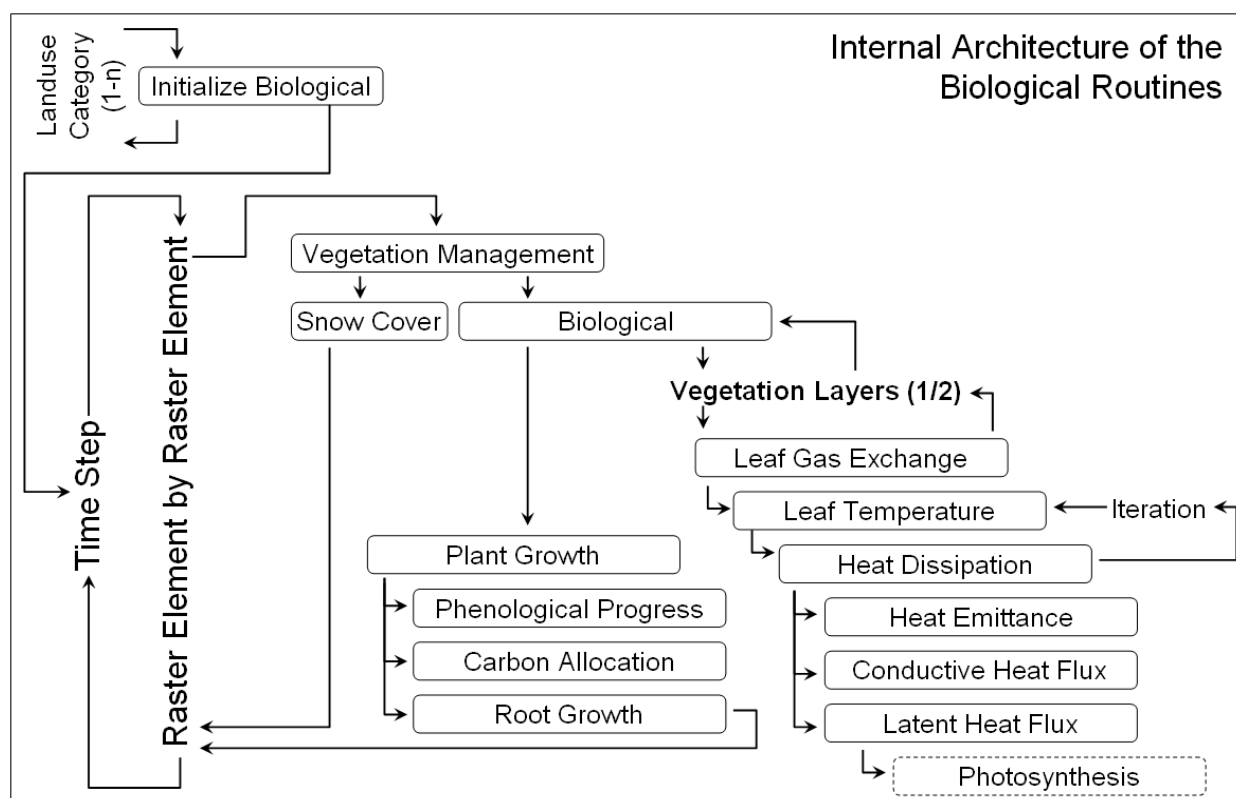


Figure 3.14: Flowchart of the biological subroutines of PROMET.

The vegetation cover is modelled for two vegetation layers, so that the leaf gas exchange routines have to be called twice for every time step (fig. 3.14). The leaf energy balance is solved subsequently for the sunlit and shaded parts of the leaves of both vegetation layers. Figure 3.14 also illustrates that the actual photosynthesis is a byproduct of the efforts concerned with the determination of the latent heat flux from the leaf. When the leaf energy balance is finally solved, the resulting carbon fixation is passed on to the plant growth routine, where the newly generated biomass is utilized according to the phenological stage of the canopy (see section 3.3.3.6.2).

The biological submodels of PROMET require a set of variables from the preceding model time step. Important parameters for example are the already accumulated biomass, the growth stage that has been reached by the vegetation type of the currently modelled proxel, the overall depth and density of the root system et cetera. When a model run is initialized, this information is not available for the very first time step. The model therefore was equipped with a subroutine that only is called once for the first time step and initializes the most determinant variables of the biological submodels. The initialisation is dynamic to some degree, so that the model run can be started on a user-defined day of the year.

In a first step it is decided, whether the modelled canopy is a perennial type and therefore requires the biological submodel at any time of the year, or if the cover type is of a seasonal kind. The non-perennial crops are discerned into winter and spring crops. If the starting day of the modelled time window lies beyond the vegetation period, the variables are set to zero and

the model run commences without the biological submodels running. If the starting day lies within the vegetation period of the currently modelled canopy type, the explicit initialisation is started.

The determinant that is used to initialise all other important variables is the leaf area index. It is assumed that the annual course of the LAI can generally be structured into four phases (*fig. 3.15, left*):

- A period, where the leaf area is at its minimum ( $LAI_{ini}$ ),
- a period of increasing leaf area,
- a time of maximum LAI values ( $LAI_{max}$ ) and
- a time, where the leaf area decreases.

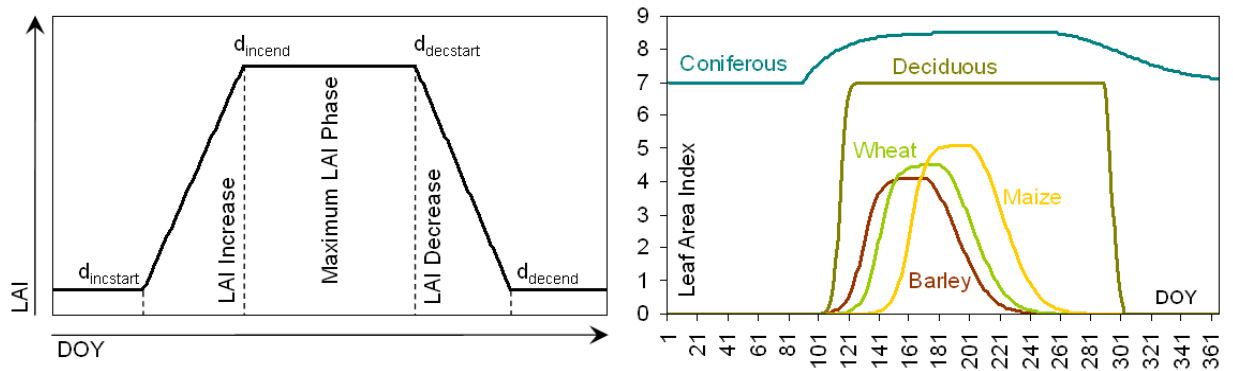


Figure 3.15: Phases of LAI development (*left*) and LAI curves for selected crops used for the initialization of the first time step.

With a simple function, the green leaf area index is assumed in dependence of the DOY (eqs. 3.28-31). For every crop, a different parameter set is used that modifies the course of the function (*fig. 3.15, right*). The boundaries of the functions are the days of the year, where the phases of LAI development are changing. While  $d$  is the currently modelled day,  $d_{incstart}$  is the day when the leaf area starts to increase,  $d_{incend}$  the day when it stagnates,  $d_{decstart}$  the day when the leaf area starts to decrease again and  $d_{decend}$  marks the completion of the senescent phase.

$$LAI = LAI_{ini} \quad \begin{array}{l} \text{If } d \text{ is lower than} \\ d_{incstart} \text{ or } d \text{ is greater} \\ \text{than } d_{decend} \end{array} \quad (\text{Eq. 3.28})$$

$$LAI = \frac{(LAI_{ini} \cdot LAI_{max})}{[LAI_{ini} + (LAI_{max} - LAI_{ini})]} \cdot e^{[-k_1 \cdot (d - d_{incstart})]} \quad \begin{array}{l} \text{If } d \text{ is greater than} \\ d_{incstart} \text{ and } d \text{ is lower} \\ \text{than } d_{incend} \end{array} \quad (\text{Eq. 3.29})$$

$$LAI = LAI_{max} \quad \begin{array}{l} \text{If } d \text{ is greater than} \\ d_{incend} \text{ and } d \text{ is lower} \\ \text{than } d_{decstart} \end{array} \quad (\text{Eq. 3.30})$$

$$LAI = LAI_{ini} + e^{\{-k_2 \cdot [d - (d_{decstart} - 1)]\}^2} \cdot (LAI_{max} - LAI_{ini}) \quad \begin{array}{l} \text{If } d \text{ is greater than} \\ d_{decstart} \text{ and } d \text{ is lower} \\ \text{than } d_{decend} \end{array} \quad (\text{Eq. 3.31})$$

For the equations 3.29 and 3.30,  $k_1$  and  $k_2$  are coefficients that modify the gradient of the LAI increase and decrease.

This method is considered to provide reasonable initialisation values for the agricultural crops as well as for the natural grasslands in the colline altitudinal belt. However, the different appearances of natural canopies at higher altitudinal vegetation zones are not accounted for in this approach. This would lead to the failure that for example coniferous forests on alpine sites above 1500 m sea level height, where the spruce forest is gradually superseded by dwarf-pines, would be initialized with the same large leaf area that they are supposed to develop in the plain regions of the alpine foreland. To account for this problem, all pixels of the input data set for the Upper Danube Basin that are populated with coniferous trees (see appendix A.8.1) were analysed with respect to their altitude and their annual mean temperature. It was found that a strong correlation of elevation and annual mean temperature exists ( $r^2 = 0.96$ , *fig. 3.16, left*), so that the annual mean temperature could well be consulted for the differentiation of the altitudinal vegetation zones.

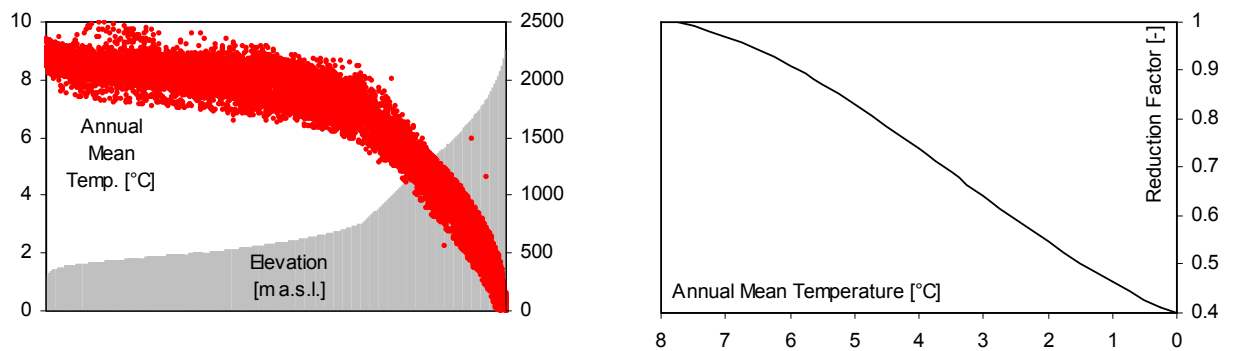


Figure 3.16: Relation of long-term annual mean temperature and terrain elevation for coniferous sites within the Upper Danube Basin (*left*) and factor reducing the leaf area of coniferous forest in dependence of the annual mean temperature of the last modelled year (*right*).

If the observed or interpolated annual mean temperature of a modelled pixel falls below 8 °C, which within the Upper Danube Basin normally is the case for elevations that exceed 600 m a.s.l. (*fig. 3.16, left*), the determined leaf area values are reduced by a factor that is based on a third-degree polynomial of the annual mean temperature of the preceding model year (*fig. 3.16, right, eq. 3.32*).

$$R_{LAI} = -0.0013 \cdot T_{avg}^3 + 0.0133 \cdot T_{avg}^2 + 0.0524 \cdot T_{avg} + 0.3986 \quad (\text{Eq. 3.32})$$

Taking the reduction factor into account, the initial leaf area for proxels located at “cold” sites reads (*eq. 3.33*):

$$LAI = LAI \cdot R_{LAI} \quad \text{If } T_{avg} \text{ is lower than } 8 \text{ } ^\circ\text{C} \quad (\text{Eq. 3.33})$$

When the leaf areas for all vegetation categories that either are perennial or in their active growing period are determined, the height of the canopy ( $h_c$ ) is calculated using a cultivar specific relation of leaf area and plant height ( $LH_{rel}$ ).

$$h_c = LAI \cdot LH_{rel} \quad (\text{Eq. 3.34})$$

Due to lack of better data for the first model time step, all relevant temperatures like the leaf and soil temperatures are initialised with the air temperature ( $T_a$ ) as a first guess.

With the help of the LAI development phases (*fig. 3.15*), the phenological phase is determined according to the DOY. The rate of development (see section 3.3.3.6.1) is supposed of having reached half the amount of the transition to the next growth stage, thus allowing the crop to autonomously commence its phenological development once the model run has started.

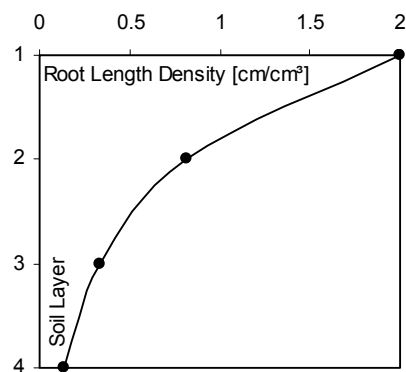
As soon as the phenological phase is known, the leaf biomass can be determined by inverting the “LAI-to-leaf-mass-per-area” relationship (*eq. 3.35*, see section 3.3.3.6.3). The leaf biomass then is extrapolated to the other plant parts that are stem, grain and root using the imported allocation percentages (see section 3.3.3.6.2).

$$B_{leaf} = LAI \cdot LMA \quad (\text{Eq. 3.35})$$

For the initialisation of all agricultural vegetation types, the root depth ( $RD$ ) is assumed as a percentage of the crop specific maximum root depth ( $RD_{max}$ , *tab. 3.02*), according to the phenological stage. Natural and perennial canopies are initialized with their specific maximum root depth.

Table 3.02: Initial root depth according to the initial growth stage.

$d < d_{incstart}$	$d_{incstart} > d < d_{incend}$	$d_{incend} > d < d_{decend}$	$d > d_{decend}$
$RD = 0.3 \cdot RD_{max}$	$RD = 0.7 \cdot RD_{max}$	$RD = RD_{max}$	$RD = 0.3 \cdot RD_{max}$



$$RLD_{L_s} = 2 \cdot e^{(L_s-1)(-0.9)} \quad (\text{Eq. 3.36})$$

Figure 3.17: Initial root length density distribution into four soil layers.

The distribution of the root density to the soil layers is initialised by an exponential function (eq. 3.36, GEWITZ AND PAGE 1974, ADIKU ET AL. 1996). Depending on the soil type, either three or four soil layers ( $L_s$ ) exist in the model that can possibly be rooted. The initial root length density of a soil layer ( $RLD_{L_s}$ ) decreases with increasing soil depth for all vegetation types (fig. 3.17).

Having passed through the initialization process, the model is able to run all biological submodels, starting from any user-defined day of the year. However, it is recommended to compute the model at least one model year in advance, before the results can be considered to be reliable. This spin-up time allows the soil water balance to adjust to the current meteorology and the biological parameters to accommodate to the climatic specifications. All model results and intermediate results presented here were generated with a spin-up phase of at least one model year.

### 3.3.3.2 Agricultural Management

Before the submodels that compute the actual plant growth are called, general agricultural management measures have to be considered.

All arable crops in the model are sowed at noontime, when their cultivar specific sowing date ( $d_{sow}$ ) is reached. The crop related variables are set to zero and the root depth is set to a sowing depth of 3 cm. Most important, the planting process activates all biological submodels for the crop, which had been skipped during the fallow period, so that the active growing process can commence. The natural and perennial crops do not have a specific sowing date, but are starting with active growth as soon as there is no snow cover signalled. An exception is made for deciduous forest, whose period of active growth is started with the emergence of leaves. This determinant phenological step is controlled by the phenology submodel (see section 3.3.3.6.1.3.2). For all agricultural crops, the growth period lasts until the cultivar specific harvest date ( $d_{har}$ ) is reached. When the crop is harvested at noontime, the biomass, plant height and LAI variables are set to zero and the active growth is aborted. The portion of the biomass that is considered as “harvestable” depends on the crop type. While for cereals only the grain mass is harvested, for silage crops and grassland the whole aboveground biomass is collected. The harvestable part of the accumulated biomass is transformed into harvest mass ( $B_{har}$ ) using a linear relation between biomass and grain harvest. Also the units are transformed from  $\text{kg m}^{-2}$  to a unit of  $\text{t ha}^{-1}$  applying a factor of 10 (eq. 3.37).

$$B_{har} = (B_{grain} \cdot m + b) \cdot 10 \quad (\text{Eq. 3.37})$$

Figure 3.18 shows the stable correlation of grain biomass and grain yield for winter wheat that could be obtained from field measurements of two wheat test sites. The location of the test sites as well as the applied measuring techniques can be followed in section 4.1.



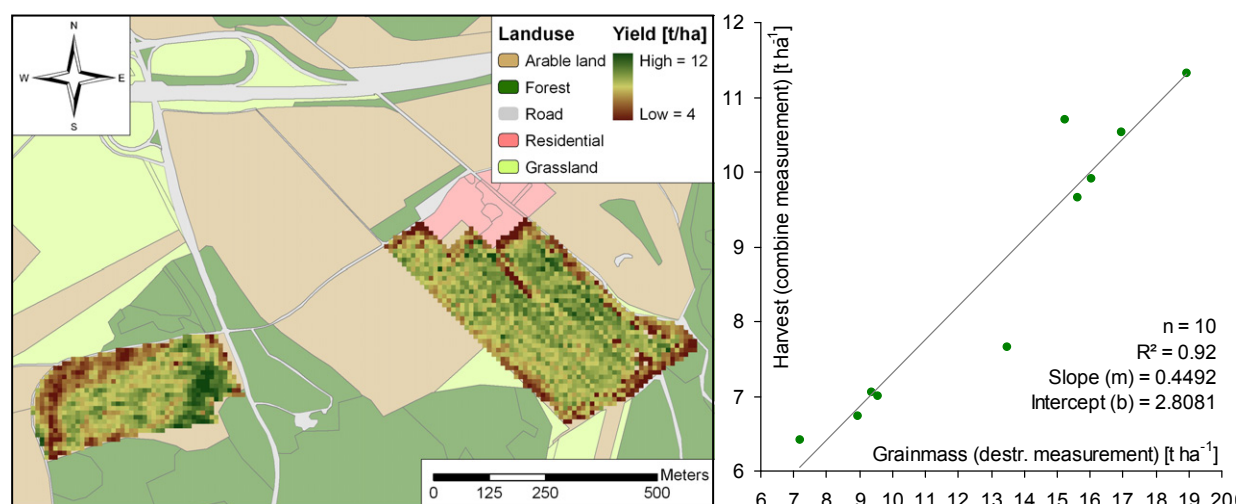


Figure 3.18: Combine harvester yield measurements for the test sites “Kochfeld” and “Hofanger” (compare section 4.1) in front of a GIS based land use map (left). Derivation of a relation between dry grain mass and measured grain yield (right).

On ten sample points, five for each test field, the dry grain mass including the straw part of the spikes was measured shortly before the fields were harvested (see section 4.1.4). The spatial distribution of the usable harvested mass was recorded during the harvest with a DGPS supported measurement system on a combine harvester. The combine measurements were corrected with the overall weight of the harvested freight and resulted in maps of obtained yield. The yield maps were compared with the destructive field measurements by integrating both into a GIS (fig. 3.18, left).

The correlation of fruit biomass and harvested grains (fig. 3.18, right) shows that the yield of winter wheat is approximately 70 % of the fruit biomass. Unfortunately, for all other arable crops no explicit yield measurements could be obtained, so that the relations had to be estimated in the style of the winter wheat measurements or were derived from the parallel analysis of model results and agricultural harvest statistics respectively (BAYERISCHES STAATSMINISTERIUM FÜR LANDWIRTSCHAFT UND FORSTEN 2004 and 2006). Table 3.03 gives an overview of the parameters applied for the conversion of biomass to yield for different crops.

Table 3.03: Parameters used for the transformation of harvested biomass [ $\text{kg m}^{-2}$ ] to yield [ $\text{t ha}^{-1}$ ].

Crop Type	Slope [m]	Intercept [b]
Hop	0.0391	0.1321
Oat	1.0282	0.0000
Oleaginous	0.2562	0.1053
Potato	2.7201	1.3457
Rye	0.7383	0.0000
Sugar	4.6454	2.3387
Summer Wheat	1.1685	0.0358
Winter Barley	0.6668	0.1315
Legumes	0.7314	0.0283
Winter Wheat	4.4922	2.8081
Other	1.0000	0.0000

For the grassland crop types, the harvested mass equals the aboveground biomass. Paying respect to the fact that grassland can be cut more than once a year, the harvest mass is accumulated during the season. Besides that, the cutting of the grassland is modelled parallel to the harvest of arable crops, but the initialization of the cutting is variable. For intensive grassland, the first cut is initialised as soon as the LAI has developed to a value of four. If this is not the case until the 20<sup>th</sup> of June, the meadow is cut anyway. The second cut happens in the model, when the LAI again has recovered to a value of four, but not before the 20<sup>th</sup> of July and not after the 15<sup>th</sup> of August. The last of three possible cuts per season then follows between the 20<sup>th</sup> of September and the 20<sup>th</sup> of October. For extensive grassland, only two cuts per season are possible, the first occurring not before the 15<sup>th</sup> of June and not until the LAI has developed to a value of four. The second cut for extensive grassland is possible in autumn between the 20<sup>th</sup> of September and the 20<sup>th</sup> of October.

Once in a model year during winter time some variables have to be reset for the natural canopies as well as for the perennial agricultural grasslands. For example a part of the root system is supposed to die during wintertime, thus avoiding unnatural accumulations of root mass. Also the number of accumulated cuts of grasslands has to be reset for the next season.

### 3.3.3.3 Leaf Energy Balance

The basis of all calculations, applied for the modelling of the biological processes in PROMET, is the energy balance of the leaf. It consists of the energy input through absorbed radiation on one side and three kinds of energy dissipation from the leaf on the other (*fig. 3.19*).

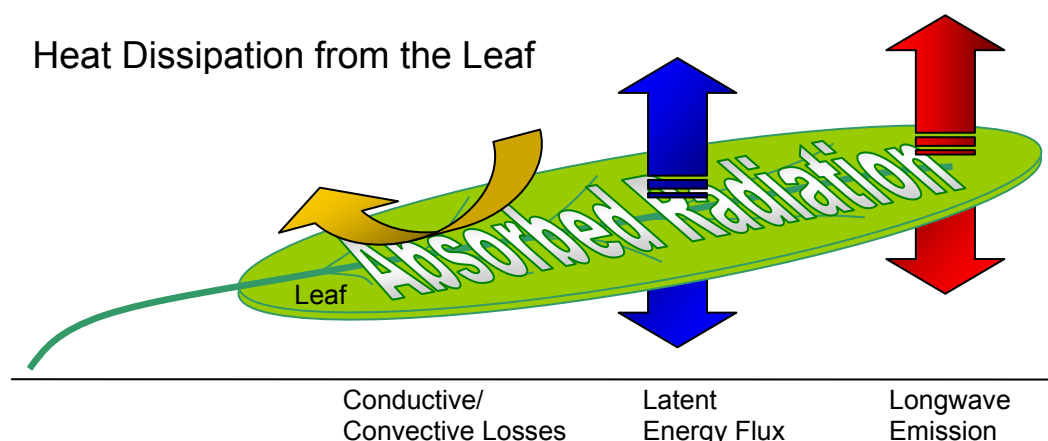


Figure 3.19: Components of the leaf energy balance of PROMET biological.

The solution of the leaf energy balance is performed through an iteration that approximates a balanced equilibrium between the energy that is gained by the leaf via the absorption of radiation on one hand and the energy that is lost due to heat dissipation from the leaf at a specific leaf temperature on the other. The dissipation of energy from the leaf consists of three

components, as there are the heat loss through emission, the conductive heat dissipation and the latent heat flux (fig. 3.19). Those three fluxes have to be calculated for every iteration step, since they all are highly dependent on the temperature of the leaf. According to the internal architecture of the model, the whole iteration has to be performed four times for every element of the raster data set at each time step, because the sunlit and the shaded parts of the leaf area have to be calculated for both of the vegetation layers successively (fig. 3.20).

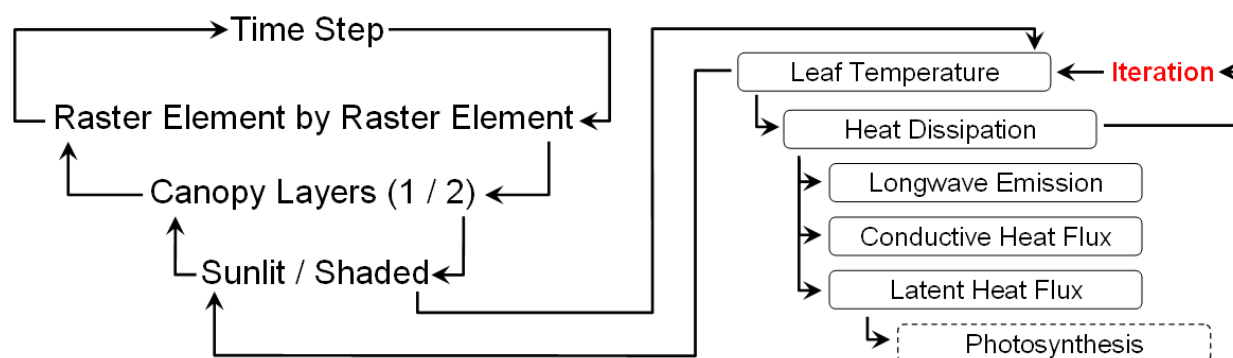


Figure 3.20: Iteration loop for the calculation of the leaf energy balance, indicating that one model time step requires the initialization of four iterations per raster element.

It therefore is of consequence to aspire the least number of iterations possible. This is accomplished by applying an efficient iteration rule that is capable of solving the required fluxes by applying no more than three iteration steps for most cases. The iteration method is briefly described in the following section.

### 3.3.3.4 Iterative Determination of the Leaf Temperature

The leaf temperature for either sunlit or shaded leaves in a particular canopy layer is determined through the energy balance of the leaf. The equilibrium leaf temperature, i.e. the temperature at which energy losses equal energy gains, is determined iteratively. Applying an initial estimate for the leaf temperature ( $T_{l,ini}$ ) as well as the energy input to the leaf, a new temperature estimate ( $T_{l,est}$ ) is calculated, at which heat losses due to emission, convective losses and latent heat transfer equal the energy input, which again is composed of the absorbed short and long wave radiation. Since all energy losses are sensitive to temperature (see sections 3.3.3.4.1 - 3), the heat dissipation is calculated for a number of temperatures, until the gains and losses differ by no more than a threshold. The critical threshold was assumed with  $5 \text{ W m}^{-2}$  for all calculations presented in the context of this work.

Usually, the leaf temperature from the preceding time step is chosen as the initial leaf temperature. If the leaf temperature has not changed significantly since the last time step, the initial estimate might be good enough and the iteration can possibly be avoided in order to save computing time. If the initial temperature estimate does not produce an energy loss that is sufficiently close to the gain, the iteration is begun. Since the relationship between the total

energy loss and the leaf temperature is nearly linear, the iteration can be kept rather simple. At first, a range of possible leaf temperatures and their corresponding energy losses is spanned, based on the initial temperature. If the initial temperature produces a heat loss that lies above the equilibrium radiation (*fig. 3.21, left*), then the initial temperature ( $T_{l,ini}$ ) is used as the upper boundary ( $T_{l,upp}$ ) for the first iteration step, while the lower boundary ( $T_{l,low}$ ) is assumed to be 10 K below (*fig. 3.21, right*). In figure 3.21, the energy fluxes  $diss_{upp}$  and  $diss_{low}$  represent the heat dissipations that correspond with the upper and the lower boundary of the estimated leaf temperature.

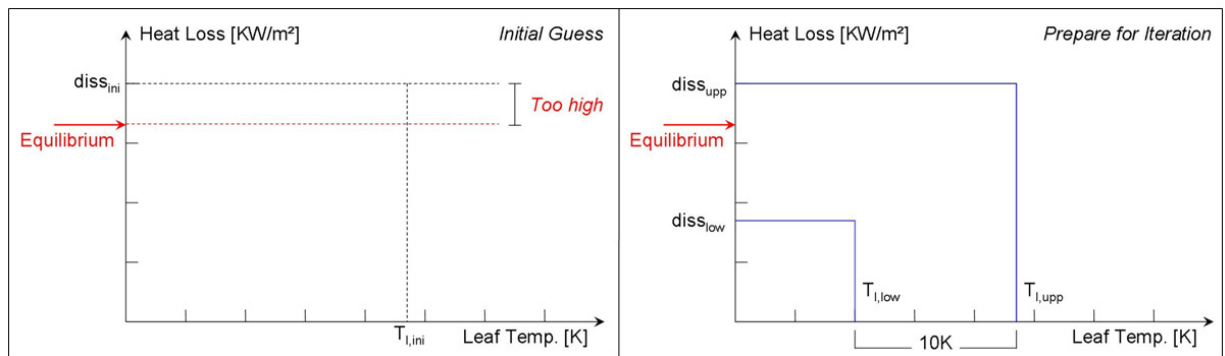


Figure 3.21: Initial estimate for the iterative solution of the leaf energy balance. The exemplary initial estimate is far too high (left), so the iteration is started with the initial intermediate temperature being applied as upper boundary (right).

For an initial estimate that happens to produce a heat loss that falls below the equilibrium, the opposite will be the case, so that the initial estimate will be used as the lower boundary, while the upper boundary will be assumed 10 K above. In a second step, an intermediate temperature is estimated applying a linear interpolation (*eq. 3.38*) between the equilibrium radiation ( $rad_{eq}$ ) and the chosen extreme temperatures with their corresponding heat dissipations (*fig. 3.22, left*).

$$T_{l,int} = T_{l,upp} + \left[ \frac{(T_{l,upp} - T_{l,low})}{(diss_{upp} - diss_{low})} \right] \cdot (Rad_{eq} - diss_{low}) \quad (\text{Eq. 3.38})$$

The energy loss for this temperature is calculated and its closeness to the desired energy equilibrium is assessed. If the result is not sufficiently close, a second iteration is performed (*fig. 3.22, right*). For the second iteration, the temperature boundaries are shifted according to the result of the first iteration. If the intermediate temperature of the first iteration step produces a total energy loss that lies below the equilibrium (*fig. 3.22, left*), this can be taken as an indication that the leaf temperature was assumed too cold and that the correct solution will be found between the intermediate temperature of the first iteration and the upper temperature boundary. Consequently, the second iteration is started with the intermediate temperature serving as the new lower bound of the estimation range (*fig. 3.22, right*).

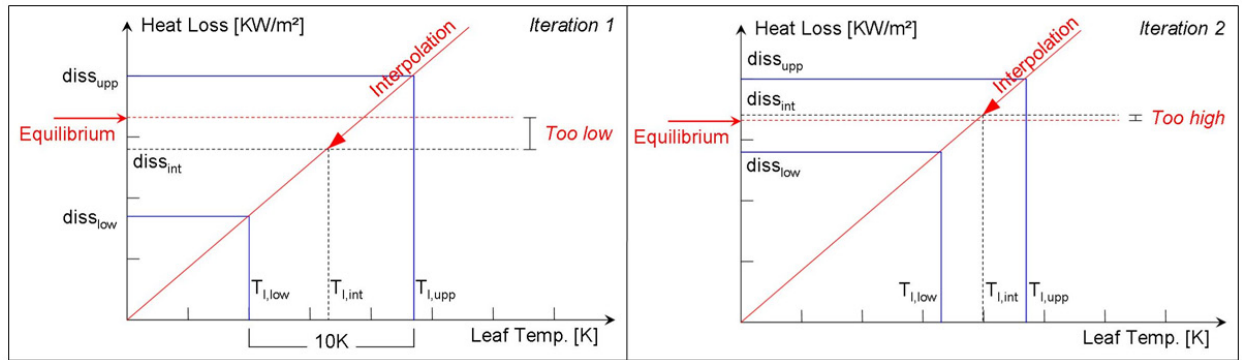


Figure 3.22: Exemplary results of the iteration steps 1 and 2. For the first iteration step, the intermediate temperature was assumed too low (left), so that for the second iteration step it is used as the lower temperature boundary (right).

For the second iteration, it may be the case that the leaf temperature is assumed too warm, so that the intermediate temperature happens to exceed the equilibrium temperature. In this case, the boundaries of the estimate are redistributed the other way round. The intermediate temperature of the second iteration step then will be used as the upper boundary for the third iteration step (fig. 3.23, left).

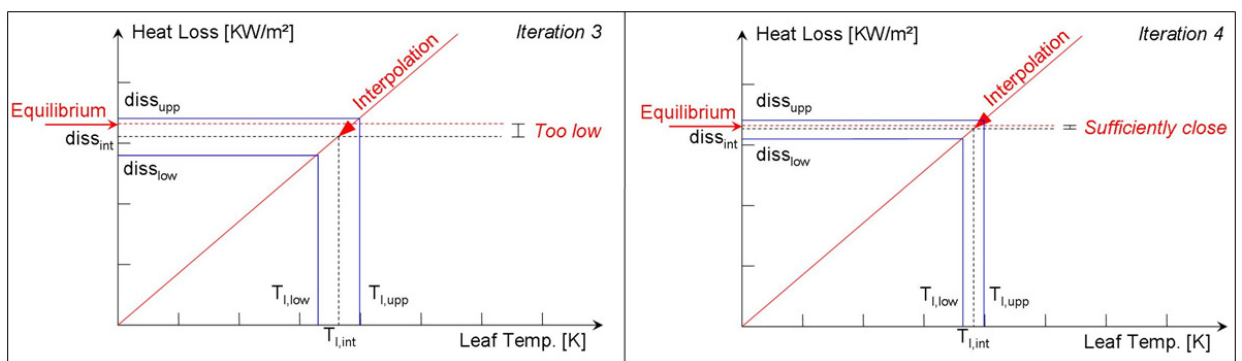


Figure 3.23: Exemplary results of the iteration steps 3 and 4. For the third iteration step, the leaf temperature again is assumed too low, only to meet the requirements of the threshold with the fourth iteration.

This swaying calculation proceeds until the critical threshold is satisfied or the correct temperature is found (fig. 3.23, right). However, experiences have shown that for most cases two or three iteration steps are sufficient when a tolerance to failure of  $5 \text{ W m}^{-2}$  is accepted. Thereby it has to be remembered that the three ways of heat dissipation (see sections 3.3.3.4.1 - 3) have to be calculated for every iteration step. The leaf temperature therefore is highly sensible to external influences (fig. 3.24).

Figure 3.24 traces the daily course of modelled leaf temperatures for a winter wheat stand. During the night, naturally the complete stand is shaded and only the shade temperatures are calculated. Both vegetation layers are emitting energy according to their temperature and therefore fall below the air temperature during night time.

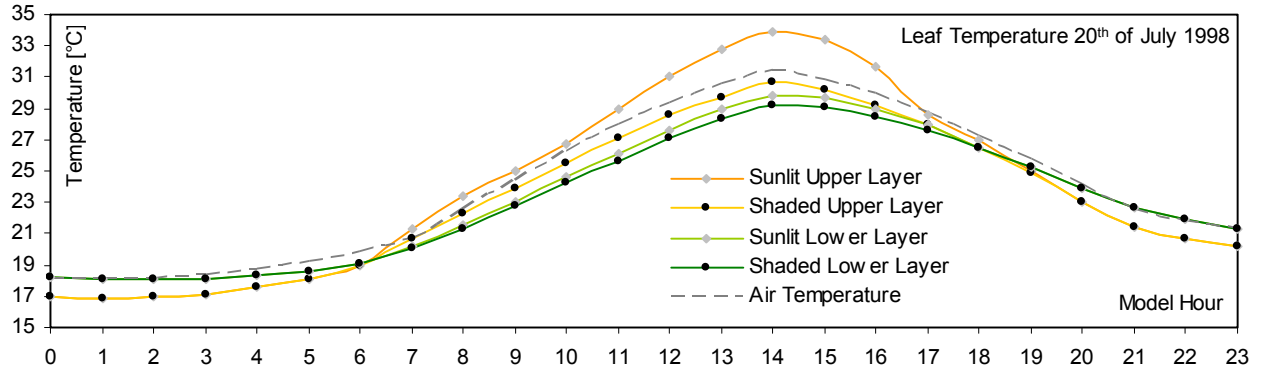


Figure 3.24: Daily course of the modelled leaf temperature of a wheat stand on a hot summer day (20<sup>th</sup> of July 1998), discerned into two canopy layers as well as into sunlit and shaded leaves.

The lower canopy layer is shielded by the upper canopy layer and therefore does not cool as much as the lower layer. As soon as the sun rises (at 6 am), the temperatures start to diverge. The energy input from above causes the upper layer to heat up more rapidly than the lower layer, so that at 7 am it is warmer than the lower layer. At the same time, the temperature of the sunlit leaves of the upper canopy layer exceeds the air temperature, while the lower vegetation layer as well as the shaded leaves stay beneath it, due to the increasing amount of latent heat that is transported from the leaves with the transpiration. The energy input of the sunlit leaves in the upper layer is rather high, so that the loss of latent heat cannot fully compensate the energy input. As a consequence, the leaves heat up until they have reached a temperature that lies 2.5 degrees above the air temperature and nearly five degrees above the shaded leaves of the lower layer. From the temperature maximum (at 2 pm) on, the temperatures start to converge again. As soon as the sun angles are too low to irradiate the leaves, the temperature of the sunlit leaves decreases rapidly, so that at sunset (8 pm) the sun temperatures again equal the shade temperatures.

#### 3.3.3.4.1 Longwave Emission

The emission of heat from the leaf is calculated applying the Stefan-Boltzmann-Law of emission successively for the estimated leaf temperature of both, the shaded and the sunlit leaves (eq. 3.39).

$$Diss_{rad} = \alpha_{leaf} \cdot \sigma \cdot 0.002 \cdot T_{l,est}^4 \quad (Eq. 3.39)$$

According to Kirchhoff's law, the emissivity of the leaf is assumed to equal its absorptivity ( $\alpha_{leaf}$ ). The overall absorptance of the leaf is set to 96 % according to NOBEL (1991). While  $\sigma$  is the Stefan-Boltzmann constant, the factor 0.002 converts the physical unit from  $W m^{-2}$  to  $KW m^{-2}$  and at the same time doubles the emitted energy, taking into account that long wave radiation is

emitted on both sides of the leaf (*fig. 3.19*). The applied temperature ( $T_{l,est}$ ) is the estimated leaf temperature of the current iteration step.

### 3.3.3.4.2 Sensible Heat Flux

The conductive heat loss, or the sensible heat flux from the leaf respectively, depends on three major conditions, as there are the temperature gradient between the leaf and the surrounding air, the thermal conductivity of the air and the inhibition of energy transport through the boundary layer that exists between leaf and atmosphere.

The temperature gradient ( $\Delta T$ ) depends on the difference of the air temperature ( $T_a$ ) to the currently estimated leaf temperature (*eq. 3.40*).

$$\Delta T = T_{l,est} - (T_a + 273.16) \quad (\text{Eq. 3.40})$$

The thermal conductivity of the air ( $tca$ ) is approximated through a linear relation (*eq. 3.41*) according to measurements from NOBEL (1991, *fig. 3.25, left*).

$$tca = (24343 \cdot 10^6) + (67143 \cdot 10^9) \cdot T_a \quad (\text{Eq. 3.41})$$

The thickness of the boundary layer ( $tbl$ ) according to NOBEL (1991) depends on the width of the leaf ( $wl$ ) and the wind velocity ( $u$ ), as displayed in equation 3.42 and figure 3.25 (right).

$$tbl = 0.004 \cdot \sqrt{\frac{wl}{u}} \quad (\text{Eq. 3.42})$$

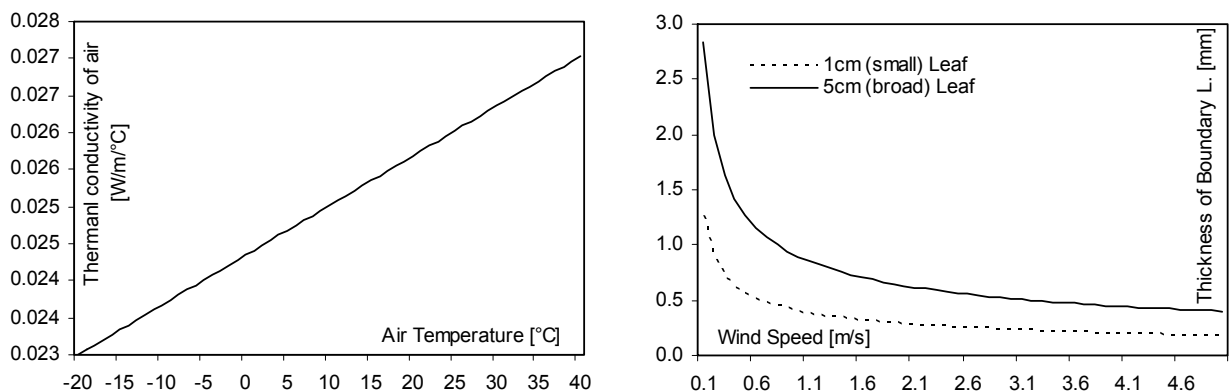


Figure 3.25: Coefficient of the thermal conductivity of air in dependence of the air temperature (left) and thickness of the boundary layer in dependence of the wind velocity and the width of the leaf (right).

With increasing wind speed, the thickness of the boundary layer is reduced (*fig. 3.26*), while it is generally thinner for small leaves than it is for broad ones (*fig. 3.25, right*).



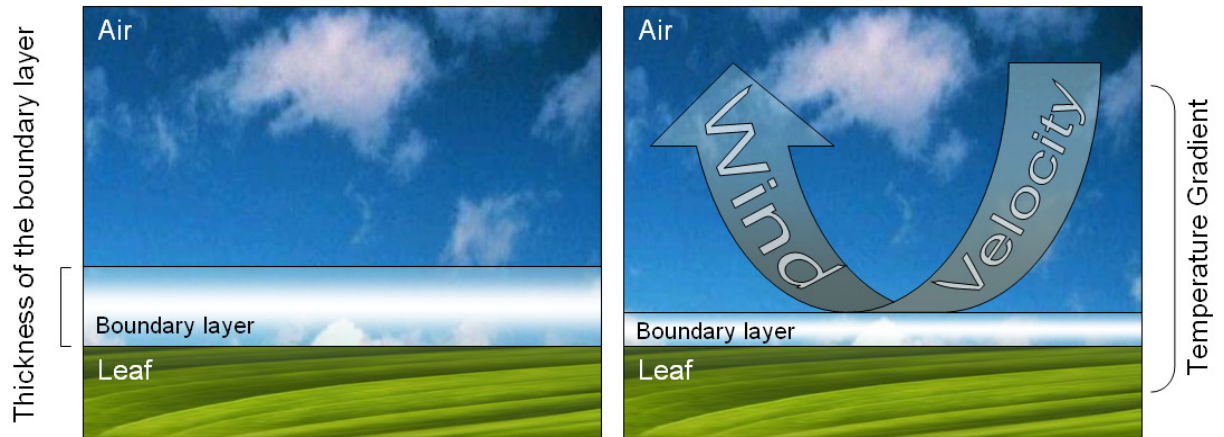


Figure 3.26: Thickness of the boundary layer in dependence of the wind velocity.

The sensible heat flux from the leaf then can be written as equation 3.43, where the denominator of 1000 accounts for the conversion from  $\text{W m}^{-2}$  to  $\text{KW m}^{-2}$  and the factor of 2 for the double sided exposure of the leaf.

$$diss_{sens} = 2 \cdot \frac{tca}{tbl} \cdot \left( \frac{\Delta T}{1000} \right) \quad (\text{Eq. 3.43})$$

#### 3.3.3.4.3 Latent Heat Flux

The third and most determinant loss of energy from the leaf is the amount of energy that is transported from the plant via the stream of latent heat, which escapes through the stomata. This process can most adequately be described with the term transpiration. The driving force of the transpiration stream is the vapour pressure gradient between the leaf and the surrounding air. Nonetheless, two barriers are inhibiting the latent heat flux. The determinant resistance that inhibits the gas exchange between the leaf and the atmosphere is the cuticle of the leaf, whose conductivity is regulated through the stomata of the epidermis. A second barrier is opposed to the transpiration stream by the resistance of the boundary layer that surrounds the leaf surface. The conductance of the boundary layer ( $g_a$ ) for water vapour can be described as equation 3.44 following NOBEL (1991).

$$g_a = \frac{d_{wv}}{tbl} \cdot 1000 \cdot \frac{P}{R \cdot T_{l,est}} \quad (\text{Eq. 3.44})$$

Besides the gas constant ( $R$ ) and the actual air pressure ( $P$ ), this requires the determination of the thickness of the boundary layer ( $tbl$ , see previous section) and the diffusion coefficient of water vapour ( $d_{wv}$ ).



The diffusion coefficient of water vapour can be approximated through a linear relation with the Celsius degree air temperature ( $T_a$ ) following NOBEL (1991, eq. 3.45).

$$d_{wv} = 2.126 \cdot 10^{-5} + 1.48 \cdot 10^{-7} \cdot T_a \quad (\text{Eq. 3.45})$$

Based on the assumption that a correct physical description of growth processes will apply to every form of vegetation growth, all vegetation types are described through the same physical routines in PROMET. Nonetheless, an exception has to be made here for the calculation of the boundary layer surrounding the needles of coniferous species. The alternative calculation of the conductance of the boundary layer for H<sub>2</sub>O accounts for the bunching of needles around coniferous twigs (eq. 3.46). The needles shield each other against atmospheric influences, producing a space of reduced wind speed which leads to an inhibited conductivity of the boundary layer (JARVIS ET AL. 1976).

$$g_a = \frac{g_a}{1.67 \cdot \left( \sum_{bl}^{0.43} \right)} \quad (\text{Eq. 3.46})$$

The influence of the reduction can be regulated through a scaling parameter ( $\Sigma_{bl}$ ) that was assumed with a value of 1 for the calculations that are presented here.

The calculation of the stomatal conductance ( $g_s$ ) requires the simulation of all processes that are related to the leaf photosynthesis and which are described in detail within the following section (3.3.3.5). Since these processes are highly correlated with the leaf temperature, they are repeatedly calculated for every iteration step until the correct leaf temperature is found (see section 3.3.3.4).

After the stomatal conductivity has been determined through the photosynthesis routine, the overall conductivity of the leaf ( $g_l$ ) that consists of the two inhibiting barriers stomata ( $g_s$ ) and boundary layer ( $g_a$ ) is calculated (eq. 3.47).

$$g_l = 1 / \left( \frac{1}{g_a} + \frac{1}{g_s} \right) \quad (\text{Eq. 3.47})$$

The flux of transpired water for the currently estimated leaf temperature and the current time step than is described as equation 3.48, where  $\Delta e$  represents the vapour pressure deficit and  $P$  is the current air pressure with the physical unit mbar. For the calculation of the vapour pressure deficit ( $\Delta e = e_l - e_a$ ), the vapour pressure within the leaf ( $e_l$ ) is assumed to equal the saturation

pressure, while the atmospheric vapour pressure ( $e_a$ ) is determined through the relative humidity of the surrounding air.

$$E_{Tflux} = \frac{\Delta e}{P \cdot g_l} \quad (\text{Eq. 3.48})$$

For the final determination of the total heat loss, the transpiration flux has to be transformed into a physical unit of KW m<sup>-2</sup> using an approximation of the latent heat of vaporization (kJ mmol<sup>-1</sup>) according to NOBEL (1991, eq. 3.49).

$$diss_{lat} = E_{Tflux} \cdot \left[ 450643 \cdot 10^{-7} - 429143 \cdot 10^{-10} \cdot \left( T_{l,est} - 273.16 \right) \right] \quad (\text{Eq. 3.49})$$

Now, the total heat loss ( $diss_{tot}$ ) for the currently estimated leaf temperature can be summed (eq. 3.50) by combining the results of the equations 3.39, 3.43 and 3.49.

$$diss_{tot} = diss_{rad} + diss_{sens} + diss_{lat} \quad (\text{Eq. 3.50})$$

### 3.3.3.5 Net Primary Production

The innermost core of the biological submodels of PROMET consists of the net photosynthesis model for C<sub>3</sub> species by FARQUHAR, VON CAEMMERER AND BERRY (1980), including extensions and improvements developed by FALGE (1997) for the modelling of forest growth as well as adaptations to the simulation of C<sub>4</sub> species applying a method after CHEN ET AL. (1994).

#### 3.3.3.5.1 Carboxylation Limitations

The modelling of the net photosynthesis rate is based on the enzyme kinetics of Ribulose-1.5-Biphosphate-Carboxylase-Oxygenase (RuBisCO). The concentration of the competitive gases CO<sub>2</sub> and O<sub>2</sub> is taken into account, while the relation of the concentration of Ribulose-1.5-Biphosphate (RuBP) and the number of active RuBisCO enzymes is monitored. The stomatal conductance is modelled in dependence of the assimilation rate, the relative air humidity and the gradient of the CO<sub>2</sub> concentration, applying an empirical function after BALL ET AL. (1987).

This model was chosen for an implementation into PROMET, because it includes the explicit reaction of the assimilation rate on the CO<sub>2</sub> concentration within the leaf ( $C_i$ ). The internal CO<sub>2</sub> concentration again is connected through the stomata to the CO<sub>2</sub> concentration of the atmosphere ( $C_a$ ), which, besides the temperature, is the determining variable when the impact of climate change is assessed with a physically based model.

The rate of carboxylation is limited by two determinant situations. For low CO<sub>2</sub> concentrations within the leaf, the fixation rate of RuBisCO and the concentration of CO<sub>2</sub> and O<sub>2</sub> determine the assimilation rate ( $w_c$ ), while for high CO<sub>2</sub> concentrations the photosynthesis is limited by the rate of the electron transport or the rate of RuBP regeneration ( $w_j$ ) respectively (see section 1.5). The rate of net photosynthesis according to FARQUHAR ET AL. (1980) then reads as (eq. 3.51):

$$np = \left(1 - \frac{\Gamma^*}{C_i}\right) \cdot \text{MIN}\{w_c; w_j\} - 0.5 \cdot r_d \quad (\text{Eq. 3.51})$$

The term  $0.5 \times r_d$  here represents the fraction of the dark respiration ( $r_d$ ) during daytime, which can best be described as the mitochondrial respiration. The symbol  $\Gamma^*$  stands for the CO<sub>2</sub> compensation point, i.e. the assimilation rate where the oxygen production of the photosynthesis process exceeds the oxygen demand of the mitochondrial respiration. The CO<sub>2</sub> compensation point is calculated following FALGE (1997, eq. 3.52) in dependence of the maximum velocity of oxygenation ( $V_{o_{max}}$ ) and carboxylation ( $V_{c_{max}}$ ) with  $O_2$  representing the internal oxygen concentration within the leaf and  $\tau$  standing for a dimensionless factor that describes the substrate specificity:

$$\Gamma^* = \frac{0.5 \cdot V_{o_{max}} \cdot K_c \cdot 1000 \cdot O_2}{V_{c_{max}} \cdot K_o} = \frac{0.5 \cdot 1000 \cdot O_2}{\tau} \quad (\text{Eq. 3.52})$$

By multiplying the numerator with a factor of 1000, the compensation point is converted from the physical unit of ml l<sup>-1</sup> to  $\mu\text{l l}^{-1}$ .

The parameters  $r_d$ ,  $\tau$ ,  $K_c$  and  $K_o$  are temperature dependent and are all four described through an exponential Arrhenius-function (FARQUHAR AND WONG 1984, MEDLYN ET AL. 2002b, eq. 3.53):

$$\left(r_d / \tau / K_c / K_o\right) = \left(r_{d25} / \tau_{25} / K_{c25} / K_{o25}\right) \cdot e^{\frac{Ea_{(r_d, \tau, c, o)} \cdot (T_{l,est} - 298.16)}{R \cdot (T_{l,est} \cdot 298.16)}} \quad (\text{Eq. 3.53})$$

The temperature, used here for the definition of the kinetic constants, is the leaf temperature from the current estimate for the latent heat flux ( $T_{l,est}$ ), while the parameters  $r_{d25}$ ,  $\tau_{25}$ ,  $K_{c25}$  and  $K_{o25}$  are holding the value of the corresponding Michaelis-Menten constants at 25 °C.  $Ea_{rd}$ ,  $Ea_\tau$ ,  $Ea_c$  and  $Ea_o$  are representing the activation energies of the respective processes with the unit J mol<sup>-1</sup>, while the constant  $R$  stands for the gas constant with a value of 8.31 J K<sup>-1</sup> mol<sup>-1</sup>.

The competitive conversion of CO<sub>2</sub> (carboxylation rate  $w_c$ , eq. 3.54) and O<sub>2</sub> (oxygenation rate  $w_o$ , eq. 3.55) by RuBisCO under saturated RuBP conditions is modelled following FARQUHAR ET AL. (1980):

$$w_c = \frac{V_{c_{\max}} \cdot c_i}{c_i + K_c \cdot \left(1 + \frac{O_2}{K_o}\right)} \quad (\text{Eq. 3.54})$$

$$w_o = \frac{V_{o_{\max}} \cdot O_2}{O_2 + K_o \cdot \left(1 + \frac{C_i}{K_c}\right)} = \frac{w_c \cdot \Gamma^*}{0.5 \cdot C_i} \quad (\text{Eq. 3.55})$$

The temperature dependency of the maximum velocity of the carboxylation ( $V_{c_{\max}}$ ), which is needed for the calculation of  $w_c$  and  $w_o$ , is described as a complex Arrhenius-function (JOHNSON ET AL. 1942, MEDLYN ET AL. 2002a and b, eq. 3.56), mostly parallel to the other temperature dependent parameters, while the calculation of  $V_{o_{\max}}$  can be avoided through substitution (eq. 3.55).

$$V_{c_{\max}}(T_{l,est}) = V_{c_{\max 25}} \cdot e^{\frac{E_{a_{vc_{\max}}}(T_{l,est} - 298.16)}{298.16 \cdot R \cdot T_{l,est}}} \cdot \left( \frac{1 + e^{\frac{298.16 \cdot \Delta s - E_{a_{vc_{\max}}}}{298.16 \cdot R}}}{1 + e^{\frac{T_{l,est} \cdot \Delta s - E_{d_{vc_{\max}}}}{T_{l,est} \cdot R}}} \right) \quad (\text{Eq. 3.56})$$

In equation 3.56, the variable  $E_{d_{vc_{\max}}}$  stands for the deactivation energy of the process, while  $\Delta s$  is a term that describes the entropy in  $\text{J K}^{-1} \text{mol}^{-1}$ . The general course of the correlation of the chemical processes in the leaf with the leaf temperature is illustrated in figure 3.27 for the Arrhenius-functions of the simple (fig. 3.27, left) and the complex type (fig. 3.27, right).

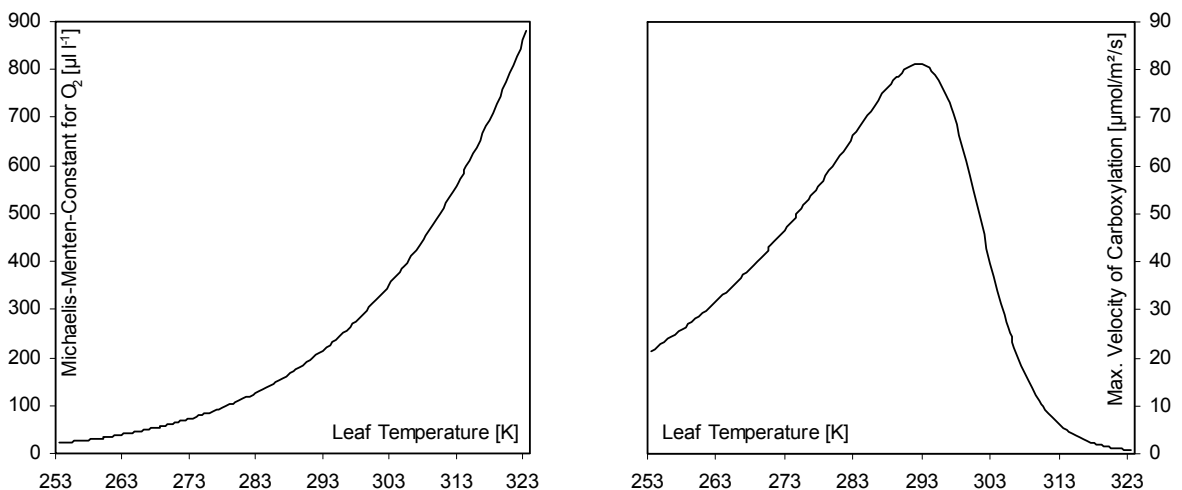


Figure 3.27: Arrhenius-function of the simple type for the calculation of the temperature dependency of the Michaelis-Menten constant for Oxygen (left) and complex Arrhenius-function for the calculation of the maximum velocity of carboxylation for a range of common leaf temperatures (right).

If not enough RuBP is present, the photosynthesis in the model is limited by the rate of regeneration of RuBP, which is the case for CO<sub>2</sub> saturated conditions in the mesophyll of the leaf. In this case, the rate of photosynthesis ( $p_m$ ) is smaller than the rate of RuBP conversion ( $w_c + w_o$ ). For the regeneration of one RuBP molecule, four electrons have to be transported for the provision of the needed chemical energy (see section 1.5.2, FARQUHAR AND VON CAEMMERER 1982). The degree of the limitation due to the electron transport is accounted for in equation 3.57.

$$w_j = w_c \cdot \frac{p_m}{w_c + w_o} \quad (\text{Eq. 3.57})$$

Remembering equations 3.54 and 3.55,  $w_j$  can also be described simplified as equation 3.58:

$$w_j = \frac{p_m}{1 + \frac{2 \cdot \Gamma^*}{C_i}} \quad (\text{Eq. 3.58})$$

The modelling of C<sub>4</sub> species here demands an extra treatment, for the C<sub>4</sub> photosynthesis is supposed to be solely controlled by the PEPcarboxylase (CHEN ET AL. 1994, see section 1.5.2.2). Therefore, the electron limited rate of carboxylation  $w_j$  is determined according to CHEN ET AL. (1994) as (eq. 3.59) for all C<sub>4</sub> crops:

$$w_j = \frac{p_m \cdot C_i}{C_i \cdot K_c} \quad (\text{Eq. 3.59})$$

The rate of leaf photosynthesis under saturated CO<sub>2</sub> conditions ( $p_m$ , eq. 3.61) is modelled in dependence of the absorbed photosynthetic active radiation ( $aPAR$ ) and the temperature dependent rate of RuBP regeneration at saturated light and CO<sub>2</sub> conditions ( $P_{ml}$ , eq. 3.60). The temperature dependency of the potential rate of the RuBP regeneration is modelled using the complex Arrhenius-Function (eq. 3.60) with  $J_{max}$  representing the maximum rate of the electron transport through the photo system II.

$$p_{ml}(T_{l,est}) = J_{\max 25} \cdot e^{\frac{Ea_{J_{\max}}(T_{l,est}-298.16)}{298.16 \cdot R \cdot T_{l,est}}} \cdot \left( \frac{1 + e^{\frac{298.16 \cdot \Delta s - Ea_{J_{\max}}}{298.16 \cdot R}}}{1 + e^{\frac{T_{l,est} \cdot \Delta s - Ed_{J_{\max}}}{T_{l,est} \cdot R}}} \right) \quad (\text{Eq. 3.60})$$

The light dependency of photosynthesis is well known. A well established (FALGE 1997, TENHUNEN ET AL. 1976) empiric equation after SMITH (1937) therefore is used (eq. 3.61), where  $\alpha$  is the light use efficiency at saturated  $\text{CO}_2$ , when no photorespiration takes place, featuring a physical unit of mol  $\text{CO}_2$  per mol photons, and  $aPAR$  is the absorbed photosynthetic radiation.

$$P_m = \frac{\alpha \cdot aPAR}{\sqrt{1 + \frac{\alpha^2 \cdot aPAR^2}{P_{ml}^2}}} \quad (\text{Eq. 3.61})$$

The radiation input here has to be converted from  $\text{W m}^{-2}$  to a quantum flux density of  $\mu\text{mol photons of PAR m}^{-2} \text{ s}^{-1}$ . This is accomplished by using a simple conversion factor of 4.56  $\mu\text{mol per Joule PAR}$  (LARCHER 1994, GOUDRIAAN AND VAN LAAR 1994, YIN AND VAN LAAR 2005).

### 3.3.3.5.2 $\text{CO}_2$ Diffusion

The last variable that is needed, before the assimilation rate that corresponds with the currently estimated leaf temperature can be computed, is the concentration of  $\text{CO}_2$  at the location where the carboxylation takes place, i.e. within the leaf. A fixed ratio between atmospheric and intercellular  $\text{CO}_2$  could be applicable (RODRIGUEZ ET AL. 1999), because observations have shown that under a wide range of conditions the ratio stays constant at about 0.7 for  $\text{C}_3$  and about 0.4 for  $\text{C}_4$  plants (GOUDRIAAN AND VAN LAAR 1978, WONG ET AL. 1979). Later it has been found that the  $C_i/C_a$  ratio depends on the air-to-leaf water vapour deficit (COLLATZ ET AL. 1992, LEUNING 1995, ZHANG AND NOBEL 1996). Analytical solutions are available for the derivation of the  $C_i/C_a$  ratio (COLLATZ ET AL. 1992, BALDOCCHI 1994), but they are averted here in favour of a simplified assumption following YIN AND VAN LAAR (2005, eq. 3.62) that derives the internal  $\text{CO}_2$  concentration as a linear function of the vapour pressure deficit and the gradient of concentration between the leaf and the atmosphere.

$$C_i = 1 - \left( \frac{1 - \Gamma^*}{C_a} \right) \cdot [c_0 + c_1 \cdot (e_l - e_a)] \quad (\text{Eq. 3.62})$$

Here  $e_l$  and  $e_a$  represent the vapour pressure within the leaf and in the atmosphere respectively, while  $c_0$  and  $c_1$  are empirical input coefficients. The adjustment of the input coefficients was derived by YIN AND VAN LAAR (2005) from observed data by MORISON AND GIFFORD (1983). The default value for  $c_0$  is 0.14 for both  $\text{C}_3$  and  $\text{C}_4$  species, while  $c_1$  is initialised with a value of 0.116 for  $\text{C}_3$  and of 0.195 for  $\text{C}_4$  species.  $C_i$  derived from equation 3.62 is used as a first guess. The internal  $\text{CO}_2$  concentration is needed to determine, whether the dominating limitation is due to

the Rubisco activity or to the electron transport, that is to say if either  $w_c$  or  $w_j$  applies. The true  $\text{CO}_2$  concentration cannot be determined until the actual net photosynthesis has been computed. For the calculation of the stomatal conductance for  $\text{H}_2\text{O}$  ( $g_s$ ), a widely recognized model developed by BALL ET AL. (1987) is applied (eq. 3.63). There,  $g_{\min}$  is the minimum conductance, i.e. the conductance of the leaf cuticle when the stomata are closed,  $gfac$  is the BALL ET AL. (1987) coefficient of stomatal conductance that describes the sensitivity of the stomatal reaction upon environmental factors,  $np$  is the net rate of carbon fixation,  $rh$  is the relative humidity of the surrounding air and  $C_s$  is the concentration of  $\text{CO}_2$  at the leaf surface.

$$g_s = g_{\min} + \frac{gfac \cdot 1000 \cdot (np + 0.5 \cdot r_d) \cdot rh}{C_s} \quad (\text{Eq. 3.63})$$

Assuming a molecular diffusion between leaf surface and atmosphere within the boundary layer, the  $\text{CO}_2$  concentration at the leaf surface can be derived from Fick's diffusion law (eq. 3.64).

$$C_s = C_a - \frac{1.6 \cdot np \cdot 1000}{g_a} \quad (\text{Eq. 3.64})$$

The denominator  $g_a$  here is the conductivity of the boundary layer calculated after NOBEL (1991, see section 3.3.3.4.3, eq. 3.44), the factor of 1000 compensates the different physical units between  $np$  and  $g_a$  (mmol to  $\mu\text{mol}$ ), while the factor 1.6 results from the difference of the diffusion behaviour of  $\text{H}_2\text{O}$  and  $\text{CO}_2$  (FARQUHAR AND SHARKEY 1982).

### 3.3.3.5.3 Analytical Solution

The derivation of the photosynthesis parameters introduced above finally leads to a system of equations that consists of four equations with four unknowns, as there are the net photosynthesis ( $np$ ), the concentration of  $\text{CO}_2$  at the leaf surface ( $C_s$ ), the stomatal conductance ( $g_s$ ) and the internal concentration of  $\text{CO}_2$  ( $C_i$ ). This system of equations could be solved by iteration (FALGE 1997), but since this computation already has to be performed successively for every iteration step for the sunlit and the shaded leaves of two vegetation layers and again for each time step (see section 3.3.3.4), an analytical solution following BALDOCCHI (1994) was favoured here in order to save computing time. According to BALDOCCHI (1994), the equation describing the net carbon fixation (eq. 3.51) can be reconverted to equation 3.65 by applying the auxiliary variables  $a$  ( $\mu\text{mol m}^{-2}$  leaf area  $\text{s}^{-1}$ ),  $b$  ( $\mu\text{l l}^{-1}$ ),  $d$  ( $\mu\text{l l}^{-1}$ ) and  $e$  (-), which are initialized according to table 3.04.

$$C_i = \frac{a \cdot d + b \cdot (np + 0.5 \cdot r_d)}{a - e \cdot (np + 0.5 \cdot r_d)} \quad (\text{Eq. 3.65})$$

The auxiliary variables are holding values that are initialized according to table 3.04 (left) or to table 3.04 (right) respectively, depending on the conditions that are currently limiting the carbon fixation rate. If the photosynthesis is currently limited by RuBisCO or the  $\text{CO}_2/\text{O}_2$  concentration,  $w_c$  will be lower than  $w_j$ . If the rate of the electron transport for the regeneration of RuBP is limiting the carbon fixation rate,  $w_j$  will be smaller than  $w_c$ .

Table 3.04: Initialisation of the auxiliary variables applied to the analytical solution of the photosynthesis related equation system, depending on the nature of the limitation of the carbon fixation rate.

If $w_c < w_j$ ( $\text{CO}_2$ is limiting)	If $w_j < w_c$ (Electron transport is limiting)
$a = Vc_{\max}$	$a = 4 \cdot p_m$
$b = K_c \cdot (1 + \text{O}_2 / K_o)$	$b = 8 \cdot \Gamma^*$
$d = \Gamma^*$	$d = \Gamma^*$
$e = 1$	$e = 4$

For the solution of this equation system, two different derivations of the internal  $\text{CO}_2$  concentration are necessary. The first can be calculated by applying Fick's diffusion law to the diffusion from the leaf surface into the mesophyll as well, so that equation 3.64 is converted to equation 3.66:

$$C_i = C_s - \frac{1.6 \cdot np \cdot 1000}{g_s} \quad (\text{Eq. 3.66})$$

If the equations for the determination of  $g_s$  (eq. 3.63) and  $C_s$  (eq. 3.64) then are inserted into equation 3.64, the second computation for  $C_i$  can be derived (eq. 3.67) with the assistance of another set of auxiliary variables (tab. 3.05, bottom).

$$C_i = \frac{\kappa \cdot np^2 + \beta \cdot np + \gamma \cdot C_a}{\lambda \cdot np + \gamma} \quad (\text{Eq. 3.67})$$

This expression for the internal  $\text{CO}_2$  concentration (eq. 3.67) is equated with equation 3.51, which was introduced at the beginning of this section, and then transformed until a cubic equation for  $np$  can be derived (eq. 3.68).



$$np^3 \cdot o_1 + np^2 \cdot o_2 + np \cdot o_3 + o_4 = 0 \quad (\text{Eq. 3.68})$$

With the assistance of the auxiliary variables determined in table 3.05 (bottom), another set of auxiliary variables ( $o_{1-4}$ ) can be initialized (tab. 3.05, top).

Table 3.05: Initialization of the auxiliary variables  $o_{1-4}$  applied to the solution of the cubic equation system for the determination of the net photosynthesis rate and initialization of the auxiliary variables kappa, beta, gamma and lambda for the calculation of the internal  $\text{CO}_2$  concentration.

$o_1 = e \cdot \kappa$ $o_2 = b \cdot \lambda + e \cdot \beta - (a - e \cdot 0.5 \cdot r_d) \cdot \kappa$ $o_3 = (a \cdot d + b \cdot 0.5 \cdot r_d) \cdot \lambda + b \cdot \gamma \cdot C_a - (a - e \cdot 0.5 \cdot r_d) \cdot \beta$ $o_4 = (a \cdot d + b \cdot 0.5 \cdot r_d) \cdot \gamma - (a - e \cdot 0.5 \cdot r_d) \cdot \gamma \cdot C_a$
<p>With:</p> <hr style="border-top: 1px dashed black;"/> $\kappa = 1600^2 \cdot (1 - rh \cdot gfac / 1.6 + g_{\min} / g_a)$ $\beta = 1600 \cdot C_a \cdot (g_a \cdot rh \cdot gfac / 1.6 - 2 \cdot g_{\min} - g_a) - 1600^2 \cdot 0.5 \cdot r_d \cdot rh \cdot gfac / 1.6$ $\gamma = C_a \cdot g_{\min} \cdot g_a + 1000 \cdot 0.5 \cdot r_d \cdot g_a \cdot rh \cdot gfac$ $\lambda = 1600 \cdot (g_a \cdot rh \cdot gfac / 1.6 - g_{\min})$

Following a solution scheme for cubic equations after BRONSTEIN AND SEMENDJAJEW (1984), the equation is transformed to the normal form of a cubic equation through a division by  $o_1$  (eq. 3.69) and the help of the auxiliary variables  $r$ ,  $s$ , and  $t$  (tab. 3.06).

$$np^3 + np^2 \cdot r + np \cdot s + t = 0 \quad (\text{Eq. 3.69})$$

Table 3.06: Initialisation of the auxiliary variables  $p$ ,  $q$ ,  $r$ ,  $s$ ,  $t$ ,  $y$  and  $dis$  applied to the solution of the cubic equation for  $np$ .

$r = o_2 / o_1$ $s = o_3 / o_1$ $t = o_4 / o_1$ $dis = (p/3)^3 + (q/2)^2$	$p = (3 \cdot s - r^2) / 3$ $q = 2 \cdot r^3 / 27 - r \cdot s / 3 + t$ $y = np + r / 3$
---	---

Via substitution with the auxiliary variables  $y$ ,  $p$  and  $q$  (tab. 3.06, right), a reduced equation is generated that can be written as equation 3.70:

$$y^3 + y \cdot p + q = 0 \quad (\text{Eq. 3.70})$$

In dependence of the algebraic sign of the discriminant (*dis*, *tab. 3.06, left*) and the auxiliary variable  $p$ , either one real and two conjugated complex solutions, or three real solutions will be available, which can be computed with the help of the auxiliary variables  $v1$  and  $v2$  (*tab. 3.07*).

Table 3.07: Initialisation of the auxiliary variables  $v1$  and  $v2$  applied to the solution of the reduced equation for  $np$ .

$v1 = (\text{sgn } q) \cdot \sqrt{\frac{ p }{3}}$ <p style="text-align: center; margin-top: 5px;">Sgn <math>q</math> = algebraic sign of <math>q</math></p>	<div style="border-left: 1px dashed black; height: 100%;"></div>	$v2 = \frac{q}{2 \cdot v1^3}$
---	--	-------------------------------

If  $p$  is larger than zero, only one real solution for the net photosynthesis rate exists (*eq. 3.71*).

$$np = -2 \cdot v1 \cdot \sinh\left(\frac{\log(v2 + \sqrt{v2^2 + 1})}{3}\right) - \frac{r}{3} \quad (\text{Eq. 3.71})$$

sinh = Sinus hyperbolicus

If  $p$  is smaller than zero and the discriminant (*dis*) is larger than zero, there also is only one real solution for  $np$  (*eq. 3.72*).

$$np = -2 \cdot v1 \cdot \cosh\left(\frac{\log(v2 + \sqrt{v2^2 - 1})}{3}\right) - \frac{r}{3} \quad (\text{Eq. 3.72})$$

cosh = Cosinus hyperbolicus

But, if  $p$  is smaller than zero, while the discriminant is zero or above, the equation system results in three real solutions for the rate of the net photosynthesis ( $np_{1-3}$ , *eqs. 3.73a-c*).

$$np_1 = -2 \cdot v1 \cdot \cos\left(\frac{\text{acos}(v2)}{3}\right) - \frac{r}{3} \quad (\text{Eq. 3.73a})$$

acos = Arcus Cosinus

$$np_2 = -2 \cdot v1 \cdot \cos\left(\frac{\text{acos}(v2) + 2 \cdot \pi}{3}\right) - \frac{r}{3} \quad (\text{Eq. 3.73b})$$

$$np_3 = -2 \cdot v1 \cdot \cos\left(\frac{\text{acos}(v2) + 4 \cdot \pi}{3}\right) - \frac{r}{3} \quad (\text{Eq. 3.73c})$$

The most complex solution therefore at least returns three different results. The subsequent decision tree according to FALGE (1997) will lead to the correct rate of net photosynthesis.

If  $\kappa$  is larger than zero:

- If all three solutions ( $np_{1-3}$ ) are positive, the smallest solution is the correct one.
- If only one of the solutions is negative, this will be the one to select.
- For all other cases, the greatest solution will be the right one.

If  $\kappa$  is smaller than zero:

- The third real solution ( $np_3$ ) will always be the correct one.

For the case that  $\kappa$  exactly equals zero, the equation system for the net rate of carbon fixation is reduced from a cubic to a quadratic equation system (eq. 3.74).

$$np^2 \cdot o_2 + np \cdot o_3 + o_4 = 0 \quad (\text{Eq. 3.74})$$

For this occurrence, the auxiliary variables  $o_{2-4}$  (tab. 3.08, top) are initialised slightly different from the ones that are used for the solution of the cubic equation (tab. 3.05, top).

Table 3.08: Initialization of the auxiliary variables  $o_{2-4}$  applied to the solution of the quadratic equation system for the determination of the net photosynthesis rate.

$$\begin{aligned} o_2 &= b \cdot \lambda + e \cdot \beta \\ o_3 &= (a \cdot d + b \cdot 0.5 \cdot r_d) \cdot \lambda + b \cdot \gamma + e \cdot \gamma \cdot C_a - (a - e \cdot 0.5 \cdot r_d) \cdot \beta \\ o_4 &= (a \cdot d + b \cdot 0.5 \cdot r_d) \cdot \gamma - (a - e \cdot 0.5 \cdot r_d) \cdot \gamma \cdot C_a \end{aligned}$$

With:

$$\begin{aligned} \beta &= -1600 \cdot C_a \cdot g_{\min} - 1600^2 \cdot 0.5 \cdot r_d \cdot rh \cdot gfac / 1.6 \\ \gamma &= C_a \cdot g_{\min} \cdot g_a + 1000 \cdot 0.5 \cdot r_d \cdot g_a \cdot rh \cdot gfac \\ \lambda &= 1600 \cdot g_a \end{aligned}$$

The reduced quadratic equation for  $np$  (eq. 3.74) has two possible solutions (eqs. 3.75a and b), from which the second ( $np_2$ ) is the correct one.

$$np_1 = \frac{-o_3 + \sqrt{o_3^2 - 4 \cdot o_2 \cdot o_4}}{2 \cdot o_2} \quad (\text{Eq. 3.75a})$$

$$np_2 = \frac{-o_3 - \sqrt{o_3^2 - 4 \cdot o_2 \cdot o_4}}{2 \cdot o_2} \quad (\text{Eq. 3.75b})$$

When  $np$  finally is determined, the other unknowns can subsequently be calculated. By inserting the result for  $np$  into equation 3.64,  $C_s$  is derived. From  $np$  and  $C_s$ , the stomatal conductance  $g_s$  can be derived through equation 3.63. In a last step, the internal concentration of  $\text{CO}_2$  ( $C_i$ ) is computed by inserting  $np$ ,  $C_s$  and  $g_s$  into equation 3.66. At the end of the calculation it becomes evident, whether the first guess for the internal  $\text{CO}_2$  concentration drawn from equation 3.62 had been correct. If it turns out that the first guess was wrong to such a degree that the dominating limitation is other than estimated, the calculation has to be repeated with the changed initialisation set for the auxiliary variables  $a$ ,  $b$   $d$  and  $e$  according to table 3.04.

Figure 3.28 shows the daily course of the modelled net primary production and the stomatal conductivity of a deciduous forest. The model result was extracted from the middle of the Upper Danube catchment (459 m a.s.l.) for a randomly chosen warm spring day (7<sup>th</sup> of May 2003). The pictured time of the year is the most active growth period for the deciduous forest, during which the trees are rapidly developing their full leaf area. The rates of the net primary production therefore reach very high values of about  $5.7 \mu\text{mol m}^{-2} \text{s}^{-1}$  at noontime. The stomatal conductivity more or less traces the course of the NPP, although during the afternoon hours, when the temperatures and the radiation input are high, the conductivity is slightly reduced. During night time, the photosynthetic activity stops, since the processes involved are only active in the presence of light (see section 1.5.1 and 1.5.2). In the absence of radiation, the NPP becomes slightly negative due to respiration processes.

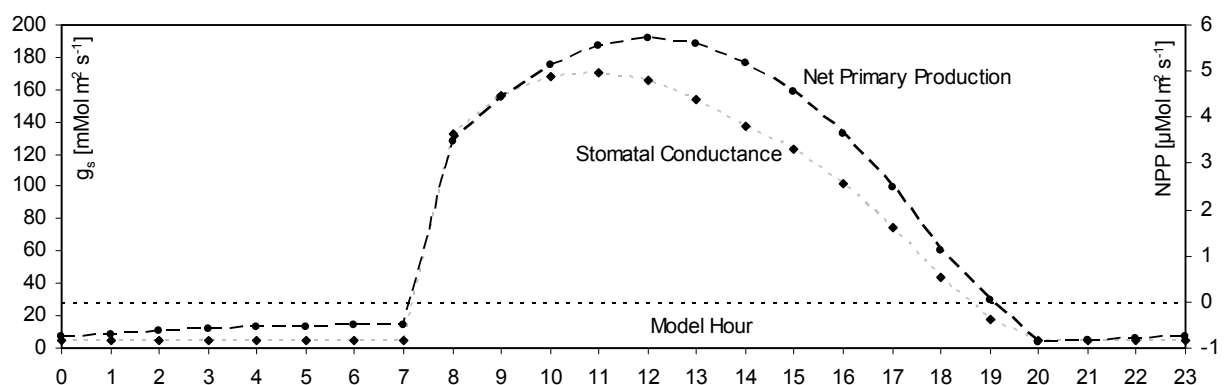


Figure 3.28: Exemplary model results for the photosynthetic activity of a deciduous forest on the 7<sup>th</sup> of May 2003, indicating the parallel development of the daily course of net primary production and the directly related stomatal conductivity. The graphs show model results that were averaged for the sunlit and the shaded parts of the two canopy layers.

The stomatal conductance displayed here, is the stomatal conductance that is determined through the NPP, assuming an abundant water supply. It therefore can more adequately be termed the “potential” stomatal conductivity, while the overall conductivity of the leaf also

depends on the resistance of the boundary layer (see section 3.3.3.4.2) and the soil water supply (see the following section).

#### 3.3.3.5.4 Stomatal Conductance

It was outlined in section 3.3.3.5.2 through equation 3.62 that the stomatal conductivity depends on an ensemble of conditions. A low rate of the net primary production will lead to a low stomatal conductivity. Also a low relative humidity at the leaf surface will cause a closing of the stomata (BALL ET AL. 1987). This is all due to the general paradox of transpiration:

Every plant cell requires a minimum amount of  $H_2O$  for the maintenance of the cell turgor. The plant therefore has to reduce the loss of humidity to the absolute minimum, while at the same time the gas exchange with respect to  $CO_2$  has to be maintained at an optimal rate (TAIZ AND ZEIGER 2000). So, if the energy balance or the  $CO_2$  supply does not allow for an effective carboxylation, the stomata will remain closed. High  $CO_2$  concentrations at the leaf surface will also result in a reduced conductivity, simply because it is no longer necessary for the plant to open the stomata as long as the  $CO_2$  concentration already allows for an effective photosynthesis. The competitive exchange of  $CO_2$  and  $H_2O$  therefore is reduced under elevated  $CO_2$  conditions (SAGE 1994, WULLSCHLEGER ET AL. 2002). The opening of the stomata is caused by an increased cell turgor within the so called guard cells, a pair of which each stoma is equipped with (HOPKINS 1999, *fig. 3.29*).

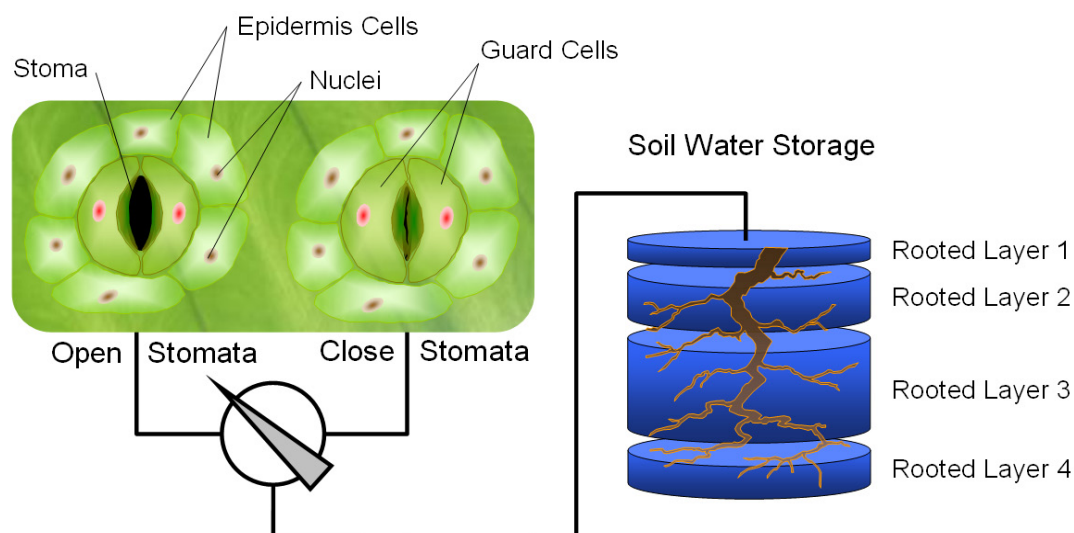


Figure 3.29: The dependence of stomatal aperture on the cell water content is represented in the model through a direct linkage with the soil water storage of the rooted soil layers.

As long as ideal conditions favour the carboxylation, a continuous stream of water vapour is extracted from the leaf. If the cell water household meets its lower limit, the stomata will not be able to open any more and the conductivity is reduced to the conductivity of the cuticle, i.e. the minimal stomatal conductivity ( $g_{min}$ ). Another parameter of the numerator of equation 3.62, which is directly scaling the stomatal conductivity, is the stomatal sensitivity coefficient  $gfac$

(BALL ET AL. 1987). In PROMET, the cell water household is represented by a direct linkage between the *gfac* and the extractable soil water storage of each soil layer that is connected to the root system of the plant (fig. 3.29).

Before the assimilation rate can be calculated, the availability of soil moisture is assessed. The root length densities ( $\text{cm cm}^{-3}$ , see section 3.3.3.6.4) for each soil layer are multiplied with the thickness of their corresponding soil layer (cm), so that the absolute root length (cm) per soil layer is available. In a second step, the percentage of the root length per soil layer is calculated in relation to the absolute root length of the soil profile. For each of the four soil layers, the inhibition (*inh<sub>i</sub>*) due to the soil water supply is assessed, according to the percentage of root length within each layer (*rl<sub>i</sub>*). The relation of the leaf water potential to the stomatal resistance can be described through a loading function following JARVIS AND MORISON (1981, eq. 3.76) that only is applied for potential differences that return a solution between zero and 1. In equation 3.76, the symbol  $\Psi_i$  is the suction in the current soil layer,  $\Psi_0$  is the threshold of suction that initiates the inhibition, while  $a_\psi$  and  $b_\psi$  are scaling parameters.

$$inh_i = rl_i \cdot \{[(\Psi_i + r_r) - \Psi_0] \cdot a_\psi + b_\psi\} \quad (\text{Eq. 3.76})$$

Water transport from the soil into the xylem of the plant is encouraged as soon as the suction of the stream of transpiration exceeds the soil potential. According to BISCOE ET AL. (1976), the rate of transpiration is directly related to the difference of leaf and soil potential, but the potential difference is not zero, when no transpiration takes place. This mainly is due to the resistance of the roots, which is represented in equation 3.76 through the parameter  $r_r$ . The resistance of the transition from soil to the root was assumed with 0.4 MPa, while the critical threshold ( $\Psi_0$ ) was set to 1 MPa for all vegetation types. According to investigations from BOYER (1976), the parameter  $a_\psi$  was adjusted to -2 for cereals, to -1.25 for maize, to -1 for grassland and to -0.94 for forest vegetation types, while the offset  $b_\psi$  was assumed with a value of 1 for all crops. If the sum of suction power and root potential does not exceed the threshold, the inhibition is set to one, so that no inhibition is modelled for the concerned soil layer. The stomatal sensitivity coefficient *gfac* then is reduced according to the weighted inhibition for all of the four soil layers (eq. 3.77).

$$gfac = gfac \cdot \left( \sum_{i=1}^4 inh_i \right) \quad (\text{Eq. 3.77})$$

Of course, the inhibition due to the soil moisture storage can only scale the stomatal conductivity within the boundaries that are given by the other parameters from equation 3.62 and which are also steering the stomatal aperture. But in extreme cases, where none of the

rooted soil layers is able to yield water, it can cause a total closing of the stomata, reducing the conductivity to the permeability of the cuticle.

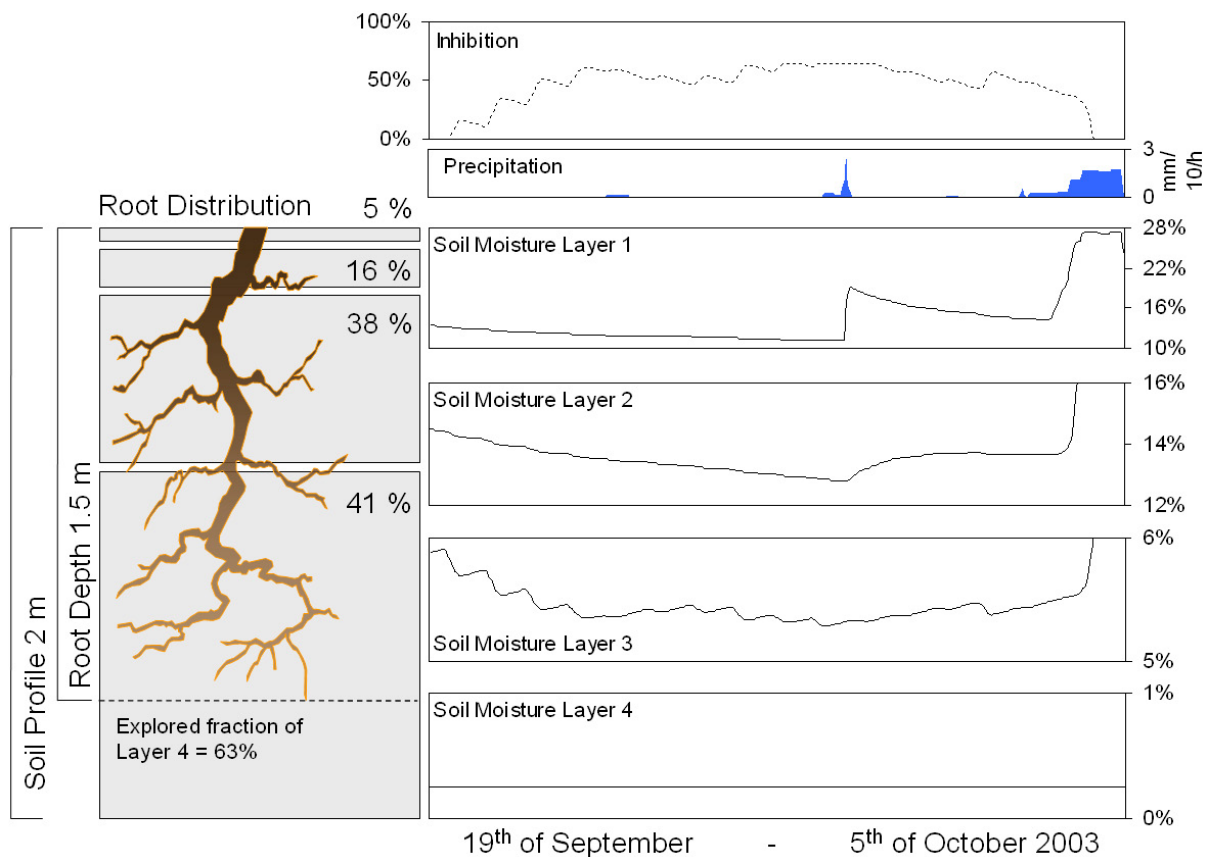


Figure 3.30: Model soil profile indicating the root distribution of a fully developed deciduous forest and the soil moisture situation of four soil layers as well as the precipitation during a dry period of the summer of 2003. For this example, the inhibition of the stomatal conductance due to the soil moisture is determined through the hydrological dynamics in the soil layer 3.

Figure 3.30 shows exemplary model results for the inhibition of the stomatal conductance due to the soil moisture induced *g<sub>fac</sub>*-reduction. During the pictured period, ranging from the 19<sup>th</sup> of September to the 5<sup>th</sup> of October 2003, the displayed root system of the deciduous forest is fully developed. 41 % of the total root mass is located at a soil depth that is assigned to the soil layer 4. This soil layer is completely dry, so that nearly half of the root system cannot contribute to the water supply of the tree. A small part (21 %) of the root system is located in the soil layers 1 and 2, while the remaining 38 % are found in soil layer 3. All three upper rooted soil layers are depleted, gradually increasing the inhibition factor. Due to the root distribution, the inhibition is mainly determined through the moisture of the third soil layer. In the middle of the pictured period, a small rainfall event causes a jump of the soil moisture in the two upper soil layers, but since the precipitation sum is quite small, already the third soil layer does not profit from it. Since this is the layer, which in this case determines the inhibition, the inhibition factor stays more or less constant at a high level of 65 %. Only when, at the beginning of October, several successive days with precipitation are refilling the soil water storage of the upper layers, the inhibition factor is reduced to zero and the water uptake continues freely.

### 3.3.3.6 Plant Growth

The newly fixed carbon that has been accumulated from the gross primary production of the shaded and the sunlit leaves of both vegetation layers has to be transformed into biomass and must be distributed to the different parts of the plant. Thus, the physical properties of the canopy are defined that form the basis for the calculations in the next time step.

#### 3.3.3.6.1 Phenology

The phenological behaviour of the modelled vegetation categories greatly influences the seasonal variation of the water balance related variables. By determining the stages of major growth activity on one hand and the phases of maturity, where biomass and transpiration activity are subdued, on the other, the annual course of evapotranspiration is controlled. The most determinant phenological consequence therefore is the duration of the active growing period or the phases of winterly dormancy respectively.

##### 3.3.3.6.1.1 Crop Phenology

In PROMET, the phenological phases of the agricultural crops are discerned into eleven stages that are following the model of the major BBCH growth stages (*tab. 3.09*, BIOLOGISCHE BUNDESANSTALT FÜR LAND- UND FORSTWIRTSCHAFT 1997).

*Table 3.09: Phenological stages in PROMET and their relation to the international BBCH code.*

Stage	Growth Phase	BBCH
9	<i>vegetative</i> PREGERMINATION	≈ 00-03
10	<i>vegetative</i> GERMINATION	≈ 05
0	<i>vegetative</i> EMERGENCE	≈ 09
1	<i>vegetative</i> LEAF_DEVELOPMENT	≈ 10-19
2	<i>vegetative</i> SIDESHOTS_DEVELOPMENT	≈ 20-29
3	<i>vegetative</i> STEM_ELONGATION	≈ 30-39
4	<i>vegetative</i> HARVESTABLE_VEGETATIVE_PARTS	≈ 40-49
5	<i>generative</i> INFLORESCENCE	≈ 50-59
6	<i>generative</i> FLOWERING	≈ 60-69
7	<i>generative</i> FRUIT_DEVELOPMENT	≈ 70-77
8	<i>generative</i> MATURITY	≈ 83-99

The general possibility for the start of plant growth is given, when the model time reaches the predefined sowing day of a crop. The phenological phase is set to “pregermination” and a flag that signals dynamic growth activity is set, enabling the biologically related submodels. The sowing depth is assumed with 3 cm, suiting the majority of the modelled crops (ITADA 2005, LÜBKE ENTRUP AND ÖHMICHEN 2000, GEISLER 1980, FISCHBECK ET AL. 1999). The uppermost soil compartment is modelled with a thickness of 5 cm and therefore the conditions within that layer are determining the germination. If the soil temperature in the first soil layer is above the freezing point and at the same time the soil moisture exceeds the wilting point, the germination



is initiated. From then on, the average daily thermal time ( $dTT_{avg}$ , eq. 3.78) is observed in dependence of the air temperature at model day  $i$  and model hour  $j$  ( $T_{a,i,j}$ ) and of the cultivar specific base temperature ( $T_b$ ).

$$dTT_{avg} = \frac{\sum_{j=0}^{23} (T_{a,i,j} - T_b)}{24} \quad (\text{Eq. 3.78})$$

The leaves are starting to penetrate the surface, when a cultivar specific heat threshold, assumed for the emergence, is exceeded. The determination and the progress of the following phenological phases is modelled in dependence of the air temperature. For all temperature related decisions, a set of cultivar specific cardinal temperatures  $T_b$  (base),  $T_o$  (optimum) and  $T_c$  (ceiling) is used. In PROMET, there exist three combinations of absolute values for the cardinal temperatures for each crop type. The application of the different temperature sets is variable and depends on the current growth stage. The cardinal temperatures on one hand are used for the restriction of sub- or supraoptimal temperatures, where no development is possible, but also determine the calculation of the hourly temperature effect that is modelled using a response function (eq. 3.79) following YIN AND VAN LAAR (2005).

$$hT_{eff}(T_{a,i,j}) = \left[ \left( \frac{T_c - T_{a,i,j}}{T_c - T_o} \right) \cdot \left( \frac{T_{a,i,j} - T_b}{T_o - T_b} \right)^{\frac{T_o - T_b}{T_c - T_o}} \right]^{c_i} \quad (\text{Eq. 3.79})$$

The hourly temperature effect ( $hT_{eff}$ ) is calculated with  $T_{a,i,j}$  representing the current hourly air temperature and  $c_i$  the temperature response curvature coefficient. Due to lack of more precise data, a value of 1.0 is considered to be applicable for the curvature coefficient (YAN AND HUNT 1999).

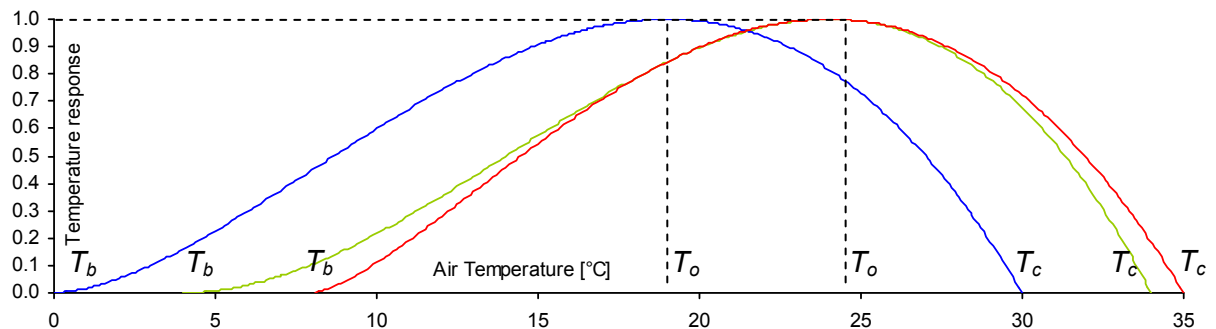


Figure 3.31: Exemplary response curve of the hourly temperature effect for three different sets of cardinal temperatures that apply to winter wheat crops.

Equation 3.79 results in a bell-shaped curve that varies between 0 and 1 and reaches its maximum when the current air temperature equals the optimum temperature of the currently modelled crop (fig. 3.31). If the hourly temperature effect is greater than zero, the hourly thermal time ( $hTT$ ) is defined as (eq. 3.80):

$$hTT = T_{a,i,j} - T_b \quad (\text{Eq. 3.80})$$

As long as the modelled crop is within the vegetative phase and has not reached the stage of inflorescence, the hourly rate of vernalisation ( $Vn_h$ ) is calculated for the winter crops, parallel to the calculation of the hourly temperature effect, but with a different set of boundary temperatures ( $VnT_b$ ,  $VnT_o$ ,  $VnT_c$ ) that apply to the vernalisation habits of the cultivar (eq. 3.81).

$$Vn_h(T_{a,i,j}) = \left[ \left( \frac{VnT_c - T}{VnT_c - VnT_o} \right) \cdot \left( \frac{T - VnT_b}{VnT_o - VnT_b} \right)^{\frac{VnT_o - VnT_b}{VnT_c - VnT_o}} \right]^{c_i} \quad (\text{Eq. 3.81})$$

At the end of every modelled day, the temperature effect, the hourly thermal time as well as the vernalisation rate are averaged for the actual day. If the average vernalisation rate is above zero, the day is considered as an effective vernalisation day ( $Vd_{eff}$ ). The effective vernalisation days again are used to compute the overall vernalisation effect, which increases with the number of accumulated vernalisation days (eq. 3.82, fig. 3.32, left).

$$Vn_{eff} = \frac{Vd_{eff}^5}{5766503.90625 + Vd_{eff}^5} \quad (\text{Eq. 3.82})$$

The length of the day, and with that the possible duration of energy input from the sun, influences the speed of development differently for specific crop types. For so called “short day” plants, which are crops that are supposed to switch from vegetative to generative growth under conditions with short day lengths like potato (*solanum tuberosum*), and for day neutral plants like maize (*zea mays*), the light effect is assumed to be constant (HOPKINS 1995). For all other “long day” crop types it is modelled explicitly.

The astronomic length of the day (LOD) or the daily photoperiod respectively (eq. 3.84) is determined after YIN AND VAN LAAR (2005). First the declination of the sun ( $\delta$ ) has to be calculated in dependence of the day of year (DOY, eq. 3.83).

$$\delta = -\arcsin\left(\sin\left(23.45 \cdot \frac{\pi}{180}\right) \cdot \cos\left(\frac{2\pi \cdot (DOY + 10)}{365}\right)\right) \quad (\text{Eq. 3.83})$$

The daily photoperiod ( $D_{lp}$ ) then is determined by the current latitude ( $\varphi$ ) and the twilight angle ( $\alpha^*$ , eq. 3.84), which was assumed with  $-2^\circ$  according to YIN AND VAN LAAR (2005).

$$D_{lp} = 12 \cdot \left(1 + \frac{2}{\pi}\right) \cdot \arcsin \left( \frac{-\sin\left(\alpha^* \cdot \frac{\pi}{180}\right) + \sin\left(\frac{\varphi \cdot \pi}{180}\right) \cdot \sin(\delta)}{\cos\left(\frac{\varphi \cdot \pi}{180}\right) \cdot \cos(\varphi)} \right) \quad (\text{Eq. 3.84})$$

The light effect curve is calculated using a method that follows STRECK ET AL. (2003) with  $p_{sen}$  representing the sensitivity of the cultivar to the LOD and  $M_{op}$  describing the minimal optimum day length (eq. 3.85). The sensitivity parameter was assumed with 0.3, representing an average value for different species of winter cereals (STRECK ET AL. 2003).

$$L_{eff} = 1 - e^{-p_{sen} \cdot (D_{lp} - M_{op})} \quad (\text{Eq. 3.85})$$

The light effect increases with longer photoperiods, but shows saturation at day lengths of twelve hours and above (fig. 3.32, right).

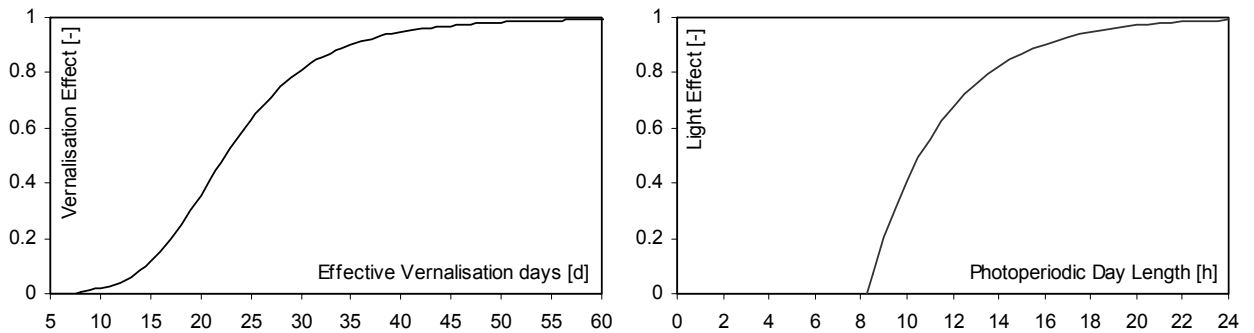


Figure 3.32: Dependence of the vernalisation effect on the absolute number of effective vernalisation days (left). Exemplary light effect for winter wheat in dependence of the photoperiodic day length (right).

Finally, the daily development rate ( $\omega_i$ ) is determined, discerned into vegetative and generative phases of growth (eq. 3.86a and b) and limited by a cultivar specific maximum development rate ( $\omega_{i,max}$ ):

$$\begin{array}{ll} \text{Vegetative growth} & \text{Generative growth} \\ \omega_i = \omega_{i,max} \cdot hT_{eff} \cdot L_{eff} \cdot Vn_{eff} & \omega_i = \omega_{i,max} \cdot hT_{eff} \end{array} \quad (\text{Eq. 3.86a/b})$$

For the progress of the phenological stages, the daily development rate is accumulated until a cultivar specific threshold is surpassed and the transition to the next growth stage is initiated (fig. 3.33).

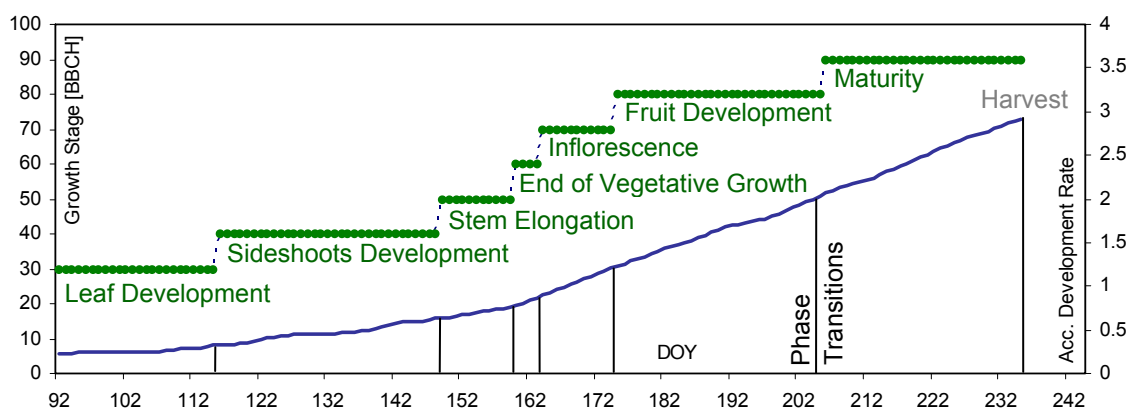


Figure 3.33: Exemplary curve of the modelled phenologic development for the wheat test site "Hofanger" (see section 4.1) during the summer months of the season 2004, indicating the accumulation of the development rate and the thresholds that initiate the transition to the next phenological stage.

Figure 3.33 shows an exemplary course of the modelled accumulated development rate of a wheat field in combination with the corresponding phase transitions. It becomes evident that the transition of the growth stages accelerates during the summer months, only to slow down again after the growth activity has switched from vegetative to generative growth, i.e. after the development of an inflorescence.

#### 3.3.3.6.1.2 Grassland and Natural Vegetation Phenology

The phenological stages of the natural vegetation categories as well as those of agricultural grasslands are modelled analogously to the phenological development of the arable land. Since grassland is considered to be a perennial land cover, there is no sowing date defined. When the agricultural grassland is cut, the growth stage is reset to the stage of "leaf development" and the accumulation of the daily development rate starts anew. The phenological development of natural grassland is reset during wintertime to prepare the initial conditions for the next season.

#### 3.3.3.6.1.3 Forest Phenology

In PROMET, a temperature based approach is used to simulate both, the spring activation that signals the beginning of the growing season as well as the autumnal defoliation that ends the vegetation period (HANK AND MAUSER 2007). A simplified version of the EXP55 model by CANNEL AND SMITH (1983) LN55, modified, verified and parameterized by MENZEL (1997), was used for the reproduction of the start of "leaf emergence" for deciduous trees as well as for the incidence of "mayshoot" in case of the coniferous trees. For the deciduous trees, the discard of the leaves in autumn is modelled in dependence of frost occurrence according to SCHNEIDER (1999).

##### 3.3.3.6.1.3.1 Deciduous Trees

The model implicitly divides the wintery dormancy of trees into two phases. First, the endogenous dormancy that is determined by inner restrictions has to be neutralized by a

winterly chill impulse. If the inner dormancy is resolved, the start of growth is secondarily inhibited by external conditions, resulting in an exogenously determined dormancy. The chill impulse, which is essential for the neutralization of the endogenous dormancy, is calculated by accumulating the chill days ( $CD$ ) that occur when the daily mean temperature ( $DMT$ ) falls below a plant specific temperature threshold ( $t_bCD$ , eq. 3.87).

$$CD = \min\left(\sum_{d_1}^d 1; CD_{\min}\right) \quad \text{if } DMT \text{ is below } t_bCD \quad (\text{Eq. 3.87})$$

The term  $d_1$  is marking the start day of the accumulation, while  $d$  is representing the currently modelled day. The possible accumulation of chill days starts on the first of November ( $d_1$ ) and continues until the necessary amount of chill days ( $CD_{\min}$ ) is accumulated. Since *fagus sylvatica* (beech) with an area percentage of 39.24 % is the most common deciduous tree in the alpine foreland (LWF 2004, see appendix A.4), it was assumed that the regional deciduous forest is largely represented by that tree type. Therefore, the threshold value ( $t_bCD$ ) of 9 °C that applies to beech trees (*tab. 3.10*) was chosen for the calculation of the chill days. The actual amount of temperature below the threshold is unessential, since each chill day is weighted equally. For beech trees, a sum of 83 chill days is considered to be the critical threshold that ends the endogenous dormancy (*tab. 3.10*). From the day, when the inner dormancy is overcome, the daily mean temperature is accumulated in form of thermal degree days ( $TDD$ , eq. 3.88).

$$TDD = \sum_{i=1}^n (\overline{T_{a,i}} - T_b) \quad (\text{Eq. 3.88})$$

In equation 3.88, the term  $T_{a,i}$  holds the daily mean air temperature on day  $i$  while  $T_b$  represents the plant specific base temperature assumed with 6 °C for beech trees (*tab. 3.10*). At the same time, the chill days are further accumulated until they either reach an assumed maximum amount of chill days ( $CD_{\max}$ ) or the critical temperature sum ( $TT_{crit}$ ) is surmounted by the thermal degree days (eq. 3.89).

$$CD = \min\left(\sum_{d_1}^d 1; CD_{\max}\right) \quad \text{if } DMT \text{ is below } t_bCD \quad (\text{Eq. 3.89})$$

If the thermal degree days sum up to a value that exceeds the calculated critical emergence temperature, the growing season is activated. The TDDs that are necessary to overcome the exogenous dormancy, decrease with an increasing number of accumulated chill days (eq. 3.90),

so that the threshold will become lower, the longer it takes for the forest to reach the critical temperature sum and the more chill days occur during that time (fig. 3.34, left).

$$TT_{crit} = a + b \cdot \ln(CD) \quad (\text{Eq. 3.90})$$

The parameters  $a$  and  $b$  are plant specific and are assumed for *fagus sylvatica* with  $a = 1708.4645$  and  $b = -312.0680$  (tab. 3.10). If the temperature threshold definitely is not exceeded, the leaf emergence is enforced after a maximum amount of chill days has been accumulated ( $CD_{max}$ ).

The reduction of the critical temperature threshold depends on the tree type, but the parameterization for beech trees seems to represent an average course of the function compared to other regional trees (fig. 3.34, left). An exemplary model run for a deciduous forest is shown in figure 3.34 (right). The accumulation of the chill days starts at the beginning of November. At the 22<sup>nd</sup> of January, the minimum sum of chill days is already surpassed and the endogenous dormancy is replaced by the exogenous dormancy. While the critical emergence temperature decreases with the further accumulating chill days, the temperature starts to sum up from the 3<sup>rd</sup> of March onwards, when the average air temperature surpasses the base temperature of 6 °C for the first time in the year. The graphs finally meet at the 30<sup>th</sup> of April, causing the leaf emergence to be initiated.

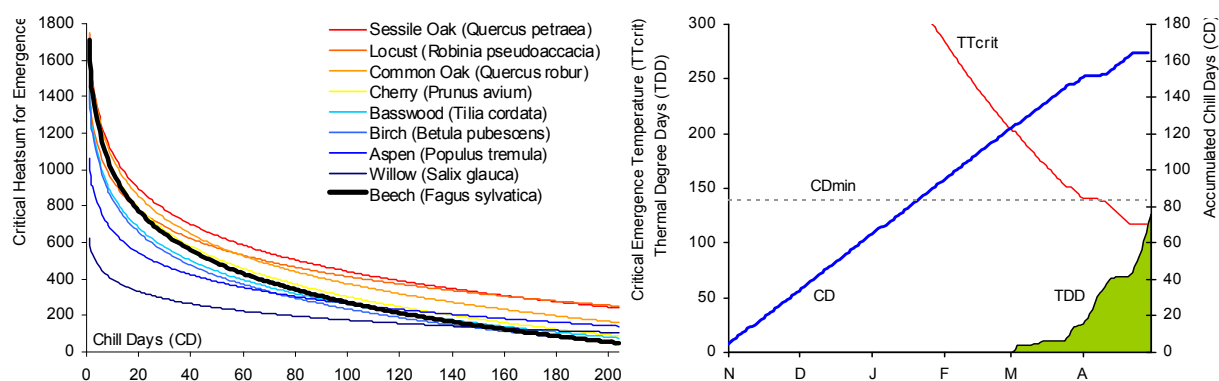


Figure 3.34: Left: Critical temperature sum for the leaf emergence ( $TT_{crit}$ ) of different deciduous tree types. Right: Example of modelled leaf emergence for a deciduous forest in the East of the Upper Danube Basin indicating the variables involved (model year 1998, 467 m a.s.l.).

The defoliation at the end of the growing season is modelled using an approach that depends on the occurrence of consecutive frost events (SCHNEIDER 1999). From the 1<sup>st</sup> of September on, the minimum day temperatures are logged. If the minimum day temperature falls below zero on consecutive days and accumulates to a frost sum of -3.0 °C, the defoliation is initialized, resulting in a rapid decrease of the leaf biomass. If the accumulation of the frost sum is interrupted by a warmer day with no frost occurring, the frost sum is reset to zero. The latest possible day for the defoliation is the day of year 334, i.e. the 30<sup>th</sup> of November (MENZEL 1997).

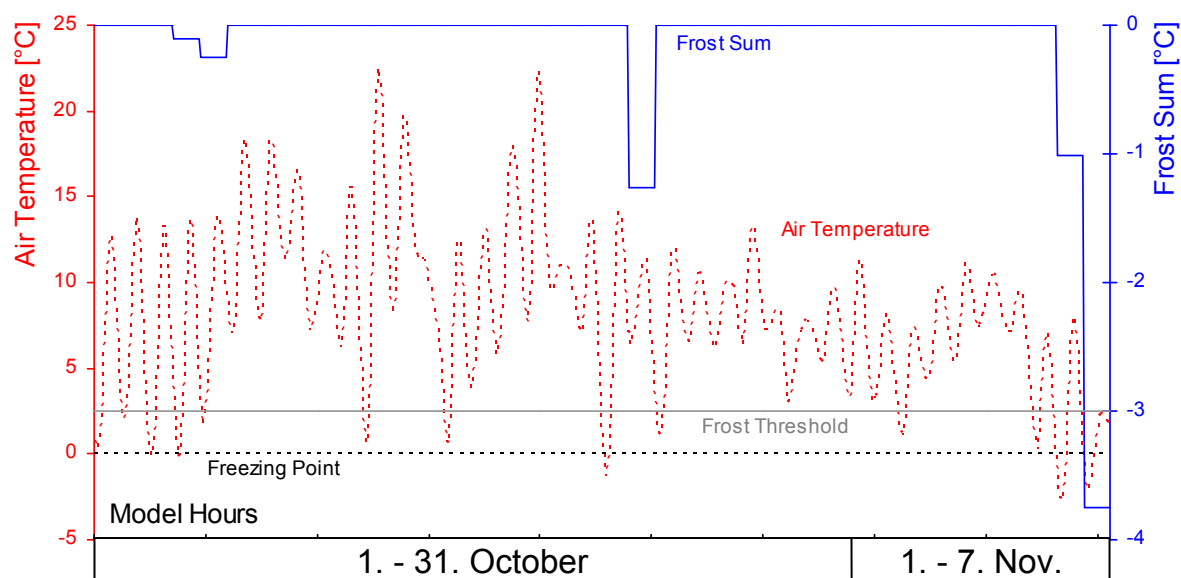


Figure 3.35: Example of modelled defoliation for a deciduous forest in the East of the Upper Danube Basin (model year 1987, 467 m a.s.l.) showing hourly values of air temperature and the resulting frost sum as well as the critical boundaries of 0 °C for the air temperature (dashed) and -3.0 °C for the frost sum (solid).

Figure 3.35 pictures an exemplary course for the accumulation of frost temperatures. Short frost events at the beginning and middle of October do not lead to a defoliation of the trees, as long as they do not penetrate the critical frost sum of -3.0 °C. Two days with consecutive frost events, falling well below the freezing point, finally induce the discard of the leaves of the exemplary forest on the 7<sup>th</sup> of November (fig. 3.35).

### 3.3.3.6.1.3.2 Coniferous Trees

Coniferous trees in the model are parameterized according to the requirements of *picea abies* (spruce), because with an area percentage of 65.06 % (LWF 2004, see appendix A.4) they represent the predominant coniferous tree type in the Upper Danube Basin.

Table 3.10: Parameters used for the description of the phenological behaviour of deciduous and coniferous trees (MENZEL 1997).

	Deciduous ( <i>fagus sylvatica</i> )	Coniferous ( <i>picea abies</i> )
$d_1$ (DOY)	305	305
$t_b$ CD (°C)	009	009
$t_b$ (°C)	006	005
$a$ (-)	1708.4645	1615.5578
$b$ (-)	-0312.0680	-0247.0063
CD <sub>min</sub> (d)	083	076
CD <sub>max</sub> (d)	204	244

Spruce trees are an all season vegetation type that does not discard its needles during wintertime. But the start of the growth activity in spring is characterized by a sudden increase of the leaf/needle area, if the external conditions are favourable. The incidence of this phenological shift is modelled analogously to the leaf emergence of deciduous trees, but with a parameter set that meets the behaviour of the spruce tree type (tab. 3.10, right, fig. 3.36, left).

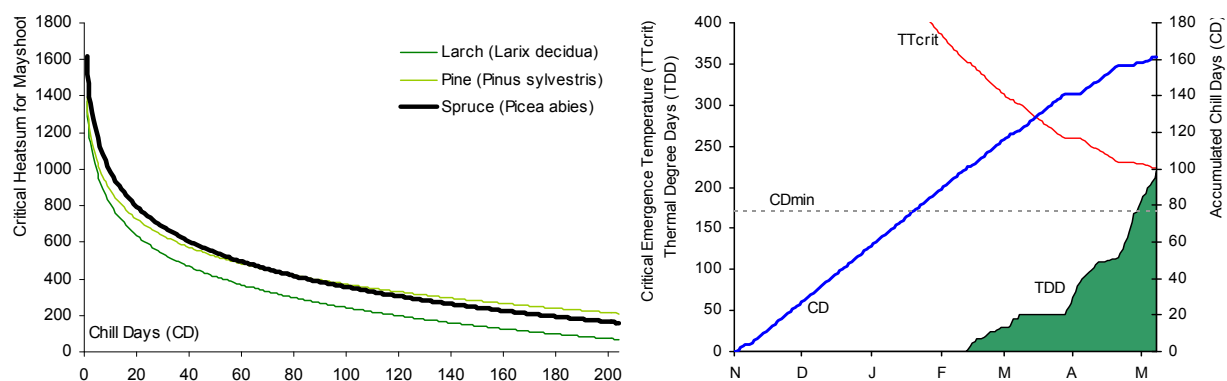


Figure 3.36: Left: Critical temperature sum for the mayshoot ( $TT_{crit}$ ) of different coniferous tree types. Right: Example of modelled mayshoot for a coniferous forest in the middle of the Upper Danube Basin indicating the variables involved (model year 1998, 554 m a.s.l.).

Figure 3.36 (right) indicates that the accumulated chill days for an exemplary coniferous site already surpass the threshold for the neutralization of the internal dormancy on the 20<sup>th</sup> of January of the model year 1998. Still the temperatures are low so that the accumulation of thermal degree days does not commence until the 13<sup>th</sup> of February. A late snow event during March even stops the TDDs from further development, while the chill days keep accumulating and contribute to the descent of the critical temperature threshold. Rising air temperatures, from the middle of April onwards, finally lead to a rapid development of the TDDs and to an initiation of mayshoot on the 8<sup>th</sup> of May 1998.

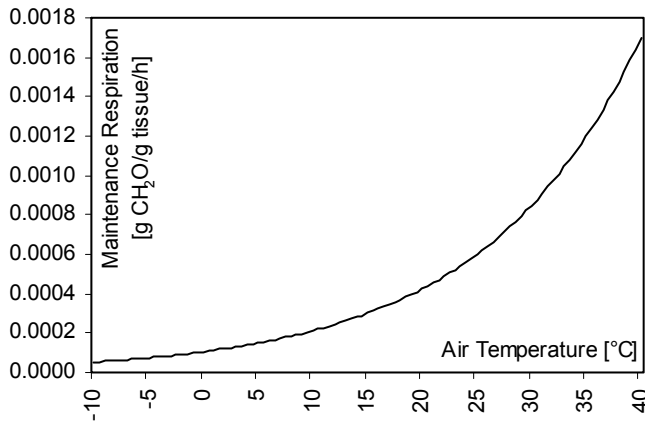
### 3.3.3.6.2 Carbon Allocation

The photosynthesis module, as described in section 3.3.3.5, simulates the amount of fixed carbon for a time step in form of the net primary production (NPP) for one square metre of leaf area. The absolute net primary production of a plant though is determined through the amount of carbon that is oxygenated due to respiration processes. The respiration again is determined by the overall biomass that has to be maintained. Therefore, the rate of carbon fixation is exported from the photosynthesis routine in form of the gross primary production (GPP). Since the GPP is already calculated in a spatial unit (per square metre leaf area, see section 3.3.3.5), it can easily be extrapolated to the whole canopy and again to the whole landscape via the LAI. The extrapolation is done for the two modelled vegetation layers and their sunlit and shaded parts separately. Before the total amount of fixed carbon of the current time step is exported from the leaf gas exchange submodel, the four different rates of productivity are summed.

The actual amount of newly available biomass though is determined by the net primary production (NPP), which again is the result of the GPP minus the amount of carbon that is continuously spent for the production of adenosine triphosphate (ATP) on one hand and for the maintenance of the cell structure the cell turgor or the turnover of organic structures on the other (HOPKINS 1999). An approach after JONES (1991, cited in ADIKU ET AL. 2006) is used for the estimation of the maintenance respiration ( $R_m$ , fig. 3.37) in dependence of the air temperature



( $T_a$ ), with  $k_m$  representing the maintenance respiration rate at 25 °C (assumed with  $6 \times 10^{-4}$ ) and  $b_m$  standing for the maintenance respiration coefficient (assumed with  $693 \times 10^{-4}$ , eq. 3.91).



$$R_m = k_m \cdot e^{b_m \cdot (T_a - 25)} \quad (\text{Eq. 3.91})$$

Figure 3.37: Maintenance respiration in dependence of the air temperature.

In addition to the maintenance respiration, the efficiency of conversion ( $E$ ) has to be accounted for. It is a fixed proportion of 25 % of the GPP ( $P_g$ ) that is dedicated to the canopy gross respiration as proposed by MCCREE (1970). The residual is considered as the net primary production ( $P_n$ , eq. 3.92), after it has been converted from carbon to glucose ( $\text{CH}_2\text{O}$ ) in a last step, so that the NPP finally reads:

$$P_n = E \cdot (2.5 \cdot P_g - (R_m \cdot B_{tot})) \quad (\text{Eq. 3.92})$$

In equation 3.92, the factor of 2.5 accounts for the conversion of carbon (molar mass =  $12 \text{ g mol}^{-1}$ ) to glucose (molar mass =  $30 \text{ g mol}^{-1}$ ), while  $B_{tot}$  is the total biomass that has already been accumulated and now requires energy for the maintenance respiration. Of course, the dry biomass as observed in the field does not only consist of pure carbon or glucose respectively, but rather is a composition of proteins, cellulose, lipids, organic acids and minerals (PENNING DE VRIES ET AL. 1989, MOHREN 1987).

Table 3.11: Divisors for the reduction of pure glucose to dry biomass (SCHNEIDER 1999).

Plant part	g Glucose per g Biomass
Leaf	1.60
Stem	1.54
Root	1.47
Grain	1.50

Thus, the net primary production has to be reduced, according to the percentages that can be allocated to the different plant parts. The demand of glucose for the production of dry biomass varies for the different organs of the plant and also for different kinds of plants. For PROMET, a

parameterization that is supposed to apply to most of the modelled landuse types is used (*tab. 3.11*, SCHNEIDER 1999).

The modelled amount of phytomass now has to be allocated to the different parts of the plant. This process is highly dependent on the growth stage and greatly influences the appearance of the plant and also its further development. A parameter set for each landuse type provides information on the allocation percentage of the different plant parts in dependence of the phenological phase. Figure 3.38 gives an example of the parameterization for winter wheat. The parameter sets for the other landuse categories are listed in the appendix (A.8.1 – 22).

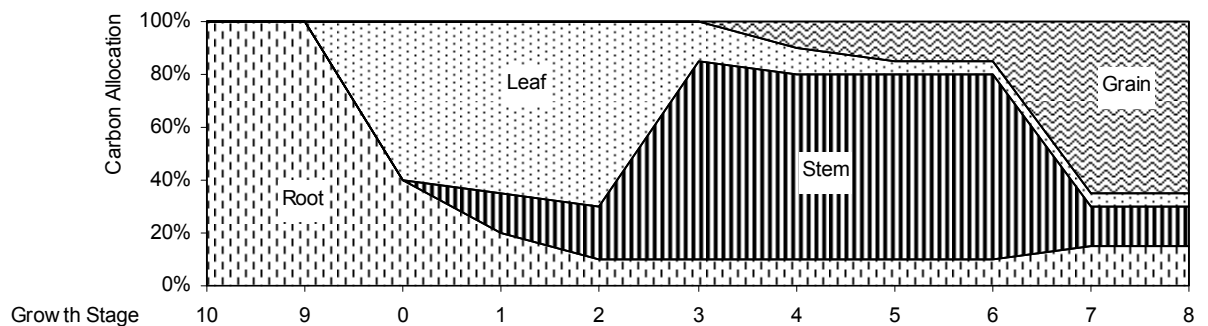


Figure 3.38: Allocation of the distribution of the net primary production to the different plant parts in dependence of the phenological phase. Exemplary parameters for winter wheat.

During the first phenological phases, the growth of the wheat root system requires all of the assimilated glucose. When the stand reaches the stage of emergence, the leaf development gains most of the productivity and the development of the stem commences. With phase 3 (stem elongation, see *tab. 3.09*) the stem starts to shoot and soon requires most of the assimilated carbon (*fig. 3.39*). With the flowering (stage 6), a fruit is slowly developing until, during stage 9 (fruit development), 60 % of the total assimilate are concentrated within the grains. The growth stage dependent distribution of biomass to the different plant parts mostly follows the allocation percentages applied in the vegetation models CERES (HODGES AND RITCHIE 1991) or DSSAT (TSUIJ ET AL. 1994) for the agricultural landuse categories, while for the forested areas, the allocation is steered according to MOHREN (1987, 1994) for coniferous and following the model of KRAMER (1995) for deciduous trees.

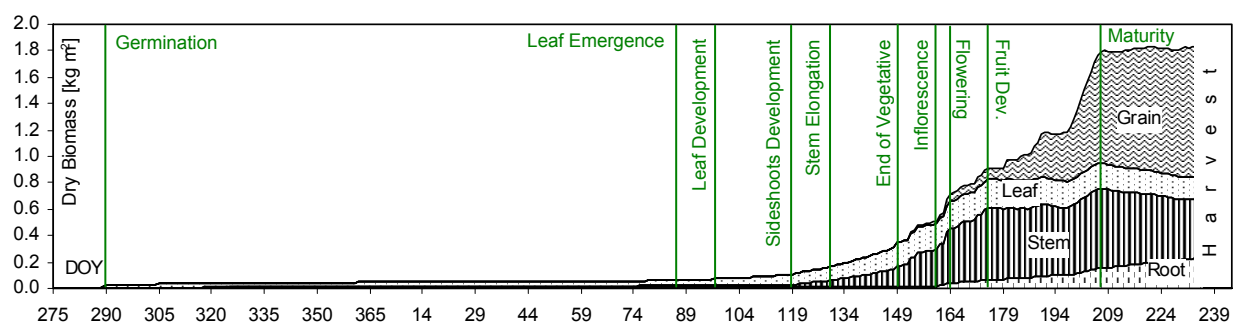


Figure 3.39: Modelled accumulation of biomass and distribution to the different plant parts in dependence of the phenological stage. Exemplary course of development for a winter wheat site during the growth season 2003/2004.

When the crop has reached the phenological stage of fruit development (stage 7), the leaf and stem biomass starts to decrease by a crop specific percentage per model hour (eq. 3.93).

$$B_{leaf} = B_{leaf} \cdot (1 - B_{dec}) \quad (\text{Eq. 3.93})$$

This accounts for the loss of leaves that are gradually turning brown during the ripening process. Analogously, the stem and the root biomass are reduced when the crop has exceeded the growth stage of maturity, accounting for the simulation of senescence.

### 3.3.3.6.3 Aboveground Parameters

The parameter, which is most intensively determining the assimilation capacity of the modelled plants, is the leaf area. It represents the absolute area that intercepts the sunlight and provides energy for all chemical processes in the plant cells. In PROMET, the leaf area is modelled in form of the green leaf area index (LAI), which is defined as half the developed area of green vegetation elements (leaf chlorophyll content higher than  $15 \mu\text{g cm}^{-2}$ ) per unit of horizontal soil (PRIVETTE ET AL. 2001). The LAI in the model develops in dependence of the absolute phytomass that has been assigned to the leaves of the plant. It is assumed that a stable relationship exists between the dry leaf mass and the leaf area that accounts for the physical structure of the leaf (i.e. thickness, stability etc.). For the crops wheat and maize, this relationship could be derived from field measurements. Figure 3.40 (left) shows the reasonably stable relation ( $r^2 = 0.57$ ) of measured LAI values and dry leaf biomass, which is the result of destructive field measurements for the wheat test site “Hofanger” in 2004 (see section 4.1.3).

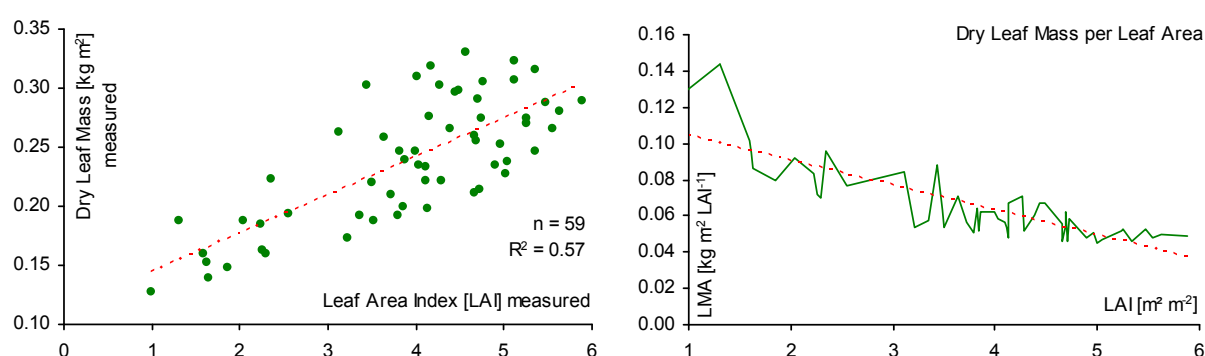


Figure 3.40: Derivation of the leaf mass per leaf area for winter wheat, based on field measurements of the vegetation period 2004. Correlation of measured LAI with measured dry leaf mass (left) and course of the leaf mass area with increasing LAI values (right).

Figure 3.40 (right) indicates, that the relative leaf mass area is not independent of the absolute LAI value. The larger the overall leaf area gets, the lower the leaf mass that has to be dedicated to the generation of the leaf area becomes. However, the relation of LMA to LAI seems to stabilize for LAI values that are larger than three. Due to lack of data for the other landuse

categories, besides wheat and maize, the LMA for each crop ( $LMA_c$ ) was assumed to be stable for the whole growing period. The actual green leaf area therefore is modelled as (eq. 3.94):

$$LAI = \frac{B_{leaf}}{LMA_c} \quad (Eq. 3.94)$$

The mapping of LAI values with a stable LMA though seemed not to be appropriate for perennial landuse categories that are not harvested or cut in the course of the year and do not discard their leaves respectively. Those are landuse categories like the natural grasslands (natural, alpine) as well as coniferous forest. The leaf area for those categories is determined using the initialisation function in dependence of the DOY and the phenological stage, as described in section 3.3.3.1, with respect to the current average annual air temperature of the modelled proxel (section 3.3.3.1, eqs. 3.28 – 3.31). In the case of coniferous forest, the day when the leaf area starts to increase ( $d_{incstart}$ ), is determined through the incidence of mayshoot that tends to happen later in the year for colder regions of higher elevation (fig. 3.41).

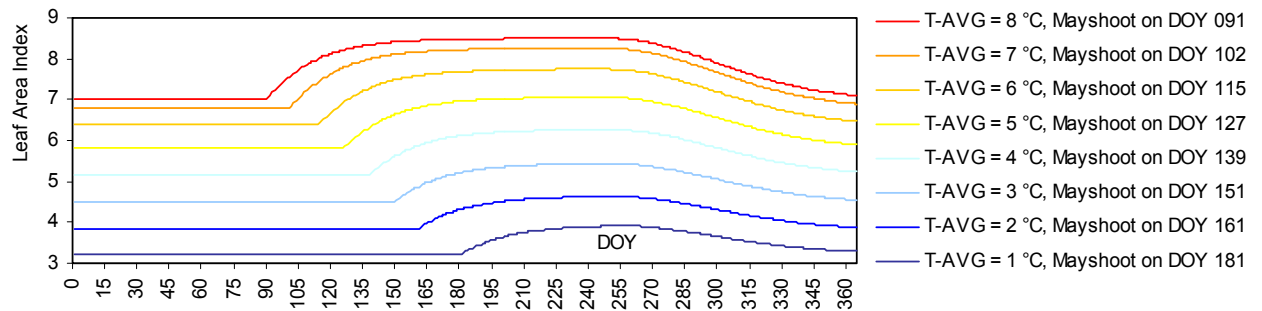


Figure 3.41: Courses of modelled leaf area values for coniferous forest depending on the annual mean air temperature as well as on the incidence of mayshoot.

For the description of the aboveground appearance of the plants and for the calculation of the interaction of plant and atmosphere (see section 3.3.2), the absolute height of the canopy ( $H_c$ ) is an important variable, which is determined as a linear function of the leaf area (eq. 3.95). In contrast to the relation of leaf area to leaf mass, the relation of leaf area to plant height is variable during the vegetation period. This is due to the fact that the leaf area decreases more rapidly than the plant height during senescence.

$$H_c = LAI \cdot LH_{rel} \quad (Eq. 3.95)$$

The relation  $LH_{rel}$  decreases by a constant amount per hour during the senescent growth stages, thus avoiding an unnaturally rapid decrease of the canopy height with decreasing green leaf areas. For deciduous forests, the canopy height is determined by applying the relation to

the stem biomass instead of the LAI, due to the fact that the green LAI turns zero during wintertime, while the height of the forest has to be maintained until the leaf growth starts again in spring.

#### 3.3.3.6.4 Root Growth

The development of the root system determines the access of the plant to the soil water storage and it therefore represents the basis for all transpiration and gas exchange processes (see section 3.3.3.5.4). Regarding the root development, two different directions have to be discerned. On one hand the root growth towards deeper soil depths progresses during the growing season, while at the same time a ramification and densification of the root system at soil depths that already have been conquered by the roots takes place (HOPKINS 1999). The root growth in PROMET is implemented mostly following the model of CERES (HODGES AND RITCHIE 1991).

A large fraction of 40 % of the biomass that has been allocated to the roots is used for the formation of the root reticulum and of mucilage for the protection of the root meristem (RITCHIE 1998). Only 60 % of the newly allocated biomass is used for the root length increase ( $RL_{inc}$ ). In addition, a relation of root mass to root length ( $R_{ml}$ ) divides the newly developed root biomass into fractions that are used for the increase of the root length on one hand and the increase of root thickness on the other (eq. 3.96).

$$RL_{inc} = incB_{root} \cdot 0.6 \cdot R_{ml} \quad (Eq. 3.96)$$

The parameterisation of the fraction  $R_{ml}$  is based on measured data by GREGORY ET AL. (1978) and was assumed with  $1.05 \times 10^4$  cm root length per gram of root biomass. The root growth towards deeper soil depths progresses in dependence of the hourly thermal time ( $hTT$ ), with an assumed lengthening of 0.1 cm per thermal degree hour, so that under ideal conditions, i. e. during a warm and moist summer day, maximum root growth rates of up to 3 cm per day are theoretically possible until the crop specific maximum root depth ( $RD_{max}$ ) is reached or the depth of the deepest soil layer of the current soil profile ( $SD_{max}$ ) is penetrated (eq. 3.98). The root development though is inhibited by the water supply of the deepest rooted soil layer ( $RL_{max}$ ). The soil moisture conditions for each soil layer are represented by a soil moisture deficit factor ( $SM_{def}$ , eq. 3.97) following SCHNEIDER (1999).

$$SM_{def} = 4 \cdot \frac{(\theta_l - \theta_{pf\ 4.2, RL_{max}})}{(\theta_{fc, RL_{max}} - \theta_{pf\ 4.2, RL_{max}})} \quad (Eq. 3.97)$$

This factor is only computed, if less than 25 % of the total extractable soil water is available at the soil depth where the roots are growing. It then depends on the actual soil moisture ( $\theta$ ), the wilting point ( $\theta_{pf4.2,l}$ ) and the total extractable soil water in the respective soil layer (fig. 3.42). The amount of water that can possibly be extracted by the canopy is defined as the field capacity ( $\theta_{fc,l}$ ) minus the wilting point of the soil type that dominates the currently computed soil layer.

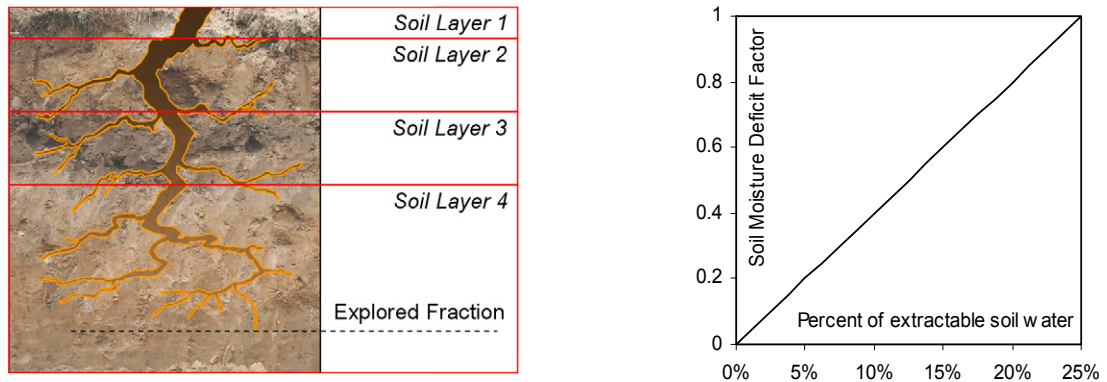


Figure 3.42: Soil profile with four layers and root system, explaining the rooted fraction of a soil layer (left) and dependence of the soil moisture deficit factor on the amount of total extractable soil water (right).

An additional inhibition of the root growth towards unexplored soil layers is the physical resistance of the soil structure that is represented by the factor  $R_p$ . This resistance factor signalizes the preference of the root growth, when a soil layer of certain structural characteristics is passed. It is defined in dependence of the soil grain size and the compactness of the soil material based on analyses of the effective rooting depth for agricultural sites conducted by the AG BODEN (2005).

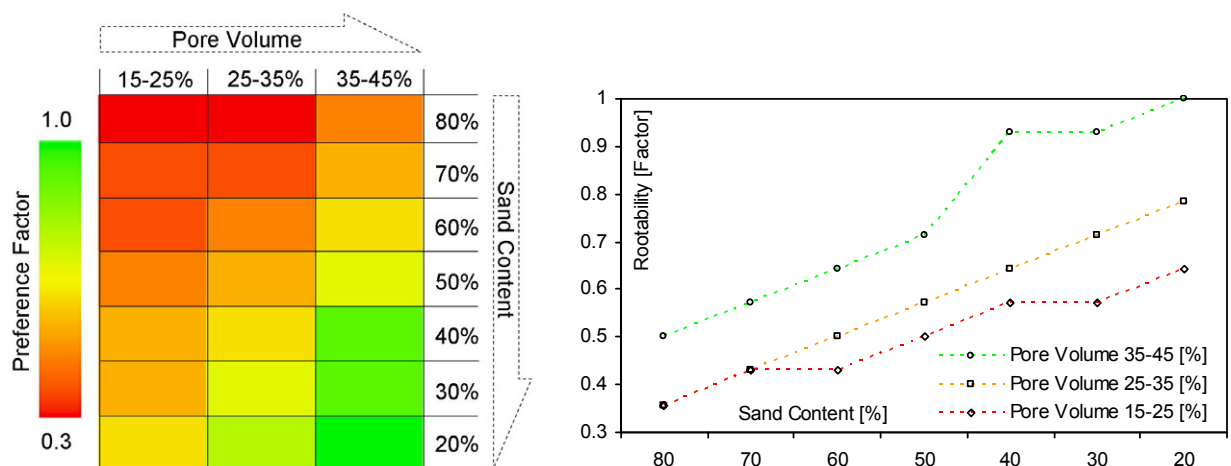


Figure 3.43: Root preference factor according to soil grain size and soil compactness (left: colour chart, right: diagram).

It appears that the rootability of the soil increases with decreasing sand content, due to the better water supply that is associated with smaller soil particles, but decreases again if the compactness of the soil is getting too high, accounting for the reduced aeration of the soil (AG

BODEN 2005, *fig. 3.43*). Taking all inhibitions into account, the root depth on a theoretic model day  $i$  ( $RD_i$ ) is computed as (*eq. 3.98*):

$$RD_i = \text{MIN} \left[ RD_{\max}; SD_{\max}; RD_{i-1} + (hTT \cdot 0.1) \cdot \sqrt{R_p \cdot SM_{def}} \right] \quad (\text{Eq. 3.98})$$

Parallel to the root depth, the density of the root system in the different soil layers has to be determined. For each soil layer, a root length density factor ( $RLD_{fac}$ ) is calculated (*eq. 3.99*, SCHNEIDER 1999) with  $Z_l$  representing the thickness of the rooted soil layer and  $N_{def}$  standing for the nitrogen deficit factor:

$$RLD_{fac,l} = \text{MIN} \left[ SM_{def}; N_{def} \right] \cdot R_p \cdot Z_l \quad (\text{Eq. 3.99})$$

The nitrogen deficit is modelled for each soil layer as a function of the total mineral nitrogen content of the soil layer with the unit  $\text{kg N ha}^{-1}$  after JONES AND KINIRY (1986) and GODWIN (1987) respectively (*eq. 3.100*).

$$N_{def} = 1.0 - \left( 1.17 \cdot e^{-0.15 \cdot N_{tot}} \right) \quad (\text{Eq. 3.100})$$

Thus, PROMET already provides an interface for a nitrogen model input. But since the nitrogen cycle is not modelled explicitly yet, the nitrogen deficit factor ( $N_{def}$ ) was assumed with 1.0 for all soil layers. As a consequence, the soil moisture deficit factor is the only inhibiting parameter for the root length density. The root length density factor is reduced for the lowest rooted soil layer according to the explored fraction of that layer (*fig. 3.42, left*) and is accumulated for the whole soil profile ( $RLD_{fac,tot}$ ).

The increase of root length ( $RL_{inc}$ ), which has been determined due to the newly developed root biomass (*eq. 3.98*), then is distributed to the soil layers according to the root length density factor, so that the root length density at a model time step ( $i$ ) for each soil layer ( $l$ ) can be described as (*eq. 3.101*):

$$RLD_{l,i} = RLD_{l,i-1} + \left\{ \frac{\left[ (RLD_{fac,l} \cdot RL_{inc}) / RLD_{fac,tot} \right]}{Z_l} \right\} - (R_{sen} \cdot RLD_{l,i-1}) \quad (\text{Eq. 3.101})$$

For each time step, a small proportion of the root length ( $R_{sen}$ ) is supposed to die back (STEINGROBE ET AL. 2001) and therefore is subtracted from the root density that already has been accumulated.

Figure 3.44 shows an exemplary course of modelled root development for a winter crop. After the seedling has germinated during a warm autumn, the first hairs of the roots already penetrate the third soil layer (*fig. 3.44, left*). Nonetheless, with exception of the first soil layer, which only has a thickness of 5 cm and contains the majority of the root hairs produced during the germination, the root system is very thready, showing root length densities of less than 0.1 cm cm<sup>-3</sup> (*fig. 3.44, right*). With the beginning of November (DOY 305), the root growth stagnates during the winter season. In spring, the root growth not only accelerates its course towards the full depth of the soil profile, but also strengthens the root system by allocating root biomass into the densification of the relative root lengths. In the middle of May (DOY 130), the deepest soil layer is accessed completely and its full water reservoir is made accessible for the stream of transpiration.

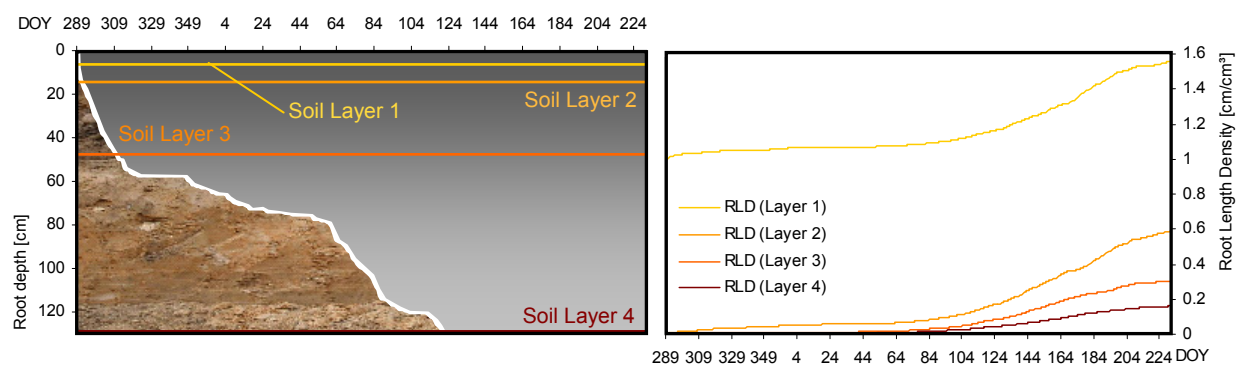


Figure 3.44: Exemplary course of modelled root development of a winter wheat site in the middle of the Upper Danube Basin (352 m a.s.l.) from the 15<sup>th</sup> of October 1998 to the 18<sup>th</sup> of August 1999. Rooting depth of the winter crop penetrating the four layers of the soil profile (*left*) and corresponding development of the root length densities for each soil layer (*right*).

### 3.3.4 Input Parameters

Even the most physically based model requires parameters that are steering the internal processes or are defining certain limits and value ranges in order to minimize the accumulation of failures during a model run. For PROMET, the parameters needed for the operation can be discerned into three categories.

On one hand, spatial input data has to be provided in form of a GIS that includes information on the terrain, the soil types and the landuse categories covered by the modelled area. A second kind of parameter set then includes the attributes that are corresponding with the soil or landuse categories that are mapped by the GIS. Finally, the model needs meteorological driving inputs that cover the modelled time frame and have to be provided in form of meteorological network data. This section is intended to give an overview about the parameters applied for the generation of the model results presented in this work.



### 3.3.4.1 Spatial Parameters

PROMET is a raster based model that is applicable on variable scales. The spatial resolution of the GIS input data set is determining the model resolution. For this work, the raster data was processed to meet a 1 x 1 km grid, so that a single raster element describes an area of one square kilometre. The raster data set has a dimension of 430 lines and 425 columns, comprising an area of  $182.750 \times 10^3 \text{ km}^2$ . From this total area,  $76.214 \times 10^3 \text{ km}^2$  are situated within the boundaries of the Upper Danube Basin. The parts of the GIS that lie beyond the watershed are masked from the computation.

#### 3.3.4.1.1 Landuse

The spatial patterns of the different landuse categories were derived from the CORINE land cover product of the European Environment Agency. Since the CORINE land cover map only identifies major landuse types such as “artificial”, “agricultural”, “forest/natural”, “wetlands” and “water bodies”, the classification had to be modified and adapted in order to represent the natural variability of the Upper Danube landscape (*fig. 3.45*).

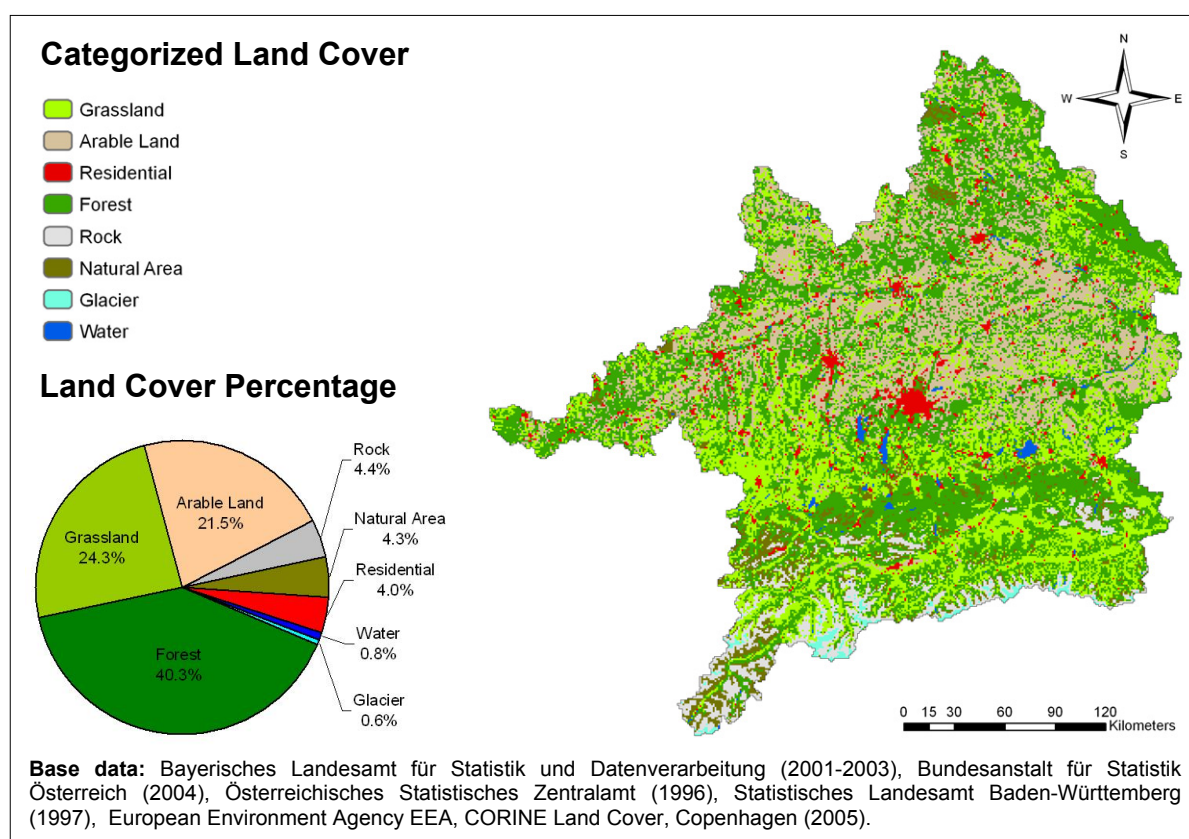


Figure 3.45: Aggregated land use map of the Upper Danube Basin based on the EEA CORINE Land cover classification, corrected and adjusted to match the regional agricultural statistics.

Especially the agricultural landuse types had to be provided on a more detailed level, due to the entirely different seasonal behaviour of the miscellaneous crops. This was accomplished by

distributing the agricultural crops according to agricultural statistics on the communal level. Thus, the percental distribution of different agricultural crops is based on statistic records, ensuring a realistic representation of the land use diversity with a spatial accuracy on the communal level. Since the exact location of single crops within the borders of a community cannot be derived from this information, the land cover map is supposed to be static, disregarding the interannual crop rotation or long-term landuse changes.

Figure 3.45 pictures aggregated major land cover categories, roughly indicating the spatial landuse patterns of the Upper Danube Basin. The largest part, with about 40 % of the total area, is forested, followed by grassland with 24 % and arable land with 21 %. Due to the high alpine areas in the South of the Upper Danube, about 4 % of the area is classified as non-vegetated rock surface, while an equally large part is labelled as natural area, mostly representing alpine pastures. Another 4 % of the area is considered as sealed or artificial, tracing the distribution of the major urban agglomerations. The existence of large surface water bodies that contribute to the land cover map with nearly 1 % is due to the glacial forming processes of the last ice age (see section 2.2). A small part of the high alpine crests in the South of the Upper Danube is classified as glaciated. Due to reasons of visualization, the displayed image (*fig. 3.45*) only features the major landuse categories. A detailed landuse map that provided the GIS layer for the model runs can be found in the appendix (A.5).

When the area percentages of the landuse categories are analysed at the full detail level, the domination of forest and grassland becomes even more apparent. Figure 3.46 ranks the discerned landuse types according to their percental contribution to the total catchment area. Together, forest and grassland apply to more than 60 % of the total area, whereas coniferous forest alone contributes to that proportion with about 25 %. Among the arable landuse types, winter wheat, silage crops (mostly represented by maize) and winter barley are dominating.

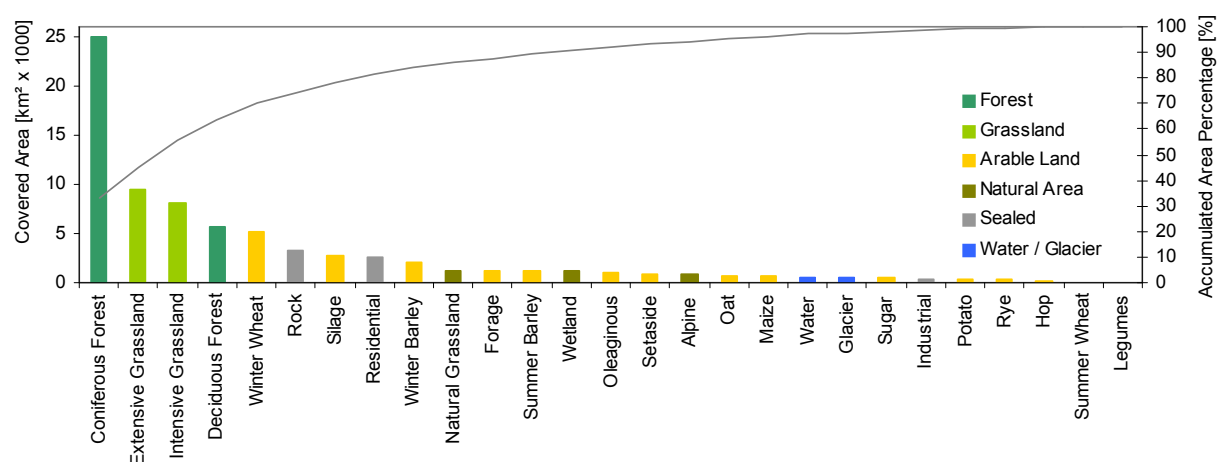


Figure 3.46: Areas of the Upper Danube, covered by the discerned land use categories with their accumulated area percentages.

### 3.3.4.1.2 Soil Texture

The Upper Danube Basin features soil types that mostly are tracing the geologic units (compare section 2.2, *fig. 2.04*). The soil map was derived through a blending of different soil maps, available from the federal agency of geosciences and resources (BGR 2000, MUERTH 2008). For the GIS database, 15 different soil categories are discerned. Figure 3.47 shows the soil types categorized according to their particle size.

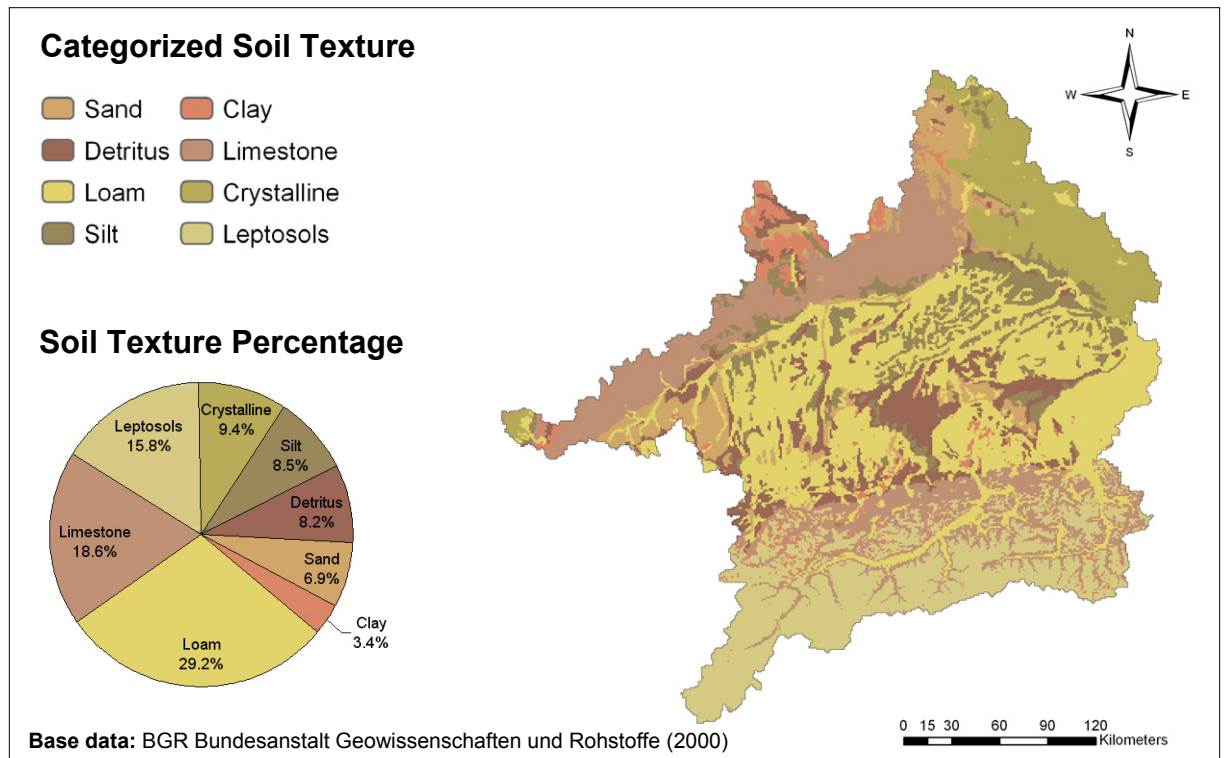


Figure 3.47: Map of aggregated soil texture types, based on the German Soil Survey Map 1 : 1000 000 (BGR 2002).

The distribution of the soil types shows a more balanced course than that of the landuse categories (*fig. 3.48*). The most frequently represented soils are leptosols, characterising shallow and relatively young soils with a straightforward A-C profile, which are typical for a periglacial landscape.

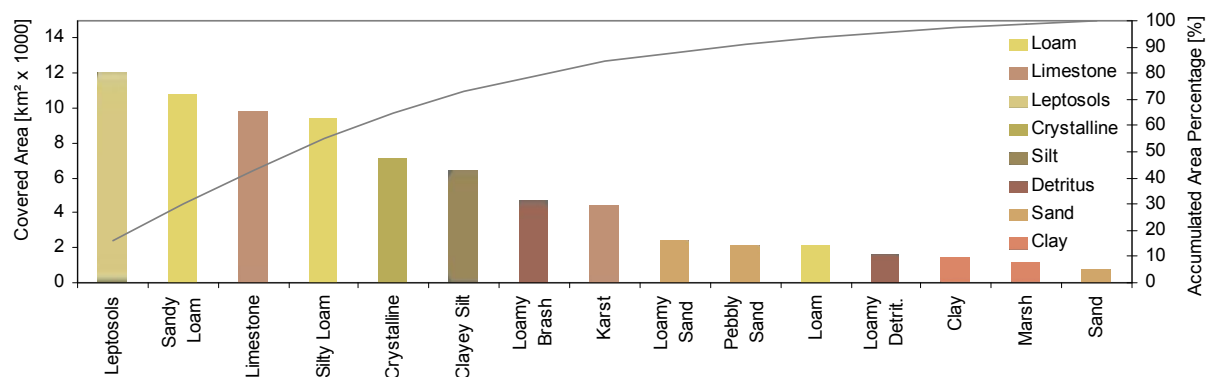


Figure 3.48: Areas of the Upper Danube, covered by the explicit soil texture categories with their accumulated area percentages.

The agriculturally used regions mostly are located on sandy to silty loam sites. An exception is represented by the gravel fields that surround the agglomeration of Munich in the middle of the Upper Danube Basin (*fig. 3.47*). A more detailed soil map, picturing all discerned soil types, can be found in the appendix (A.6).

### 3.3.4.1.3 Digital Elevation Model

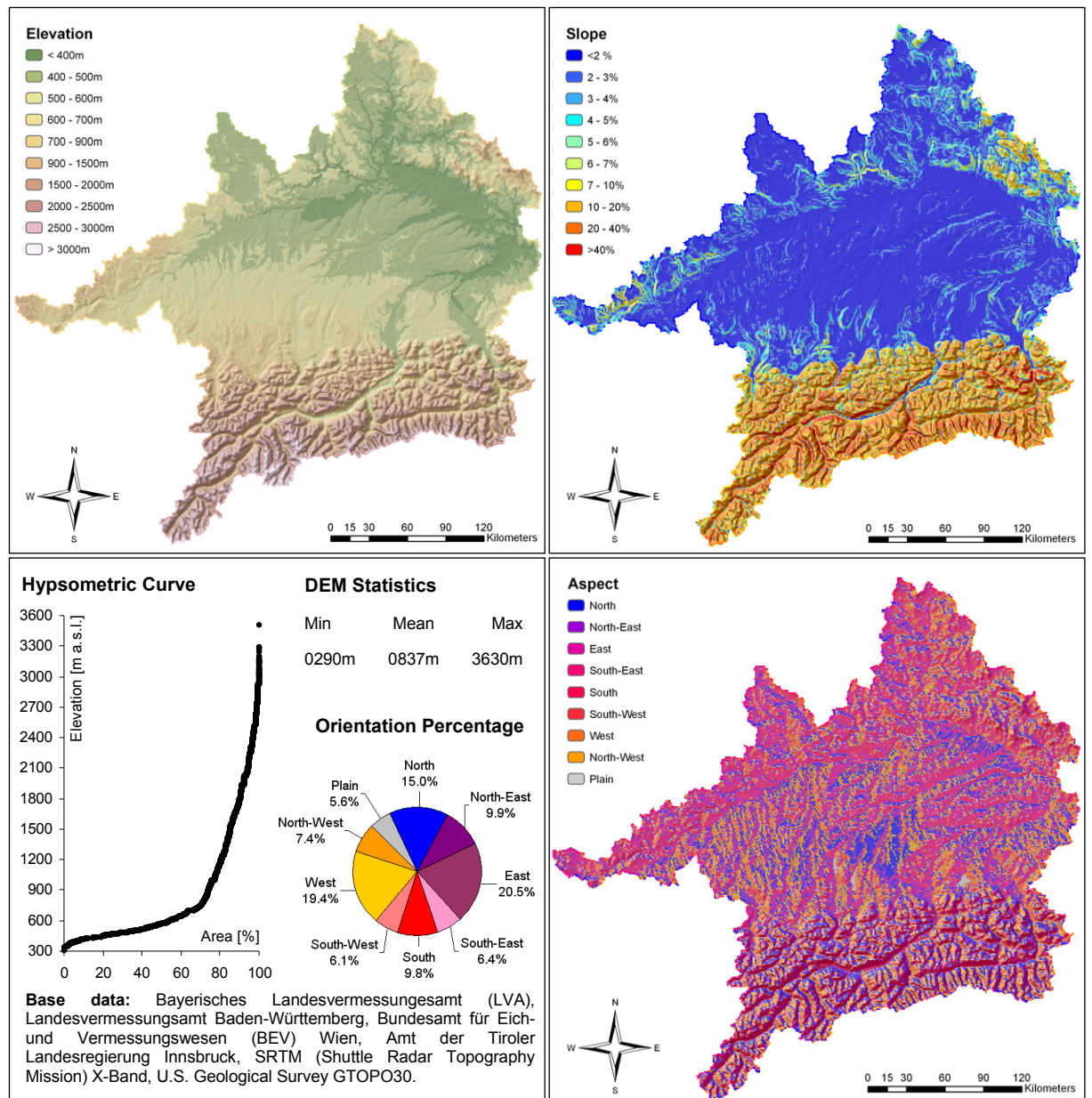


Figure 3.49: Top left: Digital elevation model mosaic for the Upper Danube Basin (relief 2 x vertical exaggeration); Top right: Slope derived from the DEM; Bottom left: Hypsometric curve, statistics and percentages of terrain exposure derived from the DEM; Bottom, right: Terrain orientation (9 major categories) derived from the DEM.

Providing a digital elevation model for a large area such as the Upper Danube Basin, whose boundaries are not tracing administrative borders, is a difficult task, since the administration of geodetic data is generally managed by the regional authorities. The DEM applied for the



simulation of the Upper Danube Basin therefore is a mosaic that was combined from six elevation models of different origin (*fig. 3.49, bottom left*).

The DEM expresses the high relief energy of the Upper Danube through its statistics. The absolute values, averaged for the 1 x 1 km raster, are ranging from low heights of 290 m above the sea level at the main gauge in the East of the basin, up to the high crests of the Rhaetian Alps in the South-West with 3630 m (i.e. Piz Bernina 4048 m). The standard deviation of approximately 680 m emphasizes the undulating surface of the terrain. The mean elevation is found at 837 m (*fig. 3.49, bottom left*). The hypsometric curve of the DEM shows a characteristic bend at a height of 800 m. More than 70 % of the total area is located below that mark. The curve again steepens its course at about 2500 m above the sea level, a height that is only exceeded by approximately 2 % of the DEM area. The alpine height of 3000 m only is exceeded by 0.2 % of the DEM (*fig. 3.49, bottom left*).

Along the alpine hillsides, the DEM shows steep slopes of up to 40 % (*fig. 3.49, top right*). Also the low mountain ridges of the Bavarian Forest and the Swabian Alb are characterized through steep hillsides, while the alpine foreland, due to the glacial gravel plains, shows a more balanced relief. The mean slope lies at about 9 %, while the standard deviation is 12.5 %.

Equally large areas, with a percentage of about 20 %, are oriented towards the East and the West (*fig. 3.49, bottom right*). With 15 % and approximately 10 % respectively, the terrain is exposed to the North and to the South. 5.6 % of the area is classified as horizontal, showing no significant orientation. Overall, the Upper Danube seems to face all directions more or less equally distributed.

#### 3.3.4.1.4 Mask and Subcatchments

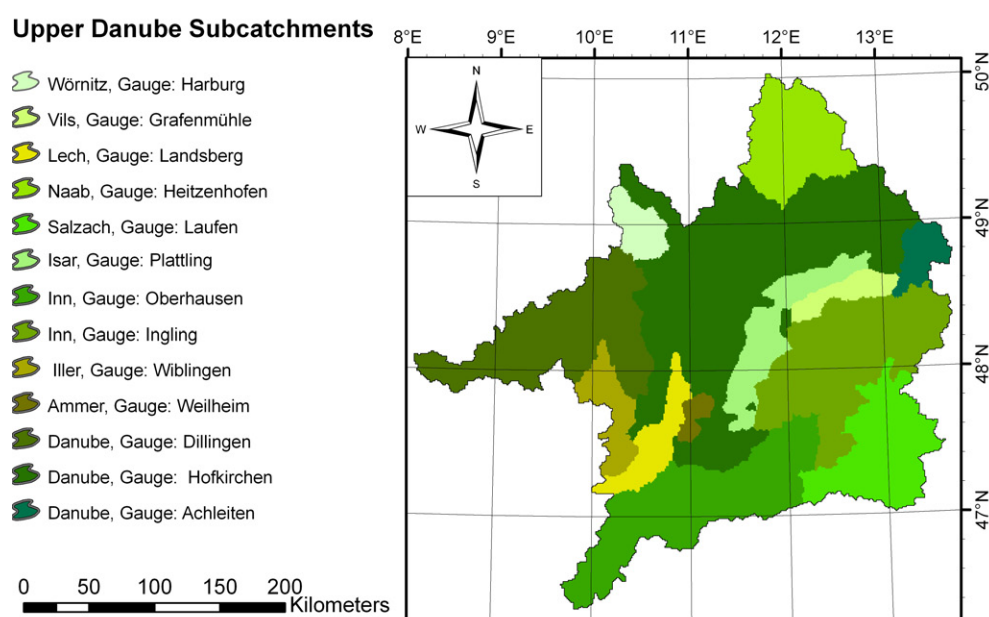


Figure 3.50: Mask layer as applied for the model runs, including the major Upper Danube subcatchments.

In PROMET, the calculation can be limited to the borders of a mask layer. In this case, the overall mask naturally traces the watershed of the Upper Danube Basin (*fig. 3.50*). The mask layer may also carry information on subcatchment areas that can be derived through a topographic parameterization of the DEM. If information on subcatchment areas is provided, the model can be adjusted to export model results for selected areas within the superior mask, enabling an assessment of the models behaviour for the drainage areas of single tributaries. Figure 3.50 shows the mask layer applied for the model runs including a selection of the major subcatchments.

### 3.3.4.2 Parameter Attributes

While the GIS layers for the soil textures and the land cover carry the information where the discerned categories are located, an associated parameter table provides the attributes of the various mapped soil or vegetation categories.

#### 3.3.4.2.1 Landuse Parameters

The imported plant properties on one hand include information on the agricultural management of the land cover category, like the dates of sowing and harvest, but also physical parameters that describe the cultivar specific efficiency of carbon fixation. Table 3.12 lists the crop specific parameters that are required for the description of the different land cover properties within the biological routines of PROMET.

For the generation of the model results that are presented in the scope of this thesis, the plant physiological parameters were adjusted according to different authors or were based on own measurements respectively. For the parameters that are steering the plant chemism, settings taken from FALGE ET AL. (1996), FALGE (1997), FALGE ET AL. (1997) and WARING AND RUNNING (1998) were applied for the simulation of the leaf gas exchange of the forest types. C<sub>3</sub> grasses and connatural cereals were parameterized according to FARQUHAR ET AL. (1980), while the carboxylation of C<sub>4</sub> plants is modelled using parameters taken from CHEN ET AL. (1994).

The phenology model, as well as the above- and belowground development of grassland and cereals, was initialised according to RITCHIE (1991), HODGES AND RITCHIE (1991), RITCHIE (1993) and SCHNEIDER (1999), while for maize, parameters taken from JONES AND KINIRY (1986) and KINIRY AND BONHOMME (1991) are applied. The phenological development of the forest landuse categories was parameterized according to CANNEL AND SMITH (1983) and MENZEL (1997). Where in-field data could be provided, the parameters were adjusted according to own observations. A detailed illustration of the parameters that were applied for the generation of the model results presented in this work can be found in the appendix (A.8.1 - 27).

Table 3.12: Crop input parameters required for the PROMET biological model.

Parameter	Unit
Position in the land cover hierarchy	[Flags]
Grey value corresponding with the landuse GIS layer	[DN]
Leaf mass per leaf area	[kg m <sup>-2</sup> ]
Day of sowing	[DOY]
Day of harvest	[DOY]
Ratio LAI to height	[m m <sup>-2</sup> leaf area]
Minimum (initial-) LAI	[m <sup>2</sup> m <sup>-2</sup> ]
Maximum LAI	[m <sup>2</sup> m <sup>-2</sup> ]
Start of LAI-increase phase (initialization)	[DOY]
End of LAI-increase phase (initialization)	[DOY]
Start of LAI-decrease phase (initialization)	[DOY]
End of LAI-decrease phase (initialization)	[DOY]
Plant specific LAI-increase constant 1 (initialization)	[-]
Plant specific LAI-increase constant 2 (initialization)	[-]
Width of the leaf	[m]
Carboxylation capacity at 25 °C	[μMol m <sup>-2</sup> leaf area second <sup>-1</sup> ]
Maximum rate of electron transport through PS II at 25 °C	[μMol electron <sup>-1</sup> m <sup>-2</sup> leaf area second <sup>-1</sup> ]
Michaelis-Menten constant for oxygen at 25 °C	[μmol mol <sup>-1</sup> ]
Michaelis-Menten constant for carbon at 25 °C	[μmol mol <sup>-1</sup> ]
Respiration capacity at 25 °C	[g CO <sub>2</sub> m <sup>-2</sup> leaf area second <sup>-1</sup> ]
Light use efficiency	[Mol CO <sub>2</sub> m <sup>-2</sup> leaf area]
Ball-Berry coefficient for stomatal conductance	[-]
Minimum leaf conductance through cuticle	[mmol m <sup>-2</sup> s <sup>-1</sup> ]
Internal concentration of oxygen in the leaf	[ml l <sup>-1</sup> ]
Fraction of dark respiration during daytime	[fraction]
Light-effect (longday / shortday crop type)	[Flag]
Cardinal temperatures - 3 sets for different growth stages	[°C]
Maximum biomass decrease per hour for senescence	[kg h <sup>-1</sup> ]
Heat sum needed for leaf emergence	[°C]
Relation of root mass to root length	[cm g <sup>-1</sup> m <sup>-2</sup> ]
Root senescence factor	[-]
Maximum root depth	[cm]
Allocationfactors for leaf biomass	[fraction]
Allocationfactors for stem biomass	[fraction]
Allocationfactors for root biomass	[fraction]
Allocationfactors for grain biomass	[fraction]
Vernalisation temperatures (minimum, optimum, maximum)	[°C]
CO <sub>2</sub> diffusion coefficient 1	[-]
CO <sub>2</sub> diffusion coefficient 2	[1 kPA <sup>-1</sup> ]

Some of the input parameters that are steering the kinetics of photosynthesis have to be adjusted after they are imported from the parameter files, accounting for the different growth conditions in alpine environments. This only is the case for forest and for grassland vegetation types, since they both are represented in alpine and in plain terrain simultaneously. The carboxylation capacity, the maximum rate of electron transport and the respiration capacity at 25 °C are elevated by a factor of 1.42 for grassland, located on sites that feature annual mean temperatures (*AMT*) above 8.5 °C (eq. 3.102).

$$V_{c_{\max 25}}, J_{\max 25}, r_{d25} = (V_{c_{\max 25}}, J_{\max 25}, r_{d25}) \cdot 1.42 \quad \text{if } AMT > 8.5 \text{ °C} \quad (\text{Eq. 3.102})$$

For forest vegetation types, the three important parameters are adjusted to meet the reduction of the transpiration activity with increasing terrain elevation as proposed by FALGE ET AL. (1996) and KÖSTNER (2001). The carboxylation capacities and with them the possible stomatal conductance (see section 3.3.3.5.4) are modelled to decrease linearly from sites showing annual mean temperatures of greater than 8.5 °C to high alpine locations, where the annual mean temperatures are around zero and no growth is possible. This gradual shift is traced through the calculation of an elevation factor ( $eFac$ ) that is correlating the terrain elevation with the local annual mean temperatures (eq. 3.103).

$$eFac = -213.75 \cdot AMT + 2270.2 \quad (\text{Eq. 3.103})$$

The carboxylation capacity ( $V_{c_{max25}}$ ) then is adjusted according to equation 3.104a for deciduous and according to equation 3.104b for coniferous tree types.

$$V_{c_{max25}} = -0.0333 \cdot eFac + 103.33 \quad \text{for deciduous trees} \quad (\text{Eq. 3.104a})$$

$$V_{c_{max25}} = -0.025 \cdot eFac + 92.5 \quad \text{for coniferous trees} \quad (\text{Eq. 3.104b})$$

Both, the maximum rate of electron transport ( $J_{max25}$ ) and the respiration capacity ( $r_{d25}$ ) are scaled linearly preserving their natural relation to the carboxylation capacity according to equations 3.105 and 3.106 respectively.

$$J_{max25} = V_{c_{max25}} \cdot 0.4 \quad (\text{Eq. 3.105})$$

$$r_{d25} = V_{c_{max25}} \cdot 0.013 \quad (\text{Eq. 3.106})$$

In combination with the reduced leaf area, as it is assumed for sites with lower AMTs (see section 3.3.3.1), this reduction is supposed to map the natural sequence from fully developed forests at colline heights towards slowly developing dwarf pine stands, which are marking the timber line at alpine elevations.

#### 3.3.4.2.2 Soil Parameters

Like the cultivar specific plant properties, the soil properties for each soil texture category are imported via ascii input files. The parameters that are needed for the modelling of the soil processes were adjusted following RAWLS ET AL. (1992), DYCK AND PESCHKE (1995) and MUERTH (2008). The soil relevant parameters are listed in table 3.13. The parameterisation of the different soil types, applied for the generation of the model results presented here, can be found in the appendix (A.9).



Table 3.13: Soil input parameters, analogously required for both, the Penman-Monteith and the biological PROMET model.

Parameter	Unit
Number of soil layers	[-]
Soil temperature	[°C]
Ground water level	[m]
Permeability	[cm second <sup>-1</sup> ]
Effective pore volume	[%]
Pore size distribution index	[-]
Bubbling pressure head	[-]
Layer thickness	[cm]
Clay content	[m <sup>3</sup> m <sup>-3</sup> ]
Sand content	[m <sup>3</sup> m <sup>-3</sup> ]
Organic matter	[m <sup>3</sup> m <sup>-3</sup> ]
Retention water content	[%]
Cumulative pore volume	[%]
Initial Pf-value	[Pf]

### 3.3.4.3 Observational Networks

The model requires several meteorological input parameters that can be imported from input files in a tabular form, as there are precipitation, air temperature, relative humidity, wind velocity and the radiation balance, which is derived from the observed cloud cover according to MÖSER AND RASCHKE (1984). The meteorological data is provided by operational observation networks such as that of the German Weather Service, which are recording data at certain hours of the day. In case of the stations that are operated by the German Weather Service, the measurements are documented at the so called “Mannheimer” hours at 7:30 am, 2:30 pm and 9:30 pm. The raster based model structure though requires the provision of discrete values for all relevant meteorological variables at the location of every raster element for each time step, i.e. for all hours of the day in this case. The imported network data consequently has to be interpolated in temporal as well as in spatial terms.

In the model, the temporal interpolation precedes the spatial interpolation. The temperature, the relative humidity, the wind velocity as well as the cloud cover are supposed to be continuous parameters that could sufficiently be described through a cubic spline interpolation. The disaggregation of the precipitation records has to take into account that the rainfall occurs in discrete events and cannot be described through a simple interpolation. Two types of rainfall are discerned. Precipitation that falls in form of a steady rain with a low intensity is divided from events of a short duration with high rainfall intensity, such as showers or thunderstorms.

The spatial interpolation is based on the assumption that an elevation dependency applies to all meteorological input parameters. This dependency can either be formulated through physical relations or elevation regressions. Since the regression method is due to produce failures at the locations where direct observations are available, i.e. at the locations of the weather stations, the resulting residuals also are interpolated. In order to minimize the deviations, a cubic inverse

distance loading function is applied here, that is taking six surrounding weather stations into account. The interpolated residuals then are added to the trend plane that is derived from the elevation regression, reducing the deviations between the measurements and the interpolation. Since the meteorological interpolation is not the central issue of this work, the related procedures are not further discussed here. For a more detailed description of the interpolation methods it is referred to LUDWIG (2000) and to MARKE (2008).

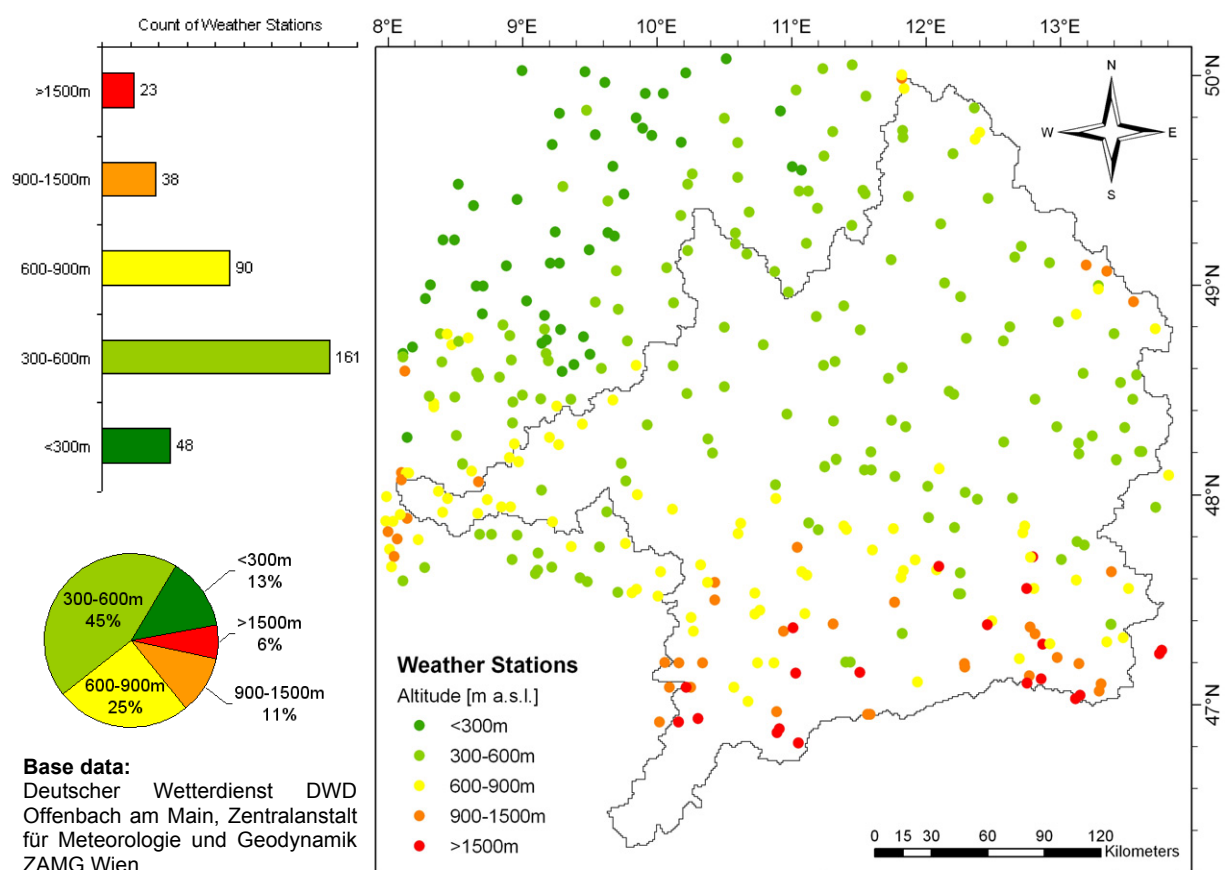


Figure 3.51: Map of the weather stations used for the meteorological interpolation for the Upper Danube Basin, indicating the spatial pattern and the elevations of the observation sites.

For the modelling of the Upper Danube catchment, data could be obtained from observation networks of the German Weather Service and the Austrian Central Agency of Meteorology. In total, data from 360 stations was revised and combined to generate a continuous data set that covers the years from 1960 to 2006 with a satisfying density and an adequately uniform spatial distribution (fig. 3.51). Due to the difficulties of the installation and operation of permanent weather stations in mountainous terrain, the density of the observation network decreases significantly with increasing elevation (fig. 3.51, left). The elevation range of 300 to 600 m above the sea level is most densely covered by weather stations with 45 % of the network being located at those heights. Only 23 stations or 6 % of the network respectively are measuring meteorological data at alpine heights above 1500 m.

## **4. Model Validation**

In the course of the development of a model for the interactive simulation of landsurface processes, the highest priority is the maintenance of a physically based process description in combination with a minimum application of empiric relations. The general assumption of such a modelling approach is that an accurate physical description of the involved processes will lead to realistic model results. A monitoring of the models quality and accuracy consequently can be accomplished by comparing the model results to measured data. It is a problem that not all of the parameters that are mapped by the model can be covered by a validation effort. Nonetheless, the verification of every parameter that actually can be investigated increases the overall reliability of the model (JONES 1991).

In this work, the validation process is performed for selected model parameters that could be supported with reference data. First, the model is tested on the micro scale for single test fields, where the reference data could be collected by means of a field campaign. When the model has proven its functionality on the small scale, the methods can be transferred to the larger landscape or meso scale. There, the models accuracy is tested for single landuse categories in the first instance and in a second step for the whole variety of crops that are representing the natural variety of the entire mapped landscape. This is accomplished on one hand by comparing the model results with calculations of a control model, which already has proven its reliability on the mesoscale, and by referencing with literature data on the other.

### **4.1 Field Scale Validation**

Before the models reliability on the landscape scale is tested, the model has to prove its functional efficiency for single land use categories. Since PROMET is able to process input data for different spatial resolutions and therefore is applicable on different scales, model runs were initiated that were limited to the spatial extension of single fields, tilled with a single crop type. This is a spatial scale that enables the collection of validation data by means of field measurements.

#### **4.1.1 Selection of Test Sites**

The selection of the test area was determined by several factors, as there are the existence of feasible test sites, their accessibility and the chance to find farmers that are willing to cooperate, since all the test sites that were worked on in the course of this thesis are private property. The test area finally chosen for the measurement campaigns is located near the town of Gilching, a

middle sized town belonging to the commuter belt of Munich, whose city centre lies 25 km in the South-West from the capital. Gilching is part of the administrative district Starnberg, a region that lies within the Northern Bavarian foothills, embedded between the Ammersee in the West and the Starnberger See in the East. The test area is more or less directly located in the heart of the Upper Danube catchment (fig. 4.01, left).

As mentioned above, the selection of the test sites was determined by several important factors, including the natural premises as well as the availability of cooperative farmers. In terms of natural conditions it was considered to be necessary to find a C<sub>3</sub> and a C<sub>4</sub> crop (see section 1.5.2) for comparison of the two carbon cycle systems that at the same time would provide large enough acreage to be mapped by the model. Since the ground truth sampling is destructive and may cause some damage to the crop, it is a difficult task to persuade farmers to entrust their acres. Within the test area Gilching, four test sites finally could be arranged. A wheat field (*Triticum aestivum* L.) tilled with an elite wheat cultivar “Achat” and a maize stand (*Zea mays* L.) of the cultivar “Magister” were chosen for the sampling seasons 2004 and 2005 respectively (fig. 4.01).

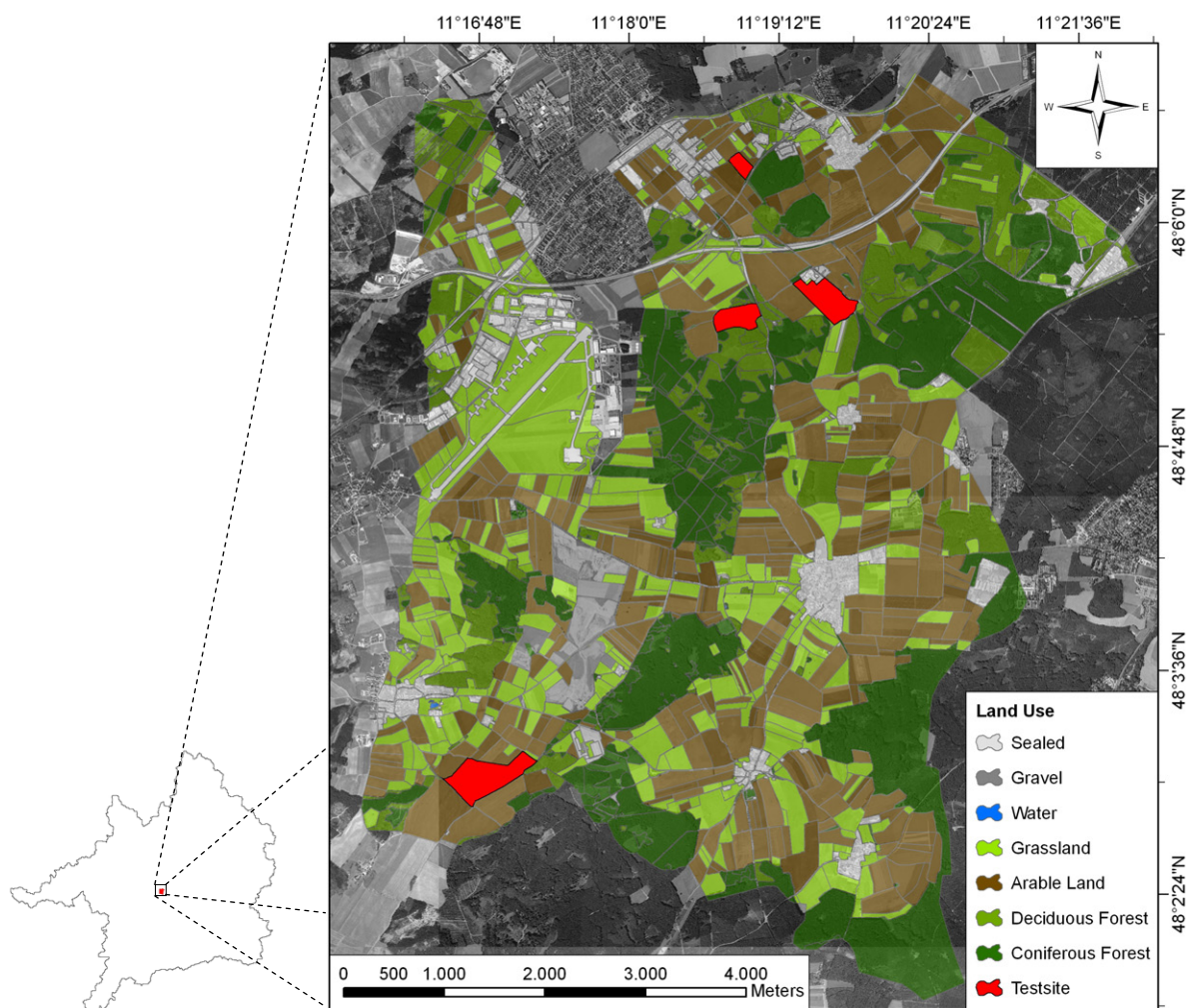


Figure 4.01: Test sites 2004/2005 embedded in a generalised landuse map (generated from field data 2005) with their relative position within the Upper Danube Basin (left). Background: Digital orthorectified aerial photograph mosaic of the season 2003 kindly provided by the Bavarian Land Surveying Office.

Three of the test sites are located next to the autobahn Munich-Lindau (A96), while one maize site lies more in the South near the village of “Hochstadt”. The different sites were named according to their respective location.

#### 4.1.2 Test Sites 2004

For the sampling year 2004, two test sites, one for each crop could be acquired. The wheat site lies in front of Hüll manor, whose proprietor has already been cooperating with the University of Munich in several projects. With a size of 14.32 ha, the site is medium sized for Bavarian acreages (BAYERISCHES STAATSMINISTERIUM FÜR LANDWIRTSCHAFT UND FORSTEN 2006). It is located on a moraine ridge of the Ammer-Loisach glacier that dates from the Saale/Riß ice age (see section 2.2). The moraine ridge causes a relatively coarse relief with an absolute height difference of 12 m and slopes of up to 10 % within the field. Also the orientation of the field is split due to the moraine ridge. While the Northern half is exposed to the North-West, the Southern half slopes to the South-East (*fig. 4.01, left*). A weather station of the Bavarian agrometeorological network is positioned in the very middle of the test site. The predominant soil particle size is loamy silt, composed of a Braunerde soil type (*fig. 4.11, top middle*), which corresponds to cambisols in the FAO classification system.

The maize site with 3.63 ha is even smaller. It has a mostly rectangular shaped contour and is situated on top of a small hill in the East of the village of Argelsried. The Southern part steeply slopes towards a country road with a maximum slope of 12 % and an absolute height difference of 9 m. With exception of the Southern corner, the whole field is oriented to the North. The dominant soil particle size is coarse loam, with loamy silt in the Eastern corner of the field (*fig. 4.13, top middle*).

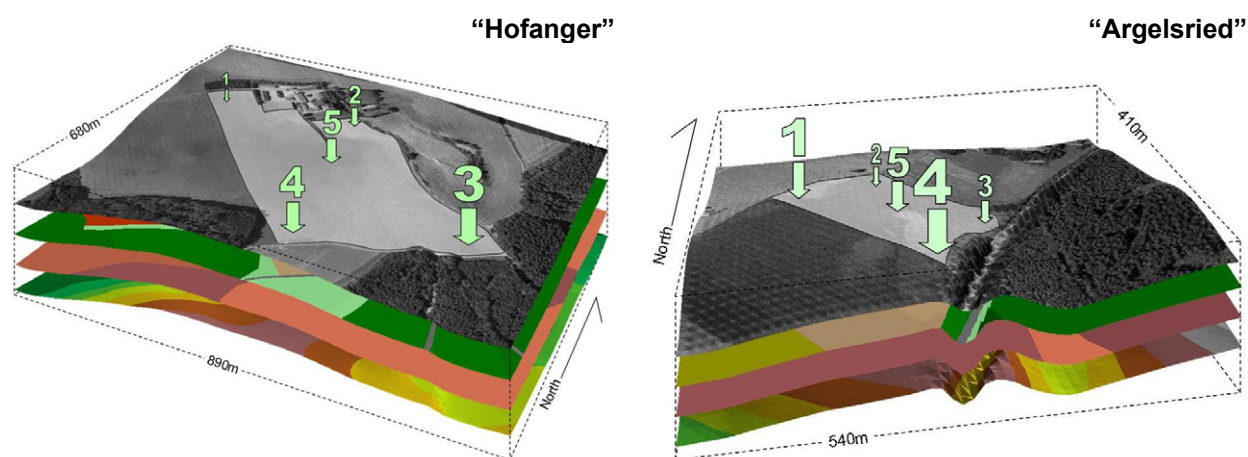


Figure 4.02: 3D-Block image of the test sites “Hofanger” (left) and “Argelsried” (right), indicating the geometry and the terrain situation of the fields as well as the position of the sampling points of the field campaign. The images include four layers (aerial photograph, landuse map, soil map, digital elevation model).



### 4.1.3 Test Sites 2005

The sampling period 2005 also featured a field campaign on one wheat field and one maize site. The wheat site has a size of 8.5 ha and again belongs to the acreage of Hüll manor, while the maize site is located more in the South of the test area near the village of Hochstadt (*fig. 4.01*). With a size of 22.02 ha, the maize field represents a somewhat larger Bavarian acre. The average acreage of typical farms in Bavaria is 26.1 ha, normally split into 14 fields, resulting in average field acreages of only 1.8 ha (BAYERISCHES STAATSMINISTERIUM FÜR LANDWIRTSCHAFT UND FORSTEN 2006). Both fields show a very even surface with no significant relief (*fig. 4.03, left and right*). However, the wheat site is slightly oriented towards the North, while the maize site mainly is facing an Easterly direction. The whole extent of the wheat site is modelled with a sandy loam soil particle size (*fig. 4.12, top middle*), while the maize site also is composed of sandy loam but with a streak of clay loam that intersects the main body of the field (*fig. 4.14, top middle*).

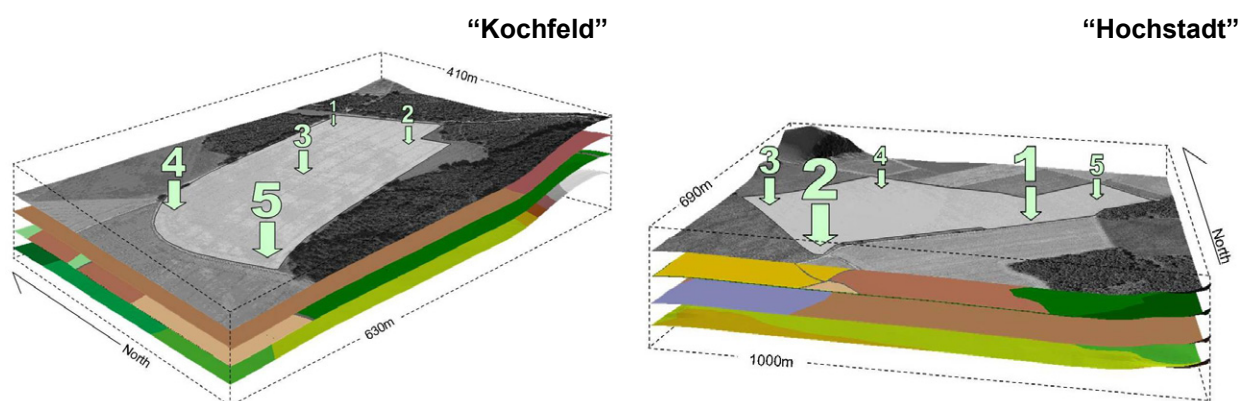


Figure 4.03: 3D-Block image of the test sites “Kochfeld” (left) and “Hochstadt” (right), indicating the geometry and the terrain situation of the fields as well as the position of the sampling points of the field campaign. The images include four layers (aerial photograph, landuse map, soil map, digital elevation model).

### 4.1.4 Field Campaign

With the help of student assistants, two field campaigns were conducted during the vegetation periods of the years 2004 and 2005. For both of the growing seasons, a variety of plant parameters was monitored with a weekly sampling interval. All data resulting from the field work for the years 2004 and 2005 was collected in the frame of the DFG funded project “Coupled Analysis of Vegetation Chlorophyll and Water Content Using Hyperspectral, Bidirectional Remote Sensing”. Besides the biomass and phenology parameters, which are presented in the scope of this work, the project collected detailed data concerning the vertical distribution of chlorophyll, carbon and nitrogen within the canopy.

#### 4.1.4.1 Defining a Sampling Pattern

For every test site, five sampling points were defined, one at every corner and a fifth right in the middle of the field, thus creating an equally distributed sampling pattern for each test site (*fig. 4.04, right*). The sampling points were selected from aerial photographs and located in the field using handheld GPS receivers of the type *Garmin eTrex* (*fig. 4.04, left*). Table 4.01 lists the exact geographic locations of the sampling points for all four of the test fields of the two sampling years.

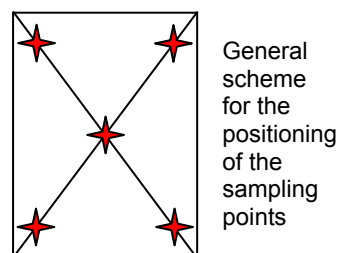


Figure 4.04: GPS positioning of sampling points (left) and general pattern for the positioning of sampling points within a test field (right).

Table 4.01: GPS - Coordinates of the sampling points of the four test fields (Geographic, WGS 84).

<b>"Hofanger" 2004 (Wheat)</b>	<b>Easting</b>	<b>Northing</b>	<b>Altitude</b>
Sample Point 1	11°19'21.5"	48°05'37.5"	583 m a.s.l.
Sample Point 2	11°19'30.0"	48°05'36.6"	583 m a.s.l.
Sample Point 3	11°19'45.3"	48°05'29.4"	579 m a.s.l.
Sample Point 4	11°19'41.5"	48°05'26.1"	584 m a.s.l.
Sample Point 5	11°19'34.4"	48°05'31.9"	590 m a.s.l.
<hr/>			
<b>"Argelsried" 2004 (Maize)</b>	<b>Easting</b>	<b>Northing</b>	<b>Altitude</b>
Sample Point 1	11°18'44.5"	48°06'15.5"	574 m a.s.l.
Sample Point 2	11°18'49.3"	48°06'18.1"	567 m a.s.l.
Sample Point 3	11°18'54.9"	48°06'14.9"	565 m a.s.l.
Sample Point 4	11°18'51.6"	48°06'11.3"	573 m a.s.l.
Sample Point 5	11°18'50.3"	48°06'15.0"	571 m a.s.l.
<hr/>			
<b>"Kochfeld" 2005 (Wheat)</b>	<b>Easting</b>	<b>Northing</b>	<b>Altitude</b>
Sample Point 1	11°18'55.8"	48°05'28.9"	572 m a.s.l.
Sample Point 2	11°18'56.5"	48°05'24.9"	572 m a.s.l.
Sample Point 3	11°18'48.1"	48°05'24.8"	573 m a.s.l.
Sample Point 4	11°18'40.1"	48°05'26.7"	573 m a.s.l.
Sample Point 5	11°18'39.7"	48°05'21.4"	574 m a.s.l.
<hr/>			
<b>"Hochstadt" 2005 (Maize)</b>	<b>Easting</b>	<b>Northing</b>	<b>Altitude</b>
Sample Point 1	11°17'05.7"	48°02'58.0"	612 m a.s.l.
Sample Point 2	11°16'43.9"	48°02'48.0"	616 m a.s.l.
Sample Point 3	11°16'32.3"	48°02'52.7"	615 m a.s.l.
Sample Point 4	11°16'48.1"	48°03'01.0"	612 m a.s.l.
Sample Point 5	11°17'08.6"	48°03'02.1"	611 m a.s.l.

#### 4.1.4.2 Field Methods

The Department of Geography of the Ludwig-Maximilians-Universität of Munich has experience of many years with the procedures of field sampling campaigns. In the course of field work in the frame of several projects, a set of methods for the sampling of aboveground vegetation parameters was established that is briefly introduced in the following.

##### 4.1.4.2.1 Meteorology

In the years 1989 to 1991, the Bavarian Ministry of Agriculture and Forestry installed a network of 122 weather stations, designed to meet the requirements of agricultural applications. The stations of this agro-meteorological network are supervised by the Bavarian Agricultural Regional Office and provide mostly consistent data for the past 15 years. Free of charge, the data is available via the internet (<http://www.lfl.bayern.de/agm/>). The weather station that was consulted here, is the station number 72 located at Gut Hüll in Krailing, Bavaria (*fig. 4.05*).



<b>Height above sea level:</b>	580 m
<b>Latitude:</b>	48° 05' 36" N
<b>Longitude:</b>	11° 19' 35" E
<b>Long term temperature avg.:</b>	7 – 8 °C
<b>Long term precipitation avg.:</b>	850 – 1000 mm
<b>In operation since:</b>	05-03-1990

Figure 4.05: Weather station Nr. 72 of the agro-meteorological network Bavaria ([www.lfl.bayern.de](http://www.lfl.bayern.de)).

As an additional advantage it can be considered that the weather station no. 72 is directly placed in the middle of the test site “Hofanger” of the sampling year 2004, allowing for a comparative analysis of the meteorological interpolation quality of PROMET (see section 3.3.4.3). Before the meteorological data was applied to a comparative analysis with model results, the data were tested for consistency.

##### 4.1.4.2.2 Phenology

Parallel to the growth stages as they are modelled in PROMET (see section 3.3.3.6.1, *tab. 3.09*), the phenological development of the test sites was monitored according to the internationally recognized BBCH-Code (Federal **B**iological Institute – Federal **B**ureau of Species - **C**hemical Industry, BIOLOGISCHE BUNDESANSTALT FÜR LAND- UND FORSTWIRTSCHAFT 1997). The classification system categorizes the growth stages of different crops by applying a decimal code, ranging from 0 (sowing) to 99 (ripeness, harvested, *fig. 4.06*).



### Growth Stages of Cereals (BBCH)

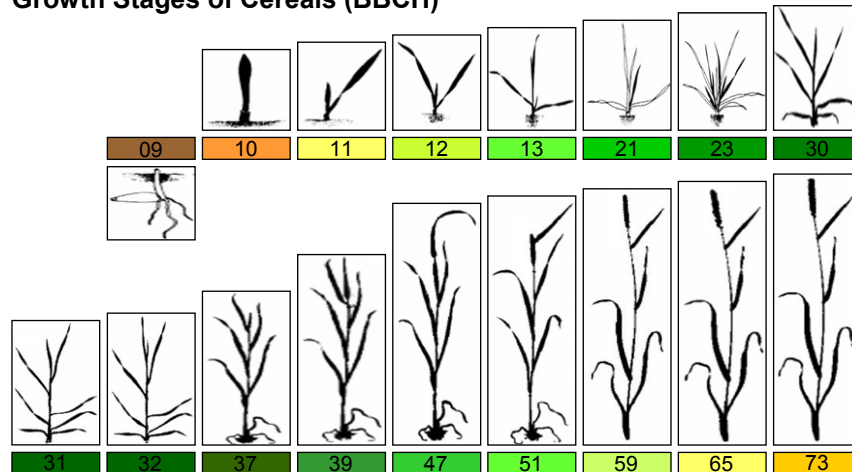


Figure 4.06: Decimal code of BBCH growth stages with their corresponding observable features. Modified after BIOLOGISCHE BUNDESANSTALT FÜR LAND- UND FORSTWIRTSCHAFT (1997).

By comparing detailed descriptions and images of the observable aboveground features of the different phenological stages of both investigated crops, the accurate determination of the current stage of development can be accomplished with reliable precision by an experienced operator.

#### 4.1.4.2.3 Canopy Height

The height of the canopy was determined for two levels applying a folding rule (fig. 4.07, left). On every sampling point, a set of ten measurements was averaged for the leaf and for the sprout level (fig. 4.07, right).

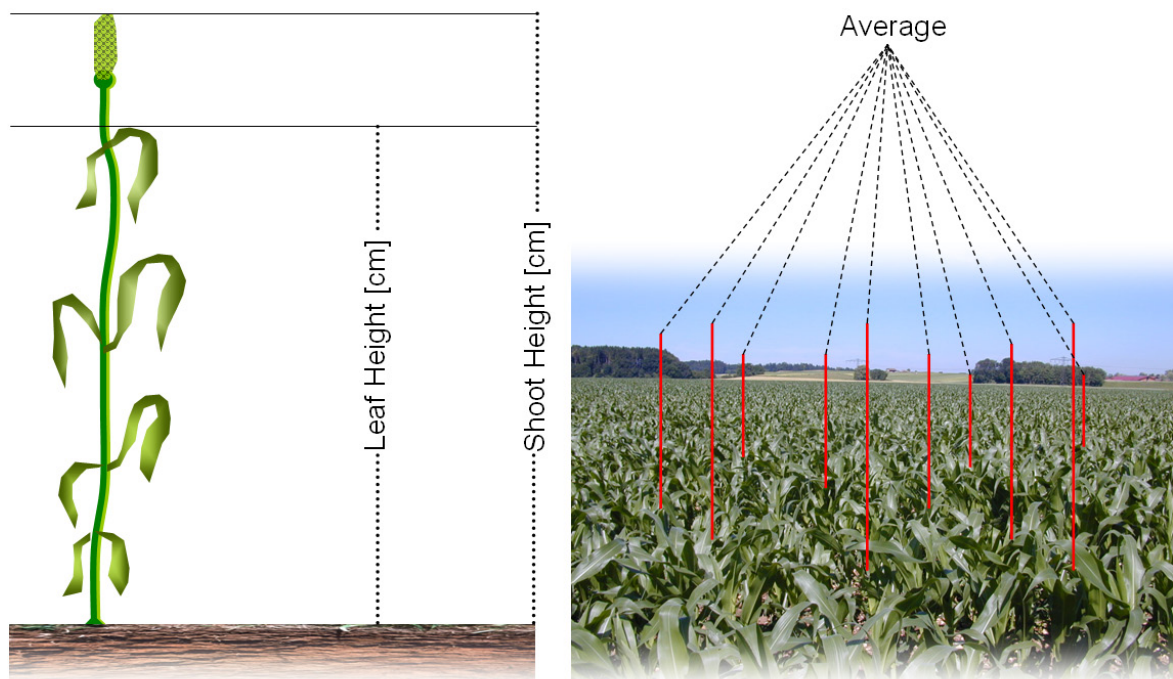


Figure 4.07: Principle of measuring the height of a canopy in the field.

#### 4.1.4.2.4 Stand Density

The density of a canopy stand is defined as the number of plants per square metre ground. It depends on the row distance and the sowing rate, which again is determined by the adjustments of the sowing machine and the rate of germination. The rate of germination is related to the type of seed that has been used. Not every seedling is bound to emerge in spring, but once the seedlings have emerged, the stand density nearly is constant for the growth period. Therefore it is sufficient to measure the stand density once in a season for every test site, usually at the end of June, when both crops (maize and wheat) are showing clear sowing tracks. Two different methods were applied. In 2004, the number of plants along one metre of a sowing track was counted and extrapolated by multiplying the result by the number of sowing tracks per metre (*fig. 4.08, left*). In 2005, a cardboard model, resembling precisely a quarter of square metre, was inserted at a randomly chosen section of the field, but in direct neighbourhood to the regular sampling points (*fig. 4.08, right*).

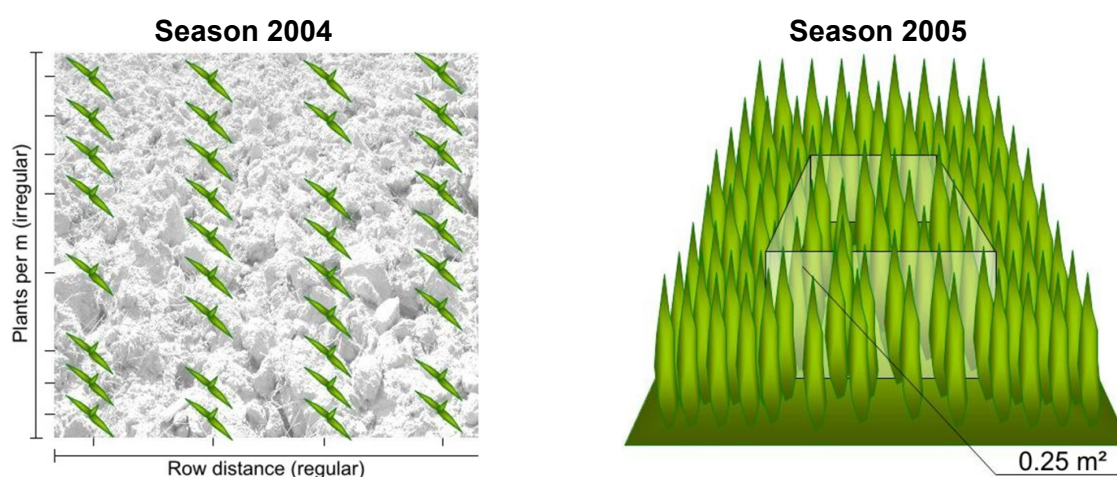


Figure 4.08: Method of the stand density measurements of the season 2004 (left) and 2005 (right).

All the shoots encircled by the cardboard were counted manually. The process was repeated five times and the results were averaged and multiplied by four to generate the final value of plants per m<sup>2</sup>. Both methods produced reliable values, although the stand density showed clear variations. The average stand density for the maize site for example was 11.5 plants per square metre for the year 2005, whereas in 2004 the maize site only counted 9.5 plants per m<sup>2</sup>.

#### 4.1.4.2.5 Dry Biomass

For the biomass sampling, three plants along one sowing track were cut directly above the ground on each sampling point. The plant parts then were neatly packed into waterproof plastic bags in order to preserve the inner humidity of the sample. After the samples had been transported to the laboratory, they were divided manually into the fractions stem, leaf and fruit to be weighed on a laboratory scale. When the wet weight was listed, the samples were dried for at least 24 hours at 85 °C in a drying oven with a constant air supply. When the samples were

thoroughly dry, the weighing was repeated and the final weight was calculated following the subsequent equations (eqs. 4.01 and 4.02).

$$WetWeight [g \cdot m^{-2}] = \left( \frac{WetSampleWeight [g] - ContainerWeight [g]}{3 [plants]} \right) \cdot StandDensity [plants \cdot m^{-2}] \quad (Eq. 4.01)$$

$$DryWeight [g \cdot m^{-2}] = \left( \frac{DrySampleWeight [g] - ContainerWeight [g]}{3 [plants]} \right) \cdot StandDensity [plants \cdot m^{-2}] \quad (Eq. 4.02)$$

The whole chain of the weighing cycles was conducted equally for all three aboveground plant fractions (fig. 4.09).

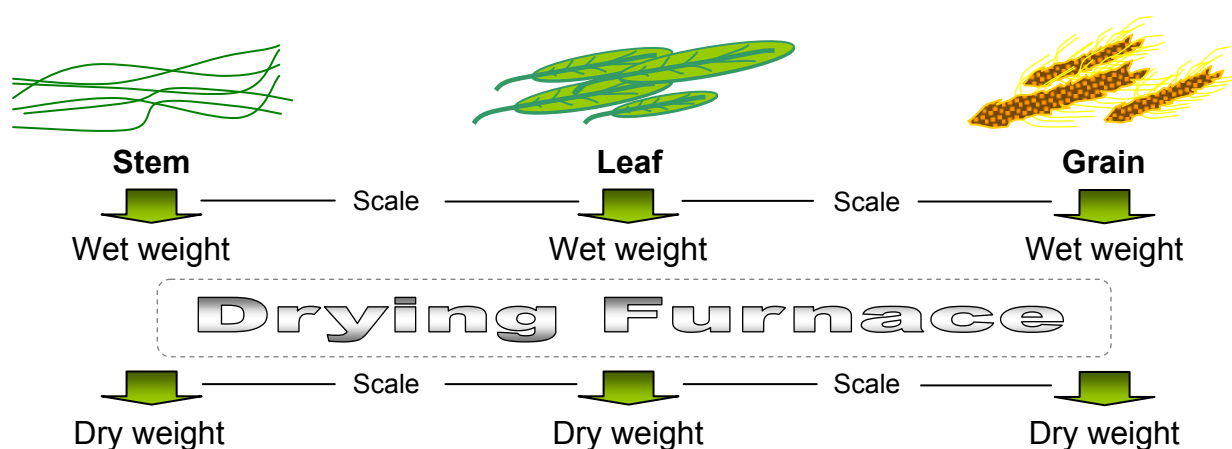


Figure 4.09: Weighing chain for the determination of the dry biomass for different plant parts.

#### 4.1.4.2.6 Leaf Area Index (LAI)

During the 2004 campaign, the relative leaf area was measured on both test sites at a weekly interval, although with a slight offset to the general field days. The offset is due to the requirement of special irradiative conditions for the LAI measurements. While rainfall generally prevents a measurement, sunny conditions are not in favour of the technique either, for the instrument is requiring a diffuse illumination situation.

The measurement itself was conducted with the help of two LI-COR *LAI-2000* instruments. The measuring technique combines a measurement of sky brightness above the canopy with measurements beneath the canopy, while the sensor is viewing skywards. In practice, four „below” measurements are taken to achieve a suitable spatial average for the corresponding sampling point. To exclude the effect of the operator and the shadow he is casting during the measurements, the *LAI-2000* was operated using a 180° azimuth view. Below and above canopy measurements were carried out at identical heights and azimuth directions.

The *LAI-2000* working principle is based on measurements of the gap fraction at five zenith angles. The data that have to be supplied are the path lengths of view through the canopy at

those five angles (*fig. 4.10*). Therefore the LAI-2000 sensor has five concentric rings that make up a field of view extending from zenith ( $0^\circ$ ) to near the horizon ( $74^\circ$ ).



Figure 4.10: Principle of a leaf area measuring cycle with the LI-COR LAI-2000 instrument.

If the sensor is viewing the sky, the  $0^\circ$  detector is measuring the brightness straight overhead, while the 5<sup>th</sup> detector is measuring the brightness of a ring centred at  $68^\circ$  subtending  $13^\circ$ . Five values of canopy transmittance are calculated from these readings by dividing corresponding below and above pairs. From the transmittance at all five zenith angles, the LAI is calculated as output. For more details on the measurement principle it is referred to LI-COR (1992). The resulting LAI values are means and standard deviations of one measurement cycle, which consists of one measurement above and four recordings below the canopy (*fig. 4.10*).

#### 4.1.5 Field Scale Modelling

For the model application on the field scale, local GIS data sets were constructed for each of the four test sites. As mentioned in section 3.1, the spatial resolution of the model calculations is determined by the spatial resolution of the digital elevation model. For the modelling on the field scale, a 10 x 10 m elevation model was kindly provided by the Bavarian land surveying office. The detailed DEM allowed the derivation of the required terrain parameters (elevation, slope and aspect) for all four test sites (*figs. 4.11, 4.12, 4.13, 4.14, bottom row*). Soil information in terms of soil texture and soil type was provided through the generalization of a digital geologic map provided by the Bavarian State Office of Geology, while the landuse information was based on own mapping campaigns (*figs. 4.11, 4.12, 4.13, 4.14, top middle and right*).

Since the field scale modelling is limited to the boundaries of the test area Gilching (*fig. 4.01*), a subset of 19 stations was clipped from the available meteorological network (*fig. 3.51*). Figure 4.15 shows the meteorological subset in spatial relation to the modelled test fields.



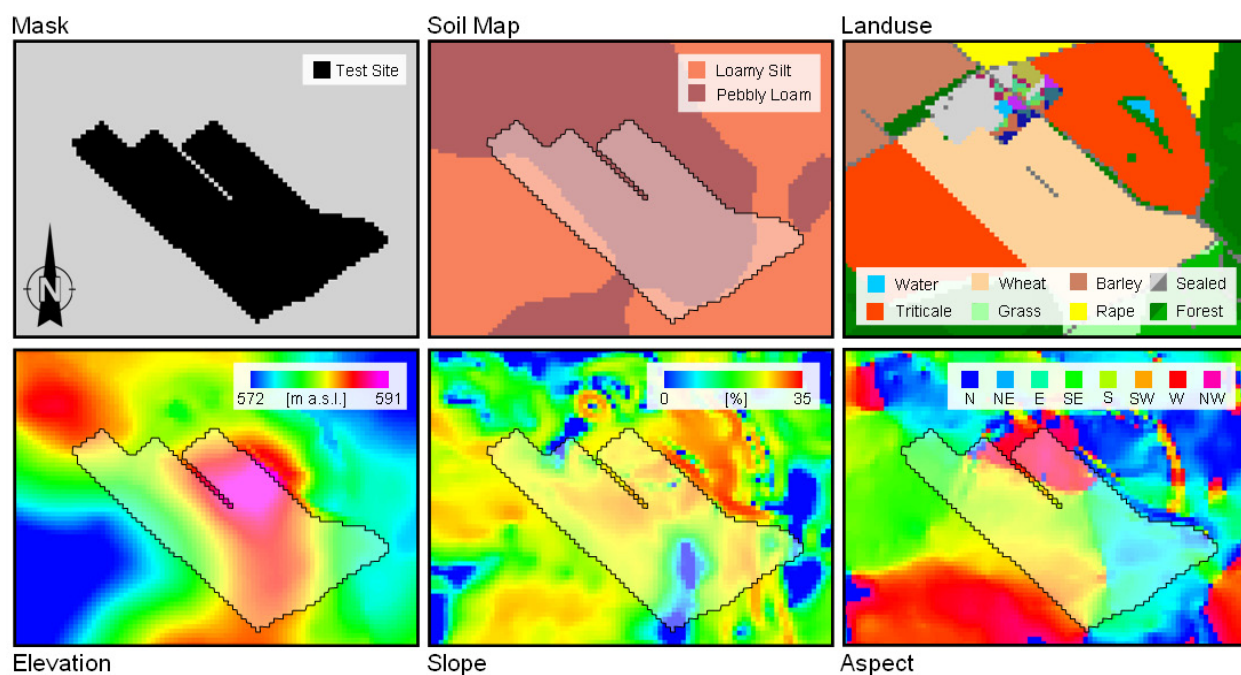


Figure 4.11: 10 x 10 m resolution GIS data set for the field scale modelling of the 2004 wheat test site "Hofanger". Top left: Mask layer, top middle: Soil particle size, top right: Land use, bottom left: Elevation [m a.s.l.], bottom middle: Slope [%] and bottom right: Aspect. All figures comprise an area of 890 by 680 m.

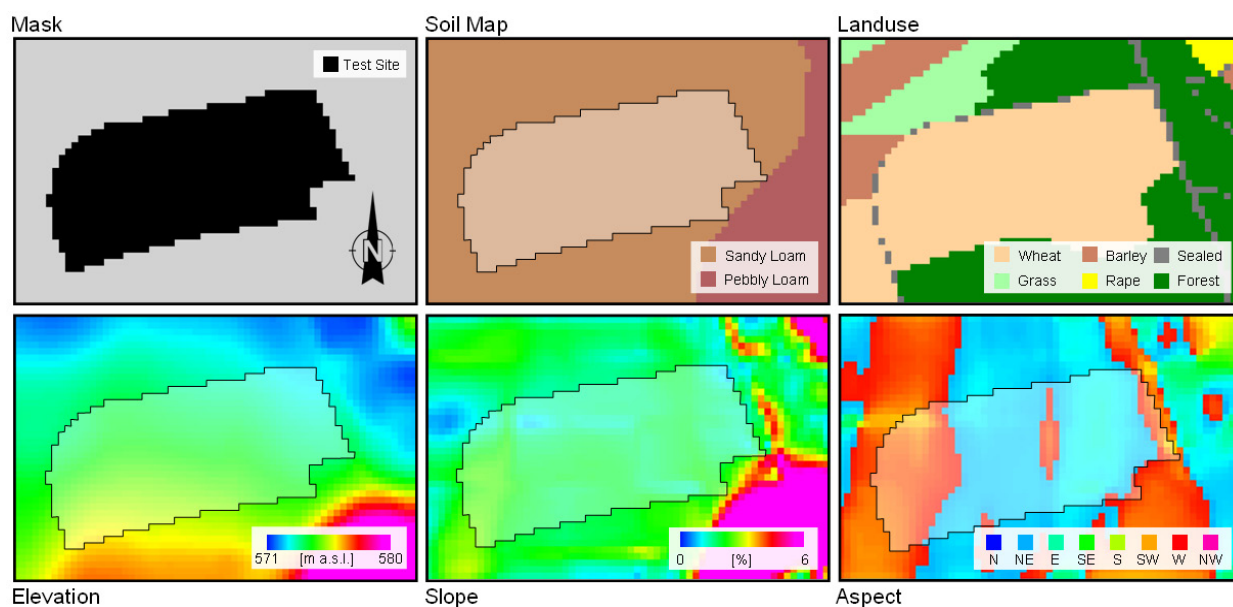


Figure 4.12: 10 x 10 m resolution GIS data set for the field scale modelling of the 2005 wheat test site "Kochfeld". Top left: Mask layer, top middle: Soil particle size, top right: Land use, bottom left: Elevation [m a.s.l.], bottom middle: Slope [%] and bottom right: Aspect. All figures comprise an area of 630 by 410 m.

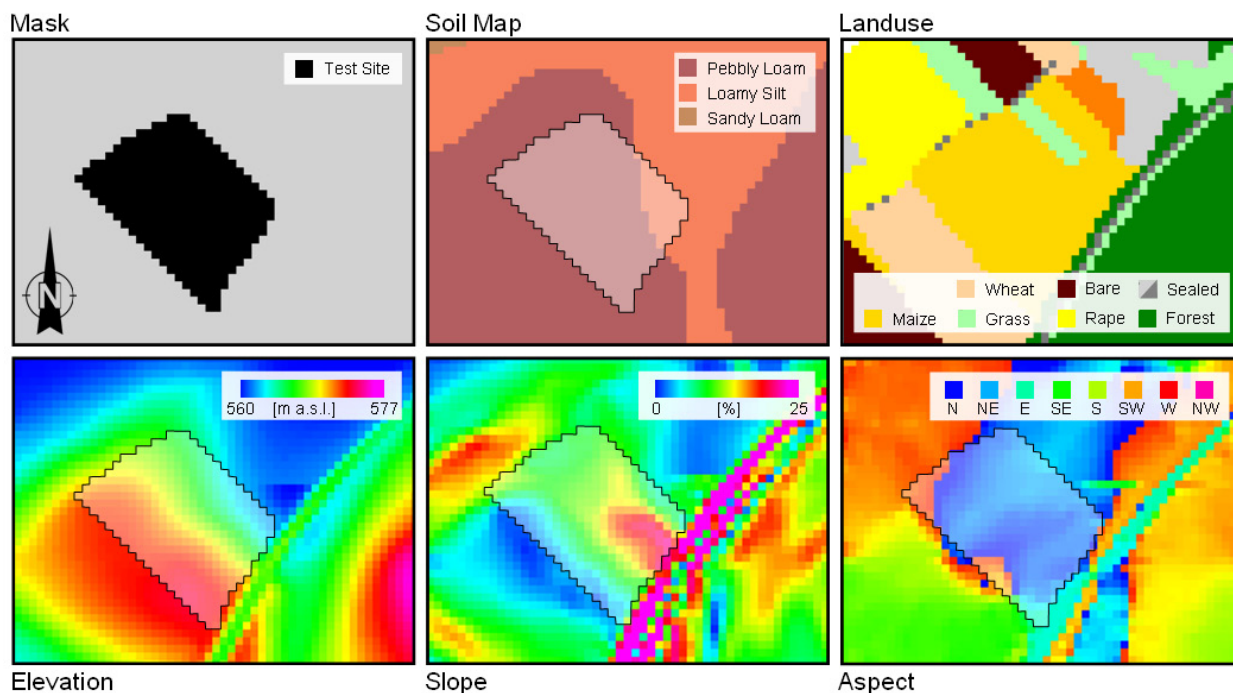


Figure 4.13: 10 x 10 m resolution GIS data set for the field scale modelling of the 2004 maize test site "Argelsried". Top left: Mask layer, top middle: Soil particle size, top right: Land use, bottom left: Elevation [m a.s.l.], bottom middle: Slope [%] and bottom right: Aspect. All figures comprise an area of 530 by 410 m.

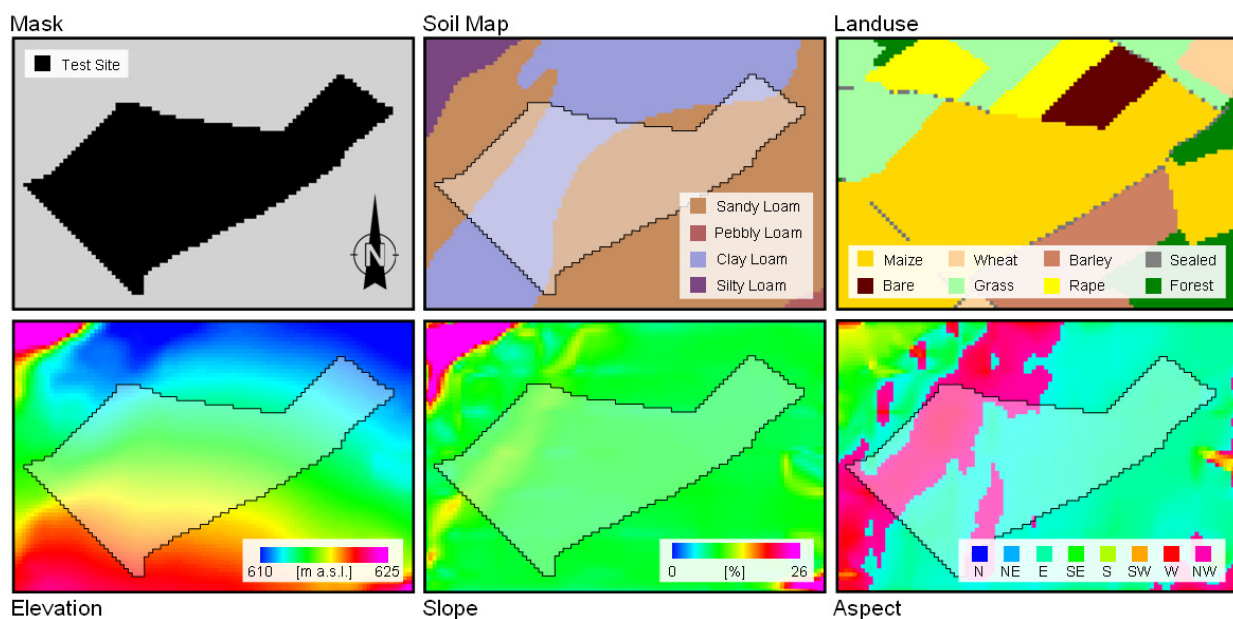


Figure 4.14: 10 x 10 m resolution GIS data set for the field scale modelling of the 2005 maize test site "Hochstadt". Top left: Mask layer, top middle: Soil particle size, top right: Land use, bottom left: Elevation [m a.s.l.], bottom middle: Slope [%] and bottom right: Aspect. All figures comprise an area of 1000 by 680 m.

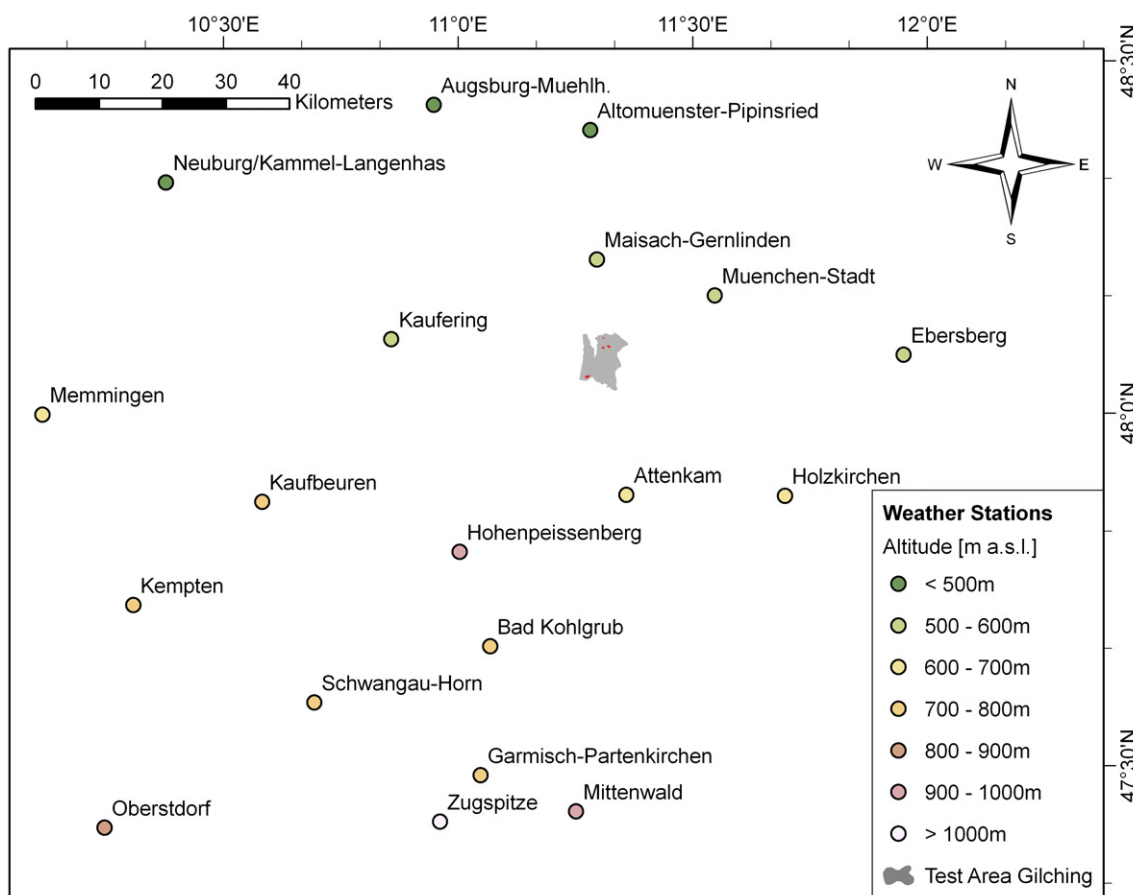


Figure 4.15: Subset of German-Weather-Service stations applied for the modelling of the field scale in the test area Gilching.

#### 4.1.6 Field Scale PROMET vs. Field Measurements

For the assessment of the model quality in comparison with field measurements, model runs were performed applying the field scale GIS data sets introduced in the previous section. A spin-up period of one model year was considered to grant an adequate initialisation time, where the model was allowed to balance the soil water storage according to the input meteorology. Due to the fact that PROMET does not feature a detailed description of the nutrient cycles (see section 3.3.3.6.4), the preceding crop was assumed to equal the respective target crop. The points that had been mapped by the field campaigns (*tab. 4.01*) were located via GIS methods and extracted from the spatial model results. Measured and modelled data were compared for the accumulated biomasses of the different aboveground plant parts, as well as for the plant height, leaf area and phenological development of the respective crops.

##### 4.1.6.1 Meteorology

Among the meteorological parameters that are determining the plant growth in the model, three parameters are of particular importance. The radiation balance of the canopy surface determines the energy budget that is available for the photosynthetic processes (see section 3.3.1), while the precipitation interacts with the canopy by replenishing the soil water storage on

one hand and by wetting the leaves and thus diverting energy for the interception evaporation on the other (see section 3.3.2.2). The temperature finally determines the velocity of the chemical reactions that are driving the photosynthesis within the chloroplasts (see section 3.3.3.5). For the assessment of the quality of the meteorological interpolation, only temperature and rainfall were investigated, due to the debatable quality of the radiation sensors of the agro-meteorological weather station. The modelled meteorology was extracted from the 10 x 10 m raster of the model results for the days that are determining the growth season of the winter crop of 2004 (October 1<sup>st</sup> 2003 to August 31<sup>st</sup> 2004) at the location of the weather station in the direct middle of the test site “Hofanger”.

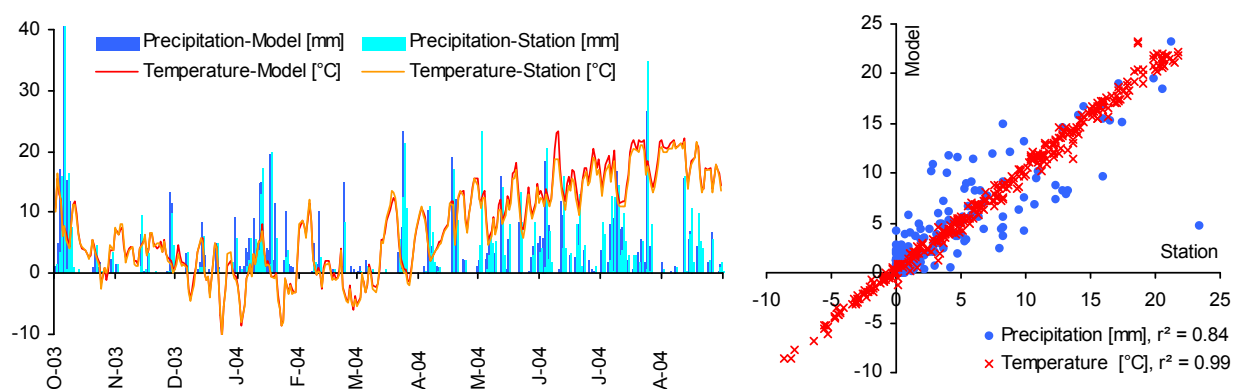


Figure 4.16: Interpolated vs. measured precipitation and temperature for the weather station No. 72 of the agro-meteorological network Bavaria. Annual course (left) and correlation (right) for the growth cycle of the wheat test field “Hofanger” from October 2003 to August 2004.

Figure 4.16 indicates a good interpolation of meteorological parameters in the case of the mean air temperature with a coefficient of determination of 0.99, a slope of 1.03 and a Nash-Sutcliffe efficiency coefficient of 0.98 (NASH AND SUTCLIFFE 1970). Sound results also are achieved for the rainfall ( $r^2 = 0.84$ , slope = 0.82, Nash-Sutcliffe = 0.94). Deviations between modelled and measured precipitation occur, when local weather events such as thunderstorms are registered by the weather station at the field, while they are not mapped by the gauging stations that are surrounding the test field. The station of the German Weather Service that is nearest to the test field (Maisach-Gernlinden, fig. 4.15) is located at a linear distance of nearly 14 kilometres. Considering the absolute sums, the model interpolated slightly more precipitation than it was recorded by the weather station as well as slightly warmer temperatures. In total, the meteorological situation at the field is well reproduced by the model, so that the meteorological interpolation can be considered to be adequate for simulations on the field scale.

#### 4.1.6.2 Winter Wheat 2004

The life cycle of the 2004 winter crop is spanned between the date of sowing (15<sup>th</sup> of October 2003) and harvest (22<sup>nd</sup> of August 2004). Only the main growth period during the summer months is covered by the field campaign, so that a subset of the model results, ranging from the



1<sup>st</sup> of April to the 31<sup>st</sup> of August 2004, could be analyzed in comparison with field measurements. The data recorded at the five sampling points in the field (see section 4.1.2) were averaged and compared to the model results, which were extracted from the modelled data sets at the locations corresponding to the sampling points and equally were averaged for the comparison. Besides the courses of modelled and measured average results, figure 4.17 also indicates the absolute ranges of the modelled growth parameters (dashed lines).

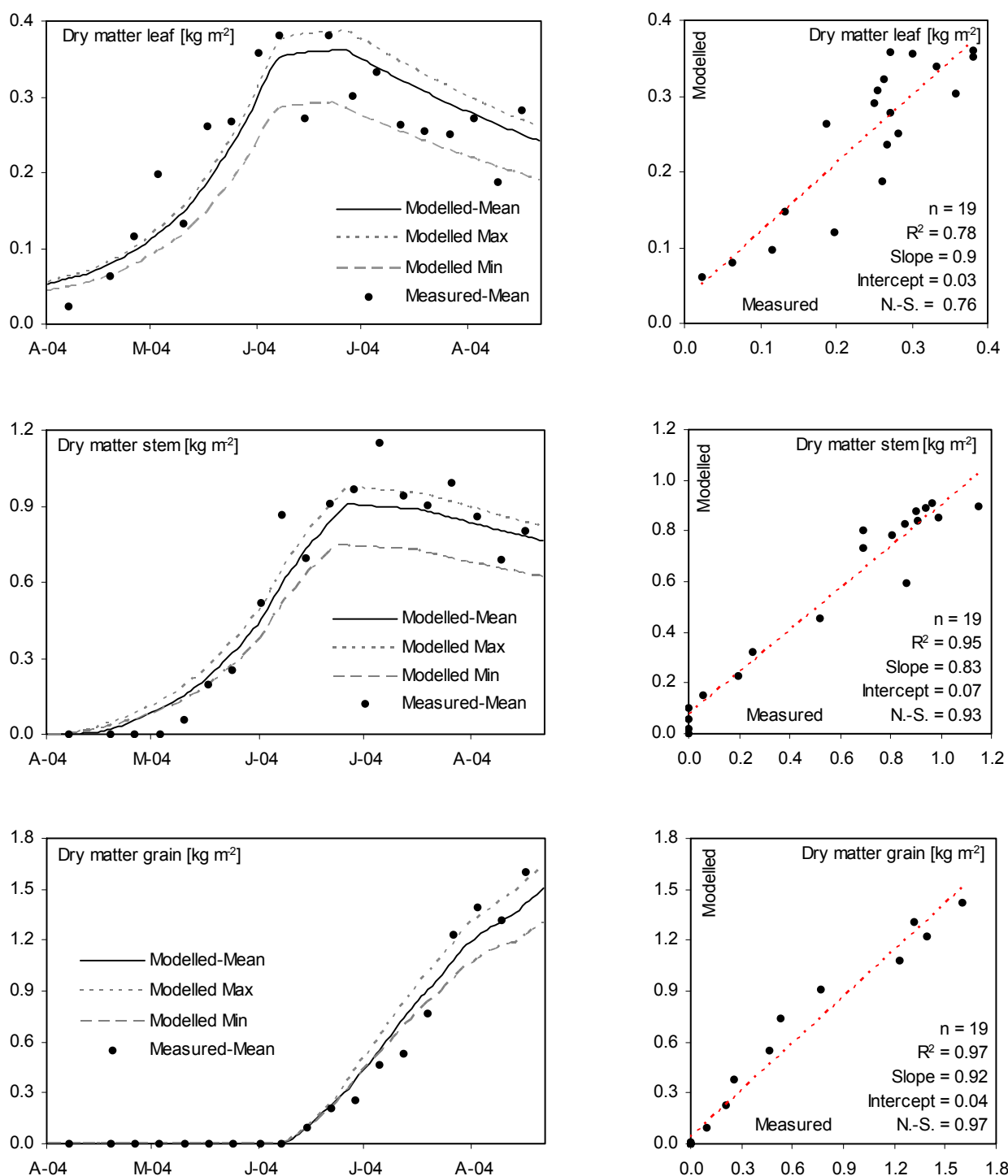


Figure 4.17: Modelled vs. measured aboveground dry biomass for the sampling period of the wheat test field "Hofanger" from April 1<sup>st</sup> to August 31<sup>st</sup> 2004. Course of development (left) and correlation including coefficients of determination and Nash-Sutcliffe coefficients (right) discerned into the plant parts leaf (top), stem (middle) and grain (bottom).

For the three aboveground plant parts “stem”, “leaf” and “grain”, the modelled values reasonably match the field data concerning their magnitude and also their course. This results in stable coefficients of model efficiency. The Nash-Sutcliffe coefficients are varying between 0.76 for the leaves (*fig. 4.17, top right*) and 0.97 for the weight of the fruit (*fig. 4.17, bottom right*). In addition, the slopes of the regression lines stay close to a value of one and the intercept values also are low, both indicating a non-biased representation of the measured biomasses through the model. The scattering of the measured data clearly shows that the measured biomass is the result of destructive measuring techniques (see section 4.1.4.2.5). This representation of the natural variability of the stand in the reference data is resulting in jumps and steps that can be found throughout the field measurements. The scattering of the values is highest for the leaf biomass and lowest for the grain dry weight, leading to an increasing accuracy of the model results from leaf to grain mass. Nonetheless, the natural variability seems to be approximately mapped by the model, since the modelled extremes are mostly enveloping the measured range.

The most determining factor, concerning the realistic representation of the carbon allocation to the different parts of the plant, is a correct modelling of the phenological progress. The phenological modelling is mainly determined by the air temperature (see section 3.3.3.6.1). The sensible representation of the air temperature by the model consequently leads to a sound mapping of the phenological stages (*fig. 4.18*).

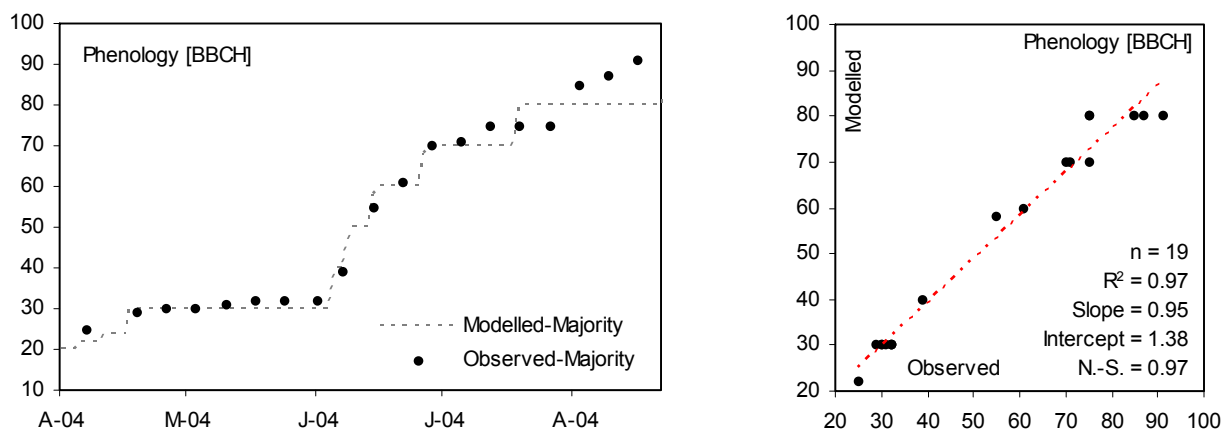


Figure 4.18: Modelled vs. observed plant phenology. Course of development (left) and correlation (right) for the sampling period of the wheat test field “Hofanger” from April 1<sup>st</sup> to August 31<sup>st</sup> 2004.

Figure 4.18 shows that the process of hibernation is well traced by the model, as well as the rapid development that characterizes the month of June. Most of the deviations are due to the model’s incapability of mapping single growth stages between the major classes, while the observations include the finer measures between the decimal steps. The BBCH stage 80 (maturity) is the highest grade of development that is modelled, so that during the ripening the modelled value stays constant. A reasonable mapping of the leaf area is of great importance, since it determines the interception of sunlight energy for all photosynthetic reactions. The rapid increase of the leaf area in spring as well as the steady decrease during the ripening phase is

well reproduced by the model, although it slightly over-predicts the accumulation of leaf area during late May (*fig. 4.19, left*). The high coefficient of correlation of 0.88 may be due to the bunching of LAI-measurements for leaf area indices greater than four and the relatively small number of measurements for low LAI-values.

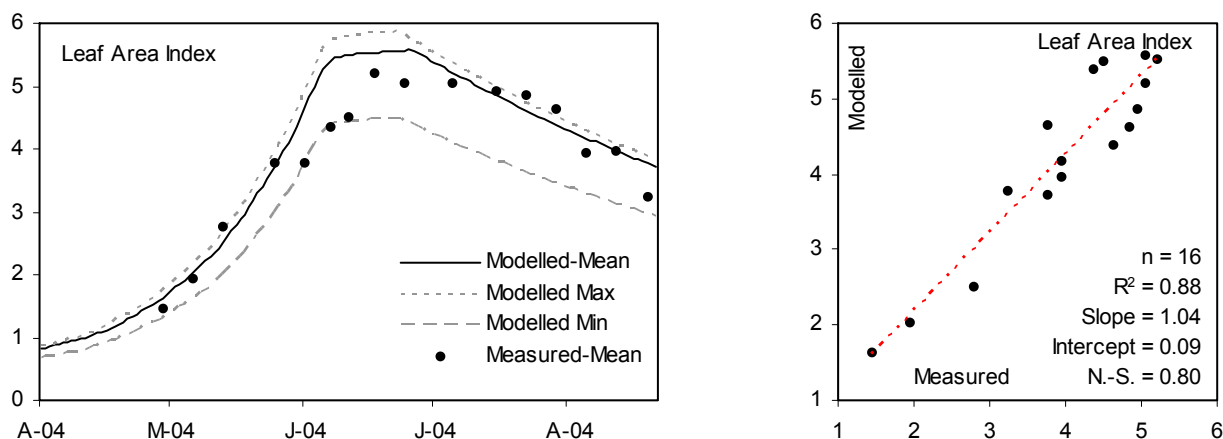


Figure 4.19: Modelled vs. observed leaf area index. Course of development (*left*) and correlation (*right*) for the sampling period of the wheat test field "Hofanger" from April 1<sup>st</sup> to August 31<sup>st</sup> 2004.

Since the plant height is modelled as a function of the LAI (see section 3.3.3.6.3), it shows an analogue trend. Spring canopy heights are over-predicted, while the decrease of height after growth stage 70 (fruit development) is well reproduced by the model (*fig. 4.20*).

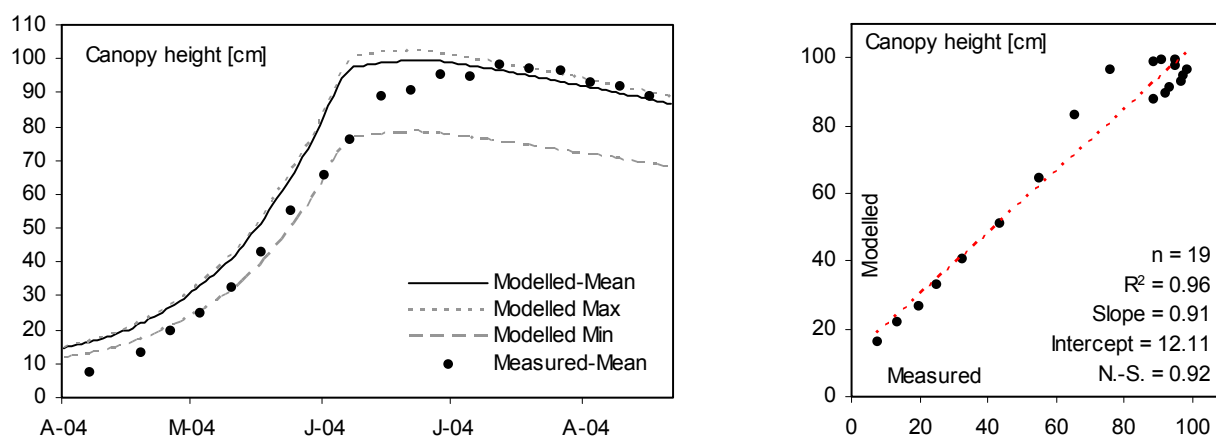


Figure 4.20: Modelled vs. observed overall canopy height. Course of development (*left*) and correlation (*right*) for the sampling period of the wheat test field "Hofanger" from April 1<sup>st</sup> to August 31<sup>st</sup> 2004.

The model results for the test field Hofanger showed high correlations concerning R<sup>2</sup> as well as Nash-Sutcliffe coefficients for all of the observed aboveground plant parameters, as could already be shown by HANK ET AL. (2007). Especially the good representation of the phenological progress results in a realistic simulation of the biomass allocation to the different plant parts. For a continuative and more detailed interpretation of the displayed data, the digital acre file ("Schlagkartei") of the test field is available in the appendix (A.10).

#### 4.1.6.3 Winter Wheat 2005

Parallel to the modelling of the wheat test site 2004, a model run was conducted for the second C<sub>3</sub> test site “Hofanger”. The winter crop was sowed the 15<sup>th</sup> of October 2004 and harvested on August 19<sup>th</sup> 2005. In-field data was available for the time from April to August 2005. Instead of going through the full comparison like for the previous test site, only the results of the confrontation of modelled and measured plant parameters are summarized in table 4.02.

Table 4.02: Assessment of the model results for the aboveground physiological plant parameters of the wheat test site “Hofanger” (April 1<sup>st</sup> to August 31<sup>st</sup> 2005) in comparison with field measurements.

Parameter	[n]	N.-S.	Slope [m]	Intercept [b]	Coeff. of Determination [R <sup>2</sup> ]
Leaf Biomass:	18	0.49	0.52	0.11 [kg m <sup>-2</sup> ]	0.51
Stem Biomass:	18	0.71	0.70	0.09 [kg m <sup>-2</sup> ]	0.73
Grain Biomass:	18	0.85	0.93	0.02 [kg m <sup>-2</sup> ]	0.87
Leaf Area Index:	7	0.86	0.95	0.30 [-]	0.89
Canopy Height:	18	0.91	0.83	16.72 [cm]	0.97
Phenology:	18	0.94	0.94	-0.83 [-]	0.97

The 2005 wheat test site shows somewhat weaker results than those that could be achieved for the 2004 wheat site. The slopes of the regression lines indicate that the model tends to underestimate the biomass accumulation with increasing overall biomasses, while the stable coefficients of correlation and of model efficiency show that the annual course seems to be accurately represented. The relatively high intercept values for the leaf and for the stem biomasses indicate that low biomasses are more likely to be overrated by the model. Due to strong scattering of the measured data, the results for the leaf biomass are the weakest. For the season of 2005, no LAI measurements were conducted in the field. The LAI comparison presented in table 4.02 applies leaf area values that are based on an ESA ENVISAT/MERIS remote sensing product (BEAM-VISAT, TOA\_Veg, see BACOUR ET AL. 2006) and were extracted for the test site from satellite imagery of the summer 2005. The LAI is soundly traced by the model and also the quality of the other plant parameters emphasizes the stability of the model for the simulation of the carbon allocation of C<sub>3</sub> species on the field scale. For a continuative interpretation of the displayed data, the digital acre file is available in the appendix (A.11).

#### 4.1.6.4 Maize 2004

Due to the different pathways of carbon assimilation that are characterising C<sub>3</sub> and C<sub>4</sub> species (see section 1.5), the modelling of the C<sub>4</sub> photosynthesis slightly differs from the method that is applied for the C<sub>3</sub> metabolism (see section 3.3.3.5). The results of the field scale model runs for the maize test site therefore are again presented in more detail.

The growth cycle of a maize stand strongly differs from that of a winter crop. The sowing window in the alpine foreland ranges from April 20<sup>th</sup> to the middle of May (FISCHBECK ET AL. 1999), while the maize crops usually are harvested during the first week of October

(SCHWERTMANN ET AL. 1987). Field measurements were available on 20 dates from May to September for the summer of 2005. Figure 4.21 lists the averaged field measurements and model results for the five sampling points of the maize test site “Argelsried”.

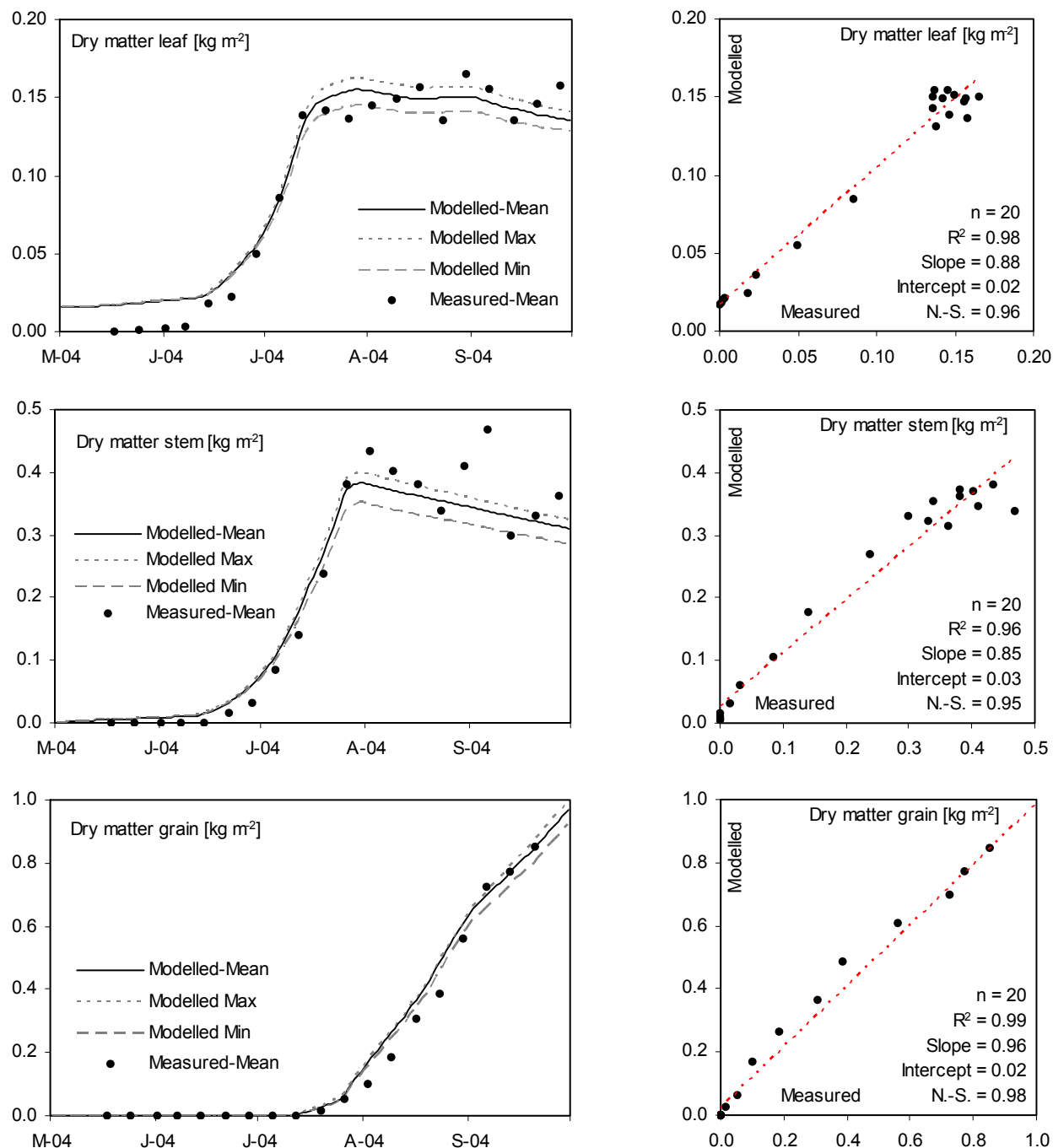


Figure 4.21: Modelled vs. measured aboveground dry biomass for the sampling period of the maize test field “Argelsried” from May 1<sup>st</sup> to September 30<sup>th</sup> 2004. Course of development (left) and correlation including coefficients of determination and Nash-Sutcliffe coefficients (right) discerned into the plant parts leaf (top), stem (middle) and grain (bottom).

The development of the aboveground plant physiology is well traced by the model for all three plant parts. Strong coefficients of model efficiency between 0.95 for the stem biomass and 0.98 for the grain biomass as well as the slopes of the regression lines confirm the visual impression of a strong correlation between modelled and measured data.

The regression line for the leaf biomass (*fig. 4.21, top right*) shows a noticeable offset from the zero intercept. This is due to a systematic feature of the model algorithm. Since the whole photosynthesis depends on the absorption of light by the leaves, growth can only be modelled, if the leaf area is above zero. However, the algorithm worked out to react unstably for very small leaf areas. Consequently, the modelled leaf area is set to a default minimum value as soon as the leaf emergence is initiated in the model. It was shown in section 3.3.3.1 that the relation of leaf area to leaf mass is assumed to be constant. So with the setting of a minimum leaf area, also a minimal leaf mass is initialized that in this case disturbs the correlation by assuming a leaf mass of about  $20 \text{ g m}^{-2}$  throughout the month of May, while the measurements are still showing very low leaf biomasses.

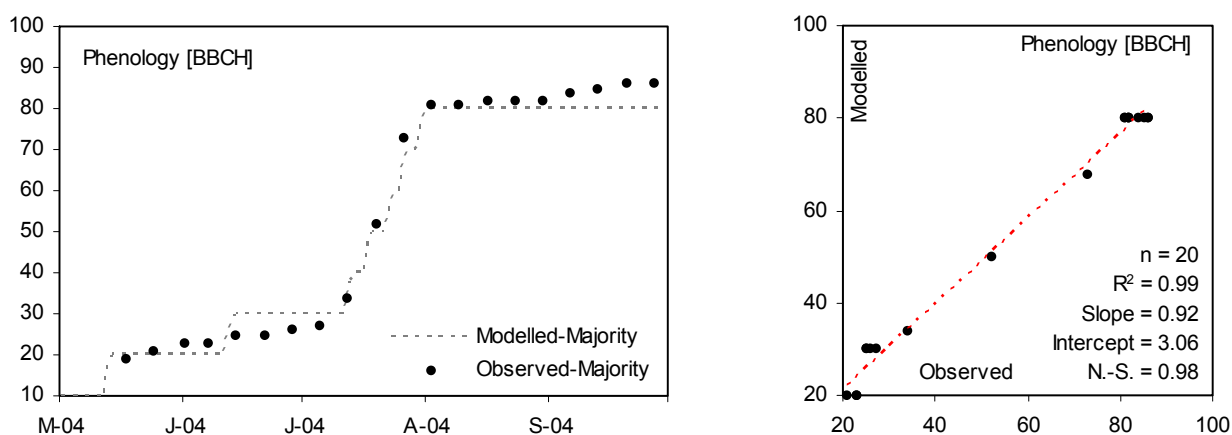


Figure 4.22: Modelled vs. observed plant phenology. Course of development (left) and correlation (right) for the sampling period of the maize test field "Argelsried" from May 1<sup>st</sup> to September 30<sup>th</sup> 2004.

For the modelling of the phenological progress, the same restrictions apply as for the wheat sites. Only the major decimal steps are modelled, but nonetheless, the course of development is well traced by the model. The maize site is characterized by an extremely rapid progress of the phenological stages during the month of July (*fig. 4.22*).

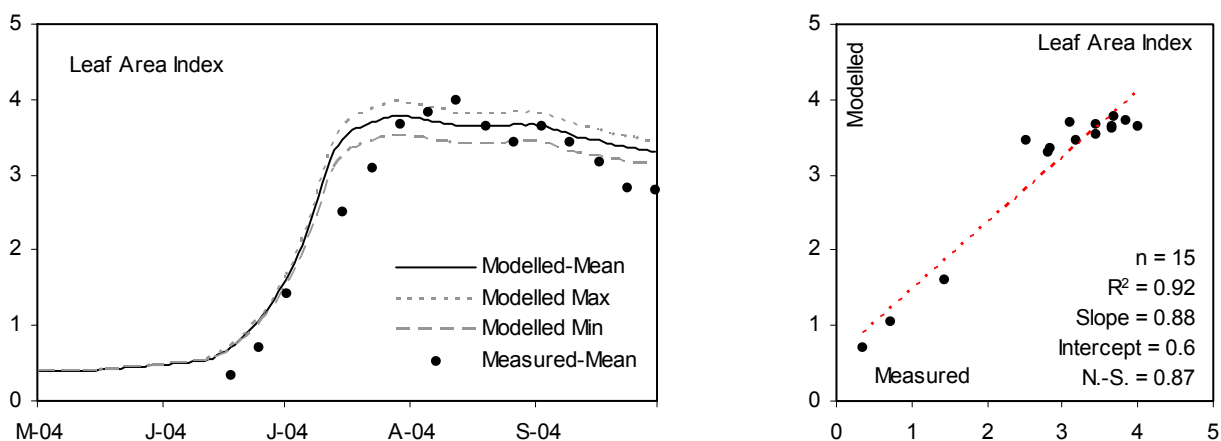


Figure 4.23: Modelled vs. observed leaf area index. Course of development (left) and correlation (right) for the sampling period of the maize test field "Argelsried" from May 1<sup>st</sup> to September 30<sup>th</sup> 2004.

The representation of the leaf area index by the model suffers the same restrictions that are disturbing the course of the leaf biomass. For the early growth stages, the leaf area like the leaf mass is overrated. However, the lines seem to match quite closely for the further course of the year. The relatively high coefficient of correlation of 0.88 may here also be due to the bunching of LAI measurements within a value range between 2 and 4, while only few measurements exist for low leaf areas (*fig. 4.23*).

Since the plant height is modelled as a function of the LAI, it also is overestimated for the early growth stages, clearly showing through the offset of the regression line that accumulates to nearly 24 cm at the y-axis. The constantly high canopy height of more than 250 cm again is well traced by the model, even during the phase of ripening trough late August and September.

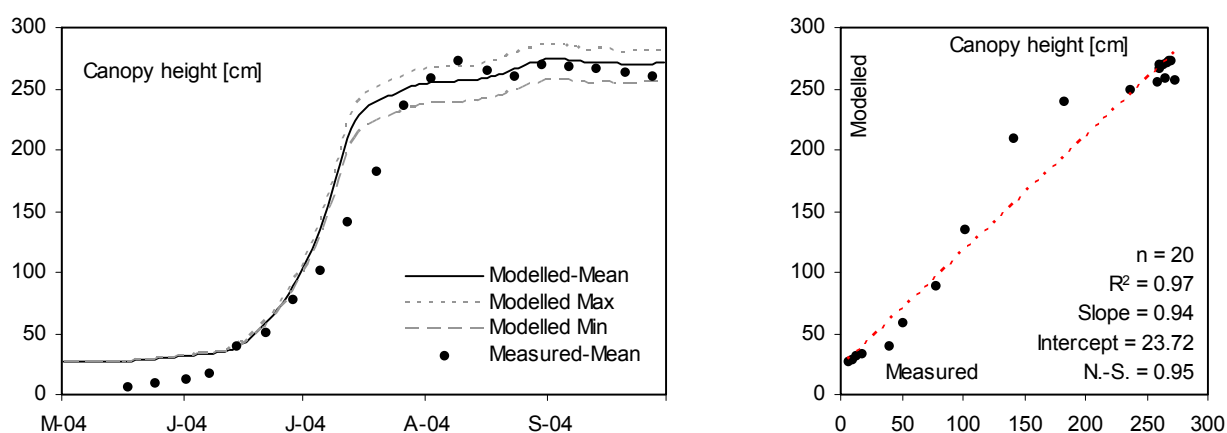


Figure 4.24: Modelled vs. observed overall canopy height. Course of development (left) and correlation (right) for the sampling period of the maize test field "Argelsried" from May 1<sup>st</sup> to September 30<sup>th</sup> 2004.

The courses of the modelled aboveground parameters for the C<sub>4</sub> test site "Argelsried" showed reasonable to high correlations for all of the observed plant features. The model seems to be capable of a sound reproduction of the carbon allocation also of C<sub>4</sub> species on the field scale.

#### 4.1.6.5 Maize 2005

To support the stable results that could be achieved for the maize test site 2004, a model run on the second C<sub>4</sub> site was conducted. Reducing the full comparison like it was displayed for the previous test site, only the results of the confrontation of modelled and measured plant parameters are summarized in table 4.03.

Table 4.03: Assessment of the model results for the aboveground physiological plant parameters of the maize test site "Hochstadt" (May 1<sup>st</sup> to September 30<sup>th</sup> 2005) in comparison with field measurements.

Parameter	[n]	N.-S.	Slope [m]	Intercept [b]	Coeff. of Determination [R <sup>2</sup> ]
Leaf Biomass:	17	0.70	0.61	0.04 [kg m <sup>-2</sup> ]	0.94
Stem Biomass:	17	0.78	0.66	0.07 [kg m <sup>-2</sup> ]	0.97
Grain Biomass:	17	0.92	0.94	0.09 [kg m <sup>-2</sup> ]	0.91
Canopy Height:	17	0.80	0.95	51.87 [cm]	0.93
Phenology:	18	0.97	0.88	7.11 [-]	0.98

The second maize test site also shows high coefficients of determination as well as of model efficiency, but the generally lower slopes of the regression lines are indicating that the model tends to underestimate the biomasses for this test site at least for higher values. Unfortunately, no leaf area measurements could be acquired for the maize site in 2005, so that no correlation for the LAI is included in table 4.03. Due to the strong correlation of plant height and leaf area and the high correlation of measured and modelled canopy height, it can be deduced that the LAI is reasonably reproduced by the model as well.

#### 4.1.6.6 Yield

For the 2004 wheat test site “Hofanger”, a digital yield map could be acquired, that is based on measurements of an impingement sensor. The sensor is mounted on a combine harvester and monitors the pressure of the threshing good at a constant rate. The spatial allocation of the yield measurements is managed via DGPS. The combine measurement was corrected by comparing the absolute sum of measured yield for the stand with the total weight harvested.

For a comparison with the model results, the original yield map was resampled to meet the models micro scale resolution of 10 x 10 m (*fig. 4.25*). Apart from the marginal regions with lower yield, the measured yield variation of the stand was between 7 and 10 t ha<sup>-1</sup>, indicating that the crop was developed strongly and homogeneously. With a total harvest of 142.7 t, the average yield of the 14.44 ha site was 9.88 t ha<sup>-1</sup> (see appendix A.10).

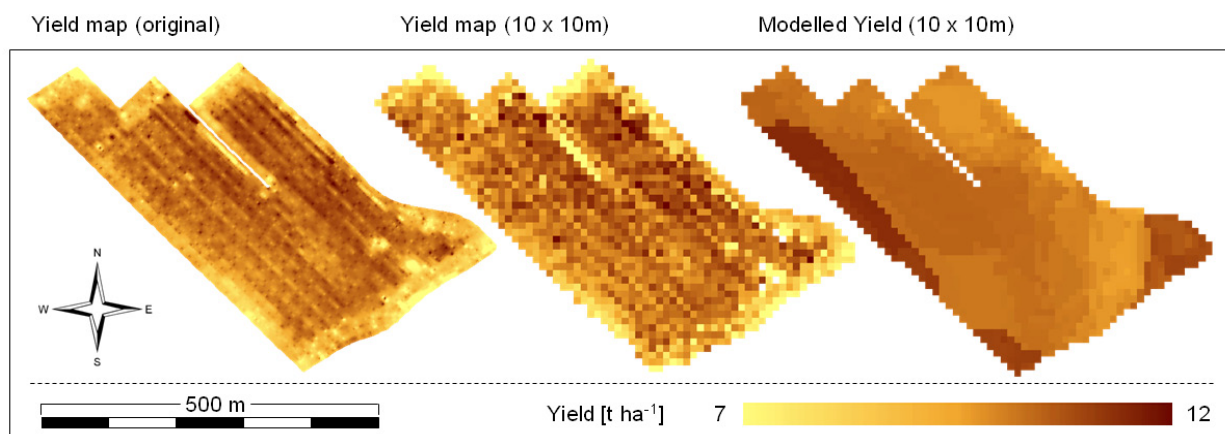


Figure 4.25: Yield map based on a combine measurement in full and resampled resolution compared to the modelled yield of the season 2004 for the wheat test site “Hofanger”.

The model returned a total yield of 157.31 t on 14.31 ha. The size of the field as it is represented in the model is 0.13 ha smaller than in reality, due to the coarsening of the shape according to the DTM resolution of 10 x 10 meters. The modelled yield ranges from 9.99 to 11.7 t ha<sup>-1</sup>, combined with a mean value of 10.99 t ha<sup>-1</sup> and a standard deviation of 0.28. The variability of the measured yield is much higher, returning a standard deviation of 1.25, while the mean measured yield value is 9.88 t ha<sup>-1</sup>. The average yield therefore is overestimated by 1.11 t



ha<sup>-1</sup> in the model results, while the absolute yield is overestimated by 14.61 tons. A major restriction here is based on the fact that the model is not able to reproduce mechanically inflicted yield losses such as windbreak or the lower plant densities at the field margins that are due to machine induced stress. The spatial variability of the yield measurement therefore was not fully mapped by the model. Only the productive zone on top of the moraine ridge at the eastern middle of the field (*fig. 4.25*) seems to be traced by the model results. Nonetheless, the average yield is well reproduced, especially if the mechanically stressed areas of the crop are disregarded. In that case, the average measured yield would increase to 10.41 t ha<sup>-1</sup> and thus reduce the deviation between modelled and measured average yield to 0.58 t ha<sup>-1</sup>.

The average values indicate that the model is capable of the reproduction of grain yield in a realistic dimension, but they do not contain information concerning the spatial representation of heterogeneities within the stand. Here the direct comparison of the yield map with the modelled yield reveals that the severe underestimation of yield variability by the model results in a clouded correlation of the data. Nonetheless, the absolute deviations are limited. 43 % of the field area does not exceed a deviation of 0.5 t ha<sup>-1</sup> (*fig. 4.26, left*). Only the field regions that are exposed to mechanical stress at the field margins or along the cart track, which intersects the field at a North-West to South-East direction, show deviations above 1.5 t ha<sup>-1</sup> (*fig. 4.26, right*).

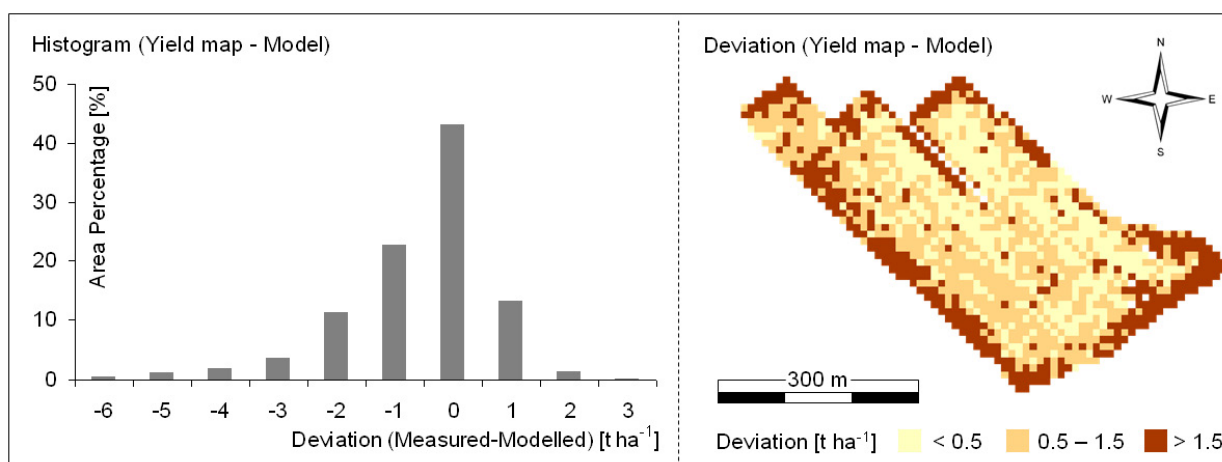


Figure 4.26: Spatial pattern of the absolute differences between measured and modelled yield (right) and histogram of the area percentages with their corresponding deviations (left) for the wheat test site "Hofanger" season 2004 (right).

These deviations are mainly due to external conditions that are not included in the model. For example, the soil map that was applied for the model runs is rather coarse (*fig. 411, upper middle*). This may be appropriate for a generalised modelling on a larger scale, but for the field scale it turns out that the local heterogeneity of soil characteristics can be traced in the plant development and therefore is represented in the measured yield map, while it cannot be regarded in the model. Also, the model does not yet contain an explicit description of the nutrient cycle and consequently is unable to map fertilization effects. Last but not least human and environmental interference is not included in the model, so that wind break, pests and

diseases but also yield loss caused by browsing game and damage due to the operation of machines cannot be reproduced. A possibility, to make information on these natural events available to the model, is the application of remote sensing techniques. Due to that reason an interface has been constructed to include remotely sensed measurements of leaf absorptivity in the course of the model runs. Since the topic of this work is the preparation of a physically based model that is designed for a mapping of possible future scenarios rather than for a best possible representation of agricultural situations, this approach is not further discussed here. Considering the spatial results of the model runs on the field scale, it becomes apparent that the lack of “natural” information leads to a reduced heterogeneity of the model results. Figure 4.27 pictures the modelled overall biomass that was fixed on all four of the field scale test sites.

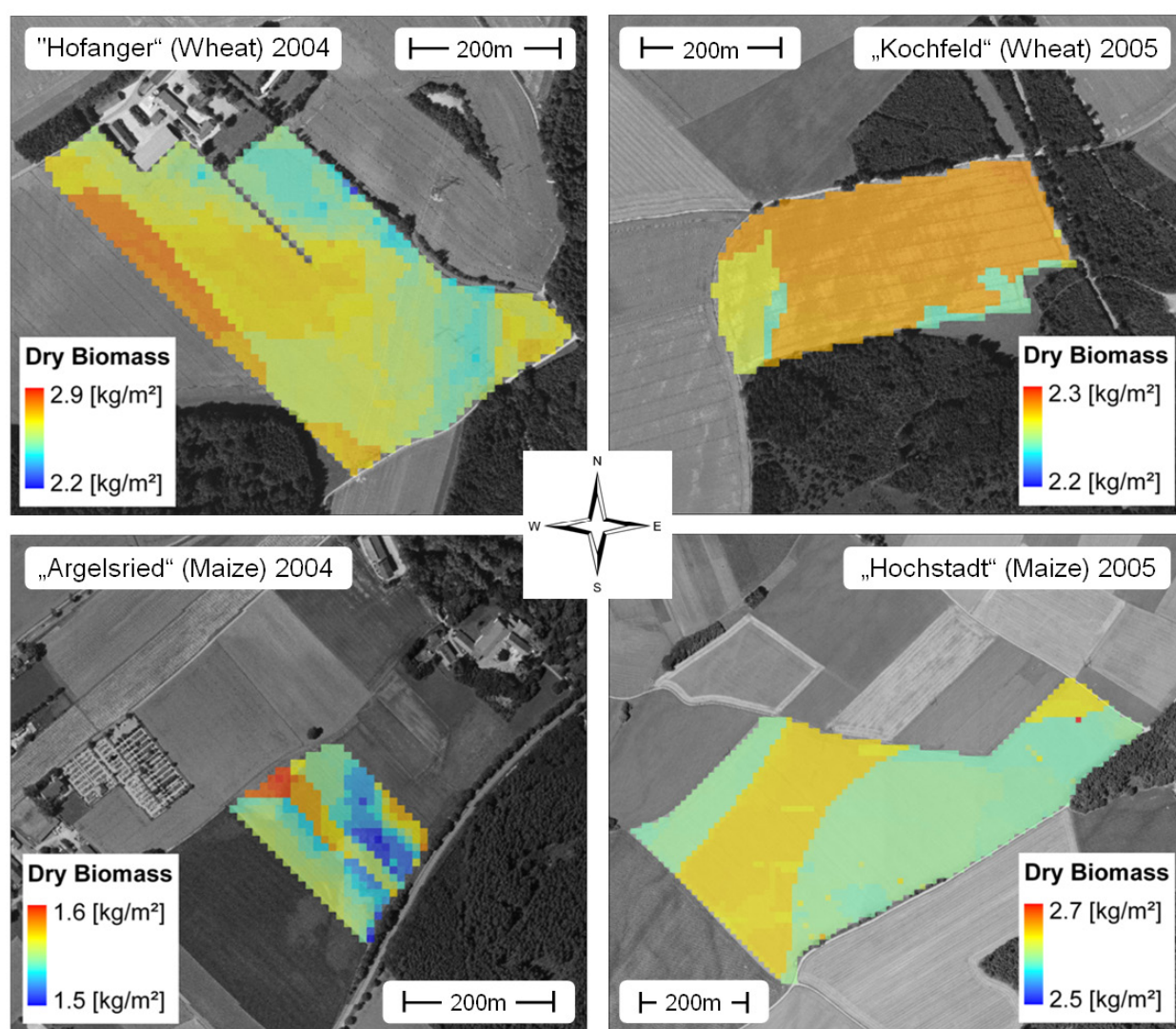


Figure 4.27: Field scale model results for the accumulated overall biomass (root, stem, grain and leaf) for the respective growth cycles of the four test sites “Hofanger” (top left), “Kochfeld” (top right), “Argelsried “ (bottom left) and “Hochstadt” (bottom right). The backdrop shows orthorectified b/w aerial photographs recorded during the aerial survey 2003 that were kindly provided by the Bavarian Land Surveying Office.

Besides the test sites “Hofanger” and “Argelsried” (fig. 4.27, left), the test fields are rather homogenous concerning their predominant soil types as well as their relief. Nonetheless, the

results show a certain spatial variability that mostly corresponds with the applied soil map. The soil particle sizes that are provided by the soil map, as well as the terrain orientation with respect to the exposure to sunlight as derived from the DEM seem to have a strong effect on the modelled productivity.

## **4.2 Meso Scale Validation**

For the testing of the PROMET model on the meso scale, model runs covering the past 46 years from 1960 to 2006 were conducted for the whole Upper Danube Basin, applying the input data described in section 3.3.4 et sequentes. Selected results from this reference time series are analysed and compared to measured and observed data in this section. The validation on the mesoscale commences with a comparative analysis of the modelled aboveground carbon fixation with measured biomass data that is derived from field campaigns. In a second step, the models capability of mapping the landscape evapotranspiration is assessed by comparing the model results with a reference model that was applied to the same time period using identical meteorological and geographical input data. Finally, the performance of the phenology model for forests is analysed in comparison with literature data.

### **4.2.1 PROMET vs. Field Measurements for Selected Proxels**

The model results, which were acquired by applying the input data set for the whole Upper Danube Basin as described in section 3.3.4, are compared to field measurements of different land use categories in this section. Field data was available from historic field campaigns that were carried out at the University of Munich in the frame of the project “Biospheric Aspects of the Hydrological Cycle – BAHC” as part of the International Geosphere Biosphere Programme – IGBP (OPPELT 2002). The measurements provide information at weekly intervals for the vegetation period of the years 1999, 2000 and 2001. In total, 11 test sites, all located in the South-West of the city of Munich, were available that covered the crops wheat, maize and oat as well as intensive and extensive grassland. A table, listing the geographic positions, names and crop types of the available test sites, which could be resorted to for the model parameterization and validation as they are displayed in figure 4.28, can be found in the appendix (A.12).

The collected data for the cereal and maize crops contains plant physiological parameters such as the dry biomass for the three aboveground plant parts stem, leaf and grain, while for the grasslands only the overall aboveground dry matter was sampled. For both, the crops and the grasslands, the overall plant height was measured at each sampling date, while the phenological stage was exclusively determined for the agricultural crop test sites. Of course, questions of scale arise, when field measurements are compared to model outputs that are the

result of a simulation on a relatively coarse resolution of 1 x 1 km. The land use categories represented in the model are very likely to differ from the actual land cover type that could be found at the exact geographic location in nature. Figure 4.28 compares the exact location of the available test sites with the corresponding proxels of the land cover map that was used for the model runs (see section 3.3.4.1.1). With exception of four winter wheat test sites in the Eastern centre of the map, none of the sampled cultivars seems to represent a landuse majority that shows in the model landuse patterns.

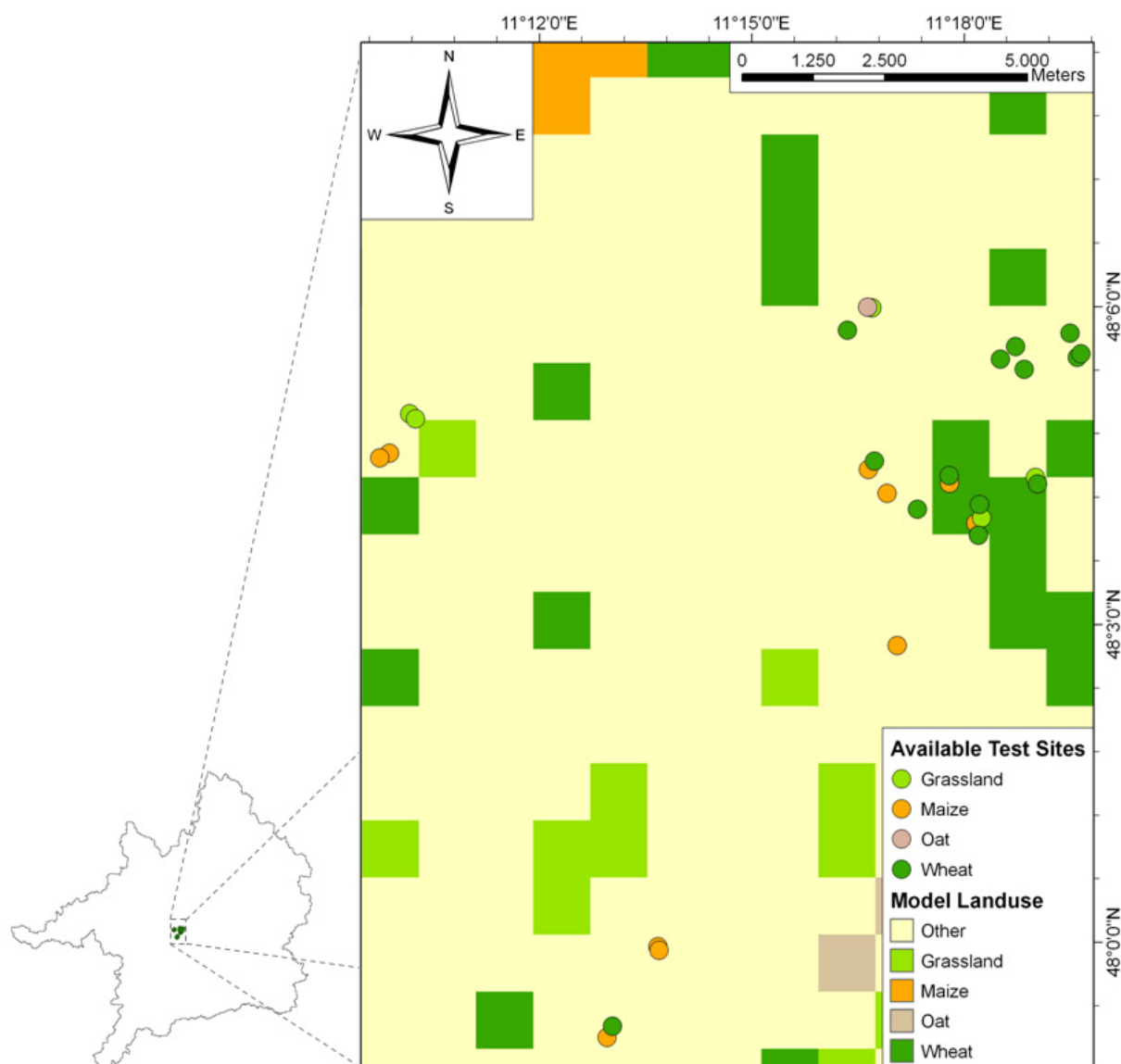


Figure 4.28: Available test sites for different landuse categories with their spatial situation compared to the 1x1 km landuse majority applied for the mesoscale model runs. Indication of the position of the general test area in the heart of the Upper Danube Basin.

The models capability of mapping the aboveground physiology of the crops wheat and maize already was described in the previous section, so that the display of the model results for the test fields on the landscape scale is skipped here and only the two mapped vegetation types that were not tested on the field scale (grassland and oat) are presented here in detail. The

testing of the grassland vegetation types is of great importance due to the high area percentage that they make up in the landuse map of the Upper Danube. The modelling of the oat crop can be interpreted as an example for agricultural spring crops.

Due to the discrepancy between the aggregated landuse map applied for the model runs on the landscape scale and the actual position of the test fields, the landuse map was adjusted in a way that it mapped the respective crops at their best possible geographic location. Table 4.04 lists the adjustments of the landuse map that were necessary for the calculation of the test results.

Table 4.04: Adjustment of the 1 x 1 km model landuse map due to the representation of the available test fields at their exact geographic position.

GIS Row	GIS Column	Original Land Cover	Adjusted Land Cover	Test Site	Seasons
231	240	Winter Wheat	Intensive Grassland	Unterbrunn	1999
228	238	Coniferous Forest	Oat	St. Gilgen	1999
229	230	Coniferous Forest	Extensive Grassland	Inning 2	1999-2001

#### 4.2.1.1 Intensive Grassland

As was mentioned in section 3.3.3.2, the modelling of intensive grassland is characterized by three cuts that can occur during a season. As exemplary test site, the meadow "Unterbrunn" was chosen, which is located in the East of the test area and provided sampling data from April to September of the season 1999. The measured aboveground dry matter clearly features the cuttings at the end of May and at the end of July as well as the late cut in September. The model almost perfectly traces the accumulation of aboveground biomass for the intensive grassland site. The period of reduced growth that follows the second cut also is well represented in the model results (fig. 4.29).

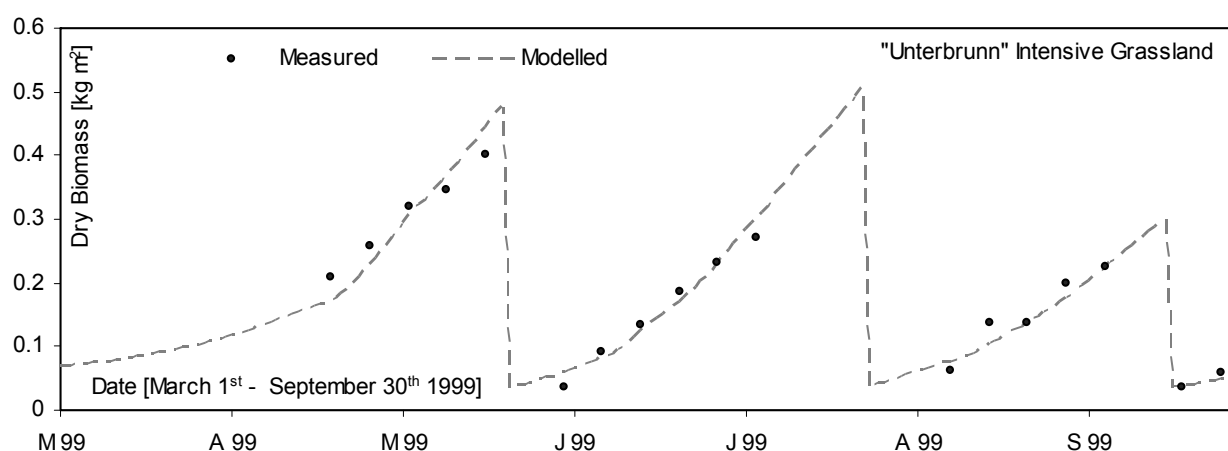


Figure 4.29: Course of modelled and measured total aboveground dry biomass of the intensive grassland test site "Unterbrunn". Results from a single proxele, modelled at a resolution of 1 x 1 km, compared to field measurements of the season 1999.

Due to the exact modelling of the cuts, which to some degree surely is coincidental in this case, the measured and the modelled aboveground biomass are highly correlated, showing a Nash-Sutcliffe coefficient of 0.96, combined with an almost ideal slope of 1.05 and a small intercept of only 0.01 kg m<sup>-2</sup> (fig. 4.30, left). The results are weaker for the canopy height, which is mostly due to a strong overestimation of height for the growth period before the first cut. For the rest of the growth season after the first cut, the plant height is far better reproduced by the model, but nonetheless the regression results are disturbed, resulting in a moderate coefficient of correlation of 0.7 with a slope of 0.87 and an intercept of 9 cm (fig. 4.30, right).

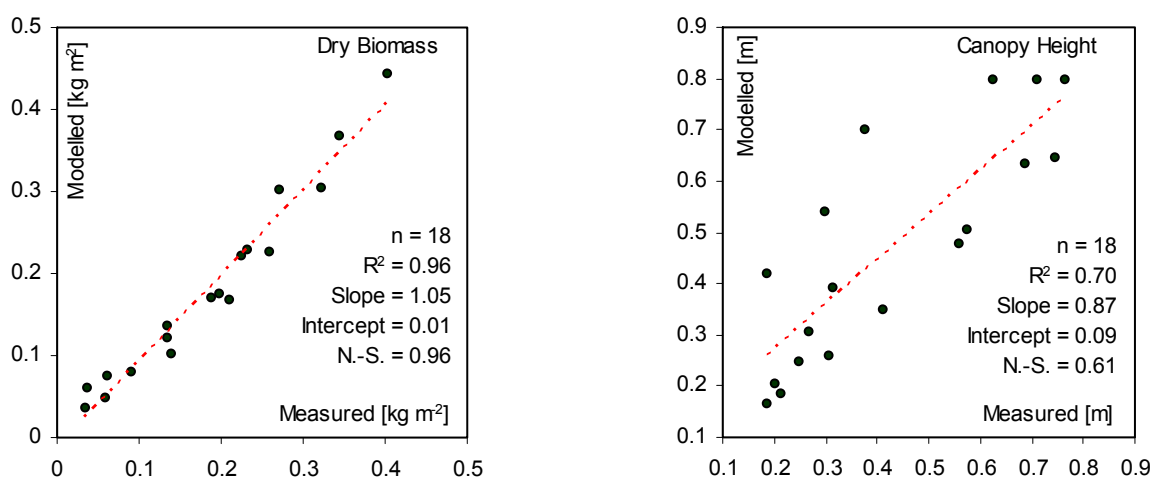


Figure 4.30: Modelled vs. measured dry biomass (left) and canopy height (right) of the intensive grassland test site “Unterbrunn” for the growth season 1999.

The results could prove that the model is able to reproduce the accumulation of biomass for grassland vegetation types on the coarse 1 x 1 km scale with a high accuracy. Also the standard mapping of the agricultural management seems to apply well to the alpine foreland, resulting in a realistic representation of the meadow cuts for intensive grassland.

#### 4.2.1.2 Extensive Grassland

For the quality assessment of the model with respect to the modelling of extensive grassland types, the test site “Inning 2” was chosen, which is located in the West of the test area and provides field data from three successive years (1999, 2000 and 2001).

Regarding figure 4.31, it becomes apparent that although the destructive field measurements show high scattering, the model clearly overestimated the biomass accumulation in spring before the first cut at least for the years 2000 and 2001, while for 1999 the spring growth was mapped quite accurately. The absolute values are rarely met by the model, but the comparison shows that the overall representation of the biomass accumulation is modelled within a likely range and with a realistic annual course. Although the dates of the meadow cuts are variable in the model as well as in the field, the standard mapping of agricultural measures may not apply to all sites equally.



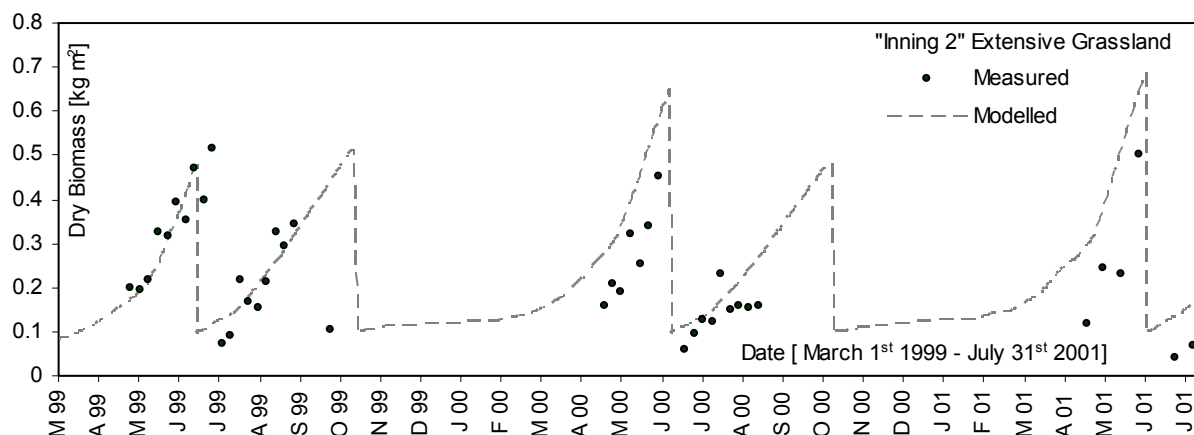


Figure 4.31: Course of modelled and measured dry biomass of the extensive grassland test site "Inning 2". Results from a single proxel, modelled at a resolution of 1 x 1 km, compared to field measurements of the seasons 1999, 2000 and 2001.

Exclusively considering the growth season 1999, which is the season that provides the highest density of field measurements, it can be recognized that the first of the two cuts that are possible on extensive grassland sites, is conducted about 10 days earlier in the model than it was observed in the field (*fig. 4.32, left*). The second cut in turn is modelled two weeks later than it was observed, severely disturbing the correlation. If these deviations, which are due to the models ignorance of the farmers decisions, are neglected, the correlation of modelled and measured biomass returns a satisfying coefficient of model efficiency of 0.79 (*fig. 4.32, right*).

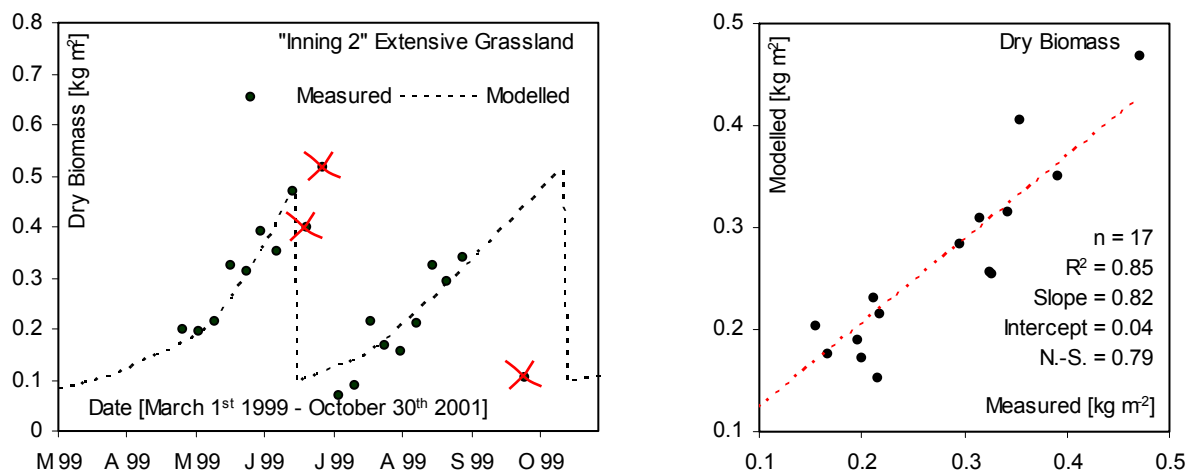


Figure 4.32: Course of modelled and measured dry biomass, indicating the errors that possibly occur due to the modelling of management measures (*left*), and modelled versus measured dry biomass of the extensive grassland test site "Inning 2" for the season 1999.

The testing of the model for extensive grassland showed that the model is able to reproduce the biomass allocation for extensive grasslands with a satisfying accuracy. Deviations are likely to occur, when the agricultural management in the model is not adequately representing the decisions that farmers are making in the field. Here again, remote sensing techniques would offer a possibility to increase the models certainty with respect to agricultural management measures as could already be shown by SCHNEIDER (1999).

### 4.2.1.3 Spring Crops (Oat)

The previous sections analysed the models behaviour for the growth simulation of winter C<sub>3</sub> crops (wheat), summer C<sub>4</sub> crops (maize) and perennial C<sub>3</sub> grasslands. A fourth agricultural group is formed by C<sub>3</sub> spring crops, which are exemplarily represented here by the oat test site “St. Gilgen”.

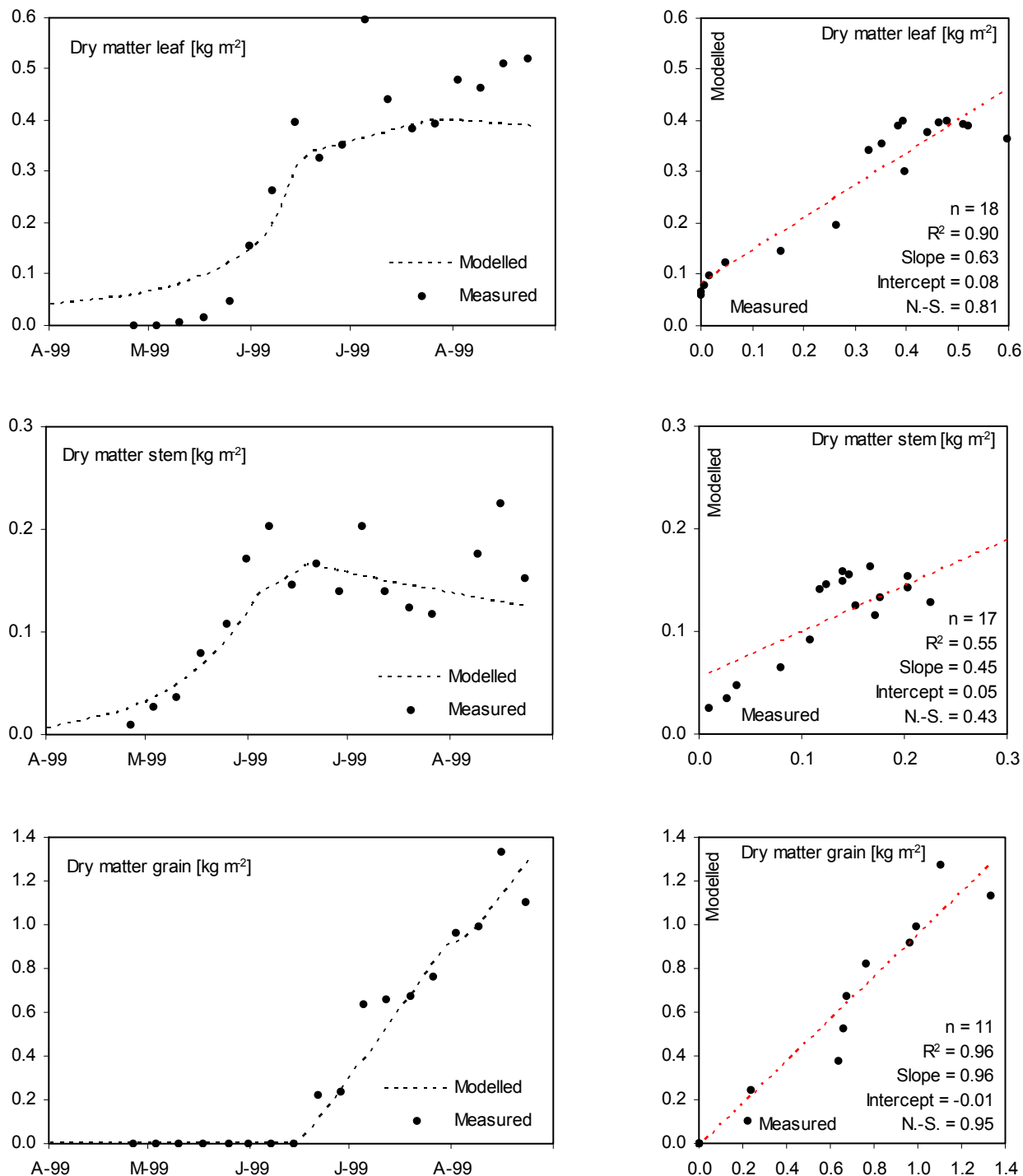


Figure 4.33: Modelled vs. measured aboveground dry biomass for the sampling period of the oat test site “St. Gilgen” from April 1<sup>st</sup> to August 31<sup>st</sup> 1999. Course of development (left) and correlation including coefficients of determination (right) discerned into the plant parts leaf (top), stem (middle) and grain (bottom).



The important growth determining management dates for oat crops in the alpine foreland are the 20<sup>th</sup> of March for the sowing and the 15<sup>th</sup> of August for the harvest (SCHWERTMANN ET AL. 1987). Due to a relatively wet August of the year 1999, the test site “St. Gilgen” was not harvested until the 25<sup>th</sup> of August, when the stand had developed to a stage of full ripeness.

Figure 4.33 pictures the model results for the biomass allocation to the aboveground plant parts in comparison with measured data for the growth season from April to August 1999. The model results again are derived from a single 1 x 1 km proxel and therefore do not contain a range of variability. The modelled biomasses for the spring crop show similar characteristics as those achieved for the winter crops. Again, the scatter in the field measurements is high for the leaf and for the stem biomass, while the grain biomass shows a somewhat lesser variability. The correlation of measured and modelled dry biomass thus is highest for the grains with a coefficient of model efficiency of 0.95 (*fig. 4.33, bottom right*) and weakest for the stem biomass, resulting in a moderate coefficient of correlation of 0.55 (*fig. 4.33, middle right*). The course of the measured leaf development shows a constant increase of leaf mass until harvest, while the model simulates a slight decrease of the leaf mass that accompanies the ripening (*fig. 4.33, top left*). During the early growth stages, the leaf mass again is overrated by the model, due to the reasons discussed in section 4.1.6.4, while the biomass increase of the grains after the flowering (stage 60) is adequately met by the model. In total, the correlation of measured and modelled biomass accumulation for the spring crop on the mesoscale shows weaker results than those that could be achieved for the winter crops on the field scale. This may be due to the higher scatter of the destructive field measurements for the oat crop, taking into account that the differentiation of the plant parts in the laboratory is somewhat more difficult for the filigree oat ears than it is for the wheat plants.

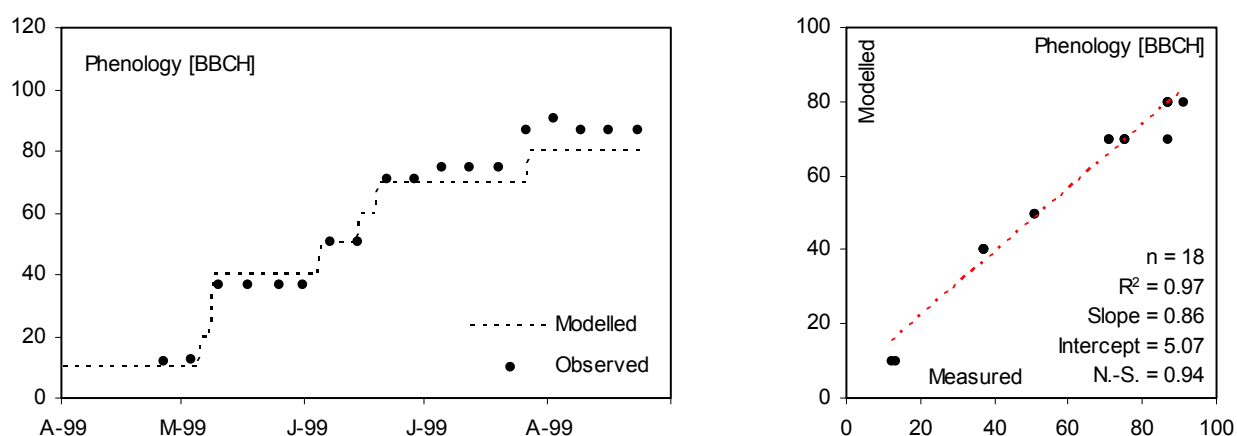


Figure 4.34: Modelled vs. observed plant phenology. Course of development (left) and correlation (right) for the sampling period of the oat test site “St. Gilgen” from April 1<sup>st</sup> to August 31<sup>st</sup> 1999.

According to GEISLER (1980), oat crops are harvested shortly before they have reached a state of dead ripeness in order to avoid the loss of grains through drop-out during the harvesting process. The phenological phase 80 (Maturity) for the oat site therefore is shorter compared to

the previously discussed crops (*fig. 4.34, left*). Nonetheless, the progress of the phenological stages of the spring crop, which naturally develops devoid of a winterly chill phase, is well traced by the model.

The height of the canopy, parallel to the leaf biomass, is overrated during the growth stage of leaf development, but is slightly underestimated for the summer months (*fig. 4.35, left*). During the stage of maturity, the measured canopy height decreases, while the model misleadingly still simulates a slight increase of the canopy height. Besides these deviations, the annual course seems to be adequately mapped.

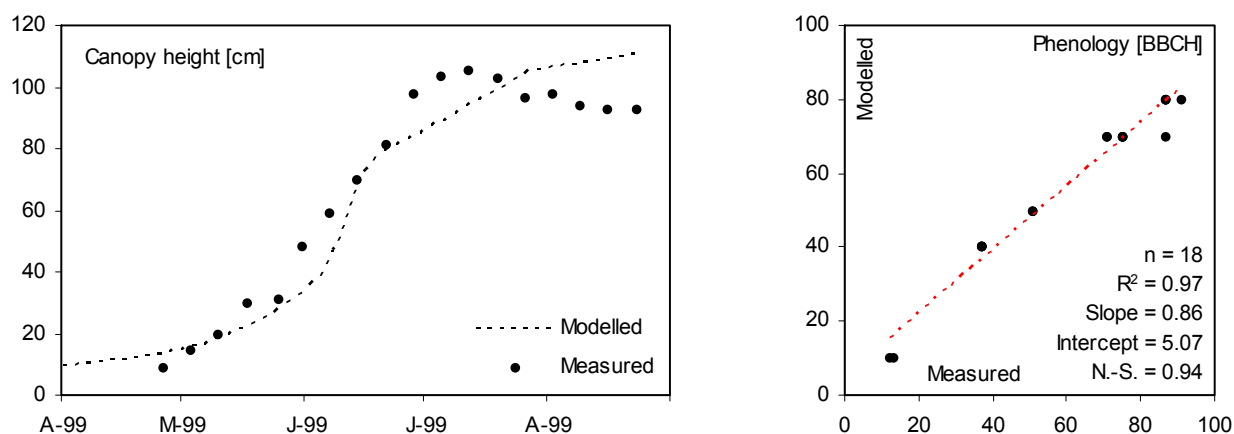


Figure 4.35: Modelled vs. observed overall canopy height. Course of development (left) and correlation (right) for the sampling period of the oat test site "St. Gilgen" from April 1<sup>st</sup> to August 31<sup>st</sup> 1999.

The validation results for the modelling of the exemplary spring crop on the mesoscale turned out to be somewhat weaker than those that could be achieved for the other agricultural crop types on the field scale. This, besides other reasons, surely is also due to the discrepancy that is likely to exist between measurements from a single field and model results derived from a proxel with a spatial extent of 1 x 1 km. Nonetheless, the model can be considered to be capable of a realistic representation of plant physiological parameters also for spring crops.

#### 4.2.2 Relating the Coupled Approach to a Reference Model

In the previous section, measured data was applied to the assessment of modelled parameters. Unfortunately, not all parameters that are modelled and are playing an important role for the simulation of natural surface processes can easily be measured. The variable that surely is most difficult to measure on a larger scale is the evapotranspiration. However, the evapotranspiration can secondarily be assessed on the catchment scale via the runoff that is measured at the gauges of the respective river basins, applying the general storage equation (see section 3.3.2.2, eq. 3.18). Due to the stable relation of the inflows and outflows of the water balance components, a model that is driven with measured precipitation data and already has

been referenced with measured runoff data is likely to simulate realistic rates of evapotranspiration as well. Therefore, the referencing of a model through a comparison of the model results with outputs of a second control model that applies a different approach, but uses the same input data and already is known to produce good results, is a convenient and valid method for the quality assessment of variables that would be hard to measure in the field.

#### 4.2.2.1 The Penman-Monteith-PROMET

PROMET in its current version offers the possibility to choose two different calculation paths for the modelling of evapotranspiration processes (MAUSER AND BACH 2008). If the explicit biological model, which is the main topic of this work and has been described in detail in section 3, is switched off, PROMET is perfectly able to calculate the landsurface water balance with an alternative approach. The explicit canopy model is reduced to a simplified vegetation routine, applying a productivity of transpiration approach following BALDOCCHI ET AL. (1987). In this approach, the leaf area, the plant height and the root depth are modelled as static functions of the DOY. The actual landsurface evapotranspiration ( $ET_a$ ) is calculated applying the Penman-Monteith-Equation (eq. 4.03, PENMAN 1956, MONTEITH 1965), where  $L^*$  is the specific heat of evaporation per mm,  $s$  is the gradient of the vapour pressure curve,  $R_n$  is the radiation balance,  $G$  is the ground heat flux,  $p$  is the air density,  $c_p$  is the specific heat of air,  $r_a$  is the aerodynamic resistance,  $e_s(T_a)-e$  is the saturation deficit in dependence of the air temperature ( $T_a$ ) and the saturation pressure ( $e_s$ ),  $\gamma$  is the psychrometric constant and  $r_s$  finally is the stomatal resistance.

$$ET_a = \frac{1}{L^*} \cdot \frac{s \cdot (R_n - G) + \frac{p \cdot c_p}{r_a} \cdot (e_s(T_a) - e)}{s + \gamma \cdot \left(1 + \frac{r_s}{r_a}\right)} \quad (\text{Eq. 4.03})$$

PROMET applied with the Penman-Monteith approach has proven its reliability in a number of publications for various watersheds of different sizes (i.e. MAUSER AND STRASSER 1997, MAUSER AND SCHÄDLICH 1998, STRASSER 1998, LUDWIG 2000) and therefore can legitimately be consulted as a reference model for the biological model version.

#### 4.2.2.2 PROMET\_Biological vs. PROMET\_Penman-Monteith

A comparative analysis of the modelled water balance components of the Penman-Monteith model on one hand and the biological model on the other was conducted by setting both models up to a reference model run. Thereby, the same geographic data base, the same meteorological input data and the same computer was applied to both models. The reference model run was performed for the years of 1960 to 2006 applying the input data set for the Upper Danube

catchment as described in section 3.3.4. The results for the first model year (1960) were neglected in order to allow both models to adapt to the meteorological situation and to settle their soil water balances. As the models are compared in order to assess the quality of the biological model with respect to the major water household components, the hydrologic year, ranging from the 1<sup>st</sup> of November to the 31<sup>st</sup> of October, was applied as the temporal base unit for the analysis.

#### 4.2.2.2.1 Selected Reference Proxels

The results for the evapotranspiration components of the modelled reference data were extracted for a set of 22 proxels, each representing one of the vegetation landuse categories that are accounted for in the input data set. For the selection of the random reference proxels, extreme locations like high elevations etc. were avoided in order to create a data survey that represents more or less average conditions of the Upper Danube area. A list of the reference proxels chosen for this survey is available in the appendix (A.13). Since only the biological routines are to be tested here, the inanimate landuse categories were neglected for this analysis. Due to the differences of the description of the vegetation growth activity of the two model approaches, the results for the evapotranspiration components partly feature strong deviations (*fig. 4.36*).

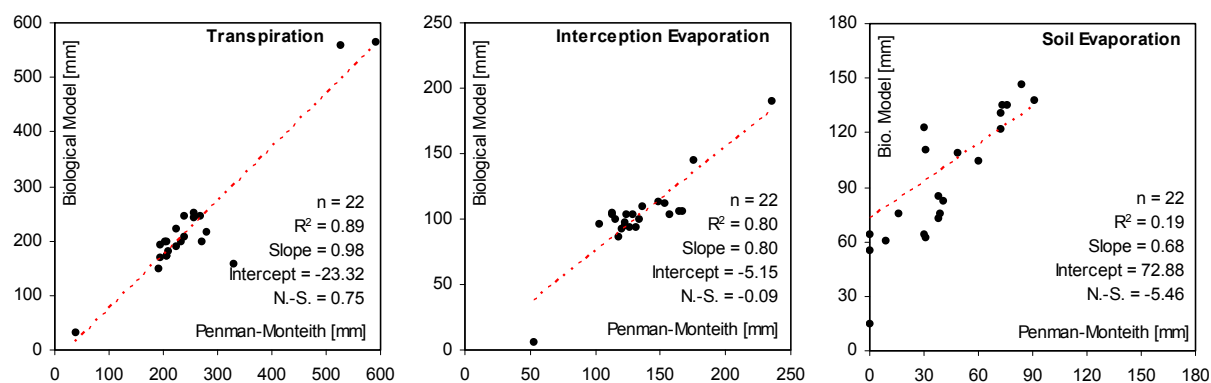


Figure 4.36: Modelled annual evapotranspiration of the hydrological year 1999, discerned into transpiration (left), interception evaporation (middle) and soil evaporation (right) for 22 different vegetation landuse proxels. Correlation between modelled results applying the Penman-Monteith approach and the biological model.

The best correlation between both models exists for the transpiration, where small deviations are more or less balanced between both models. Keeping the direct relation of the aboveground plant physiology to the interception capacity of the landsurface in mind (see section 3.3.2.2), the deviations that occur between the different model approaches for the interception evaporation are not surprising, since both models follow entirely different vegetation modelling strategies. For all landuse categories, the biological model reports somewhat lower sums of interception evaporation than the Penman-Monteith model. Strong deviations, which also are due to the different modelling strategies, were mapped for the soil evaporation. While the Penman-

Monteith approach only simulates soil evaporation until the modelled vegetation has developed to a full canopy closure, the biological model is calculating soil evaporation applying an explicit soil temperature model, which is driven by the energy that is transmitted even through the closed canopy above (MUERTH 2008). The biological model consequently calculates soil evaporation for the whole course of the year. Due to that discrepancy, the biological model returned much higher rates of soil evaporation than the Penman-Monteith approach. The results of the comparative model runs for the hydrological year 1999 are summarized in table 4.05.

Table 4.05: Annual sums of evapotranspiration components [mm] for the hydrological year 1999, modelled with the Penman-Monteith approach and deviations of the results achieved with the biological model.

Landuse	Precip.	Penman-Monteith Model [mm]				Deviation of the Biological Model			
		Trans.	Evap.	Interc.	Sum	Trans.	Evap.	Interc.	Sum
Coniferous Forest	1124	525	0	235	760	+33	+ 15	- 45	+ 3.41
Extensive Grassland	860	279	31	115	425	- 63	+ 80	- 14	+ 2.44
Intensive Grassland	786	270	30	123	424	- 70	+ 93	- 20	+ 2.77
Deciduous Forest	728	593	0	175	768	- 27	+ 64	- 30	+ 6.46
Winter Wheat	625	224	72	123	419	- 33	+ 58	- 25	- 0.42
Silage	946	205	38	132	375	- 7	+ 47	- 37	+ 2.66
Winter Barley	811	205	74	123	402	- 31	+ 62	- 28	+ 2.61
Natural Grassland	723	237	9	166	412	+ 8	+ 52	- 60	+ 0.18
Forage	884	193	30	112	335	- 25	+ 34	- 9	+ 0.71
Summer Barley	895	207	31	103	341	- 25	+ 31	- 7	- 0.71
Wetland	732	330	0	157	487	- 172	+ 229	- 54	+ 3.88
Oleaginous	812	195	38	148	381	- 1	+ 35	- 34	- 0.15
Setaside	739	255	16	164	435	- 5	+ 60	- 58	- 2.72
Alpine	1494	38	0	53	91	- 7	+ 55	- 47	+ 0.83
Oat	806	205	76	137	417	- 31	+ 60	- 26	+ 2.34
Maize	810	239	84	126	450	- 33	+ 62	- 33	- 3.16
Sugar	799	223	41	153	417	- 1	+ 42	- 41	- 0.61
Potato	736	257	60	117	434	- 15	+ 45	- 31	- 1.45
Rye	733	231	48	120	400	- 33	+ 61	- 27	+ 0.26
Hop	834	267	91	129	487	- 23	+ 47	- 26	- 0.96
Summer Wheat	858	190	72	113	375	- 40	+ 50	- 8	+ 2.65
Legumes	839	203	39	133	375	- 3	+ 37	- 34	+ 0.72

Although the evapotranspiration components partly show strong deviations, the overall annual sum of evapotranspiration is reproduced by both models at nearly the same level with only minor deviations (*table 4.05, right*). This may be due to the fact that both models were provided with the same supply of energy and water, since identical meteorological input data was used for both models. The deviations between both models are the combined result of the different algorithms that are applied for the evaporation components, of the differences of the modelled agricultural management measures and of the differences of the parameterization of both models. The landuse category “wetland” may serve as a somewhat extreme example. Table 4.05 shows that for this land cover extremely high deviations exist between the evapotranspiration components of both models, although they nearly evaporate the same overall sum during the hydrological year. While the annual evapotranspiration in the Penman-

Monteith model mainly consists of transpiration, the biological model predominantly mapped soil evaporation. The example shows that both models may be behaving different for the discerned evapotranspiration components, but both affect the annual water balance in a comparable dimension.

Despite the good match of the annual sums, the seasonal course of both models may noticeably differ. These variations especially increase during phases of active growth, when the differences of the two methods concerning the description of the vegetation behaviour are more determining. The figures 4.37 - 39 are showing the course of daily evapotranspiration rates for a single exemplary proxel, tilled with a maize silage crop as it is common for the Upper Danube. The maize site in the Penman-Monteith model already returns transpiration rates from the 1<sup>st</sup> of March on, while the biological model does not start the active growth before the 25<sup>th</sup> of April. The first reason for differences between the model concepts therefore results from differences of the description of the agricultural management measures. For the first parallel month of active growth, the curves fit closely, but during June and July the Penman-Monteith approach produces peaks that clearly exceed the transpiration rates that are simulated by the biological model (*fig. 4.37*).

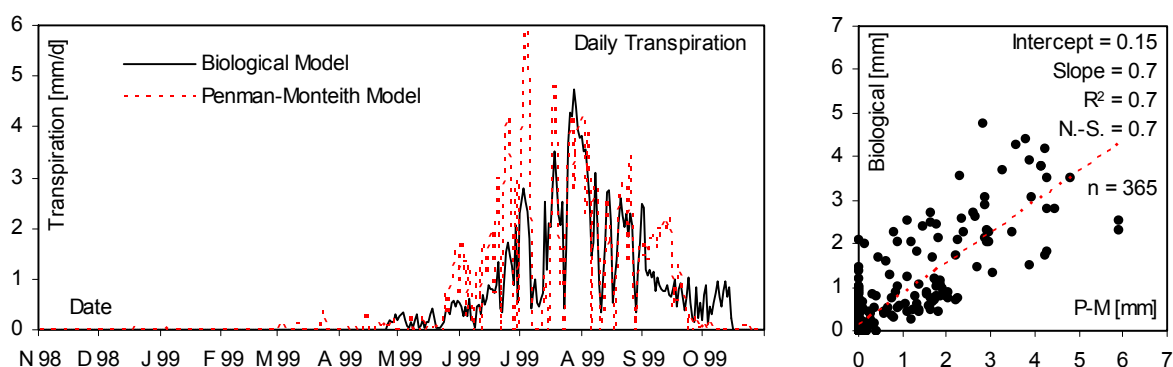


Figure 4.37: Daily rates of transpiration of a silage proxel, calculated via the biological and the Penman-Monteith model for the hydrological year 1999. Annual course (left) and correlation of both models (right).

The P.-M. model also returned days with absolute zero transpiration throughout the summer, which were not mapped by the biological model. This is due to the biological model returning small values of transpiration even when it is raining, while the P.-M. model is not constructed to produce transpiration in that case. However, the overall correlation of the daily rates of transpiration of both models is reasonably good, returning a Nash-Sutcliffe coefficient of model efficiency of 0.7 (*fig. 4.37, right*).

The interception evaporation in both models is determined by the provision of rainfall and radiation on one hand and the amount of water that can possibly be intercepted by the canopy on the other. This interception storage capacity greatly depends on the modelled plant physiological parameters, especially on the leaf area. Since the P.-M. model is restricted to a static description of the leaf area development, the interception storage capacity is less variable

than it is returned by the biological model (*fig. 4.38, left*). This results in a distortion of the correlation at times, when the full storage capacity of the canopy is utilized and evaporates in the course of a single day (*fig. 4.38, right*). In total, the biological model tends to underestimate the storage capacity of the canopy, compared to the Penman-Monteith approach.

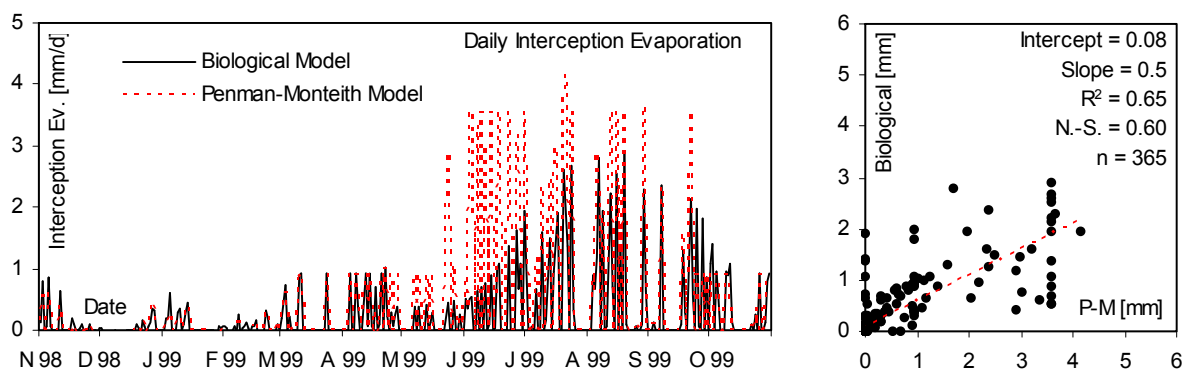


Figure 4.38: Daily rates of interception evaporation of a silage proxel, calculated via the biological and the Penman-Monteith model for the hydrological year 1999. Annual course (*left*) and correlation of both models (*right*).

As long as there is no vegetation cover modelled, which for the maize silage crop is the case from autumn to early spring, both models return almost identical rates of soil evaporation, with exception of a peak in October, which is due to differences of the available soil water storage that remains after the harvest. As soon as the canopy closure is complete, the P.-M. model ceases to produce soil evaporation, while the biological model still returns evaporation rates. Apart from these systematic differences, the correlation would be rather good (*fig. 4.39, right*).

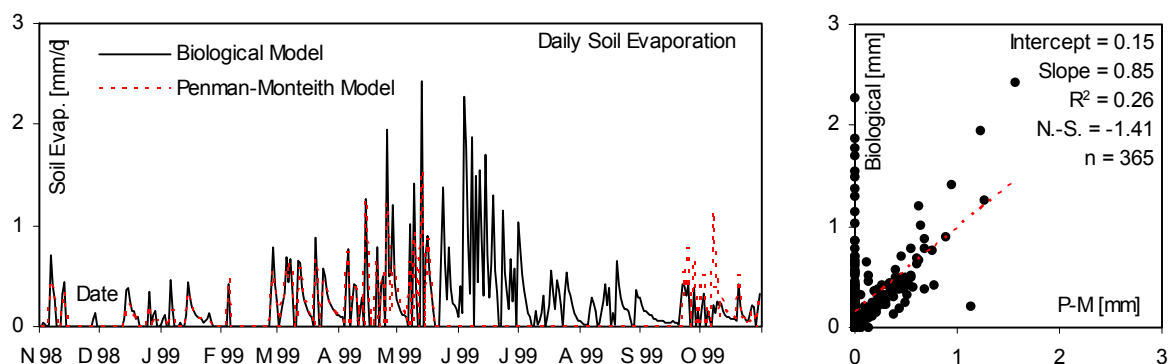


Figure 4.39: Daily rates of soil evaporation of a silage proxel, calculated via the biological and the Penman-Monteith model for the hydrological year 1999. Annual course (*left*) and correlation of both models (*right*).

Although the deviations between the two model types are noticeable, both models returned nearly identical annual sums of evapotranspiration for the 22 investigated vegetation land cover types. While the biological model on average returned less transpiration and less interception evaporation than the Penman-Monteith approach, the surplus of soil evaporation compensates for this effect, so that the dimension of the annual balance again is simulated at the same level by both models.

#### 4.2.2.2.2 Spatial Statistics

In the previous section, the two models were compared concerning the annual sums as well as the annual course of their respectively modelled evapotranspiration components. The models turned out to correlate reasonably well concerning the variability, which results from the divergent evapotranspiration behaviour of the different land use categories. However, each landuse category is represented in the data set at a characteristic spatial distribution. To assess the ability of the biological model concerning the reproduction of the spatial variability as well, the spatial results of the reference model run were analyzed for both model types.

Figure 4.40 indicates that during the long-term reference period, the biological model generally returned slightly less evapotranspiration than the Penman-Monteith approach, while at the same time it featured an equally higher standard deviation. For some of the peaks, the models show a nearly parallel course (e.g. 1965-1968), while others are completely missed by the biological model (e.g. 1963). Nonetheless, both model results correlate reasonably well, although the overall average evapotranspiration for both models does not exceed an interannual variation of 70 mm (fig. 4.40, right).

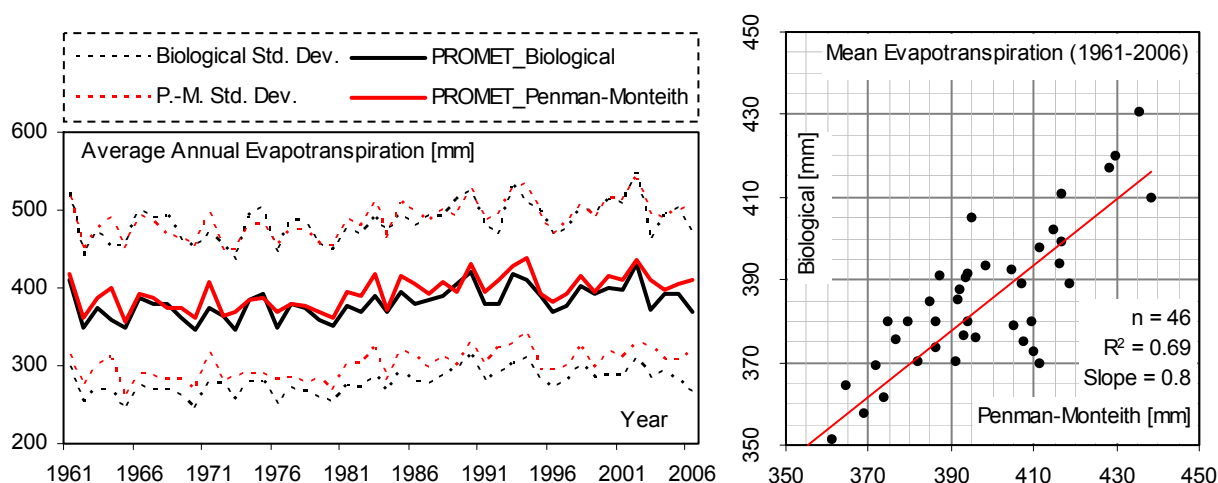


Figure 4.40: Modelled evapotranspiration for a 46-year period (1961-2006), averaged for the Upper Danube catchment area. Annual course (left) and correlation (right) of the evapotranspiration modelled by the PROMET\_Biological model and the PROMET\_Penman-Monteith model.

In order to include the mapping of the spatial patterns into the comparison, the averaged model results for the reference period were correlated for each proxel and discerned into the 27 different landuse categories that are accounted for in the input data set. Table 4.06 lists the results of this comparison, while a full overview is given in the appendix (A.14).

The correlation between both models is high for all of the different land covers. The vegetation landuse categories are characterized by slopes that slightly fall below the ideal value of one, visualizing the generally slightly lower evapotranspiration that is returned by the biological model.



Table 4.06: Spatial correlation of the annual average evapotranspiration [mm] of both, the PROMET-Penman-Monteith and the PROMET\_Biological model. Compared model results for the hydrological years of 1961 to 2006, calculated for the Upper Danube Basin.

Landuse Type	ET Penman-Monteith	ET Biological	N	N.-S.	Slope	R <sup>2</sup>
Coniferous Forest	554.99	552.93	25012	0.92	1.00	0.94
Extensive Grassland	309.35	260.87	9548	0.57	0.84	0.84
Intensive Grassland	368.85	303.31	8010	-3.61	0.83	0.61
Deciduous Forest	505.04	490.15	5681	0.92	0.97	0.95
Winter Wheat	352.70	360.52	5179	0.69	1.02	0.86
Rock	046.34	059.91	3301	0.58	1.23	0.88
Silage	379.03	326.41	2790	-1.28	0.77	0.85
Residential	063.77	063.89	2624	0.97	1.00	0.96
Winter Barley	351.18	334.34	2120	0.56	0.95	0.85
Natural Grassland	217.97	197.04	1270	0.87	0.94	0.91
Forage	303.32	298.59	1228	0.84	0.99	0.90
Summer Barley	289.23	298.89	1163	0.79	1.03	0.90
Wetland	299.34	287.87	1127	0.53	0.93	0.55
Oleaginous	369.23	322.51	989	-0.60	0.87	0.71
Set Aside	418.55	391.83	920	-0.52	0.94	0.71
Alpine Grassland	171.66	118.32	854	-1.40	0.69	0.62
Oat	337.07	293.40	770	-1.04	0.87	0.75
Maize	385.24	351.09	749	-1.03	0.91	0.74
Water	622.15	632.14	573	0.94	1.02	0.99
Sugar	390.80	399.95	434	0.43	1.02	0.79
Industrial	062.28	062.20	411	1.00	1.00	0.99
Potato	380.27	415.17	328	-0.12	1.09	0.93
Rye	332.58	311.46	293	0.68	0.94	0.80
Hop	399.87	382.12	168	0.19	0.96	0.81
Summer Wheat	316.22	296.74	85	0.38	0.94	0.83
Legumes	368.56	365.07	77	0.85	0.99	0.89
Glacier	029.92	034.91	10	-1.84	1.40	0.71

In addition to the good correlation, both models returned comparable values for the average evapotranspiration sum for the different land covers (*fig. 4.41, left*).

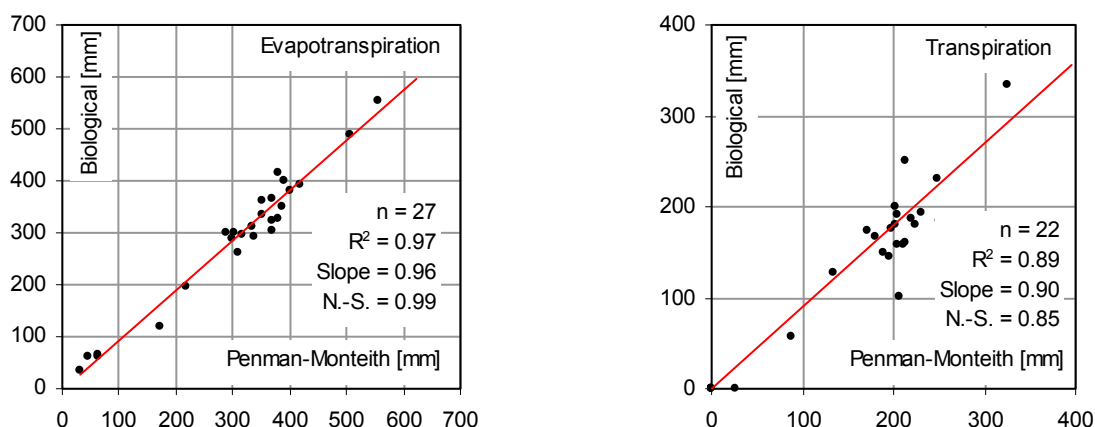


Figure 4.41: Correlation of the long-term (1961-2006) average evapotranspiration (*left*) and transpiration (*right*) modelled by the PROMET\_Biological model and the PROMET\_Penman-Monteith model.

As already could be concluded for the correlation of single proxels in the previous section, the correlation for the transpiration alone is not as good as for the plain evapotranspiration (*fig.*

4.41, right). This is mostly due to the differences of the description of the agricultural management in both models. While the soil evaporation is able to balance those differences in the case of the evapotranspiration, the transpiration alone fully features these deviations. Figure 4.42 shows a map of relative deviation between the modelled long-term evapotranspiration sums of both models. While the Northern half of the Upper Danube Basin features deviations that mostly fall below 5 %, the Southern part shows slightly higher deviations of mostly 10 – 20 %. Please note that in figure 4.42 the extremely high deviations above 40 % (pictured in red) are limited to highly elevated terrain, where the absolute evapotranspiration sums are very low. At those heights, already minimal differences of < 10 mm can result in high percental values.

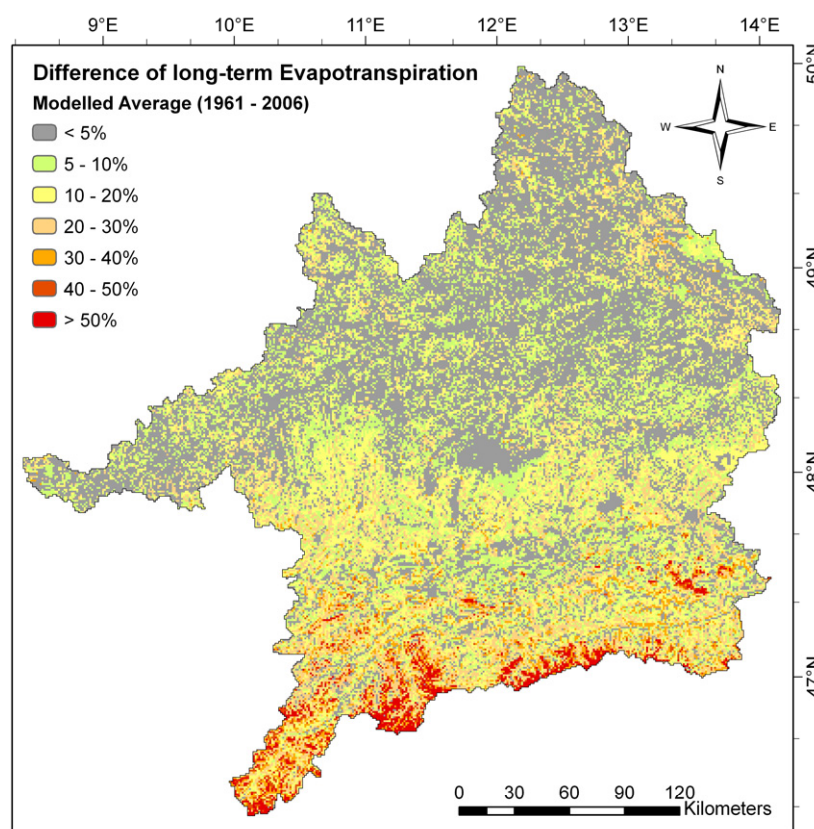


Figure 4.42: Map of deviation between the long-term (1961-2006) average evapotranspiration modelled by the PROMET\_Biological model and the PROMET\_Penman-Monteith model.

Overall, the spatial patterns of both models are matching, but small deviations exist, that are primarily due to the entirely different description of the vegetation behaviour of both models. In order to assess the consequences of these deviations on subsequent model parameters, the results of both models were also compared with respect to the modelled runoff. For the modelling of the runoff, the surplus of water that is generated on each proxel according to the general storage equation, is converted to a flux of runoff from each proxel and again is routed through a network of rivers that finally drains the catchment at the basin gauge (MAUSER AND BACH 2008). The basin gauge of the Upper Danube is represented by the gauge Achleiten as described in section 2.1. For the 46 year reference time series, both models produced very

similar rates of runoff at the main gauge, resulting in a very high correlation of the two modelling approaches (fig. 4.43, left).

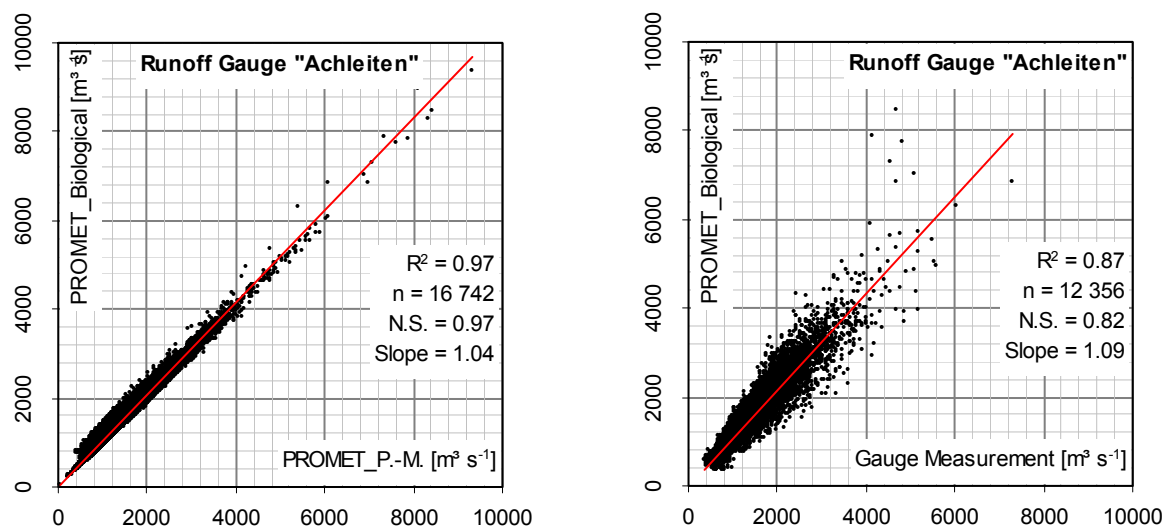


Figure 4.43: Correlation of modelled runoff for the gauge "Achleiten" by the PROMET\_Biological model and the PROMET\_Penman-Monteith model (1961-2006, left) and correlation of modelled and measured runoff for the main gauge of the Upper Danube catchment (1970-2003, right).

Both models show high correlations with the measured runoff, featuring Nash-Sutcliffe efficiency coefficients of 0.82 and 0.86 respectively. The high correlation of the Penman-Monteith approach with the measured runoff could already be shown by MAUSER AND BACH (2008). Small deviations mostly are due to an overrating of the average discharge during snowmelt periods. Floodwater and low flow peaks are precisely mapped by both model approaches. In relation to the gauge measurements, the biological model returned a similar slope of the regression line in combination with almost identical coefficients of correlation and of model efficiency respectively, compared to those that were achieved applying the Penman-Monteith approach (see tab. 4.07).

Tab. 4.07: Results for the correlation of modelled and measured runoff (1970-2003) at the main gauge of the Upper Danube catchment for the two different model approaches.

	Biological vs. Penman-Monteith	Penman-Monteith vs. Measured Runoff	Biological vs. Measured Runoff
<b>T =</b>	1961-2006	1970-2003	1970-2003
<b>N =</b>	16 742	12 356	12 356
<b>R<sup>2</sup> =</b>	0.97	0.87	0.87
<b>Slope =</b>	1.04	1.05	1.09
<b>Nash-Sutcliffe =</b>	0.97	0.86	0.82

Compared to the reference model, the biological model approach could prove to produce reliable results concerning the absolute sums as well as the spatial and temporal variability of the evapotranspiration components for the catchment area. Although the biological model generally returned slightly lower rates of evapotranspiration, the comparison with measured runoff data could reveal that the water balance seems not to be negatively affected.

### 4.2.3 Consulting External Data

For the assessment of model parameters that are not mapped by own sampling campaigns measured data may be available through publications of neighbour sciences. In this case, the ecological branch of forestry was able to contribute detailed studies concerning the phenological behaviour of trees in Southern Europe (MENZEL 1997), which allowed for a testing of the phenology submodel of the forest vegetation types.

The main phenological phases of the forested areas are of great importance to the annual water balance, as the date of the incidence of the major growth stages determines the absolute temporal range where the woodlands are able to contribute to the overall evapotranspiration of the landsurface. During the reference model run, which was calculated for the Upper Danube from 1960 to 2006, the model was reconstructed to export the date of the first incidence of the major growth stages of deciduous and coniferous woodland. Thereby, a 46-year data set of the spatially distributed incidence of the growth stages “Leaf Emergence” and “Defoliation” for deciduous trees as well as of the incidence of “Mayshoot” in the case of coniferous trees (see section 3.3.3.6.1.3) was collected. Since the Upper Danube catchment comprises a high variety of altitudes, the results were analysed for three discerned altitudinal vegetation zones as there are the so called “colline” belt, ranging from 300 to 600 m above the sea level, the “montane” level from 600 to 1500 m a.s.l. and the “alpine” altitudinal zone exceeding that mark (*fig. 4.44*).

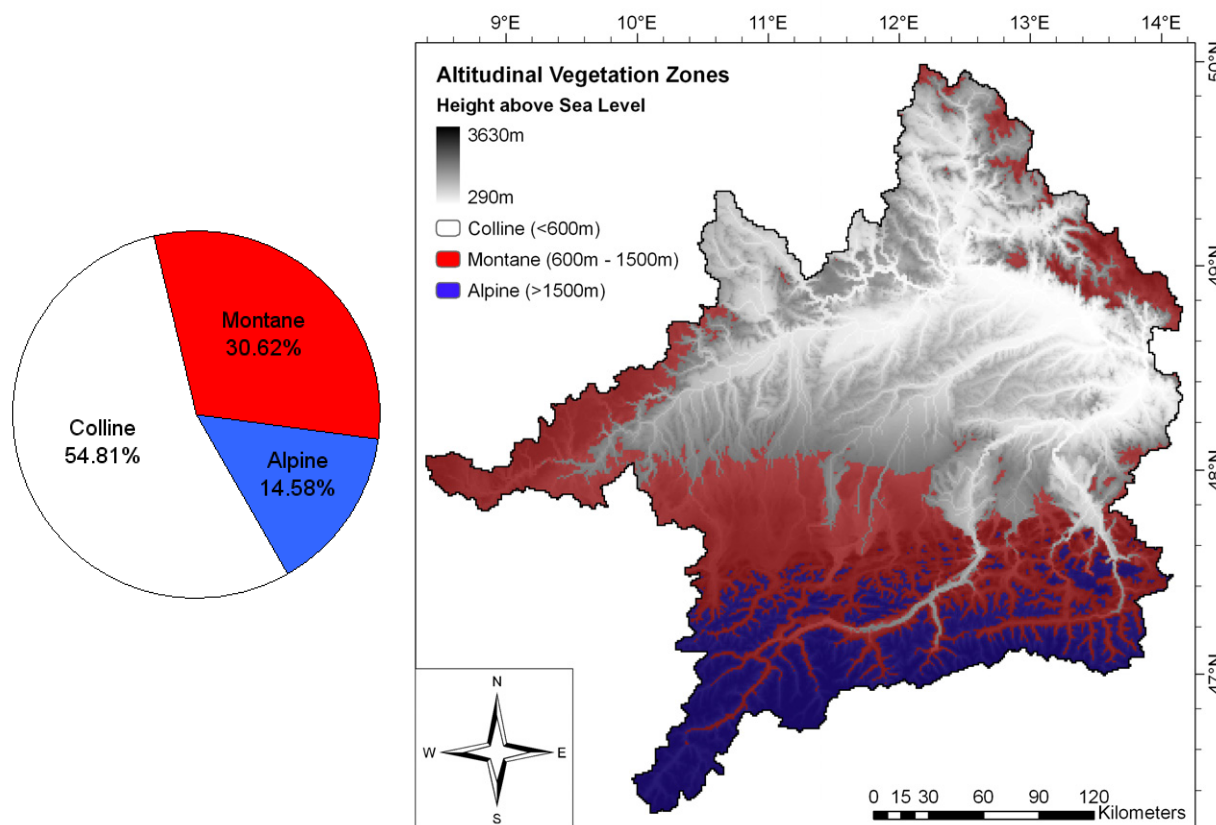


Figure 4.44: Terrain elevation within the Upper Danube Basin indicating the spatial distribution and the percentage of the altitudinal vegetation belts.

#### 4.2.3.1 Deciduous Forest Phenology

As described in section 3.3.3.6.1.3, the simulation of the forest phenology is based on the analysis of average and extreme air temperatures. Leaf emergence in spring is mainly initiated by warm weather, whereas the autumnal defoliation is dependent on the occurrence of frosty days. Increasing average air temperatures will cause the leaves to emerge earlier in spring and will delay their fall in autumn, while the contrary would be the case for a decrease of the average air temperature. When the dates of incidence of these processes are averaged for the whole Upper Danube Basin and are displayed for the 46 year time series, a data set is created that shows patterns of natural variability (*fig. 4.45* and *fig. 4.46, left*).

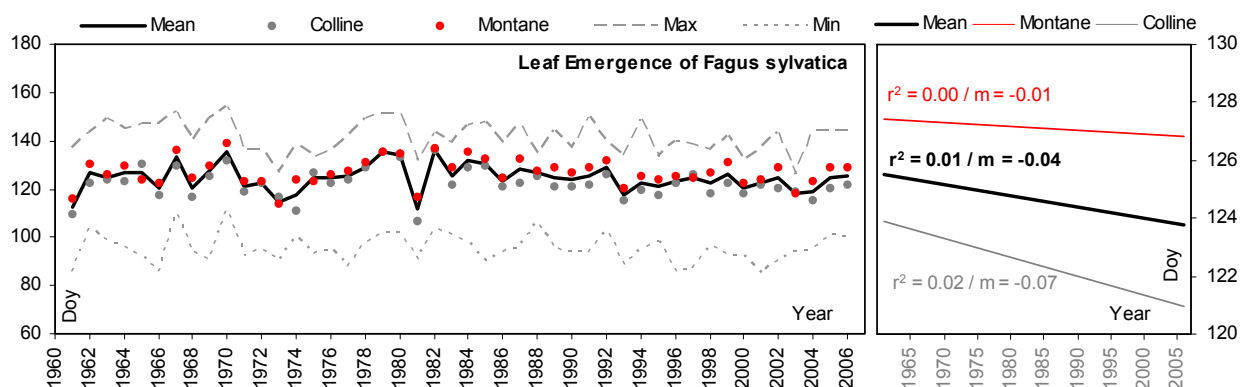


Figure 4.45: DOY of the mean and extreme modelled initiation of leaf emergence for deciduous trees in the Upper Danube Basin from 1961 to 2006, discerned into two altitudinal vegetation zones (left). Corresponding trends for the 46-year period 1961-2006 (right).

The average incidence of the modelled leaf emergence in the Upper Danube Basin varies between the DOY 86 and 154 (27<sup>th</sup> of March till 3<sup>rd</sup> of June for a non leap year) for the years 1961 to 2006, while the average incidence of the defoliation covers a range of DOY 245 to 334 (2<sup>nd</sup> of September till 30<sup>th</sup> of November for a non leap year). Figure 4.45 also indicates that the leaf emergence, according to the natural temperature gradient, occurs earlier at the colline (grey) than at the montane level (red), with exception of the years 1965, 1973 and 1975.

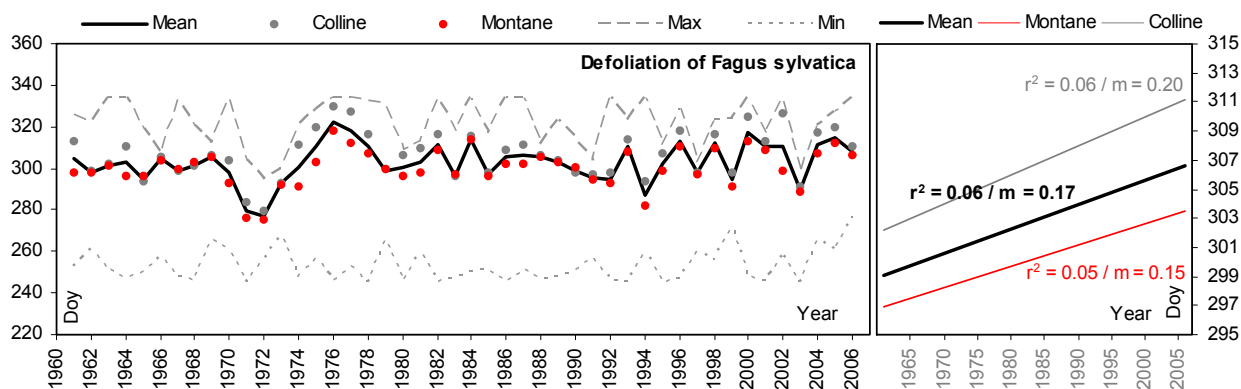


Figure 4.46: DOY of the mean and extreme modelled initiation of defoliation for deciduous trees in the Upper Danube Basin from 1961 to 2006, discerned into two altitudinal vegetation zones (left). Corresponding trends for the 46-year period 1961-2006 (right).



The dashed lines represent extreme sites within the Upper Danube catchment area. A reciprocal picture was calculated for the defoliation that continuously occurs earlier at the montane than at the colline altitudinal belt (*fig. 4.46*). Since deciduous forest is not supposed to be found at altitudes that exceed 1500 m above the sea level, no results for the alpine altitudinal zone of the Upper Danube are available.

Besides the interannual variability, both rows show a very slight trend. While the date of leaf emergence tends towards lower days of the year, i.e. an earlier incidence, with a soft slope ( $m$ ) of  $-0.04$  and a weak correlation of  $R^2 = 0.01$  (*fig. 4.45, right*), the date of defoliation develops towards higher days of the year, or a later occurrence respectively, with a slightly sharper slope of  $0.17$  and a likewise weak correlation of  $R^2 = 0.06$  (*fig. 4.46, right*). If both dates are drifting apart, this will necessarily result in a prolonged vegetation period. Indeed, the model shows a discernable increase of active growing days of deciduous forest during the past 45 years. While the absolute average length of the vegetation period showed durations of 152 to 198 days per year for the time from 1960 to 2006 (*fig. 4.47, left*), featuring a natural variability of 46 days (approx. 7 weeks), it seems to tend towards a longer duration with a slope of  $0.21$  and a weak correlation of  $R^2 = 0.06$  (*fig. 4.47, right*).

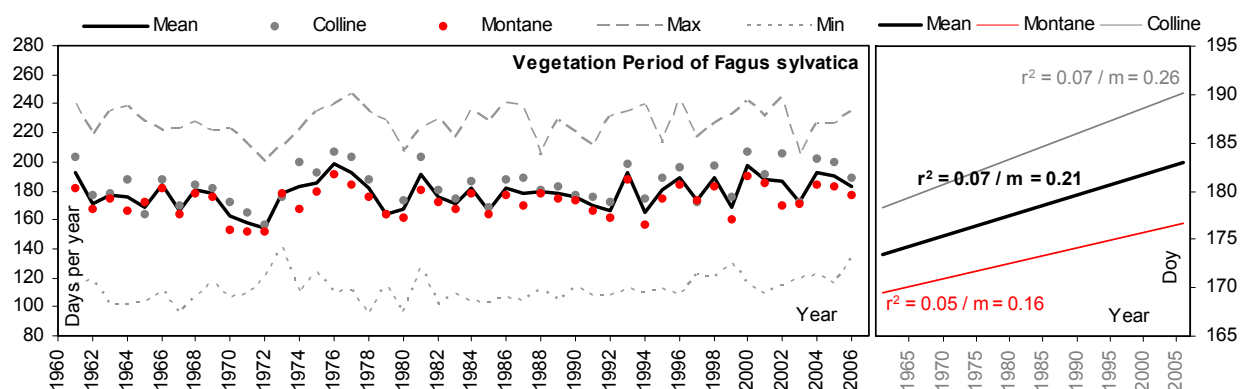


Figure 4.47: Mean and extreme duration of the modelled vegetation period for deciduous trees in the Upper Danube Basin from 1961 to 2006, discerned into two altitudinal vegetation zones (left). Corresponding trends for the 46-year period 1961-2006 (right).

Although both phenological transitions show discernable trends, the gradual change seems to be veiled by the interannual variability, leading to weak correlations. In order to visualize the trend, the moving ten-year average (1965-2001) is calculated, based on the model data for the years 1961-2006.

Figure 4.48 shows that the trends of the moving average of leaf emergence and defoliation are more stable, although they are diluted by a cooler period during the eighties of the 20<sup>th</sup> century. Nonetheless, the modelled incidence of leaf emergence has steadily developed towards an earlier date since 1982, while the discard of the leaves was modelled to occur later in the year. If only the development from 1982 onwards was considered, the development of the vegetation period would be alarming, showing a prolongation trend of 32 days within 50 years ( $R^2 = 0.88$ ).

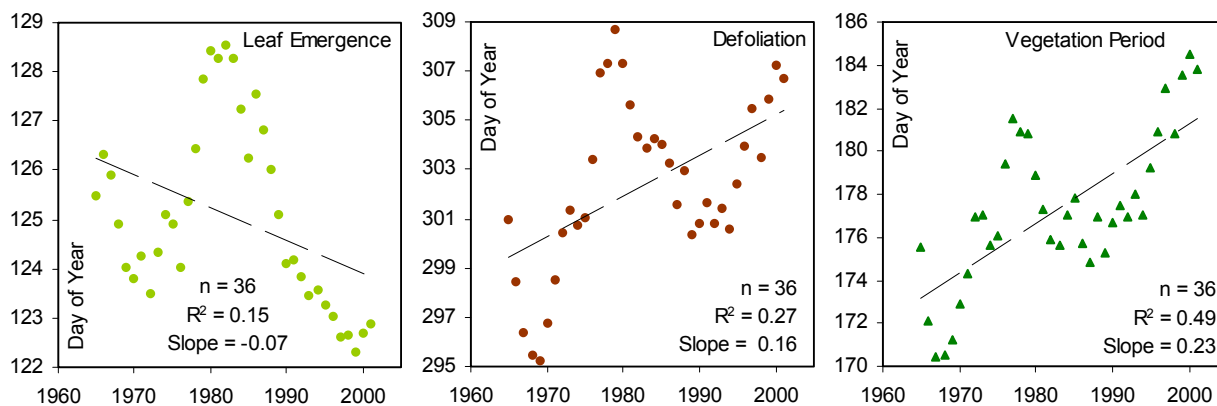


Figure 4.48: Moving 10-year averages of modelled leaf emergence, defoliation and the resulting vegetation period from 1965 to 2001, based on modelled data for the years 1961-2006.

A closer examination of the data reveals that, although the average trends still are weak and the slopes are inclining gently due to the undulating course that the change is taking, the absolute consequences can be more definite when the dates are considered in their spatial variability. Two ten year averages (1961-1970 and 1997-2006), one at each end of the reference period, were calculated and compared to each other (fig. 4.49). The maps are colourized in a way that early leaf emergence, which is technically connected to warmer temperatures, appears orange to red, while later leaf emergence is displayed green. Both maps show a strong terrain influence. It manifests for instance in the green barrier in the South that indicates the later leaf emergence that is modelled for areas with strong alpine influence, whereas the lower landscape in the middle of the basin shows light green to yellow colours, indicating a predominant incidence of leaf emergence already at the end of April.

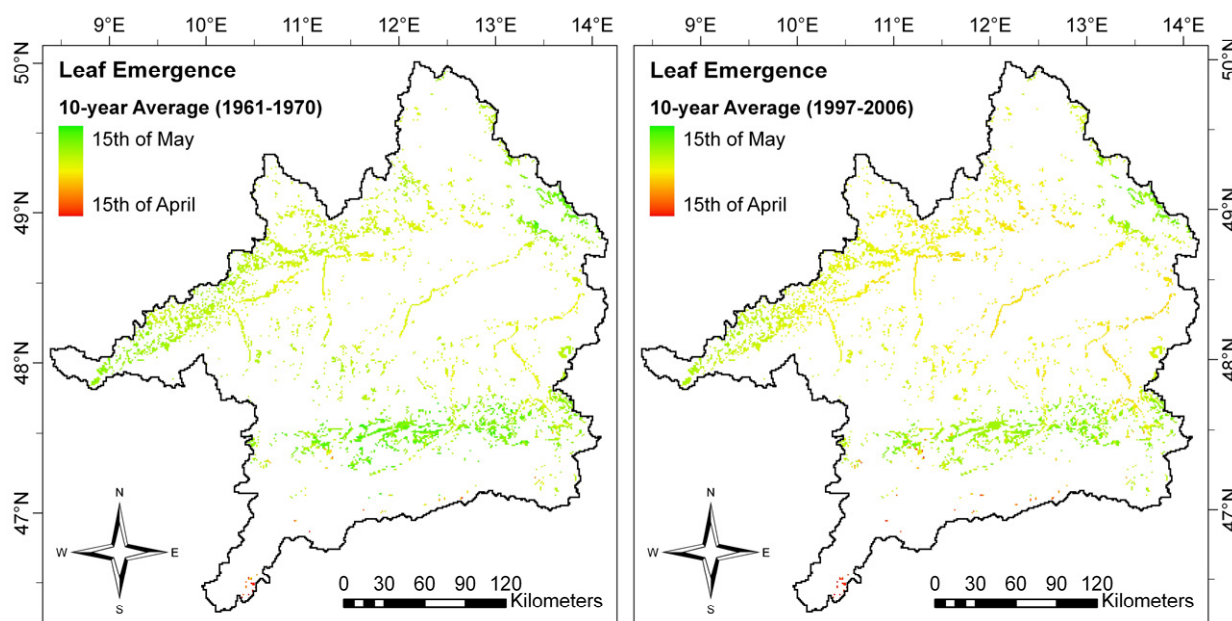


Figure 4.49: 10-year average of the initiation of leaf emergence, modelled by PROMET for the Upper Danube Basin 1961-1970 (left) and 1997-2006 (right).

A parallel picture can be observed for the defoliation (*fig. 4.50*). Only here, the orange to red colours are indicating a late incidence, which is technically due to a retarded occurrence of frost.

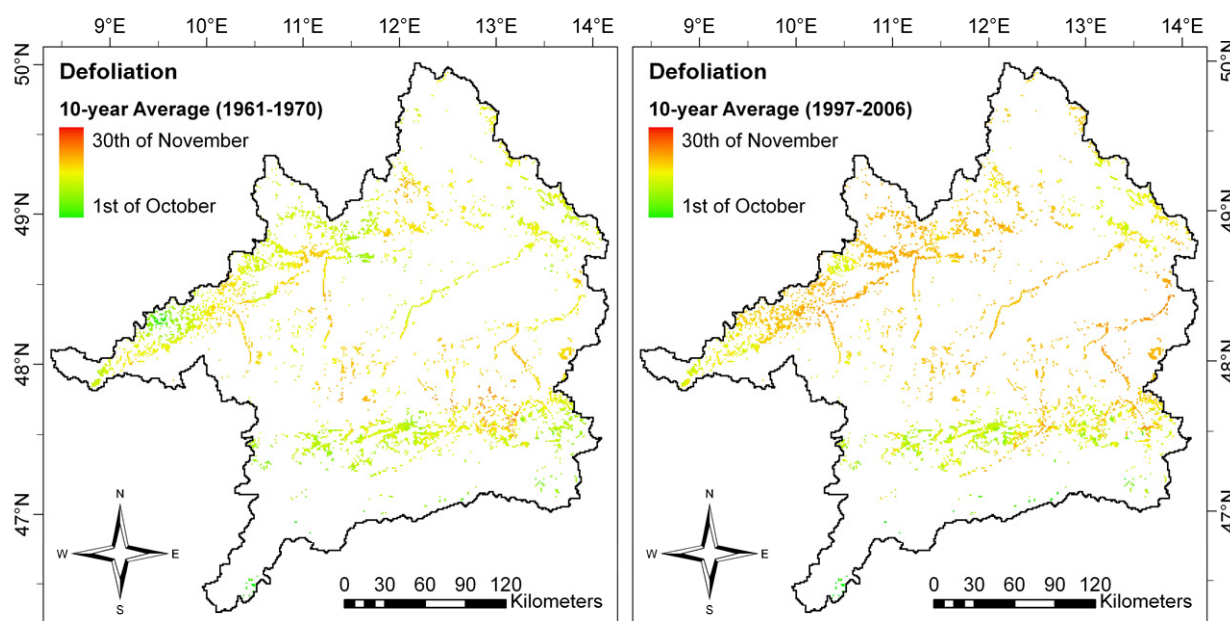


Figure 4.50: 10-year average of the initiation of defoliation, modelled by PROMET for the Upper Danube Basin 1961-1970 (left) and 1997-2006 (right).

If the two maps are subtracted, the difference of both 10-year-averages can be visualized, creating a map of mean change (*fig. 4.51*). Both phenological transitions, the leaf emergence and the defoliation, are determining the absolute duration of the vegetation period. Their diverging development results in a dominance of orange to red colours in the map of change.

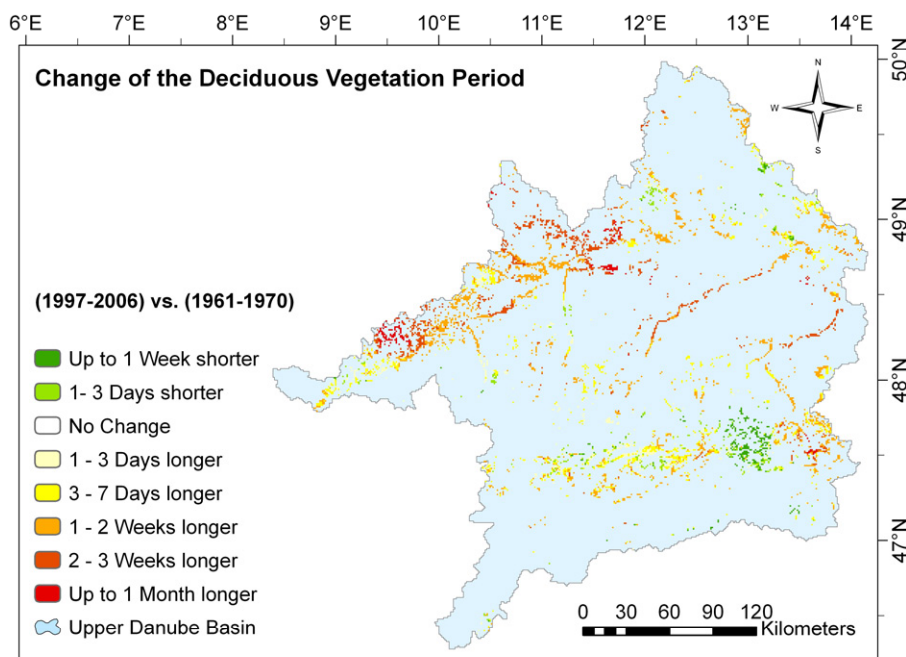


Figure 4.51: Change of the modelled 10-year average of the duration of the active growth period for deciduous trees (1997-2006 compared to 1961-1970) in the Upper Danube Basin.



The legend is coloured in a way that a change towards a prolongation of the mean duration of the vegetation period, which technically is caused by an increase of mean temperature, is displayed orange to red, while a change towards a shortening of the vegetation period, which is due to a general cooling, is displayed green.

The observed patterns imply that the sensitivity of the forest phenology in terms of temperature change is somehow connected to the terrain. Especially the low mountain ranges of the Swabian and the Franconian Alb show the largest changes with a prolongation of the 10-year average of the vegetation period of up to one month. Also a region of shorter growth periods is noticeable in the valley of the river Inn in the South-East of the basin, which is mostly caused by an earlier discard of leaves due to early frost events. While in some places the vegetation period is up to one month longer at the beginning of the 21<sup>st</sup> century compared to the sixties of the 20<sup>th</sup> century, the average prolongation for the Upper Danube sums up to 8.3 days. The landuse category “deciduous forest” in the model is parameterised like *fagus sylvatica*, due to the predominant appearance of beech trees in the Upper Danube Basin (LWF 2004). MENZEL (1997) provides a detailed report on observed development stages of trees in Europe based on the analysis of long term data of International Phenological Gardens (IPG). A set of IPGs for Europe was selected (see appendix A.15) and analysed in terms of the average incidence of phenological stages of trees (see appendix A.16). A subset of the phenological data, including the IPGs *Trier*, *Stuttgart-Hohenheim*, *Stuttgart-Weilimdorf*, *Grafrath*, *Freising-Weihestefan* and *Tharandt*, was used to generate average values and limits of variation that were supposed to apply to Southern Germany. Table 4.08 summarizes the observed incidences of leaf emergence and the modelled results for the Upper Danube Basin.

Table 4.08: Average incidence of the leaf emergence of beech trees (*fagus sylvatica*) based on observed long time data (1963-1993) of International Phenological Gardens in Europe (MENZEL 1997) and modelled results for the Upper Danube Basin.

		<b>Avg. for Europe</b>	<b>Avg. for S.-Germany</b>	<b>Min</b>	<b>Max</b>	<b>Variation</b>
<b>Observed:</b>	<i>Early</i>	123	122	92	163	71
	<i>Normal</i>	126	125	93	153	60
	<i>Late</i>	129	128	99	151	52
<b>Modelled:</b>	<i>Colline</i>		122	99	140	41
	<i>Montane</i>		127	88	154	66
	<i>Total</i>		125	88	154	66

The average dates for the incidence of the leaf emergence in Southern Germany, as derived from the literature for beech trees, are most perfectly met by the model. Observed and modelled mean leaf emergence occur on DOY 125, i.e. on the 5<sup>th</sup> of May. Also the variability of the modelled leaf emergence with 66 days is comparable to the observed dimensions. While the model results for the colline altitudinal belt feature the characteristics of early emerging IPG clones, the dates achieved for the montane level tend towards a later emergence. For the defoliation, a similar quality of the model results could be verified. The mean date of defoliation

for both, observed and modelled data, is the DOY 302 or the 29<sup>th</sup> of October respectively. Although the average incidence is perfectly met, the model seems to underestimate the variability as it is observed for Southern Germany. While the observed values vary by a range of 140 days, the model returned a maximum variation of 84 days (*tab. 4.09*). This may be due to the different observational regions, but may also be due to the fact that the discard of leaves in nature may have other reasons besides the mere temperature dependency as it is assumed in the model. It is known that the increase of atmospheric ethylene concentrations towards the end of the summer is encouraging the generation of the auxin (indole-3-acetic acid, IAA) hormone, which again is triggering the defoliation (HOPKINS 1999). These chemical processes are not accounted for in the model.

Table 4.09: Average incidence of the defoliation of beech trees (*fagus sylvatica*) based on observed long time data (1963-1993) of International Phenological Gardens in Europe (MENZEL 1997) and modelled results for the Upper Danube Basin.

		Avg. for Europe	Avg. for S.-Germany	Min	Max	Variation
<b>Observed:</b>	Total	307	302	196	336	140
	Colline		305	260	334	74
<b>Modelled:</b>	Montane		300	250	334	84
	Total		302	250	334	84

In total, the results indicate that the model is capable of returning a phenological behaviour of deciduous tree types for the leaf emergence as well as for the defoliation that very closely matches the observed dates. Consequently, the modelled absolute length of the vegetation period can be assumed to be soundly reproduced by the model.

#### 4.2.3.2 Coniferous Forest Phenology

For coniferous forest, the rapid increase of growth activity in spring, referred to as the “mayshoot”, is determined technically parallel to the leaf emergence of deciduous trees. Since coniferous trees may surmount the altitude of 1500 m, all three altitudinal zones (colline = grey, montane = red, alpine = blue) are discerned here.

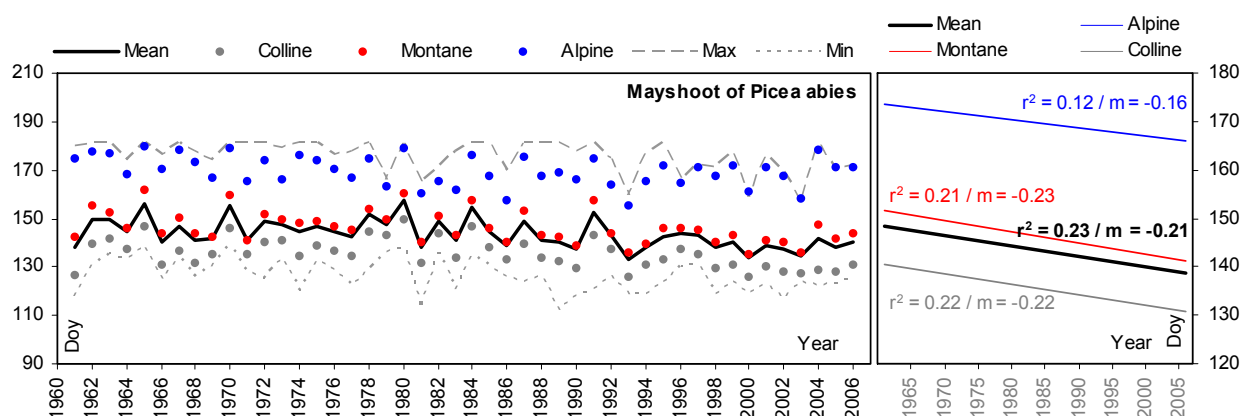


Figure 4.52: Modelled average and extreme incidence of coniferous mayshoot for the Upper Danube Basin (1961-2006), discerned into three altitudinal vegetation zones (left). Corresponding trends for the 46-year period 1961-2006 (right).

The late incidences that are modelled for the high alpine coniferous sites are biasing the average towards a later occurrence of mayshoot. The average incidence of modelled mayshoot for the whole Upper Danube Basin therefore stays close to the dates that were modelled for the montane altitudinal belt (*fig. 4.52, left*). Nonetheless, the coniferous trees generally seem to develop towards an earlier incidence of the mayshoot, although the slopes are quite small and the regressions are veiled by the interannual variability (*fig. 4.52, right*). Surprisingly, the average values trace a parallel development for all three altitudinal belts.

A more differentiated picture is revealed, when the spatial patterns are taken into account. Figure 4.53 emphasizes the effect of the terrain elevation on the incidence of phenological stages. Clearly the alpine barrier is discernable in cyan to blue colours, which are indicating a late incidence of the mayshoot. Also the trees that are covering the Black Forest in the West of the catchment and the Bohemian Forest in the East are characterised by a later mayshoot. In figure 4.53, the majority of the alpine foreland is represented by yellow colours in the left frame, while orange to red colours are dominating in the right frame. This already implies that a change of phenological behaviour is noticeable comparing the two averaged decades.

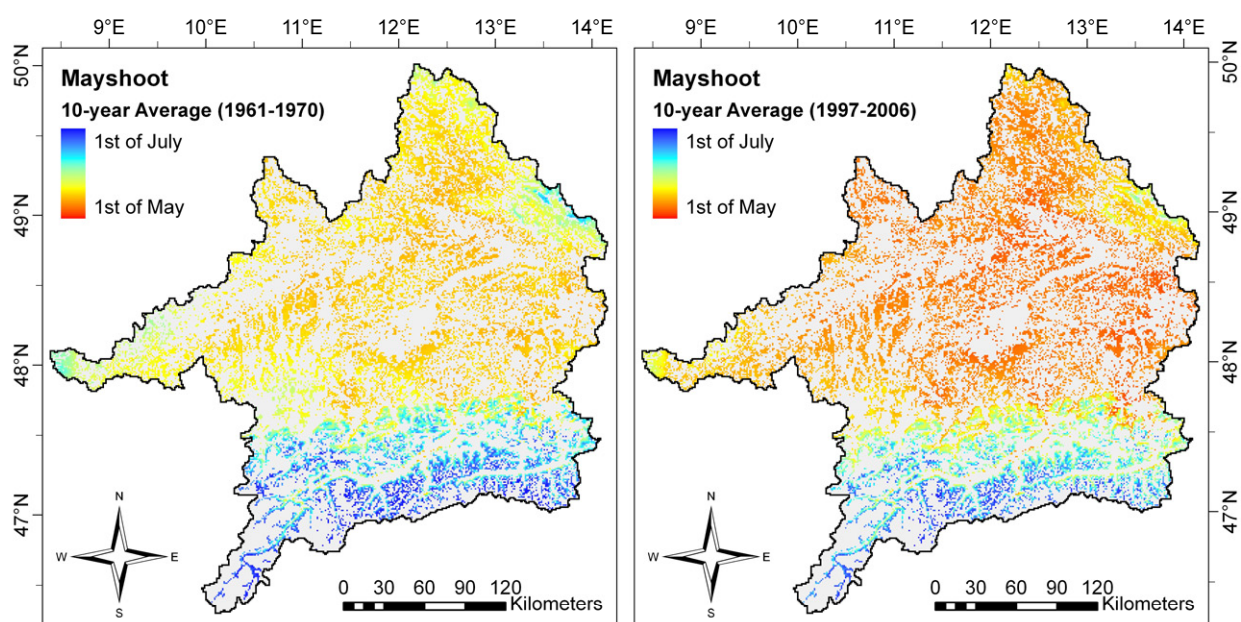


Figure 4.53: Modelled 10-year average of the initiation of mayshoot for coniferous trees 1961-1970 (left) compared to 1997-2006 (right) for the Upper Danube Basin.

By subtracting the two 10-year averages, a map of average change can be created (*fig. 4.54*). With exception of a small area in the South-West of the basin, the mayshoot was modelled earlier for the 10-year average from 1997-2006 than for the period from 1961-1970. In the average, the earlier incidence of mayshoot sums up to 7.69 days for the whole Upper Danube area. Based on the analysis of IPG data, CHMIELEWSKI (2001) could prove that the beginning of the active vegetation period in central Europe has shifted to an earlier incidence by 8 days during the past 30 years. The modelled change therefore matches the observed change quite

well. Again, the low mountain ranges of the Swabian Alb as well as of the Black and the Bohemian Forest are the regions that are most intensively affected by the change, featuring an earlier occurrence of mayshoot of up to three weeks in the average.

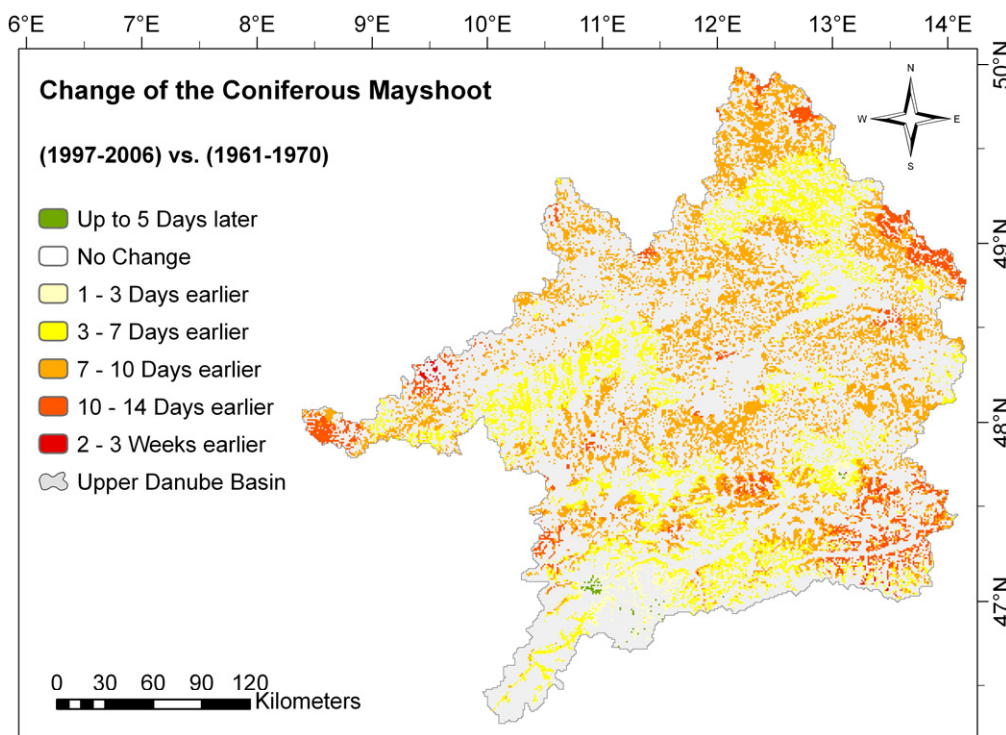


Figure 4.54: Change of the modelled 10-year average of the incidence of mayshoot for coniferous trees (1997-2006 compared to 1961-1970) in the Upper Danube Basin.

A summary of the model results and the observed data for coniferous forest is listed in table 4.10. Although the alpine regions are somewhat biasing the average, the model well meets the observed dates for the mayshoot in Southern Germany.

Table 4.10: Average incidence of the mayshoot of spruce trees (*picea abies*) based on observed long time data (1963-1993) of International Phenological Gardens in Europe (MENZEL 1997) and modelled results for the Upper Danube Basin.

		<b>Avg. for Europe</b>	<b>Avg. for S.-Germany</b>	<b>Min</b>	<b>Max</b>	<b>Variation</b>
<b>Observed:</b>	<i>Early</i>	127	128	73	179	106
	<i>Normal</i>	134	134	80	194	114
	<i>Late</i>	138	139	82	201	119
<b>Modelled:</b>	<i>Colline</i>		130	112	159	47
	<i>Montane</i>		141	117	181	64
	<i>Alpine</i>		169	140	181	41
	<i>Total</i>		139	112	181	69

The average modelled dates for the Upper Danube correspond to the observed values of a “late” IPG clone, while the average for the colline zone lies between the “early” and the “middle” observed date. Although the model simulated the incidence of mayshoot precisely concerning the average, it does not trace the full temporal variability of the observed values. Since the progress of phenological stages is also determined by the local situation of water supply,

shading and so forth, this lack of variability may be due to the relatively coarse 1 x 1 km spatial resolution of the model. In order to investigate in how far the lack of spatial variability is accompanied with a reduced temporal variability, observed time series are required in addition to the average dates. Eleven of the currently operated IPGs are located next to the Upper Danube catchment (*fig. 4.55*).

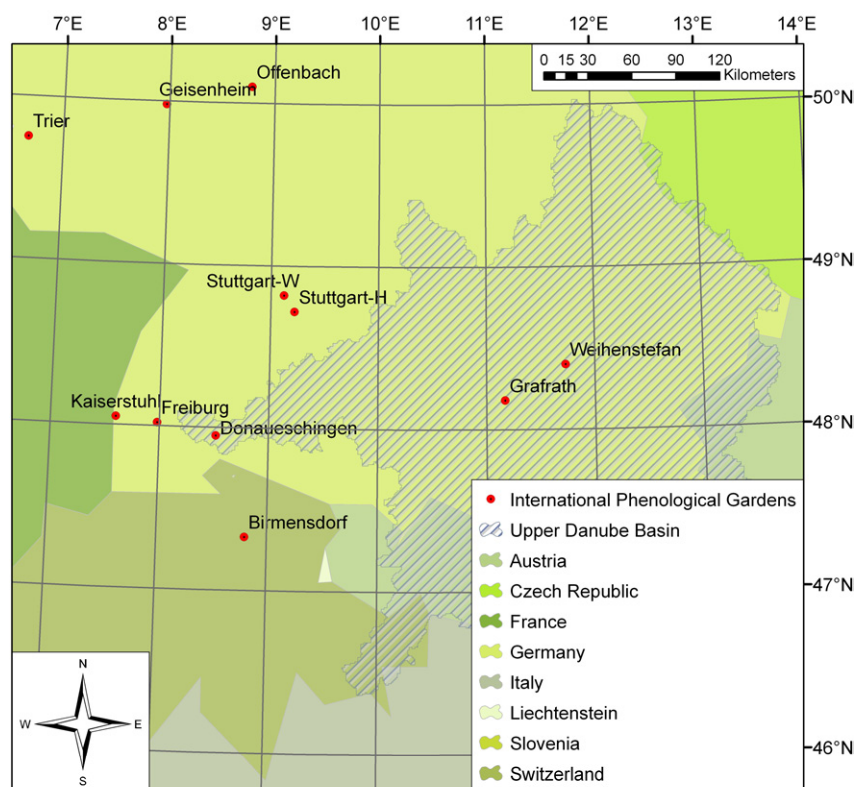


Figure 4.55: International Phenological Gardens located next to and within the Upper Danube Basin.

While no time series of the modelled forest species could be acquired for the three IPGs that actually are located within the boundaries of the Upper Danube Basin (*Donaueschingen*, *Grafrath* and *Weihenstephan*, *fig. 4.55*), the database of the garden *Offenbach* could be accessed, since the time series for *picea abies* already are published by MENZEL (1997). The IPG contributed time series of the observed incidence of mayshoot (IPG phase 2) for three IPG clones of *picea abies* 121 (early), 122 (middle), 123 (late) for a period of 1959 to 1993. For the years of 1961 to 1993, the observed and the modelled data overlap and allow for a comparative analysis (*fig. 4.56*). Since the location of the IPG *Offenbach* lies beyond the borders of the Upper Danube catchment area, a site that features comparable annual mean temperatures was selected for the comparison. An analysis of long term data provided by the German Weather service returned that the city of *Offenbach* features an annual mean temperature of 10.3 °C, while the warmest region within the Upper Danube can be found in the valley of the river Inn with annual mean temperatures of up to 10.1 °C for the respective period. A proxel of the model



data set, taken from the Inn valley in the South-East of the Upper Danube Basin, therefore was selected for the comparison.

Figure 4.56 shows that the model is capable of tracing the temporal variability of the observed time series. While some of the peaks are perfectly reproduced by the model (1974, 1981, 1983), it completely misses the observed peak of early mayshoot in 1969. The best fit between modelled and observed dates could be achieved for the IPG clone 122, which is associated with an average behaviour (MENZEL 1997). The correlation between the modelled mayshoot and the dates observed for the “middle” clone 122 (*fig. 4.56, right*) indicates, that the model is likely to reproduce the mayshoot rather later than it is observed. This may be due to the different geographic positions of observed and modelled dates. The IPG Offenbach, being located in the South-East of Frankfurt, is characterized by the low terrain elevation of 99 m above the sea level, while the lowest altitude that can be found within the borders of the Upper Danube Basin is 290 m above the seal level. The resulting differences of the annual mean temperature that discerns the IPG Offenbach from the Inn valley, which provided the test proxel, may well account for the deviations.

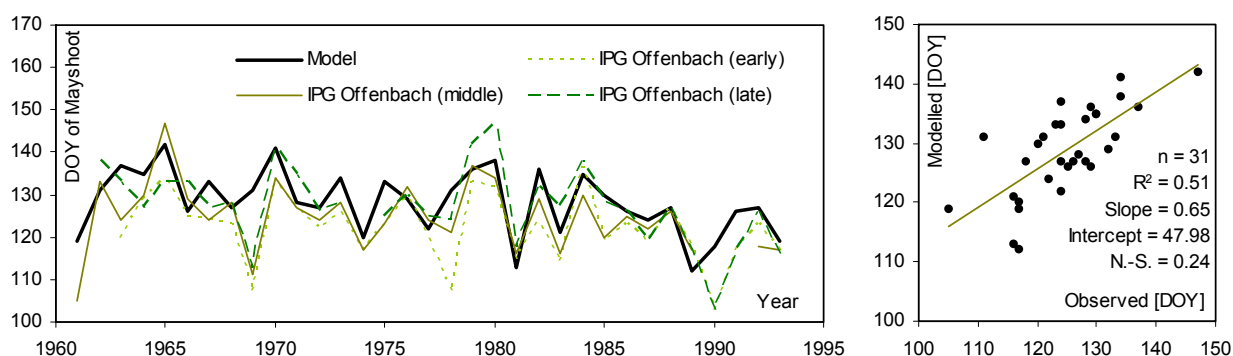


Figure 4.56: Course of observed and modelled incidence of mayshoot of *picea abies* for a time series from 1961 to 1993 (left) and correlation of modelled and observed (middle) mayshoot dates.

The model could prove its capability of a precise reproduction of the average incidence of major phenological stages for deciduous and coniferous forest trees. It also returned realistic spatial distributions of the investigated phenological transitions. For coniferous sites it could further be shown that the model is able to trace temporal patterns at a reasonable level. The model results for the reference model period from 1961 to 2006 also are carrying a strong indication that considerable changes of the phenological behaviour of trees already are occurring. The modelled changes reasonably match the changes of phenological phases as they are observed for central Europe in the literature by CHMIELEWSKI (2001) and CHMIELEWSKI AND RÖTZER (2001). The following sections will include an investigation on the further development of those changes under the impact of a possible future climate.

## 5. Modelling Climate Scenarios

For the assessment of a possible future climate, it is necessary to find an international standard that allows for the comparison of the results that are derived from different models. Only recently, the efforts of the scientists that are participating in the Intergovernmental Panel on Climate Change were honoured in relation with the Nobel Prize for peace 2007. The work of the IPCC obviously is most widely known and is thought to be perceived as a decision support for politicians worldwide. Thus, for the modelling of climate scenarios in this work, an international standard was found in the emission scenarios that were published in the special report on emissions scenarios (SRES) by the IPCC (2000, 2007).

However, there still is a large uncertainty in the literature that surrounds both, future emissions and the possible developments of their underlying driving forces. The uncertainties range from inadequate scientific understanding of the problems, due to data gaps or lack of data, to the inherent uncertainties of future events in general (IPCC 2000). To account for those uncertainties, scenario families that are based on different assumptions of future human behaviour are used to describe the range of possible future emissions.

### 5.1 The IPCC CO<sub>2</sub>-Emissions-Scenarios

The scenarios developed by the IPCC are based on assumptions of future development of determinant variables such as technology, governance, and behavioural patterns. The SRES emissions scenarios were developed in a way that they do not include simple catastrophic future projections, but endeavour to discuss more likely futures that regard the balance of future developments, which also might be complementary.

Table 5.01: IPCC scenario families, discerned into scenario groups with their major characteristics (IPCC 2000).

Scenario Family:	A1				A2	B1	B2
Scenario Group:	A1C	A1G	A1B	A1T	A2	B1	B2
Population growth:	low	low	low	low	high	low	medium
GDP growth:	very high	very high	very high	very high	medium	high	medium
Energy use:	very high	very high	very high	high	high	low	medium
Landuse changes:	low-med	low-med	low	low	med/high	high	medium
Resource availability:	high	high	medium	medium	low	low	medium
Technological development:	rapid	rapid	rapid	rapid	slow	medium	medium
Change favouring:	coal	oil & gas	balanced	nonfossil	regional	efficiency	as usual

In total, four scenario families based on four different future storylines were developed by the IPCC, listed in table 5.01, where the respective assumptions on the future development of central socioeconomic issues that are associated with each scenario are displayed.

### 5.1.1 The Scenario Families

As can be derived from table 5.01, the four scenario families are based on a variety of assumptions that are concerning the future development of a set of driving forces. While the “A”-families are scenarios, where economics are the driving factors, the „B“-families are scenarios, where environmental policies are the determinant force. Each scenario family is accompanied by a storyline that accounts for the assumed changes. Briefly, these storylines are summarized according to the IPCC (2000) in the following:

- **A1 storyline and scenario family:** This storyline is based on the assumption of a future world of very rapid economic growth, combined with a low population growth. It assumes the rapid introduction of new and more efficient technologies. Major underlying themes are the convergence among regions, capacity building and increased cultural and social interactions. Also a substantial reduction of regional differences of per capita income is hypothesized. The A1 scenario family develops into four groups that describe alternative directions of technological change concerning the energy system. The discerned groups are the A1C (favouring “clean coal” technologies), the A1G (favouring “fossil oil- and gas” technologies), the A1B (“balanced” development of energy technologies) and the A1T (transition towards solar and nuclear technologies) scenarios.
- **The A2 storyline and scenario family:** This storyline describes a very heterogeneous future world. The basic theme is self-reliance and preservation of local identities. Fertility patterns across regions converge very slowly, which results in high population growth. Economic development is primarily regionally oriented. Consequently both, the per capita economic growth as well as the technological change, are more fragmented and slower than in other storylines.
- **The B1 storyline and scenario family:** This storyline pictures a convergent world with a low population growth as assumed in the A1 storyline, but with rapid changes of economic structures towards a service and information economy. This is supposed to go along with reductions of material intensity and the introduction of clean and resource-efficient technologies. This scenario emphasizes global solutions that lead to economic, social and environmental sustainability, including improved equity. Additional climate initiatives are neglected.
- **The B2 storyline and scenario family:** This storyline outlines a world, where local solutions to economic, social and environmental sustainability are emphasized. Basic assumptions are a moderate population growth, intermediate levels of economic



development and less rapid and more diverse technological change than in the B1 and A1 storylines. While the scenario is also oriented towards environmental protection and social equity, it focuses on local and regional levels.

This variety of assumptions of human behaviour leads to different carbon dioxide and other greenhouse gas (GHG) emissions scenarios that again are resulting in changes of the global average temperature (*tab. 5.02*).

Table 5.02: Projected globally averaged surface warming at the end of the 21<sup>st</sup> century for different model cases (IPCC 2007).

Temperature Change °C (2090-2099 relative to 1980-1999)		
Case	Best estimate	Likely Range
Constant year 2000 concentrations:	0.6	0.3 - 0.9
B1 scenario:	1.8	1.1 - 2.9
A1T scenario:	2.4	1.4 - 3.8
B2 scenario:	2.4	1.4 - 3.8
A1B scenario:	2.8	1.7 - 4.4
A2 scenario:	3.4	2.0 - 5.4
A1FI scenario:	4.0	2.4 - 6.4

Table 5.02 includes two extreme reference scenarios. On the lower boundary of possible temperature changes stands the assumption of constant CO<sub>2</sub> emissions, as they were recorded in the year 2000. The upper boundary of possible global temperatures is formed by a scenario that extremely relies on the consumption of fossil fuels and therefore results in the most extreme temperature change (A1FI, *fig. 5.01*).

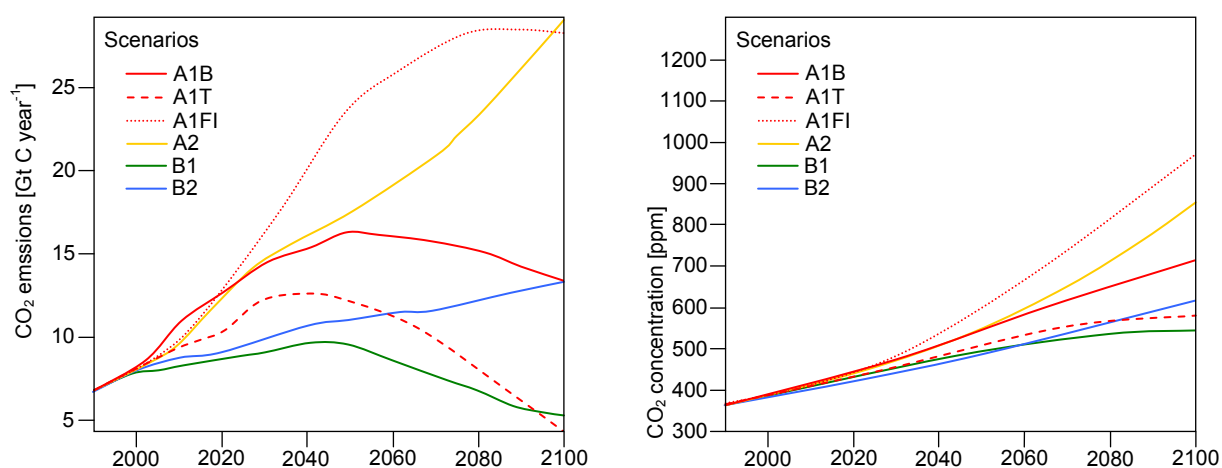


Figure 5.01: Anthropogenic emissions of CO<sub>2</sub> (left) and resulting atmospheric CO<sub>2</sub> concentrations (right) for six illustrative SRES scenarios for a time frame from 1990 to 2100 (IPCC 2007, modified).

The “constant CO<sub>2</sub>” as well as the A1FI scenario represent the most extreme positions and therefore can be considered to be the most unlikely. However, since economy is assumed to be the determining variable also in the future, the A1T (transition between fossil fuel usage and

renewable energy) and A1B (fossil fuels reach a balance with renewable energy sources) scenarios are the most widely recognized projections. The A1B scenario was chosen as the scenario basis for all calculations presented in this work, due to the moderate course it is taking and the high probability that is associated with the A1B storyline.

In that context it has to be mentioned that each scenario is represented not only by a core line of development, but by a range of possible realizations for each storyline. These ranges are defined through the boundaries that are calculated for the diverse realizations of the respective marker scenarios by a set of different environmental and socioeconomic models, a so called ensemble. Figure 5.02 pictures the increase of global mean temperature, modelled according to the projected green house gas emissions by the IPCC (2007).

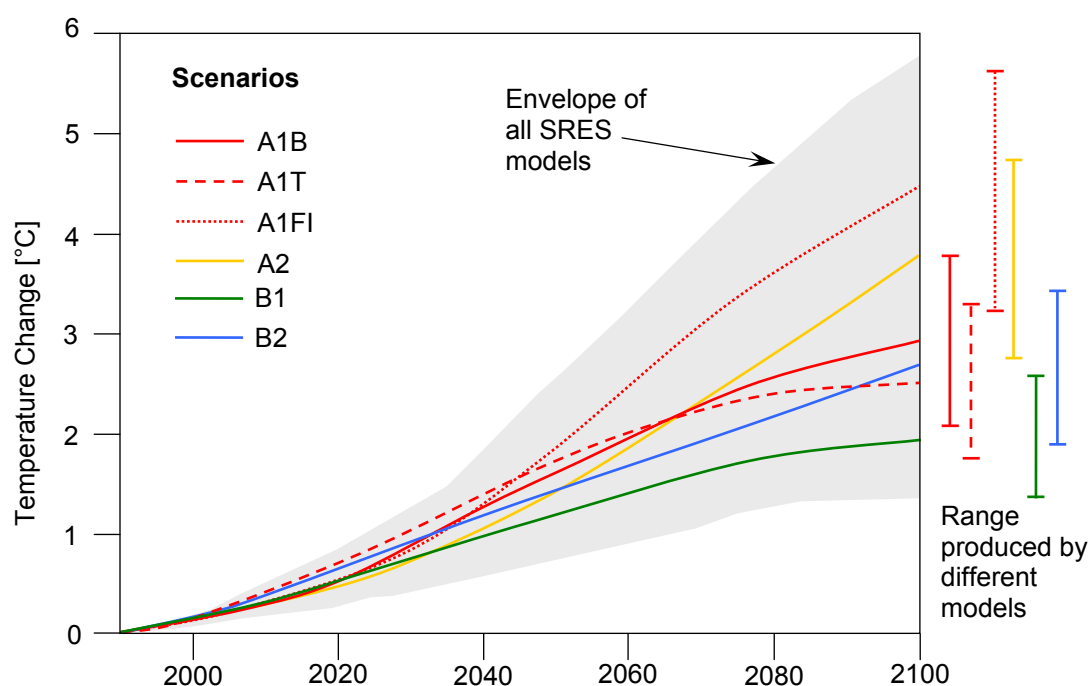


Figure 5.02: Global average temperature projections for the six illustrative SRES scenarios. The shading is the envelope based on all six model projections (with climate sensitivity in the range 1.7 to 4.2 °C). The bars on the right hand side indicate the range produced by different models for the respective storylines (IPCC 2007, modified).

The coloured lines represent the average of model runs with model ensembles, while the coloured bars on the right indicate the range of the ensemble results for the respective scenarios. The grey shading outlines the overall range of modelled possible temperature increases.

The first group of A1 scenarios, which includes the A1B scenario, assumes a balanced progress across all resources and technologies from energy supply to end use, as well as balanced land-use changes. The term balanced in this context is defined as not relying too heavily on one particular energy source or landuse development respectively. The basic conception of a balanced development assumes similar improvement rates for all sorts of energy supply and end use technologies (IPCC 2007).

## 5.2 Adapting PROMET to the Simulation of Climate Scenarios

Since PROMET is a model that entirely relies on physical descriptions of the modelled processes (see section 3.1 et seq.), the algorithms themselves do not need to be altered, when the model is confronted with climate parameters that deviate from the observed conditions of the validation time period. The basic assumption is that the model will produce realistic results, when the meteorological input data sets are modified in a way that they can provide a realistic image of a changing climate. The increase of the atmospheric CO<sub>2</sub> concentration thereby has to be considered separately from the expected temperature increase. While the ascent of the atmospheric CO<sub>2</sub> concentration is a global phenomenon, its local consequences can differ strongly from the global average. Accordingly, the modelled change of the CO<sub>2</sub> concentration is assumed with the globally projected range of the IPCC A1B scenario, while the modelled temperature increase is based on the A1B scenario, but is adjusted by a local impact factor that applies to the observed and expected trends for the Upper Danube region.

### 5.2.1 Modelling the Increase of Atmospheric Carbon Dioxide

Likely projections of the future development of the human emission behaviour are published by the IPCC for the different scenario families and storylines mentioned above. Usually, the published data is derived from economic calculations and is presented with a unit of giga-tons of carbon emissions per year. For the plant growth activities modelled here, only the atmospheric concentration of CO<sub>2</sub> is of direct consequence (see section 3.3.3.5.2). With a rough calculation, applying the parameters listed in table 5.03, the emitted tons of C can easily be converted into the resulting atmospheric concentration of CO<sub>2</sub>.

Table 5.03: Parameters for the conversion of annual CO<sub>2</sub> emissions to atmospheric CO<sub>2</sub> concentrations.

<b>Earth surface area:</b>	510 000 000	[km <sup>2</sup> ]
<b>Mean air pressure:</b>	1.033	[kg cm <sup>-2</sup> ]
<b>Molecular weight of air:</b>	28.8	[g mol <sup>-1</sup> ]
<b>Molecular weight of carbon:</b>	12	[g mol <sup>-1</sup> ]
<b>Molecular weight of CO<sub>2</sub>:</b>	44	[g mol <sup>-1</sup> ]
<b>Global mass of air:</b>	5.2683 x 10 <sup>18</sup>	[kg]
<b>Global mass of air:</b>	5268300	[gt]
<b>Global mass of air:</b>	1.82927 x 10 <sup>20</sup>	[mol]
<b>Atmospheric CO<sub>2</sub>-concentration (1970):</b>	328.9	[ppm]

Four parameters have to be known, as there is the overall area of the earth's surface with 510 x 10<sup>6</sup> km<sup>2</sup>, the mean global air pressure with 1.033 kg cm<sup>-2</sup>, the annual mass of emitted carbon as well as the atmospheric CO<sub>2</sub>-concentration that applies to the year 1970. The latter two of the required parameters are taken from the special report on emissions scenarios (IPCC 2000, *fig.*

5.04, left). First, the emissions are converted into a physical unit of grams and again into a unit of mol via the molecular weight of carbon (eq. 5.01).

$$Emission [molC \cdot year^{-1}] = \frac{(Emission [gtC \cdot year^{-1}] \cdot 10^{15})}{MolarMassOfC [g \cdot mol^{-1}]} \quad (Eq. 5.01)$$

In order to calculate the CO<sub>2</sub>-concentration, the global mass of the atmosphere with a physical unit of mol is required, which is determined following equation 5.02:

$$GlobalAirMass [mol] = \frac{(EarthSurface [km^2] \cdot 10^{10}) \cdot MeanAirPressure [kg \cdot cm^{-2}]}{MolarMassOfAir [g \cdot mol^{-1}]} \quad (Eq. 5.02)$$

The increase of the CO<sub>2</sub> concentration due to the emitted carbon then can be expressed as equation 5.03, with 0.47 representing an empiric conversion factor that accounts for the conversion of C to CO<sub>2</sub> as well as for the CO<sub>2</sub> fixation of natural carbon sinks, like the terrestrial and marine re-absorption of emitted carbon (SHAFFER AND SARMIENTO 1995).

$$CO_2 \text{ increase} [ppm \cdot year^{-1}] = \left[ \left( \frac{Emission [molC \cdot year^{-1}]}{GlobalAirMass [mol]} \right) \cdot 0.47 \right] \cdot 10^6 \quad (Eq. 5.03)$$

Figure 5.03 (left) shows the annual carbon emission due to human activities as projected by the IPCC for the moderate A1B scenario and the ascent of the atmospheric CO<sub>2</sub> concentrations, which results from the accumulation of the annual increases calculated via equation 5.03 (fig. 5.03, right). It is pictured that the A1B scenario includes a reduction of the annual C emissions from the year 2050 onwards. Nonetheless, the atmospheric concentrations continue to increase in the scenario until they have reached an elevation of nearly 560 ppm in the year 2060.

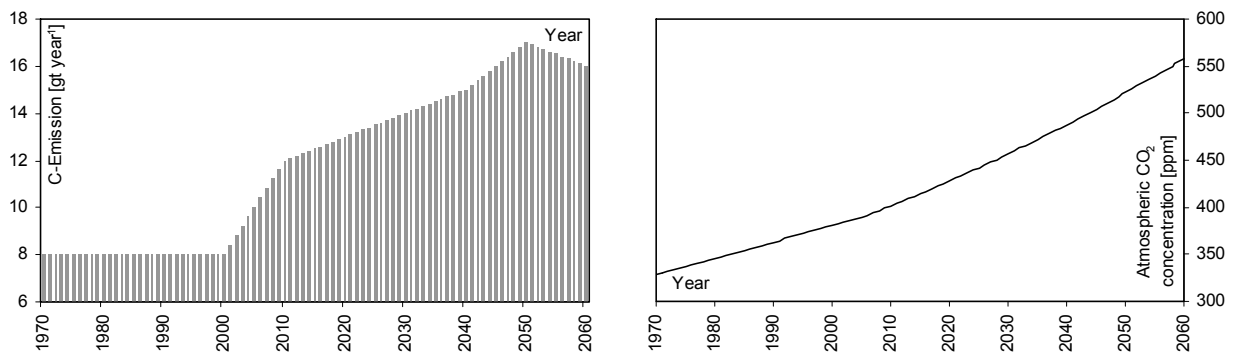


Figure 5.03: Annual emissions of carbon due to human activity according to the IPCC A1B storyline (IPCC 2000, left) and resulting atmospheric CO<sub>2</sub> concentrations (right) for a time period of 1970 to 2060.

In the model, the derived curves of increasing atmospheric CO<sub>2</sub> concentrations are traced applying third order polynomials. The course of the A1B scenario as shown in figure 5.03 (right)

for example is represented by equation 5.04, where the term “ $d1970$ ” is holding the accumulated model days since the 1<sup>st</sup> of January 1970.

$$CO_2 \text{ concentration [ppm]} = -3 \cdot 10^{-12} \cdot d1970^3 + 3 \cdot 10^{-7} \cdot d1970^2 + 5 \cdot 10^{-4} \cdot d1970 + 328.9 \quad (\text{Eq. 5.04})$$

This may well represent the global trend, but for local sites the  $CO_2$  concentrations are subject to fluctuations. This variability is simulated by overlaying the generated curve at first with an annual variation and in a second step with diurnal oscillations. The daily variability again shows a distinct seasonality. The simulated fluctuations are based on measurements from OHTAKI (1982), which were supposed to be applicable to the Northern hemisphere. In the course of the year, the mean concentrations are supposed to vary about a range of 10 ppm. While the minimum is found during the most active growth period in July, the maximum is assumed for the month of January (fig. 5.04).

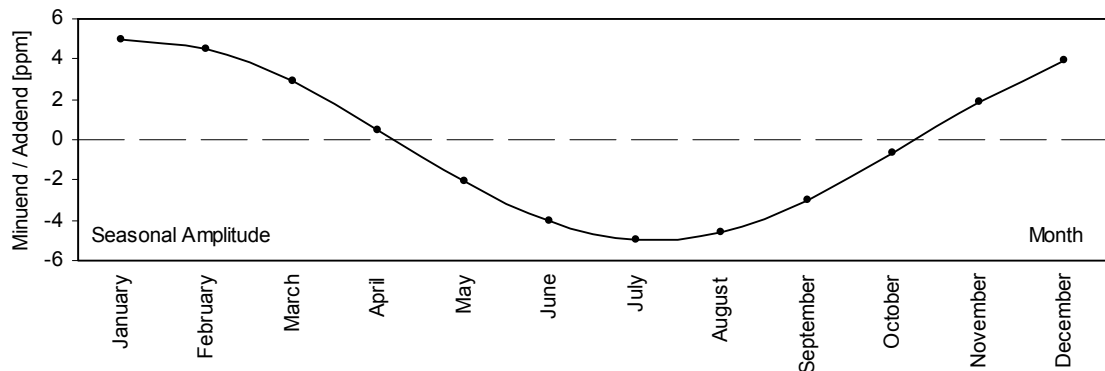


Figure 5.04: Monthly adds or minuends respectively for the simulation of the seasonal amplitude of the atmospheric  $CO_2$  concentration, based on measurements taken from OHTAKI (1982).

The daily course of the  $CO_2$  concentration is characterized by a maximum during the early morning hours and a minimum in the evening (fig. 5.05). The amplitude of the diurnal oscillations according to OHTAKI (1982) is highest for the summer with 7–15 ppm (here assumed with 10 ppm) and lowest during the winter months with 2–3 ppm (here assumed with 2.8 ppm).

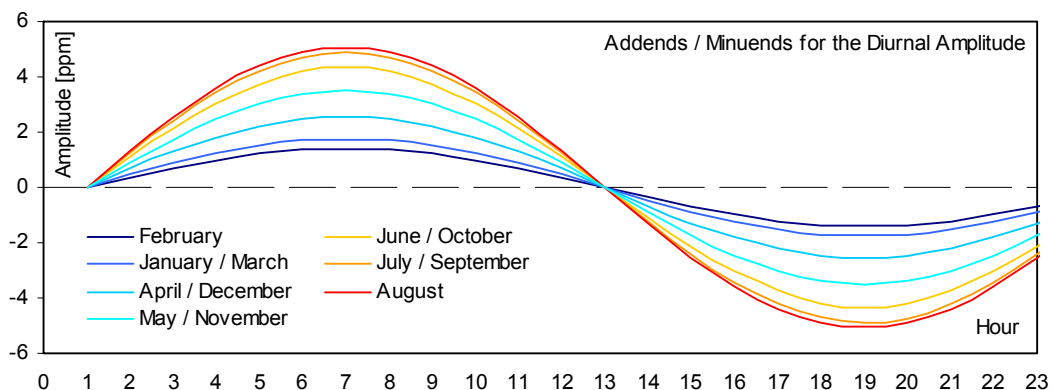


Figure 5.05: Seasonal variation of the hourly adds or minuends respectively for the simulation of the diurnal amplitude of the atmospheric  $CO_2$  concentration, based on measurements taken from OHTAKI (1982).

When both, the seasonal and the diurnal amplitudes, are taken into account, the modelled atmospheric CO<sub>2</sub> concentration resembles the oscillating course of natural measurement series (fig. 5.06, right).

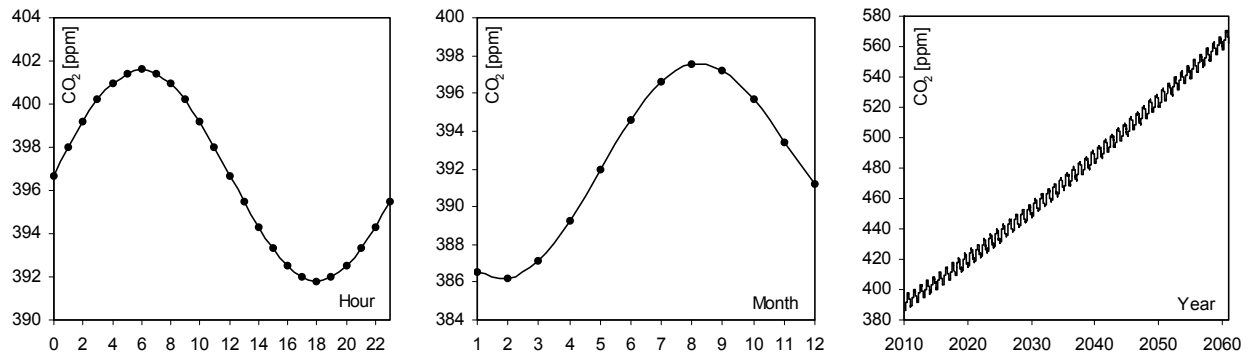


Figure 5.06: Modelled atmospheric CO<sub>2</sub> concentration for a summer day (25<sup>th</sup> of July 2010, left), for the course of the year 2010 (middle) and for a time period from 2010-2060 (right).

## 5.2.2 Modelling the Corresponding Change of Temperature and Rainfall

The change of the annual mean temperature, as it is observed around the globe, mainly is the result of the increasing concentration of climate gases in the atmosphere. However, the change of temperature has to be considered independently from the change of the CO<sub>2</sub> concentration, when the global perspective is neglected and investigations on a regional scale are put into focus. The reaction of local ecosystems on elevated GHG concentrations may result in measurably higher or lower manifestations of temperature change compared to the changes that are observed for the global average. For the modelling of the Upper Danube, long-term meteorological series (1960-2006) were analyzed with respect to their temperature trend and compared to the projected global trends as they are assumed by the IPCC (2007, fig. 5.07).

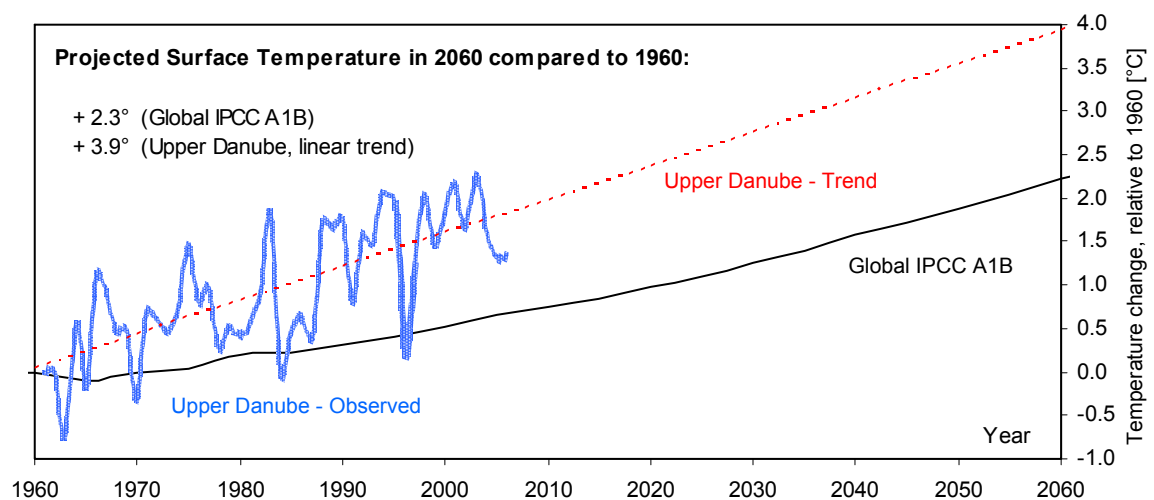


Figure 5.07: Observed annual mean air temperature of the meteorological stations that were applied for the modelling of the Upper Danube Basin (1960-2006), relative to the average annual temperature of 1960, including the trend of the regional temperature increase. Both are compared to the global relative temperature increase as it is assumed by the IPCC A1B scenario (IPCC 2007).

It can be deduced from figure 5.07 that the impact of climate change for the Upper Danube region concerning the increase of average temperature (+ 3.9 °C in 2060 compared to 1960) is elevated by a factor of 1.7 compared to the assumed global average temperature reaction (+ 2.3 °C in 2060 compared to 1960). The climate scenario generated for this work consequently features a projection of the temperature increase according to the IPCC A1B scenario, but additionally incorporates an impact factor of 1.7. The elevated temperature increase more adequately suits the conditions in the Upper Danube, continuing the historically mapped course (compare *figs. 5.07, 5.09 and 5.10*).

Due to the interconnectedness of climatic processes, the change of temperature will also lead to a change of the seasonal patterns and annual sums of precipitation. For the generation of projected meteorological data, this causes the problem that not only the temperature change has to be applied to the model, but also the change of precipitation has to be integrated, while at the same time the statistical features of the input meteorology have to be preserved in the scenario meteorology. This can easily be maintained by exclusively applying combinations of climate parameters that already have been measured in the past, instead of generating thoroughly artificial meteorological combinations.

The projected weather data applied for this work therefore is the result of a stochastic analysis of measured meteorological data (MAUSER ET AL. 2007), following the example of the stochastic weather generators WGEN (RICHARDSON 1981) or LARS-WG (RACSO ET AL. 1991, SEMENOV ET AL. 1998). The procedure is based on the assumption that the sum and the intensity of precipitation are connected with certain temperature events. Through a statistical analysis of the covariance of the weekly precipitation sums ( $P$ ) and the weekly mean temperatures ( $T$ ), which are recorded in the historic climate time series, the assumption is derived that the weekly rainfall can be expressed as a function of the corresponding weekly mean temperature (eq. 5.05, MAUSER ET AL. 2007).

$$\bar{P} = f(\bar{T}) \quad (\text{Eq. 5.05})$$

This allows for a selection of rainfall events that are statistically connected to a specified temperature and therefore ensures the maintenance of the original statistic attributes of the temperature and rainfall data series. The measured data thereby are intersected into observation weeks, the smallest unit where weather patterns that manifest in stable relations of temperature and rainfall were assumed to be adequately mapped, so that for each week of the year the mean temperature and average precipitation sum as well as their covariance is available. These parameters are representing the average seasonal dependence of temperature and rainfall and are forming the basis of a dicing process, which employs a coupled

two stage random number generator (IMSL 2003) and uses the weekly means and covariances of temperature and rainfall to determine pairs of interdependent random numbers (fig. 5.08).

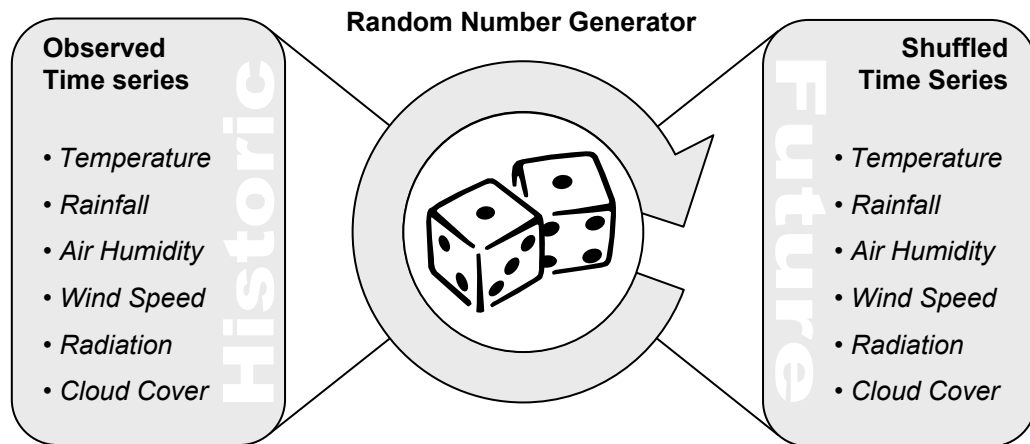


Figure 5.08: Generation of artificial meteorological data applying a stochastic weather generator.

By imposing a positive temperature trend on the result of the first random number selection, the stochastic generation of the new weather series can be combined with certain conditional features. In this example, the increase of annual mean temperature, as proposed by the IPCC A1B scenario and amplified by the impact factor of 1.7, has to be mapped by the shuffled weather data, so that the statistics of the newly generated temperature series trace a gradual increase of mean temperature, which is picturing the specified temperature increase of 3.9 °C until the year 2060 compared to 1960 (2.3 °C “IPCC” x 1.7 “impact factor”  $\approx$  3.9 °C, figs. 5.07, 5.09 and 5.10).

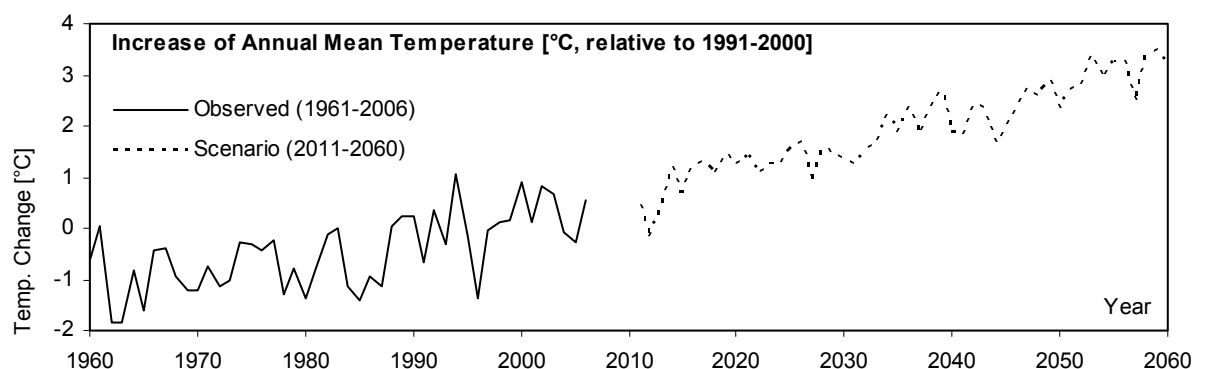


Figure 5.09: Annual mean temperatures relative to the 10-year average of 1991-2000 observed by the meteorological stations, which were applied for the modelling of the Upper Danube (solid, see section 3.3.4.3), and stochastically rearranged annual mean temperatures, applying a local impact factor of 1.7 to the IPCC A1B scenario (dashed).

The second random number, which represents the corresponding rainfall, is drawn considering the previously determined covariance of temperature and precipitation. Following the course of the randomly generated pairs of temperature and rainfall, the measured weeks then are rearranged by selecting the weekly averages that most closely meet the randomly selected pair of temperature and rainfall by applying a Euclidian nearest neighbour distance metric. Through



this continuous process of dicing and selecting, the observed data of temperature and rainfall for all weeks of the measured data base are shuffled and a new chain of weather weeks is recombined, gradually generating new meteorological data series.

The additionally required meteorological data besides temperature and precipitation like relative humidity, wind velocity, radiation and cloud cover (see section 3.3.4.3) are also taken from the selected historic observation week and are added to the new meteorological data set. For more details concerning the stochastic generation of future weather data it is referred to MAUSER ET AL. (2007). The procedure results in a time series of a user-defined length of possible future meteorological data, featuring statistical characteristics that are matching the historic measurement series (*fig. 5.09*).

However, the future weather chain is limited to the observed extremes. With a prolonged future extension and more extreme climatic situations, the probability of recurrence of certain extreme historic events increases. For the period that is modelled here with a moderate future extension of 50 years (2011-2060), the observed data base provided an adequate variability, so that the introduced method produced a statistically likely realization of the future climate. Due to the methodical characteristic of rearranging measured data, the generated future weather data can rather be termed “stochastically nearest neighbour resampled” (MAUSER ET AL 2007) than synthetic.

### **5.2.3 Selected Scenario Storylines**

Each scenario storyline can be composed of not one, but of a multitude of feasible realizations. The absolute number of possible combinations is determined by the statistic population of measured weather data that can be applied to the stochastic shuffling for the compilation of the new weather series. For the generation of a climate scenario that would satisfy the specifications required in the scope of this work, a more or less average realization of the IPCC A1B scenario was created and modified according to the trend that is implied by the observed time series, applying the regional impact factor of 1.7 as described above. The base data consisted of 377 weather stations, which provided records for a 46-year time period from 1960 to 2006. The scenario was constructed to cover a time period that comprises the forthcoming 50 years from 2011 to 2060 and generally was designed to avoid extreme realizations. In order to assess the models sensitivity with respect to the changed climate, a so called baseline scenario run also was initialized that was designed to feature no discernable temperature trend. Also the atmospheric concentration of carbon dioxide was limited to a static value that applies to 1970 ( $\approx 326$  ppm) for the baseline scenario. To enable a separate mapping of the models sensitivity with respect to the atmospheric CO<sub>2</sub> concentration, the model was also tested in combination with a hypothetical scenario that combines the positive temperature trend of the A1B storyline with a constant carbon dioxide concentration.

Figure 5.10 pictures the trend of the modelled temperature increase within the boundaries of the Upper Danube Basin, while the spatial manifestation of the temperature change is visualized in the appendix (A.17.1).

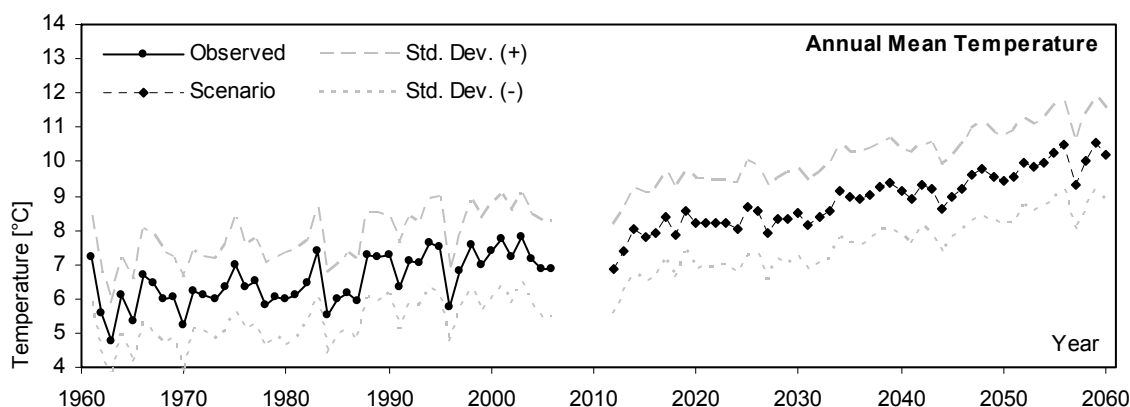


Figure 5.10: Development of the modelled annual mean temperature for the Upper Danube Basin. Model results based on observed data (1960-2006) and modelled temperatures applying to the regionally adapted IPCC A1B climate scenario (2011-2060), including the respective standard deviations from the area average.

As described above, the rainfall is technically connected to the selected temperature events. Parallel to the expectations enunciated by the IPCC (2007), the scenario includes a slight increase of wintery precipitation in combination with a decrease of rainfall during the summer half-year. The changes are to some extent balancing the annual precipitation sums, but the absolute amount of rainfall during the scenario is strongly decreasing (fig. 5.11).

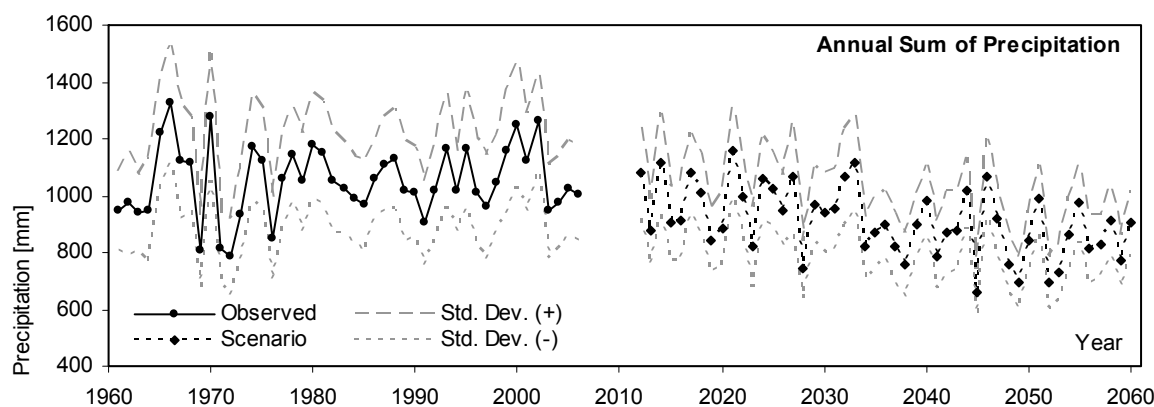


Figure 5.11: Development of the annual sums of precipitation for the Upper Danube Basin. Model results based on observed data (1960-2006) and modelled rainfall applying to the regionally adapted IPCC A1B climate scenario (2011-2060), including the respective standard deviations from the area average.

The average sum of precipitation for the reference period (1961-2006) was modelled with 1050 mm per year, while for the scenario (2011-2060) the modelled average featured 908 mm of rainfall per year (tab. 4.05, also see appendix A.17.2).

Considering the change of the precipitation sums for the respective half-years of the model period, the diverging change of the precipitation patterns becomes even more apparent.

Table 5.04: Statistical features of the meteorological input data, summarized for the reference and the scenario model period.

	Reference (1960-2006)		Scenario (2011-2060)	
	Average	Std. Dev.	Average	Std. Dev.
<b>Temperature:</b>	6.54 °C	2.48 °C	8.89 °C	2.59 °C
<b>Summer Precipitation:</b>	630.40 mm	203.67 mm	478.82 mm	132.30 mm
<b>Winter Precipitation:</b>	420.14 mm	138.01 mm	429.39 mm	126.16 mm
<b>Total Precipitation:</b>	1050.54 mm	333.61 mm	908.21 mm	247.10 mm

While the wintery rainfall, although somewhat diluted, continues its slight trend towards higher sums (reference slope = 0.92 mm a<sup>-1</sup>, scenario slope = 0.62 mm a<sup>-1</sup>), the summer precipitation decreases strongly during the scenario period, featuring a slope of - 4.54 mm a<sup>-1</sup> (fig. 5.12). The statistical features of the meteorological driving parameters are summarized in table 5.04 for the reference and the scenario period.

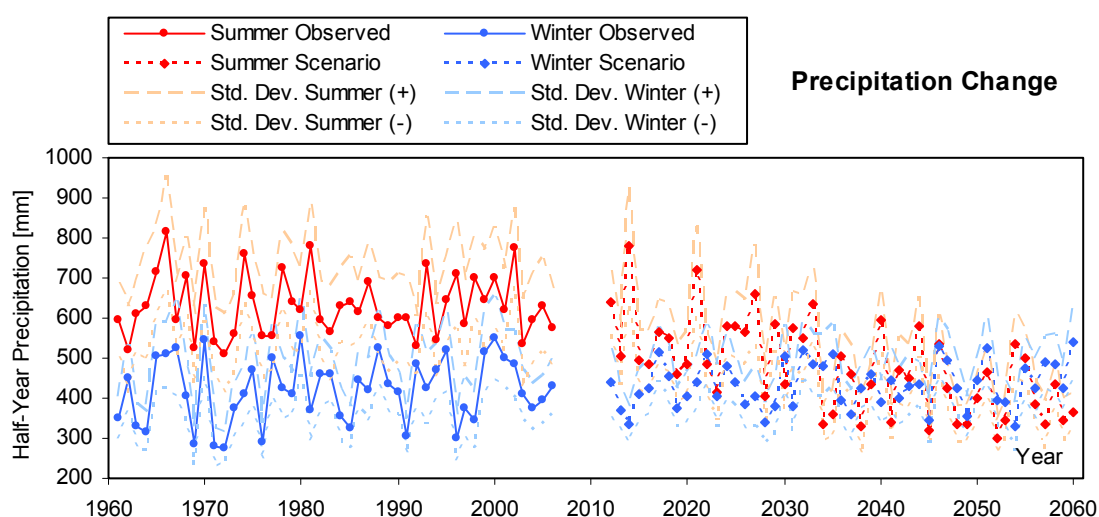


Figure 5.12: Development of annual precipitation sums for the Upper Danube Basin discerned into the summer (May-October) and winter half-year (November-April). Model results based on observed data (1960-2006) and modelled rainfall applying to the regionally adapted IPCC A1B climate scenario (2011-2060), including the respective standard deviations from the area average.

The strong decrease of the summer rainfall, which amounts to more than 150 mm less summer precipitation during the scenario period compared to the reference average, in combination with the expected increase of the annual mean temperature is supposed to have a definite impact on the modelled vegetation parameters. A set of selected model results that are supposed to adequately describe the catchments reaction to the assumed climate change are presented in the following section.

## 6. The Scenario Results

In this section, the results of the scenario model runs for the future years of 2011 to 2060 are analyzed in comparison to the model results of the reference time series (1961-2006). The temporal basis for all results presented here again is the hydrological year, ranging from the 1<sup>st</sup> of November to the 31<sup>st</sup> of October of the respective model year.

### 6.1 Phenology

For the scenario model runs, the development of major phenological stages of forest trees was mapped parallel to the examples presented in section 4.2.3.2. Figure 6.01 pictures the modelled course of the average duration of the vegetation period of deciduous trees, which is determined by the modelled incidence of leaf emergence in spring and by the discard of the leaves in autumn. The trend towards longer periods of active growth per year, which already can be perceived in the reference time series from 1961 to 2006, is continued for the scenario period, but is intensified under the scenario conditions (reference slope =  $0.23 \text{ d a}^{-1}$ , scenario slope =  $0.42 \text{ d a}^{-1}$ , see *tab. 6.01*). The strong variability between the single years that characterises the model results is also continued for the scenario (*fig. 6.01*). The standard deviation of about 16 days from the area average is nearly the same for the reference and the scenario period, indicating that the original spatial heterogeneity of the Upper Danube is preserved in the scenario (also see appendix A.17.5).

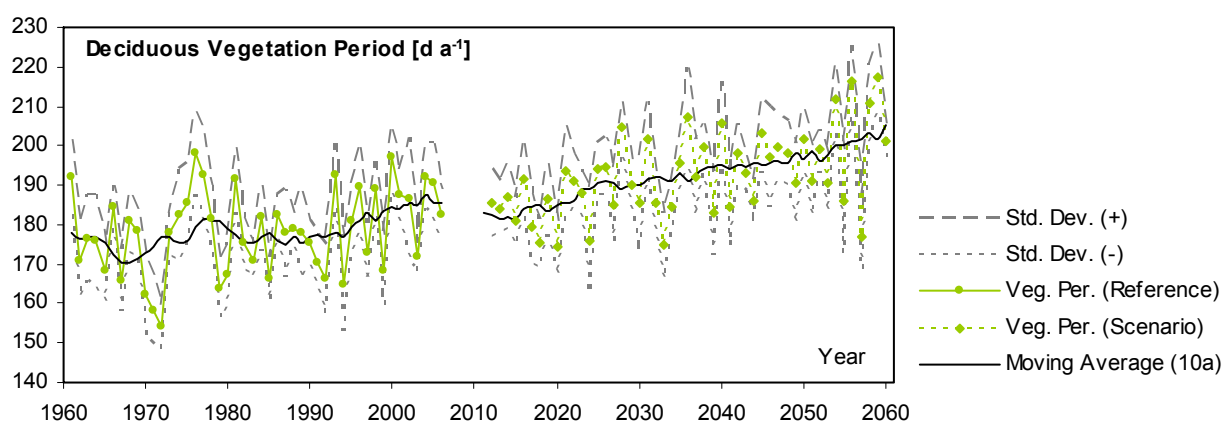


Figure 6.01: Course of the average duration of the vegetation period of deciduous trees within the Upper Danube Basin, modelled for the reference period from 1961 to 2006 and for the modified IPCC A1B scenario from 2011 to 2060, including the moving 10-year average and the respective standard deviations from the area mean.

A parallel picture can be observed for the incidence of the mayshoot of coniferous trees, which continues its gradual shift towards earlier incidence (*fig. 6.02*). Here, the change is even more

definite, which may be due to the considerably higher count of coniferous proxels (25 013 km<sup>2</sup>) compared to the deciduous areas (5 681 km<sup>2</sup>). Coniferous trees are covering all zones of the Upper Danube more or less equally, while the more sparsely distributed deciduous areas are mostly concentrated along the major watercourses (*fig. 6.01*), which may tend to feature more balanced temperatures.

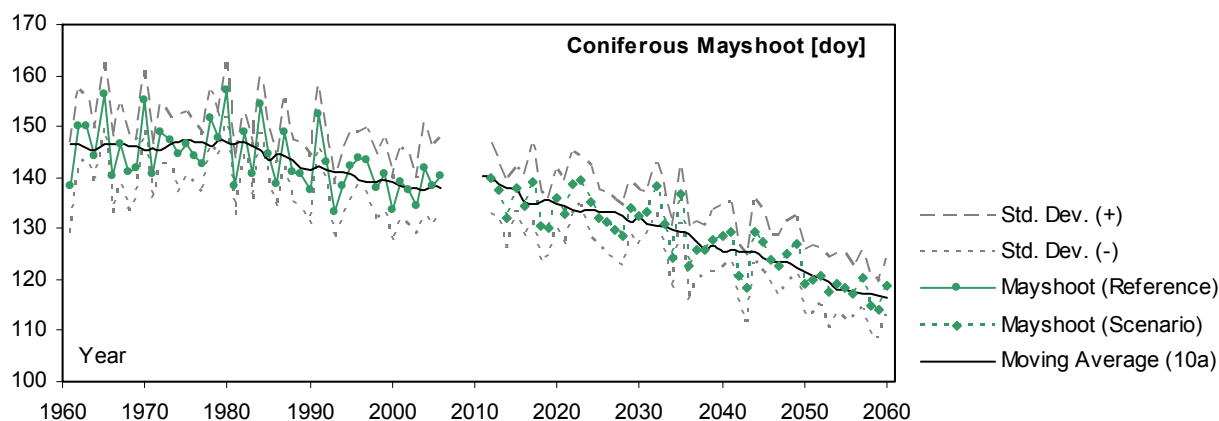


Figure 6.02: Course of the average incidence of mayshoot of coniferous trees within the Upper Danube Basin, modelled for the reference period from 1961 to 2006 and for the modified IPCC A1B scenario from 2011 to 2060, including the moving 10-year average and the respective standard deviations from the area mean.

With exception of the defoliation, the trends that were observed for the reference period are continued during the scenario for all phenological transitions. Although the observed trends are sustained, they show more definite correlations and steeper slopes for the scenario (*tab. 6.01*). According to the trend, the vegetation period was modelled to lengthen by about four days in the average during every decade, mostly due to an earlier incidence of the leaf emergence in spring. On average, the period of active growth was modelled 14 days longer for the scenario period than it was mapped for the reference series. The discard of the leaves does not show a discernable trend during the scenario, although it is modelled to occur nearly seven days later compared to the reference average. This may be due to a veiling of the trend through the strong variation of the discard between the respective model years. The coniferous mayshoot again shows a strong trend and was modelled to happen 15 days earlier for the scenario average compared to the reference results. If the data view is restricted to the recent history of the reference time series, only considering the years from 1980 onwards, while the 60ies and 70ies of the previous century are neglected, the trends are almost perfectly projected into the future by the scenario.

Table 6.01 summarizes the trends and averages that were modelled for the reference and for the scenario period. In order to accentuate the directions of the development, the trends presented in table 6.01 are based on the moving 10-year average of both time series, shown as solid black lines in *figs. 6.01* and *6.02*.

Table 6.01: Trends of the moving 10-year average of the modelled phenological behaviour of forest trees within the Upper Danube Basin and modelled average incidence of the major phenological phases, discerned into the reference period from 1961 to 2006 and the scenario period from 2011 to 2060.

	Reference (1961 – 2006)	Scenario (2011 – 2060)
<b>Deciduous Leaf Emergence</b>		
N =	46	50
R <sup>2</sup> =	0.19	0.96
Slope =	- 0.06 [DOY a <sup>-1</sup> ]	- 0.42 [DOY a <sup>-1</sup> ]
Average =	124.67 [DOY]	117.28 [DOY]
Average Std. Dev. =	5.87 [DOY]	5.75 [DOY]
<b>Deciduous Defoliation</b>		
N =	46	50
R <sup>2</sup> =	0.40	--
Slope =	+ 0.17 [DOY a <sup>-1</sup> ]	--
Average =	302.89 [DOY]	309.73 [DOY]
Average Std. Dev. =	10.70 [DOY]	11.05 [DOY]
<b>Deciduous Vegetation Period</b>		
N =	46	50
R <sup>2</sup> =	0.55	0.96
Slope =	+ 0.23 [d a <sup>-1</sup> a <sup>-1</sup> ]	+ 0.42 [d a <sup>-1</sup> a <sup>-1</sup> ]
Average =	178.23 [d]	192.45 [d]
Average Std. Dev. =	16.56 [d]	16.80 [d]
<b>Coniferous Mayshoot</b>		
N =	46	50
R <sup>2</sup> =	0.80	0.99
Slope =	- 0.23 [DOY a <sup>-1</sup> ]	- 0.47 [DOY a <sup>-1</sup> ]
Average =	143.65 [DOY]	127.96 [DOY]
Average Std. Dev. =	12.27 [DOY]	11.71 [DOY]

Figure 6.03 visualizes the spatial manifestation of average changes for deciduous (left) and coniferous trees (right), that could be discerned between the reference and the scenario period.

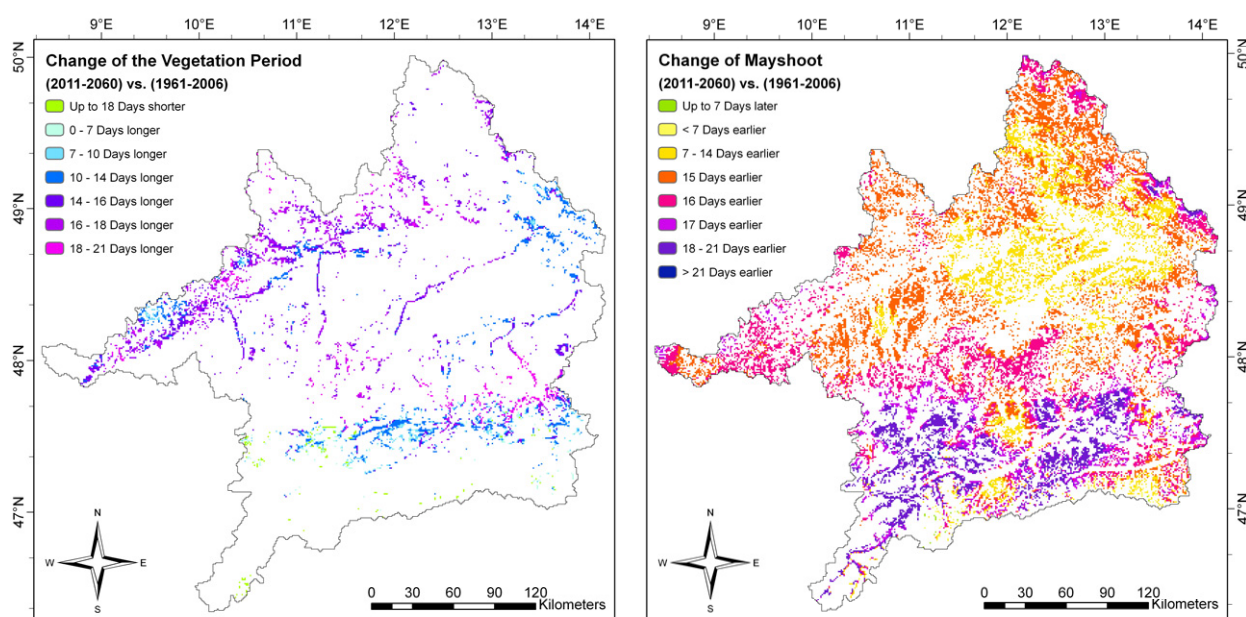


Figure 6.03: Map of change of the average duration of the vegetation period of deciduous trees (left) and of the incidence of mayshoot of coniferous forests (right) within the Upper Danube Basin, picturing the difference between the model results achieved for the reference period from 1961 to 2006 and for the modified IPCC A1B scenario from 2011 to 2060.

While the prolongation of the vegetation period is strongest in the valley of the river Inn that lies in the South-East of the basin, a slight shortening of the vegetation period was mapped for some proxels in the South-West of the catchment area (*fig. 6.03, left*). The shift towards earlier dates of the incidence of mayshoot is strongest for the mountainous regions of the Alps and the Black Forest, while it is lowest for the central region of the Danube valley itself (*fig. 6.03, right*). The spatial patterns of the average dates of the phenological transitions are displayed in the appendix (A.17.3 - 6).

Since the phenology model that is applied to the agricultural landcover types also is based on a temperature related approach, it is likely that a more rapid progress of the modelled phenological phases can be expected under elevated average temperature conditions, although a more detailed analysis of this development has not been completed yet.

## 6.2 Biological Productivity

In order to assess the temporal development of the overall modelled biological productivity, which can be defined as the accumulated annual net primary production (NPP), the assimilated biomass was summed for the different plant parts, so that the absolute biomass was available that was allocated for each proxel during the hydrological year. The accumulated biomass was averaged for all proxels of the Upper Danube data set that are assigned to vegetation landuse types and thereby returned time series of modelled average biological productivity in terms of annual sums of NPP for the Upper Danube Basin. The model results picture a clear trend towards increasing biological productivity within the Upper Danube catchment that equally applies to the reference and to the scenario period (*fig. 6.04*).

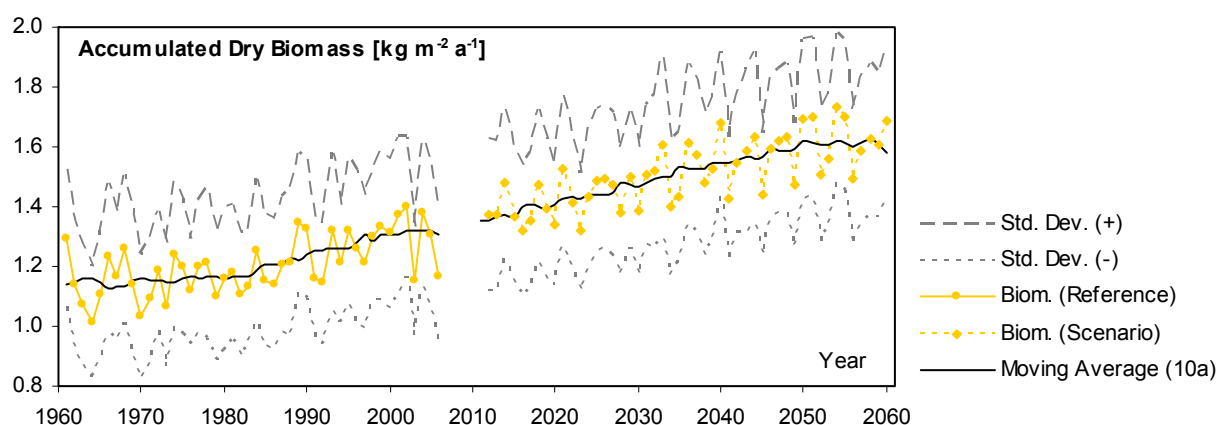


Figure 6.04: Course of the average annual accumulation of dry biomass for the Upper Danube Basin, modelled for the reference period from 1961 to 2006 and for the modified IPCC A1B scenario from 2011 to 2060, including the moving 10-year average and the respective standard deviations from the area mean.

The slope of the increase of biomass accumulation is slightly steeper for the scenario compared to the reference period, indicating an average additional productivity of roughly 500 kg ha<sup>-1</sup> for



every decade (tab. 6.02). The results for both periods are featuring comparable standard deviations from the area average, indicating that the spatial diversity is reasonably preserved in the scenario.

Table 6.02: Trends of the moving 10-year average of the modelled biological productivity within the Upper Danube Basin and modelled average biomass allocation, discerned into the reference period from 1961 to 2006 and the scenario period from 2011 to 2060.

	Reference (1961 – 2006)	Scenario (2011 – 2060)
N =	46	50
R <sup>2</sup> =	0.90	0.96
Slope =	+ 0.0047 [kg m <sup>-2</sup> a <sup>-1</sup> a <sup>-1</sup> ]	+ 0.0058 [kg m <sup>-2</sup> a <sup>-1</sup> a <sup>-1</sup> ]
Average =	1.21 [kg m <sup>-2</sup> a <sup>-1</sup> ]	1.51 [kg m <sup>-2</sup> a <sup>-1</sup> ]
Average Std. Dev. =	0.45 [kg m <sup>-2</sup> a <sup>-1</sup> ]	0.48 [kg m <sup>-2</sup> a <sup>-1</sup> ]

The average productivity was modelled to be elevated by about 3 tons per hectare for the scenario compared to the reference period. Several factors are contributing to this development. The generally higher temperatures are causing accelerated chemical reactions according to the van't Hoff rule, while the increased atmospheric CO<sub>2</sub> supply additionally encourages the allocation of carbon. Also the longer duration of the vegetation period, which could equally be detected in the control and in the scenario results (see sections 4.2.3 and 6.1), contributes to higher annual sums of accumulated biomass. Figure 6.05 pictures the diverging courses of differently modelled future annual biomass accumulations for the case of an exemplary grassland proxel, taken from the middle of the Upper Danube Basin. The scenario period is divided into three storylines, including the baseline scenario devoid of any trend, the locally adapted IPCC A1B scenario, which was applied for all spatial results that are presented here, and the A1B scenario in combination with the hypothetical assumption of a constant atmospheric CO<sub>2</sub> concentration, the latter being included to enable the investigation of the models sensitivity concerning the carbon dioxide supply.

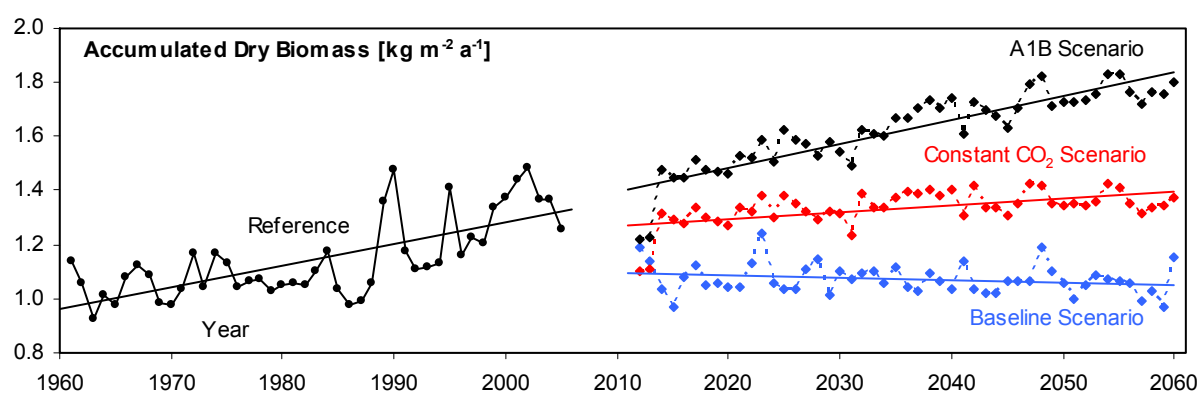


Figure 6.05: Biological productivity of an intensive grassland proxel from the middle of the Upper Danube catchment (457 m a.s.l.), calculated for the reference period (1961-2006) and for three different future storylines including the modified A1B scenario with and without assumed CO<sub>2</sub> increase and the unbiased baseline scenario (2011-2060).



The grassland proxel features a definite increase of biological productivity for the years 1961 to 2006 that also characterises the spatial average (compare *figs. 6.04* and *6.05*). The baseline scenario shows no discernable trend (slope = -0.0009,  $R^2 = 0.04$ ), indicating the non-biased behaviour of the model for constant external conditions, while the hypothetical constant CO<sub>2</sub> scenario shows a soft increase (slope = 0.0025,  $R^2 = 0.30$ ), but at the same time significantly lower productivities compared to the “normal” A1B scenario. The diverging development of the A1B scenario and the constant CO<sub>2</sub> scenario are revealing the strong influence that the supply of carbon dioxide is exerting on the modelled carbon allocation. The slightly increasing trend of the constant CO<sub>2</sub> scenario, compared to the levelled development that applies to the baseline scenario, again pictures the isolated influence of the temperature change on the chemical reactions that are steering the simulation of the carbon allocation. However, the increasing trend of the reference period (slope = 0.008,  $R^2 = 0.52$ ) is almost perfectly continued into the future for the combination of the CO<sub>2</sub> and temperature development that was assumed for the modified A1B scenario (slope = 0.009,  $R^2 = 0.80$ ). The assumptions that were made for the scenario therefore seem to picture a likely realization of the future development of the photosynthetic activity under climate change conditions.

Despite the average trend, the spatial manifestation of the possible local changes is of importance. Especially the agricultural areas in the foreland of the Alps benefit from the change, showing an increased allocation of biomass of up to 4 t ha<sup>-1</sup> on average (*fig. 6.06, left*).

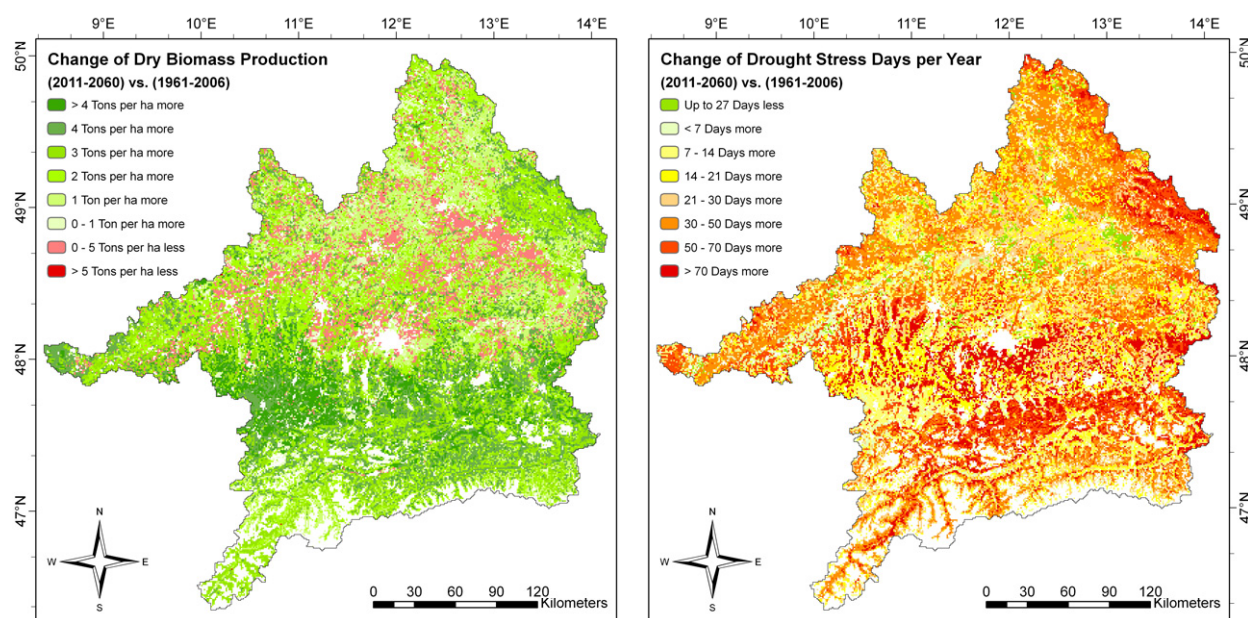


Figure 6.06: Map of change of the average annual accumulation of dry biomass (left) and of the average annual count of water stress days (right) for the Upper Danube Basin, picturing the difference between the model results achieved for the reference period from 1961 to 2006 and for the modified IPCC A1B scenario from 2011 to 2060.

Nonetheless it is striking that not the entire catchment area shows increased rates of biomass allocation as would be assumed from the influence that the changed environmental conditions

are taking. The central area of the Danube valley itself features lower rates of productivity during the scenario, indicated by predominantly light red colours in figure 6.06 (left). This anomaly is due to the limiting effect of the water supply that characterizes this agriculturally intensely used region. Already during the reference period, the model results for the Danube valley locally report up to 200 days of limited growth due to water stress per year, indicating that the water supply is a growth limiting factor throughout the vegetation period (see appendix A.17.7 - 8). The region consequently is unable to transform the growth encouraging changing climatic conditions into an increased productivity, because it already has been producing near the naturally limited maximum in the past. The accelerated progress of the phenological phases under the increased temperature conditions may also contribute to a decrease of productivity through a shortened phase of generative growth. The spatial manifestation of the combined changes results in a gradual shift of the agricultural productivity from the North to the South of the catchment area under scenario conditions.

### 6.3 Drought Stress

In order to picture the development of water stress events under climate change conditions, the absolute occurrences of limited photosynthetic activity due to water stress situations were assessed by counting the absolute number of days featuring a growth limitation that could be traced to the water supply. As was described in section 3.3.3.5.4, the modelled conductance of the leaves with respect to water vapour is determined by several factors. The reduction of stomatal conductivity that is triggered by the water supply can be assessed separately from the other causes, like for example the CO<sub>2</sub> supply, since it manifests in the model through a temporarily reduction of the BALL ET AL. (1987) coefficient for stomatal conductance (*g<sub>fac</sub>*). If a vegetated proxel during the model runs features a water stress induced growth reduction at least during one model time step, the actual model day is counted as a water stress event. The absolute intensity of the water stress thereby is neglected and only the actual occurrence of water stress is accumulated for the hydrological years of the model period in the form of so called “water stress days”. Preparing an average indicator of the water stress situation for the model area, it is not sufficient to simply average the count of mapped water stress days, for the absolute number of proxels that actually are featuring water stress may vary between the model years. In order to bridge that problem, the averaging has to be extended to all vegetated areas within the model data set, i.e. all proxels that would potentially be able to yield water stress days. This can be accomplished by relating the absolute number of water stress days (*WSD*) of all proxels that actually reported water stress (*n*) to the total number of vegetated proxels (*N*, eq. 6.01).

$$WSD_{avg} = \frac{\sum_{i=1}^n WSD_i}{N} \quad (\text{Eq. 6.01})$$

The spatial averaging resulted in time series of the modelled average number of water stress days per year. Although already the results for the reference period showed an increase of the average count of water stress events (see *tab. 6.03*), figure 6.07 features a severe increase of the slope of the trend for the Upper Danube under scenario conditions, as they were assumed for the modified A1B storyline (also see *tab. 6.03*). Not only the average number of days that are counted as water stress days increases for the scenario, but also the absolute count of proxels that actually are reporting water stress is modelled to rise, significantly biasing the average towards intensified average drought stress. While the average count of stress affected proxels was 44 833 for the reference, more than 13 500 km<sup>2</sup> additionally reported water stress for the scenario in the average (*tab. 6.03*). This implies that not only the absolute number of water stress events per season is increasing, but also areas that did not show water stress effects during the reference period, are becoming sensitive to the water supply under the impact of a possible future climate of the kind as it was applied here with the modified A1B storyline. The highest increase of water stress events therefore is mapped for regions that were featuring low numbers of water stress days during the reference period like for example the Northern rim of the Alps, while the regions that already showed high stress impact during the reference period did report less determinant changes (*fig. 6.06, right*).

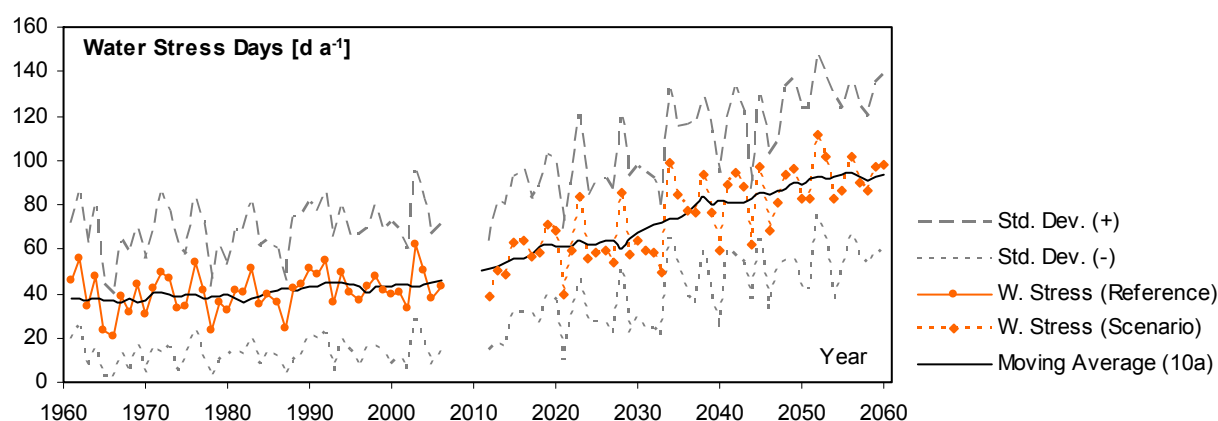


Figure 6.07: Course of the average annual count of water stress days within the Upper Danube Basin, modelled for the reference period from 1961 to 2006 and for the modified IPCC A1B scenario from 2011 to 2060, including the moving 10-year average and the respective standard deviations from the area mean.

Water stress and biological productivity are reciprocally determining each other in the model. If the water stress is high, only reduced growth is possible, while at the same time the probability for the occurrence of water stress is increased during phases of rapid growth, when high rates of transpiration occur. An increase of drought stress during the early growth stages therefore will lead to reduced or crippled growth, which again will result in a reduced number of dry stress

events for the rest of the year, simply because the plants are too weakly developed to transpire amounts of water that would overstrain the soil water supply. The central region of the Danube valley, which was showing lower rates of productivity during the scenario compared to the reference period as discussed in the previous section, therefore even reports a slight decrease of the water stress days during the scenario (*fig. 6.06, right*). Visualizations of the spatial patterns of the average water stress limitation modelled for the reference and for the scenario period for the region of the Upper Danube are available in the appendix (A.17.8).

Table 6.03: Trends of the moving 10-year average of the modelled water stress events within the Upper Danube Basin and modelled average count of water stress days per year, discerned into the reference period from 1961 to 2006 and the scenario period from 2011 to 2060.

	Reference (1961 – 2006)	Scenario (2011 – 2060)
N =	46	50
R <sup>2</sup> =	0.47	0.97
Slope =	+ 0.19 [d a <sup>-1</sup> a <sup>-1</sup> ]	+ 0.95 [d a <sup>-1</sup> a <sup>-1</sup> ]
Average =	40.70 [d a <sup>-1</sup> ]	74.66 [d a <sup>-1</sup> ]
Average Std. Dev. =	55.50 [d a <sup>-1</sup> ]	67.51 [d a <sup>-1</sup> ]
Average Affected Area =	44833.54 [km <sup>2</sup> ]	58353.31 [km <sup>2</sup> ]

## 6.4 Water Cycle Components

The modelled components of the water balance for the climate scenario situation on one hand are the result of the changed temperature and rainfall environment, but on the other hand comprise all the changes that have been provoked in the biological activity by the CO<sub>2</sub>, temperature and water supply changes. Higher rates of biological productivity, which are induced by accelerated chemical reactions under elevated temperature conditions, as well as prolonged vegetation periods, may result in increased sums of evapotranspiration, while a more frequent occurrence of water stress again may reduce the annual evapotranspiration significantly. The evapotranspiration therefore combines a whole variety of reactions and consequently can be considered to be a parameter that most sensitively summarizes the response of the landsurface to climate change.

The modelled course of the average annual sum of transpiration (*fig. 6.08*) shows a faintly increasing trend for the reference period. This trend is inversed for the scenario, where the transpiration rates are slightly decreasing on average (see *tab. 6.04*). The increase of the transpiration sums in the reference series is developing parallel to the increasing biological activity that also was mapped for this period. But, while the biological activity was modelled to continue its course towards higher rates of biomass accumulation, the transpiration is slightly reduced under scenario conditions. An increase of transpiration activity can be traced to two facts. Increasing temperatures are contributing to an intensification of transpiration by provoking higher rates of gas exchange through accelerated chemical reactions on one hand, but on the other hand are directly influencing the gas exchange by increasing the leaf-to-atmosphere water

vapour deficit. If only the temperature was accounted for in the climate scenario, these effects could be expected to extend their course into the future, continuing the trend of increasing transpiration rates. But two factors are exerting a counter influence that is exceeding the positive trend, forcing the development into a downward direction again. As was described in section 5.2.3, the elevated temperature is accompanied by a significant decrease of summer precipitation. This results in a strong increase of drought stress events, which naturally are inhibiting the transpiration. In addition to this effect, the level of the atmospheric CO<sub>2</sub> concentration was increased during the scenario according to the IPCC A1B storyline. An increase of the concentration of carbon dioxide at the leaf surface is modelled to lead to a reduced conductivity of the stomata (see section 3.3.3.5.4), which again results in reduced rates of transpiration. Due to the increased efficiency of the gas exchange under elevated CO<sub>2</sub> conditions, the photosynthetic processes in the leaf can be maintained at a high rate, while at the same time less water vapour is lost through the gas exchange (SAGE 1994). This stomatal reaction can be equally observed for both C<sub>3</sub> and C<sub>4</sub> species (TYREE AND ALEXANDER 1993).

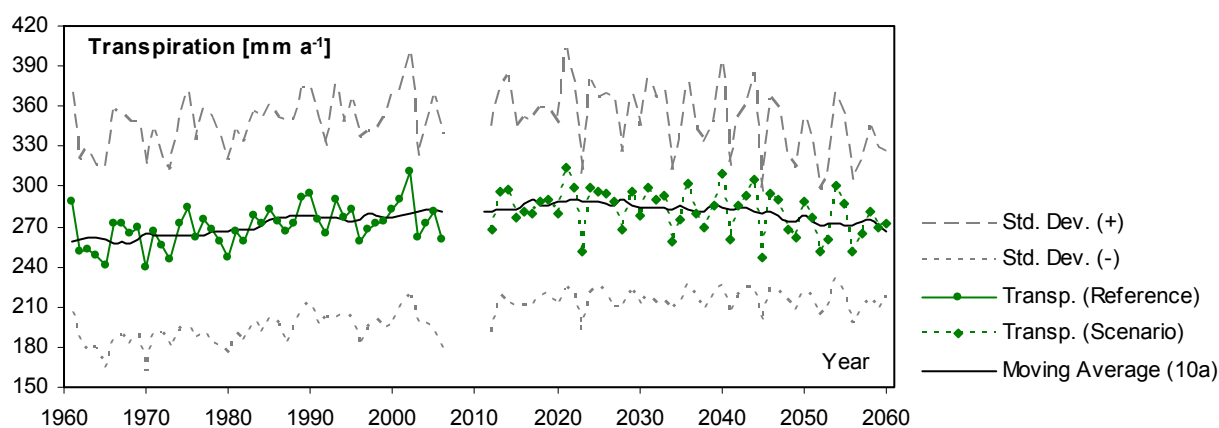


Figure 6.08: Course of the average annual sum of transpiration within the Upper Danube Basin, modelled for the reference period from 1961 to 2006 and for the modified IPCC A1B scenario from 2011 to 2060, including the moving 10-year average and the respective standard deviations from the area mean.

Table 6.04: Trends of the moving 10-year average of the modelled transpiration and evapotranspiration within the Upper Danube Basin and modelled average of both water cycle components, discerned into the reference period from 1961 to 2006 and the scenario period from 2011 to 2060.

	Reference (1961 – 2006)	Scenario (2011 – 2060)
<b>Transpiration</b>		
N =	46	50
R <sup>2</sup> =	0.90	0.64
Slope =	+ 0.58 [mm a <sup>-1</sup> a <sup>-1</sup> ]	- 0.34 [mm a <sup>-1</sup> a <sup>-1</sup> ]
Average =	269.77 [mm a <sup>-1</sup> ]	281.95 [mm a <sup>-1</sup> ]
Average Std. Dev. =	155.35 [mm a <sup>-1</sup> ]	134.08 [mm a <sup>-1</sup> ]
<b>Evapotranspiration</b>		
N =	46	50
R <sup>2</sup> =	0.82	0.20
Slope =	+ 0.84 [mm a <sup>-1</sup> a <sup>-1</sup> ]	- 0.12 [mm a <sup>-1</sup> a <sup>-1</sup> ]
Average =	380.91 [mm a <sup>-1</sup> ]	403.22 [mm a <sup>-1</sup> ]
Average Std. Dev. =	205.84 [mm a <sup>-1</sup> ]	187.06 [mm a <sup>-1</sup> ]

Figure 6.09 pictures rates of transpiration that correspond to the biological activity displayed in figure 6.05 for an exemplary grassland site. Although this proxel is only showing a moderate water stress impact and therefore does not feature the decreasing trend of the transpiration for the scenario that characterizes the average development, it almost ideally demonstrates the increased efficiency of the gas exchange under elevated CO<sub>2</sub> conditions. The highest increase of transpiration is mapped for the hypothetic constant CO<sub>2</sub> scenario (slope = 1.26, R<sup>2</sup> = 0.65), whereas the baseline scenario again shows no definite trend (slope = -0.13, R<sup>2</sup> = 0.02).

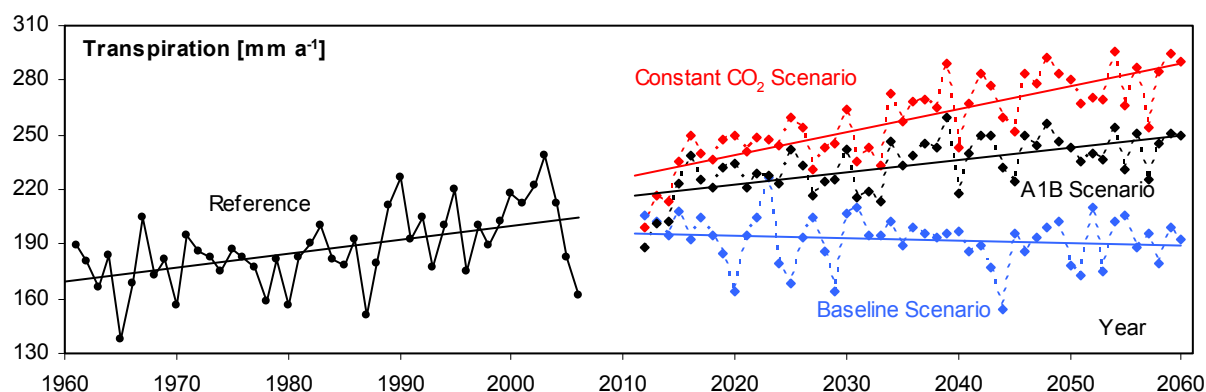


Figure 6.09: Annual sums of transpiration of an intensive grassland proxel from the middle of the Upper Danube catchment (457 m a.s.l.), calculated for the reference period (1961-2006) and for three different future storylines including the modified A1B scenario with and without assumed CO<sub>2</sub> increase and the unbiased baseline scenario (2011-2060).

While the “normal” A1B scenario showed the highest productivity among the different storylines (fig. 6.05), the mapped transpiration rates are subdued compared to the constant CO<sub>2</sub> scenario (slope = 0.67, R<sup>2</sup> = 0.40), accounting for the increased efficiency of gas exchange under elevated CO<sub>2</sub> conditions. Again, the modified A1B storyline features the smoothest continuation of the development of the transpiration rates that were modelled for the reference conditions (slope = 0.77, R<sup>2</sup> = 0.25).

Despite the decreasing average trend of the transpiration, the modelled average sum of transpiration is slightly higher for the scenario period compared to the reference results, although it is likely that the decrease of transpiration will continue if the scenario is expanded further into the future and the atmospheric CO<sub>2</sub> concentration is even more elevated.

Since the transpiration is a major component of the overall evapotranspiration, the average course of the total evapotranspiration is strongly determined by the development of the transpiration rates and therefore follows similar characteristics, although at a higher absolute level. The course of the evapotranspiration also is characterized by a slight increase during the reference period that is partly compensated by an even slighter decrease under the scenario conditions (fig. 6.10). The inanimate components of the evapotranspiration, the soil and the interception evaporation, are continuing their increasing course during the scenario, mostly due to the elevated water vapour deficit that is associated with the increased average temperatures.



The decline of the evapotranspiration under scenario conditions therefore is not as strong as that of the mere transpiration (*fig. 6.10, tab. 6.04*).

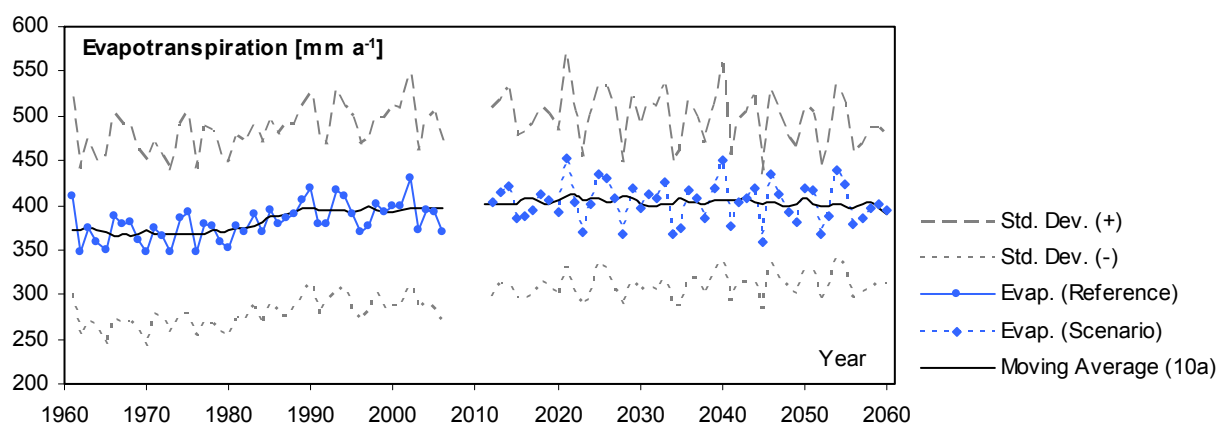


Figure 6.10: Course of the average annual sum of evapotranspiration within the Upper Danube Basin, modelled for the reference period from 1961 to 2006 and for the modified IPCC A1B scenario from 2011 to 2060, including the moving 10-year average and the respective standard deviations from the area mean.

Besides their parallel temporal development, the transpiration and the evapotranspiration are featuring similar spatial patterns. The change of the transpiration and of the evapotranspiration shows a striking North to South gradient, that optically divides the catchment area into a Northern part that features lower and a Southern part that shows higher evapotranspiration sums for the scenario conditions (*fig. 6.11*).

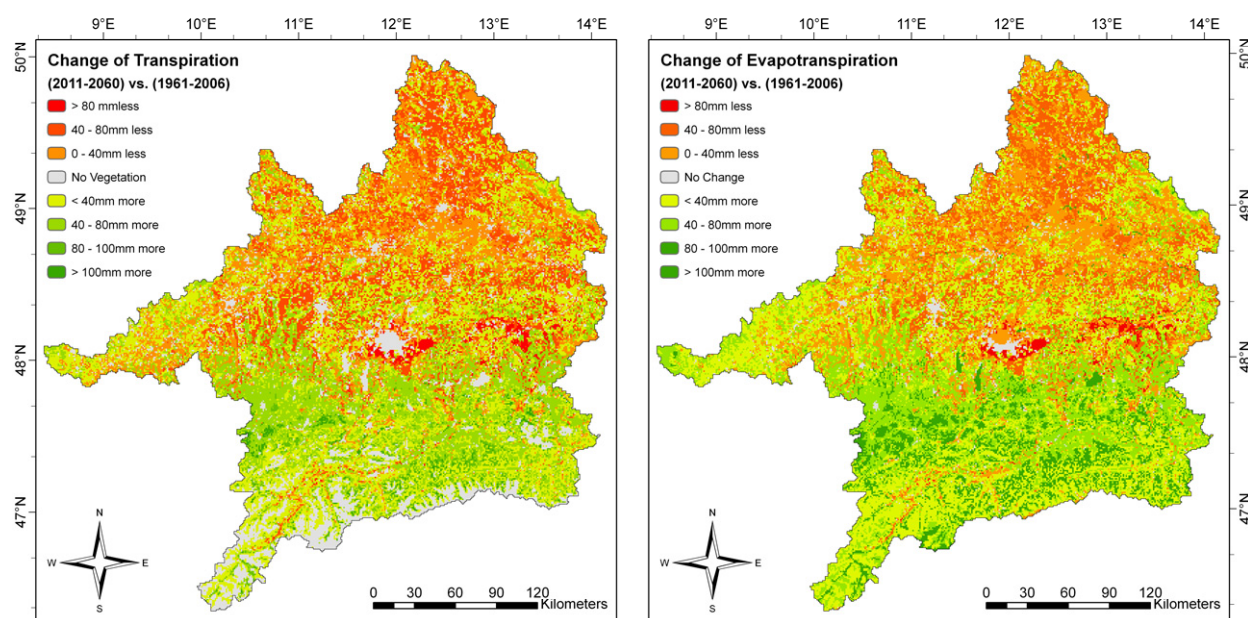


Figure 6.11: Map of change of the average annual sum of transpiration (left) and evapotranspiration (right) within the Upper Danube Basin, picturing the difference between the model results achieved for the reference period from 1961 to 2006 and for the modified IPCC A1B scenario from 2011 to 2060.

Obviously, the water supply is determining the spatial manifestation of the evapotranspiration. While the Northern part only features a small increase of water stress events during the

scenario period, the absolute frequency of drought stress is very high (see appendix A.17.8). The Southern part in contrast is the region that shows the most intense increase of drought stress events during the scenario (*fig. 6.06, right*), although it still features moderate water stress frequencies (see appendix A.17.8) and therefore is able to contribute to a higher evapotranspiration. The change of the evapotranspiration, in accordance with the other scenario results, is pointing towards a shift of the landscape characteristics that is progressing from North to South for the course of the scenario and is gradually accessing the alpine regions.

Spatial representations of the respective average sums of both, the transpiration and the evapotranspiration, that were calculated for the reference and the scenario period are available in the appendix (A.17.9 - 10).

The decrease of the summer precipitation and the generally elevated evapotranspiration both are contributing to a decrease of runoff during the course of the climate scenario (*fig. 6.12*). Nonetheless, the decrease of the discharge rates is somewhat diluted by the negative trend of the transpiration that partly compensates the decline of the rainfall. Although the absolute decrease of the average runoff at the main gauge of the Upper Danube catchment is veiled by the seasonal variability of the discharge to some degree, the expected trend features an average decline of nearly  $400 \text{ m}^3 \text{ s}^{-1}$ , or nearly a third of the average discharge rate respectively, in 50 years time (*fig. 6.12*). The high peaks of flood events that are characterising the observed gauge data are maintained for the scenario period to some degree (e.g. July of the year 2014, see *fig. 6.12*), while the runoff minima of the scenario are consistently lower compared to the reference series, indicating that the seasonal distribution of the rainfall is likely to lead to a significant decrease of the base flow during the summer months.

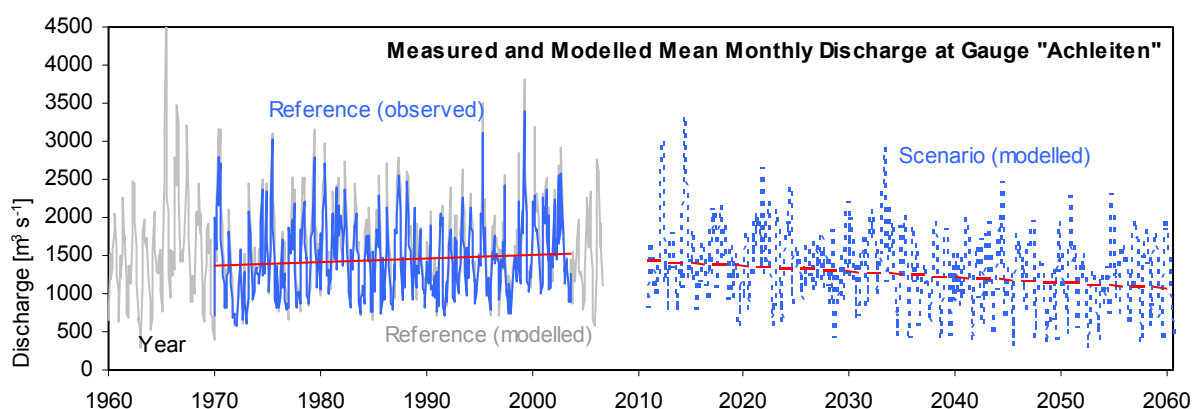


Figure 6.12: Monthly average rates of discharge for the main gauge of the Upper Danube Basin "Achleiten" (287 m a.s.l.). Measured data (1970-2003) and modelled runoff for the reference period (1970-2006) and the modified IPCC A1B climate scenario (2011-2060).

All of the investigated parameters showed dynamic reactions to the environmental changes that were assumed for the climate scenario. The reactions manifested in clearly discernable trends, while all parameters featured a preserved temporal and spatial variability that clearly matches



the fluctuations modelled for the observed conditions of the reference period. The baseline scenario was spot-checked for a set of reference proxels and did not return any trends as expected. This can be taken as an indication that the observed future trends are not due to a systematic bias of the model, but exclusively represent the models reaction to the climate scenario. The results therefore can be considered to provide a reliable information basis that does not feature extreme trends, but nonetheless is clearly giving notice of the directions of the changes that are likely to happen in a possible future that may resemble the assumptions that were made here for the regionally adapted IPCC A1B scenario.

## 7. Conclusion and Outlook

In the course of this work, a powerful instrument for the assessment of climate change enquiries has been constructed, validated and applied to a climate scenario. In order to achieve an active response of biological landsurface activities to climate change impacts, a biochemically based model of photosynthesis was integrated into a multiscale land surface model. The resulting coupled model approach then was applied to the mesoscale river catchment of the Upper Danube, firstly for reasons of model validation and secondly in order to launch investigations on the sensitivity of the modelled landsurface processes to altered environmental conditions.

The quality assessment of the coupled model approach was conducted on different scales, ranging from the detailed microscale of single test acres to the mesoscale of a diverse landscape. In comparison with measured and observed data, the model could prove its capability of a sound reproduction of aboveground plant physiological parameters, such as biomass, leaf area, canopy height and stages of phenological progress. The newly developed coupled model approach therefore can adequately be applied to studies that are concerned with plant physiological enquiries. At the mesoscale, the model was able to soundly trace evapotranspiration and runoff rates of a validated reference model. Consequently, the coupled model approach may well be applied to investigations concerning the dynamics of the landsurface water balance. The phenology model, which was applied for the description of the phenological progress of forest trees and which is supposed to have a determinant influence on the water balance of the river catchment, was able to closely reproduce phenological dates as they are documented in the literature. In total, the diverse validation efforts all returned good results, so that the new coupled model approach can be considered to be adequately developed and may well be confronted with future modelling enquiries.

The dynamic response of the model to changed environmental conditions was tested by applying the model to the simulation of a climate scenario. The attention thereby was directed to a moderate scenario rather than to extreme projections, thus increasing the plausibility of the simulation. The basis of the climate scenario was found in the internationally acknowledged IPCC A1B storyline as proposed by the Special Report on Emissions Scenarios by the Intergovernmental Panel on Climate Change, ensuring international comparability of the model results. By generating future meteorological driving parameters through a rearrangement of measured weather data, the feasibility of the future weather patterns can be considered to be high. The model results for the climate scenario featured variations and standard deviations that well matched the statistical characteristics of the reference model results, but at the same time returned clear trends of a possible future development for a selection of landsurface

parameters. A spot-checking of the model behaviour for a control scenario, which was constructed to feature constant temperature, rainfall and CO<sub>2</sub> conditions, could prove that the modelled trends are exclusively due to the models reaction to the changed environment parameters and cannot be traced to a general systematic bias of the model system. The modelled future projections therefore can be considered to represent a reasonable perspective of possible future developments.

Nonetheless, the model in its current configuration is still suffering some restrictions that might be subjected to a further development. For example, the model is assuming ideal nutrient conditions for the plant growth, unaware of possible fertilisation measures and atmospheric nitrogen depositions. Although the modelled biological activity is limited by the water supply and determined according to the temperature as well as to the supply of atmospheric carbon dioxide, which both are steering the velocity and the efficiency of the chemical reactions within the chloroplast, it does not include an explicit description of the nitrogen cycle. This nutrient cycle though determines the maintenance of the supply of the Rubisco receptor enzyme and therefore strongly influences the overall biological productivity (HANK ET AL. 2006). Also the reaction of the stomatal conductivity on atmospheric CO<sub>2</sub> enrichment may be influenced by the nitrogen status of the plant (KATTGE ET AL. 1997).

For a more intensive application of the model on the field scale, e.g. in the function of an agricultural production model, a further development with respect to a detailed description of the nutrient cycle and possible fertilization effects will be of utmost importance. If the model shall be applied as a model of agricultural production, additional management actions will have to be included in the algorithms. Also the realistic representation of mechanically inflicted yield losses, such as hailstorms, windbreak etc. will have to be taken care of in future versions of the model.

A simplifying assumption, which may be restricting the models applicability for investigations of drought stress effects, is that the vegetation routines do not explicitly account for crop damages due to longer phases of water shortage yet. The modelled plants are currently supposed to recover completely after a drought stress event, neglecting the loss of leaves or the desiccation of roots and twigs. An integration of a simulation of structural damage that gradually progresses with increasing drought stress intensity and duration will be a sensible expansion of the models functionality.

A reasonable approach for the integration of information on management actions, mechanically inflicted yield losses, pests and diseases or possible drought damages is represented by remote sensing techniques. A parameter that might account for a variety of those external restrictions for example is the fraction of absorbed photosynthetically active radiation. The so called fAPAR can be derived from remote sensing data with high precision. Especially hyperspectral remote sensing systems, which are capable of monitoring the behaviour of chlorophyll absorptance at

high spectral resolution for the respective spectral domain, could easily supply this information and thereby would greatly enhance the models functionality.

Concerning the photosynthesis core model it has to be critically considered that the model does not yet include an adaptive reaction of the plant metabolism to the atmospheric CO<sub>2</sub> enrichment under scenario conditions, as it was observed by KÖRNER (2006). The strong influence of the carbon dioxide supply on the modelled net rate of carbon allocation that could be verified in the scenario results therefore may be overrated to some degree. Model enhancements towards a more detailed reaction of the vegetation cover on elevated CO<sub>2</sub> conditions, such as those summarized for example by FANGMEIER AND JÄGER (2001), would greatly increase the reliability of the model predictions for larger climate scenarios that are ranging further into the future.

Another restriction of the model in its current version is the basic assumption of a static land cover. For small time periods, like those which are comprised by the calculations presented in the context of this work, static land cover information might be adequate, assuming a representation of the different land use categories that is balanced over the years due to the regionally adapted crop rotation. For the modelling of larger time periods under assumed climate change conditions, which may exceed 50 years of future projection, the regional composition of crops and natural areas is likely to change. For example, the lower water supply during the summer months will require the cultivation of crops that are more resistant to water stress. Also the elevation of annual mean temperatures may increase the risk of forest fires, which again may lead to an increased representation of natural succession areas in the landuse map. At the same time, the timberline may access more elevated terrain according to the rising temperatures, gradually expanding the forested areas in the alpine region. It has to be assumed that adaptations to the changed environment will be enforced, which will have to be considered when the future development of a natural entity, such as that of a river catchment, is investigated for larger time periods.

A validation study by MUERTH (2008) that was based on remote sensing data could reveal that the landsurface energy balance, modelled with the introduced approach, features lower than expected landsurface temperatures for vegetated proxels. First investigations are pointing towards an overestimation of the sensible heat flux from the leaves, combined with a slight underestimation of the canopy absorptance. The further improvement of the description of the leaf surface energy exchange therefore will be a sensible next step for the future development of the model.

A general difficulty that accompanies the modelling of detailed biological processes, as they occur in the cells of green plants, is the relatively high number of required specific input parameters. While for the landuse categories that are presented in detail within this work, the parameterization can be considered to be sufficiently developed, other land cover types remain that still need to be investigated further in order to provide improved adjustments for important

parameters. Although the model is physically based and is supposed not to be calibrated in any way, an application of the model under entirely different natural conditions may involve the adaptation of some of the parameters. Also an application in geographic regions that differ strongly from the premises of a central European landscape may raise the need to include further land cover types. For example a model application in extremely dry environments would have to result in an implementation of the Crassulacean Acid Metabolism (CAM) besides the  $C_3$  and  $C_4$  pathways, which are part of the endeavours of this thesis.

The development of a model is a process that features constant enhancements and improvements. It is one of the particularities of model development, which contributes to the fascination of this scientific field, that a model rarely is finished completely. Suggestions concerning a further development of the model always remain and provide interesting challenges for future work. The coupled PROMET\_Biological model here makes no exception. Although the model has reached a stage of development that well enables a model application for diverse scientific enquiries, the restrictions mentioned above provide appealing opportunities of improvement. It is a task that should gratefully be accepted in order to strengthen the role of computer aided modelling and decision support systems worldwide. While the increased reliability of computer aided simulations will lead to a better understanding of the concerned processes, the new cognition again will improve the hypotheses that are the basis of the model algorithms. This cycle of improvements is supposed to result in thoroughly developed decision support systems that will be able to reliably assist humanity with the management of the diverse challenges that the future changes of our environment may hold.

## 8. Summary

The central issue of this thesis is concerned with the investigation of vegetation related landsurface parameters under the impact of changing climate conditions. The spatial extent of the study is limited to the borders of the Upper Danube drainage basin, according to the requirements of the cooperative Project GLOWA-Danube (Global change of the Hydrological Cycle), funded by the German Ministry of Education and research (BMB+F).

In the frame of global change research, computer aided modelling has developed to an important resource during the last decades. Thereby models, which are capable of mapping landsurface parameters at high spatial and temporal resolution, play an important role. For investigations that are concerned with global change enquiries, models are required that are based on physical relations and whose description of the involved processes is accomplished by applying a minimum of empiricism. The application of physically based models requires the important basic assumption that the physical process description will also be stable, if the model is exposed to external conditions that are different to those of contemporary reference periods. Before a model can be applied to such investigations, it has to prove its functionality in comparison with measured data. A physically based model that has been validated through measurements, should consequently be capable of producing reliable information also when it is exposed to changed external conditions, like in a future scenario for example, at least as long as the variability of the external parameters is limited to a valid physical range.

Current publications are indicating that the dynamic behaviour of the vegetation cover often is inadequately accounted for in studies that are investigating the impacts of climate change with respect to the landsurface water cycle. In order to enable a dynamic feedback between the animate land cover and the atmosphere, which might be sensitive enough to trace active reactions of the vegetation cover on changing climatic conditions, the physically based land surface process model PROMET (Process of Radiation Mass and Energy Transfer Model) was enhanced by an explicit description of the growth activity of different plant types.

A well-established model of  $C_3$  photosynthesis was combined with a model approach for the description of the conductivity between leaf and atmosphere and furnished with extensions concerning the description of the  $C_4$  metabolism. Also a parameterization that applies to the modelling of forest trees was included. The outstanding character of this model is based on the description of the rate of photosynthetic activity as the result of the competing limitations due to the carbon dioxide supply on one hand and the possible rate of electron transport through the cell organs on the other. The model consequently includes an explicit description of the enzyme kinetics of the receptor enzyme ribulose-1.5-biphosphate-carboxylase/oxygenase (RUBISCO),

as well as of the active gas exchange between the location of the carbon fixation (chloroplast) and the atmosphere. The energy that is required for the photosynthesis is provided as the result of an explicitly modelled energy balance of the leaf, where energy inputs in form of absorbed radiation on one hand and energy losses in form of the sensible heat flux, emissions from the leaf and the loss of latent heat due to the stream of transpiration on the other are accounted for. The results of the photosynthesis routines, especially the rate of net carbon fixation and the rate of transpiration, are scaled from the microscale (leaf) to the mesoscale (landscape) via the Leaf Area Index (LAI). The photosynthetic products are distributed to the different plant organs following the example of the CERES growth models and in that way are determining the physiological appearance of the modelled canopy. In order to account for the seasonal dynamics of plant development, a modelling of the progress of phenological stages was integrated. While for some of the natural vegetation types static seasonal phases are assumed, the determination of the growth stages of agricultural crops as well as of grassland is modelled dynamically. A special relevance with respect to the landscape water balance is associated with the phenological behaviour of forest trees. The incidence of the determinant growth stages of forest therefore is also simulated dynamically.

In order to test the stability of the applied physical relations, the model was subjected to an intensive validation program. First of all, the sensitivity of the model algorithms was investigated at the high resolution field scale (10 m). For this spatial scale, field measurements could be acquired by means of intensive field campaigns that were conducted in the frame of the project „Coupled Analysis of Vegetation Chlorophyll and Water Content Using Hyperspectral, Bidirectional Remote Sensing“, which was funded by the German research Foundation (DFG). Two stands of winter wheat, representing  $C_3$  crops, and two fields of maize, exemplary for  $C_4$  crops, could be acquired as test sites for the campaigns. For both plant types, the model achieved good to very good results concerning the overall biomass production and the allocation of the assimilates to the different aboveground plant parts. Also the development of the leaf area and of the canopy height was well reproduced by the model. A detailed analysis of the models potential concerning the yield estimation of agricultural sites could reveal that, although the model is well able to reproduce the mean yield, it proved to be insensitive to the mapping of zones of low productivity, which are due to mechanically induced stress or to the occurrence of pests and diseases respectively. The modelled agricultural yield therefore tends to be generally overestimated.

In a second step, the model was applied to a coarser spatial resolution of 1 km, which applies to the mesoscale, and again was compared to field measurements. For extensive as well as for intensive grassland, the model could prove that the accumulation of biomass and the height of the canopy are reproduced realistically. Although the measures of agricultural management as they are accounted for in the model, like e.g. the different count of cuts per season for intensive

and extensive grassland, were well mapped, discrepancies of management actions may temporarily lead to strong deviations between modelled and measured parameters.

Some modelled parameters cannot easily be measured in their spatial manifestation, like for example evapotranspiration. For the investigation of the models capability with respect to the simulation of the evapotranspiration components, a comparison with a reference model was conducted. Only a model that is thoroughly validated for different scales and regions can be applied as reference source. Concerning the reproduction of the landscape evapotranspiration, the reliability of the reference model has to be assessed through the comparative analysis of modelled runoff rates with hydrographs that are measured at the gauge of the drainage area. The PROMET model, besides the biological approach that is presented in this thesis, is capable of calculating the landsurface evapotranspiration alternatively applying the Penman-Monteith equation. This is accomplished in combination with a straightforward description of the vegetation activity, which is more or less restricted in terms of dynamics, although seasonally variable. Thanks to the parallel architecture of both models (PROMET\_Penman-Monteith and PROMET\_Biological), a comparative analysis could be conducted that was based on identical input data for a reference period of 1961 to 2006. For this 46-year period, both models returned analogue annual sums of evapotranspiration, although the annual courses of the evapotranspiration components partly differed noticeably. The biological PROMET returned slightly less evapotranspiration on average, combined with a somewhat higher spatial variability, than the PROMET-Penman-Monteith approach. The annual sum of evapotranspiration was well traced by the biological model, concerning the temporal course as well as the spatial variability. The relative deviations between both models stayed below 20 % for nearly the whole Upper Danube Basin. An equally good correlation was found between the modelled runoff of both model approaches. Compared to measured runoff data, the biological approach and the Penman-Monteith model likewise returned good results.

The functionality of the model with respect to a mapping of the determinant phenologic phases of forest trees finally could be investigated in comparison with data taken from the literature. The literature values are based on the analysis of long-term data, which is derived from the European network of International Phenological Gardens. It could be shown that the mean incidences as well as the temporal dynamics of the phenologic phases are well documented by the model. The high temporal variability that characterises the observed data though could not be traced with its full range by the model.

Considering the good results of the different validation efforts it can be stated that the model soundly demonstrated its capability concerning the precise reproduction of a variety of structural landsurface variables on different scales under observed climatic conditions. An application of the model to the calculation of climate scenarios therefore seems appropriate.



In order to enable comparability with international research approaches, the internationally acknowledged global change scenarios developed by the Intergovernmental Panel on Climate Change (IPCC), were basically applied. The moderate A1B emissions scenario, which is based on the assumption of a balanced future development of different energy technologies, was selected and modified by a regional impact factor that was assumed to apply to the local situation of the Upper Danube catchment. The impact factor was determined through an analysis of the measured long-term data of 360 weather stations from the Upper Danube region. The change of the annual mean temperature that was accounted for in the scenario model runs adds up to an increase of the average temperature of roughly 3.4 °C until the year 2060 compared to the time period of 1980 to 1999, while the increase of the atmospheric CO<sub>2</sub> concentration was modelled to meet a value of roughly 550 ppm in the year 2060. The meteorological input data required for the modelling of the future scenarios was generated through a shuffling of the measured relations of temperature and rainfall, based on a stochastic approach. In order to assess the models sensitivity with respect to changing climatic conditions, a baseline scenario also was calculated. This control scenario featured constant annual mean temperatures from the year 2006 on, without a discernable increasing trend. The atmospheric concentration of carbon dioxide also was assumed to stay constant at a level that applies to 1970 ( $\approx$  326 ppm) for the baseline scenario.

Being applied to the regionally adapted IPCC A1B climate scenario, the model returned clear statements, projecting a possible future development of selected landsurface parameters within the Upper Danube area. Concerning the phenological behaviour of forest trees, the model simulated a strong trend towards earlier incidence of the leaf emergence of deciduous as well as of the mayshoot of coniferous trees, contributing to a significant elongation of the vegetation period. These longer phases of active growth in combination with the rising temperatures and the elevated supply of atmospheric carbon dioxide led to an increase of biological activity in the model results that manifested in increasing rates of biomass accumulation for the Upper Danube area. The increased biological activity in combination with the strong decrease of summer precipitation, which was assumed in the climate scenario, again led to an escalating frequency of drought stress events in the Upper Danube Basin. Not only the average count of water stress events per year was modelled to increase, but also a spatial extension of the regions that are affected by drought stress was mapped by the model. This general increase of water stress and the significant decrease of summer precipitation entailed a slight decline of the transpiration and evapotranspiration of the Upper Danube area in the scenario results. The modelled decline of the summer precipitation also resulted in a noticeable decrease of the modelled average discharge rates at the main gauge of the basin. The base flow rates during the summer months thereby are likely to be primarily affected.

Since the model results for the scenario period featured temporal and spatial variations and standard deviations that were closely matching the statistics of the reference period, while at the same time they showed clear trends though they were avoiding extreme realizations, the scenario assumptions can be considered to be reliable. The baseline scenario, which was spot-checked for a set of reference proxels, did not return any trends as expected, indicating that the observed future trends are not of systematic origin.

Although, within the scope of this work, the coupled model approach has been developed to a degree that well justifies an application to scientific issues, there still remain fields that may be subjected to further enhancements, based on the perception that a model never is developed completely, but rather is always open to constant modifications and improvements. For instance the implementation of an explicit description of the nutrient fluxes would greatly enhance the models functionality with respect to agricultural purposes. In the context of agricultural applications, a dynamic coupling of the model with remote sensing techniques is especially promising. Also it may be the case that some of the landuse specific parameters may have to be refined or adjusted for an application of the model in natural conditions that strongly differ from the central European premises, which were basically consulted for the development of the model.

The further development of the introduced model approach is an appealing challenge, which might considerably contribute to the improvement of computer aided decision support systems. It can be assumed that the progress of the development of physically based models due to a more profound understanding of the processes on one hand and the sophistication and refinement of the model algorithms that result from the increase of knowledge on the other, may contribute to the development of reliable systems, that will be able to sustainably assist humanity with the handling of future environmental challenges.

## 9. Zusammenfassung (German)

Die vorliegende Arbeit beschäftigt sich mit der Untersuchung von vegetationsbezogenen Landoberflächenparametern unter dem Einfluss sich ändernder Klimabedingungen. Die räumliche Basis bildet dabei das Einzugsgebiet der oberen Donau, entsprechend der Anforderungen des vom Deutschen Bundesministerium für Bildung und Forschung (BMB+F) geförderten Verbundprojektes GLOWA-Danube (Globaler Wandel des Wasserkreislaufs).

Im Laufe der letzten Jahrzehnte haben sich computergestützte Modelle zu wichtigen Werkzeugen der Forschung entwickelt. Im Rahmen der Global Change Forschung nehmen Modelle, die in der Lage sind Landoberflächenprozesse in hoher räumlicher und zeitlicher Auflösung zu reproduzieren, eine besonders wichtige Rolle ein. Für Untersuchungen im Zusammenhang mit Global Change Fragestellungen sind Modelle vonnöten, die vorwiegend auf physikalischen Beziehungen basieren und deren Prozessbeschreibung dementsprechend auf ein Minimum an empirischen Annahmen beschränkt ist. Bei der Arbeit mit physikalisch basierten Modellen wird die wichtige Grundannahme getroffen, dass die physikalischen Algorithmen auch dann stabil sind, wenn das Modell mit externen Bedingungen konfrontiert wird, die von denen aktueller Referenzzeiträume abweichen. Bevor ein Modell aber für eine solche Untersuchung angewendet werden kann, muss seine Funktionalität im Vergleich mit gemessenen Daten überprüft werden. Ein solcherart validiertes und physikalisch basiertes Modell, sollte, entsprechend der Grundannahme der physikalischen Stabilität, in der Lage sein, auch für veränderte externe Bedingungen, wie sie z.B. in Zukunftsszenarien angewendet werden, verlässliche Aussagen treffen zu können, solange sich die Variabilität der externen Bedingungen innerhalb gültiger physikalischer Grenzen bewegt.

In der aktuellen Literatur wird beschrieben, dass das dynamische Verhalten der Vegetationsdecke in zeitgenössischen Studien zur Untersuchung von Auswirkungen des Klimawandels auf den Landschaftswasserhaushalt nur unzureichend berücksichtigt wird. Um eine dynamische Rückkopplung zwischen der belebten Landoberfläche und der Atmosphäre herzustellen, die auch in der Lage ist eine aktive Reaktion der Vegetationsdecke auf sich verändernde klimatische Bedingungen abzubilden, wurde im Rahmen dieser Arbeit das physikalisch basierte Landoberflächenprozessmodell PROMET (Process of Radiation Mass and Energy Transfer Model) um eine explizite Beschreibung des Wachstumsverhaltens verschiedener Pflanzentypen erweitert.

Dazu wurde ein etabliertes Modell zur Berechnung der Photosynthese von  $C_3$  Pflanzen mit einem Modellansatz zur Beschreibung der Leitfähigkeit zwischen Blatt und Atmosphäre kombiniert und mit Erweiterungen für die Beschreibung des  $C_4$  Metabolismus, sowie einer

Parametrisierung für die Modellierung von Waldbäumen versehen. Die prinzipbedingte Besonderheit dieses Modellansatzes ist, dass die photosynthetische Aktivität als potenzielle Assimilationsrate beschrieben wird, die durch das Angebot an verfügbarem Kohlendioxid auf der einen und durch die Elektronentransportkapazität der Mitochondrien auf der anderen Seite limitiert wird. Das Modell beinhaltet dementsprechend eine explizite Beschreibung der Enzymkinetik des Rezeptorenzyms Ribulose-1.5-Biphosphat-Carboxylase/Oxygenase (RUBISCO), sowie des aktiven Gaswechsels zwischen dem Ort der Kohlenstofffixierung (Chloroplast) und der Atmosphäre. Die zur Photosynthese benötigte Energie wird dem Modell als Restglied einer explizit modellierten Energiebilanz der Blattoberfläche zur Verfügung gestellt, wobei Energieinputs in Form von absorbierter Strahlung auf der einen und Energieverluste in Form von fühlbarer Wärme, langwelliger Ausstrahlung und latentem Wärmeverlust durch den Transpirationsstrom auf der anderen Seite berücksichtigt werden.

Die Ergebnisse der Photosyntheseroutinen, hervorzuheben sind hier die Raten der netto Kohlenstofffixierung sowie der Transpiration, können mit Hilfe des Blattflächenindex (LAI) von der Mikroskala (Blatt) auf die Mesoskala (Landschaftsebene) transponiert werden. Die Produkte der Photosynthese werden in Anlehnung an die CERES Wachstumsmodelle in die verschiedenen Pflanzenorgane verteilt und bestimmen so das äußere Erscheinungsbild der modellierten Vegetationsdecke. Um auch die jahreszeitliche Dynamik der Vegetationsentwicklung zu berücksichtigen, wurde eine Modellierung des Fortschreitens der phänologischen Phasen integriert. Während für einige natürliche Vegetationstypen feste Phasen in Abhängigkeit der Jahreszeit angenommen werden, erfolgt die Bestimmung der Wachstumsstadien von Ackerpflanzen und Grünland dynamisch. Eine besondere Bedeutung im Hinblick auf den Landschaftswasserhaushalt kommt der phänologischen Entwicklung von Waldbäumen zu. Sie wurde dementsprechend ebenfalls dynamisch implementiert.

Um die physikalische Stabilität der verwendeten Beziehungen zu überprüfen, wurde das Modell einer intensiven Validierung unterzogen. Dabei wurde zunächst das Verhalten der Modellalgorithmen auf der hoch aufgelösten Feldskala (10 m) untersucht. Die entsprechenden Messdaten konnten auf dieser Skala durch intensive Geländemessungen bereitgestellt werden, die im Rahmen des von der deutschen Forschungsgemeinschaft (DFG) geförderten Projektes „Coupled Analysis of Vegetation Chlorophyll and Water Content Using Hyperspectral, Bidirectional Remote Sensing [Gekoppelte Analyse des Chlorophyll- und Wassergehaltes von Vegetation mit Hilfe von hyperspektraler, bidirektionaler Fernerkundung]“ erhoben wurden. Als Testflächen standen hierfür zwei Winterweizenfelder ( $C_3$ ) sowie zwei Maisfelder ( $C_4$ ) zur Verfügung. Das Modell zeigte für beide Pflanzentypen gute bis sehr gute Ergebnisse im Bezug auf die Gesamtbiomasseproduktion und die Allokation der Assimilate in den verschiedenen oberirdischen Pflanzenteilen. Auch die Entwicklung der Blattfläche und der Bestandeshöhe wurde vom Modell gut reproduziert. Eine Analyse des Potentials zur Ertragsmodellierung von

landwirtschaftlichen Flächen konnte zeigen, dass das Modell zwar in der Lage ist mittlere Erträge gut zu reproduzieren, jedoch Niederertragszonen, die auf mechanische oder parasitische Beeinträchtigungen des Wachstums zurückzuführen sind, ignoriert und dementsprechend zu einer Überschätzung des Ertrages neigt.

In einem zweiten Schritt wurde das Modell auf einer, der Mesoskala entsprechenden, größeren räumlichen Auflösung von 1 km angewendet und wiederum mit Messdaten verglichen. Für extensiv und intensiv bewirtschaftete Grünlandflächen konnte gezeigt werden, dass die Akkumulation der Biomasse, sowie die Bestandeshöhe vom Modell realistisch wiedergegeben werden. Obwohl die im Modell abgebildeten landwirtschaftlichen Maßnahmen, wie z. B. die unterschiedliche Anzahl der Wiesenschnitte bei extensiv und intensiv genutzten Flächen, teilweise gut erfasst wurden, können diesbezügliche Diskrepanzen temporär zu hohen Abweichungen zwischen Modell und Messung führen.

Um auch Modellparameter zu untersuchen, die sich einer direkten Messbarkeit ihrer flächenhaften Ausprägung entziehen, wie z.B. die Evapotranspiration, wurde ein Vergleich mit einem Modell angestrebt, dessen Verlässlichkeit im Bezug auf die Berechnung der Gebietsverdunstung bereits im Vergleich mit Pegel-Abflussdaten bewiesen wurde. Das Modell PROMET ermöglicht die Berechnung der Landoberflächenverdunstung neben dem hier vorgestellten Ansatz auch entsprechend der Penman-Monteith Methode, allerdings in Kombination mit einer zwar jahreszeitlich variablen, aber aufgrund von mehrheitlich statischer Parametrisierung insgesamt eingeschränkt dynamischen Beschreibung der Vegetationsaktivität. Durch die parallel gestaltete Architektur der beiden Modelle (PROMET\_Penman-Monteith und PROMET\_Biological), ließ sich eine vergleichende Analyse durchführen, die auf identischen Eingabedaten für einen Referenzzeitraum von 1961 bis 2006 berechnet wurde. Beide Modelle zeigten analoge Jahressummen der Evapotranspiration für diese 46-jährige Zeitreihe, obgleich die jährlichen Verläufe von Trans- und Evapotranspiration teilweise große Unterschiede aufwiesen. Das PROMET\_Biological Modell simulierte im Mittel geringfügig kleinere Verdunstungsraten als das Penman-Monteith Modell, allerdings in Kombination mit einer gesteigerten räumlichen Variabilität. Die Jahressummen der Evapotranspiration wurden vom Biological Modell hinsichtlich des zeitlichen Verlaufs und auch der räumlichen Variabilität gut wiedergegeben. Die relativen Abweichungen zwischen beiden Modellen blieben unterhalb einer Schwelle von 20 % für den größten Teil des Einzugsgebietes der Oberen Donau. Ebenfalls gute Korrelationen wurden hinsichtlich der modellierten Abflüsse erzielt. Im Vergleich mit gemessenen Abflussdaten, konnten beide Modellansätze, der explizite Gaswechselansatz und die Penman-Monteith-Methode, vergleichbar gute Ergebnisse verzeichnen.

Die Funktionalität des Modells im Hinblick auf die Abbildung der wesentlichen phänologischen Phasen von Waldbäumen konnte schließlich im Vergleich mit Literaturwerten, die auf der Analyse von Messdaten des Europäischen Netzwerks der Internationalen Phänologischen

Gärten beruhen, untersucht werden. Es zeigte sich, dass die mittleren Eintrittstermine, sowie die zeitliche Dynamik der Phasen, sehr gut vom Modell erfasst werden. Die hohe zeitliche Variabilität der aus Beobachtungen stammenden Eintrittstermine konnte in den Modellergebnissen allerdings nicht erreicht werden.

Insgesamt konnte gezeigt werden, dass der vorgestellte Modellansatz in der Lage ist, eine Vielzahl an Landoberflächen- und Vegetationsvariablen unter gegenwärtigen Klimabedingungen auf unterschiedlichen Skalen mit hoher Genauigkeit wiederzugeben, so dass eine Anwendung des Modells für die Berechnung von Landoberflächenprozessen unter Szenarienbedingungen angemessen erscheint.

Um die Vergleichbarkeit mit internationalen Studien zu gewährleisten, wurden die international anerkannten Global Change Szenarien des Intergovernmental Panel on Climate Change (IPCC) als Ausgangsbasis verwendet. Das moderate A1B Emissions-Szenario, das von einer zukünftigen Ausgewogenheit bei der Entwicklung von verschiedenen Energietechnologien ausgeht, wurde mit einem lokalen Wirkungsfaktor verrechnet, der sich aus der Analyse der vorhandenen Messdaten aus 360 Klimastationen des Einzugsgebietes der oberen Donau und seiner unmittelbaren Umgebung ergab. Die bei der Modellierung berücksichtigte mittlere Temperaturerhöhung beträgt dementsprechend ca. 3.9 °C bis zum Jahr 2060 im Vergleich zum Temperaturmittel des Jahres 1960, bei einem gleichzeitigen Anstieg der atmosphärischen Kohlendioxidkonzentration auf ca. 550 ppm. Die meteorologischen Eingabedaten, die für die Modellierung der Zukunftsszenarien erforderlich waren, wurden durch eine Neuordnung der gemessenen Temperatur-Niederschlagsbeziehungen bereitgestellt, die auf einem stochastischen Verfahren basiert. Um die Sensitivität des Modells im Bezug auf eine Änderung der klimatischen Verhältnisse zu untersuchen, wurde zusätzlich ein Vergleichsszenario berechnet. Das Vergleichs-, oder Basislinienszenario geht von einer konstanten, trendfreien Entwicklung der Jahresmitteltemperatur ab dem Jahr 2006 aus. Die atmosphärische Kohlendioxidkonzentration wurde für das Basislinienszenario als konstant auf dem Niveau von 1970 ( $\approx 326$  ppm) angenommen.

Die Anwendung des Modells auf das regional angepasste IPCC A1B Szenario ergab deutliche Aussagen bezüglich der zukünftigen Entwicklung ausgewählter Landoberflächenparameter innerhalb des Einzugsgebietes der Oberen Donau. Im Bezug auf die phänologische Entwicklung von Waldbäumen wurde vom Modell unter Szenariobedingungen eine starke Tendenz zu einem verfrühten Einsetzen des Blattaustriebs von Laubbäumen sowie des Maitriebs von Nadelbäumen simuliert, was in einer deutlichen Verlängerung der Vegetationsperiode im Modell resultierte. Diese verlängerten Wachstumsphasen wiederum führten, in Verbindung mit der dem Wachstum förderlichen erhöhten Temperatur sowie der erhöhten atmosphärischen Kohlendioxidkonzentration, zu einer Zunahme der photosynthetischen Aktivität, die sich in einem starken Ansteigen der jährlichen

Trockenmassefixierung widerspiegelte. Die erhöhte Wachstumsaktivität, zusammen mit den im Szenario als stark rückläufig angenommenen Sommerniederschlägen, zog ein starkes Ansteigen der Häufigkeit von Trockenstressereignissen im Einzugsgebiet nach sich. Die Simulation signalisierte nicht nur eine Zunahme der mittleren Häufigkeit von Trockenstressereignissen, sondern auch eine räumliche Ausdehnung der von Wasserstress betroffenen Gebiete. Die allgemein höhere Trockenstressbelastung und der signifikante Rückgang der Sommerniederschläge im Klimaszenario führten zu einem leichten Absinken der modellierten Transpirations- sowie der Gesamtverdunstungssummen des Einzugsgebietes der Oberen Donau. Trotz der leicht verringerten Verdunstungsraten, führte der modellierte Rückgang der Sommerniederschläge zu einer spürbaren Abnahme der Abflusssummen am Hauptpegel des Einzugsgebietes. Es ist anzunehmen, dass die sommerlichen Niedrigwasserabflüsse von dieser Entwicklung besonders betroffen sein werden.

Die Modellergebnisse für den Szenarienzeitraum zeigten zeitliche und räumliche Varianzen und Standardabweichungen, die mit den statistischen Eigenschaften der Ergebnisse des Referenzzeitraumes vergleichbar waren. Obwohl die Szenarienrechnungen entsprechend des moderat gewählten Klimaszenarios keine extremen Zukunftsperspektiven zeichnen, identifizierten die Modellrechnungen eindeutige Trends für eine mögliche zukünftige Entwicklung ausgewählter Landoberflächenparameter. Das Vergleichsszenario, bei dem Temperatur, Niederschlag und die atmosphärische Kohlendioxidkonzentration als konstant angenommen wurden, zeigte in stichprobenartigen Untersuchungen erwartungsgemäß keine eindeutigen Tendenzen. Eine systematische Ursache kann demnach für die aus den Szenarienrechnungen abgeleiteten Trends ausgeschlossen werden.

Obwohl der gekoppelte Modellansatz im Rahmen dieser Arbeit bis zu einer Reife entwickelt wurde, die einen Einsatz des Modells für wissenschaftliche Fragestellungen rechtfertigt, so ergeben sich, entsprechend der grundsätzlichen Annahme dass ein Modell niemals gänzlich fertig entwickelt und ständigen Veränderungen und Verbesserungen unterworfen sein wird, selbstverständlich Möglichkeiten der Weiterentwicklung. Beispielsweise würde die Implementierung einer expliziten Beschreibung der Nährstoffflüsse die Anwendbarkeit des Modells für landwirtschaftliche Fragestellungen deutlich erhöhen. Im Zusammenhang mit einer landwirtschaftlichen Anwendung erscheint eine dynamische Kopplung des Modells mit Fernerkundungsmethoden besonders vielversprechend. Ebenso ist nicht auszuschließen, dass einige der landnutzungsspezifischen Modellparameter noch verfeinert, bzw. für eine Anwendung des Modells in bisher nicht berücksichtigten Naturräumen, angepasst werden müssen.

Die Weiterentwicklung des hier vorgestellten Modellansatzes ist eine anspruchsvolle und reizvolle Herausforderung, die einen wesentlichen Beitrag zur Verbesserung von computergestützten Entscheidungsunterstützungssystemen leisten kann. Es ist davon auszugehen, dass die

fortschreitende Entwicklung physikalisch basierter Modelle durch eine Verbesserung des Verständnisses der abgebildeten Prozesse auf der einen und eine daraus hervorgehende Verfeinerung der Modellalgorithmen auf der anderen Seite, dazu beitragen wird verlässliche Systeme zu schaffen, die in der Lage sein werden die Menschheit beim Umgang mit zukünftigen klimatisch bedingten Herausforderungen nachhaltig zu unterstützen.



## 10. References

- ACC AND SCN (United Nations Administrative Committee on Coordination and Standing Committee on Nutrition) (Edt.) (2004): Fifth report on the world nutrition situation: Nutrition for improved development outcomes. Geneva, pp. 143.
- ADIKU, S. G. K., BRADDOCK, R. D. AND ROSE, C. W. (1996): Modeling the effect of varying soil water on root growth dynamics of annual crops. *Plant and Soil*, Volume 185, Issue 1, pp. 125–136.
- ADIKU, S. G. K., REICHSTEIN, M., LOHILA, A., DINH, N. Q., AURELA, M., LAURILA, T., LUEERS, J. AND TENHUNEN, J. D. (2006): PIXGRO: A model for simulating the ecosystem CO<sub>2</sub> exchange and growth of spring barley. *Ecological Modelling*, Volume 196, Issue 1-2, pp. 149-162.
- AG BODEN (2005): Bodenkundliche Kartieranleitung - 5. Auflage [Instructions to Pedologic Field Mapping- 5<sup>th</sup> edition]. Hannover, pp. 392.
- ARNELL, N. AND LIU, C. (2001): Hydrology and water resources. In: MCCARTHY, J. J., CANZIANI, O. F., LEARY, N. A., DOKKEN, D. J. AND WHITE, K. S. (Eds.): Climate Change 2001: Impacts, Adaptation and Vulnerability, contribution of Working Group II to the Third Assessment Report of the Intergovernmental Panel on Climate Change. Cambridge University Press, pp. 191-233.
- BACOUR, C., BARET, F., BEAL, D., WEISS, M. AND PAVAGEAU, K. (2006): Neural network estimation of LAI, fAPAR, fCover and LAIxCab, from top of canopy MERIS reflectance data: Principles and validation. *Remote Sensing of Environment*, Volume 105, Issue 4, pp. 313-325.
- BALDOCCHI, D. D. (1994): An analytical solution for coupled leaf photosynthesis and stomatal conductance models. *Tree Physiology*, Volume 14, Issue 7-9, pp. 1069–1079.
- BALDOCCHI, D. D., HICKS, B. B. AND CAMARA, P. (1987): Canopy stomatal resistance model for gaseous deposition to vegetated canopies. *Atmospheric Environment*, Volume 21, Issue 1, pp. 91-101.
- BALL, J., WOODROW, I. AND BERRY, J. (1986): A model predicting stomatal conductance and its contribution to the control of photosynthesis under different environmental conditions. *Progress in Photosynthesis Research*, Volume 4, pp. 221-224.
- BARTHEL, R., ROJANSCHI, V., WOLF, J. AND BRAUN, J. (2005): Large-scale water resources management within the framework of GLOWA-Danube. Part A: The groundwater model. *Physics and Chemistry of the Earth*, Volume 30, Issue 6-7, pp. 372-382.
- BASSHAM, J., BENSON, A. AND CALVIN, M. (1950): The path of carbon in photosynthesis. *Journal of Biological Chemistry*, Volume 185, Issue 2, pp. 781-787.
- BAUMGARTNER, A. AND LIEBSCHER, H. J. (1996): Allgemeine Hydrologie: Quantitative Hydrologie 2. Auflage [Universal Hydrology: Quantitative Hydrology 2<sup>nd</sup> Edition]. Borntraeger, Berlin, pp. 693.

- BAYERISCHES LANDESAMT FÜR STATISTIK UND DATENVERARBEITUNG (Edt.) (2001-2003): Ergebnisse der Agrarstrukturerhebung 1995. Datenbankabfragen des Bayerischen Landesamtes für Statistik und Datenverarbeitung. [Results of the Agricultural Composition Census 1995. Data Base Queries of the Bavarian State Office for Statistics and Data Handling]. München.
- BAYERISCHES STAATSMINISTERIUM FÜR LANDWIRTSCHAFT UND FORSTEN (Edt.) (2006): Bayerischer Agrarbericht 2006 [Bavarian Agricultural Report 2006]. Referat Bayerische Agrarpolitik, Sonderaufgaben, Agrarstatistik, Wirtschaftsbeobachtung. München, pp. 240.
- BAYERISCHES STAATSMINISTERIUM FÜR LANDWIRTSCHAFT UND FORSTEN (Edt.) (2004): Land- und Forstwirtschaft in Zahlen – Daten und Fakten 2004 [Agriculture and Forestry in Numbers - Data and Facts 2004]. Referat Öffentlichkeitsarbeit Agrarstatistik, Wirtschaftsbeobachtung, München.
- BERRY, J. AND FARQUHAR, G. (1978): The CO<sub>2</sub> concentrating function of C<sub>4</sub> photosynthesis. A biochemical model. In: HALL, D., COOMBS, J. AND GOODWIN, T. (Eds.): Proceedings of the 4<sup>th</sup> International Congress on Photosynthesis. The Biochemical Society, Reading, London, England, pp. 119-131.
- BETTS, R. A., BOUCHER, O., COLLINS, M., COX, P. M., FALLOON, P. D., GEDNEY, N., HEMMING, D. L., HUNTINGFORD, C., JONES, C. D., SEXTON, D. M. AND WEBB, M. J. (2007): Projected increase in continental runoff due to plant responses to increasing carbon dioxide. *Nature*, Volume 448, Issue 7157, pp. 1037-1041.
- BETTS, R. A., COX, P. M., LEE, S. E. AND WOODWARD, F. I. (1997): Contrasting physiological and structural vegetation feedbacks in climate change simulations. *Nature*, Volume 387, Issue 6635, pp. 796-799.
- BGR - BUNDESANSTALT FÜR GEOWISSENSCHAFTEN UND ROHSTOFFE (Edt.) (2000): Legende zur Bodenübersichtskarte 1:1 Mio. [Legend of the Soil Survey Map 1:1 Mio.]. Hannover.
- BIOLOGISCHE BUNDESANSTALT FÜR LAND- UND FORSTWIRTSCHAFT (Edt.) (1997): Growth Stages of Mono- und Dicotyledonous Plants. Blackwell Wiss.-Verlag, Berlin, Wien, pp. 158.
- BISCOE, P. V., COHEN, Y. AND WALLACE, J. S. (1976): Community water relations. Daily and seasonal changes of water potential in cereals. *Philosophical Transactions of the Royal Society of London*, Volume B 273, pp. 565-580.
- BLFW – BAYERISCHES LANDESAMT FÜR WASSERWIRTSCHAFT (Edt.) (1999): Deutsches Gewässerkundliches Jahrbuch – Donaugebiet 1995 [German Hydrological Yearbook – Danube Area 1995]. Munich, pp. 307.
- BJÖRKMAN, O., DEMMING, B. (1987): Photon yield of oxygen evolution and chlorophyll fluorescence characteristics at 77 K among vascular plants of diverse origin. *Planta*, Volume 170, Issue 4, pp. 489–504.
- BMU - BUNDESMINISTERIUM FÜR UMWELT, NATURSCHUTZ UND REAKTORSICHERHEIT (Edt.) (2003): Hydrologischer Atlas von Deutschland [Hydrological Atlas of Germany]. Berlin.
- BONDEAU, A., SMITH, P., ZAEHLE, S., SCHAPHOFF, S., LUCHT, W., CRAMER, W., GERTEN, D., LOTZE-CAMPEN, H., MÜLLER, C., REICHSTEIN, M. AND SMITH, B. (2007): Modelling the role of agriculture for the 20th century global terrestrial carbon balance. *Global Change Biology*, Volume 13, Issue 3, pp. 679-706.

- BOTKIN, D. B., JANAK, J. F. AND WALLIS, J. R. (1972): Some ecological consequences of a computer model of forest growth. *Journal of Ecology*, Volume 60, pp. 849-872.
- BOUMAN, B. A. M., VAN KEULEN, H., VAN LAAR, H. H. AND RABBINGE, R. (1996): The 'School of de Wit' crop growth simulation models: A pedigree and historical overview. *Agricultural Systems*, Volume 52, Issue 2-3, pp. 171-198.
- BOX, E. O. (1981): Macroclimate and plant forms: An introduction to predictive modeling in phytogeography. *Tasks for Vegetation Science*. Dr. W. Junk BV Publ., The Hague, pp. 271.
- BOYER, J. S. (1976): Water deficits and photosynthesis. In: KOZLOWSKI, T. T. (Edt.): *Water Deficits and Plant Growth*. New York: Academic Press, Volume 4, pp. 153–190.
- BRAUN, M (2007): The Segmentation of Reflectances from Moderate Resolution Remote Sensing Data for the Retrieval of Land Cover Specific Leaf Area Index. Ph.D., LMU München: Fakultät für Geowissenschaften, pp. 223.
- BRONSTEIN, I. N. AND SEMENDJAJEW, K. A. (1981): Taschenbuch der Mathematik [Pocket Book of Mathematics]. 21/22. Edition Harri Deutsch. Frankfurt am Main, pp. 838.
- BUCKLEY, T. AND FARQUHAR, G. D. (2004): A new analytical model for whole-leaf potential electron transport rate. *Plant Cell and Environment*, Volume 27, Issue 12, pp. 1487-1502.
- BUNDESANSTALT FÜR STATISTIK ÖSTERREICH (Edt.) (2004): Ergebnisse der Agrarstrukturerhebung 1995 [Results of the Agricultural Composition Census 1995]. M. Dötzl, Austria, Wien.
- CAMPBELL, G. S. (1986): Extinction coefficients for radiation in plant canopies calculated using an ellipsoidal inclination angle distribution. *Agricultural and Forest Meteorology*, Volume 36, Issue 4, pp. 317-321.
- CAMPBELL, G. S. AND NORMAN, J. M. (1998): *An Introduction to Environmental Biophysics*. 2<sup>nd</sup> Edition, Springer-Verlag, New York, pp. 281.
- CANNEL, M. G. R. AND SMITH, R. I. (1983): Thermal time, chill days and prediction of budburst in *Picea sitchensis*. *Journal of Applied Ecology*, Volume 20, pp. 951-963.
- CAO, M. AND WOODWARD, F. I. (1998): Dynamic responses of terrestrial ecosystem carbon cycling to global climate change. *Nature*, Volume 393, Issue 6682, pp. 249-252.
- CHEN, D. X., COUGHENOUR, M. B., KNAPP, A. K. AND OWENSBY, C. E. (1994): Mathematical simulation of C<sub>4</sub> grass photosynthesis in ambient and elevated CO<sub>2</sub>. *Ecological Modelling*, Volume 73, Issue 1-2, pp. 63-80.
- CHMIELEWSKI, F.-M. (2001): Markante Veränderungen in der Vegetationsentwicklung seit dem Ende der achtziger Jahre [Distinctive Changes in the Development of Vegetation since the End of the Eighties]. In: Deutsche Meteorologische Gesellschaft (Edt.): *Mitteilungen der DMG*, Volume 1.
- CHMIELEWSKI, F.-M. AND RÖTZER, T. (2001): Response of tree phenology to climate change across Europe. *Agricultural and Forest Meteorology*, Volume 108, Issue 2, pp. 101-112.
- CIONCO, R. M. (1965): A Mathematical Model for Air Flow in a Vegetative Cover. *Journal of Applied Meteorology*, Volume 4, Issue 4, pp. 517–522.

- COLLATZ, G. J., RIBAS-CARBO, M. AND BERRY, J. A. (1992): Coupled photosynthesis-stomatal conductance model for leaves of C<sub>4</sub> plants. *Australian Journal of Plant Physiology*, Volume 19, Issue 5, pp. 519-538.
- COX, P. M., BETTS, R. A., BUNTON, C.B., ESSERY, R. L. H., ROWNTREE, P. R. AND SMITH, J. (1999): The impact of new land surface physics on the GCM simulation of climate and climate sensitivity. *Climate Dynamics*, Volume 15, Issue 3, pp. 183-203.
- CRAMER, W., BONDEAU, A., SCHAPHOFF, S., LUCHT, W., SMITH, B. AND SITCH, S. (2004): Tropical forests and the global carbon cycle: Impacts of atmospheric CO<sub>2</sub>, climate change and rate of deforestation. *Philosophical Transactions of the Royal Society of London, Series B*, Volume 359, Issue 1443, pp. 331-343.
- CRAMER, W., SHUGART, H. H., NOBLE, I., WOODWARD, F. I., BUGMANN, H., BONDEAU, A., FOLEY, J. A., GARDNER, R. R., LAUENROTH, W. K., PITELKA, L. F. AND SUTHERST, R. W. (1999): Ecosystem Composition and Structure. In: WALKER, B. H., STEFFEN, W. L., CANADELL, J. AND INGRAM, J. S. I. (Eds.): *The Terrestrial Biosphere and Global Change: Implications for Natural and Managed Ecosystems*. Cambridge University Press, Cambridge, pp. 190-228.
- DE BAETS, S., POESEN, J., KNAPEN, A. AND CALINDO, P. (2007): Impact of root architecture on the erosion-reducing potential of roots during concentrated flow. *Earth Surface Processes and Landforms*, Volume 32, Issue 9, pp. 1323-1334.
- DE WIT C. T., BROUWER, R. AND PENNING DE VRIES, F. W. T. (1970): The simulation of photosynthetic systems. In: SETLIK, I. (Ed.): *Prediction and measurement of photosynthetic productivity*. Proceedings IBP/PP Technical Meeting Trebon 1969, Pudoc, Wageningen, The Netherlands, pp. 47-50.
- DE WIT, C. T. (Ed.) et al. (1978): *Simulation of assimilation, respiration and transpiration of crops*. Pudoc, Wageningen, pp. 141.
- DE WIT, M. AND STANKIEWICZ, J. (2006): Changes in surface water supply across Africa with predicted climate change. *Science*, Volume 311, pp. 1917-1921.
- DINGMAN, S. L. (1994): *Physical Hydrology*. Macmillan Publishing Company, New York, pp. 575.
- DYCK, S. AND PESCHKE, G. (1995): *Grundlagen der Hydrologie, 3. Auflage [Basics of Hydrology, 3<sup>rd</sup> Edition]*. Verlag für Bauwesen, Berlin.
- EAGLESON, P. S. (1978): Climate, soil, and vegetation 3, A simplified model of soil moisture movement in the liquid phase. *Water Resources Research*, Volume 14, Issue 5, pp. 722-730.
- ELLENBERG, H. SEN. (1996): *Vegetation Mitteleuropas mit den Alpen, in ökologischer, dynamischer und historischer Sicht [The Vegetation of Central Europe and the Alps from an Ecologic, Dynamic and Historic Point of View]*. Verlag Eugen Ulmer, Stuttgart, 5<sup>th</sup> Edition, pp. 1096.
- EVANS J. R. (1987): The dependence of quantum yield on wavelength and growth irradiance. *Australian Journal of Plant Physiology*, Volume 14, Issue 1, pp. 69-79.
- FALGE, E. (1997): *Die Modellierung der Kronendachtranspiration von Fichtenbeständen (Picea abies (L.) Karst.) [Modelling the Crown Transpiration of Spruce Stands]*. Ph.D., Univ. of Bayreuth, Bayreuther Forum Ökologie, Band 48, pp. 221.

- FALGE, E., GRABER, W., SIEGWOLF, R. AND TENHUNEN, J. D. (1996): A model of the gas exchange response of *Picea abies* to habitat conditions. *Trees-Structure and Function*, Volume 10, Issue 5, pp. 277-287.
- FALGE, E., RYEL, R. J., ALSHEIMER, M. AND TENHUNEN, J. D. (1997): Effects of stand structure and physiology on forest gas exchange: A simulation study for Norway spruce. *Trees – Structure and Function*, Volume 11, Issue 7, pp. 436-448.
- FANGMEIER, A. AND JÄGER, H.-J. (2001): Wirkungen erhöhter CO<sub>2</sub>-Konzentrationen [Impacts of elevated CO<sub>2</sub> concentrations]. In: GUDERIAN, R. (Edt.): Handbuch der Umweltveränderungen und Ökotoxikologie. Volume 2 A, Terrestrische Ökosysteme, Springer, Berlin, pp. 382-433.
- FARQUHAR, G. D. (1979): Models describing the kinetics of ribulose biphosphate carboxylase-oxygenase. *Archives of Biochemistry and Biophysics*, Volume 193, Issue 2, pp. 456-468.
- FARQUHAR, G. D. AND VON CAEMMERER, S. (1982): Modeling of photosynthetic response to environmental conditions. In: LANGE, O. L., NOBEL, P. S., OSMOND, C. B. AND ZIEGLER, H. (Eds.): Physiological Land Ecology. *Encyclopedia of Plant Physiology*, New Series, Volume 12B, Springer-Verlag, Berlin, pp. 549-588.
- FARQUHAR, G. D. AND VON CAEMMERER, S. (1982): Modelling of photosynthetic response to environmental conditions. *Encyclopedia of Plant Physiology*, Volume 12B, pp. 549 - 587.
- FARQUHAR, G. D. AND SHARKEY, T. D. (1982): Stomatal conductance and photosynthesis. *Annual Review of Plant Physiology*, Volume 33, pp. 317–345.
- FARQUHAR, G. D., VON CAEMMERER, S. AND BERRY, J. A. (1980): A biochemical model of photosynthetic CO<sub>2</sub> assimilation in leaves of C<sub>3</sub> species. *Planta*, Volume 149, Issue 1, pp. 78-90.
- FARQUHAR, G. D., VON CAEMMERER, S. AND BERRY, J. A. (2001): Models of Photosynthesis. *Plant Physiology*, Volume 125, pp. 42-45.
- FARQUHAR, G. D. AND WONG, C. S. (1984): An empirical model of stomatal conductance. *Australian Journal of Plant Physiology*, Volume 11, Issue 3, pp. 191–210.
- FIELD, C. B. (2000): Plant Physiology of the "Missing" Carbon Sink. *Plant Physiology*, Volume 125, pp. 25-28.
- FIELD, C., JACKSON, R. AND MOONEY, H. (1995): Stomatal responses to increased CO<sub>2</sub>: Implications from the plant to the global scale. *Plant Cell and Environment*, Volume 18, Issue 10, pp. 1214–1255.
- FISCHBECK, G., HEYLAND, K.-U. AND KNAUER, N. (1999): Spezieller Pflanzenbau [Specific Crop Production]. Verlag Eugen Ulmer Stuttgart, 2<sup>nd</sup> edition = UTB-Taschenbuch, Volume 111, pp. 336.
- FISCHER, K. (2006): Geomorphologie der Berchtesgadener Alpen [Geomorphology of the Berchtesgaden Alps]. Nationalpark Berchtesgaden, Forschungsbericht 50, pp.171.
- FLOHN, H. (1971): Arbeiten zur allgemeinen Klimatologie [Publications on Universal Climatology]. Wissenschaftliche Buchgesellschaft., Darmstadt, pp. 315.
- FOLEY, J. A. (1995): An equilibrium model of the terrestrial carbon budget. *Tellus*, Volume 47, Issue 3, pp. 310–319.

- FOLEY, J. A., PRENTICE, I. C., RAMANKUTTY, N., LEVIS, S., POLLARD, D., SITCH, S. AND HAXELTINE, A. (1996): An integrated biosphere model of land surface processes, terrestrial carbon balance and vegetation dynamics. *Global Biogeochemical Cycles*, Volume 10, Issue 4, pp. 693–709.
- FRIEND, A. D., STEVENS, A. K., KNOX, R. G. AND CANNELL, M. G. R. (1997): A process-based, terrestrial biosphere model of ecosystem dynamics (Hybrid v3.0). *Ecological Modelling*, Volume 95, Issue 2-3, pp. 249– 287.
- GASH, J. H. C. (1979): An analytical model of rainfall interception in forests. *Quarterly Journal of the Royal Meteorological Society*, Volume 105, Issue 443, pp. 43-55.
- GASH, J. H. C., ROSIER, P. T. W. AND RAGAB, R. (2007): A note on estimating urban roof runoff with a forest evaporation model. *Hydrological Processes*, John Wiley & Sons, Ltd., Early View, Digital Object Identifier: 10.1002/hyp.6683, pp. 4.
- GEDNEY, N., COX, P. M., BETTS, R. A., BOUCHER, O., HUNTINGFORD, C. AND STOTT, P. A. (2006): Detection of a direct carbon dioxide effect in continental river runoff records. *Nature*, Volume 439, Issue 7078, pp. 835-838.
- GEISLER, G. (1980): Pflanzenbau. Ein Lehrbuch - Biologische Grundlagen und Techniken der Pflanzenproduktion [Plant Cultivation. A Textbook – Biological Basics and Techniques of Plant Production]. Verlag Paul Parey, Berlin und Hamburg, 2<sup>nd</sup> new and enhanced edition 1988, pp. 480.
- GEWITZ, A. AND PAGE, E. R. (1974): An empirical mathematical model to describe plant root systems. *Journal of Applied Ecology*, Volume 11, pp. 773-778.
- GODWIN, D. C. (1987): Simulation of nitrogen dynamics in wheat cropping systems. Ph.D., University of New England, pp. 348.
- GOUDRIAAN, J. AND VAN LAAR, H. H. (1978): Relations between leaf resistance, CO<sub>2</sub> concentration and CO<sub>2</sub> assimilation in maize, beans, lalang grass and sunflower. *Photosynthetica*, Volume 12, pp. 241–249.
- GOUDRIAAN, J. AND VAN LAAR, H. H. (1994): Modelling Potential Crop Growth Processes. Kluwer Academic Publishers, pp. 258.
- GREGORY, P. J., MCGOWAN, M., BISCOE, P. V. AND HUNTER, B. (1978): Water relations of winter wheat 1: Growth of the root system. *Journal of Agricultural Science*, Cambridge, Volume 91, pp. 91–102.
- GRIMMOND, C. S. B. AND OKE, T. R. (1991): An evapotranspiration-interception model for urban areas. *Water Resources Research*, Volume 27, pp. 1739-1755.
- HALL, A. E. AND BJÖRKMAN, O. (1975): Model of leaf photosynthesis and respiration. In: GATES, D. M. AND SCHMERL, R. B. (Eds.): *Ecological studies*, Volume 12. Springer, Berlin Heidelberg New York.
- HALL, D. O., ROSILLO-CALLE, F., WILLIAMS, R. AND WOODS, J. (1993): Biomass for Energy: Supply Prospects. In: JOHANSSON, T. B., KELLY, H., REDDY, A. AND WILLIAMS, R. (Eds.): *Renewable Energy: Sources for Fuel and Electricity*. Island Press, Washington, DC, pp. 593-652.

- HANK, T. AND MAUSER, W. (2007): Modeling the Impact of Climate Change on the Phenological Development of Forest Trees in the Upper Danube Basin. In: Proceedings of "Managing Alpine Future", International Conference on Global Change, 15-17 October 2007, Innsbruck, Austria.
- HANK, T., OPPELT, N. AND MAUSER W. (2006): Simulation of a winter wheat site using the physically based SVAT model WHNSIM. In: Proceedings of the 8<sup>th</sup> International Conference on Precision Agriculture, 23-26 July 2006, Minneapolis (USA).
- HANK, T., OPPELT, N. AND MAUSER, W. (2007): Physically based modelling of photosynthetic processes. In: STAFFORD, J. V.: *Precision Agriculture '07*, Skiathos, Greece, 03-06 June 2007, Wageningen Academic Publisher, The Netherlands, pp. 165-172.
- HATCH, M. D. AND SLACK, C. R. (1977): Photosynthesis by sugar cane leaves. A new carboxylation reaction and the pathway of sugar formation. *Biochemical Journal*, Volume 101, pp. 103–111.
- HAXELTINE, A. AND PRENTICE, I. C. (1996): BIOME3: An equilibrium terrestrial biosphere model based on ecophysiological constraints, resource availability, and competition among plant functional types. *Global Biogeochemical Cycles*, Volume 10, Issue 4, pp. 693–710.
- HAXELTINE, A. AND PRENTICE, I. C. (1997): A general model for the light-use efficiency of primary production. *Functional Ecology*, Volume 10, pp. 551-561.
- HEATHCOTE, I. W. (1998): *Integrated Watershed Management: Principles and Practices*. John Wiley & Sons Inc., New York, pp. 440.
- HINTERMAIER-ERHARD, G. AND ZECH, W. (1997): *Wörterbuch der Bodenkunde [Dictionary of Pedology]*. Ferdinand Enke Verlag Stuttgart.
- HODGES, T. AND RITCHIE, J. T. (1991): The Ceres-Wheat phenology model. In: HODGES, T. (Edt.): *Predicting crop phenology*. CRC Press, Boston. pp. 133–141.
- HOPKINS, W. G. (1999): *Introduction to Plant Physiology*. John Wiley and Sons, New York, pp. 512.
- HUNGATE, B. A., REICHSTEIN, M., DIJKSTRA, D., JOHNSON, D., HYMUS, G. AND TENHUNEN, J. D. (2002): Evapotranspiration and soil water content in a scrub-oak woodland under carbon dioxide enrichment. *Global Change Biology*, Volume 8, pp. 289-298.
- HUNTLEY, B. (1991): How plants respond to climate change: Migration rates, individualism and the consequences for plant communities. *Annals of Botany*, Volume 67, Issue 1, pp. 15–22.
- IPCC (2000): NAKIC-ENOVIC, N., ALCAMO, J., DAVIS, G., DE VRIES, B., FENHANN, J., GAFFIN, S., GREGORY, K., GRÜBLER, A., YONG JUNG, T., KRAM, T., LA ROVERE, E. L., MICHAELIS, L., MORI, S., MORITA, T., PEPPER, W., PITCHER, H., PRICE, L., RIAHI, K., ROEHL, A., ROGNER, H.-H., SANKOVSKI, A., SCHLESINGER, M., SHUKLA, P., SMITH, S., SWART, R., VAN ROOIJEN, S., VICTOR, N. AND DADI, Z. (Eds.): *Special Report on Emissions Scenarios. A Special Report of Working Group III of the Intergovernmental Panel on Climate Change*. Cambridge University Press, Cambridge, UK, pp. 612.
- IPCC (2001): HOUGHTON, J. T., DING, Y., GRIGGS, D. J., NOGUER, M., VAN DER LINDEN, P. J., DAI, X., MASKELL, K. AND JOHNSON, C. A. (Eds.): *Climate Change 2001: The Scientific Basis. Contribution of Working Group I to the Third Assessment Report of the Intergovernmental Panel on Climate Change*. Cambridge, UK: Cambridge University Press, pp. 881.

- IPCC (2007): SOLOMON, S., QIN, D. AND MANNING, M. (Eds.): Climate Change 2007: The Physical Science Basis. Contribution of Working Group I to the Fourth Assessment Report of the Intergovernmental Panel on Climate Change. Cambridge, UK: Cambridge University Press, pp. 996.
- IMSL (2003): IMSL Fortran Library User's Manual. Version 5.0, IMSL Houston, pp. 947.
- ITADA - Institut Transfrontalier d'Application et de Développement Agronomique / Grenzüberschreitendes Institut zur rentablen umweltgerechten Landwirtschaft (2005): Nachhaltige Maisproduktion am Oberrhein: Konzeption und vertiefte Auswertung von Anbausystemen [Sustainable Maize Production in the Upper Rhine. Concept and Analysis of Cropping Systems]. Colmar, France, pp. 151.
- JARVIS, P. G. AND MORISON, J. I. L. (1981): The control of transpiration and photosynthesis by the stomata. In: JARVIS, P. G. AND MANSFIELD, T. A. (Eds.): Stomatal physiology. Society for Experimental Biology Seminar Series 8. Cambridge University Press, pp. 694.
- JARVIS, P. G., JAMES, G. B., AND LANDSBERG, J. J. (1976): Coniferous forest. In: MONEITH, J. L. (Edt.): Vegetation and the Atmosphere. Volume II, Case Studies, London, Academic Press, pp. 171-240.
- JERZ, H. (1993): Das Eiszeitalter in Bayern - Erdgeschichte, Gesteine, Wasser, Boden. Geologie von Bayern II [The Ice Age in Bavaria – Geology, Bedrock, Water, Soil. Geology of Bavaria II]. Schweizerbart'sche Verlagsbuchhandlung, Stuttgart, pp. 243.
- JOHNSON, F. H., EYRING, H. AND WILLIAMS, R. (1942): The nature of enzyme inhibitions in bacterial luminescence: sulfanilamide, urethane, temperature and pressure. *Journal of Cellular and Comparative Physiology*, Volume 20, Issue 2, pp. 247-268.
- JONES, C. A. AND KINIRY, J. R. (1986): CERES-Maize - A simulation model of maize growth and development. Texas A&M University Press, pp.194.
- JONES, H. G. (1992): Plants and Microclimate. 2<sup>nd</sup> Edition. Cambridge University Press, pp. 428.
- JONES, J. W. (1991): Crop growth, development and production modeling. In: Proceedings of the Symposium on Automated Agriculture for the Future. American Society of Agricultural Engineers, Chicago, IL, 1–17 December, pp. 447–457.
- KANNEGANTI, V. R. AND FICK, G. W. (1991): A warmseason annual grass growth model parameterized for corn and sudangrass. *Agricultural Systems*, Volume 36, Issue 4, pp. 439-470.
- KATTGE, J., GRÜTERS, U., HOFFSTADT, J., FANGMEIER, A. AND JÄGER, H.-J. (1997): Reaktion des Wasserhaushaltes von Wildkräutern auf erhöhte CO<sub>2</sub>-Konzentrationen der Atmosphäre [Reaction of the water balance of wild herbs on elevated atmospheric CO<sub>2</sub> concentrations]. *Verhandlungen der Gesellschaft für Oekologie*, Volume 27, pp. 273-282.
- KINIRY, J. R. AND BONHOMME, R. (1991): Predicting maize phenology. In Hodges, T. (Edt.): Physiological aspects of predicting crop phenology. CRC Press, pp. 115–131.
- KLÜPFEL, W. (1926): Über Reliefmorphogenie und zyklische Landschaftsgenerationen [Relief Morphology and Cyclic Landscape Formations]. Verlag Springer Berlin / Heidelberg, *International Journal of Earth Sciences*, Volume 17, Issue 6, pp. 401-417.



- KÖPPEN, W. (1936): Das geographische System der Klimate [The Geographic System of Climates]. In: KÖPPEN, W. AND GEIGER, R. (Eds.): Handbuch der Klimatologie. Gebrüder Borntraeger, Berlin, pp. 1–46.
- KÖRNER, C. (2000): Biosphere responses to CO<sub>2</sub> enrichment. *Ecological Applications*, Volume 10, Issue 6, pp. 1590-1619.
- KÖRNER, C. (2006): Plant CO<sub>2</sub> responses: An issue of definition, time and resource supply. *New Phytologist*, Volume 172, Issue 3, pp. 393-411.
- KÖSTNER, B. (2001): Evaporation and transpiration from coniferous and broad-leaved forests in Central Europe - relevance of patch-level studies. *Meteorology and Atmospheric Physics*, Volume 75, Issue 1-4, pp. 69-82.
- KORTSCHAK, H. P., HARTT, C. E. AND BURR, G. O. (1965): Carbon dioxide fixation in sugarcane leaves. *Plant Physiology*, Lancaster, Volume 40, Issue 2, pp. 209–213.
- KRAMER, K. (1995): Modelling comparison to evaluate the importance of phenology for the effects of climate change on growth of temperate-zone deciduous trees. *Climate-Research*, Volume 5, Issue 2, pp. 119-130.
- KUNTZE, H., ROESCHMANN, G. AND SCHWERDTFEGER, G. (1994): Bodenkunde. 5. neu bearbeitete und erweiterte Auflage [Pedology. Revised and Enhanced 5<sup>th</sup> Edition]. Stuttgart, Ulmer UTB, pp. 424.
- LANGENSCHIEDT, E. (2001): Geologie der Berchtesgadener Berge [Geology of the Berchtesgaden Mountains]. 2<sup>nd</sup> Edition, pp. 160.
- LARCHER, W. (1994): Ökophysiologie der Pflanze. [Physiological Plant Ecology]. Verlag Eugen Ulmer, Deutschland, pp. 408.
- LARCHER, W. (1995): Physiological plant ecology. 3<sup>rd</sup> edition, Springer, New York, USA, pp. 506.
- LENIHAN, J. M., DALY, C., BACHELET, D. AND NEILSON, R. P. (1998): Simulating broad-scale fire severity in a dynamic global vegetation model. *Northwest Science*, Volume 72, pp. 91–103.
- LEUNING, R. (1995): A critical appraisal of a combined stomatal-photosynthesis model for C<sub>3</sub> plants. *Plant Cell and Environment*, Volume 18, Issue 4, pp. 339-355.
- LI-COR BIOSCIENCES (Edt.) (1992): LAI-2000 Plant Canopy Analyzer - Operating Manual, Lincoln, USA.
- LONG, S. P., AINSWORTH, E. A., LEAKEY, A. D. B., NÖSBERGER, J. AND ORT, D. R. (2006): Food for thought: lower-than-expected crop yield stimulation with rising CO<sub>2</sub> concentrations. *Science*, Volume 312, Issue 5782, pp. 1918–1921.
- LÜDEKE, M. K. B., BADECK, F. W., OTTO, R. D., HÄGER, C., DÖNGERS, S., KINDERMANN, J., WÜRTH, G., LANG, T., JÄKEL, U., KLAUDIUS, A., RAMGE, P., HABERMEHL, A. AND KOHLMAIER, G. H. (1994): The Frankfurt Biosphere Model: A global process-oriented model for the seasonal and long-term CO<sub>2</sub> exchange between terrestrial ecosystems and the atmosphere. *Climate Research*, Volume 4, Issue 2, pp. 143–166.
- LUDWIG, R. (2000): Die flächenverteilte Modellierung von Wasserhaushalt und Abflußbildung im Einzugsgebiet der Ammer [Spatially Distributed Modelling of Water Balance and Runoff Formation in the Ammer Catchment]. In: Münchener Geographische Abhandlungen, Series B, Volume 32, pp. 173.

- LUDWIG, R., BARTHEL, R., WILLEMS, W. AND MAUSER, W. (2005): Coupled hydrologic process modelling in the Upper Danube using the integrated expert system DANUBIA. *Geophysical Research Abstracts*, European Geosciences Union General Assembly, Vienna, Volume 7.
- LUDWIG, R., MAUSER, W., NIEMEYER, S., COLGAN, A., STOLZ, R., ESCHER-VETTER, H., KUHN, M., REICHSTEIN, M., TENHUNEN, J., KRAUS, A., LUDWIG, M., BARTH, M. AND HENNICKER, R. (2003): Web-based modeling of water, energy and matter fluxes to support decision making in mesoscale catchments – the integrative perspective of GLOWA-Danube. *Physics and Chemistry of the Earth*, Volume 28, Issue 14-15, pp. 621 – 634.
- LÜTKE ENTRUP, N. AND OEHMICHEN, J. (Eds.) (2000): Lehrbuch des Pflanzenbaues. Bd. 1: Grundlagen; Bd. 2: Kulturpflanzen [Textbook of Plant Cultivation, Vol 1: Basics, Vol 2: Economic Plants]. Verlag Thomas Mann, Gelsenkirchen, pp. 823 and pp. 856.
- LWF - BAYERISCHE LANDESANSTALT FÜR WALD UND FORSTWIRTSCHAFT (Edt.) (2004): Erfolgreich mit der Natur – Ergebnisse der zweiten Waldinventur in Bayern [Successful with Nature – Results of the Second Forest Inventory in Bavaria]. Bavarian Regional Office of Forest and Forestry, Munich, pp. 16.
- MARKE, T. (2008): Development and Application of a Model Interface to couple Land Surface Models with Regional Climate Models for Climate Change Risk Assessment. PhD, Faculty of Geosciences, LMU Munich, in preparation.
- MAUSER, W. AND BACH, H. (2008): PROMET – A Physical Hydrological Model to Study the Impact of Climate Change on the Water Flows of Medium Sized, Complex Watersheds. *Journal of Hydrology*, accepted.
- MAUSER, W. AND LUDWIG, R. (2002): GLOWA-DANUBE – A research concept to develop integrative global changes of the water cycle. In: BENISTON, M. (Edt.): Climatic Change: Implications for the Hydrological Cycle and for Water Management. *Advances in Global Change Research*, Volume 10, Kluwer Academic Publishers, Dordrecht and Boston, pp. 171-188.
- MAUSER, W. AND SCHÄDLICH, S. (1998): Modelling the spatial distribution of Evapotranspiration on different scales using remote sensing data. *Journal of Hydrology*, Volume 212-213, pp. 250-267.
- MAUSER, W. AND STRASSER, U. (1997): Modelling actual evapotranspiration of the Weser catchment with the multiscale SVAT model PROMET. In: DIEKKRÜGER, B. AND RICHTER, O. (Eds.): *Landschaftsökologie und Umweltforschung*, Braunschweig, Volume 25, pp. 161-164.
- MAUSER, W., PRASCH, M. AND STRASSER, U. (2007): Physically based Modelling of Climate Change Impact on Snow Cover Dynamics in Alpine Regions using a Stochastic Weather Generator. Proceedings of the International Congress on Modelling and Simulation MODSIM07, Christchurch, New Zealand, Proceeding, submitted.
- MCCREE, K. J. (1970): An equation for the rate of respiration for white clover plants grown under controlled conditions. In: SETLIK, I. (Edt.): Prediction and Measurement of Photosynthetic Productivity. Centre for Agricultural Publishing and Documentation, Wageningen, pp. 221–229.
- MCNEVIN, D. B., VON CAEMMERER, S. AND FARQUHAR, G. D. (2006): Determining RuBisCO activation kinetics and other rate and equilibrium constants by simultaneous multiple non-linear regression of a kinetic model. *Journal of Experimental Botany*, Volume 57, Issue 14, pp. 3883-3900.

- MEDLYN, B. E., DREYER, E., ELLSWORTH, D. S., FORSTREUTER, M., HARLEY, P. C., KIRSCHBAUM, M. U. F., LE ROUX, X., MONTPIED, P., STRASSEMAYER, J., WALCROFT, A., WANG, K. AND LOUSTAU, D. (2002): Temperature response of parameters of a biochemically-based model of photosynthesis. II. A review of experimental data. *Plant Cell and Environment*, Volume 25, Issue 9, pp. 1167–1179.
- MEDLYN, B. E., LOUSTAU, D. AND DELZON, S. (2002): Temperature response of parameters of a biochemically based model of photosynthesis. I. Seasonal changes in mature maritime pine (*Pinus pinaster* Ait.). *Plant, Cell and Environment*, Volume 25, Issue 9, pp. 1155–1165.
- MENZEL, A. (1997): Phänologie von Waldbäumen unter sich ändernden Klimabedingungen [Forest Phenology under Changing Climatic Conditions]. In: Forstliche Forschungsberichte München, Volume 164, Munich, pp. 147.
- MENZEL, A., SPARKS, T. H., ESTRELLA, N., KOCH, E., AASA, A., AHAS, R., ALM-KÜBLER, K., BISSOLLI, P., BRASLAVSKÁ, O., BRIEDE, A., CHMIELEWSKI, F.-M., CREPINSEK, Z., CURNEL, Y., DAHL, A., DEFILA, C., DONNELLY, A., FILELLA, Y., JATCZAK, K., MAGE, F., MESTRE, A., NORDLI, Ø., PEÑUELAS, J., PIRINEN, P., REMIŠOVÁ, V., SCHEIFINGER, H., STRIZ, M., SUSNIK, S., VAN VLIET, A. J. H., WIELGOLASKI, F.-E., ZACH, S. AND ZUST, A. (2006): European phenological response to climate change matches the warming pattern. *Global Change Biology*, Volume 12, pp. 1969-1976.
- MEYER, R. K. F. AND SCHMIDT-KALER, H. (1997): Auf den Spuren der Eiszeit südlich von München – östlicher Teil [Tracing the Ice Age in the South of Munich – Eastern Part]. In: Wanderungen in die Erdgeschichte. Verlag F. Pfeil, München, Volume 8, pp. 142.
- MEYNEN, E. AND SCHMITHÜSEN, J. (1953): Handbuch der naturräumlichen Gliederung Deutschlands [Handbook of the Natural Landscape Units of Germany]. Bundesanstalt für Landeskunde, Bad Godesberg, pp. 1339.
- MIRSCHHEL, W. AND WENKEL, K.-O. (2007): Modelling soil-crop interactions with AGROSIM model family. In: KERSEBAUM, K.-C., HECKER, J.-M., MIRSCHEL, W. AND WEGEHENKEL, M. (Eds.): Modelling water and nutrient dynamics in soil crop systems : Proceedings of the workshop on "Modelling water and nutrient dynamics in soil-crop systems" held on 14 - 16 June 2004 in Müncheberg, Germany, Springer Verlag, Dordrecht, pp. 59-73.
- MÖSER, W. AND RASCHKE, E. (1984): Incident solar radiation over Europe estimated from METEOSAT data. *Journal of Applied Meteorology*, Volume 23, Issue 1, pp. 166-170.
- MOHREN, G. M. J. (1987): Simulation of forest growth, applied to douglas fir stands in the Netherlands. PhD, Wageningen, the Netherlands. pp. 184.
- MOHREN, G. M. J. (1994): Modelling Norway spruce growth in relation to site conditions and atmospheric CO<sub>2</sub>. In: VEROUSTRAETE, F. AND CEULEMANS, R. (Eds.): Vegetation, modelling and climate change effects. SPB Academic Publishing, The Hague, pp. 7-22.
- MONTEITH, J. L. (1965): Evaporation and environment. In: FOGG, G. E. (Edt.): The state and movement of water in living organisms (= Symposia of the Society for Experimental Biology), Cambridge University Press, pp. 205-234.
- MONTEITH, J. L. (Edt.) (1976): Vegetation and the atmosphere. Vol II, Case studies, London: Academic press, pp. 458.
- MONTEITH, J. L. AND UNSWORTH, M. H. (1990): Principles of Environmental Physics (2<sup>nd</sup> Edition). Edward Arnold, London, pp. 440.

- MOORE, R., CLARK, W. D. AND VODOPICH, D. (1998): Botany. 2<sup>nd</sup> edition, McGraw-Hill/Wm. C. Brown Publishers, Dubuque, pp. 919.
- MORISON, J. I. L. AND GIFFORD, R. M. (1983): Stomatal sensitivity to carbon dioxide and humidity: A comparison of two C<sub>3</sub> and two C<sub>4</sub> grass species. *Plant Physiology*, Volume 71, Issue 4, pp. 789-796.
- MUERTH, M. (2008): A Soil Temperature and Energy Balance Model for Integrated Assessment of Global Change Impacts at the Regional Scale. PhD, Faculty of Geosciences, LMU Munich, submitted.
- MURRAY, F. W. (1967): On the computation of saturation vapor pressure. *Journal of Applied Meteorology*, Volume 6, Issue 1, pp. 203-204.
- NASH, J. E. AND SUTCLIFFE, J. V. (1970): River flow forecasting through conceptual models part I — A discussion of principles. *Journal of Hydrology*, Volume 10, Issue 3, pp. 282-290.
- NEILSON, R. P. (1995): A model for predicting continental-scale vegetation distribution and water balance. *Ecological Applications*, Volume 5, Issue 2, pp. 362-385.
- NEILSON, R. P. AND MARKS, D. (1994): A global perspective of regional vegetation and hydrological sensitivities from climatic change. *Journal of Vegetation Science*, Volume 5, pp. 715-730.
- NOBEL, P. S. (1991): Physiochemical and Environmental Plant Physiology. Academic Press, San Diego, pp. 635.
- OHTAKI, E. (1982): Atmospheric carbon dioxide variations at Uoshima Island, Seto Inland Sea, Japan. *Meteorology and Atmospheric Physics*, Volume 32, Issue 1, pp. 89-97.
- OKE, T. R. (1978): Boundary Layer Climate. 2<sup>nd</sup> Edition, Methuen & Co., Oxon, New York, pp. 435.
- OPPELT, N. (2002): Monitoring of Plant Chlorophyll and Nitrogen Status Using the Airborne Imaging Spectrometer AVIS. PhD. Faculty of Geosciences, LMU Munich, pp. 196.
- ÖSTERREICHISCHES STATISTISCHES ZENTRALAMT (1996): Ergebnisse der landwirtschaftlichen Statistik im Jahr 1995 [Results of the Agricultural Statistics for the Year 1995]. *Beiträge zur Österreichischen Statistik*, Volume 1205, Wien.
- PAN, Y., MCGUIRE, A. D., MELILLO, J. M., KICKLIGHTER, D. W., SITCH, S. AND PRENTICE, I. C. (2002): A biogeochemistry-based dynamic vegetation model and its application along a moisture gradient in the continental United States. *Journal of Vegetation Science*, Volume 13, Issue 3, pp. 369-382.
- PARTON, W. J., SCURLOCK, J. M. O., OJIMA, D. S., GILMANOV, T. G., SCHOLES, R. J., SCHIMEL, D. S., KIRCHNER, T., MENAUT, J.-C., SEASTEDT, T., GARCIA MOYA, E., KAMNALRUT, A. AND KINYAMARIO, J. L. (1993): Observations and modeling of biomass and soil organic matter dynamics for the grassland biome worldwide. *Global Biogeochemical Cycles*, Volume 4, pp. 785-809.
- PEISKER, M. (1976): Ein Modell der Sauerstoffabhängigkeit des Photosynthetischen CO<sub>2</sub> Gaswechsels von C<sub>3</sub> Pflanzen [A Model of the Oxygen Dependency of Photosynthetic CO<sub>2</sub> for the Gas Exchange of C<sub>3</sub> Species]. *Kulturpflanzen*, Volume 24, pp. 221-235.

- PENG, C. H. (2000): From static biogeographical model to dynamic global vegetation model: A global perspective on modeling vegetation dynamics. *Ecological Modelling*, Volume 135, Issue 1, pp. 33-54.
- PENG, C. H., GUIOT, J. AND VAN CAMPO, E. (1998): Estimating changes in terrestrial vegetation and carbon storage: Using palaeoecological data and models. *Quaternary Science Reviews*, Volume 17, Issue 18, pp. 719-735.
- PENMAN, H. L. (1956): Estimating evaporation. *Transactions of the American Geophysical Union*, Volume 37, pp. 43-46.
- PENNING DE VRIES, F. W. T., JANSEN, D. M., TEN BERGE, H. F. M. AND BAKEMA, A. (1989): Simulation of Ecophysiological Processes of Growth in Several Annual Crops. Simulation Monographs, 29. PUDOC, Wageningen, The Netherlands, pp. 271.
- POTTER, C. S. AND KLOOSTER, S. A. (1999): Dynamic global vegetation modelling for predicting of plant functional types and biogenic trace gas fluxes. *Global Ecology and Biogeography*, Volume 8, pp. 473-488.
- PRENTICE, I. C., BARTLEIN, P. J. AND WEBB, T. (1991): Vegetation and climate change in Eastern North America since the last glacial maximum. *Ecology*, Volume 72, Issue 6, pp. 2038-2056.
- PRENTICE, I. C., CRAMER, W., HARRISON, S. P., LEEMANS, R., MONSERUD, R. A. AND SOLOMON, A. M. (1992): A global biome model based on plant physiology and dominance, soil properties and climate. *Journal of Biogeography*, Volume 19, pp. 117-134.
- PRIESTLEY, C. H. B. AND TAYLOR, R. J. (1972): On the assessment of surface heat flux and evaporation using large-scale parameters. *Monthly Weather Review*, Volume 100, Issue 2, pp. 81-92.
- PRIVETTE, J. L., MORISETTE, J., BARET, F., GOWER, S. T. AND MYNENI, R. B. (2001): Summary of the International Workshop on LAI Product Validation. *Earth Observer*, Volume 13, Issue 3, pp. 18-22.
- RACSKO, P., SZEIDL, L., AND SEMENOV, M. (1991): A Serial Approach to Local Stochastic Weather Models. *Ecological Modelling*, Volume 57, Issue 1-2, pp. 27-41.
- RAICH, J. W., RASTETTER, E. B., MELILLO, J. M., KICKLIGHTER, D. W., STEUDLER, P. A., PETERSON, B. J., GRACE, A. L., MOORE, B. AND VOROSMARTY, C. J. (1991): Potential net primary productivity in South America: application of a global model. *Ecological Applications*, Volume 1, Issue 4, pp. 399-429.
- RAMSAY, J. G. (1981): Tectonics of the Helvetic Nappes. Geological Society of London, *Special Publications*, Volume 9, pp. 293-309.
- RASTETTER, E. B., RYAN, M. G., SHAVER, G. R., MELILLO, J. M., NADELHOFFER, K. J., HOBBIIE, J. E. AND ABER, J. D. (1991): A general model describing the response of the C and N cycles in terrestrial ecosystems to changes in CO<sub>2</sub>, climate and N deposition. *Tree Physiology*, Volume 9, Issue 1-2, pp. 101-126.
- RAWLS, W. J., AHUJA, L. R., BRAKENSIEK, D. L. AND SHIRMOHAMMADI, A. (1991): Infiltration and Soil Water Movement. In: MAIDMENT, D. R. (Ed.): *Handbook of Hydrology*. McGraw Hill, New York, pp. 5-51.
- RICHARDSON, C. W. (1981): Stochastic simulation of daily precipitation, temperature and solar radiation. *Water Resources Research*, Volume 17, Issue 1, pp. 182-190.

- RICKMAN, R. W., WALDMAN, S. AND KLEPPER, B. L. (1996): MODWh3: A development driven winter wheat growth simulation. *Agronomy Journal*, Volume 88, Issue 2, pp. 176-185.
- RITCHIE, J. T. (1991): Wheat phasic development. In: HANKS, R. J. AND RITCHIE, J. T. (Eds.): Modeling plant and soil systems. *Agronomy Monograph*, Volume 31, ASA, CSSSA, SSSA, Madison, WI, pp. 31-54.
- RITCHIE, J. T. (1993): Genetic specific data for crop modeling. In: PENNING DE VRIES, F., TENG, P. AND METSELAAR, K. (Eds.): Systems approaches for agricultural development. Kluwer Academic Publishers, Dordrecht, Netherlands, pp. 77-93.
- RITCHIE, J. T. (1998): Soil water balance and plant water stress. In: TSUJI, G. Y., HOOGENBOOM, G. AND THORNTON, P. K. (Eds.): Understanding Options for Agricultural Production. Kluwer Academic Publishers, pp. 41-54.
- RODRIGUEZ, D., VAN OIJEN, M. AND SCHAPENDONK, A. H. C. M. (1999): LINGRA-CC: a sink-source model to simulate the impact of climate change and management on grassland productivity. *New Phytologist*, Volume 144, Issue 2, pp. 359–368.
- RUNNING, S. W. AND COUGHLAN, J. C. (1988): A general model of forest ecosystem processes for regional applications. I. Hydrologic balance, canopy gas exchange and primary production processes. *Ecological Modelling*, Volume 42, Issue 2, pp. 125–154.
- RZD - REGIONALE ZUSAMMENARBEIT DER DONAULÄNDER (Edt.) (1986): Die Donau und ihr Einzugsgebiet. Eine hydrologische Monographie. Teil 1: Texte, Teil 2: Tabellen, Teil 3: Karten [The Danube and its Catchment – A Hydrologic Monography. Part 1: Texts, Part 2: Tables, Part 3: Maps]. Bayerisches Landesamt für Wasserwirtschaft, Munich.
- SAGE, R. F. (1994): Acclimation of photosynthesis to increasing atmospheric CO<sub>2</sub>: The gas exchange perspective. *Photosynthesis Research*, Volume 39, Issue 3, pp. 351-368.
- SCHNEIDER, K. (1999): Gekoppelte, flächenverteilte Modellierung von Pflanzenwachstum und Verdunstung im Ammereinzugsgebiet mit dem prozeßorientierten Evapotranspirations- und Vegetationsmodell PROMET-V [Coupled and Spatially Distributed Modelling of Plant Growth and Evapotranspiration in the Ammer Catchment with the Process Oriented Evapotranspiration and Vegetation Model PROMET-V]. Professorial Dissertation, Faculty of Geosciences, LMU Munich, pp. 263.
- SCHWERTMANN, U., VOGL, W. AND KAINZ, M. (1987): Bodenerosion durch Wasser - Vorhersage des Abtrags und Bewertung von Gegenmaßnahmen [Soil Erosion through Water – Prediction of Degradation and Assessment of Counter Measures]. 2<sup>nd</sup> Edition, Ulmer, Stuttgart, pp. 64.
- SELLERS, P. J., BOUNOUA, L., COLLATZ, G. J., RANDALL, D. A., DAZLICH, D. A., LOS, S. O., BERRY, J. A., FUNG, I., TUCKER, C. J., FIELD, C. B. AND JENSEN, T. G. (1996): Comparison of radiative and physiological effects of doubled atmospheric CO<sub>2</sub> on climate. *Science*, Volume 271, pp. 1402–1406.
- SEMENOV, M. A., BROOKS, R. J., BARROW, E. M. AND RICHARDSON, C. W (1998): Comparison of the WGEN and LARS-WG stochastic weather generators in diverse climates. *Climate Research*, Volume 10, Issue 2, pp. 95-107.
- SHAFFER, G. AND SARMIENTO, J. (1995): Biogeochemical cycling in the global ocean: A new, analytical model with continuous vertical resolution and high-latitude dynamics. *Journal of Geophysical Research*, Volume 100, Issue C2, pp. 2659–2672.

- SHAW, R. H. AND PEREIRA, A. R. (1982): Aerodynamic Roughness of Plant Canopy: A Numerical Experiment. *Agricultural Meteorology*, Volume 26, Issue 1, pp. 51–65.
- SITCH, S., SMITH, B., PRENTICE, I. C., ARNETH, A., BONDEAU, A., CRAMER, W., KAPLAN, J., LEVIS, S., LUCHT, W., SYKES, M., THONICKE, K. AND VENEVSKY, S. (2003): Evaluation of ecosystem dynamics, plant geography and terrestrial carbon cycling in the LPJ Dynamic Vegetation Model. *Global Change Biology*, Volume 9, Issue 2, pp. 161–185.
- SMITH, E. L. (1937): The influence of light and carbon dioxide on photosynthesis. *Journal of General Physiology*, Volume 20, Issue 6, pp. 807–830.
- STATISTISCHES LANDESAMT BADEN-WÜRTTEMBERG (Edt.) (1997): Agrarberichterstattung 1995. Ergebnisse für landwirtschaftliche Vergleichsgebiete und Kreise [Agricultural Report 1995. Results for Comparable Agricultural Regions and Districts]. Volume 519, Stuttgart.
- STEINGROBE, B., SCHMID, H., GUTSER, R. AND CLAASSEN, N. (2001): Root production and root mortality of winter wheat grown on sandy and loamy soils in different farming systems. *Biology and Fertility of Soils*, Volume 33, Issue 4, Springer, Heidelberg, pp. 331-339.
- STRASSER, U. (1998): Regionalisierung des Wasserkreislaufs mit einem SVAT-Modell am Beispiel des Weser-Einzugsgebiets [Regionalization of the Water Cycle using a SVAT Model, Exemplary for the Weser Catchment]. In: Münchener Geographische Abhandlungen, Series B, Volume 28, pp. 146.
- STRECK, N. A., WEISS, A., XUE, Q. AND BAENZIGER, P. S. (2003): Incorporating a chronology response into the prediction of leaf appearance rate in winter wheat. *Annals of Botany*, Volume 92, Issue 2, pp. 181–190.
- TAIZ, L. AND ZEIGER, E. (2000): Physiologie der Pflanzen [Plant Physiology]. 2<sup>nd</sup> Edition. Spektrum Akademischer Verlag, Heidelberg, Berlin, pp. 773.
- TENHUNEN, J., WEBER, J., YOCUM, C. AND GATES, D. (1976): Development of a photosynthesis model with an emphasis on ecological applications. II. Analysis of a data set describing the P M surface. *Oecologia*, Berlin, Volume 26, Issue 2, pp. 101–119.
- TROLL, C. AND PAFFEN, K. H. (1964): Karte der Jahreszeiten-Klimate der Erde [Map of Seasonal Climates of the Earth]. *Erdkunde*, Volume 18, Issue 1, pp. 5-28.
- TSUJI, G. Y., UEHARA, G. AND BALAS, S. (Eds.) (1994): DSSAT Version 3 Volumes 1, 2, and 3. International Benchmark Sites Network for Agrotechnology Transfer, University of Hawaii, Honolulu, HI.
- TYREE, M. T. AND ALEXANDER, J. D. (1993): Plant water relations and the effects of elevated CO<sub>2</sub>: A review and suggestions for future research. In: ROZEMA, J., LAMBERS, H., VAN DE GEIJN, S. C. AND CAMBRIDGE, M. L. (Eds.): CO<sub>2</sub> and biosphere. Kluwer Academic Publishers, Dordrecht, pp. 47-62.
- VAN DIJK, A. I. J. M. AND BRUIJNZEEL, L. A. (2001): Modelling rainfall interception by vegetation of variable density using an adapted analytical model. Part 2. Model validation for a tropical upland mixed cropping system. *Journal of Hydrology*, Volume 247, pp. 239–262.
- VAN LAAR, H. H., GOUDRIAAN, J. AND VAN KEULEN, H. (Eds.) (1997): SUCROS97: Simulation of crop growth for potential and water-limited production situations. *Quantitative Approaches in Systems Analysis*, Volume 14, pp. 52.

- VON CAEMMERER, S. (2000): Biochemical models of leaf photosynthesis. *Techniques in Plant Sciences*, Volume 2, CSIRO Publishing, Australia, pp. 165.
- WARING, R. H. AND RUNNING, S. W. (1998): Forest Ecosystems - Analysis at multiple scales. 2<sup>nd</sup> edition. San Diego: Academic Press, pp. 370.
- WARREN, R. (2006): Impacts of global climate change at different annual mean global temperature increases. In: SCHELLNHUBER, H. J., CRAMER, W., NAKICENOVIC, N., WIGLEY, T. AND YOHE, G. (Eds.): Avoiding Dangerous Climate Change. Cambridge Univ. Press, Chapter 11, pp. 93–100.
- WEINGART, P., ENGELS, A. AND PANSEGRAU, P. (2000): Risks of communication: discourses on climate change in science, politics, and the mass media. *Public Understanding of Science*, Volume 9, pp. 261-283.
- WIGLEY, T. M. L. AND JONES, P. D. (1985): Influences of precipitation changes and direct CO<sub>2</sub> effects on streamflow. *Nature*, Volume 314, Issue 6007, pp. 149-152.
- WOHLFAHRT, G., BIANCHI, K. AND CERNUSCA, A. (2006): Leaf and stem maximum water storage capacity of herbaceous plants in a mountain meadow. *Journal of Hydrology*, Volume 319, Issue 1-4, pp. 383-390.
- WONG, S. C. (1979): Elevated atmospheric partial pressure of CO<sub>2</sub> and plant growth. I. Interactions of nitrogen nutrition and photosynthetic capacity in C<sub>3</sub> and C<sub>4</sub> plants. *Oecologia*, Volume 44, Issue 1, pp. 68-74.
- WONG, S. C., COWAN, I. R. AND FARQUHAR, G. D. (1979): Stomatal conductance correlates with photosynthetic capacity. *Nature*, Volume 282, Issue 5737, pp. 424–426.
- WOODWARD, F. I., SMITH, T. M. AND EMANUEL, W. R. (1995): A global land primary productivity and phytogeography model. *Global Biogeochemical Cycles*, Volume 9, pp. 471–490.
- WULLSCHLEGER, S. D., GUNDERSON, C. A., HANSON, P. J., WILSON, K. B. AND NORBY R. J. (2002): Sensitivity of stomatal and canopy conductance to elevated CO<sub>2</sub> concentration - interacting variables and perspectives of scale. *New Phytologist*, Volume 153, Issue 3, pp. 485–496.
- YAN, W. AND HUNT, L. A. (1999): An equation modeling the temperature response of plant growth and development using only the cardinal temperatures. *Annals of Botany*, Volume 84, Issue 5, pp. 607-614.
- YIN, X. AND VAN LAAR, H. (2005): Crop Systems Dynamics. An Ecophysiological Simulation Model for Genotype-By-Environment Interactions. Wageningen Academic Publishers, Wageningen, The Netherlands, pp. 155.
- ZHANG, H. AND NOBEL, P. S. (1996): Dependency of ci/ca and leaf transpiration efficiency on the vapor pressure deficit. *Australian Journal of Plant Physiology*, Volume 23, Issue 5, pp. 561-568.



# 11. Curriculum Vitae

## Personal

Name: Tobias Benedikt Hank  
 Date of Birth: 7<sup>th</sup> of May 1978  
 Place of Birth: Munich / Upper Bavaria / Germany  
 Age: 29  
 Nationality: German  
 Degree: Dipl. Geogr. (*phys. Univ.*)  
 Marital Status: Unmarried  
 Postal Address: Agnesstraße 2 / II  
 D-80801 Munich / Germany  
 Affiliation: LMU Munich / Faculty of Geosciences / Dept. of Geography  
 Chair of Geography and Geographic Remote Sensing  
 Luisenstrasse 37 / III / 428  
 D-80333 Munich / Germany  
 Telephone: +49 (0)89 / 2180 - 6689  
 Email: t.hank@iggf.geo.uni-muenchen.de

## Scientific Career

Since 5 / 2007: Lecturer at the Department of Geography of the Ludwig-Maximilians-Universität Munich (Germany).  
 Since 5 / 2004: Scientific researcher at the chair of Geography and Geographic Remote Sensing at the LMU-Munich.  
 2003: Working student at the „Ground Truth Center Oberbayern (GTCO)“ in Germering (Germany).  
 2001 / 2002: Employee at the „Gesellschaft für Angewandte Fernerkundung (GAF) AG“ in Munich.  
 1998 – 2003: Student assistant at the chair of Geography and Geographic Remote Sensing at the LMU-Munich.

---

### School and Education

- 2004 - 2007: PhD studies at the LMU-Munich (Germany).
- 2004: Degree with distinction in physical Geography at the LMU-Munich. Subsidiary subjects: Zoology, Remote Sensing.
- 2004: Diploma Thesis: “*Simulation eines Weizenstandortes mit dem physikalisch basierten Modell WHNSIM – Möglichkeiten der Validierung mit Hilfe von hyperspektraler Fernerkundung* [Simulation of a Stand of Winter Wheat using the Physically Based Model WHNSIM – Potential of Hyperspectral Remote Sensing for Validation Purposes]”.
- 2000 – 2004: Advanced studies of physical Geography at the LMU-Munich.
- 2000: Intermediate diploma in physical Geography at the LMU-Munich.
- 1998 – 2000: Elementary studies of physical Geography at the LMU-Munich.
- 1997: High-School-Degree at the “*Ludwig-Thoma-Gymnasium*” in Prien am Chiemsee (Germany).
- 1985 – 1997: Comprehensive school „*FWS Chiemgau*“ in Prien am Chiemsee (Germany).
- 1984 – 1985: Primary school „*Grund- und Volksschule*“ in Feldkirchen-Westerham (Germany).

---

### General Conscription

- 1997 – 1998: Alternative civilian service at the „*CARITAS Kontaktstelle für Behinderte* [CARITAS Contact Point for Challenged People]“ in Rosenheim (Germany).

**A Biophysically Based Coupled Model Approach  
For the Assessment of Canopy Processes  
Under Climate Change Conditions**

Dissertation der Fakultät für Geowissenschaften  
der Ludwig-Maximilians-Universität München



**APPENDIX**

vorgelegt von:

*Tobias Benedikt Hank*

aus München

Eingereicht am 30. April 2008

## Table of Contents

<b>12.</b>	<b>Appendix</b>	
A.1	List of Symbols	001
A.2	DOY-Table for Normal Years	014
A.3	DOY-Table for Leap Years	015
A.4	Species of Bavarian Forests	016
A.5	Map of Landuse	017
A.6	Map of Soil Texture	018
A.7	Map of Terrain Elevation	019
A.8	Parameters Applied to the Modelled Landcover Types (1 – 27)	020
A.8.1.	Coniferous Forest	020
A.8.2.	Extensive Grassland	021
A.8.3.	Intensive Grassland	022
A.8.4.	Deciduous Forest	023
A.8.5.	Winter Wheat	024
A.8.6.	Silage	025
A.8.7.	Winter Barley	026
A.8.8.	Natural Grassland	027
A.8.9.	Forage	028
A.8.10.	Summer Barley	029
A.8.11.	Wetland	030
A.8.12.	Oleaginous	031
A.8.13.	Set Aside	032
A.8.14.	Alpine Grassland	033
A.8.15.	Oat	034
A.8.16.	Maize	035
A.8.17.	Sugar	036
A.8.18.	Potato	037
A.8.19.	Rye	038
A.8.20.	Hop	039
A.8.21.	Summer Wheat	040
A.8.22.	Legumes	041
A.8.23.	Rock	042

---

A.8.24.	Residential Areas	042
A.8.25.	Water	042
A.8.26.	Glacier	042
A.8.27.	Industrial	042
A.9	Parameters of Selected Soil Types	043
A.10	Acre File of the Wheat Test Site "Hofanger" Season 2004	044
A.11	Acre File of the Wheat Test Site "Kochfeld" Season 2005	045
A.12	Available Historic Test Sites	046
A.13	List of Selected Reference Proxels	047
A.14	Long-Term Annual Evapotranspiration (Biological vs. Penman-Monteith)	048
A.15	Selected International Phenological Gardens of Europe	051
A.16	Long-Time Records of Phenological Phases in Europe	052
A.17	Reference and Scenario Period – Selected Model Results	053
A.17.1.	Annual Mean Temperature	053
A.17.2.	Annual Sum of Precipitation	053
A.17.3.	Leaf Emergence of Deciduous Forest	054
A.17.4.	Defoliation of Deciduous Forest	054
A.17.5.	Vegetation Period of Deciduous Trees	055
A.17.6.	Mayshoot of Coniferous Forest	055
A.17.7.	Biological Productivity	056
A.17.8.	Drought Stress	056
A.17.9.	Transpiration	057
A.17.10.	Evapotranspiration	057

## 12. Appendix

### A.1 List of Symbols

#### Radiation - Page 31 et seq.

Symbol	Caption	Unit
$A_c$	= Albedo of the canopy	[%]
$A_s$	= Albedo of bare soil	[%]
$aLW_1$	= Absorbed long wave rad. upper veg. layer	[W m <sup>-2</sup> ]
$aLW_2$	= Absorbed long wave rad. lower veg. layer	[W m <sup>-2</sup> ]
$aPAR_{dif}$	= Absorbed diffuse PAR	[W m <sup>-2</sup> ]
$aPAR_{dir}$	= Absorbed direct PAR	[W m <sup>-2</sup> ]
$\alpha_{lw}$	= Leaf absorptivity for long wave radiation	[%]
$\alpha_{nir}$	= Leaf absorptivity for near Infrared	[%]
$\alpha_{par}$	= Leaf absorptivity for PAR	[%]
$\alpha_{sw}$	= Leaf absorptivity for short wave radiation	[%]
$\beta_l$	= Leaf angle	[°]
$fPAR$	= Fraction of PAR	[%]
$K_{dif}$	= Extinction coefficient for diffuse radiation	[-]
$K_{ed}$	= Extinction coeff. for ellipsoidal canopies	[-]
$LAI$	= Leaf area Index	[m <sup>2</sup> m <sup>-2</sup> ]
$LA_1$	= Leaf area of the upper veg. layer	[m <sup>2</sup> ]
$LA_2$	= Leaf area of the lower veg. layer	[m <sup>2</sup> ]
$LA_{sun1}$	= Sunlit leaf area of the upper veg. layer	[m <sup>2</sup> ]
$LA_{sun2}$	= Sunlit leaf area of the lower veg. layer	[m <sup>2</sup> ]
$LW$	= Incoming long wave radiation	[W m <sup>-2</sup> ]
$\rho_{cpy}^H$	= Canopy hemispherical reflection coeff.	[-]
$S_{f1}$	= Fraction of shaded leaf area upper layer	[%]
$S_{f2}$	= Fraction of shaded leaf area lower layer	[%]
$SW_{dif}$	= Incoming shortwave diffuse radiation	[W m <sup>-2</sup> ]
$SW_{dir}$	= Incoming shortwave direct radiation	[W m <sup>-2</sup> ]

**Radiation (continued) - Page 31 et seq.**

<b>Symbol</b>	<b>Caption</b>	<b>Unit</b>
$\sigma$	= Stefan-Boltzmann constant ( $5.6704 \times 10^{-8}$ )	[W m <sup>-2</sup> K <sup>-4</sup> ]
$T_{c1}$	= Canopy temperature upper veg. layer	[K]
$T_{c2}$	= Canopy temperature lower veg. layer	[K]
$tPAR_{dif}$	= Fraction of transmitted diffuse PAR	[-]
$tPAR_{dir}$	= Fraction of transmitted direct PAR	[-]
$T_s$	= Soil surface temperature	[K]
$\chi$	= Canopy shape parameter	[0 - 1]
$\Psi$	= Solar zenith angle	[°]

**Surface Processes - Page 36 et seq.**

<b>Symbol</b>	<b>Caption</b>	<b>Unit</b>
$c_p$	= Specific heat of air	[J g <sup>-1</sup> K <sup>-1</sup> ]
$dis_0$	= Zero plane displacement height	[m]
$\Delta I$	= Intercepted water storage	[mm]
$\Delta I_{max}$	= Maximum interception capacity	[mm]
$\Delta s_{snow}$	= Snow water storage	[mm]
$\Delta s_{soil}$	= Soil water storage	[mm]
$e$	= Saturation pressure	[mb]
$E_I$	= Interception evaporation	[mm]
$E_p$	= Latent heat of potential evaporation	[W m <sup>-2</sup> h <sup>-1</sup> ]
$e_s$	= Saturation deficit	[mb]
$E_S$	= Soil evaporation	[mm]
$E_T$	= Transpiration	[mm]
$fCOVER$	= Fractional cover	[%]
$\gamma$	= Psychrometric constant	[mb °C <sup>-1</sup> ]
$H_c$	= Height of the canopy	[m]
$H_m$	= Measurement height	[m]
$K$	= Von Karman constant (0.41)	[-]

### Surface Processes (continued) - Page 36 et seq.

Symbol	Caption	Unit
$L$	= Latent heat of vaporization	[J g <sup>-1</sup> ]
$L^*$	= Specific heat of evaporation per mm	[J g <sup>-1</sup> ]
$LAI$	= Leaf Area Index	[m <sup>2</sup> m <sup>-2</sup> ]
$LW$	= Incoming long wave radiation	[W m <sup>-2</sup> ]
$M_{air}$	= Molar mass of air (28.97)	[g mol <sup>-1</sup> ]
$M_{H_2O}$	= Molar mass of water (0.0180153)	[kg mol <sup>-1</sup> ]
$O_{lw}$	= Outgoing long wave radiation	[W m <sup>-2</sup> ]
$O_{sw}$	= Outgoing shortwave radiation	[W m <sup>-2</sup> ]
$p$	= Air density	[g m <sup>-3</sup> ]
$P_{eff}$	= Effective precipitation	[mm]
$P_{int}$	= Intercepted precipitation	[mm]
$R$	= Gas constant (8.314472...)	[J K <sup>-1</sup> mol <sup>-1</sup> ]
$r_a$	= Aerodynamic resistance	[s m <sup>-1</sup> ]
$R_i$	= Interflow	[mm]
$R_n$	= Radiation balance	[W m <sup>-2</sup> ]
$R_s$	= Surface runoff	[mm]
$s(T_l)$	= Slope of the saturation pressure curve	[Pa K <sup>-1</sup> ]
$SW_{dif}$	= Incoming shortwave diffuse radiation	[W m <sup>-2</sup> ]
$SW_{dir}$	= Incoming shortwave direct radiation	[W m <sup>-2</sup> ]
$T_l$	= Leaf temperature	[K]
$u^*$	= Friction velocity	[m s <sup>-1</sup> ]
$u(z)$	= Wind velocity at height z	[m s <sup>-1</sup> ]
$z$	= Height above ground	[m]
$z_m$	= Roughness length	[m]



**Biological Initialisation - Page 45 et seq.**

<b>Symbol</b>	<b>Caption</b>	<b>Unit</b>
$B_{leaf}$	= Leaf biomass	[kg m <sup>-2</sup> ]
$d$	= Model day	[DOY]
$d_{decend}$	= Day of end of LAI decrease phase	[DOY]
$d_{decstart}$	= Day of start of LAI decrease phase	[DOY]
$d_{incend}$	= Day of end of LAI increase phase	[DOY]
$d_{incstart}$	= Day of start of LAI increase phase	[DOY]
$e$	= Eularian number (2.718281828459...)	[const.]
$h_c$	= Canopy height	[m]
$k_1$	= Coefficient of LAI-increase curve	[-]
$k_2$	= Coefficient of LAI-decrease curve	[-]
$LAI$	= Leaf Area Index	[m <sup>2</sup> m <sup>-2</sup> ]
$LAI_{ini}$	= Initial (minimum) Leaf Area Index	[m <sup>2</sup> m <sup>-2</sup> ]
$LAI_{max}$	= Maximum Leaf Area Index	[m <sup>2</sup> m <sup>-2</sup> ]
$LH_{rel}$	= Relation of LAI to canopy height	[m m <sup>-2</sup> leaf area]
$LMA$	= Cultivar specific leaf mass area	[kg m <sup>-2</sup> leaf area]
$L_s$	= Number of soil layer	[-]
$RD$	= Root depth	[cm]
$RD_{max}$	= Maximum root depth	[cm]
$R_{LAI}$	= LAI reduction factor	[0 - 1]
$RLD_{L_s}$	= Root length density at a soil layer	[cm cm <sup>-3</sup> ]
$T_{avg}$	= Annual mean temperature	[°C]

**Agricultural Management - Page 49 et seq.**

<b>Symbol</b>	<b>Caption</b>	<b>Unit</b>
$B_{grain}$	= Grain biomass	[kg m <sup>-2</sup> ]
$B_{har}$	= Harvest mass	[t ha <sup>-1</sup> ]
$d_{har}$	= Harvest date	[DOY]
$d_{sow}$	= Sowing date	[DOY]

### Agricultural Management (continued) - Page 49 et seq.

Symbol	Caption	Unit
$m$	= Slope of grain mass to harvest relation	[-]
$b$	= Intercept of grain mass to harvest relation	[t ha <sup>-1</sup> ]

### Leaf Temperature - Page 52 et seq.

Symbol	Caption	Unit
$\alpha_{leaf}$	= Absorptivity of the leaf	[%]
$Diss_{int}$	= Heat dissipation at intermediate temp.	[KW m <sup>-2</sup> ]
$Diss_{sens}$	= Heat dissipation due to conduction	[KW m <sup>-2</sup> ]
$Diss_{Lat}$	= Latent heat dissipation	[KW m <sup>-2</sup> ]
$Diss_{low}$	= Heat dissipation at lower boundary	[KW m <sup>-2</sup> ]
$Diss_{rad}$	= Heat dissipation due to emission	[KW m <sup>-2</sup> ]
$Diss_{tot}$	= Total heat dissipation	[KW m <sup>-2</sup> ]
$Diss_{upp}$	= Heat dissipation at upper boundary	[KW m <sup>-2</sup> ]
$dwv$	= Diffusion coefficient of water vapour	[m <sup>2</sup> s <sup>-1</sup> ]
$\Delta e$	= Saturation deficit	[mbar]
$\Delta T$	= Temperature gradient	[K]
$e_a$	= Atmospheric vapour pressure	[mbar]
$e_l$	= Vapour pressure in the leaf	[mbar]
$E_{Tflux}$	= Transpiration	[mmol m <sup>-2</sup> leaf area s <sup>-1</sup> ]
$g_a$	= Boundary layer conductivity for H <sub>2</sub> O	[mmol m <sup>-2</sup> leaf area s <sup>-1</sup> ]
$g_l$	= Leaf conductivity to H <sub>2</sub> O	[mmol m <sup>-2</sup> leaf area s <sup>-1</sup> ]
$g_s$	= Stomatal conductivity for H <sub>2</sub> O	[mmol m <sup>-2</sup> leaf area s <sup>-1</sup> ]
$P$	= Air pressure	[Pa / mbar]
$R$	= Gas constant (8.314472...)	[J K <sup>-1</sup> mol <sup>-1</sup> ]
$rad_{eq}$	= Equilibrium radiation	[KW m <sup>-2</sup> ]
$\sigma$	= Stefan-Boltzmann constant (5.6704 x 10 <sup>-8</sup> )	[W m <sup>-2</sup> K <sup>-4</sup> ]
$\Sigma_{bl}$	= Scaling factor for the bunching of needles	[-]
$T_a$	= Air temperature	[°C]

### Leaf Temperature (continued) - Page 52 et seq.

Symbol	Caption	Unit
$tbl$	= Thickness of boundary layer	[m]
$tca$	= Thermal conductivity of air	[W m <sup>-1</sup> °C <sup>-1</sup> ]
$T_{l,est}$	= Estimated leaf temperature	[K]
$T_{l,low}$	= Lower boundary of the est. leaf temp.	[K]
$T_{l,ini}$	= Initial leaf temperature	[K]
$T_{l,upp}$	= Upper boundary of the est. leaf temp.	[K]
$u$	= Wind velocity	[m s <sup>-1</sup> ]
$wl$	= Width of leaf	[m]

### Photosynthesis - Page 59 et seq.

Symbol	Caption	Unit
$\alpha$	= Light use efficiency	[mol CO <sub>2</sub> mol photons <sup>-1</sup> ]
$aPAR$	= Absorbed photosynthetic radiation	[μmol photons m <sup>-2</sup> leaf area s <sup>-1</sup> ]
$c_0$	= Empirical input coefficient 1	[-]
$c_1$	= Empirical input coefficient 2	[1 kPA <sup>-1</sup> ]
$C_a$	= Atmospheric CO <sub>2</sub> concentration	[ppm]
$C_i$	= Internal (leaf) CO <sub>2</sub> concentration	[ppm]
$\Delta s$	= Entropy term	[J K <sup>-1</sup> mol <sup>-1</sup> ]
$e$	= Eulerian number (2.718281828459...)	[const.]
$e_a$	= Atmospheric vapour pressure	[mbar]
$Ea_{J_{max}}$	= Activation energy	[J mol <sup>-1</sup> ]
$Ea_{V_{C_{max}}}$	= Activation energy	[J mol <sup>-1</sup> ]
$Ea_{(rd,\tau,c,o)}$	= Activation energies	[J mol <sup>-1</sup> ]
$Ed_{J_{max}}$	= Deactivation energy	[J mol <sup>-1</sup> ]
$Ed_{V_{C_{max}}}$	= Deactivation energy	[J mol <sup>-1</sup> ]
$e_l$	= Vapour pressure in the leaf	[mbar]
$\Gamma^*$	= CO <sub>2</sub> compensation point	[μl l <sup>-1</sup> ] / [ml l <sup>-1</sup> ]
$gfac$	= Stomatal sensitivity parameter	[-]

## Photosynthesis (continued) - Page 59 et seq.

Symbol	Caption	Unit
$g_{\min}$	= Conductance of the cuticle	[mmol m <sup>-2</sup> leaf area s <sup>-1</sup> ]
$g_s$	= Stomatal conductivity for H <sub>2</sub> O	[mmol m <sup>-2</sup> leaf area s <sup>-1</sup> ]
$J_{\max 25}$	= Max. rate of electron transport at 25 °C	[ $\mu$ mol e <sup>-1</sup> m <sup>-2</sup> leaf area s <sup>-1</sup> ]
$K_c$	= Michaelis-Menten constant for C	[ $\mu$ l l <sup>-1</sup> ]
$K_{c25}$	= Michaelis-Menten constant for C at 25 °C	[ $\mu$ l l <sup>-1</sup> ]
$K_o$	= Michaelis-Menten constant for O	[ml l <sup>-1</sup> ]
$K_{o25}$	= Michaelis-Menten constant for O at 25 °C	[ml l <sup>-1</sup> ]
$np$	= Rate of net leaf photosynthesis	[ $\mu$ mol m <sup>-2</sup> leaf area s <sup>-1</sup> ]
$O_2$	= Internal (leaf) concentration of oxygen	[ml l <sup>-1</sup> ]
$p_m$	= Rate of photosynthesis at saturated CO <sub>2</sub>	[ $\mu$ mol m <sup>-2</sup> leaf area s <sup>-1</sup> ]
$p_{ml}$	= Potential rate of RuBP regeneration	[ $\mu$ mol m <sup>-2</sup> leaf area s <sup>-1</sup> ]
$R$	= Gas constant (8.314472...)	[J K <sup>-1</sup> mol <sup>-1</sup> ]
$\tau_{25}$	= Substrate specificity at 25 °C	[-]
$r_d$	= Dark respiration	[ $\mu$ mol m <sup>-2</sup> leaf area s <sup>-1</sup> ]
$r_{d25}$	= Respiration capacity at 25 °C	[g CO <sub>2</sub> m <sup>-2</sup> leaf area s <sup>-1</sup> ]
$rh$	= Relative air humidity	[%]
$\tau$	= Substrate specificity	[-]
$T_{l,est}$	= Estimated leaf temperature	[K]
$Vc_{\max}$	= Maximum speed of carboxylation	[mmol m <sup>-2</sup> leaf area s <sup>-1</sup> ]
$Vc_{\max 25}$	= Carboxylation capacity at 25 °C	[ $\mu$ mol m <sup>-2</sup> leaf area s <sup>-1</sup> ]
$Vo_{\max}$	= Maximum rate of oxygenation	[ $\mu$ mol m <sup>-2</sup> leaf area s <sup>-1</sup> ]
$w_c$	= RuBisCO limited rate of carboxylation	[ $\mu$ mol m <sup>-2</sup> leaf area s <sup>-1</sup> ]
$w_j$	= Carboxylation rate ltd. by electron transp.	[ $\mu$ mol m <sup>-2</sup> leaf area s <sup>-1</sup> ]
$w_o$	= RuBisCO limited rate of oxygenation	[ $\mu$ mol m <sup>-2</sup> leaf area s <sup>-1</sup> ]

### Photosynthesis, analytical solution - Page 64 et seq.

Symbol	Caption	Unit
$a$	= Auxiliary variable	$[\mu\text{mol m}^{-2} \text{ leaf area s}^{-1}]$
$b$	= Auxiliary variable	$[\mu\text{l l}^{-1}]$
$\beta$	= Auxiliary variable	$[\text{ppm}^2 (\text{mmol m}^{-2} \text{ s}^{-1})^2 (\mu\text{mol m}^{-2} \text{ s}^{-1})^{-1}]$
$d$	= Auxiliary variable	$[\mu\text{l l}^{-1}]$
$dis$	= Discriminant, auxiliary variable	$[(\text{mmol m}^{-2} \text{ s}^{-1})^6]$
$e$	= Auxiliary variable	$[-]$
$\gamma$	= Auxiliary variable	$[\text{ppm} (\text{mmol m}^{-2} \text{ s}^{-1})^2]$
$\kappa$	= Auxiliary variable	$[\text{ppm} (\text{mmol m}^{-2} \text{ s}^{-1})^2 (\mu\text{mol m}^{-2} \text{ s}^{-1})^{-1}]$
$\lambda$	= Auxiliary variable	$[\text{ppm} (\text{mmol m}^{-2} \text{ s}^{-1})^2 (\mu\text{mol m}^{-2} \text{ s}^{-1})^{-1}]$
$np_1$	= Solution of the quadratic/cubic eq. system	$[\mu\text{mol m}^{-2} \text{ leaf area s}^{-1}]$
$np_2$	= Solution of the quadratic/cubic eq. system	$[\mu\text{mol m}^{-2} \text{ leaf area s}^{-1}]$
$np_3$	= Solution of the cubic eq. system	$[\mu\text{mol m}^{-2} \text{ leaf area s}^{-1}]$
$o_1$	= Auxiliary variable	$[\text{ppm}^2 (\text{mmol m}^{-2} \text{ s}^{-1})^2 (\mu\text{mol m}^{-2} \text{ s}^{-1})^{-2}]$
$o_2$	= Auxiliary variable	$[\mu\text{l l}^{-1} \text{ ppm} (\text{mmol m}^{-2} \text{ s}^{-1})^2 (\mu\text{mol m}^{-2} \text{ s}^{-1})^{-1}]$
$o_3$	= Auxiliary variable	$[\mu\text{l l}^{-1} \text{ ppm} (\text{mmol m}^{-2} \text{ s}^{-1})^2]$
$o_4$	= Auxiliary variable	$[\text{ppm}^2 (\text{mmol m}^{-2} \text{ s}^{-1})^2 \mu\text{mol m}^{-2} \text{ s}^{-1}]$
$p$	= Auxiliary variable	$[(\text{mmol m}^{-2} \text{ s}^{-1})^2]$
$q$	= Auxiliary variable	$[(\text{mmol m}^{-2} \text{ s}^{-1})^3]$
$r$	= Auxiliary variable	$[\text{mmol m}^{-2} \text{ s}^{-1}]$
$s$	= Auxiliary variable	$[(\text{mmol m}^{-2} \text{ s}^{-1})^2]$
$t$	= Auxiliary variable	$[(\text{mmol m}^{-2} \text{ s}^{-1})^3]$
$v1$	= Auxiliary variable	$[-]$
$v2$	= Auxiliary variable	$[\text{mmol m}^{-2} \text{ s}^{-1}]$
$y$	= Auxiliary variable	$[\mu\text{mol m}^{-2} \text{ s}^{-1}]$

### Stomatal Conductance - Page 70 et seq.

Symbol	Caption	Unit
$a_{\Psi}$	= Multiplicative scaling parameter	[-]
$b_{\Psi}$	= Additive scaling parameter	[-]
$inh_i$	= Inhibition due to water stress in soil layer i	[0 – 1]
$rl_i$	= Fraction of root length in soil layer i	[%]
$r_r$	= Root resistance	[MPa]
$\Psi_i$	= Soil suction power in layer i	[MPa]
$\Psi_0$	= Soil suction power threshold for inhibition	[MPa]

### Crop Phenology - Page 73 et seq.

Symbol	Caption	Unit
$\alpha^*$	= Twilight angle	[°]
$c_i$	= Temperature response curvature coeff.	[-]
$D_{tp}$	= Daily photoperiod	[h]
$dTT_{avg}$	= Average daily thermal time	[°C]
$hT_{eff}$	= Hourly temperature effect	[0-1]
$hTT$	= Hourly thermal time	[°C]
$L_{eff}$	= Light effect	[0 - 1]
$M_{op}$	= Minimal optimum day length	[h]
$p_{sen}$	= Photoperiod-sensitivity-parameter	[1 h <sup>-1</sup> ]
$\pi$	= Pi (3.14159265358979...)	[const.]
$\varphi$	= Geographic latitude	[°]
$\delta$	= Declination of sun	[°]
$T_{a,i,j}$	= Air temp. on model day i and model hour j	[°C]
$T_b$	= Base temperature	[°C]
$T_c$	= Ceiling temperature	[°C]
$T_o$	= Optimum temperature	[°C]
$Vd_{eff}$	= Effective vernalisation day	[d]
$Vn_{eff}$	= Vernalisation effect	[0 - 1]

**Crop Phenology (continued) - Page 73 et seq.**

<b>Symbol</b>	<b>Caption</b>	<b>Unit</b>
$VnT_b$	= Vernalisation base temperature	[°C]
$Vn_h$	= Hourly vernalisation rate	[-]
$VnT_c$	= Vernalisation ceiling temperature	[°C]
$VnT_o$	= Vernalisation optimum temperature	[°C]
$\omega_i$	= Daily development rate	[-]
$\omega_{i,max}$	= Maximum daily development rate	[-]

**Forest Phenology - Page 77 et seq.**

<b>Symbol</b>	<b>Caption</b>	<b>Unit</b>
$a$	= Additive parameter for temp. threshold	[-]
$b$	= Multiplicative param. for temp. threshold	[-]
$CD$	= Chill day	[d]
$CD_{max}$	= Maximum number of chill days	[d]
$CD_{min}$	= Chill days needed for external dormancy	[d]
$d$	= Actual model day	[d]
$d_1$	= Model start day	[d]
$\overline{T_{a,i}}$	= Mean air temperature on model day i	[°C]
$T_b$	= Base temperature	[°C]
$T_b CD$	= Base temperature for chill days	[°C]
$TT_{crit}$	= Critical heat sum for emergence	[°C]
$TDD$	= Thermal degree day	[d]

**Carbon Allocation - Page 81 et seq.**

<b>Symbol</b>	<b>Caption</b>	<b>Unit</b>
$B_{dec}$	= Percentage of biomass decrease	[% h <sup>-1</sup> ]
$B_{grain}$	= Grain biomass	[kg m <sup>-2</sup> ]
$B_{leaf}$	= Leaf biomass	[kg m <sup>-2</sup> ]
$b_m$	= Maintenance respiration coefficient	[-]

## Carbon Allocation (continued) - Page 81 et seq.

Symbol	Caption	Unit
$B_{root}$	= Root biomass	[kg m <sup>-2</sup> ]
$B_{stem}$	= Stem biomass	[kg m <sup>-2</sup> ]
$B_{tot}$	= Total biomass	[kg m <sup>-2</sup> ]
$E$	= Efficiency of conversion	[%]
$H_c$	= Canopy height	[m]
$k_m$	= Maintenance respiration constant	[g CH <sub>2</sub> O g tissue <sup>-1</sup> h <sup>-1</sup> ]
$LAI$	= Leaf Area Index	[m <sup>2</sup> m <sup>-2</sup> ]
$LH_{rel}$	= Relation of LAI to canopy height	[m m <sup>-2</sup> leaf area]
$LMA_c$	= Cultivar specific leaf mass area	[kg m <sup>-2</sup> leaf area]
$P_n$	= Rate of net photosynthesis	[kg CH <sub>2</sub> O m <sup>-2</sup> h <sup>-1</sup> ]
$P_g$	= Rate of gross primary production	[kg C m <sup>-2</sup> h <sup>-1</sup> ]
$R_{LAI}$	= LAI reduction factor	[0 - 1]
$R_m$	= Maintenance respiration	[g CH <sub>2</sub> O g tissue <sup>-1</sup> h <sup>-1</sup> ]

## Root Growth - Page 86 et seq.

Symbol	Caption	Unit
$hTT$	= Hourly thermal time	[°C]
$incB_{root}$	= Increase of root biomass	[kg m <sup>-2</sup> h <sup>-1</sup> ]
$N_{def}$	= Nitrogen deficit factor	[0 - 1]
$N_{tot}$	= Total nitrogen content of the soil layer	[Kg N ha <sup>-1</sup> ]
$RD_i$	= Root depth on model day i	[cm]
$RD_{max}$	= Maximum root depth	[cm]
$RLD_{fac,l}$	= Root length density factor of soil layer l	[-]
$RLD_{fac,tot}$	= RLD factor of the soil profile	[-]
$RLD_l$	= Root length density per soil layer	[cm cm <sup>-3</sup> ]
$RLD_{l,i}$	= Root length density of soil layer l on day i	[cm cm <sup>-3</sup> ]
$RI_{inc}$	= Root length increase	[cm h <sup>-1</sup> ]
$RL_{max}$	= Deepest rooted soil layer	[1 - 4]



**Root Growth (continued) - Page 86 et seq.**

<b>Symbol</b>	<b>Caption</b>	<b>Unit</b>
$R_{ml}$	= Relation of root mass to root length	[cm kg <sup>-1</sup> ]
$R_p$	= Root preference factor	[0 - 1]
$R_{sen}$	= Root senescence percentage	[% h <sup>-1</sup> ]
$SM_{def}$	= Soil moisture deficit factor	[0 - 1]
$SD_{max}$	= Maximum soil depth	[cm]
$\theta_l$	= Soil moisture in soil layer l	[vol. %]
$\theta_{fc,l}$	= Field capacity in soil layer l	[vol. %]
$\theta_{pf\ 4.2,l}$	= Wilting point in soil layer l	[vol. %]
$Z_l$	= Thickness of the soil layer l	[cm]

**Landuse Parameter Attributes - Page 96/97**

<b>Symbol</b>	<b>Caption</b>	<b>Unit</b>
$AMT$	= Annual Mean Temperature	[°C]
$eFac$	= Increase of root biomass	[kg m <sup>-2</sup> h <sup>-1</sup> ]
$J_{max\ 25}$	= Max. rate of electron transport at 25 °C	[μmol e <sup>-1</sup> m <sup>-2</sup> leaf area s <sup>-1</sup> ]
$r_{d25}$	= Respiration capacity at 25 °C	[g CO <sub>2</sub> m <sup>-2</sup> leaf area s <sup>-1</sup> ]
$Vc_{max\ 25}$	= Carboxylation capacity at 25 °C	[μmol m <sup>-2</sup> leaf area s <sup>-1</sup> ]

**Penman-Monteith Equation - Page 132**

<b>Symbol</b>	<b>Caption</b>	<b>Unit</b>
$c_p$	= Specific heat of air	[J g <sup>-1</sup> K <sup>-1</sup> ]
$e$	= Actual vapour pressure	[kPa]
$e_s$	= Saturation vapour pressure	[kPa]
$ET_a$	= Real landsurface Evapotranspiration	[mm]
$G$	= Ground heat flux	[W m <sup>-2</sup> ]
$\gamma$	= Psychrometric constant	[kPa K <sup>-1</sup> ]
$L^*$	= Specific heat of evaporation	[J g <sup>-1</sup> ]
$p$	= Air density	[g m <sup>-3</sup> ]

**Penman-Monteith Equation (continued) - Page 132**

Symbol	Caption	Unit
$r_a$	= Aerodynamic resistance	[s m <sup>-1</sup> ]
$R_n$	= Net radiation	[W m <sup>-2</sup> ]
$r_s$	= Stomatal resistance	[s m <sup>-1</sup> ]
$S$	= Slope of saturation vapour pressure curve	[kPa K <sup>-1</sup> ]
$T_a$	= Air temperature	[°C]

**Scenario Generation - Page 158 et seq.**

$d1970$	= Days since 1 <sup>st</sup> of January 1970	[d]
$\bar{P}$	= Weekly precipitation sum	[mm]
$\bar{T}$	= Weekly mean temperature	[°C]

**Scenario Results - Page 179**

$WSD_{avg}$	= Average number of water stress days	[d]
$WSD_i$	= Annual sum of water stress day per proxel	[d]
$n$	= Number of proxels reporting water stress	[-]
$N$	= Number of vegetated proxels (68 770)	[-]

## A.2 DOY-Table for Normal Years

Days since the beginning of the year (DOYs) for normal years

	Jan.	Feb.	March	April	May	June	July	August	Sept.	Oct.	Nov.	Dec.
<b>1st</b>	1	32	60	91	121	152	182	213	244	274	305	335
<b>2nd</b>	2	33	61	92	122	153	183	214	245	275	306	336
<b>3rd</b>	3	34	62	93	123	154	184	215	246	276	307	337
<b>4th</b>	4	35	63	94	124	155	185	216	247	277	308	338
<b>5th</b>	5	36	64	95	125	156	186	217	248	278	309	339
<b>6th</b>	6	37	65	96	126	157	187	218	249	279	310	340
<b>7th</b>	7	38	66	97	127	158	188	219	250	280	311	341
<b>8th</b>	8	39	67	98	128	159	189	220	251	281	312	342
<b>9th</b>	9	40	68	99	129	160	190	221	252	282	313	343
<b>10th</b>	10	41	69	100	130	161	191	222	253	283	314	344
<b>11th</b>	11	42	70	101	131	162	192	223	254	284	315	345
<b>12th</b>	12	43	71	102	132	163	193	224	255	285	316	346
<b>13th</b>	13	44	72	103	133	164	194	225	256	286	317	347
<b>14th</b>	14	45	73	104	134	165	195	226	257	287	318	348
<b>15th</b>	15	46	74	105	135	166	196	227	258	288	319	349
<b>16th</b>	16	47	75	106	136	167	197	228	259	289	320	350
<b>17th</b>	17	48	76	107	137	168	198	229	260	290	321	351
<b>18th</b>	18	49	77	108	138	169	199	230	261	291	322	352
<b>19th</b>	19	50	78	109	139	170	200	231	262	292	323	353
<b>20th</b>	20	51	79	110	140	171	201	232	263	293	324	354
<b>21st</b>	21	52	80	111	141	172	202	233	264	294	325	355
<b>22nd</b>	22	53	81	112	142	173	203	234	265	295	326	356
<b>23rd</b>	23	54	82	113	143	174	204	235	266	296	327	357
<b>24th</b>	24	55	83	114	144	175	205	236	267	297	328	358
<b>25th</b>	25	56	84	115	145	176	206	237	268	298	329	359
<b>26th</b>	26	57	85	116	146	177	207	238	269	299	330	360
<b>27th</b>	27	58	86	117	147	178	208	239	270	300	331	361
<b>28th</b>	28	59	87	118	148	179	209	240	271	301	332	362
<b>29th</b>	29		88	119	149	180	210	241	272	302	333	363
<b>30th</b>	30		89	120	150	181	211	242	273	303	334	364
<b>31st</b>	31		90		151		212	243		304		365

Normal Years within the model period (1960-2060)

1961	1974	1987	2001	2014	2027	2041	2054
1962	1975	1989	2002	2015	2029	2042	2055
1963	1977	1990	2003	2017	2030	2043	2056
1965	1978	1991	2005	2018	2031	2045	2057
1966	1979	1993	2006	2019	2033	2046	2058
1967	1981	1994	2007	2021	2034	2047	2059
1969	1982	1995	2009	2022	2035	2049	
1970	1983	1997	2010	2023	2037	2050	
1971	1985	1998	2011	2025	2038	2051	
1973	1986	1999	2013	2026	2039	2053	

## A.3 DOY-Table for Leap Years

Days since the beginning of the year (DOYs) for leap years\*

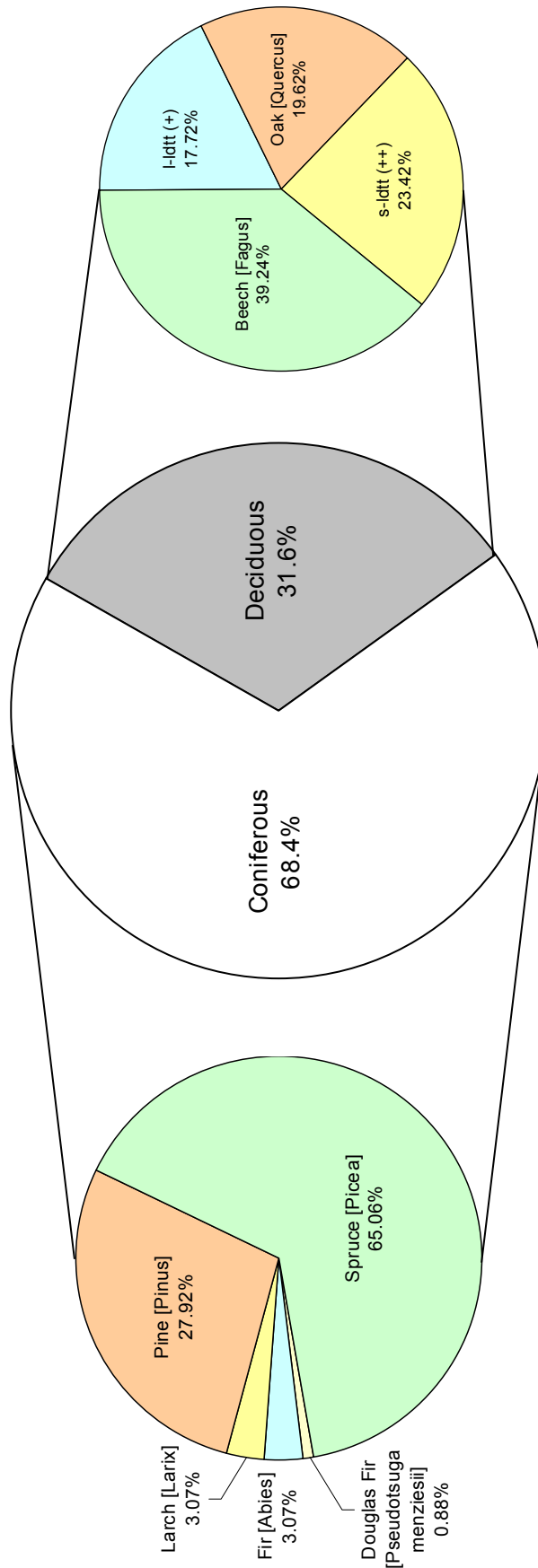
	Jan.	Feb.	March	April	May	June	July	August	Sept.	Oct.	Nov.	Dec.
<b>1st</b>	1	32	61	92	122	153	183	214	245	275	306	336
<b>2nd</b>	2	33	62	93	123	154	184	215	246	276	307	337
<b>3rd</b>	3	34	63	94	124	155	185	216	247	277	308	338
<b>4th</b>	4	35	64	95	125	156	186	217	248	278	309	339
<b>5th</b>	5	36	65	96	126	157	187	218	249	279	310	340
<b>6th</b>	6	37	66	97	127	158	188	219	250	280	311	341
<b>7th</b>	7	38	67	98	128	159	189	220	251	281	312	342
<b>8th</b>	8	39	68	99	129	160	190	221	252	282	313	343
<b>9th</b>	9	40	69	100	130	161	191	222	253	283	314	344
<b>10th</b>	10	41	70	101	131	162	192	223	254	284	315	345
<b>11th</b>	11	42	71	102	132	163	193	224	255	285	316	346
<b>12th</b>	12	43	72	103	133	164	194	225	256	286	317	347
<b>13th</b>	13	44	73	104	134	165	195	226	257	287	318	348
<b>14th</b>	14	45	74	105	135	166	196	227	258	288	319	349
<b>15th</b>	15	46	75	106	136	167	197	228	259	289	320	350
<b>16th</b>	16	47	76	107	137	168	198	229	260	290	321	351
<b>17th</b>	17	48	77	108	138	169	199	230	261	291	322	352
<b>18th</b>	18	49	78	109	139	170	200	231	262	292	323	353
<b>19th</b>	19	50	79	110	140	171	201	232	263	293	324	354
<b>20th</b>	20	51	80	111	141	172	202	233	264	294	325	355
<b>21st</b>	21	52	81	112	142	173	203	234	265	295	326	356
<b>22nd</b>	22	53	82	113	143	174	204	235	266	296	327	357
<b>23rd</b>	23	54	83	114	144	175	205	236	267	297	328	358
<b>24th</b>	24	55	84	115	145	176	206	237	268	298	329	359
<b>25th</b>	25	56	85	116	146	177	207	238	269	299	330	360
<b>26th</b>	26	57	86	117	147	178	208	239	270	300	331	361
<b>27th</b>	27	58	87	118	148	179	209	240	271	301	332	362
<b>28th</b>	28	59	88	119	149	180	210	241	272	302	333	363
<b>29th</b>	29	60	89	120	150	181	211	242	273	303	334	364
<b>30th</b>	30		90	121	151	182	212	243	274	304	335	365
<b>31st</b>	31		91		152		213	244		305		366

Leap Years\* within the model period (1960-2060)

1960	1984	2008	2032	2056
1964	1988	2012	2036	2060
1968	1992	2016	2040	
1972	1996	2020	2044	
1976	2000	2024	2048	
1980	2004	2028	2052	

\*Leap years are all years that are dividable by four without remainder. An exception is made for full centuries, which are calculated like normal years. Another exception is made, if a full century is dividable by 400 without remainder, which then is considered also to be a leap year. This for example is the case for the year 2000 of the model period.

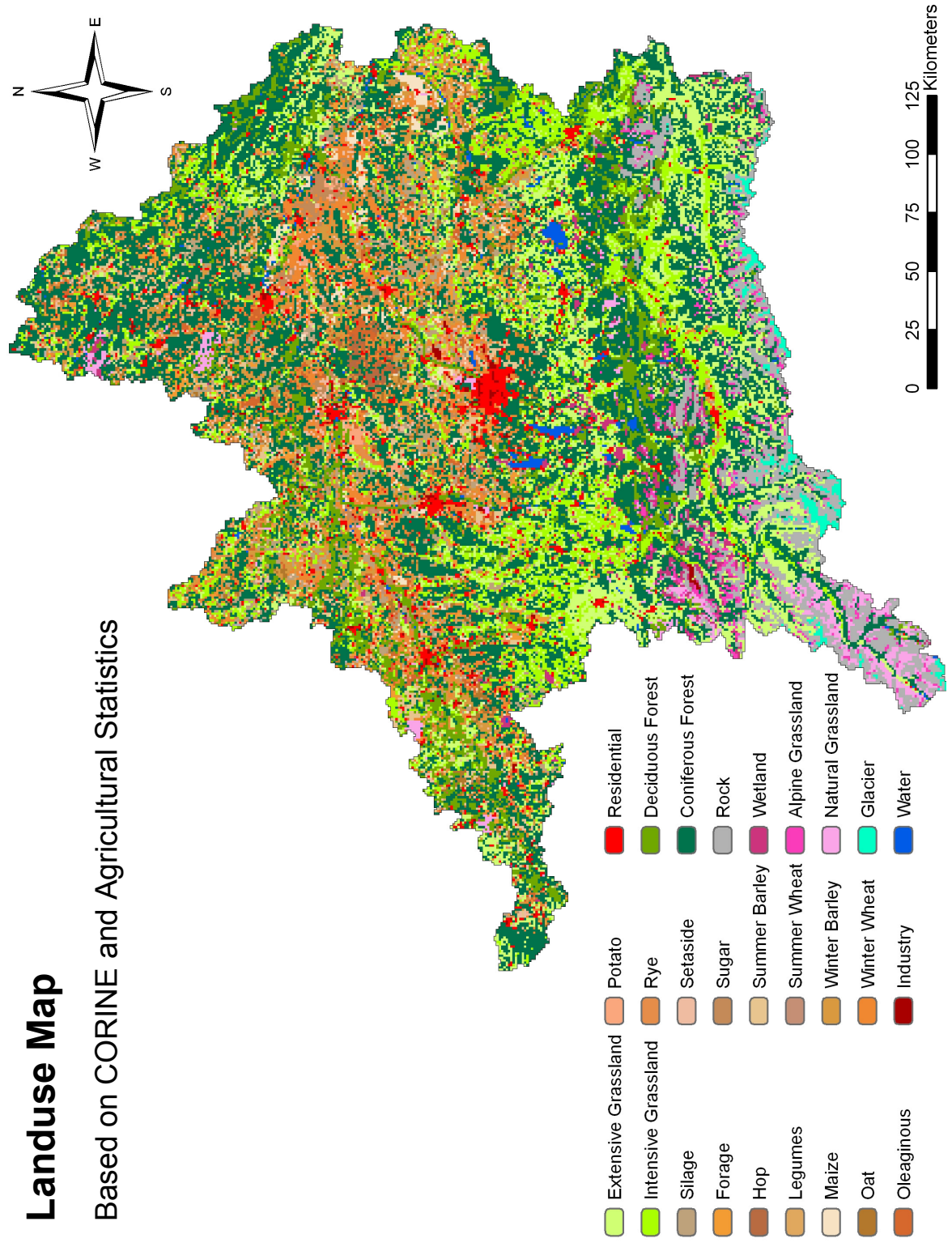
## A.4 Species of Bavarian Forests



(+) l-lttt = long-lived deciduous tree types (Hornbeam [Carpinus], Ash [Fraxinus], Sycamore [Acer pseudoplatanus], Norway Maple [Acer platanoides], Field Maple [Acer campestre], Basswood [Tilia cordata], Elm [Ulmus campestris], Cherry [Prunus cerasus], Locust [Robinia pseudoacacia], Chestnut [Aesculus], Service tree [Sorbus terminalis])

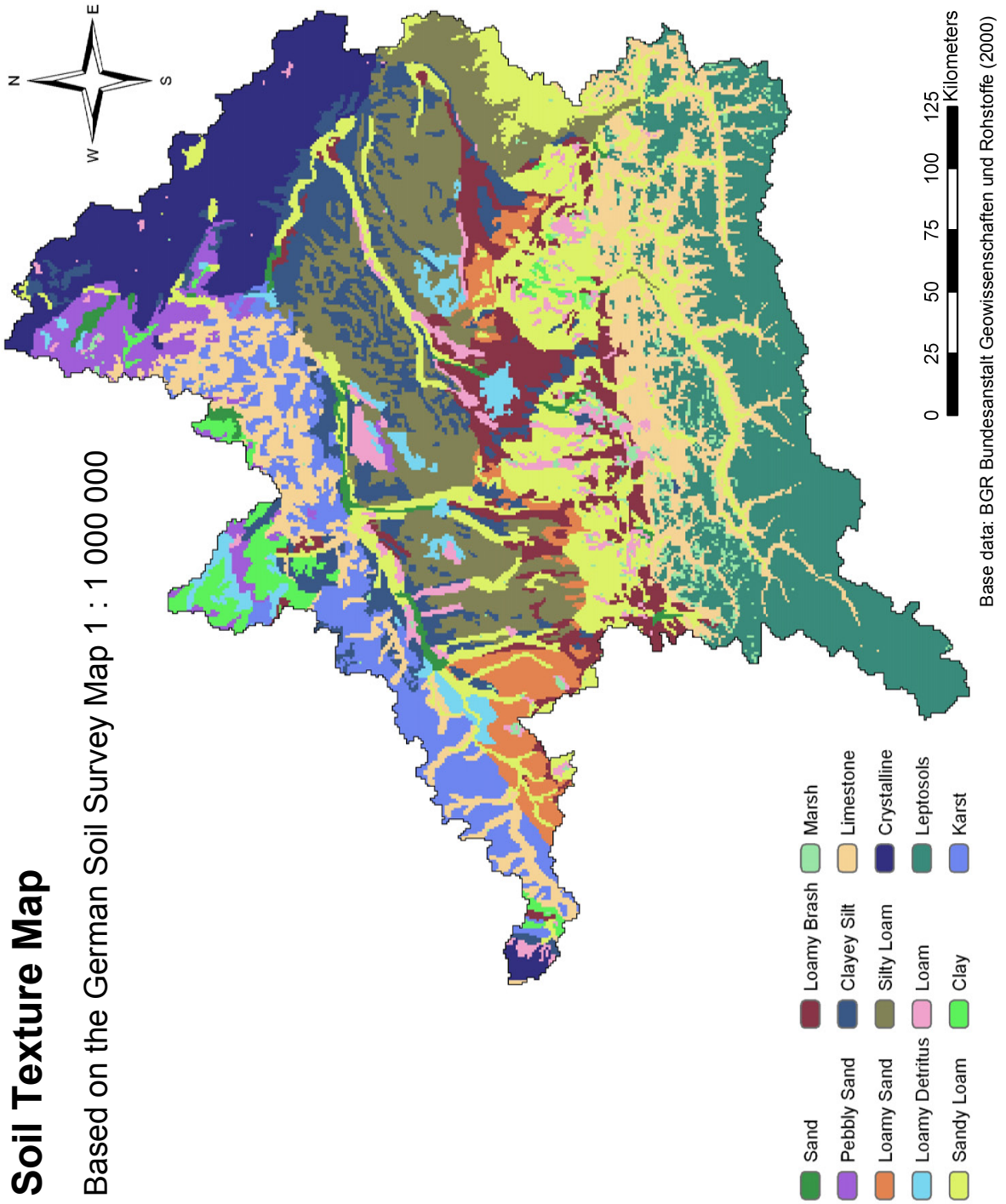
(++) s-lttt = short-lived deciduous tree types (Birch [Betula], Alder [Alnus], Poplar [Populus], Balsam Poplar [Populus balsamifera], Willow [Salix], Rowan Berry [Sorbus aucuparia], other)

## A.5 Map of Landuse



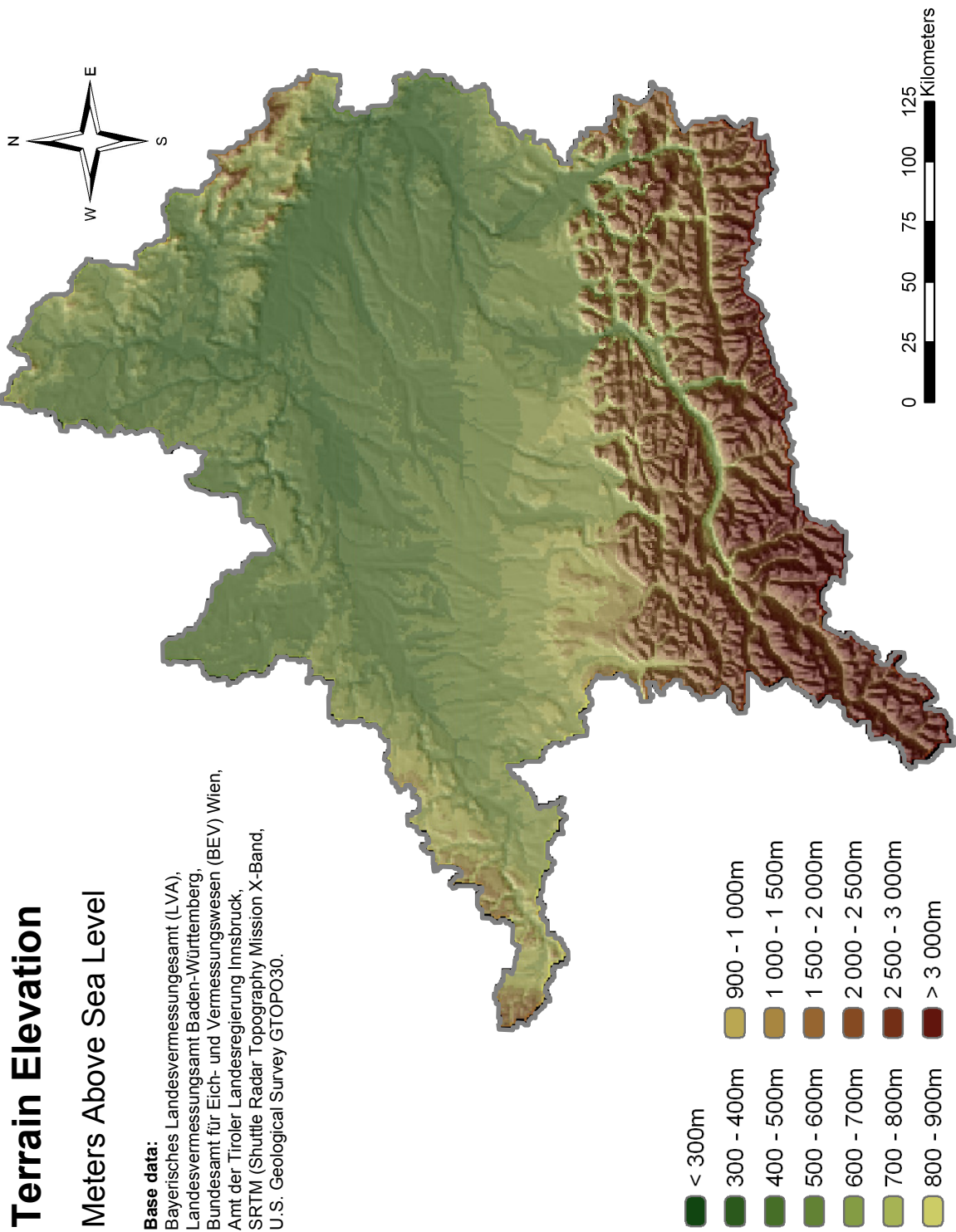
Base data: Bayerisches Landesamt für Statistik und Datenverarbeitung (2001-2003), Bundesanstalt für Statistik Österreich (2004), Österreichisches Statistisches Zentralamt (1996), Statistisches Landesamt Baden-Württemberg (1997), European Environment Agency EEA, CORINE Land Cover, Copenhagen

## A.6 Map of Soil Texture






## A.7 Map of Terrain Elevation





## A.8 Parameters Applied to the Modelled Landcover Types

### A.8.1 Coniferous Forest

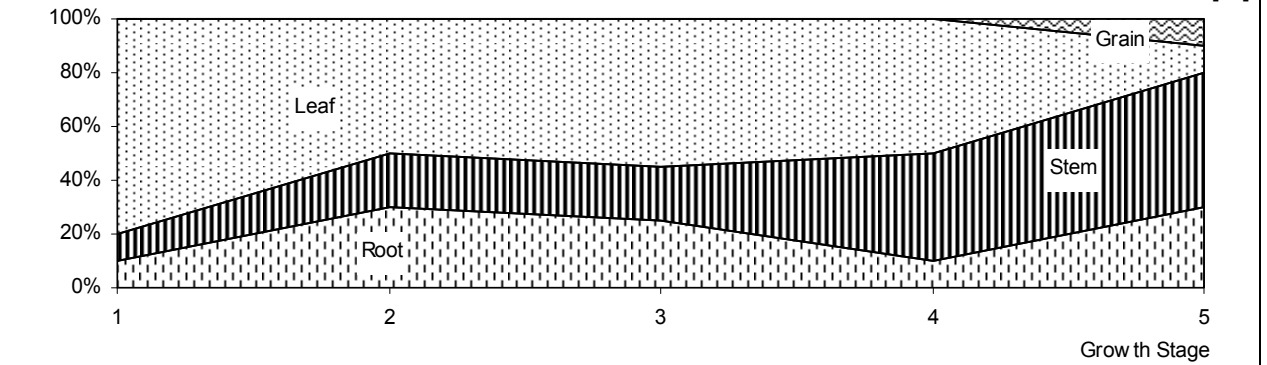


**Area percentage:** 32.82 %

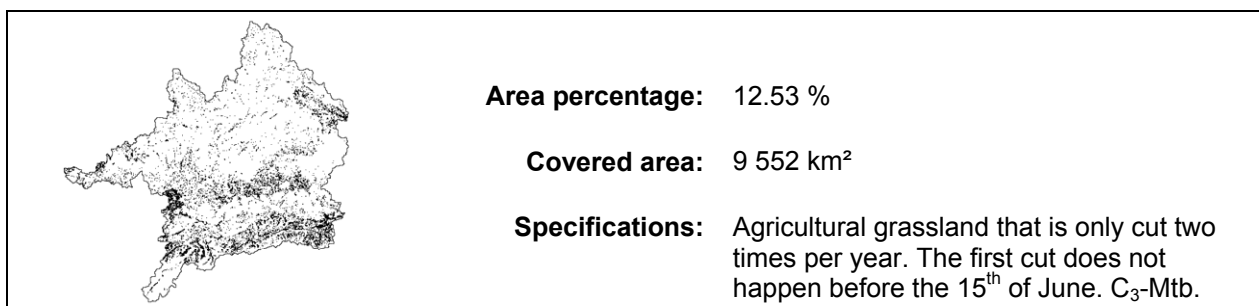
**Covered area:** 25 013 km<sup>2</sup>

**Specifications:** Forested areas with all-season large leaf areas. The predominant land use category in the Upper Danube Basin. C<sub>3</sub>-Metabolism.

Parameter	Value	Unit
$LMA_c$	0.7	[kg m <sup>-2</sup> leaf area]
$d_{sow}$	perennial	[DOY]
$d_{har}$	perennial	[DOY]
$LH_{rel}$	1.5	[m kg <sup>-1</sup> stem mass m <sup>-2</sup> ]
$LAI_{ini}$	7	[m <sup>2</sup> m <sup>-2</sup> ]
$LAI_{max}$	8.5	[m <sup>2</sup> m <sup>-2</sup> ]
$lw$	0.002	[m]
$Vc_{max25}$	dynamic	[μMol m <sup>-2</sup> leaf area s <sup>-1</sup> ]
$J_{max25}$	dynamic	[μMol e <sup>-1</sup> m <sup>-2</sup> leaf area s <sup>-1</sup> ]
$K_{o25}$	278.4	[μl l <sup>-1</sup> ]
$K_{c25}$	404.9	[ml l <sup>-1</sup> ]
$r_{d25}$	dynamic	[g CO <sub>2</sub> m <sup>-2</sup> leaf area s <sup>-1</sup> ]
$\alpha$	0.2	[Mol CO <sub>2</sub> m <sup>-2</sup> leaf area]
$gfac$	9.2	[-]
$O_2$	210	[ml l <sup>-1</sup> ]
$r_d$	0.5	[Fraction]
Long Day Crop Type	0	[Flag]
$3 \times T_b / T_o / T_c$	0, 25, 30 / 0, 25, 30 / 0, 25, 30	[°C]
$TT_{crit}$	60.4	[°C]
$RD_{max}$	130	[cm]
$VnT_b / VnT_o / VnT_c$	-1.3 / 4.9 / 15.7	[°C]
$PT_{thres,i}$	181 / 220 / 250 / 305	[DOY]
Allocation of assimilated carbon:		[%]

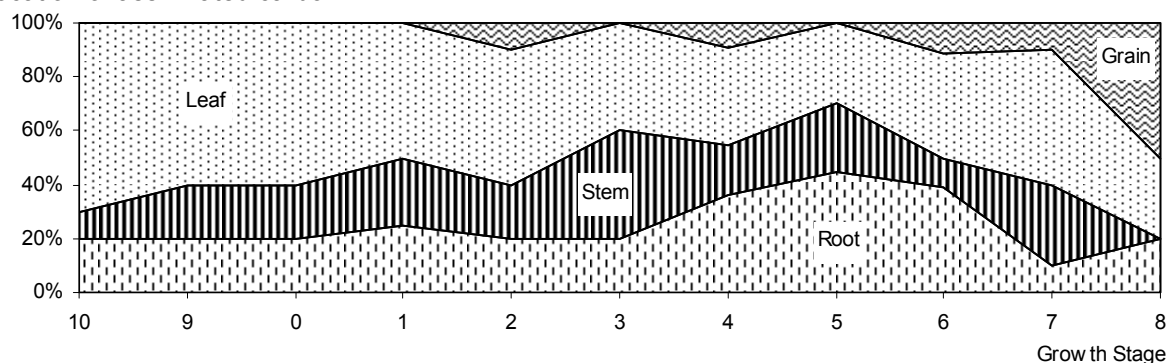


## A.8.2 Extensive Grassland

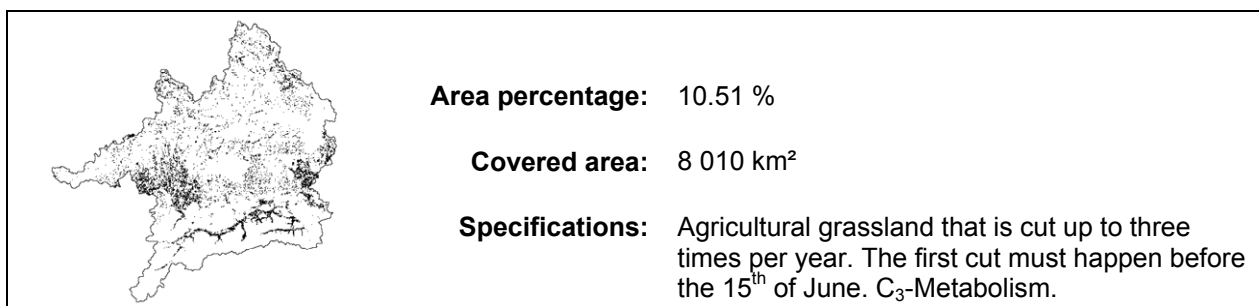


Parameter	Value	Unit
$LMA_c$	0.06	[kg m <sup>-2</sup> leaf area]
$d_{sow}$	perennial	[DOY]
$d_{har}$	perennial	[DOY]
$LH_{rel}$	0.2	[m m <sup>-2</sup> leaf area]
$LAI_{ini}$	0.8	[m <sup>2</sup> m <sup>-2</sup> ]
$LAI_{max}$	4.4	[m <sup>2</sup> m <sup>-2</sup> ]
$lw$	0.02	[m]
$Vc_{max25}$	59.1	[μMol m <sup>-2</sup> leaf area s <sup>-1</sup> ]
$J_{max25}$	30.4	[μMol e <sup>-1</sup> m <sup>-2</sup> leaf area s <sup>-1</sup> ]
$K_{o25}$	278.4	[μl l <sup>-1</sup> ]
$K_{c25}$	404.9	[ml l <sup>-1</sup> ]
$r_{d25}$	0.94	[g CO <sub>2</sub> m <sup>-2</sup> leaf area s <sup>-1</sup> ]
$\alpha$	0.05	[Mol CO <sub>2</sub> m <sup>-2</sup> leaf area]
$gfac$	14.0	[-]
$O_2$	210.0	[ml l <sup>-1</sup> ]
$r_d$	0.5	[Fraction]
Long Day Crop Type	1	[Flag]
$3 \times T_b / T_o / T_c$	0, 20, 30 / 0, 20, 35 / 0, 20, 35	[°C]
$TT_{crit}$	60.4	[°C]
$RD_{max}$	150	[cm]
$VnT_b / VnT_o / VnT_c$	-1.3 / 4.9 / 15.7	[°C]
$9 \times PT_{thres,i}$	0 / 0.2 / 0.3 / 0.45 / 0.6 / 0.9 / 1 / 1.5 / 2	[Thres.]

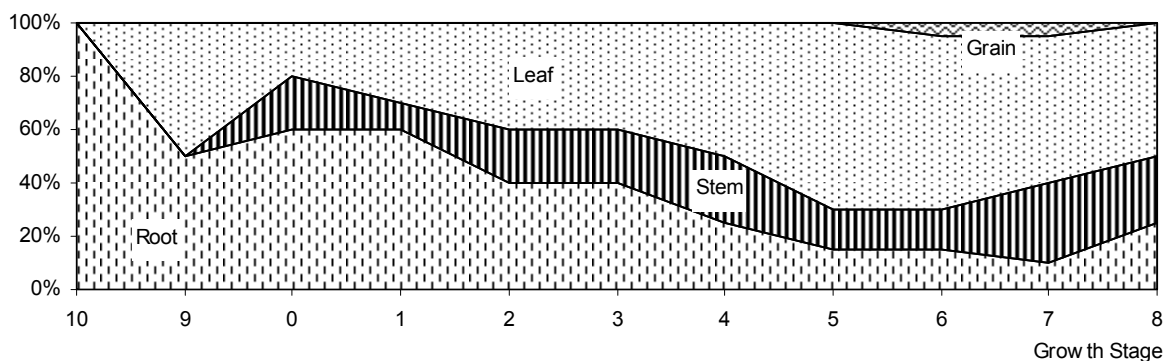
Allocation of assimilated carbon:



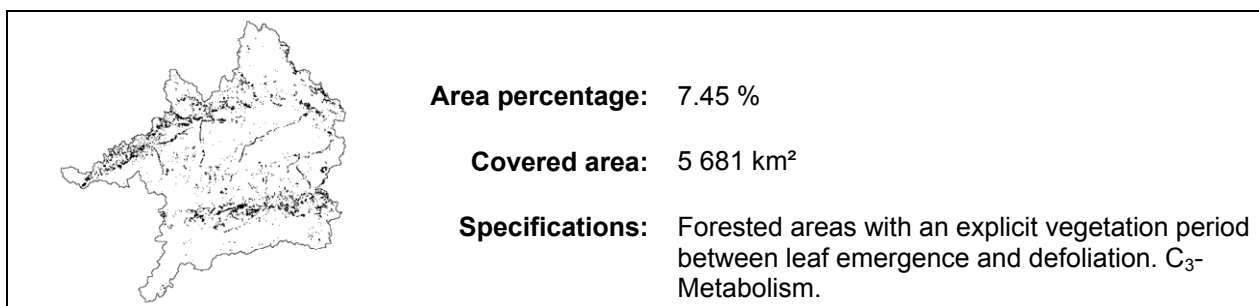
### A.8.3 Intensive Grassland



Parameter	Value	Unit
$LMA_c$	0.065	[kg m <sup>-2</sup> leaf area]
$d_{sow}$	perennial	[DOY]
$d_{har}$	perennial	[DOY]
$LH_{rel}$	0.2	[m m <sup>-2</sup> leaf area]
$LAI_{ini}$	0.8	[m <sup>2</sup> m <sup>-2</sup> ]
$LAI_{max}$	4.2	[m <sup>2</sup> m <sup>-2</sup> ]
$lw$	0.02	[m]
$Vc_{max25}$	59.1	[μMol m <sup>-2</sup> leaf area s <sup>-1</sup> ]
$J_{max25}$	30.4	[μMol e <sup>-1</sup> m <sup>-2</sup> leaf area s <sup>-1</sup> ]
$K_{o25}$	278.4	[μl l <sup>-1</sup> ]
$K_{c25}$	404.9	[ml l <sup>-1</sup> ]
$r_{d25}$	0.94	[g CO <sub>2</sub> m <sup>-2</sup> leaf area s <sup>-1</sup> ]
$\alpha$	0.045	[Mol CO <sub>2</sub> m <sup>-2</sup> leaf area]
$gfac$	16.0	[-]
$O_2$	210.0	[ml l <sup>-1</sup> ]
$r_d$	0.5	[Fraction]
Long Day Crop Type	1	[Flag]
$3 \times T_b / T_o / T_c$	0, 20, 30 / 0, 20, 35 / 0, 20, 35	[°C]
$TT_{crit}$	60.4	[°C]
$RD_{max}$	170	[cm]
$VnT_b / VnT_o / VnT_c$	-1.3 / 4.9 / 15.7	[°C]
$9 \times PT_{thres,i}$	0 / 0.2 / 0.3 / 0.45 / 0.6 / 0.9 / 1 / 1.5 / 2	[Thres.]
Allocation of assimilated carbon:		[%]

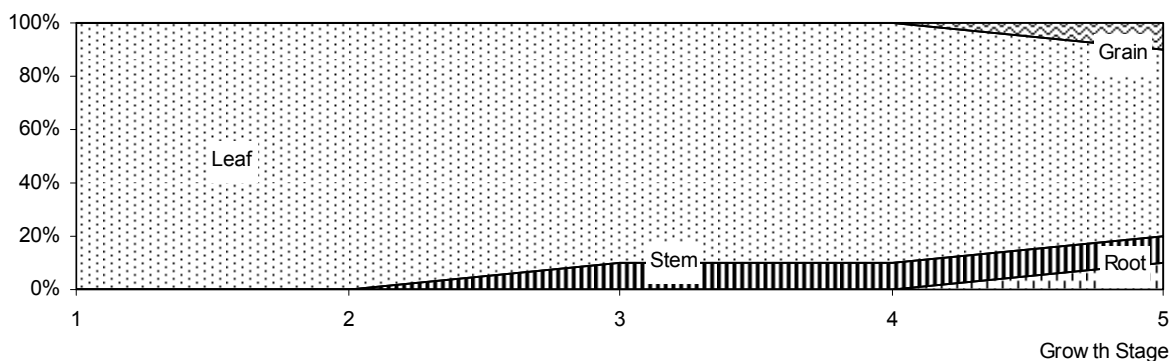


### A.8.4 Deciduous Forest

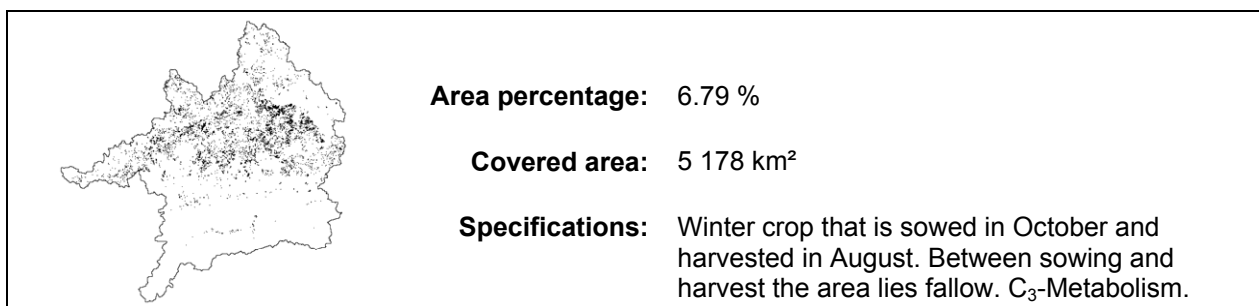


Parameter	Value	Unit
$LMA_c$	0.072	[kg m <sup>-2</sup> leaf area]
$d_{sow}$	181	[DOY]
$d_{har}$	334	[DOY]
$LH_{rel}$	1.4	[m kg <sup>-1</sup> stem mass m <sup>-2</sup> ]
$LAI_{ini}$	2.2	[m <sup>2</sup> m <sup>-2</sup> ]
$LAI_{max}$	8.2	[m <sup>2</sup> m <sup>-2</sup> ]
$lw$	0.08	[m]
$Vc_{max25}$	dynamic	[μMol m <sup>-2</sup> leaf area s <sup>-1</sup> ]
$J_{max25}$	dynamic	[μMol e <sup>-1</sup> m <sup>-2</sup> leaf area s <sup>-1</sup> ]
$K_{o25}$	278.4	[μl l <sup>-1</sup> ]
$K_{c25}$	404.9	[ml l <sup>-1</sup> ]
$r_{d25}$	dynamic	[g CO <sub>2</sub> m <sup>-2</sup> leaf area s <sup>-1</sup> ]
$\alpha$	0.11	[Mol CO <sub>2</sub> m <sup>-2</sup> leaf area]
$gfac$	13.0	[-]
$O_2$	210.0	[ml l <sup>-1</sup> ]
$r_d$	0.5	[Fraction]
Long Day Crop Type	0	[Flag]
$3 \times T_b / T_o / T_c$	0, 25, 30 / 0, 25, 30 / 0, 25, 30	[°C]
$TT_{crit}$	60.4	[°C]
$RD_{max}$	180	[cm]
$VnT_b / VnT_o / VnT_c$	-1.3 / 4.9 / 15.7	[°C]
$PT_{thres,i}$	181 / 220 / 244 / 335	[DOY]

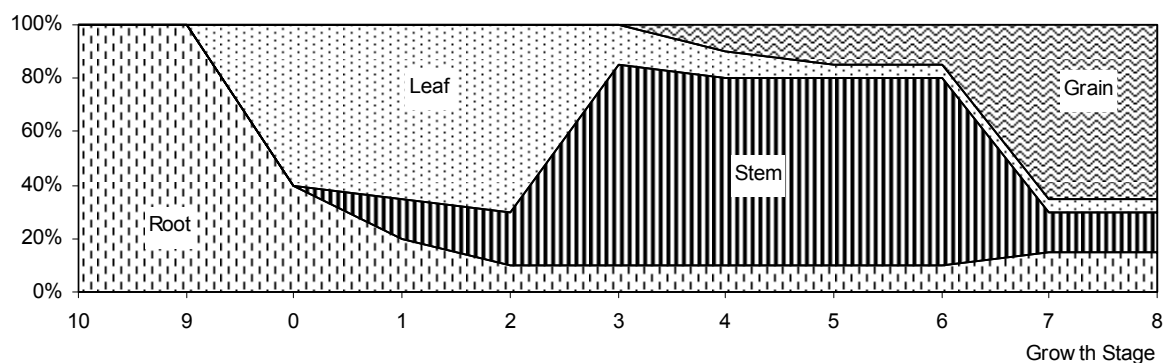
Allocation of assimilated carbon:



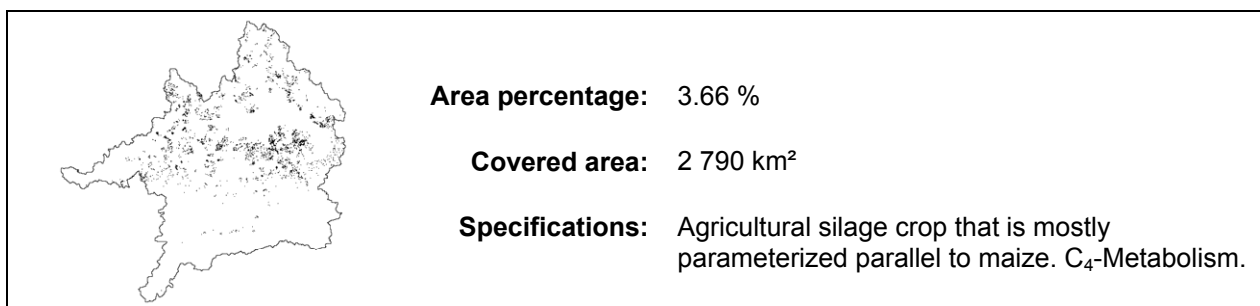
### A.8.5 Winter Wheat



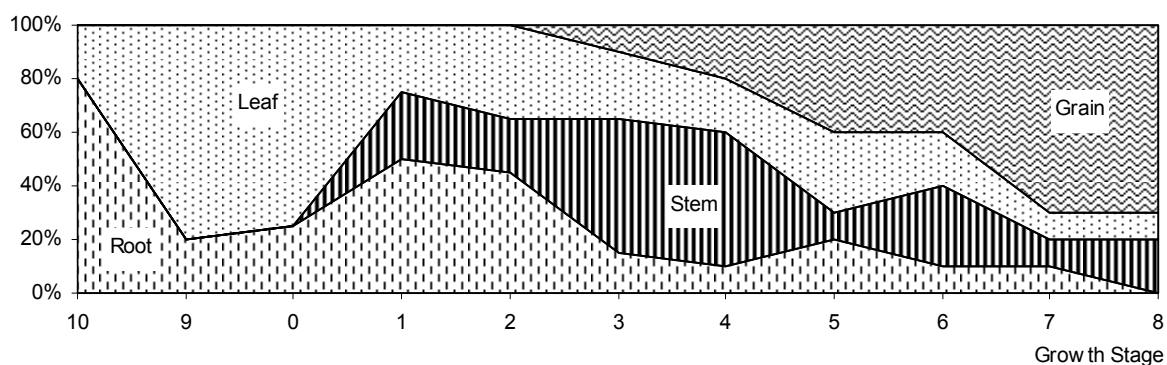
Parameter	Value	Unit
$LMA_c$	0.07	[kg m <sup>-2</sup> leaf area]
$d_{sow}$	288	[DOY]
$d_{har}$	231	[DOY]
$LH_{rel}$	0.1837	[m m <sup>-2</sup> leaf area]
$LAI_{ini}$	0.4	[m <sup>2</sup> m <sup>-2</sup> ]
$LAI_{max}$	6.0	[m <sup>2</sup> m <sup>-2</sup> ]
$lw$	0.015	[m]
$Vc_{max25}$	68.1	[μMol m <sup>-2</sup> leaf area s <sup>-1</sup> ]
$J_{max25}$	32.3	[μMol e <sup>-1</sup> m <sup>-2</sup> leaf area s <sup>-1</sup> ]
$K_{o25}$	278.4	[μl l <sup>-1</sup> ]
$K_{c25}$	404.9	[ml l <sup>-1</sup> ]
$r_{d25}$	0.93	[g CO <sub>2</sub> m <sup>-2</sup> leaf area s <sup>-1</sup> ]
$\alpha$	0.13	[Mol CO <sub>2</sub> m <sup>-2</sup> leaf area]
$gfac$	12.5	[-]
$O_2$	210.0	[ml l <sup>-1</sup> ]
$r_d$	0.5	[Fraction]
Long Day Crop Type	1	[Flag]
$3 \times T_b / T_o / T_c$	0, 19, 30 / 4, 24, 35 / 8, 24, 35	[°C]
$TT_{crit}$	60.4	[°C]
$RD_{max}$	130.0	[cm]
$VnT_b / VnT_o / VnT_c$	-1.3 / 4.9 / 15.7	[°C]
$9 \times PT_{thres,i}$	0 / 0.2 / 0.3 / 0.6 / 0.74 / 0.85 / 2.49 / 2.9 / 3.18	[Thres.]
Allocation of assimilated carbon:		[%]



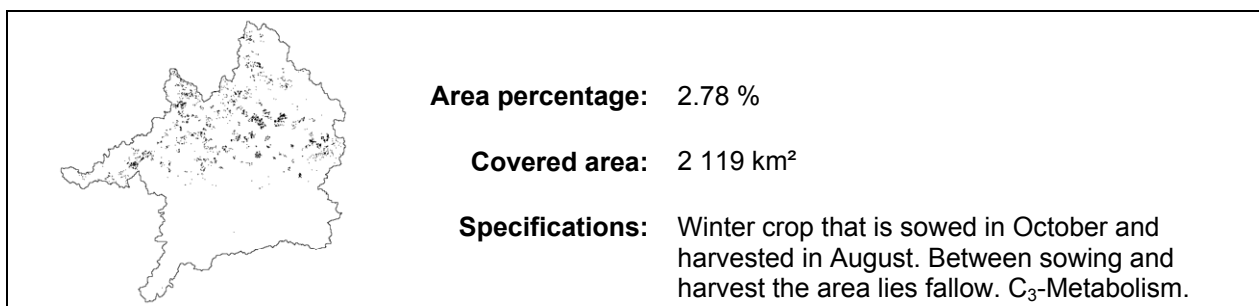
## A.8.6 Silage



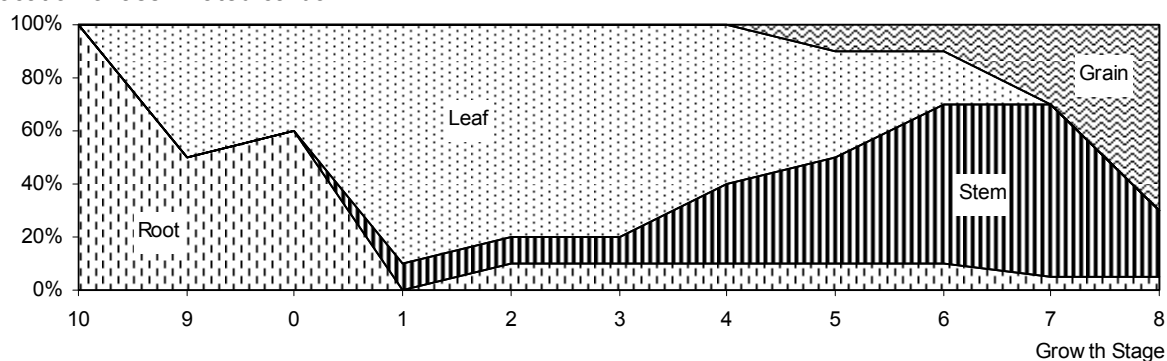
Parameter	Value	Unit
$LMA_c$	0.055	[kg m <sup>-2</sup> leaf area]
$d_{sow}$	114	[DOY]
$d_{har}$	308	[DOY]
$LH_{rel}$	0.2	[m m <sup>-2</sup> leaf area]
$LAI_{ini}$	0.4	[m <sup>2</sup> m <sup>-2</sup> ]
$LAI_{max}$	5.1	[m <sup>2</sup> m <sup>-2</sup> ]
$lw$	0.05	[m]
$Vc_{max25}$	63.1	[μMol m <sup>-2</sup> leaf area s <sup>-1</sup> ]
$J_{max25}$	29.3	[μMol e <sup>-1</sup> m <sup>-2</sup> leaf area s <sup>-1</sup> ]
$K_{o25}$	450.0	[μl l <sup>-1</sup> ]
$K_{c25}$	650.0	[ml l <sup>-1</sup> ]
$r_{d25}$	0.86	[g CO <sub>2</sub> m <sup>-2</sup> leaf area s <sup>-1</sup> ]
$\alpha$	0.34	[Mol CO <sub>2</sub> m <sup>-2</sup> leaf area]
$gfac$	9.0	[-]
$O_2$	210.0	[ml l <sup>-1</sup> ]
$r_d$	0.5	[Fraction]
Long Day Crop Type	0	[Flag]
$3 \times T_b / T_o / T_c$	10, 30, 42 / 8, 30, 42 / 8, 30, 42	[°C]
$TT_{crit}$	51.0	[°C]
$RD_{max}$	145.0	[cm]
$VnT_b / VnT_o / VnT_c$	-1.3 / 4.9 / 15.7	[°C]
$9 \times PT_{thres,i}$	0 / 0.2 / 0.3 / 0.45 / 0.65 / 0.9 / 1.0 / 1.5 / 2.0	[Thres.]
Allocation of assimilated carbon:		[%]



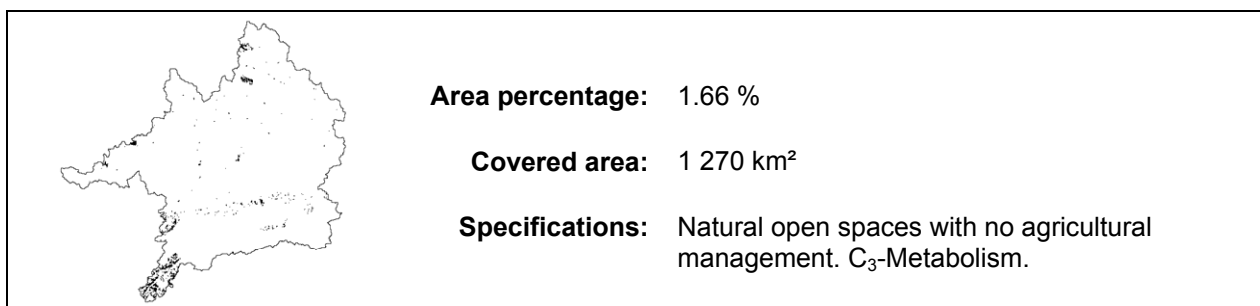
### A.8.7 Winter Barley



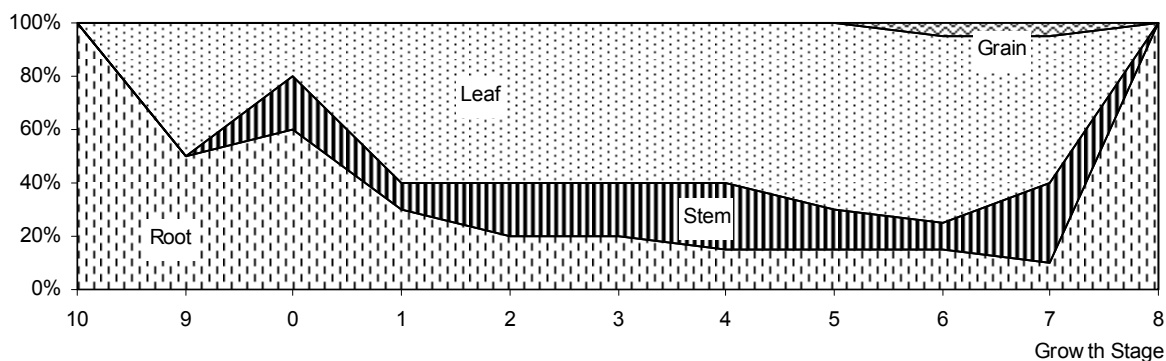
Parameter	Value	Unit
$LMA_c$	0.073	[kg m <sup>-2</sup> leaf area]
$d_{sow}$	280	[DOY]
$d_{har}$	232	[DOY]
$LH_{rel}$	0.2	[m m <sup>-2</sup> leaf area]
$LAI_{ini}$	0.4	[m <sup>2</sup> m <sup>-2</sup> ]
$LAI_{max}$	4.5	[m <sup>2</sup> m <sup>-2</sup> ]
$lw$	0.01	[m]
$Vc_{max25}$	68.1	[μMol m <sup>-2</sup> leaf area s <sup>-1</sup> ]
$J_{max25}$	32.3	[μMol e <sup>-1</sup> m <sup>-2</sup> leaf area s <sup>-1</sup> ]
$K_{o25}$	278.4	[μl l <sup>-1</sup> ]
$K_{c25}$	404.9	[ml l <sup>-1</sup> ]
$r_{d25}$	0.93	[g CO <sub>2</sub> m <sup>-2</sup> leaf area s <sup>-1</sup> ]
$\alpha$	0.0475	[Mol CO <sub>2</sub> m <sup>-2</sup> leaf area]
$gfac$	12.8	[-]
$O_2$	210.0	[ml l <sup>-1</sup> ]
$r_d$	0.5	[Fraction]
Long Day Crop Type	1	[Flag]
$3 \times T_b / T_o / T_c$	0, 19, 30 / 4, 24, 35 / 8, 24, 35	[°C]
$TT_{crit}$	60.4	[°C]
$RD_{max}$	130.0	[cm]
$VnT_b / VnT_o / VnT_c$	-1.3 / 4.9 / 15.7	[°C]
$9 \times PT_{thres,i}$	0.2 / 0.4 / 0.6 / 0.85 / 1.0 / 1.5 / 1.8 / 2.0 / 2.3	[Thres.]
Allocation of assimilated carbon:		[%]



### A.8.8 Natural Grassland

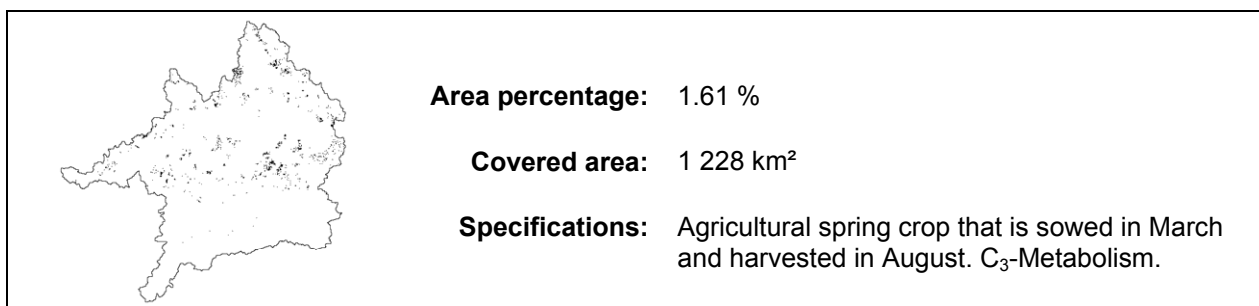


Parameter	Value	Unit
$LMA_c$	0.1	[kg m <sup>-2</sup> leaf area]
$d_{sow}$	perennial	[DOY]
$d_{har}$	perennial	[DOY]
$LH_{rel}$	0.2	[m m <sup>-2</sup> leaf area]
$LAI_{ini}$	0.8	[m <sup>2</sup> m <sup>-2</sup> ]
$LAI_{max}$	5.2	[m <sup>2</sup> m <sup>-2</sup> ]
$lw$	0.03	[m]
$Vc_{max25}$	59.1	[μMol m <sup>-2</sup> leaf area s <sup>-1</sup> ]
$J_{max25}$	30.4	[μMol e <sup>-1</sup> m <sup>-2</sup> leaf area s <sup>-1</sup> ]
$K_{o25}$	278.4	[μl l <sup>-1</sup> ]
$K_{c25}$	404.9	[ml l <sup>-1</sup> ]
$r_{d25}$	0.94	[g CO <sub>2</sub> m <sup>-2</sup> leaf area s <sup>-1</sup> ]
$\alpha$	0.078	[Mol CO <sub>2</sub> m <sup>-2</sup> leaf area]
$gfac$	16.0	[-]
$O_2$	210.0	[ml l <sup>-1</sup> ]
$r_d$	0.5	[Fraction]
Long Day Crop Type	1	[Flag]
$3 \times T_b / T_o / T_c$	0, 20, 30 / 0, 20, 35 / 0, 20, 35	[°C]
$TT_{crit}$	60.4	[°C]
$RD_{max}$	150.0	[cm]
$VnT_b / VnT_o / VnT_c$	-1.3 / 4.9 / 15.7	[°C]
$9 \times PT_{thres,i}$	0 / 0.2 / 0.3 / 0.45 / 0.6 / 0.9 / 1 / 1.5 / 2	[Thres.]
Allocation of assimilated carbon:		[%]



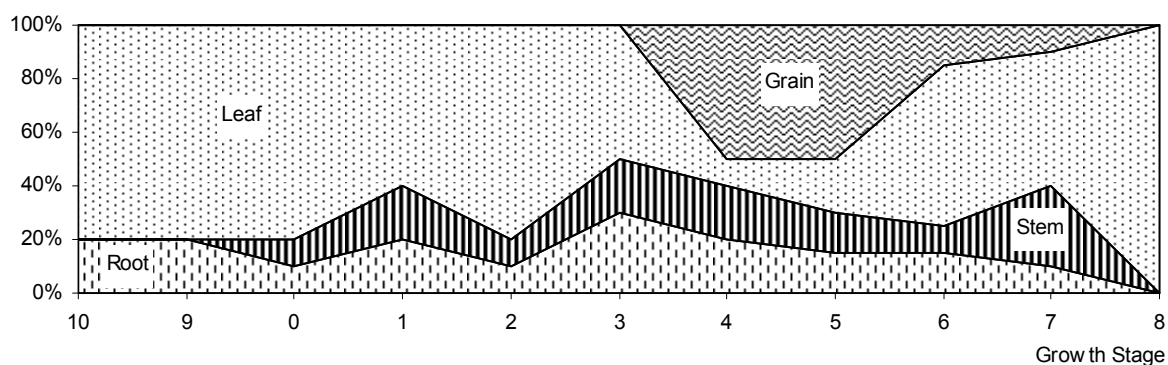


### A.8.9 Forage

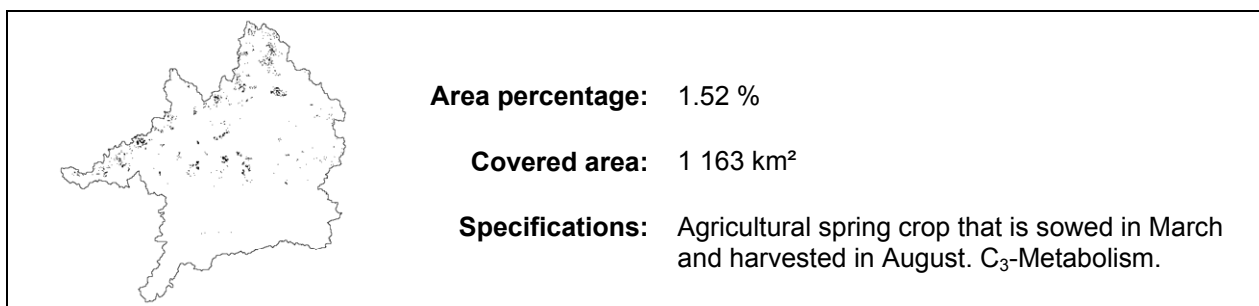


Parameter	Value	Unit
$LMA_c$	0.067	[kg m <sup>-2</sup> leaf area]
$d_{sow}$	67	[DOY]
$d_{har}$	221	[DOY]
$LH_{rel}$	0.266	[m m <sup>-2</sup> leaf area]
$LAI_{ini}$	0.4	[m <sup>2</sup> m <sup>-2</sup> ]
$LAI_{max}$	4	[m <sup>2</sup> m <sup>-2</sup> ]
$lw$	0.02	[m]
$Vc_{max25}$	59.15	[μMol m <sup>-2</sup> leaf area s <sup>-1</sup> ]
$J_{max25}$	30.4	[μMol e <sup>-1</sup> m <sup>-2</sup> leaf area s <sup>-1</sup> ]
$K_{o25}$	278.4	[μl l <sup>-1</sup> ]
$K_{c25}$	404.9	[ml l <sup>-1</sup> ]
$r_{d25}$	0.94	[g CO <sub>2</sub> m <sup>-2</sup> leaf area s <sup>-1</sup> ]
$\alpha$	0.061	[Mol CO <sub>2</sub> m <sup>-2</sup> leaf area]
$gfac$	13.5	[-]
$O_2$	210	[ml l <sup>-1</sup> ]
$r_d$	0.5	[Fraction]
Long Day Crop Type	1	[Flag]
$3 \times T_b / T_o / T_c$	0, 20, 30 / 0, 20, 35 / 0, 20, 35	[°C]
$TT_{crit}$	60.4	[°C]
$RD_{max}$	150	[cm]
$VnT_b / VnT_o / VnT_c$	-1.3 / 4.9 / 15.7	[°C]
$9 \times PT_{thres,i}$	0.0 / 0.1 / 0.5 / 1.8 / 2.8 / 3.5 / 3.9 / 4.0 / 4.1	[Thres.]

Allocation of assimilated carbon:

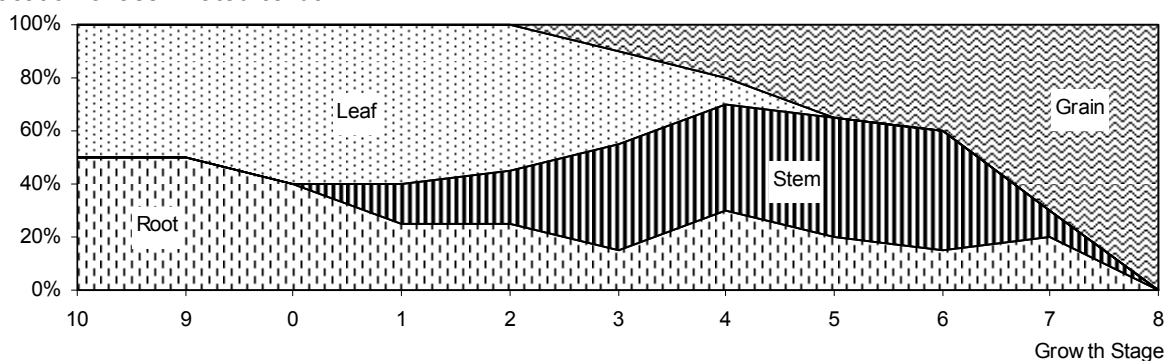


### A.8.10 Summer Barley

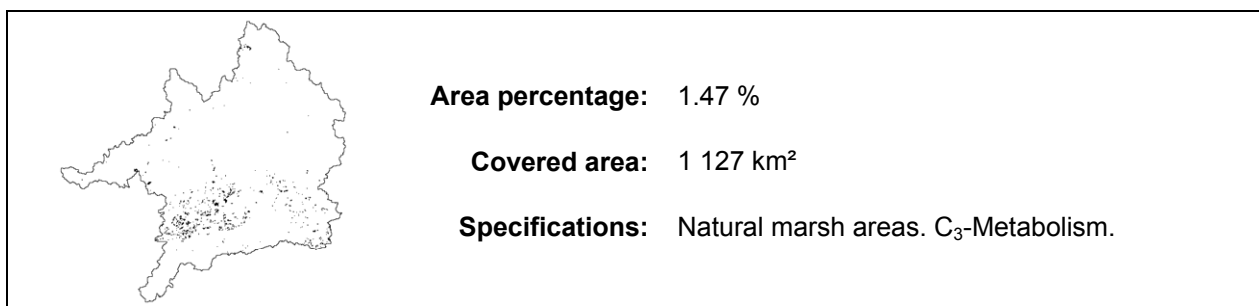


Parameter	Value	Unit
$LMA_c$	0.055	[kg m <sup>-2</sup> leaf area]
$d_{sow}$	75	[DOY]
$d_{har}$	221	[DOY]
$LH_{rel}$	0.2	[m m <sup>-2</sup> leaf area]
$LAI_{ini}$	0.4	[m <sup>2</sup> m <sup>-2</sup> ]
$LAI_{max}$	4.1	[m <sup>2</sup> m <sup>-2</sup> ]
$lw$	0.01	[m]
$Vc_{max25}$	58.3	[μMol m <sup>-2</sup> leaf area s <sup>-1</sup> ]
$J_{max25}$	42.1	[μMol e <sup>-1</sup> m <sup>-2</sup> leaf area s <sup>-1</sup> ]
$K_{o25}$	278.4	[μl l <sup>-1</sup> ]
$K_{c25}$	404.9	[ml l <sup>-1</sup> ]
$r_{d25}$	0.9	[g CO <sub>2</sub> m <sup>-2</sup> leaf area s <sup>-1</sup> ]
$\alpha$	0.056	[Mol CO <sub>2</sub> m <sup>-2</sup> leaf area]
$gfac$	14.0	[-]
$O_2$	210	[ml l <sup>-1</sup> ]
$r_d$	0.5	[Fraction]
Long Day Crop Type	1	[Flag]
$3 \times T_b / T_o / T_c$	0, 25, 37 / 0, 25, 37 / 0, 25, 37	[°C]
$TT_{crit}$	70.8	[°C]
$RD_{max}$	130	[cm]
$VnT_b / VnT_o / VnT_c$	-1.3 / 4.9 / 15.7	[°C]
$9 \times PT_{thres,i}$	0.1 / 0.3 / 0.6 / 0.8 / 1.0 / 1.2 / 1.4 / 1.6 / 1.8	[Thres.]

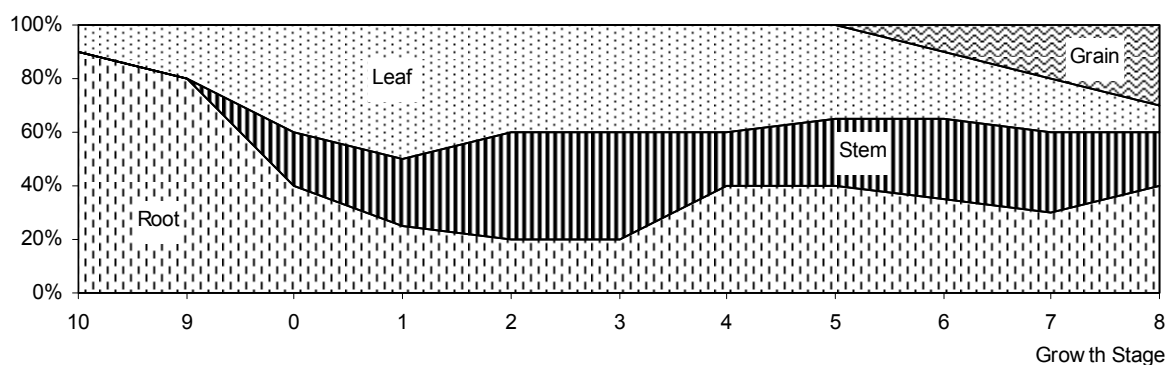
Allocation of assimilated carbon:



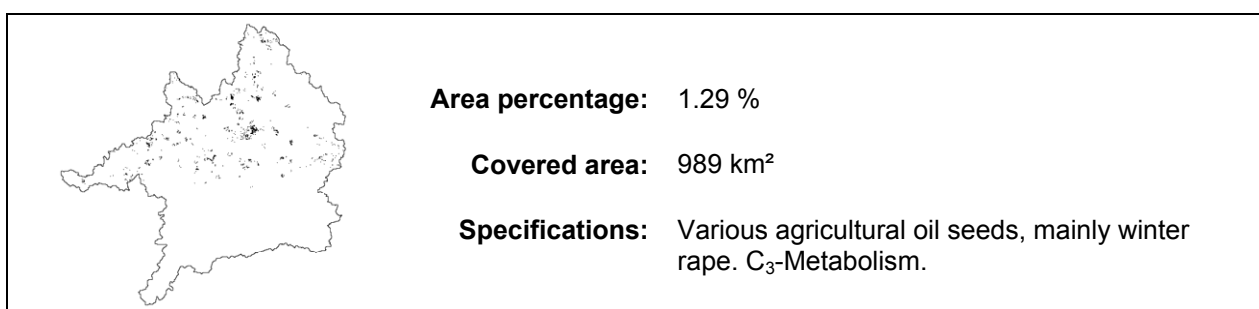
### A.8.11 Wetland



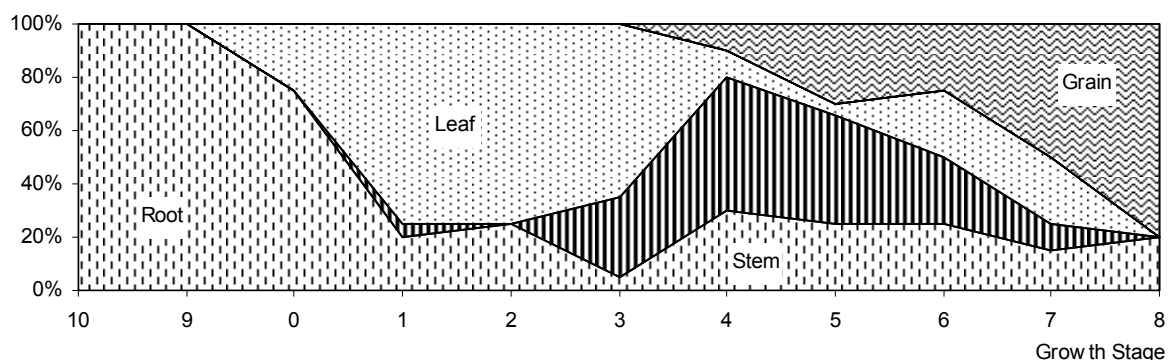
Parameter	Value	Unit
$LMA_c$	0.4	[kg m <sup>-2</sup> leaf area]
$d_{sow}$	perennial	[DOY]
$d_{har}$	perennial	[DOY]
$LH_{rel}$	0.2	[m m <sup>-2</sup> leaf area]
$LAI_{ini}$	1.2	[m <sup>2</sup> m <sup>-2</sup> ]
$LAI_{max}$	4.5	[m <sup>2</sup> m <sup>-2</sup> ]
$lw$	110	[m]
$Vc_{max25}$	40	[μMol m <sup>-2</sup> leaf area s <sup>-1</sup> ]
$J_{max25}$	20	[μMol e <sup>-1</sup> m <sup>-2</sup> leaf area s <sup>-1</sup> ]
$K_{o25}$	278.4	[μl l <sup>-1</sup> ]
$K_{c25}$	404.9	[ml l <sup>-1</sup> ]
$r_{d25}$	0.6	[g CO <sub>2</sub> m <sup>-2</sup> leaf area s <sup>-1</sup> ]
$\alpha$	0.025	[Mol CO <sub>2</sub> m <sup>-2</sup> leaf area]
$gfac$	17.0	[-]
$O_2$	210	[ml l <sup>-1</sup> ]
$r_d$	0.5	[Fraction]
Long Day Crop Type	0	[Flag]
$3 \times T_b / T_o / T_c$	0, 25, 30 / 0, 25, 30 / 0, 25, 30	[°C]
$TT_{crit}$	60.4	[°C]
$RD_{max}$	150.0	[cm]
$VnT_b / VnT_o / VnT_c$	-1.3 / 4.9 / 15.7	[°C]
$9 \times PT_{thres,i}$	0 / 0.2 / 0.3 / 0.45 / 0.65 / 0.9 / 1 / 1.5 / 2	[Thres.]
Allocation of assimilated carbon:		[%]



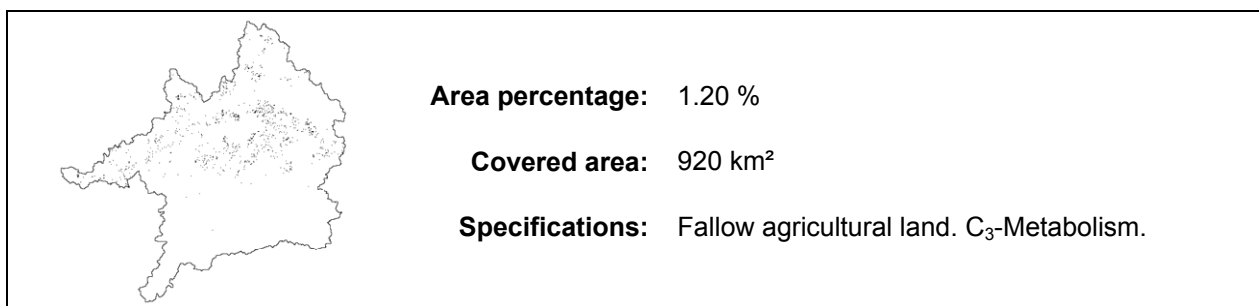
### A.8.12 Oleaginous



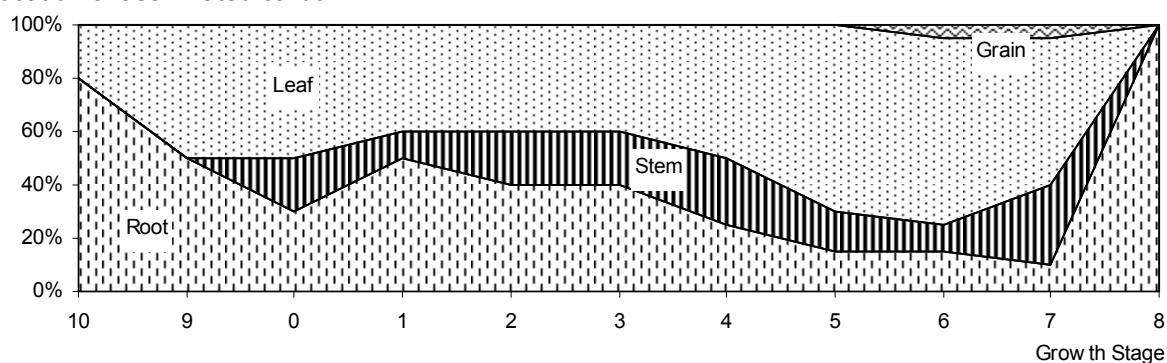
Parameter	Value	Unit
$LMA_c$	0.064	[kg m <sup>-2</sup> leaf area]
$d_{sow}$	253	[DOY]
$d_{har}$	195	[DOY]
$LH_{rel}$	0.27	[m m <sup>-2</sup> leaf area]
$LAI_{ini}$	0.8	[m <sup>2</sup> m <sup>-2</sup> ]
$LAI_{max}$	5.5	[m <sup>2</sup> m <sup>-2</sup> ]
$lw$	0.01	[m]
$Vc_{max25}$	63.1	[μMol m <sup>-2</sup> leaf area s <sup>-1</sup> ]
$J_{max25}$	29.3	[μMol e <sup>-1</sup> m <sup>-2</sup> leaf area s <sup>-1</sup> ]
$K_{o25}$	278.4	[μl l <sup>-1</sup> ]
$K_{c25}$	404.9	[ml l <sup>-1</sup> ]
$r_{d25}$	0.86	[g CO <sub>2</sub> m <sup>-2</sup> leaf area s <sup>-1</sup> ]
$\alpha$	0.046	[Mol CO <sub>2</sub> m <sup>-2</sup> leaf area]
$gfac$	16.0	[-]
$O_2$	210	[ml l <sup>-1</sup> ]
$r_d$	0.5	[Fraction]
Long Day Crop Type	1	[Flag]
$3 \times T_b / T_o / T_c$	2.5, 25, 40 / 2.5, 25, 40 / 2.5, 25, 40	[°C]
$TT_{crit}$	51	[°C]
$RD_{max}$	120	[cm]
$VnT_b / VnT_o / VnT_c$	-3.17 / 3.5 / 17.2	[°C]
$9 \times PT_{thres,i}$	0 / 0.2 / 0.3 / 0.45 / 0.65 / 0.9 / 1 / 1.5 / 2	[Thres.]
Allocation of assimilated carbon:		[%]



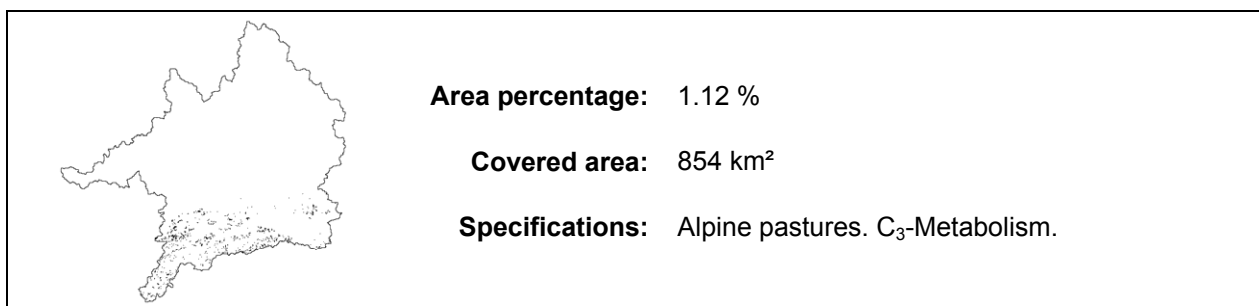
### A.8.13 Set Aside



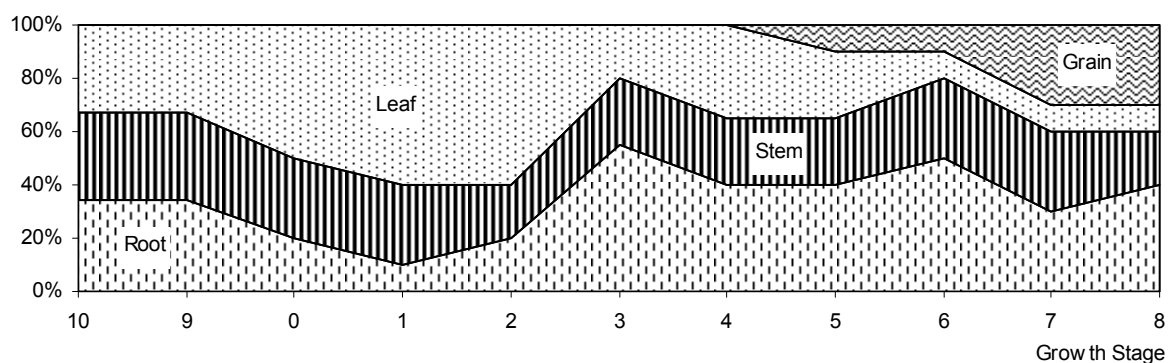
Parameter	Value	Unit
$LMA_c$	0.06	[kg m <sup>-2</sup> leaf area]
$d_{sow}$	perennial	[DOY]
$d_{har}$	perennial	[DOY]
$LH_{rel}$	0.2	[m m <sup>-2</sup> leaf area]
$LAI_{ini}$	0.8	[m <sup>2</sup> m <sup>-2</sup> ]
$LAI_{max}$	4.8	[m <sup>2</sup> m <sup>-2</sup> ]
$lw$	0.03	[m]
$Vc_{max25}$	59.1	[μMol m <sup>-2</sup> leaf area s <sup>-1</sup> ]
$J_{max25}$	30.4	[μMol e <sup>-1</sup> m <sup>-2</sup> leaf area s <sup>-1</sup> ]
$K_{o25}$	278.4	[μl l <sup>-1</sup> ]
$K_{c25}$	404.9	[ml l <sup>-1</sup> ]
$r_{d25}$	0.94	[g CO <sub>2</sub> m <sup>-2</sup> leaf area s <sup>-1</sup> ]
$\alpha$	0.0595	[Mol CO <sub>2</sub> m <sup>-2</sup> leaf area]
$gfac$	14.0	[-]
$O_2$	210	[ml l <sup>-1</sup> ]
$r_d$	0.5	[Fraction]
Long Day Crop Type	1	[Flag]
$3 \times T_b / T_o / T_c$	0, 20, 30 / 0, 20, 30 / 0, 20, 35	[°C]
$TT_{crit}$	60.4	[°C]
$RD_{max}$	150	[cm]
$VnT_b / VnT_o / VnT_c$	-1.3 / 4.9 / 15.7	[°C]
$9 \times PT_{thres,i}$	0 / 0.2 / 0.3 / 0.45 / 0.65 / 0.9 / 1 / 1.5 / 2	[Thres.]
Allocation of assimilated carbon:		[%]



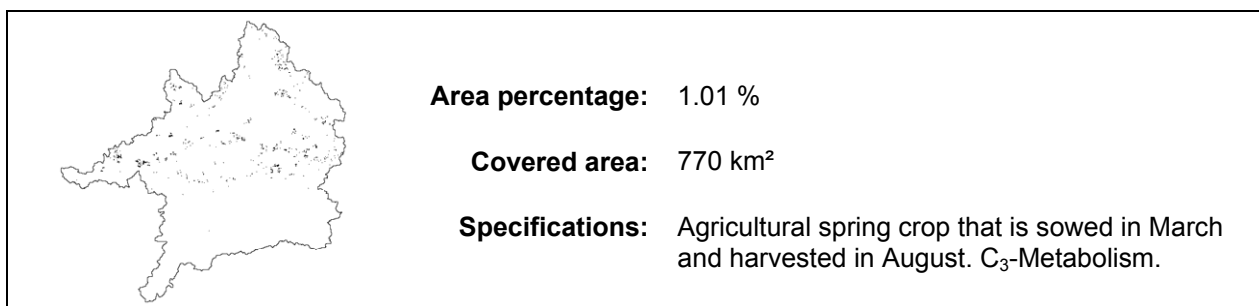
## A.8.14 Alpine Grassland



Parameter	Value	Unit
$LMA_c$	0.09	[kg m <sup>-2</sup> leaf area]
$d_{sow}$	perennial	[DOY]
$d_{har}$	perennial	[DOY]
$LH_{rel}$	0.1	[m m <sup>-2</sup> leaf area]
$LAI_{ini}$	0.8	[m <sup>2</sup> m <sup>-2</sup> ]
$LAI_{max}$	4.2	[m <sup>2</sup> m <sup>-2</sup> ]
$lw$	0.05	[m]
$Vc_{max25}$	45	[μMol m <sup>-2</sup> leaf area s <sup>-1</sup> ]
$J_{max25}$	22.5	[μMol e <sup>-1</sup> m <sup>-2</sup> leaf area s <sup>-1</sup> ]
$K_{o25}$	278.4	[μl l <sup>-1</sup> ]
$K_{c25}$	404.9	[ml l <sup>-1</sup> ]
$r_{d25}$	0.68	[g CO <sub>2</sub> m <sup>-2</sup> leaf area s <sup>-1</sup> ]
$\alpha$	0.069	[Mol CO <sub>2</sub> m <sup>-2</sup> leaf area]
$gfac$	14.0	[-]
$O_2$	210	[ml l <sup>-1</sup> ]
$r_d$	0.5	[Fraction]
Long Day Crop Type	0	[Flag]
$3 \times T_b / T_o / T_c$	0, 25, 30 / 0, 25, 30 / 0, 25, 30	[°C]
$TT_{crit}$	60.4	[°C]
$RD_{max}$	150	[cm]
$VnT_b / VnT_o / VnT_c$	-1.3 / 4.9 / 15.7	[°C]
$9 \times PT_{thres,i}$	0 / 0.03 / 0.05 / 0.1 / 0.15 / 0.2 / 0.25 / 0.3 / 0.4	[Thres.]
Allocation of assimilated carbon:		[%]

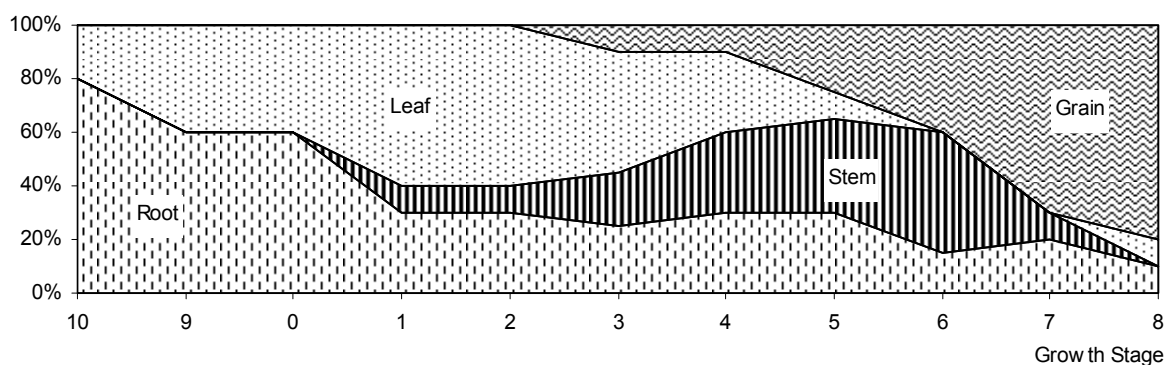


## A.8.15 Oat

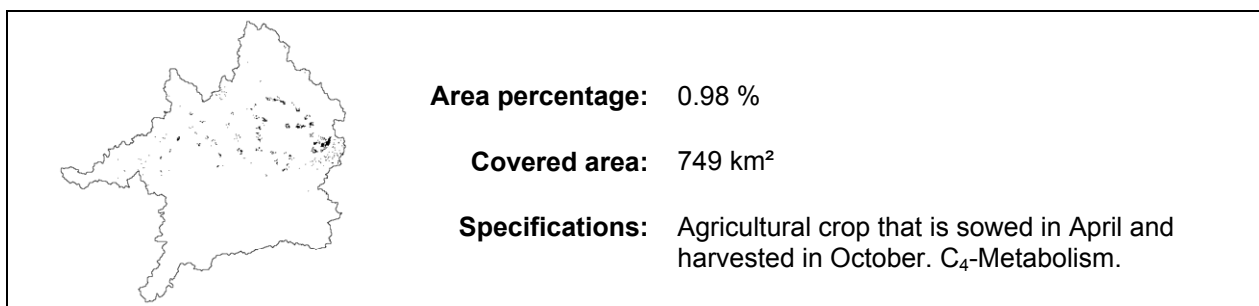


Parameter	Value	Unit
$LMA_c$	0.087	[kg m <sup>-2</sup> leaf area]
$d_{sow}$	67	[DOY]
$d_{har}$	218	[DOY]
$LH_{rel}$	0.2	[m m <sup>-2</sup> leaf area]
$LAI_{ini}$	0.4	[m <sup>2</sup> m <sup>-2</sup> ]
$LAI_{max}$	5	[m <sup>2</sup> m <sup>-2</sup> ]
$lw$	100	[m]
$Vc_{max25}$	60.6	[μMol m <sup>-2</sup> leaf area s <sup>-1</sup> ]
$J_{max25}$	20.2	[μMol e <sup>-1</sup> m <sup>-2</sup> leaf area s <sup>-1</sup> ]
$K_{o25}$	278.4	[μl l <sup>-1</sup> ]
$K_{c25}$	404.9	[ml l <sup>-1</sup> ]
$r_{d25}$	0.84	[g CO <sub>2</sub> m <sup>-2</sup> leaf area s <sup>-1</sup> ]
$\alpha$	0.3	[Mol CO <sub>2</sub> m <sup>-2</sup> leaf area]
$gfac$	7.5	[-]
$O_2$	0	[ml l <sup>-1</sup> ]
$r_d$	0.5	[Fraction]
Long Day Crop Type	1	[Flag]
$3 \times T_b / T_o / T_c$	0, 25, 37 / 0, 25, 37 / 0, 25, 37	[°C]
$TT_{crit}$	70.8	[°C]
$RD_{max}$	150.0	[cm]
$VnT_b / VnT_o / VnT_c$	-1.3 / 4.9 / 15.7	[°C]
$9 \times PT_{thres,i}$	0.0 / 0.5 / 0.8 / 1.2 / 1.5 / 1.7 / 2.0 / 2.1 / 2.5	[Thres.]

Allocation of assimilated carbon:

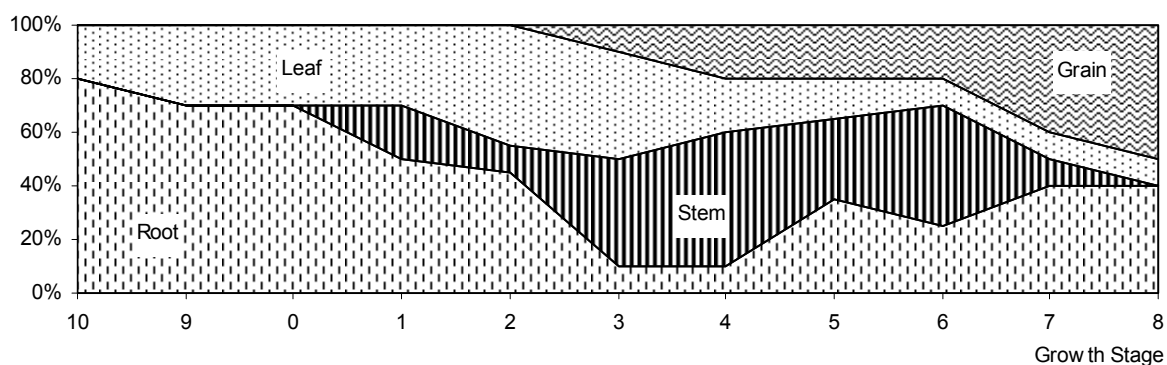


### A.8.16 Maize



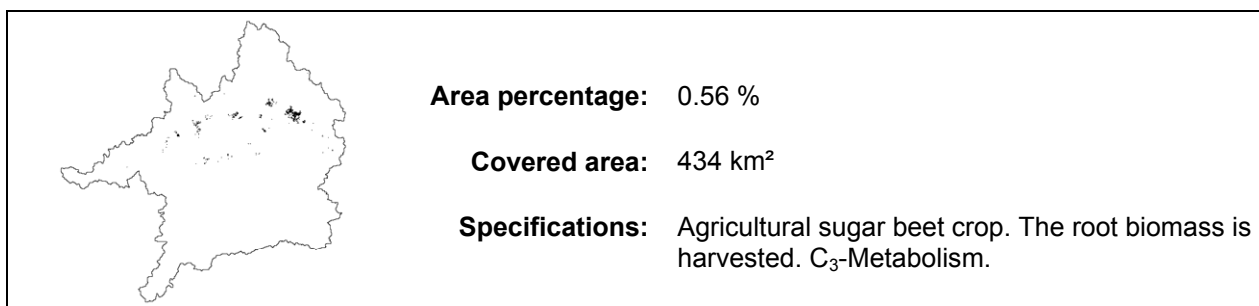
Parameter	Value	Unit
$LMA_c$	0.052	[kg m <sup>-2</sup> leaf area]
$d_{sow}$	114	[DOY]
$d_{har}$	289	[DOY]
$LH_{rel}$	0.66	[m m <sup>-2</sup> leaf area]
$LAI_{ini}$	0.4	[m <sup>2</sup> m <sup>-2</sup> ]
$LAI_{max}$	5.1	[m <sup>2</sup> m <sup>-2</sup> ]
$lw$	0.05	[m]
$Vc_{max25}$	63.1	[μMol m <sup>-2</sup> leaf area s <sup>-1</sup> ]
$J_{max25}$	29.3	[μMol e <sup>-1</sup> m <sup>-2</sup> leaf area s <sup>-1</sup> ]
$K_{o25}$	450	[μl l <sup>-1</sup> ]
$K_{c25}$	650	[ml l <sup>-1</sup> ]
$r_{d25}$	0.86	[g CO <sub>2</sub> m <sup>-2</sup> leaf area s <sup>-1</sup> ]
$\alpha$	0.38	[Mol CO <sub>2</sub> m <sup>-2</sup> leaf area]
$gfac$	8.7	[-]
$O_2$	210	[ml l <sup>-1</sup> ]
$r_d$	0.5	[Fraction]
Long Day Crop Type	0	[Flag]
$3 \times T_b / T_o / T_c$	10, 30, 42 / 8, 30, 42 / 8, 30, 42	[°C]
$TT_{crit}$	51	[°C]
$RD_{max}$	145	[cm]
$VnT_b / VnT_o / VnT_c$	-1.3 / 4.9 / 15.7	[°C]
$9 \times PT_{thres,i}$	0 / 0.01 / 0.03 / 0.59 / 1.2 / 1.5 / 2.06 / 2.5 / 2.8	[Thres.]

Allocation of assimilated carbon:



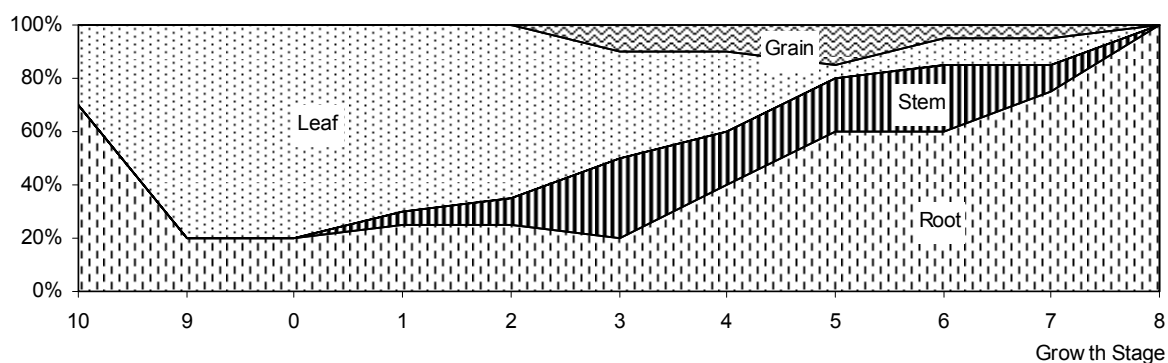


### A.8.17 Sugar

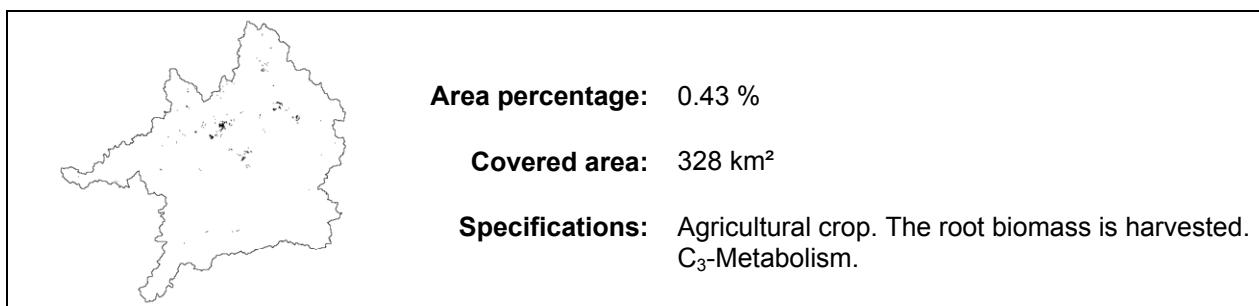


Parameter	Value	Unit
$LMA_c$	0.78	[kg m <sup>-2</sup> leaf area]
$d_{sow}$	114	[DOY]
$d_{har}$	308	[DOY]
$LH_{rel}$	0.2	[m m <sup>-2</sup> leaf area]
$LAI_{ini}$	0.4	[m <sup>2</sup> m <sup>-2</sup> ]
$LAI_{max}$	4.9	[m <sup>2</sup> m <sup>-2</sup> ]
$lw$	0.03	[m]
$Vc_{max\ 25}$	63.1	[μMol m <sup>-2</sup> leaf area s <sup>-1</sup> ]
$J_{max\ 25}$	29.3	[μMol e <sup>-1</sup> m <sup>-2</sup> leaf area s <sup>-1</sup> ]
$K_{o25}$	278.4	[μl l <sup>-1</sup> ]
$K_{c25}$	404.9	[ml l <sup>-1</sup> ]
$r_{d25}$	0.86	[g CO <sub>2</sub> m <sup>-2</sup> leaf area s <sup>-1</sup> ]
$\alpha$	0.135	[Mol CO <sub>2</sub> m <sup>-2</sup> leaf area]
$gfac$	13.0	[-]
$O_2$	210	[ml l <sup>-1</sup> ]
$r_d$	0.5	[Fraction]
Long Day Crop Type	0	[Flag]
$3 \times T_b / T_o / T_c$	10, 30, 42 / 8, 30, 42 / 8, 30, 42	[°C]
$TT_{crit}$	51	[°C]
$RD_{max}$	200	[cm]
$VnT_b / VnT_o / VnT_c$	-1.3 / 4.9 / 15.7	[°C]
$9 \times PT_{thres,i}$	0.1 / 0.2 / 0.5 / 0.7 / 0.8 / 1.0 / 1.1 / 1.3 / 1.5	[Thres.]

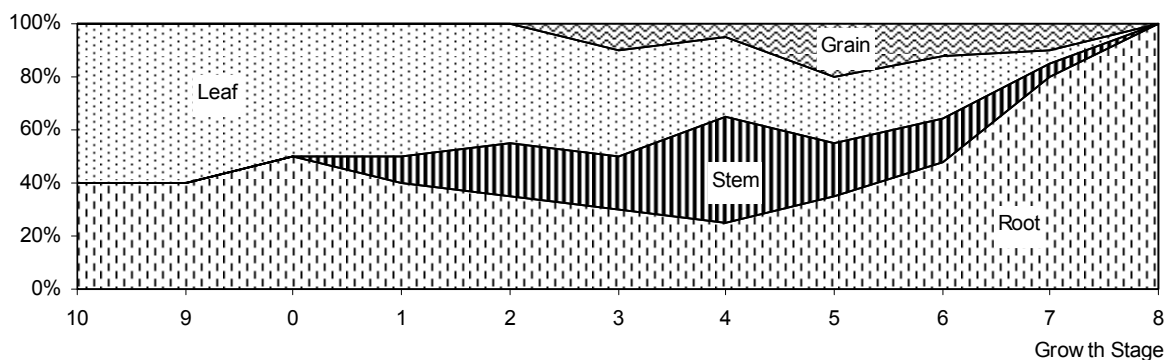
Allocation of assimilated carbon:



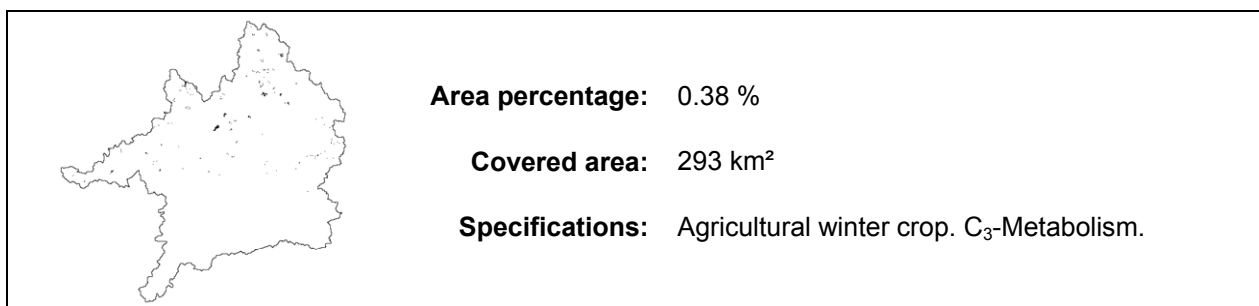
## A.8.18 Potato



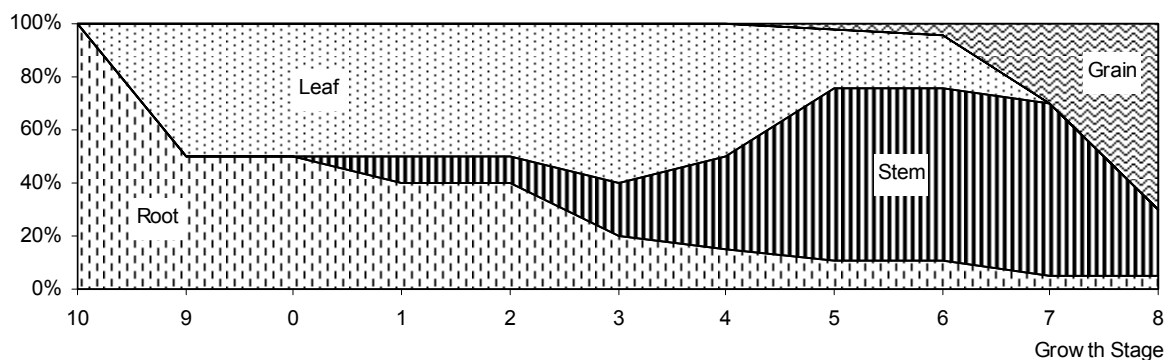
Parameter	Value	Unit
$LMA_c$	0.06	[kg m <sup>-2</sup> leaf area]
$d_{sow}$	114	[DOY]
$d_{har}$	308	[DOY]
$LH_{rel}$	0.1	[m m <sup>-2</sup> leaf area]
$LAI_{ini}$	0.3	[m <sup>2</sup> m <sup>-2</sup> ]
$LAI_{max}$	5.1	[m <sup>2</sup> m <sup>-2</sup> ]
$lw$	130	[m]
$Vc_{max25}$	63.1	[μMol m <sup>-2</sup> leaf area s <sup>-1</sup> ]
$J_{max25}$	29.3	[μMol e <sup>-1</sup> m <sup>-2</sup> leaf area s <sup>-1</sup> ]
$K_{o25}$	278.4	[μl l <sup>-1</sup> ]
$K_{c25}$	404.9	[ml l <sup>-1</sup> ]
$r_{d25}$	0.86	[g CO <sub>2</sub> m <sup>-2</sup> leaf area s <sup>-1</sup> ]
$\alpha$	0.088	[Mol CO <sub>2</sub> m <sup>-2</sup> leaf area]
$gfac$	13.5	[-]
$O_2$	0	[ml l <sup>-1</sup> ]
$r_d$	0.5	[Fraction]
Long Day Crop Type	1	[Flag]
$3 \times T_b / T_o / T_c$	10, 30, 42 / 8, 30, 42 / 8, 30, 42	[°C]
$TT_{crit}$	51.0	[°C]
$RD_{max}$	200	[cm]
$VnT_b / VnT_o / VnT_c$	-1.3 / 4.9 / 15.7	[°C]
$9 \times PT_{thres,i}$	0.0 / 0.3 / 0.6 / 0.9 / 1.2 / 1.4 / 1.6 / 1.8 / 2.0	[Thres.]
Allocation of assimilated carbon:		[%]



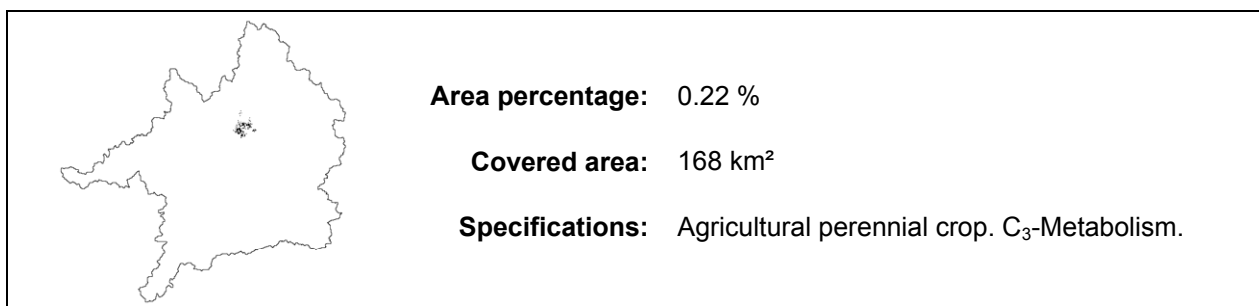
## A.8.19 Rye



Parameter	Value	Unit
$LMA_c$	0.057	[kg m <sup>-2</sup> leaf area]
$d_{sow}$	283	[DOY]
$d_{har}$	232	[DOY]
$LH_{rel}$	0.2	[m m <sup>-2</sup> leaf area]
$LAI_{ini}$	0.4	[m <sup>2</sup> m <sup>-2</sup> ]
$LAI_{max}$	4.5	[m <sup>2</sup> m <sup>-2</sup> ]
$lw$	110	[m]
$Vc_{max25}$	68.1	[μMol m <sup>-2</sup> leaf area s <sup>-1</sup> ]
$J_{max25}$	32.3	[μMol e <sup>-1</sup> m <sup>-2</sup> leaf area s <sup>-1</sup> ]
$K_{o25}$	278.4	[μl l <sup>-1</sup> ]
$K_{c25}$	404.9	[ml l <sup>-1</sup> ]
$r_{d25}$	0.93	[g CO <sub>2</sub> m <sup>-2</sup> leaf area s <sup>-1</sup> ]
$\alpha$	0.051	[Mol CO <sub>2</sub> m <sup>-2</sup> leaf area]
$gfac$	12.0	[-]
$O_2$	0	[ml l <sup>-1</sup> ]
$r_d$	0.5	[Fraction]
Long Day Crop Type	1	[Flag]
$3 \times T_b / T_o / T_c$	0, 19, 30 / 4, 24, 35 / 8, 24, 35	[°C]
$TT_{crit}$	60.4	[°C]
$RD_{max}$	180.0	[cm]
$VnT_b / VnT_o / VnT_c$	-1.3 / 4.9 / 15.7	[°C]
$9 \times PT_{thres,i}$	0.0 / 0.4 / 0.6 / 0.85 / 1.0 / 1.2 / 1.6 / 1.9 / 2.2	[Thres.]
Allocation of assimilated carbon:		[%]

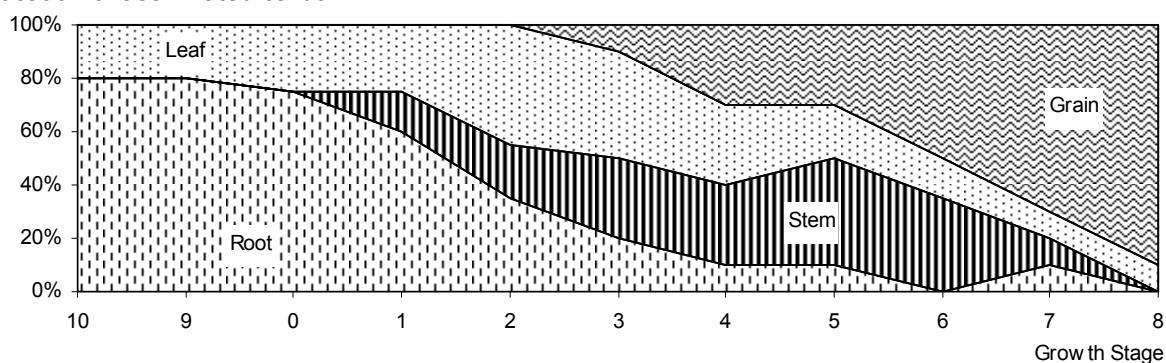


## A.8.20 Hop

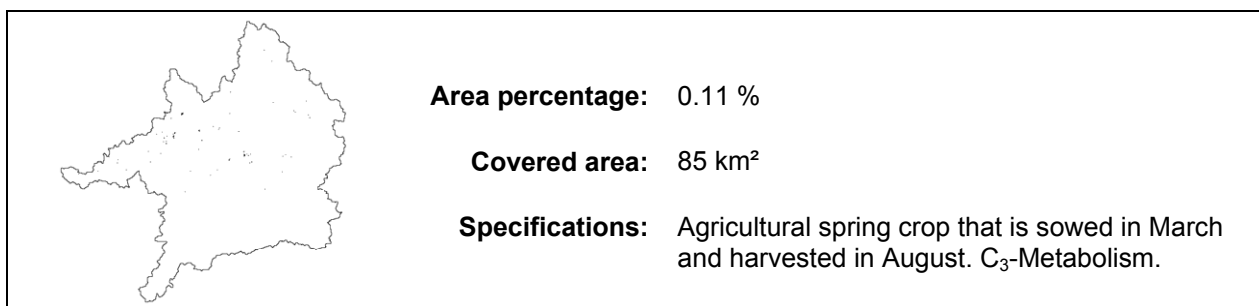


Parameter	Value	Unit
$LMA_c$	0.056	[kg m <sup>-2</sup> leaf area]
$d_{sow}$	114	[DOY]
$d_{har}$	308	[DOY]
$LH_{rel}$	1.3	[m m <sup>-2</sup> leaf area]
$LAI_{ini}$	0.5	[m <sup>2</sup> m <sup>-2</sup> ]
$LAI_{max}$	5	[m <sup>2</sup> m <sup>-2</sup> ]
$lw$	0.04	[m]
$Vc_{max25}$	63.1	[μMol m <sup>-2</sup> leaf area s <sup>-1</sup> ]
$J_{max25}$	29.3	[μMol e <sup>-1</sup> m <sup>-2</sup> leaf area s <sup>-1</sup> ]
$K_{o25}$	278.4	[μl l <sup>-1</sup> ]
$K_{c25}$	404.9	[ml l <sup>-1</sup> ]
$r_{d25}$	0.86	[g CO <sub>2</sub> m <sup>-2</sup> leaf area s <sup>-1</sup> ]
$\alpha$	0.105	[Mol CO <sub>2</sub> m <sup>-2</sup> leaf area]
$gfac$	10.5	[-]
$O_2$	210	[ml l <sup>-1</sup> ]
$r_d$	0.5	[Fraction]
Long Day Crop Type	0	[Flag]
$3 \times T_b / T_o / T_c$	10, 30, 42 / 8, 30, 42 / 8, 30, 42	[°C]
$TT_{crit}$	51	[°C]
$RD_{max}$	400	[cm]
$VnT_b / VnT_o / VnT_c$	-1.3 / 4.9 / 15.7	[°C]
$9 \times PT_{thres,i}$	0.0 / 0.2 / 0.4 / 0.75 / 1.1 / 1.5 / 2.0 / 2.5 / 2.8	[Thres.]

Allocation of assimilated carbon:

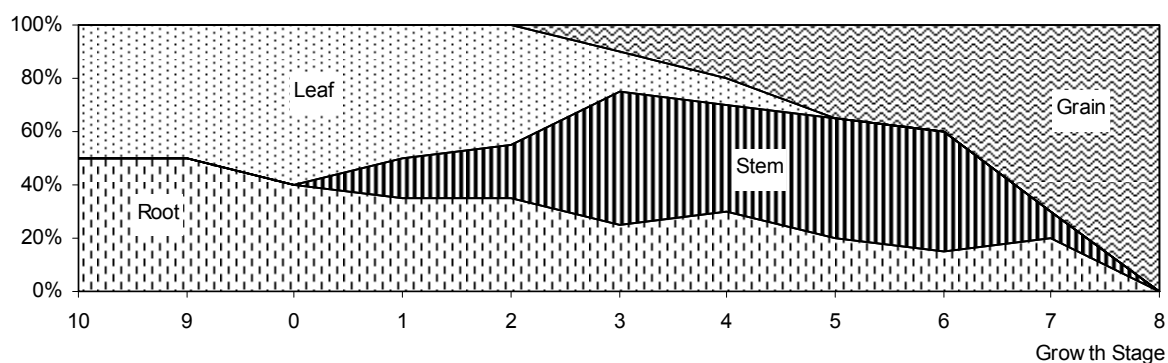


## A.8.21 Summer Wheat

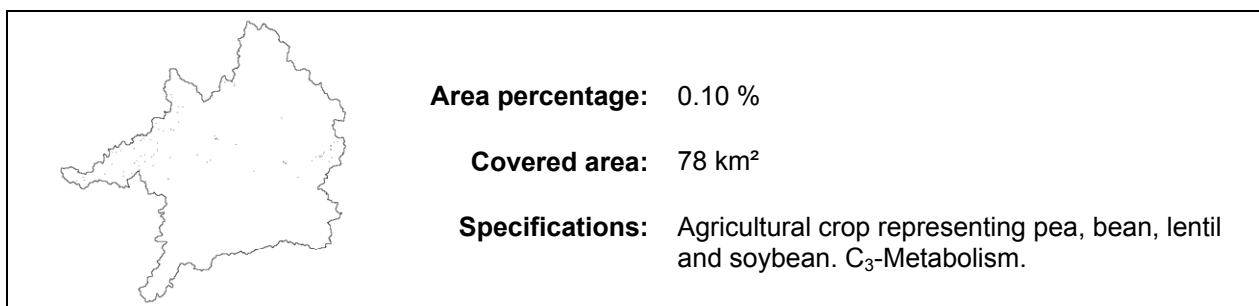


Parameter	Value	Unit
$LMA_c$	0.048	[kg m <sup>-2</sup> leaf area]
$d_{sow}$	67	[DOY]
$d_{har}$	221	[DOY]
$LH_{rel}$	0.2	[m m <sup>-2</sup> leaf area]
$LAI_{ini}$	0.4	[m <sup>2</sup> m <sup>-2</sup> ]
$LAI_{max}$	4.1	[m <sup>2</sup> m <sup>-2</sup> ]
$lw$	0.01	[m]
$Vc_{max25}$	58.3	[μMol m <sup>-2</sup> leaf area s <sup>-1</sup> ]
$J_{max25}$	42.1	[μMol e <sup>-1</sup> m <sup>-2</sup> leaf area s <sup>-1</sup> ]
$K_{o25}$	278.4	[μl l <sup>-1</sup> ]
$K_{c25}$	404.9	[ml l <sup>-1</sup> ]
$r_{d25}$	0.9	[g CO <sub>2</sub> m <sup>-2</sup> leaf area s <sup>-1</sup> ]
$\alpha$	0.049	[Mol CO <sub>2</sub> m <sup>-2</sup> leaf area]
$gfac$	12.3	[-]
$O_2$	210	[ml l <sup>-1</sup> ]
$r_d$	0.5	[Fraction]
Long Day Crop Type	1	[Flag]
$3 \times T_b / T_o / T_c$	0, 25, 37 / 0, 25, 37 / 0, 25, 37	[°C]
$TT_{crit}$	70.8	[°C]
$RD_{max}$	130	[cm]
$VnT_b / VnT_o / VnT_c$	-1.3 / 4.9 / 15.7	[°C]
$9 \times PT_{thres,i}$	0.1 / 0.4 / 0.6 / 0.8 / 1.0 / 1.2 / 1.5 / 1.7 / 2.0	[Thres.]

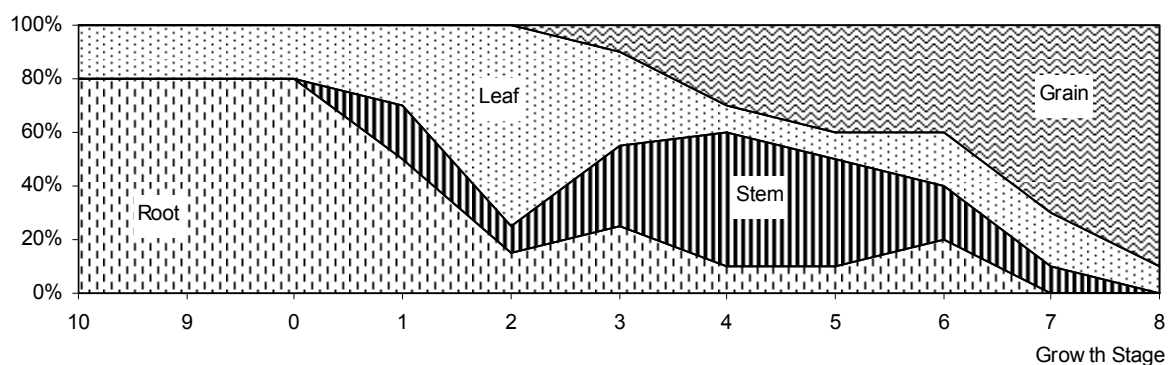
Allocation of assimilated carbon:



## A.8.22 Legumes



Parameter	Value	Unit
$LMA_c$	0.059	[kg m <sup>-2</sup> leaf area]
$d_{sow}$	114	[DOY]
$d_{har}$	308	[DOY]
$LH_{rel}$	0.3	[m m <sup>-2</sup> leaf area]
$LAI_{ini}$	0.4	[m <sup>2</sup> m <sup>-2</sup> ]
$LAI_{max}$	5.1	[m <sup>2</sup> m <sup>-2</sup> ]
$lw$	0.05	[m]
$Vc_{max25}$	63.1	[μMol m <sup>-2</sup> leaf area s <sup>-1</sup> ]
$J_{max25}$	29.3	[μMol e <sup>-1</sup> m <sup>-2</sup> leaf area s <sup>-1</sup> ]
$K_{o25}$	278.4	[μl l <sup>-1</sup> ]
$K_{c25}$	404.9	[ml l <sup>-1</sup> ]
$r_{d25}$	0.86	[g CO <sub>2</sub> m <sup>-2</sup> leaf area s <sup>-1</sup> ]
$\alpha$	0.1	[Mol CO <sub>2</sub> m <sup>-2</sup> leaf area]
$gfac$	13.0	[-]
$O_2$	210	[ml l <sup>-1</sup> ]
$r_d$	0.5	[Fraction]
Long Day Crop Type	1	[Flag]
$3 \times T_b / T_o / T_c$	10, 30, 42 / 8, 30, 42 / 8, 30, 42	[°C]
$TT_{crit}$	51	[°C]
$RD_{max}$	145	[cm]
$VnT_b / VnT_o / VnT_c$	-1.3 / 4.9 / 15.7	[°C]
$9 \times PT_{thres,i}$	0.0 / 0.2 / 0.4 / 0.55 / 0.75 / 0.9 / 1.3 / 1.7 / 2.0	[Thres.]
Allocation of assimilated carbon:		[%]

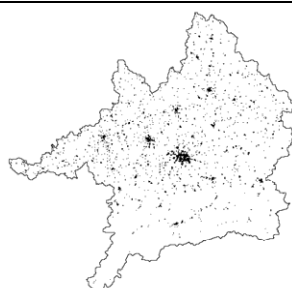


**A.8.23 Rock**

**Area percentage:** 4.39 %

**Covered area:** 3346 km<sup>2</sup>

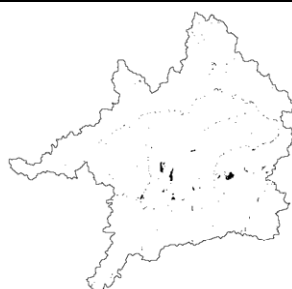
**Specifications:** Alpine areas with no vegetation cover.

**A.8.24 Residential Areas**

**Area percentage:** 3.44 %

**Covered area:** 2624 km<sup>2</sup>

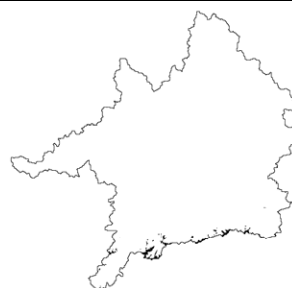
**Specifications:** Sealed urban and residential areas with the agglomeration of Munich in the middle of the catchment.

**A.8.25 Water**

**Area percentage:** 0.75 %

**Covered area:** 573 km<sup>2</sup>

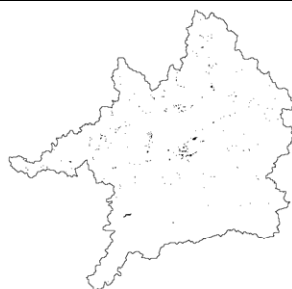
**Specifications:** Rivers, lakes and water bodies.

**A.8.26 Glacier**

**Area percentage:** 0.60 %

**Covered area:** 459 km<sup>2</sup>

**Specifications:** Alpine glaciers.

**A.8.27 Industrial**

**Area percentage:** 0.53 %

**Covered area:** 411 km<sup>2</sup>

**Specifications:** Sealed urban and suburban industrial areas.

## A.9 Parameters of Selected Soil Types

Soil Type	L	GWL	P	EPV	PDI	BPH	CC	SC	OM	RWC	CPV
Sand	1	0.483591	0.003472	43.40	500	6.57	0.01	0.95	0.15	0.51	51.50
	2	0.501178	0.002894	38.30	500	6.86	0.01	0.95	0.04	0.51	45.50
	3	0.501178	0.002894	38.30	500	6.86	0.01	0.95	0.04	0.51	45.50
	4	0.573994	0.002546	28.69	500	9.68	0.01	0.95	0.00	0.51	34.20
Pebble Sand	1	0.527114	0.003472	33.94	500	7.69	0.01	0.95	0.05	0.51	40.38
	2	0.568623	0.002546	23.36	500	9.43	0.01	0.95	0.02	0.41	27.84
	3	0.580839	0.002546	22.45	500	10.02	0.01	0.95	0.01	0.41	26.78
	4	0.541166	0.002546	25.71	500	8.23	0.01	0.95	0.00	0.41	30.60
Loam Sand	1	0.350122	0.000583	34.68	500	10.27	0.15	0.60	0.03	7.65	47.50
	2	0.402910	0.000579	32.13	500	12.38	0.10	0.65	0.01	5.10	42.28
	3	0.320699	0.000107	17.40	500	22.06	0.20	0.60	0.00	8.16	27.63
	4	0.320699	0.000107	17.40	500	22.06	0.20	0.60	0.00	8.16	27.63
Sand Loam	1	0.350122	0.000370	34.68	500	10.27	0.15	0.60	0.05	7.65	47.50
	2	0.350122	0.000583	34.68	500	10.27	0.15	0.60	0.03	7.65	47.50
	3	0.215993	0.000078	18.52	500	96.34	0.30	0.30	0.00	15.30	35.20
	4	0.318699	0.000168	25.13	500	49.99	0.20	0.35	0.00	10.20	38.50
Loam Brash	1	0.323118	0.000176	31.76	500	9.95	0.18	0.52	0.10	7.34	43.80
	2	0.323118	0.000709	31.76	500	9.95	0.18	0.52	0.03	7.34	43.80
	3	0.336956	0.000232	23.43	500	18.55	0.18	0.52	0.01	7.34	34.00
	4	0.500674	0.001019	11.48	500	7.81	0.05	0.90	0.00	1.02	14.40
Clay Silt	1	0.332799	0.000440	38.93	500	45.64	0.15	0.10	0.04	7.65	52.50
	2	0.332799	0.000121	38.93	500	45.64	0.15	0.10	0.02	7.65	52.50
	3	0.306004	0.000209	30.23	500	71.49	0.20	0.10	0.01	10.20	44.50
	4	0.300671	0.000160	27.68	500	85.52	0.20	0.10	0.00	10.20	41.50
Silt Loam	1	0.315783	0.000301	31.93	500	48.96	0.20	0.20	0.05	10.20	46.50
	2	0.315783	0.000185	31.93	500	48.96	0.20	0.20	0.01	10.20	46.50
	3	0.188196	0.000080	20.36	500	137.65	0.35	0.10	0.00	17.85	39.60
	4	0.308305	0.000142	23.42	500	75.57	0.20	0.20	0.00	9.18	35.60
Loam	1	0.261708	0.000261	28.55	500	38.21	0.30	0.30	0.03	15.30	47.00
	2	0.261708	0.000398	28.55	500	38.21	0.30	0.30	0.01	15.30	47.00
	3	0.254739	0.000184	27.28	500	70.34	0.30	0.15	0.01	15.30	45.50
	4	0.202472	0.000102	22.40	500	114.21	0.35	0.10	0.01	17.85	42.00
Clay	1	0.183315	0.000404	32.45	500	24.74	0.60	0.20	0.10	30.60	65.00
	2	0.152039	0.000457	23.53	500	61.68	0.60	0.20	0.03	30.60	54.50
	3	0.128776	0.000060	20.40	500	83.55	0.60	0.20	0.00	30.60	51.00
	4	0.128776	0.000060	20.40	500	83.55	0.60	0.20	0.00	30.60	51.00
Marsh	1	0.180000	0.001160	75.60	300	40.00	0.01	0.01	0.97	1.00	76.60
	2	0.180000	0.001160	75.60	300	40.00	0.01	0.01	0.97	1.00	76.60
	3	0.180000	0.001160	75.60	300	40.00	0.01	0.01	0.97	1.00	76.60
	4	0.302124	0.000115	37.25	300	37.74	0.25	0.15	0.01	12.75	55.00
Leptosols	1	0.281064	0.000195	31.77	800	18.10	0.30	0.30	0.10	12.24	48.10
	2	0.334324	0.000169	7.29	800	21.27	0.17	0.38	0.03	1.73	10.10
	3	0.425566	0.000141	5.53	800	16.61	0.10	0.65	0.00	1.02	7.40
	4	-	-	-	-	-	-	-	-	-	-

*L* = Soil Layer

*GWL* = Ground water level [m]

*P* = Permeability [cm/sec]

*EPV* = Effective pore volume [%]

*PDI* = Pore size distribution index [-]

*BPH* = Bubbling pressure head [-]

*CC* = Clay content [ $m^3/m^3$ ]

*SC* = Sand content [ $m^3/m^3$ ]

*OM* = Organic matter [ $m^3/m^3$ ]

*RWC* = Retention water content [%]

*CPV* = Cumulative pore volume [%]



## A.10 Acre File of the Wheat Test Site “Hofanger” Season 2004

### General Information

Size:	14.44 ha
Preceding Crops:	2001: Triticale 2002: Summer Barley 2003: Rape

### Cultivation Information

Sowing Date	15.10.2003
Cultivar:	Wheat Achat (Elite-Wheat)
Sowing Quantity:	Average: 1.20 dt/ha Total: 17.33 dt
TKG:	47.00 g
Sowing Density:	248 Seeds per m <sup>2</sup>
Germination Capacity:	97 %
Row Distance:	12 cm
Harvestdate:	22.08.2004
Total amount harvested:	1427.00 dt
Average Yield:	98.82 dt/ha

### Operation of Machines

Date	Action	Total Time [h]	hours/ha
22.07.2003	Stubble Processing	3.62	0.25
19.08.2003	Pest Management	1.97	0.14
04.09.2003	Stubble Processing	6.00	0.42
15.10.2003	Sowing	22.00	1.52
17.10.2003	Rolling	6.00	0.42
29.10.2003	Pest Management	2.15	0.15
12.03.2004	Manuring	1.23	0.09
03.04.2004	Manuring	1.54	0.11
15.04.2004	Pest Management	2.09	0.14
29.04.2004	Pest Management	1.73	0.12
30.04.2004	Manuring	1.38	0.10
18.05.2004	Pest Management	1.93	0.13
20.05.2004	Manuring	1.36	0.13
30.05.2004	Manuring	1.21	0.08
06.06.2004	Pest Management	2.36	0.16
11.06.2004	Manuring	2.06	0.14
15.06.2004	Pest Management	1.45	0.18
23.06.2004	Pest Management	2.35	0.16
22.08.2004	Harvest	10.00	0.69

### Application of Pesticides [dt]

Date	Type	Total Amount	/ha	BBCH
19.08.2003	Round Up Turbo	39.00	2.70	
29.10.2003	Schneckenkorn	45.92	3.18	05
	Fenikan	15.31	1.06	05
15.04.2004	Starane	7.36	0.51	25
	CCC	14.73	1.02	25
29.04.2004	CCC	5.92	0.41	30
18.05.2004	Input Set	5.92	0.41	32
06.06.2004	Twist	3.03	0.21	39
	Input Set	7.51	0.52	39
	Camposan	4.48	0.31	39
	Karate Zeon	1.16	0.08	39
15.06.2004	Starane	2.90	0.36	
23.06.2004	Twist	2.17	0.15	65
23.06.2004	Rogor	7.51	0.52	65
	Input Set	8.95	0.62	65

### Application of Fertilizers [dt]

Date	Type	Total Amount	/ha	N	BBCH
12.03.2004	AHL	16.66	1.15	42	VB
03.04.2004	Patentkali	18.88	1.31		
15.04.2004	AHL	4.12	0.29	10	25
29.04.2004	Natrel	16.17	1.12		30
	AHL	4.12	0.29	10	30
30.04.2004	AHL	21.08	1.46	53	30
20.05.2004	AHL	2.78	0.26	9	32
	Natrel	14.94	1.40		32
	Bittersalz	99.23	9.30		32
30.05.2004	Plammon	20.65	1.43	47	37
06.06.2004	Bor	2.02	0.14		39
	Bittersalz	150.18	10.40		39
11.06.2004	AHL	23.15	1.60	58	51

### Nutrition Balance [kg ha<sup>-1</sup>]

	N	P <sub>2</sub> O <sub>5</sub>	K <sub>2</sub> O	MgO	CaO
	Nitrate	Diphosphorpentoxide	Potassium	Magnesium	Calcium
Demand:	237.2	79.1	59.3	19.8	59.3
Input:	226.5	0.0	39.2	13.1	-179.3
Balance:	-10.7	-79.1	-20.1	-6.7	-238.6

## A.11 Acre File of the Wheat Test Site “Kochfeld” Season 2005

### General Information

Size:	8.41 ha
Preceding Crops:	2002: Triticale 2003: Summer Barley 2004: Rape

### Cultivation Information

Sowing Date	15.10.2004
Cultivar:	Wheat Achat (Elite-Wheat)
Sowing Quantity:	Average: 1.28 dt/ha Total: 10.76 dt
TKG:	50.00 g
Sowing Density:	251 Seeds per m <sup>2</sup>
Germination Capacity:	98 %
Row Distance:	12 cm
Harvestdate:	19.08.2005
Total amount harvested:	605 dt
Average Yield:	71.94 dt/ha

### Operation of Machines

Date	Action	Total Time [h]	hours/ha
18.08.2004	Stubble Processing	3,36	0.40
13.09.2004	Pest Management	1.10	0.13
15.10.2004	Sowing	11,55	1.37
04.11.2004	Pest Management	1,25	0.15
22.03.2005	Manuring	3,25	0.39
24.03.2005	Manuring	0,70	0.08
04.04.2005	Rolling	3,35	0.42
16.04.2005	Pest Management	0,98	0.12
13.05.2005	Pest Management	1,20	0.14
14.05.2005	Manuring	0,98	0.12
30.05.2005	Manuring	0,75	0.09
31.05.2005	Pest Management	1,24	0.15
10.06.2005	Manuring	1,08	0.13
30.06.2005	Pest Management	1,30	0.15
19.08.2005	Harvest	4,00	0.97

### Application of Pesticides [dt]

Date	Type	Total Amount	/ha	BBCH
13.09.2004	Round Up Turbo	22,12	2,63	
04.11.2004	Schneckenkorn	26,24	3,12	11
	Fenikan	8,75	1,04	11
16.04.2005	CCC	8,45	1,00	25
13.05.2005	Impulse	3,34	0,41	32
	CCC	4,29	0,51	32
31.05.2005	Flamenco FS	8,57	1,02	32
	Starane XL	8,57	1,02	39
	Camposan	1,71	0,20	39
	Twist	1,71	0,20	39
	Input Set	5,13	0,61	39
	Fury	0,86	0,10	39
30.06.2005	Input Set	5,59	0,66	69
	Rogor	4,64	0,55	69

### Application of Fertilizers [dt]

Date	Type	Total Amount	/ha	N	BBCH
22.03.2005	Patentkali	10,93	1,30		
24.03.2005	AHL	8,90	1,08	38	VB
16.04.2005	AHL	1,18	0,14	5	25
13.05.2005	AHL	0,84	0,10	4	32
14.05.2005	Zinksulfat	8,82	1,05		32
	AHL	17,62	2,09	75	32
30.05.2005	Piammon	13,77	1,64	54	37
31.05.2005	Bittersalz	42,41	5,04		39
31.05.2005	Bor	0,86	0,10		39
10.06.2005	AHL	12,93	1,54	55	51

### Nutrition Balance [kg ha<sup>-1</sup>]

	N	P <sub>2</sub> O <sub>5</sub>	K <sub>2</sub> O	MgO	CaO
	Nitrate	Diphosphorpentoxide	Potassium	Magnesium	Calcium
Demand:	172.7	57.6	43.2	14.4	-43.2
Input:	231.5	0.0	39.0	13.0	-177.5
Balance:	58.9	-57.6	-4.2	-1.4	-220.7

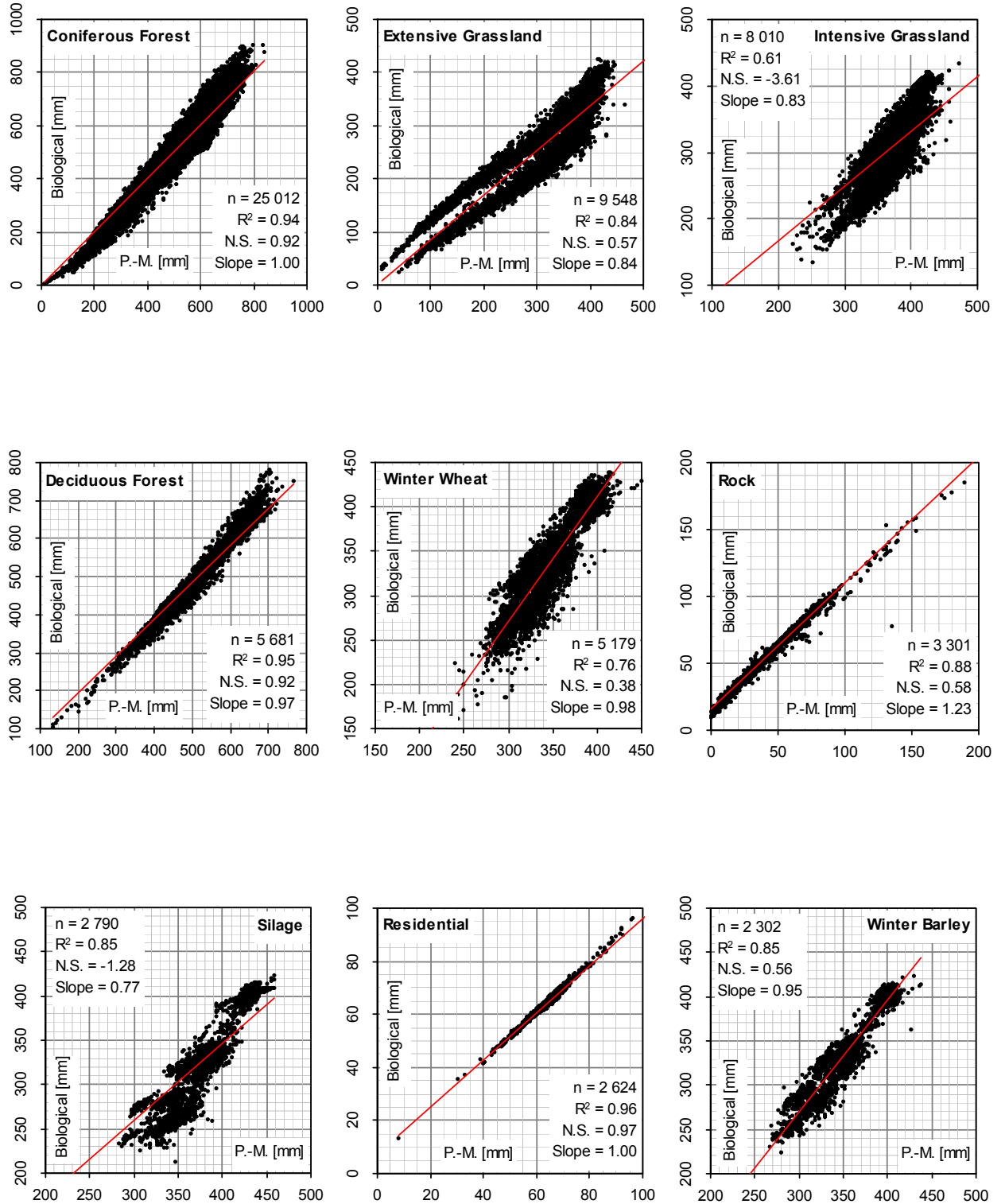
## A.12 Available Historic Test Sites

Coordinates (Gauß – Krueger)					
Longitude	Latitude	Altitude	Name	Crop	Sampling Season
44°42'33.9"	53°18'28.0"	656	"Frieding Meister 1"	Maize	1999
44°42'35.9"	53°18'22.0"	656	"Frieding Meister 2"	Maize	1999
44°41'41.6"	53°16'71.3"	675	"Frieding"	Maize	1999
44°47'61.0"	53°26'28.3"	590	"Mitterwies"	Maize	1999
44°48'09.9"	53°25'36.5"	594	"Unterbrunn"	Maize	1999
44°46'23.3"	53°29'39.4"	570	"St. Gilgen"	Oat	1999
44°41'51.5"	53°16'90.9"	672	"Frieding Weizen"	Winterwheat	1999
44°48'54.7"	53°28'43.7"	572	"Hüll"	Winterwheat	1999
44°47'60.3"	53°26'42.1"	590	"Mitterwies Weizen"	Winterwheat	1999
44°46'51.4"	53°26'13.0"	593	"Brunner"	Maize	2000
44°37'80.4"	53°27'00.5"	570	"Inning Mais 1"	Maize	2000
44°37'63.4"	53°26'92.5"	566	"Inning Mais 2"	Maize	2000
44°47'03.9"	53°25'84.0"	595	"Brunner Capo"	Winterwheat	2000
44°48'81.4"	53°28'65.5"	571	"Hüll Capo"	Winterwheat	2000
44°49'88.9"	53°28'44.0"	590	"Stürzer Bussard"	Winterwheat	2000
44°49'95.4"	53°28'50.5"	591	"Stürzer Capo"	Winterwheat	2000
44°49'11.9"	53°26'35.5"	595	"Schlaubfeld"	Extensive Grassland	2001
44°46'18.9"	53°26'55.5"	592	"DLR"	Maize	2001
44°46'63.4"	53°23'46.5"	616	"Tiefenbrunn"	Maize	2001
44°48'05.9"	53°25'57.4"	593	"Unterbrunn"	Maize	2001
44°46'30.4"	53°26'70.0"	588	"DLR Weizen"	Winterwheat	2001
44°48'95.9"	53°28'25.0"	573	"Hüll Weizen"	Winterwheat	2001
44°48'12.9"	53°25'90.0"	591	"Mitterwies Weizen"	Winterwheat	2001
44°45'87.4"	53°28'99.5"	571	"St. Gilgen Weizen"	Winterwheat	2001
44°49'77.4"	53°28'87.0"	584	"Stürzer Weizen"	Winterwheat	2001
44°48'09.9"	53°25'36.5"	594	"Unterbrunn Bussard"	Winterwheat	2001
44°48'15.8"	53°25'66.9"	593	"Unterbrunn Wiese"	Intensive Grassland	1999, 2000
44°49'15.4"	53°26'24.0"	593	"Schlaubfeld Weizen"	Winterwheat	2000, 2001
44°38'27.3"	53°27'59.6"	577	"Inning 2"	Extensive Grassland	1999, 2000, 2001
44°46'31.3"	53°29'37.7"	570	"St. Gilgen Wiese"	Extensive Grassland	1999, 2000, 2001
44°38'17.4"	53°27'69.1"	568	"Inning 1"	Intensive Grassland	1999, 2000, 2001

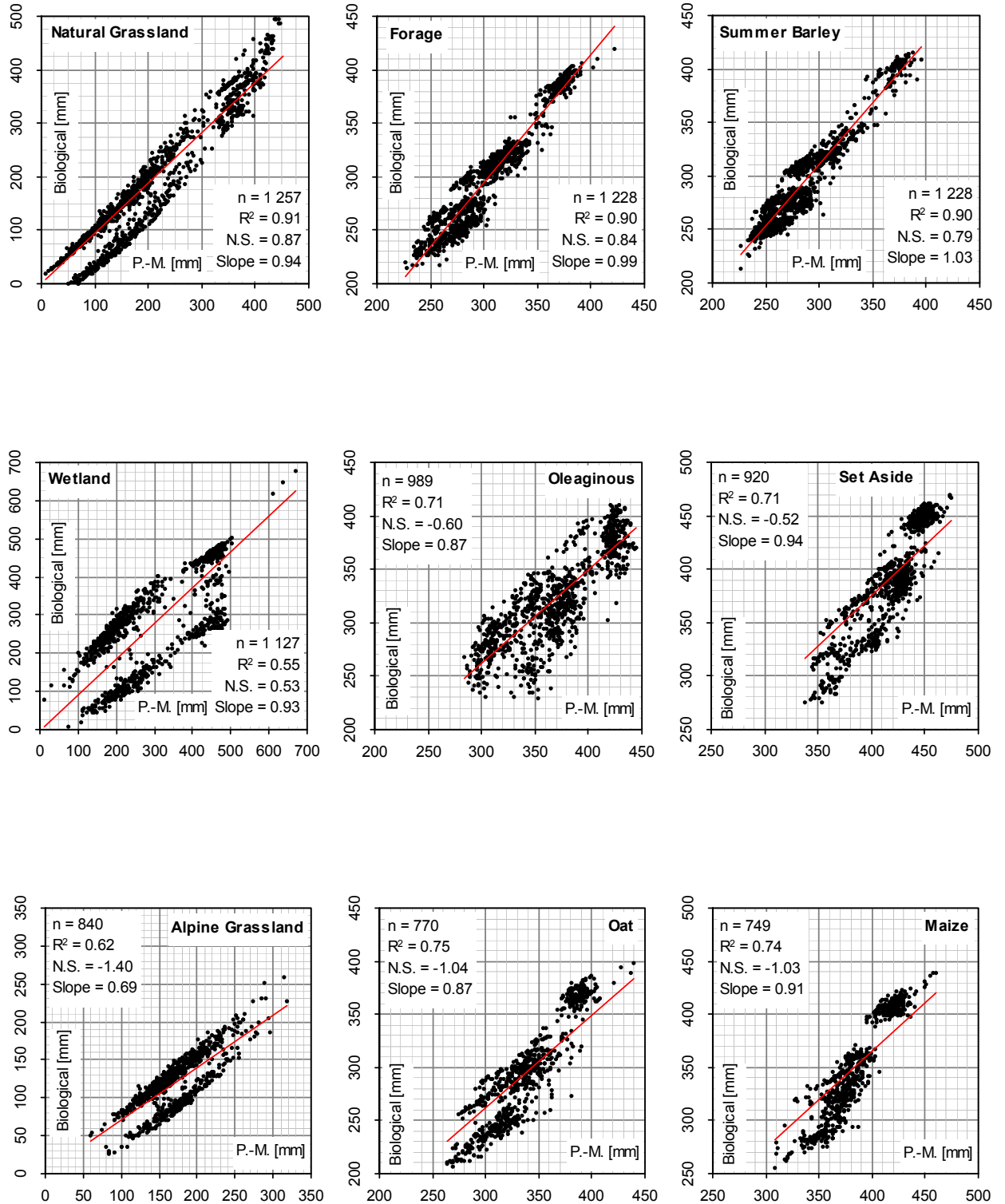
## A.13 List of Selected Reference Proxels

Area Rank	Landuse Type	GIS Row	GIS Column	Altitude
1	Coniferous Forest	224	285	552
2	Extensive Grassland	203	325	458
3	Intensive Grassland	161	289	457
4	Deciduous Forest	160	238	375
5	Winter Wheat	136	318	352
6	Rock	122	242	407
7	Silage	205	187	493
8	Residential	221	260	534
9	Winter Barley	181	272	507
10	Natural Grassland	100	283	438
11	Forage	207	251	496
12	Summer Barley	211	242	514
13	Wetland	135	243	413
14	Oleaginous	179	160	488
15	Set Aside	151	264	381
16	Alpine	350	241	2096
17	Oat	180	164	467
18	Maize	180	266	508
19	Water	240	228	553
20	Glacier	299	373	2676
21	Sugar	179	176	445
22	Industrial	199	275	466
23	Potato	164	236	396
24	Rye	167	231	402
25	Hop	171	266	459
26	Summer Wheat	208	273	493
27	Legumes	183	230	453

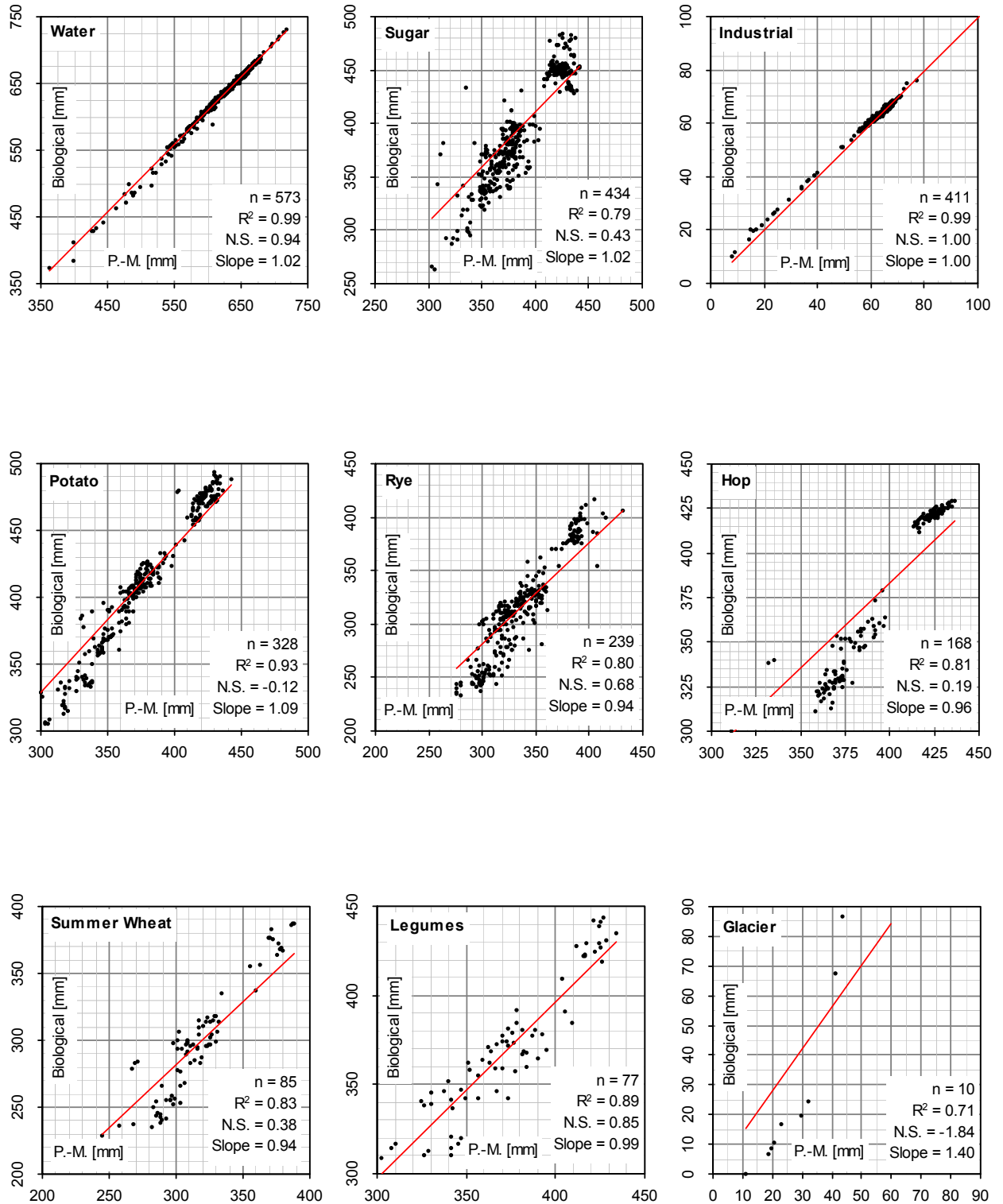
## A.14 Long-Term Annual Evapotranspiration (PROMET\_Biological vs. PROMET\_Penman-Monteith)



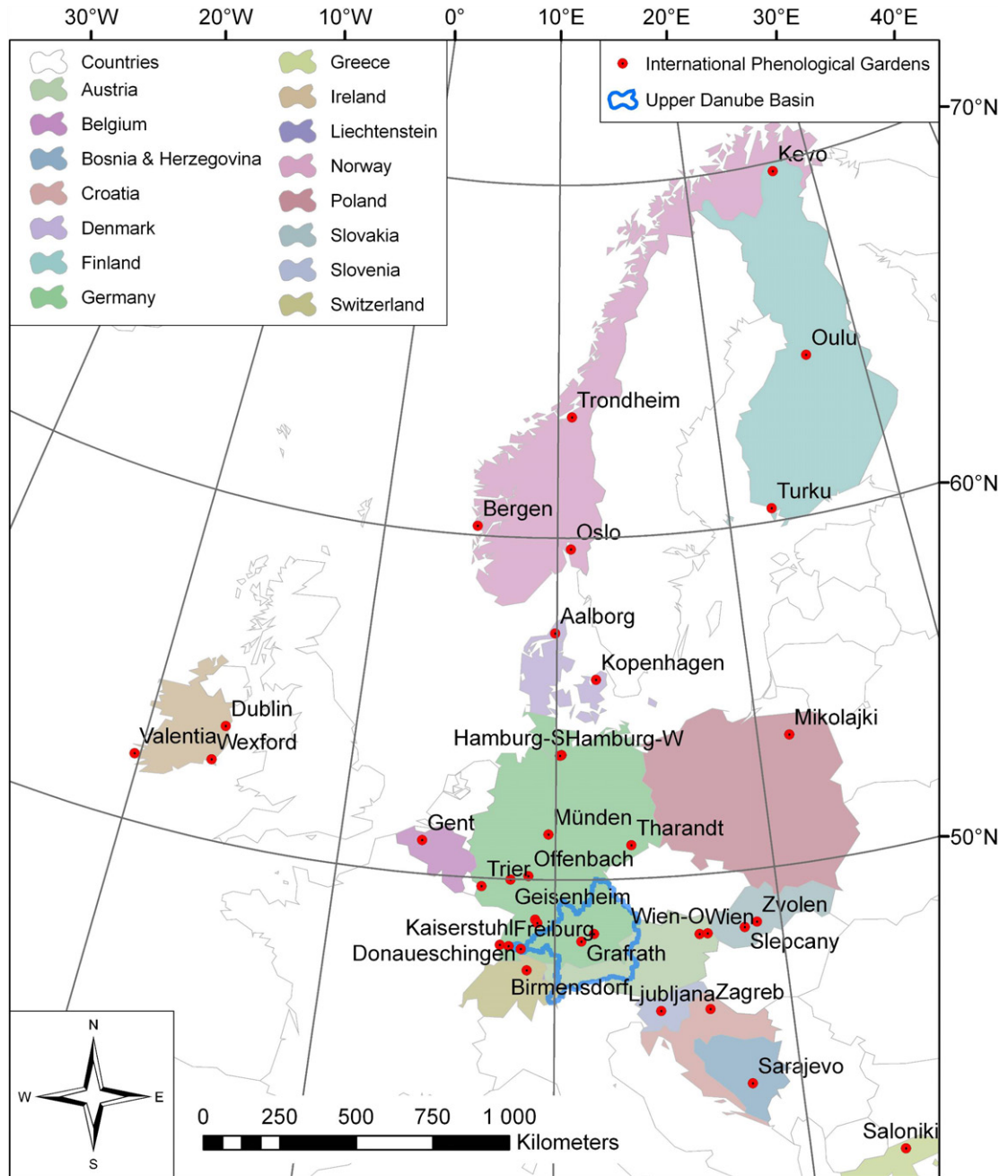
## Long-Term Annual Evapotranspiration (continued)



## Long-Term Annual Evapotranspiration (continued)



### A.15 Selected International Phenological Gardens of Europe



Base data: European borderlines (ESRI World database), locations of the IPGs after MENZEL (1997).



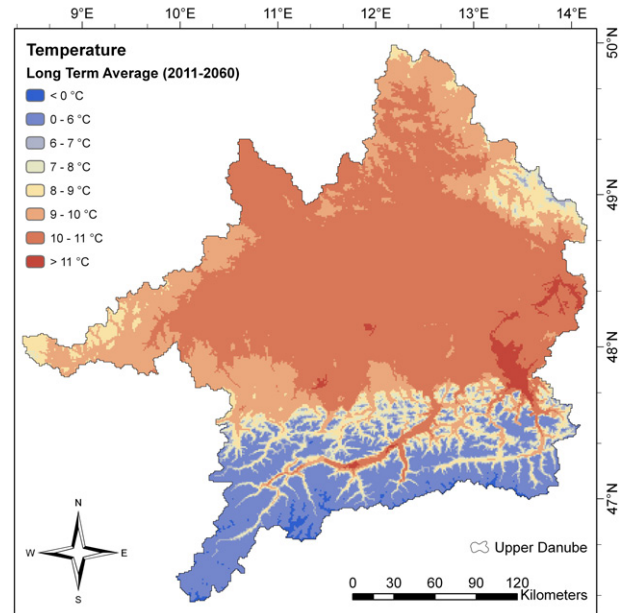
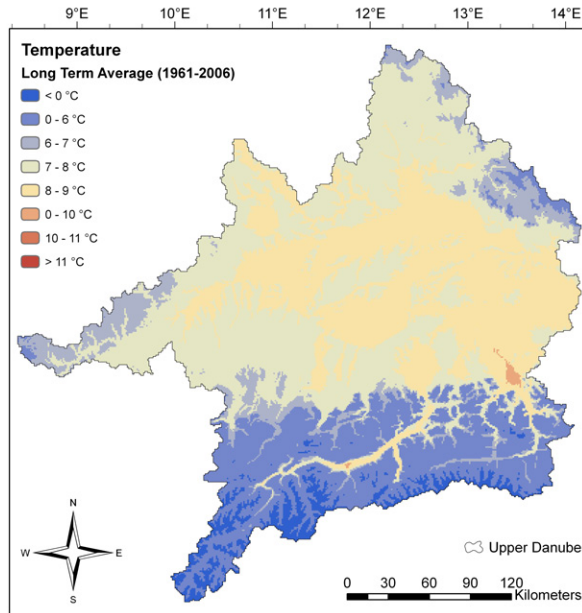
## A.16 Long-Term Records of Phenological Phases in Europe

Phenological Phase:				Leaf Emergence		May Shoot		Defoliation							
Int. Phen. Garden	Latitude	Longitude	Altitude	Beech		Spruce		Grey Poplar	Basswood	Locust	Sagewillow	Birch	Kueblenwillow	Larch	
				early	middle	late	early								middle
Common Name:				Fagus sylvatica		Picea abies									
Latin Name:															
06 Kevo	69.75°N	27.00°E	180m a.s.l.				187								
07 Oulu	64.52°N	26.45°E	115m a.s.l.			154	156					300		307	
01 Trondheim	63.48°N	10.88°E	025m a.s.l.	139		142	149							314	
08 Turku	60.38°N	22.55°E	010m a.s.l.			149	151								
02 Bergen	60.27°N	05.35°E	050m a.s.l.	132	136	139	143								
03 Oslo	59.67°N	10.78°E	095m a.s.l.			143	146					309		314	
12 Aalborg	57.23°N	09.92°E	020m a.s.l.			134	142								
09 Kopenhagen-T.	55.87°N	12.05°E	040m a.s.l.			131	139								
44 Mikolajki	53.78°N	21.58°E	127m a.s.l.			132	135								
21 Hamburg-S.	53.67°N	10.27°E	050m a.s.l.			122	136							320	
22 Hamburg-W.	53.65°N	10.20°E	046m a.s.l.	128		126						301		300	
16 Dublin	53.38°N	06.33°W	030m a.s.l.			120	126					300		326	
14 Wexford-J.F.	52.33°N	06.63°W	080m a.s.l.	118		128	123					294		294	
13 Valentia	51.93°N	10.25°W	014m a.s.l.	113	123	130	108					307		307	
23 Hann.Münden	51.33°N	09.67°E	500m a.s.l.	127	133	133	131					307		324	
18 Gent	50.98°N	03.80°E	015m a.s.l.	121		124	117					296	304		
42 Tharandt	50.98°N	13.53°E	360m a.s.l.	122	127	128	127		294	297	303	302			
24 Offenbach	50.10°N	08.78°E	099m a.s.l.	120		124	120		302	307	300				
25 Geisenheim	49.98°N	07.97°E	109m a.s.l.										311		
26 Trier	49.75°N	06.67°E	265m a.s.l.									299		315	
28 Stuttgart-W.	48.82°N	09.12°E	330m a.s.l.	119	124		115		272	293	305	313			
27 Stuttgart-H.	48.72°N	09.22°E	380m a.s.l.						304	307		308			
52 Zvolen	48.45°N	18.93°E	540m a.s.l.	119	125	126	125		306			304		310	
37 Weißenstefan	48.40°N	11.73°E	460m a.s.l.	126			138			309		307			
51 Slepčany	48.33°N	18.37°E	180m a.s.l.	117	118	120	121					303			
49 Wien	48.25°N	16.37°E	202m a.s.l.				114				300				
50 Wien-O.	48.25°N	16.72°E	150m a.s.l.	116	116		114		300	296					
36 Grafrath	48.18°N	11.17°E	540m a.s.l.	119			125					299		325	
30 Kaiserstuhl-L.	48.05°N	07.60°E	285m a.s.l.				132					312		318	
32 Freiburg	48.02°N	07.96°E	500m a.s.l.	124			124					290			
35 Donaueschingen	47.95°N	08.52°E	680m a.s.l.				150								
46 Birmensdorf	47.33°N	08.80°E	569m a.s.l.	120		128	119					305		325	
55 Ljubljana	46.07°N	14.50°E	310m a.s.l.	116	123		112					294		294	
56 Zagreb	46.03°N	16.57°E	146m a.s.l.	112	118	120	111		301			298		307	
65 Sarajevo	43.75°N	18.02°E	1000m a.s.l.	139			133				295	302			
65 Saloniki	41.25°N	23.62°E	1550m a.s.l.				144								
<b>Southern Germany (Avg. of I.P.G.s 26, 27, 28, 36, 37, 42)</b>				<b>122</b>	<b>125</b>	<b>128</b>	<b>125</b>	<b>131</b>	<b>288</b>	<b>290</b>	<b>303</b>	<b>304</b>	<b>305</b>	<b>308</b>	<b>319</b>

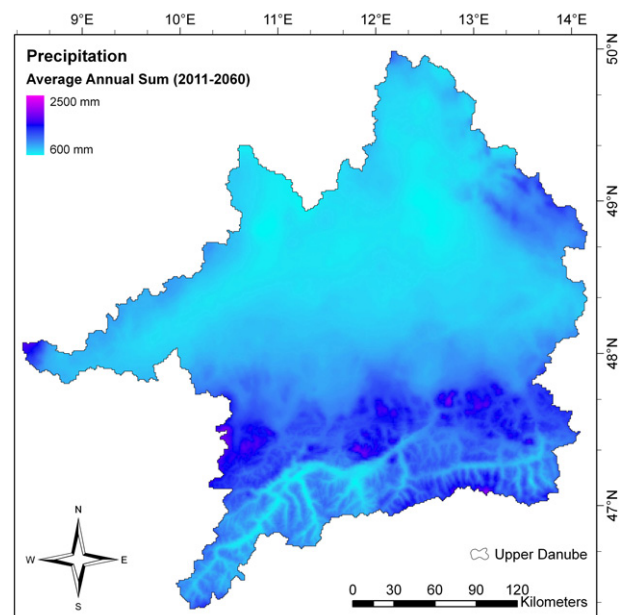
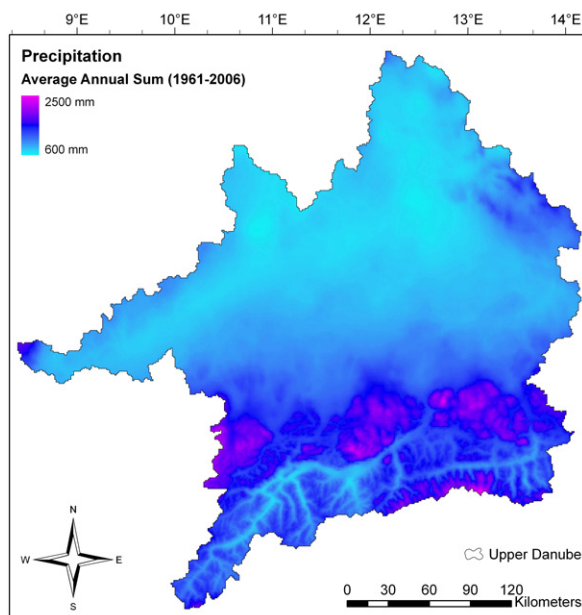
Long-Term (&gt; 30 years) average of the incidence of phenological stages of trees, recorded at International Phenological Gardens across Europe (MENZEL 1997).

## A.17 Reference and Scenario Period – Selected Model Results

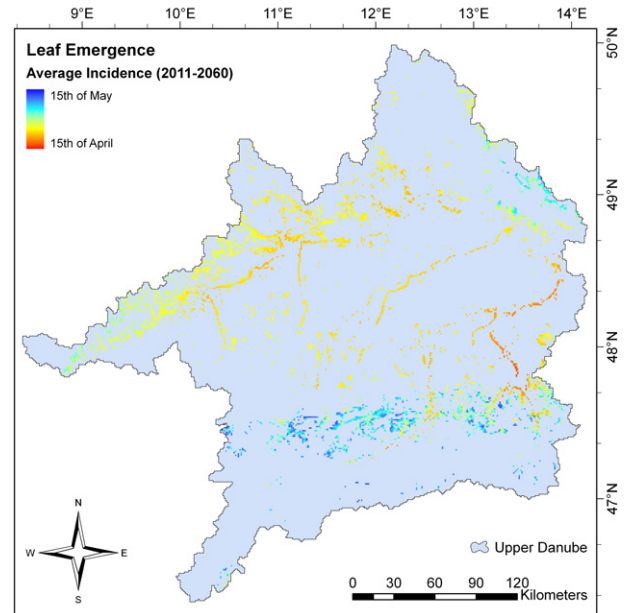
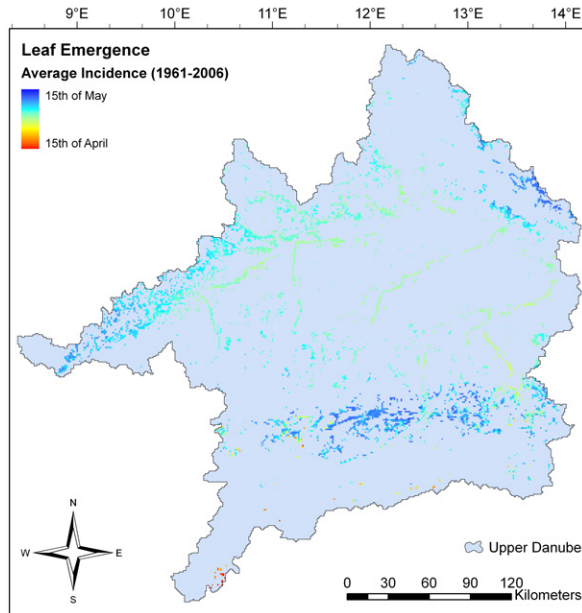
### A.17.1 Annual Mean Temperature



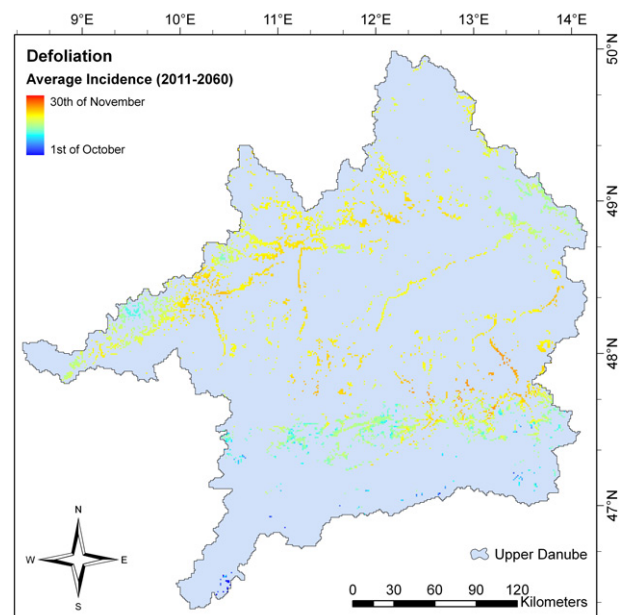
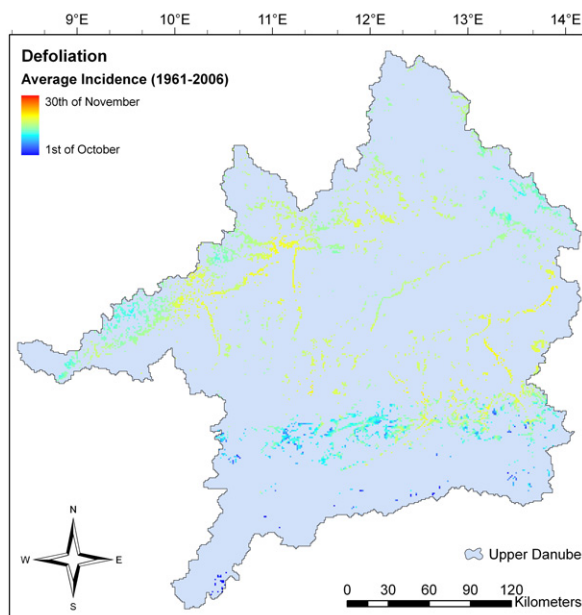
### A.17.2 Annual Sum of Precipitation



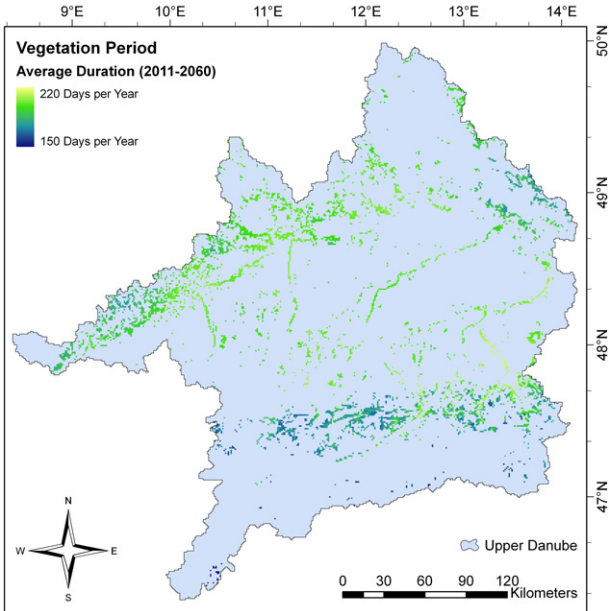
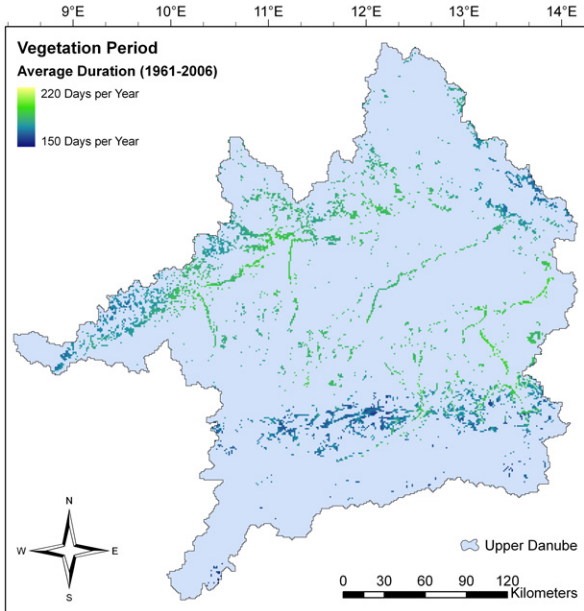
### A.17.3 Leaf Emergence of Deciduous Forest



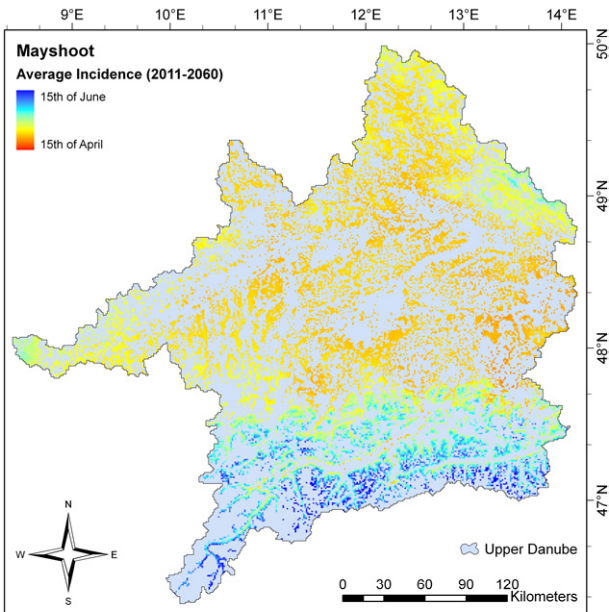
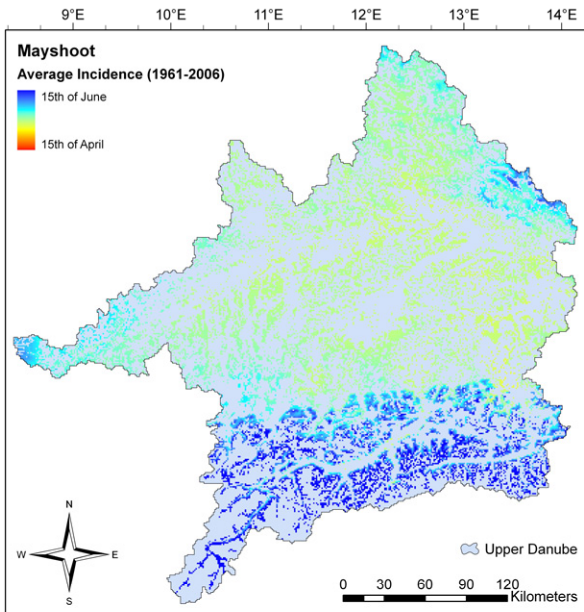
### A.17.4 Defoliation of Deciduous Forest



### A.17.5 Vegetation Period of Deciduous Trees

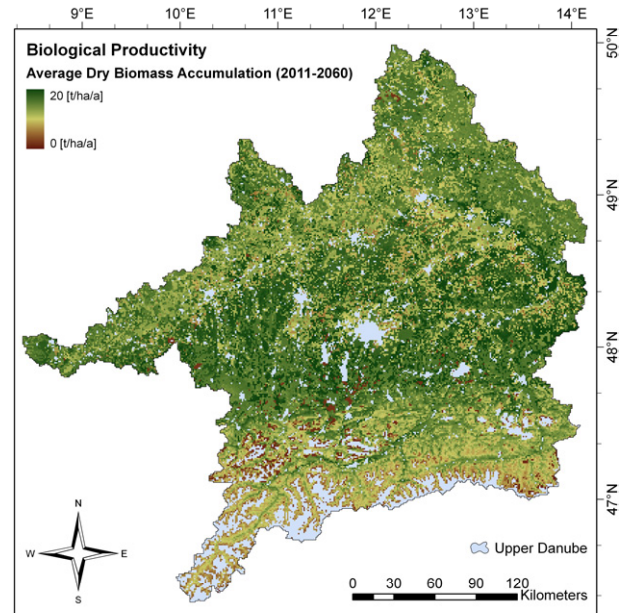
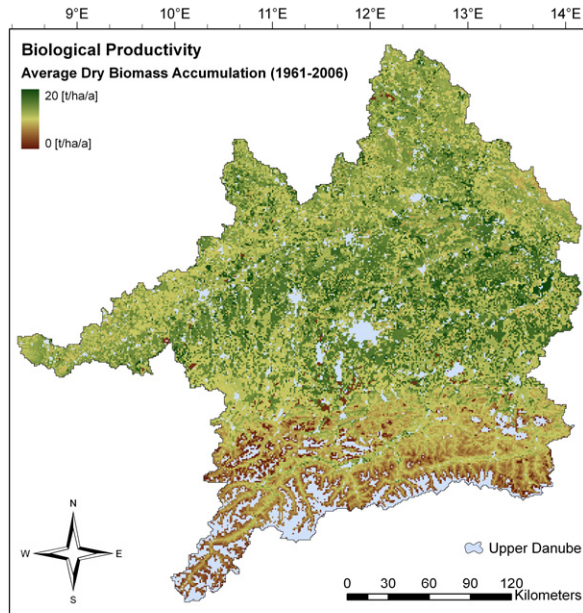


### A.17.6 Mayshoot of Coniferous Forest

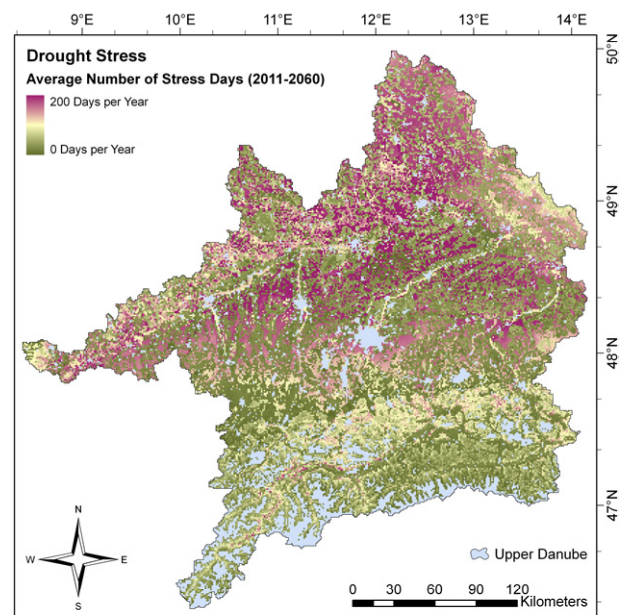
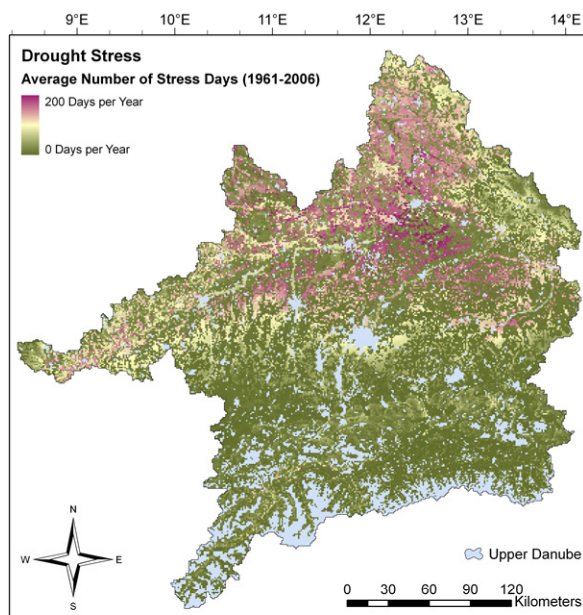




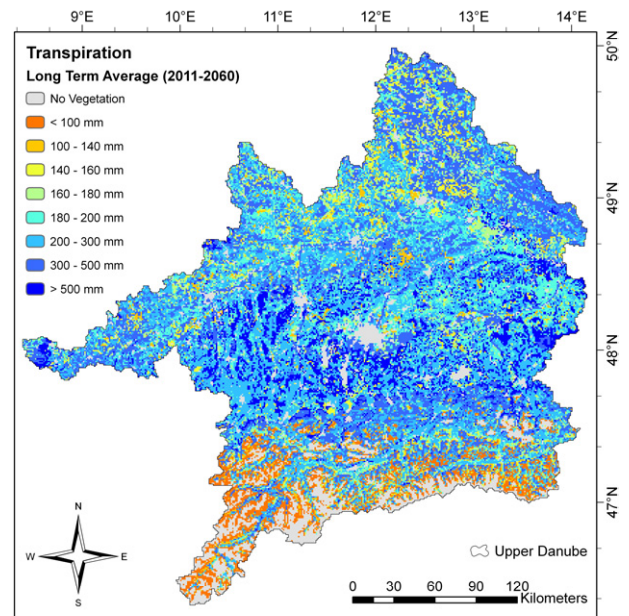
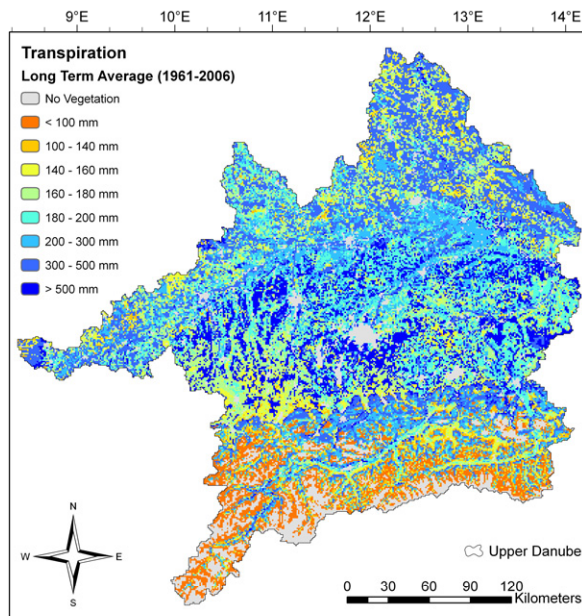
### A.17.7 Biological Productivity



### A.17.8 Drought Stress



### A.17.9 Transpiration



### A.17.10 Evapotranspiration

